THE CITY UNIVERSITY
Northampton Square London EC1V 0HB
Department of Electrical and Electronic Engineering

A STUDY OF A LINEAR INDUCTION MOTOR USING ALTERNATIVE MODELS

by

Moayed Abdullah Al-Maayouf, M.Sc.(Eng.)

A Thesis presented in The City University for the Degree of Doctor of Philosophy in Engineering.

December 1981

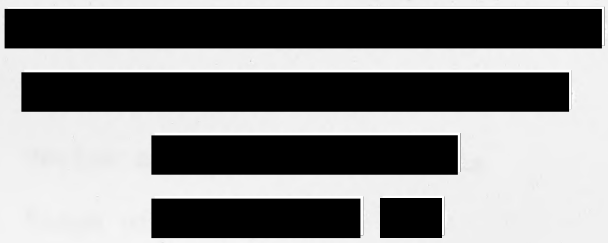

CONTENTS

ACKNOWLEDGEMENTS

The author would like to express his gratitude to Professor A.J. Ellison, Head of the Department of Electrical and Electronic Engineering at The City University, for his interest in the research, and for the use of the facilities of the Department. The author is much indebted to Mr. J. van Bueren for supervising this research and for his considerable interest and encouragement throughout the course of the research.

The author is also indebted to many friends and members of the Department of Electrical and Electronic Engineering and of the Department of Mechanical Engineering, especially to [redacted] for helpful discussions and advice.

Thanks are also due to the late [redacted] (former Superintendent) for his encouragement and useful comments during the construction of the test rig.

For their indespensible contributions and sincere assistance in the laboratory, thanks are due to [redacted] of the Central and Departmental Workshops, to [redacted] of the Electrical Machine Laboratory and to [redacted] of the Photographic Room.

The help of the staff of the Computer Centre of The City University has been of considerable value in the work. Special gratitude is due to [redacted].

The author is much indebted to [redacted] for typing the manuscript with interest and care, and gratitude is extended the the secretarial staff of the Department.

Thanks are finally due to the Ministry of Higher Education and Scientific Research of the Republic of Iraq for their generous support which enabled the author to carry out the work.

ABSTRACT

This thesis is concerned with the prediction and study of the performance characteristics of a single-sided linear induction motor both theoretically and experimentally.

In the work described here a field solution is investigated using one-, two- and three-dimensional analyses. In each of these analyses two models for the linear induction motor are studied which differ in the way of representing the primary windings.

The primary winding of the first model is represented by a current sheet which covers the teeth-slots and overhang zones, and the stator iron is extended up to the ends of the overhang winding. In the second model, the primary winding over the teeth-slots is represented by a homogenous anisotropic conductor of finite thickness which exhibits different permeabilities in directions parallel with and perpendicular to the airgap. The overhang winding is represented by a normal homogenous isotropic mass. The stator iron in this model extends only over its actual width. This model makes possible an adequate consideration of slot leakage.

In these analyses, numerical solutions describing the magnetic vector potential are obtained by the finite difference method using a successive over-relaxation iterative technique.

The three-dimensional analytical models take account of the boundaries and discontinuties in all three directions of the linear induction motor. Special studies on the boundaries of these models and their line- and dot-corners are made.

In these models, linear induction motors with and without backing iron are examined for different speeds up to 282 Km/h.

In order to verify the validity of the theoretical results of the motor without backing iron, a test rig is designed and constructed. Both theoretical and experimental results are shown for comparison purposes.

A new pole-by-pole equivalent circuit of the linear induction motor is presented. It is based on a one-dimensional analysis and takes account of longitudinal end effects. A comparison of the predicted performance is made between the equivalent circuit and the field solution of the linear induction motor with backing iron.

The state variables of the performance presented in this thesis include the forces, power, power factor, efficiency, flux and flux density distribution and a terminal voltage which is calculated numerically for each of the three phases.

Other aspects investigated are the effects of changing the topology of the machine, the use of a composite rail, the parameters affecting the significance of end effects and constant current and constant voltage drives.

LIST OF SYMBOLS

The symbols repeatedly used are listed below. Other symbols are explained in the text.

Unless otherwise stated, all quantities are expressed in rationalized m.k.s.

$\overline{A}$	:	Magnetic vector potential, Wb/m
Ax, Ay, Az	:	x,y, and z components of magnetic vector potential, Wb/m
$\overline{B}$	:	Magnetic flux density vector, Wb/m^2
B_x, B_y, B_z	:	x, y and z components of magnetic flux density, Wb/m^2
B_s	:	Steady state component of magnetic flux density in airgap, Wb/m^2
B_l	:	Entry-end effect component of magnetic flux density in airgap, Wb/m^2
C1, C2, ... C11	:	Constants and factors used in Chapter Six
d	:	Secondary conductor thickness, m
$\overline{E}$	:	Electric field intensity vector, V/m
E_x, E_z	:	x and z components of electric field intensity, V/m
E_i	:	Induced electromotive force in pole pitch i, V
E_l	:	Induced electromotive force in primary winding, V
$\overline{F}$	:	Force vector, N
F_x, F_y, F_z	:	x, y and z components of force vector, N
$\overline{f}$	:	Force density vector, N/m^3
f_x, f_y, f_z	:	x, y and z components of force density vector, N/m^3
f_{ya}	:	Attraction force density in y direction, N/m^2

f	:	Supply frequency, Hz
G	:	Goodness factor
g	:	Effective airgap length, m
$\overline{H}$	:	Magnetic field strength vector, A/m
H_x, H_z	:	x and z components of the magnetic field strength, A/m
h	:	Stator width, Mesh size, m
I	:	RMS value of phase current, A
I_1	:	RMS of the primary current, A
I_2	:	RMS of the Secondary current, A
I_m	:	RMS of the magnetizing current, A
$\overline{J}$	:	Current density vector, A/m^2
Jx, Jz	:	x and z components of the current density vector, A/m^2
$\overline{Ja}$	:	Active zone current density vector, A/m^2
$\overline{Jo}$	:	Overhang current density vector, A/m^2
J_s	:	Secondary current density, A/m^2
j	:	$\sqrt{-1}$
$\overline{K}$	:	Line current density vector, A/m
Kx, Kz	:	x and z components of the line current density vector, A/m
k	:	Wavelength factor, rad/m
K_a	:	Modules of the line current density over the active zone, A/m
K_o	:	Modules of the line current density over the overhang zone, A/m
k_1	:	Wavelength factor of the entry end wave, rad/m.
K_t	:	Coefficient of the transverse edge effect
K_s	:	Coefficient of the skin effect
K_p, K_b	:	Pitch and breadth factors of the primary winding
i,j,k	:	Labels of the node on y, x and z axes respectively

N	:	Number of turns per phase
Ne	:	Effective number of turns per phase
$\overline{P}$	:	Poynting vector, W/m^2
P_a	:	Airgap cross power density, W/m^2
P_i	:	Input power to the secondary, W
P_L	:	Secondary ohmic losses, W/m^3 or W
P_o	:	Output mechanical power, W/m^3 or W
P_s	:	Stator ohmic losses, W
Q_a	:	Reactive airgap cross power density, W/m^2
Q_s	:	Stator reactive power, W
q	:	Number of slots per pole per phase, mesh factor
R_L	:	Resistance representing the secondary ohmic losses, Ω
R_o	:	Resistance representing the output power, Ω
R_1	:	Primary resistance, Ω
S	:	Apparent power W
S_a	:	Airgap cross apparent power W/m^2 or W
S_s	:	Stator apparent power, W
s	:	Slip
T	:	Factor relating B_1 to B_s
t	:	time, sec.
$\overline{V}$	:	Velocity vector, m/sec
V_x	:	Velocity in x-direction, m/sec
V_s	:	Synchronous speed, m/sec
V	:	Primary voltage per phase, V
X_m	:	Magnetizing reactance, Ω
X_1	:	Primary leakage reactance, Ω
X_2	:	Secondary leakage reactance, Ω

Z_1	:	Primary impedance, Ω
x, y, z	:	Cartesian Co-ordinate
$\hat{x}$, $\hat{y}$, $\hat{z}$	:	Unit vectors in x, y and z directions respectively
α, β, γ	:	Factors used in the numerical solutions
δ	:	Slot angle
ε	:	Permitivity of the conductor, F/m, Tolerance factor
λ	:	Wavelength, m
μ_o	:	Permeability of free space, $4\pi \times 10^{-7}$ H/m
μ_r	:	Relative permeability
μ_i	:	Relative permeability of unsaturated iron
μ_x, μ_y	:	x and y components of relative permeability
ν	:	Reluctivity, $(1/\mu_o\mu_r)$
$\bar{\nu}$	:	Reluctivity vector
ν_x ν_y ν_z	:	x, y and z components of the reluctivity vector
ξ	:	Angle of the skew of the stator coil degree
ρ	:	Resistivity , Ω.m
σ	:	Conductivity S/m
σ_e	:	Effective conductivity S/m
τ	:	Pole pitch, m
ω	:	Angular velocity, rad/sec
ϕ	:	Electric scalar potential
Γ	:	Convergence factor
*	:	Complex conjugate
Re	:	Real part of
Im	:	Imaginary part of

IDENTITIES

$$\nabla\phi = \hat{x}\frac{\partial\phi}{\partial x} + \hat{y}\frac{\partial\phi}{\partial y} + \hat{z}\frac{\partial\phi}{\partial z}$$

$$\nabla.\bar{A} = \frac{\partial Ax}{\partial x} + \frac{\partial Ay}{\partial y} + \frac{\partial Az}{\partial z}$$

$$\nabla x\bar{A} = \hat{x}\left(\frac{\partial Az}{\partial y} - \frac{\partial Ay}{\partial z}\right) + \hat{y}\left(\frac{\partial Ax}{\partial z} - \frac{\partial Az}{\partial x}\right)$$

$$+ \hat{z}\left(\frac{\partial Ay}{\partial x} - \frac{\partial Ax}{\partial y}\right)$$

$$\nabla X(\nabla X\bar{A}) = \nabla(\nabla.A) - \nabla^2 A$$

∇ : 'del' operator

$$= \hat{x}\frac{\partial}{\partial x} + \hat{y}\frac{\partial}{\partial y} + \hat{z}\frac{\partial}{\partial z}$$

∇^2: Laplacian operator

$$= \frac{\partial^2}{\partial x^2} + \frac{\partial^2}{\partial y^2} + \frac{\partial^2}{\partial z^2}$$

CHAPTER 1

INTRODUCTION

1.1 Historical Introduction

It is fair to say that the invention of the linear motor dates back to the period of the initial invention of the electric rotary motors. However, the former was largely neglected at that time, while the development has concentrated on the rotary version.

The convenience of using a rotary motor may be related to its high efficiency and the simplicity of the analysis and application, coupled with the possibility of obtaining a wide variation in speed by the use of a gear box.

The increasing need for an improvement in transport systems early this century, caused a re-appraisal of the linear machines. Since then a considerable amount of effort has been put into the linear machine. In consequence, the interest has been growing in changing the topology and design of the linear machine. The various designs of the linear machine include single sided, double sided, transverse flux induction machines, synchronous and hybrid linear motors.

Therefore the application of the linear motor in high speed ground transportation (HSGT) for propulsion purposes is considered as the most important and exciting field in the studies of the linear motor from the performance characteristics and design point of view.

The first major application of the linear induction motor (LIM), in its single sided form, as a high speed drive occurred in the form of an aircraft launcher known as "Electropult" which

was built in 1945 by Westinghouse [1]. In this machine, the primary winding was carried on the vehicle, so that the whole of the energised portion of the machine could be used continuously, at the expense of supplying the moving members with power. The form of the machine used was that of a short (stator) with a (rotor) of "squirrel cage" type. The work was finally abandoned because of the high cost of this form of machine and in particular that of the secondary member.

In the fifth decade of this century, the use of a linear induction machine for propelling with "sheet-rotor" type was performed both theoretically and analytically by Laithwaite at Manchester University.[2, 3]

Recently, scientists and engineers in many countries have been working on the development of HSGT propelled by linear electric motors and magnetically suspended using advanced control technique.

The world situation regarding the development in HSGT is briefly described in the following notes:

United Kingdom;

The work on the Hovertrain was started in 1967 by Tracked Hovercraft Limited,[4] who built a 1.61 km (1 mile) experimental track at Earith near Cambridge, with the possibility of extension to 4.82 km (3 miles) with variable track-beam sections. The experimental vehicle RTV-31, driven by a single-sided linear induction motor, commenced tests along the track in the summer of 1972 and reached over 160 km/h on 1 mile of track. It was hoped to reach full design speed by extending the track to the greater length, but the U.K. Government closed down the project in February 1973 and since then the work on this level of application is

almost at a standstill.

West Germany;

The development of the magnetic suspension ground transport system is sponsored by the Federal Ministry for Research and Technology within the scope of the ground transport program. It began about 1970 and is preceeding in controlled project phases.[5]

Krauss-Maffei A.G. presented in 1969, the first electro-magnetically levitated functional model with linear propulsion, the Transrapid 01, then in 1971-1973 conducted test drives on a track of 930 m long with electromagnetically suspended vehicle Transrapid 03 (TR03). Another development is the transrapid 04 (TR04), which reached a maximum speed of about 250 km/h; in 1979 TR05 version was exhibited at the international exhibition in Hamburg, which included a control system specially developed for the machine.

In 1969 Messershmitt-Bolkow-Blohn GmbH also started developmental work and in 1971 presented the first passenger vehicle with an electromagnetic attraction suspension sub-system driven by a linear induction motor (double sided). This vehicle was tested on a 660 m long trail track at a speed of 90 km/h. In 1977 a projected vehicle (Komet) was tested. The vehicle incorporated a single-sided linear induction motor and was designed for a speed of 400 km/h. During the year of 1976/77, the working team Transrapid-EMS conducted tests with linear motors at the high speed.

Other phases of the program which will most probably last to the end of this century have already been planned such as system development, system test, system introduction and system utilization.

Japan;

The Railway Technical Research Institute of JNR, has been studying the propulsion, suspension, and guidance of superspeed trains for the last 15 years. In 1972 a ground primary linear induction motor car model was demonstrated on a test track 500 m long. The car was designed for operation at 60 km/h, and the suspension being inductive repulsion of superconducting magnet[6].

Japan Airlines has exerted a lot of effort to develop a ferromagnetically levitated vehicle system. Their fully fledged research activity on HSGT was started in 1974.[7] In 1975 the first electromagnetically levitated vehicle HSST-01 was completed, and the second vehicle HSST-02 in 1976. In February 1978, HSST-01 reached a maximum speed of 307.8 km/h on a 1300 m long test track. In April, 1978, manned test flights of HSST-02 were opened to the public and since then a total of more than 1,500 persons have participated in the tests.

The one-ton HSST-01, designed for high speed testing, is 4 m long, and incorporates eight electromagnets and a single-sided linear induction motor with a maximum thrust about 3000 N. The levitating power supply is taken from the batteries carried on board, and the 3-phase variable voltage variable frequency (vvvf) power for the LIM propulsion is supplied from wayside power lines through the power collectors.

The nine-seated HSST-02 has a loaded mass of 2-3 tons and has additional functions such as electromagnetics fitted to the flexible chassis for the better riding comfort and on-board rectification for the electromagnetic suspension enabling continuous levitation.

The design of a preoperational test vehicle of 80 seats is

now under way and its test flight is scheduled to be initiated in 1980 on a 15 km track at cruising speed of 300 km/h.

United States;

As part of the program to develop technology for HSGT, the US Federal Department of Transportation awarded a contract to the Garrelt Cooperation in March 1965 that has resulted in the building and testing of a Linear Induction Motor Research Vehicle (LIMRV).[8]

At the High Speed Ground Test Centre of the Department of Transportation near Pueblo, Colorado, two experimental vehicles have been tested. The first tested vehicle (LIMRV) carried a double-sided linear induction motor having an output rate of 1860 kw (2500 hp). It has so far reached speeds up to 300 km/h. The power of theLIM is provided by an on-board gas turbine alternator set of 2240 kw.

The second test vehicle, known as a Tracked Air-Cushion Research Vehicle (TACRV) was initially tested in late 1972. It was designed to be supported and guided by air cushion and propelled by 7480 kw (10,000 hp) double-sided linear induction motor up to a speed of 480 km/h. The combination of double-sided LIM propulsion and air-cushion suspension is now being considered as impracticable for HSGT, for reasons of safety and noise respectively.

In 1972, the Rohr Cooperation Co. in the U.S. demonstrated an experimental low speed vehicle employing an integrated magnetic suspension and propulsion system utilising a single-sided linear induction motor on a linear test track. The extension of the concept to high speeds (500 km/h) was proposed by Rohr in 1974, and attracted the attention of the U.S. Department of Transportation.

Canada;

The Department of Electrical Engineering in the University of Toronto supported by the Canadian Institute of Guided Ground Transport proposed and studied an electrodynamic suspension system for HSGT. The vehicle was suspended by making use of superconducting magnets on the vehicle edges interacting with aluminium plates on the guide way. The guiding clearance for typical vehicle of these systems are in the range of 10 to 25 cm. The 30-ton 100 passenger vehicle is propelled by a linear synchronous motor to a maximum speed of 500 km/h. The stator is a flat, three-phase winding embedded in the upper surface of the guideway between the aluminium levitation plates which are installed along the edges of the guideway.[9]

1.2 The State of the Art

The following are the most important sub-systems of the high-speed ground transportation system:

- propulsion
- suspension and guidance
- power supply
- control
- braking
- aerodynamics

Currently, special emphasis is put on the development of the propulsion as well as the suspension sub-system.

Propulsion

Generally speaking, linear electric motors have become of major interest as a propulsion method for HSGT. Initially, it was proposed in Britain that linear electric motors for traction purposes should have a double-sided configuration. At that time,

the double-sided motor was prefered to a single-sided configuration for two reasons. First, for a given weight the double-sided motor develops greater propulsion force than a single-sided machine. Secondly, the double-sided motor develops no force normal to the direction of motion. This motor is thus more convenient for a system in which the propulsion and suspension sub-systems are separated.

The proposal was almost accepted by other countries.[10] Later it was recognised that a double-sided motor straddling a vertical reaction rail posed severe safety problems which required precision installation, frequent inspection, and careful maintenance of the motor guideway. Designers then reverted to the single-sided configuration, where there are some factors favouring the single-sided linear electric motor, e.g. considerably reduced cost of the track, simplified track construction and vehicle operation, and less effect from environmental conditions. The losses due to entry and exit effects are likely to be less than those for a double-sided configuration.

Calculations and design procedures for single-sided longitudinal linear induction motors are largely confirmed by mutual comparison of different calculation methods and by comparison with measured data. However, various structural and technological problems such as cooling problems, control sub-systems, etc., have not been solved conclusively for the time being. Long-time tests for a vehicle at high speed are yet to be performed.

For high-speed applications the linear motor should be of large pole pitch and/or supplied at a high frequency. Increase of either of these has its own problems. The problem in U.K. was

investigated at its roots and considerable advancement in linear induction motor Topology followed.[11] The breakthrough came in the shape of the transverse-flux linear induction motor, in which the core flux is arranged to be in a plane perpendicular to the direction of the travelling magnetic field, instead of the plane which is parallel to the direction of travelling field as in the longitudinal linear induction motor. In a transverse-flux machine the pole-pitch can be extended without any difficulty and the thickness of the backing iron required can be kept very small.

Small transverse flux motors have been investigated experimentally[12]. They required somewhat greater reactive power than a longitudinal machine. This machine is, however, capable of providing both lift and guidance in addition to propulsion. There is a need for more detailed information on the cross-coupling between the three axis forces and the turning moments under dynamic conditions.

In principle, the linear induction motor is simple in structure since it is sufficient for the secondary member to be a conducting plate. A linear synchronous motor, on the other hand, needs two energised members or one member permanently magnetised.

The study of linear synchronous motors is concentrated first on the iron-core long-stator linear synchronous motor.[10] The need for energised coils, embedded in a laminated iron structure along the entire length of the track would be prohibitively expensive. For this reason not much attention has been paid to linear synchronous motors until recently when increasing interest was shown in cryogenic suspension sub-systems. Thus the preferred configuration

is the air-core long-stator linear synchronous motor with superconducting excitation. This type of propulsion was tested in 1979 on a scale close to practice at the Erlangen round track in West Germany.[5]

In so far as a suitable propulsion sub-system for high speed vehicles is concerned, it would appear that the final battle will be between a single-sided longitudinal linear induction motor and a single-sided longitudinal synchronous motor.

Suspension and Guidance;

In the last decade researchers in many countries have been working towards the possibility of replacing the wheel by a contact-free suspension and guiding sub-system. They tried to overcome the disadvantages of the wheel such as point load, maintenance, friction, noise, vibration and limited speed range.

The alternative to the wheel to suspend a vehicle on a track can be accomplished by one of the following means:

a) Air cushion suspension sub-system

b) Magnetic suspension sub-system

The air-cushion sub-system had been widely used in hovercraft.[10] However further studies are required to adapt and establish their performance for high-speed ground transportation. This type of suspension has been examined in the U.K. by Tracked Hovercraft Limited, in the process of developing the hovertrain. The same type of suspension has been examined by the U.S.A. and France.

The air-cushion suspension has a "natural" stability as it settles down by itself in the event of any change in the condition

of operation. However, further studies have shown some inconvenience of using this type for HSGT due to the high level of noise, low lift force/drag-force ratio, and frequent servicing and maintanence.

The magnetic suspension has been proposed as being the most advanced transportation technology to help further HSGT needs of future. [13,14] Many techniques of suspending vehicle magnetically have been studied widely in many countries, and the three basic versions are:

i. Electromagnetic support; utilizing ordinary electromagnets which are attracted toward a ferromagnetic rail lifting the vehicle. The equibrium position in such a scheme is unstable and hence requires elaborate active feedback control to maintain a constant airgap between the magnets and the track.

ii. Repulsion support with permanent magnets; the guiding track and vehicle are equipped with high-coercivity permanent magnets which are arranged with their like poles next to each other, thus providing repulsive forces. The problem in this case is in the stability and the cost of the guideway.

iii. Electrodynamic support; where the vehicle suspension is achieved by the repulsive forces which are produced by a relative movement between a magnetic field and an electric conductor. This magnetic field can be a travelling field which is generated by means of a polyphase winding in either the guideway or the vehicle. This means that the travelling field also provides a propulsion force as in the case of the linear induction motor.

The other version of this type of suspension is the system with magnetic coils and a conducting guideway. By using a cryogenic system (superconductive helium-cooled coils) a suspension height of 10 to 30 cm could be obtained, where a large operating clearance between the primary and the secondary of the motor is a desirable feature of a high speed vehicle.

Power Supply;

Generally, there are three basic approaches to the problem of the electric power supply to the HSGT system. First, by using a current collection system to transfer the power to the vehicle, where at least two lines are needed because of the absence of an earth return through the wheels. The second approach is to supply the power to a stator which is laid in the track. In this case the major part of the control subsystem is separated from the vehicle itself. In the third approach, power is generated on the vehicle by diesel-or gas-turbine (on-board power generation). This method is not practicle for levitated vehicles of the highest speeds.

In each system the cost of installation is likely to be expensive and for HSGT some power conditioning equipment is required either to be carried on board, or to be installed near the track so as

a) to convert a voltage or frequency,

b) to improve the power factor,

c) to provide a control sub-system cooling plant, and

d) to suppress the interference

Power collection has been achieved using almost conventional equipment at speeds up to 320 km/h, although frequent maintenance has been needed, on Japan's Tokaido line, which has an average

speed of about 185 km/h. However, at much higher speeds contact-free power transfer would be very desirable and is probably essential to avoid the problem of arcing and wear. Some methods have been suggested for this objective such as[4], inductive coupling, capacitive coupling, conduction through a plasma, and high frequency electromagnetic waves (Microwaves).

However, it can be said that there is no obvious answer to the question of how one might transfer power to a high speed vehicle which is magnetically suspended, and new ideas for the extension of existing technology, or an entirely new concept would be very useful.

Control;

Control of the total transport system is outside the scope of this introduction. Control of a vehicle which involves a coupling between suspension sub-system and propulsion sub-system is rather complicated.. Systems in which propulsion and suspension are separated offer more scope for applying the control sub-systems.

The main objective of any control sub-system in a transport system are the following:

a) stable operation

b) to ensure a tolerable journey for passengers

c) location of the vehicle; the maintenance of a safe distance between two vehicles.

d) speed regulation ; acceleration, de-acceleration, constant speed operation, and braking.

The modern high-speed ground transportation system should be provided with a general system supervisor from which the entire system can be supervised by automatic equipment.

The control of the vehicle in the HSGT is seen to be a significant part of the design of an efficient system. The capabilities of a transport system can be considerably improved and safety can be increased by the use of an appropriate control method which must be automatically operated.

Braking;

A braking sub-system is one of the most essential parts of all propulsion arrangements. The acceptable de-acceleration rate for passenger comfort would be much the same as the appropriate acceleration rate.

Braking force can be applied by pneumatic, hydraulic, electro-magnetic or electro-mechanical means.

Aerodynamics;

At the HSGT, aerodynamic effects will become extremely important. The aerodynamic drag, and hence the power required to overcome it, becomes large for a vehicle travelling close to the ground at a high speed. In consequence, the aerodynamic noise generated by the passage of a vehicle will be appreciable, and the other aspects such as the effect of natural winds on vehicle behaviour, unsteady flow effects produced by two vehicle passing each other, and compressible flow effects produced by vehicle passing through tunnels present additional problems to be studied.

Theories will therefore need to be developed to consider all these apsects for the assessment of vehicle stability control.

The performance with respect to quantity and quality is required for an advanced HSGT. Apart from high speed and transport capacity, a high standard of safety, adequate profitability and punctuality have to be the objectives. These requirements can only be met by

means of a high degree of automation for the sub-system mentioned earlier.

1.3 Review of Methods of Analysis

Generally speaking, to solve the field problem of the linear induction motor (LIM) it should be represented by a model which gives a pictorial diagram to describe the system and its behaviour. These models of LIMs are roughly classified into three categories, one-, two-, and three-dimensional models. To solve these models, there are several different techniques and in turn they may be classified as Direct, Transformation and Numerical methods.

The first and the second of the above methods are considered usually as analytical methods. However, as far as engineers are concerned, there is no principal difference between an analytical and a numerical approach. The contrast may exist as soon as one of them appears to be a comparatively inefficient technique from the point of view of cumbersome procedure, time consumed in solving the problem, and the assumptions made.

In this review of method of analysis it has only been possible to outline just some of the techniques used in the study of the LIM.

The One-Dimensional Model.

Obviously, the one-dimensional model represents the simplest form of analysis of the field problem, where the only space variation is along the axis of motion. This form of analysis is considered as the conventional approach for the design of rotating machines and for the calculations of its performance by an equivalent circuit.

Although, the one-dimensional analysis cannot accurately take into account the end effect of the LIM, several authors have attempted to modify the analysis to produce a quasi-two-dimensional analysis. For instance, the transverse edge effects are allowed for by introducing a reduction-conductivity-factor[15,16] which depends on the dimensions and the properties of members of the machine.

The other approach [17,18] is to modify the one-dimensional analysis to account for the entry and exit edge effects by deriving an empirical formula for the air-gap flux distribution which should be satisfied by the appropriate boundary condition.

Ooi[19] and North[20] have attempted to derive more general equations based on generalised machine theory. The study includes short-stator end effects and a physical interpretation for the performance degradation due to end effects.

In this thesis, two approaches are presented based on one-dimensional analysis. In the first one, a pole-by-pole equivalent circuit of the LIM is derived, while in the second approach a one-dimensional finite-difference technique is used to find out the solution of the field problem in relatively simple way. These two attempts are presented with more details later on in this thesis.

It is obvious, however, that the application of the one-dimensional model on a LIM is rather limited, since the transverse and longitudinal edge effects are not directly investigated in the analysis. In consequence, these effects may be examined better by the two-dimensional model.

The Two-Dimensional Model

The two-dimensional analysis commonly encountered is used to account for either transverse edge-effects or longitudinal-end effects. In both cases the secondary skin effects may be taken into account.

A vast amount of literature has been published dealing with the two-dimensional model of LIM.

The study of the transverse edge effects on the performance of the LIM has attracted some investigators. Analytically, it has been examined by Bolton[16], but the flux density is assumed to be normal to the stator surface and still neglects stator end-region fields. A good step towards strict treatment of transverse edge effects are the models of Preston and Reece[21], and Oberretl[22]. Although the 3-dimensional flux density distribution is obtained, the stator iron was assumed to extend to the edge of the secondary.

Numerically, the transverse edge effects on the performance of a LIM has been examined recently by Mosebach[23]. The model takes account of finite iron as well as the effects of stator fringeing and rotor end-portion leakage.

The longitudinal end effects are by far the most specific phenomena of linear motors. Many techniques have been developed to study this phenomena based on a two-dimensional model.

One approach to the problem is based on Fourier transform technique, where the model used employs infinite stator iron length and a finite length sinusoidal current sheet excitation. The predicted results have been compared with experiment[17,18,24], and have generally shown a reasonable agreement, indicating that the

major phenomena in linear motors are the consequence of finite stator winding length. However, the major shortcomings of these models include the fact that they do not consider the effects of finite stator iron length and idealized the stator winding, thus neglecting important practical effects, such as half-filled-end slots in double layer linear induction motor winding.

Analytically, this problem is attacked by Dakowicz [25] where a formulation for the airgap field distribution due to single slot current has been found, allowing the construction of arbitary winding by the superimposition of these solutions, and the fictitious reactive sheets lining the iron beyond the stator ends are used to shield the excess iron beyond the stator active zone.

Numerically, Elliot [26] has treated the problem differently by using a mesh/matrix technique, which represents the moving conductor by a discrete mesh network, each mesh span no more than one tooth pitch. Many simultaneous equations for unknown currents are solved, and by using these currents the field densities, forces and ohmic losses are obtained.

Using a finite difference technique [18, 27] the problem of finite stator iron length is overcome. The procedure is based on the formulation of the difference equations, derived from the governing equations and boundary conditions, and then solving these equations numerically..

The finite element analysis of a two-dimensional model of the LIM is used by Alwash [28]. The finite element formulation which is presented for the actual slotted model as well as the stator current sheet is based on the variational approach.

In this thesis, two models for the LIM are examined. In the first one[29, 30, 31], the tooth zone is represented by an equivalent homogenous anisotropic mass, while the other one is just the ordinary current sheet representation, which is used for comparison. In both models a finite-stator iron length is considered, as shown in more details later on.

However, even two-dimensional models cannot completely describe the performance of a linear induction machine, and a three-dimensional treatment is required.

Three-Dimensional Model

The linear induction motor has become an attractive element for propulsion of high speed ground transport. The application required an elaborate technique completely to describe the performance of the LIM.

A few authors attempted to study the performance of the LIM using the three-dimensional model. Such analysis is required to include all the phenomena in LIM due to the end effects.

An attempt to solve the problem has been made analytically by Oberretl[22]. In this approach a double-Fourier series is used successfully to account for the end effects of double-sided LIMs with a non-magnetic secondary sheet. An infinite array of adjacent primary members separated by a specific airgap is considered in both the longitudinal and transverse directions to account for both longitudinal and transverse edge effects repsectively. For mathematical tractability, a simplification of extending the iron to infinity is found necessary.

Since further substantial improvement cannot be expected from analytical methods, a numerical solution for three-dimensional models of the LIM is presented in this thesis using two models.

In the first model the shape and finite cross section of the winding are both treated. Such treatment is obviously more natural and realistic than current sheet representation which is adopted in the second model of the 3-dimentional analysis as shown later in this thesis.

1.4 Scope of the Work

The objective of this thesis is to study the performance characteristics of the longitudinal single-sided linear induction motor using alternative approaches and models as shown by the block chart in Fig. 1.1.

Generally, the electromagnetic field problems of electric machines are solved by using one or a combination of the following methods; circuit theory, field theory and a hybrid approach.

Field theory as opposed to circuit theory has become increasingly important in many electrical engineering problems, where considerable boundary conditions are imposed. By a hybrid approach is meant the combination of circuit and field theories.

The hybrid approach is based on a one-dimensional analysis. The longitudinal end effects are considered by counting the waves generated at the entry and exit ends of the stator. These waves are attenuating while travelling along the machine. The skin and transverse edge effects are considered by introducing conductivity reduction factors[16,39]. Using this approach a pole-by-pole equivalent circuit of the linear induction motor is developed.

The major part of this thesis is concerned with the field theory, in which three-, two- and one-dimensional approaches are examined.

In these approaches, numerical solutions describing the magnetic vector potential are obtained by the finite-difference method. Such solutions consist of values of the function describing the field which are determined at discrete points spaced in an ordered way over the whole field region. In this method of solution, the one partial differential equation of the field state variable

is replaced by many, simple, finite-difference equations. These take the form of linear equations connecting the potentials at adjacent points, allowing for the boundary conditions of the system. To solve the finite-difference equations using a digital computer, the successive over-relaxation (SOR) technique is used.

Having solved the problem in terms of magnetic vector potential, the flux density components and the performance state variables (forces and powers) are formulated in discrete form in terms of that quantity. Applying the method of numerical integration to the discrete form of the performance state variable gives the effective performance of the machine.

In each of the three-, two- and one-dimensional approaches two models are investigated. In the first model the primary winding is represented by a current sheet backed by iron. In the second model, the primary winding over the active zone is represented by a homogenous anisotropic mass backed by iron, but over the overhang zone the winding is represented by a homogenous isotropic mass.

In each of these models the single sided linear induction motor is examined with and without backing iron.

The results of the models without backing iron are compared with the experimental results obtained from the test rig which is constructed to verify the dynamic performance of the linear induction motor. These results are presented in Chapter 7.

In the light of the comparison of the results of the linear motor without backing iron, the predicted results obtained for the linear motor with backing iron are compared with the results

obtained from the equivalent circuit. These results are presented in Chapter 8.

There are other cases studied in this thesis, which are presented in Chapter 9. These studies include:

a) change in the secondary topology

b) composite reaction rail

c) skin and transverse edge effects

d) longitudinal end effects

e) constant current and constant voltage drives

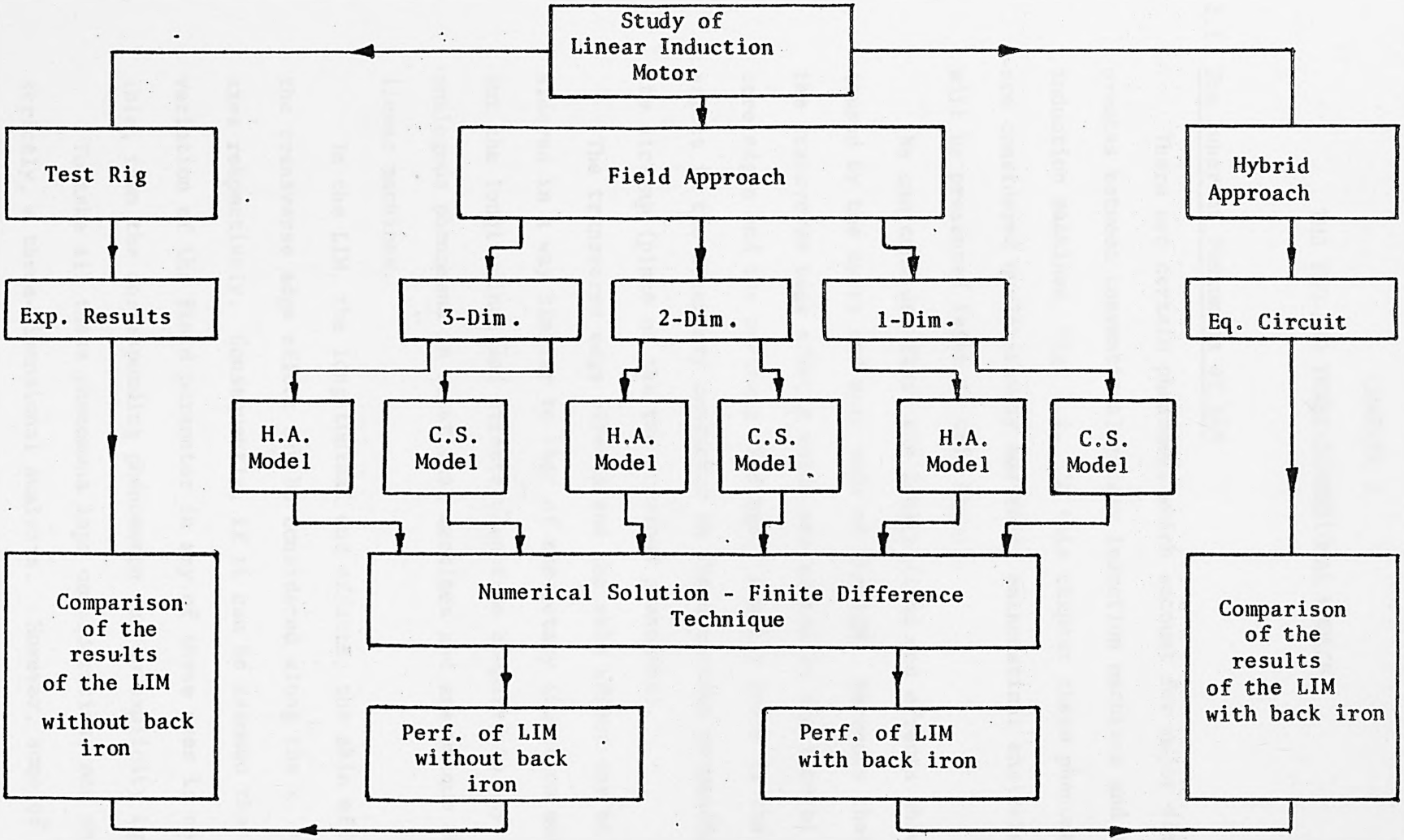

Fig. 1.1. Scope of the Work

CHAPTER 2

THE TWO-AND THREE-DIMENSIONAL MODELS

2.1 The Inherent Phenomena of LIM

There are certain phenomena which account for major differences between conventional rotary induction machines and linear induction machines, Fig. 2.1. In this chapter these phenomena are considered qualitatively and their mathematical analysis will be presented later in this thesis.

We can consider first the longitudinal end effects which are caused by the entry and exit ends of the LIM. Secondly there are the transverse edge effects which are caused by the lateral stator core edges and the overhang windings. Finally there is the skin effect in the secondary conductor in the direction perpendicular to the air-gap (plane of the two previous phenomena).

The transverse edge effects and the skin effect may be considered in a way similar to that of the rotary induction motors. But the longitudinal end effects cannot be compared to any analogous phenomena in rotational machines and are unique to linear machines.

In the LIM, the longitudinal end effects, the skin effect and the transverse edge effect can be considered along the x, y and z axes respectively. Consequently, if it can be assumed that the variation of the field parameter in any of these axes is negligible, then the corresponding phenomenon can be explicity ignored.

To take all these phenomena into consideration, one should choose, strictly, a three-dimensional analysis. However, some of these phenomena could be represented by introducing appropriate

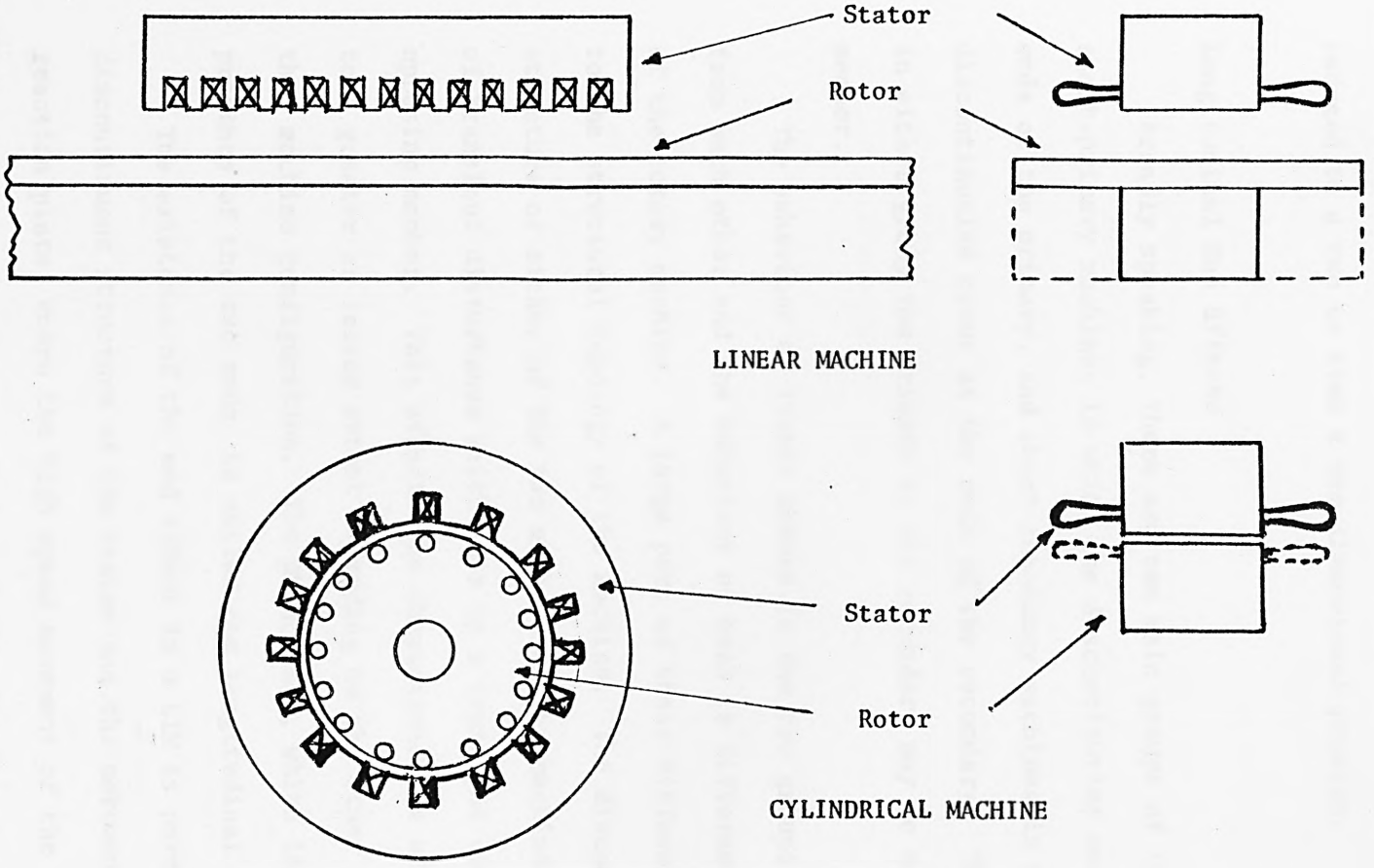

Fig. 2.1. Configurations of Electric Moving Machines

corresponding coefficients, and in this case the analysis may be reduced to a two or even a one-dimensional problem.

2.1.1 Longitudinal End Effects

Broadly speaking, there are two main groups of linear machines: short-primary machines in which the discontinuties occur at the ends of the primary, and short-secondary machines in which the discontinuties occur at the ends of the secondary. Theoretically in either group the primary or the secondary may be made the moving member.

The behaviour of linear motors in the two groups are different from each other and the behaviour of both is different from that of the rotary machine. A large part of these differences are due to the structural topology of the machine. The discontinuous structure of either of the two members of the machine causes a kind of transient disturbance which sets up a transient current in the opposing member. This affects the characteristics of the machine to a greater or lesser extent depending on the other parameter of the machine configuration. The phenomenon, which is caused by the presence of the two ends, is called the longitudinal end effect.

The existence of the end effect in a LIM is purely due to the discontinuous structure of the stator and the movement of the reaction plate, where the high speed movement of the reaction plate tends to prevent the penetration of the main flux in the case of the short stator.

In short-stator (primary) machines the transient phenomena occurring at the edges are all-important in setting the pattern of machine behaviour. On the other hand, in the case of short-rotor (secondary) machines, although some transient phenomena

must still take place at the rotor edges, the effect is of secondary importance compared with that in short-stator motors.

Another fact concerning the end effects[32] is perhaps worth mentioning here with regard to the primary winding connection. It has been found that for short-stator machines, a series connection is more favourable as it avoids over-heating of the coils close to the ends of the machine. This may occur due to the transient current being induced in the secondary conductors as they enter and leave the stator (primary) and the corresponding increase in the primary current in the end section.

For short-rotor machines, on the other hand, it is generally better to use a parallel connection to enable a reasonable working flux density to be obtained in the active section of the machine.

However, the parallel connection of the stator winding has been found[24] to be useful to compensate the influence of the end effects. It is noted that the efficiency of a series connected LIM is much degraded by the end effect.

The influence of entry and exit ends on the performance of the machine depends significantly on the speed of the LIM. An extensive literature survey on longitudinal ends effects reveals that the influence of the longitudinal end effects on the performance of the high speed LIM are of such magnitude that they cannot be ignored.

There are many other factors affecting the influence of the end effects such as number of poles, airgap length, secondary conductivity, supply frequency, pole pitch etc. Adjustment of these factors to alleviate the end effects tend to degrade the normal motor performance making it necessary to find a compromise.

The longitudinal end effect may be taken into consideration by using the equivalent circuit approach[33,34], one dimensional analysis[35,36,37], two-dimensional analysis[17,20,25,28,36,38], and three-dimensional analysis[22]. However, the accuracy of these analysis depends on the assumptions, the boundary conditions, and how realistic the configuration of the machine is.

2.1.2. Transverse Edge Effect

Usually the primary and secondary members of a LIM have finite width, and from the stability point of view the secondary is wider than the primary, Fig. 2.1. The currents in the secondary member of the machine flow in roughly elliptical paths, the secondary appears to have a resistivity greater than the natural value, cross-gap flux density varies across the stator width and is greatest at the edges of the stator. The consequences of these physical features of a LIM are the transverse edge effect, which is rather different in its origin and nature from the longitudinal edge effect. Neither is it caused by the relative motion between the primary and secondary nor does it involve transient phenomena associated with the non-uniform distribution of current and magnetic flux in the transverse direction.

The consequences of the transverse edge effect are:

(a) an increase in secondary resistivity,

(b) a tendency to be a source of armature reaction,

(c) a tendency toward lateral instability.

As a result of the above, the overall performance of the LIM is effected in an adverse manner.

The transverse edge effect may be taken into consideration either by explicitly solving the field equation or by introducing an appropriate conductivity reduction factor while the redistributed of the air-gap flux due to the action of currents flowing in the active region in the direction of motion are ignored. The transverse edge effects factor K_t is given below[16].

$$K_t = \frac{K_x^2}{K_R} \quad \frac{1 + s^2G^2K_R^2/K_x^2}{1 + s^2G^2}$$

where $K_R = 1 - R_e \left[(1 - jsG) \frac{\lambda}{a\alpha} \tanh(\alpha a)\right]$

$$K_x = 1 + R_e \left[(sG + j)\, sG \frac{\lambda}{a\alpha} \tanh(\alpha a)\right]$$

$$G = \frac{2\,\sigma\tau^2\mu_o\, f}{\pi g}$$

$$\alpha^2 = k^2 + \frac{js\omega\,\mu_o\sigma}{g} = k^2\,(1 + js\,G)$$

$$\lambda = 1/\left[1 + \frac{1}{r} \tanh(\alpha a) \tanh(k\,(C-a))\right]$$

$$r^2 = 1/\,(1 + js\,G)$$

$k = \pi/\tau$

τ = pole pitch

σ = secondary conductivity

d = secondary conductor thickness

g = effective airgap

a = stator semiwidth

C = secondary conductor semiwidth

2.1.3. Skin Effect

When a conductor of any shape carries an alternating current, the internal magnetic field tends to crowd the current towards the surface, the more so the higher the frequency. This phenomenon is called skin effect. In a high speed LIM, where there is an appreciable distance between primary and secondary and the input frequency may be higher than 100 Hz, the effect becomes significant on the performance of the LIM. It increases the effective resistance of the conductor over that for direct current and therefore increases the losses.

The skin effect may be taken into account either explicity, by solving the field equation using two-dimentional or three-dimensional analysis, or by using an appropriate conductivity correction factor (K_s) [39].

$$K_s = \frac{d(\sinh(d/ds) + \sin(d/ds))}{ds\,(\cosh(d/ds) - \cos(d/ds))}$$

where d is the secondary conductor thickness.

ds is the skin depth $= \sqrt{\frac{2}{\mu_o \sigma \omega s}}$

and the conductivity becomes $\sigma_s = \sigma/K_s$

When both transverse edge effects and skin effects are considered the effective conductivity becomes:

$$\sigma_e = \sigma/K_s K_t$$

2.2 The Analytical Models and Assumptions

As mentioned earlier, in this part of analysis the longitudinal single-sided LIM is represented by four analytical models. These are:

a) Two-dimensional model with primary winding represented by current sheet; this will be hereafter called 2DCM, Fig. 2.2a.

b) Three-dimensional model with primary winding represented by current sheet; this will be hereafter called 3DCM, Fig. 2.2.

c) Two-dimensional model with primary winding represented by homogeneous anisotropic mass; this will be hereafter be called 2DHM, Fig. 2.3a .

d) Three-dimensional model with primary winding represented by homogeneous isotropic and homogenous anisotropic masses; this will be hereafter called 3DHM, Fig. 2.3 .

For the 3DCM, the stator iron is assumed to be extended to the ends of the overhang winding, as shown in Fig. 2.2b .

In order to facilitate the analysis for the three-dimensional models, the following assumptions are made:

1) The machine is operating over the linear region of the B-H curve.

2) The primary current density is varying sinusoidally with time and with the direction of motion.

3) The current density component in y-direction is assumed to be zero.

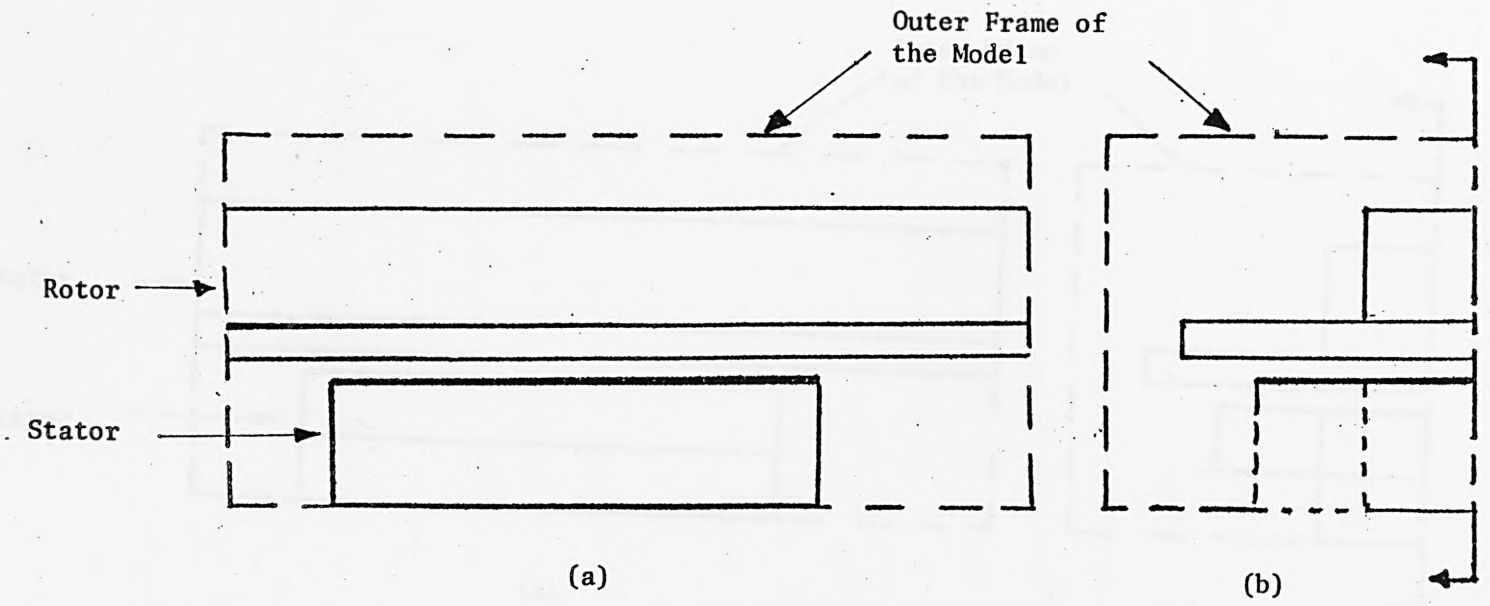

Fig. 2.2. Current sheet models of the LIM

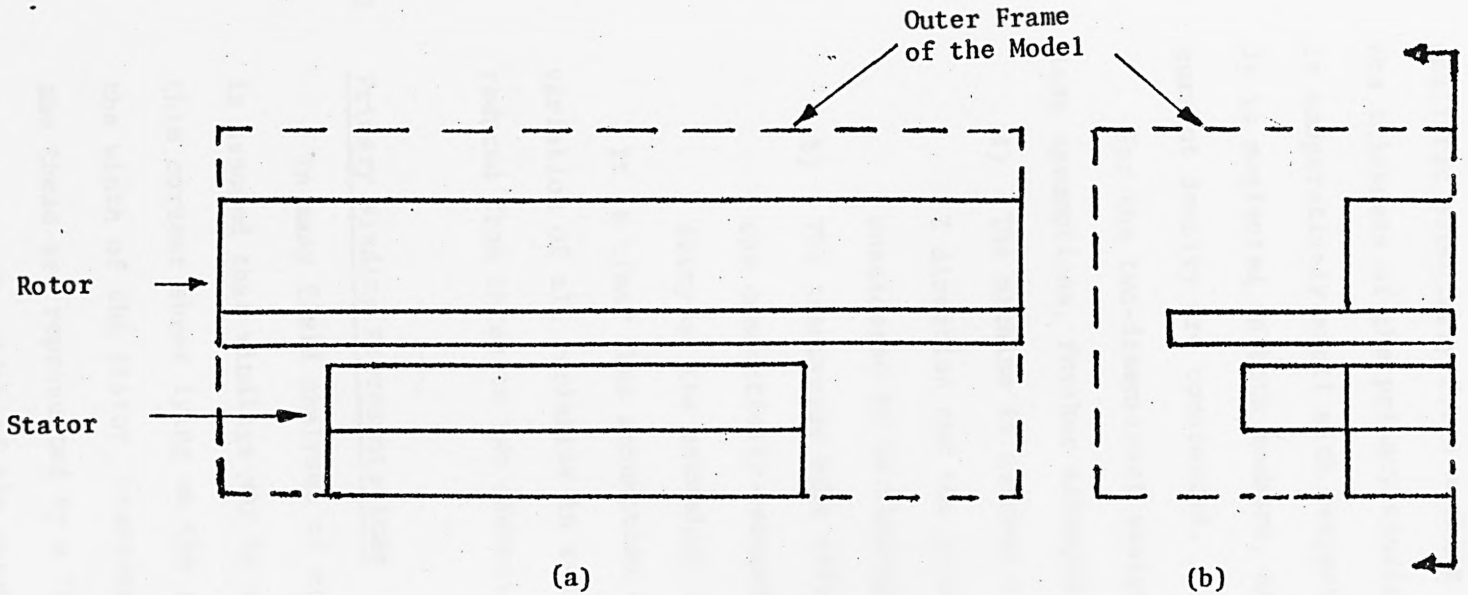

Fig. 2.3. Homogenous Anisotropic models of the LIM

It is clear that assumptions 1 and 3 are not often physically realistic especially for a machine of large power. In these models the thickness of the primary winding and the secondary conductor is comparatively small with respect to the pole pitch. Therefore Jy is neglected in both members, and only two components of the current density are considered.

For the two-dimensional analysis, and in addition to the last assumptions, further assumptions should be made:

4) The machine is assumed to be infinitely wide in the Z direction and the primary and secondary currents are considered to be flowing in this direction only.

5) The transverse edge effect is considered by introducing the conductivity-reduction factor to modify the conductivity of the secondary conductor as given earlier.

It is clear that assumption 4 means that, by ignoring the variation of all variables in z-direction, the problem will be reduced from three to two dimensions.

2.3 Primary Winding Representations

In many field analyses of electrical machine structure it is assumed that windings may be represented by an infinitesimally thin current sheet lying on the stator surface.[40,41] Over the width of the stator, transverse currents only are presented and these are represented by a 'transverse' current sheet (Kz), while over the width of the overhang windings, both transverse and longitudinal currents must flow. These are represented by a 'transverse' current sheet (Kz) and a 'longitudinal' current sheet (Kx), so that the current continuity relation ($\nabla.\overline{J} = 0$) is obeyed.

Basically, the winding of the stator is arranged as shown in Fig. 2.4a, where Z = 0 is the center of the stator core, a is the end of the core, and b is the end of the overhang winding. The solid lines represents the top layer while the broken lines represents the lower layer.

The active zone (0 < Z < a);

The fundamental wave of the line current density of the top layer is

$$K_T = \frac{K_a}{2} \cdot e^{j(\omega t - kx)}$$

The fundamental wave of the line current density of the lower layer at z = 0 is displaced by pπ radians, where p is the fractional coil pitch and is given by

$$K_L = \frac{K_a}{2} \cdot e^{j(\omega t - kx + p\pi)}$$

The resultant components of the line current density are given by

$$Kx = 0$$

and

$$Kz = \frac{K_a}{2} \cdot e^{j(\omega t - kx)} \cdot (1 - e^{+jp\pi})$$

For unchorded coil the transverse-component becomes

$$Kz = K_a \cdot e^{j(\omega t - kx)}$$

where

$$K_a = 6\sqrt{2} \quad 1 \; N_e/4\tau$$

$$Ne = N \; K_p K_b$$

N = No. of turns/phase

$$K_p = 1.0$$

$$K_b = \frac{\text{Sin } \frac{q\delta}{2}}{q \text{ Sin } \frac{\delta}{2}}$$

The overhang zone ($a < Z < 6$);

At the general point P of Fig. 2.4a the top and the lower line current density become respectively:

$$K_T = \frac{K_o}{2} \cdot e^{j(\omega t - kx + \theta)}$$

$$K_L = \frac{K_o}{2} \cdot e^{j(\omega t - kx + p\pi - \theta)}$$

where $\theta = p \frac{\pi}{2} \frac{z-a}{b-a}$ by using triangle similar value.

at $z = a \quad \theta = 0$

$z = b \quad \theta = p\frac{\pi}{2}$

The resultant transverse line current density is given by

$$Kz = (K_T - K_L) \cdot \text{Sin } \xi$$

$$= \frac{K_o}{2} \cdot e^{j(\omega t - kx)} \cdot (e^{j\theta} - e^{+j(p\pi - \theta)}) \cdot \text{Sin } \xi$$

The longitudinal line current density is

$$Kx = (K_T + K_L) \cdot \text{Cos } \xi$$

$$= \frac{K_o}{2} \cdot e^{j(\omega t - kx)} \cdot (e^{j\theta} + e^{+j(p\pi - \theta)}) \cdot \text{Cos } \xi$$

For unchorded coil the line current density components are reduced to.

$$Kz = K_o \cdot e^{j(\omega t - kx)} \cdot \text{Cos } \theta \cdot \text{Sin } \xi$$

and $$Kx = K_o \cdot e^{j(\omega t - kx)} \cdot \text{Sin } \theta \text{Cos } \xi$$

where ξ is the angle of the skew of the coil with the x-axis.

Now, since the overhang current sheet is considered as elemental sheet which is skewed at the end of the active zone by angle ξ, see Fig. 2.4b, the maximum line current density of the overhang current sheet K_o is no longer equal to the line current density of the active zone K_a. But they are related to each other by the expression.

$$K_o = \frac{K_a}{\text{Sin } \xi}$$

To sumarize, the equations of the line current density components for the active and overhang zones are as follows, (see Fig. 2.5)

at $o<Z<a$

$$Kz = \frac{K_a}{2} \cdot e^{j(\omega t - kx)} \cdot (1 - e^{jp\pi})$$

$$Kx = 0$$

and at $a<Z<b$

$$Kz = \frac{K_a}{2} \cdot e^{j(\omega t - kx)} \cdot (e^{j\theta} - e^{j(p\pi-\theta)})$$

$$Kx = \frac{K_a}{2} \cdot e^{j(\omega t - kx)} \cdot (e^{j\theta} + e^{j(p\pi-\theta)}) \cdot \text{Cot } \xi$$

The method of representing the windings by a current sheet is applied to the 2DCM and 3DCM models shown earlier. However this assumption is valid only if the coils are embedded in slots[42]. Consequently when machines possess airgap windings, as is the case of the overhang windings, the conditions for analysis using a thin current sheet are not directly applicable. Therefore for the 3DCM model, the stator iron is assumed to extend until the ends of the overhang windings, and an approximate allowance for this may be made by the modification of the current components in the overhang region, see appendix A.

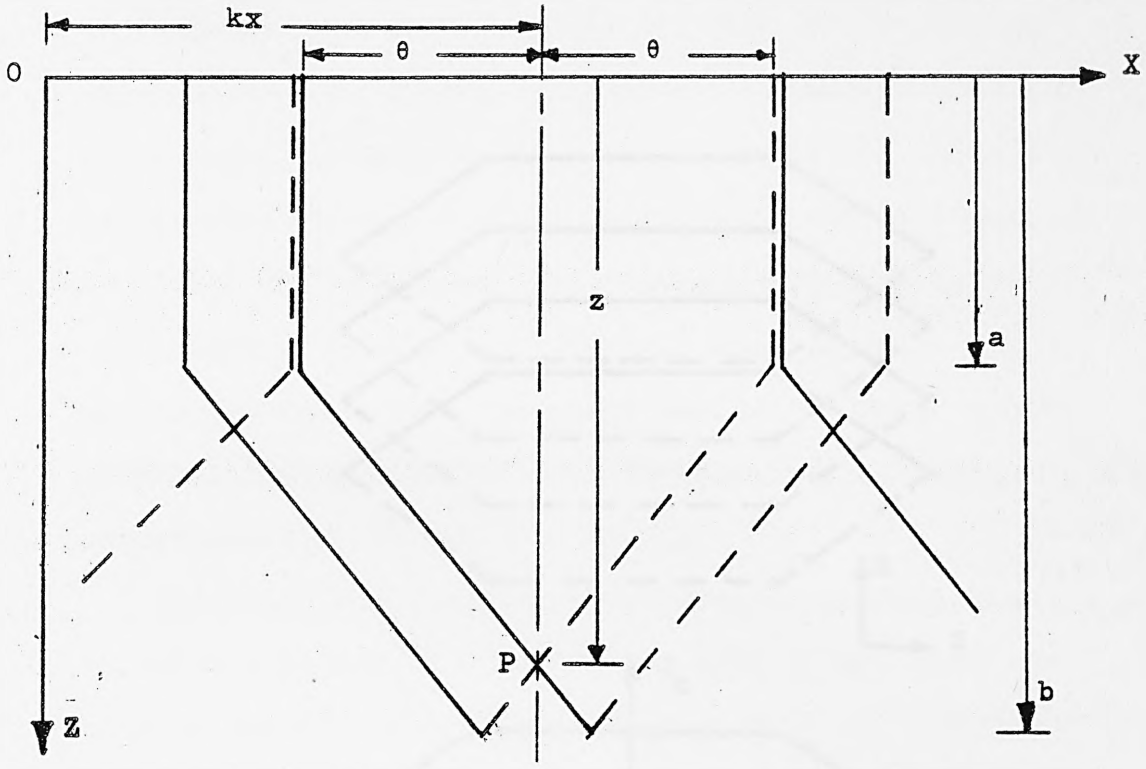

Fig. 2.4a. Stator winding configuration

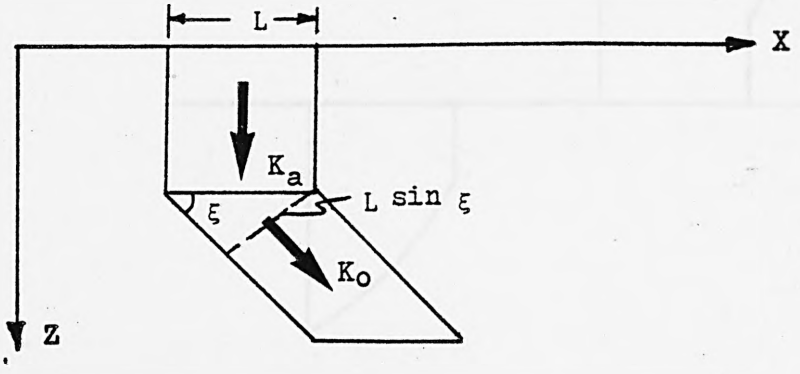

Fig. 2.4b. Elemental current sheet on stator surface

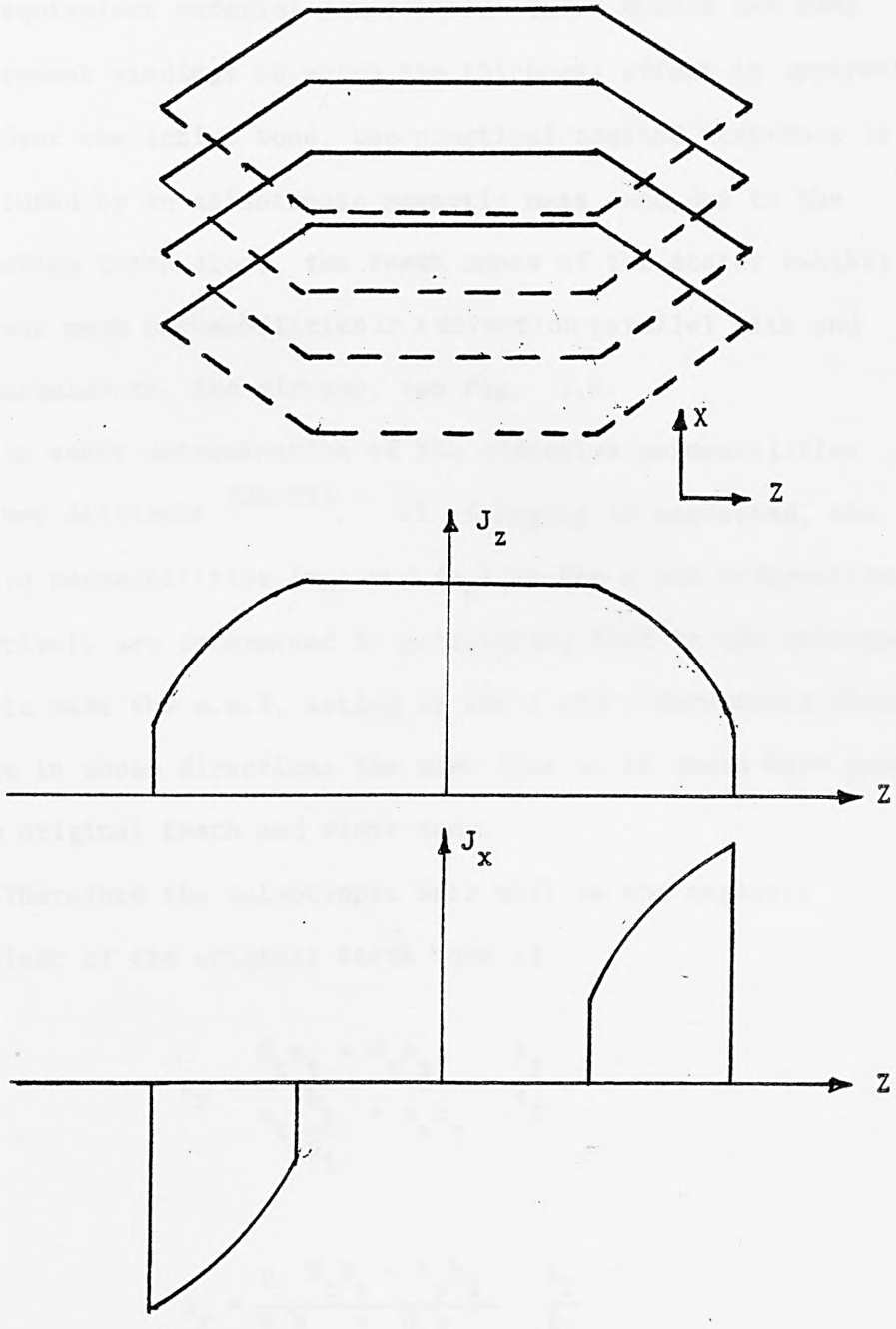

Fig. 2.5. Current distributions

In the other two models, 2DHM and 3DHM, the windings are represented by anisotropic and isotropic homogenous masses with their equivalent material properties. These models are used to represent windings in which the thickness effect is apparent.

Over the active zone, the practical toothed structure is substituted by an anisotropic magnetic mass and, due to the alternating teeth slots, the teeth zones of the stator exhibit different mean permeabilities in a direction parallel with and perpendicular to the air-gap, see Fig. 2.6.

An exact determination of the effective permeabilities is rather difficult [29-31]. If fringing is neglected, the relative permeabilities (μ_x) and (μ_y) in the x and y-direction respectively are determined by postulating that in the anisotropic magnetic mass the m.m.f. acting in the x and y-directions should produce in these directions the same flux as it would have produced in the original teeth and slots zone.

Therefore the anisotropic mass will be the magnetic equivalent of the original teeth zone if

$$\mu_x = \frac{N_t b_t + N_s b_s}{N_t \frac{b_t}{\mu_i} + N_s b_s} \quad \frac{\ell_1}{\ell_2}$$

$$\mu_y = \frac{\mu_i N_t b_t + N_s b_s}{N_t b_t + N_s b_s} \quad \frac{\ell_2}{\ell_1}$$

where N_t = No. of teeth

N_s = No. of slots

μ_i = relative permeability of the iron

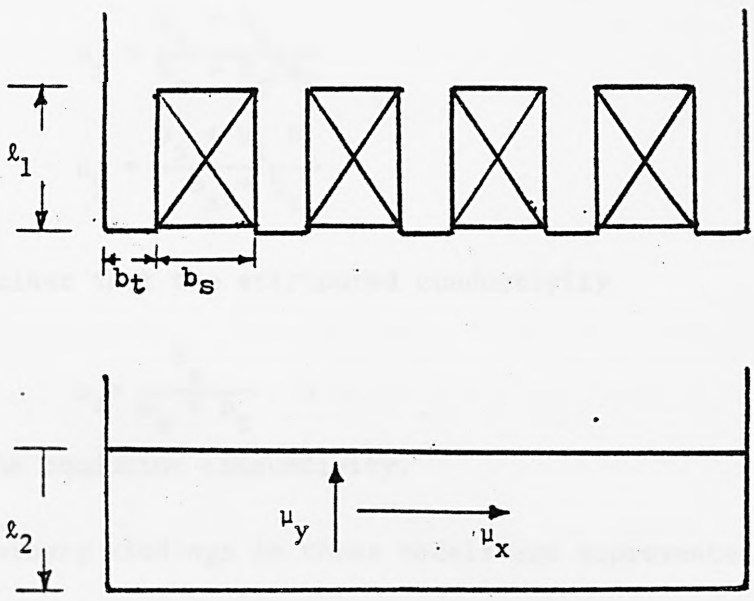

Fig. 2.6. The magnetic equivalent of the teeth zone

If $\ell_1 = \ell_2$ and $N_t = N_s$ then the last equations become

$$\mu_x = \frac{b_s + b_t}{b_s + b_t/\mu_i}$$

$$\mu_y = \frac{b_s + \mu_i\, b_t}{b_s + b_t}$$

It is clear that the attributed conductivity

$$\sigma_a = \frac{b_s}{b_s + b_t}\ \sigma$$

where σ is the conductor conductivity.

The overhang windings in these models are represented by an isotropic conducting mass with free space permeability μ_o.

The current distribution in these models has the same form as that applied to the current sheet models. However, the current density vector must be introduced and, due to assumption, that the current should be independent of y, it becomes

$$\overline{J} = J_1 e^{j(\omega t - kx)}$$

where

$$J_1 = \frac{K_1}{h}$$

CHAPTER 3

THE NUMERICAL SOLUTION

3.1 Introduction

Broadly speaking, numerical methods are very powerful and can be applied equally to steady state and transient problems, linear and non-linear, with and without regular boundaries and boundary conditions. Therefore by applying the numerical method for solving differential equations, the restrictions and limitations of the analytical approaches may be reduced.

In this thesis, numerical solution describing the magnetic vector potential (MVP) are obtained using the finite-difference method.

Starting with Maxwell's equations, the governing equations for the suggested models shown earlier are derived in terms of the magnetic vector as differential equations. Thus Laplace's and Poisson's equations are replaced by finite difference equations which connect the values of the function describing the field at surrounding nodes to that at the node under consideration.

The MVP of the nodes in a current-free or a current-carrying region can be defined by the finite difference form of the Laplace's or Poisson's equations respectively. The solution of the field is obtained by solving the resulting simultaneous equations. As the number of these simultaneous equations is very large, it becomes unreasonable to attempt a solution using methods involving the elimination of variables, determinants or matrix inversion.

Instead, some form of iterative procedure is usually adopted which exploits the simple forms of the different equations.

In this thesis, the finite-difference equations are solved using machine computation and by applying a successive over-relaxation (SOR) technique.

Having solved the field in terms of magnetic vector potential by the finite-difference method, the magnetic flux density, the forces developed, the rotor current density, the ohmic losses, and the cross-gap power can be formulated in terms of the MVP and also in discrete form.

To compute the total quantities of the above state variables of machine performance, a numerical integration method can be used.

In this chapter, the two-and three-dimensional analyses and formulation of the problem are discussed. The two-dimensional derivation is obtained by considering it as a particular case of the three-dimensional analysis.

The derived solution is for a longitudinal linear induction motor backed by iron. But since the experimental work deals with a machine without backing iron, the solution for the problem of the new topology (air backed) could be considered as a particular case of the former one.

3.2 Governing Equations

Electrodynamic equations for a slowly moving medium, which are relevant to the study of the linear induction motor include the following:

Amperes circuital law for the non-stationary electromagnetic field, where displacement currents are neglected:

$$\nabla \times \overline{H} = \overline{J} \qquad (3.1)$$

Maxwell-Faraday's Law, where the electrostatic flux density is ignored:

$$\nabla \times \overline{E} = - \frac{\partial \overline{B}}{\partial t} \tag{3.2}$$

the law of conservation of magnetic flux:

$$\nabla \cdot \overline{B} = 0 \tag{3.3}$$

and the continuity equation of the current density:

$$\nabla \cdot \overline{J} = 0 \tag{3.4}$$

The above four variables are related to each other and controlled by the material properties, defined by the constituent relations:

$$\overline{B} = \mu_r \mu_o \overline{H} \tag{3.5}$$

$$\overline{J} = \sigma \overline{E} \tag{3.6a}$$

Ohm's law for an isotropic medium moving with velocity $\overline{V}$:

$$\overline{J} = \sigma (\overline{E} + \overline{V} \times \overline{B}) \tag{3.6b}$$

$\overline{J}$ in above equations represents either the impressed current density or the conduction current density existing due to induction phenomena.

By using the magnetic vector potential $\overline{A}$, defined by

$$\nabla \times \overline{A} = \overline{B} \tag{3.7}$$

the continuity condition of eq. (3.3) can be satisfied automatically.

From eqs.(3.2) and (3.7), one obtains a generalised electric field strnegth formula.

$$\overline{E} = - \frac{\partial \overline{A}}{\partial t} - \nabla \phi \tag{3.8}$$

where ϕ is the electric scalar potential, and $\nabla\phi$ term is customarily associated with the electrostatic effects of the charges on the conductor surfaces.

Therefore, in general terms the eddy-current field equation can be obtained by combining eqs. (3.1), (3.2), (3.5), (3.6a), (3.7), and (3.8):

$$\nabla x \left(\frac{1}{\mu} \nabla X \overline{A}\right) = - \mu_o \sigma \left(\frac{\partial \overline{A}}{\partial t} + \nabla \phi\right)$$

and since the machine is considered as operating over the linear region of the B-H curve the field equation becomes

$$\nabla(\nabla . \overline{A}) - \nabla . (\nabla \overline{A}) = - \mu \mu_o \sigma \left(\frac{\partial \overline{A}}{\partial t} + \nabla \phi\right) \qquad (3.9)$$

Now $\overline{A}$ and ϕ supposed only to satisfy eqs. (3.3) and (3.9) respectively, otherwise they are arbitrary functions.

Since $(\nabla X \overline{A})$ is specified, $(\nabla . \overline{A})$ may be adopted to represent any function, but it is wise to choose it such that the foregoing differential equations have the simplest forms possible. In other words, for a conducting medium, the suppositions that are going to be made here, serve the requirements of the following constraints without the violation of eq. (3.9).

a) since the charges in the conducting media can only be distributed on surfaces, then the Laplacian of electric scalar potential ϕ exists only in the interior region

$$\nabla^2 \phi = 0$$

b) to seek uncoupled MVP equations .

Since from eqs. (3.4), (3.6a), and (3.8)

$$\nabla^2 \phi = - \frac{\partial}{\partial t} (\nabla . \overline{A})$$

Then $\bar{A}$ should be defined by

$$\nabla.\bar{A} = 0 \tag{3.10}$$

so that to satisfy requirement (a), but to satisfy the request mentioned in (b) as well, one may assume from eq. (3.9) that

$$\nabla (\nabla.\bar{A}) = \mu\mu_o\sigma\nabla\phi$$

As a matter of fact the above assumption cannot be applied except when $\nabla.\bar{A} = 0$, since this supposition without condition (3.10) implies that there is a valume charge distribution within the conductivity media.

As a consequence of this, eq. (3.9) is simplified as

$$\nabla^2\bar{A} = \mu\mu_o\sigma\frac{\partial\bar{A}}{\partial t}$$

Thus for a medium moving in the x direction with velocity V_x the field equations of a three-dimensional problem are obtained by combining eqs. (3.1), (3.2), (3.5), (3.6b), (3.7) and (3.8).

$$\frac{\partial^2 Az}{\partial x^2} + \frac{\partial^2 Az}{\partial y^2} + \frac{\partial^2 Az}{\partial z^2} = \mu\mu_o\sigma\left[\frac{\partial Az}{\partial t} - V_x.\left(\frac{\partial Ax}{\partial z} - \frac{\partial Az}{\partial x}\right)\right] \tag{3.11a}$$

$$\frac{\partial^2 Ax}{\partial x^2} + \frac{\partial^2 Ax}{\partial y^2} + \frac{\partial^2 Ax}{\partial z^2} = \mu\mu_o\sigma\frac{\partial Ax}{\partial t} \tag{3.11b}$$

while for two dimensional problem it becomes

$$\frac{\partial^2 Az}{\partial x^2} + \frac{\partial^2 Az}{\partial y^2} = \mu\mu_o\sigma\left[\frac{\partial Az}{\partial t} + V_x.\frac{\partial Az}{\partial x}\right] \tag{3.11c}$$

Again as it is simpler and more convenient to have uncoupled equations for the numerical solution, one may formulate the coupled component equation (3.11a) in more convenient manner as long as the basic equation is not violated. This could be achieved by replacing the term $\frac{\partial Ax}{\partial z}$ by its final value developed from the solution of the x-component (3.11b) using the iterative procedure which will be described later on.

For a homogeneous isotropic conducting medium carrying an impressed current density $\overline{J}$, the Poisson's equation simply becomes:

$$\nabla^2\overline{A} = - \mu\mu_o\overline{J}$$

Hence for a three-dimensional analysis it becomes

$$\frac{\partial^2 Az}{\partial x^2} + \frac{\partial^2 Az}{\partial y^2} + \frac{\partial^2 Az}{\partial z^2} = - \mu\mu_o Jz \qquad (3.12a)$$

and

$$\frac{\partial^2 Ax}{\partial x^2} + \frac{\partial^2 Ax}{\partial y^2} + \frac{\partial^2 Ax}{\partial z^2} = - \mu\mu_o Jx \qquad (3.12b)$$

while for two-dimensional analysis only the z component of Poisson's equation exists.

$$\frac{\partial^2 Az}{\partial x^2} + \frac{\partial^2 Az}{\partial y^2} = - \mu\mu_o Jz \qquad (3.12c)$$

Jz and Jx are the z- and x-components of the source current density vector respectively.

For a homogeneous isotropic non-conducting medium the field equation becomes of a Laplacian form

$$\nabla^2\overline{A} = 0$$

Hence for a three-dimensional problem it becomes

$$\frac{\partial^2 Az}{\partial x^2} + \frac{\partial^2 Az}{\partial y^2} + \frac{\partial^2 Az}{\partial z^2} = 0 \qquad (3.13a)$$

and

$$\frac{\partial^2 Ax}{\partial x^2} + \frac{\partial^2 Ax}{\partial y^2} + \frac{\partial^2 Ax}{\partial z^2} = 0 \qquad (3.13b)$$

while for two-dimensional problem it becomes

$$\frac{\partial^2 Az}{\partial x^2} + \frac{\partial^2 Az}{\partial y^2} = 0 \qquad (3.13c)$$

For a homogeneous anisotropic conducting medium, the field equations to be solved are obtained as follows.

from equations (3.1), (3.5), and (3.7)

$$\nabla \times (\bar{\nu} \cdot \nabla \times \bar{A}) = \bar{J}$$

where reluctivity vector $\bar{\nu}$ is the reciprocal of the magnetic permeability. Since J_y, and in consequence, A_y are ignored, the above equation becomes

$$-\nu_z \frac{\partial}{\partial y}\left(\frac{\partial Ax}{\partial y}\right) - \nu_y \frac{\partial}{\partial z}\left(\frac{\partial Ax}{\partial z}\right) + \nu_y \frac{\partial}{\partial z}\left(\frac{\partial Az}{\partial x}\right) = Jx$$

$$-\nu_y \frac{\partial}{\partial x}\left(\frac{\partial Az}{\partial x}\right) - \nu_x \frac{\partial}{\partial y}\left(\frac{\partial Az}{\partial y}\right) + \nu_y \frac{\partial}{\partial x}\left(\frac{\partial Ax}{\partial z}\right) = Jz$$

The above two equations are coupled due to the third term of each equation, but using the definition of $\bar{A}$ in eq. (3.10), or rather

$$\nabla (\nabla . \bar{A}) = 0$$

some alternatives for these terms could be found and these are

$$\frac{\partial^2 Az}{\partial x \partial z} = -\frac{\partial^2 Ax}{\partial x^2}$$

and

$$\frac{\partial^2 Ax}{\partial z \partial x} = -\frac{\partial^2 Az}{\partial z^2}$$

Substitution of above two alternatives in the two eddy-current equations will lead to uncoupled expressions.

$$\nu_y \left[\frac{\partial^2 Ax}{\partial x^2} + \frac{\partial^2 Ax}{\partial y^2} + \frac{\partial^2 Ax}{\partial z^2} \right] = -Jx \qquad (3.14a)$$

and

$$\nu_y \left[\frac{\partial^2 Az}{\partial x^2} \right] + \nu_x \left[\frac{\partial^2 Az}{\partial y^2} \right] + \nu_y \left[\frac{\partial^2 Az}{\partial z^2} \right] = -Jz \qquad (3.14b)$$

where ν_z is replaced by ν_y where they are considered to be equivalent to each other.

For two dimensional problem it becomes

$$\nu_y \left[\frac{\partial^2 Az}{\partial x^2} \right] + \nu_x \left[\frac{\partial^2 Az}{\partial y^2} \right] = -Jz \qquad (3.14c)$$

3.3 Finite Difference Representation of Three Dimensional Models

The importance of the finite difference method lies in the ease with which many logically complicated operations and functions may be discretized. Operations are then performed not upon continuous functions but approximately, in terms of values over a discrete point set. As the distance between points is made smaller, the approximation becomes increasingly accurate. The great advantage of this method is that operations, such as differeniation and integration, may be reduced to simple arithmetic forms which can then be conveniently programmed for automatic digital computation.

For a numerical solution, the differential expressions of the field equations mentioned in the previous section have to be transformed into difference form which connect values of the potential function at a discrete point set. The pattern according

to which the points are distributed in the medium must be known. However, it is obvious that if a completely regular distribution of points is chosen, which is uniform over the whole region considered, the same form of finite-difference equation is satisfied at all the points, and the representation of the problem is much simplified. Fig. 3.1 shows a typical three-dimensional lattice. The distances between the point 0 and the points 1, 2, 3, 4, 5 and 6 are denoted h_1, h_2, h_3, h_4, h_5, and h_6 respectively.

As mentioned earlier, the field equation of the homogenous isotropic current-free medium is of Laplacian form. In Cartesian-form, Laplace's equation is

$$\nu \left[\frac{\partial^2 A}{\partial x^2} + \frac{\partial^2 A}{\partial y^2} + \frac{\partial^2 A}{\partial z^2} \right] = 0 \qquad (3.15)$$

The difference equation of the above differential expression is developed by expanding the function (νA) in nodes 1, 2, 3, 4, 5, and 6 in terms of the values of these function at node 0, by the use of Taylor's series. Ignoring terms containing h_i to the power of (3) or more, we obtain for instance

$$\nu_1 . A_1 = \nu_o . A_o + h_1 \left(\nu_o \left.\frac{\partial A}{\partial x}\right|_o + A_o \left.\frac{\partial \nu}{\partial x}\right|_o \right) +$$

$$\frac{1}{2} h_1^2 \left(\nu_o \cdot \left.\frac{\partial^2 A}{\partial x^2}\right|_o + 2 \left.\frac{\partial \nu}{\partial x}\right|_o \cdot \left.\frac{\partial A}{\partial x}\right|_o + A_o \cdot \left.\frac{\partial^2 \nu}{\partial x^2}\right|_o \right)$$

Now as the region is considered to be homogenous, ν is assumed to be constant, therefore

$$\nu_1 . A_1 = \nu_o \cdot \left(A_o + h_1 \left.\frac{\partial A}{\partial x}\right|_o + \frac{1}{2} h_1^2 \left.\frac{\partial^2 A}{\partial x^2}\right|_o \right)$$

and

$$\nu_3 . A_3 = \nu_o \cdot \left(A_o - h_3 \left.\frac{\partial A}{\partial x}\right|_o + \frac{1}{2} h_3^2 \cdot \left.\frac{\partial^2 A}{\partial x^2}\right|_o \right)$$

multiply the 1st equation by h_3 and the second equation by h_1 and adding them yields,

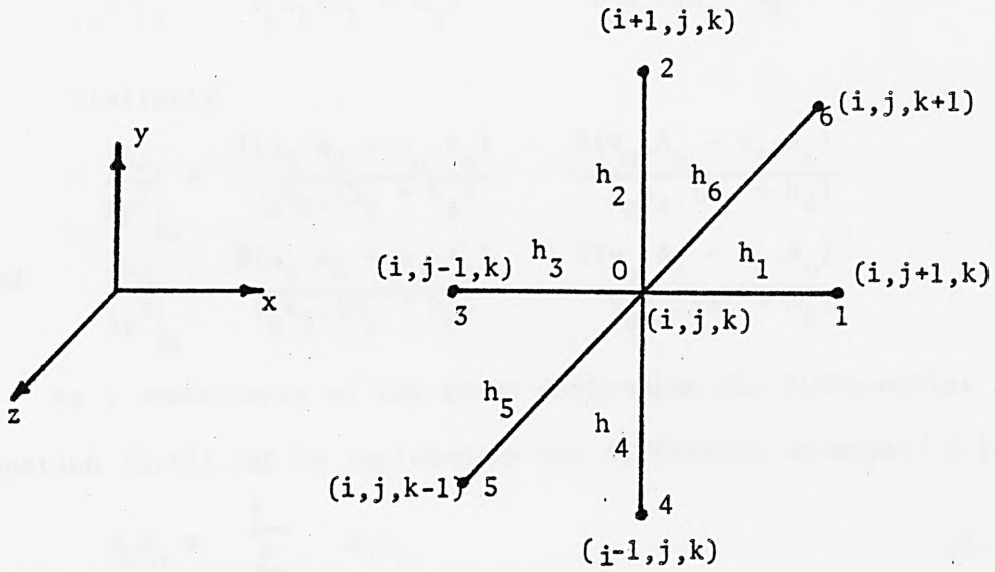

Fig. 3.1. A typical three dimensional lattice

$$\nu_1 . h_3 . A_1 + \nu_3 . h_1 . A_3 = (\nu_o h_3 + \nu_o h_1) . A_o + \tfrac{1}{2} h_1 h_3$$

$$(h_3 \nu_o + h_1 \nu_o) . \left(\frac{\partial^2 A}{\partial x^2}\right)_o$$

Hence

$$\left.\frac{\partial^2 A}{\partial x^2}\right|_o = \frac{2(A_1 \nu_1 - A_o . \nu_o)}{\nu_o h_1 (h_1 + h_3)} - \frac{2(A_o . \nu_o - A_3 . \nu_3)}{\nu_o h_3 . (h_1 + h_3)}$$

Similarly

$$\left.\frac{\partial^2 A}{\partial y^2}\right|_o = \frac{2(\nu_2 . A_2 - \nu_o . A_o)}{\nu_o h_2 . (h_2 + h_4)} - \frac{2(\nu_o . A_o - \nu_4 . A_4)}{\nu_o h_4 . (h_2 + h_4)}$$

and

$$\left.\frac{\partial^2 A}{\partial z^2}\right|_o = \frac{2(\nu_5 . A_5 - \nu_o . A_o)}{\nu_o h_5 . (h_5 + h_6)} - \frac{2(\nu_o . A_o - \nu_6 . A_6)}{\nu_o h_6 . (h_5 + h_6)}$$

As a consequence of the above derivation the differential equation (3.15) can be replaced by the difference equation (3.16)

$$\beta_o A_o = \sum_{i=1}^{6} \beta_i A_i \qquad (3.16)$$

where $\beta_o = \sum_{i=1}^{6} \beta_i$

$$\beta_1 = \frac{2\nu_1}{h_1 (h_1 + h_3)} \quad , \quad \beta_3 = \frac{2\nu_3}{h_3 (h_1 + h_3)}$$

$$\beta_2 = \frac{2\nu_2}{h_2 (h_2 + h_4)} \quad , \quad \beta_4 = \frac{2\nu_4}{h_4 (h_2 + h_4)}$$

$$\beta_5 = \frac{2\nu_5}{h_5 (h_5 + h_6)} \quad , \quad \beta_6 = \frac{2\nu_6}{h_6 (h_5 + h_6)}$$

By applying eq. (3.16) to the field differential equation derived earlier in the Governing equation section, the following corresponding finite-difference equations are obtained, see Figs. 3.1, 3.2 and 3.3

For the Homogeneous-Isotropic (HI) Non-conducting medium:

$$\bar{A}_o = \frac{1}{2 (q^2 p^2 + q^2 + p^2)} (q^2 p^2 . (\bar{A}_1 + \bar{A}_3) + p^2 . (\bar{A}_2 + \bar{A}_4) + q^2 . (\bar{A}_5 + \bar{A}_6)) \qquad (3.17)$$

For the HI conducting medium:

$$\bar{A}_o = \frac{1}{2(q^2p^2 + q^2 + p^2)} \left(q^2p^2 \cdot (\bar{A}_1 + \bar{A}_3) + p^2 \cdot (\bar{A}_2 + \bar{A}_4) + q^2(\bar{A}_5 + \bar{A}_6) + \mu_o\mu_r q^2p^2h^2\bar{J}\right) \quad (3.18)$$

For the HI conducting medium moving in x-direction at constant speed V:

$$\bar{A}_o = \frac{1}{\gamma} (\alpha \cdot \bar{A}_1 + \beta \cdot \bar{A}_3 + p^2 \cdot (\bar{A}_2 + \bar{A}_4) + q^2 \cdot (\bar{A}_5 + \bar{A}_6) + C) \quad (3.19)$$

For the homogenous anisotropic conducting medium:

$$Az_o = \frac{1}{2(s3(q^2p^2 + q^2) + p^2)} \left(q^2p^2 \cdot s3 \cdot (Az_1 + Az_3) + p^2 \cdot (Az_2 + Az_4) + q^2 s3 \cdot (Az_5 + Az_6) + \mu_o\mu_x q^2p^2h^2Jz\right) \quad (3.20a)$$

and

$$Ax_o = \frac{1}{2(q^2p^2 + q^2 + p^2)} \left(q^2p^2 \cdot (Ax_1 + Ax_3) + p^2 \cdot (Ax_2 + Ax_4) + q^2 \cdot (Ax_5 + Ax_6) + \mu_o\mu_y q^2p^2h^2Jx\right) \quad (3.20b)$$

where $\alpha = q^2p^2 (1. - 0.5\, \mu_o\mu_r\sigma\, hV_x)$

$\beta = q^2p^2 (1. + 0.5\, \mu_o\mu_r\sigma\, hV_x)$

$\gamma = 2(q^2p^2 + q^2 + p^2) + j\mu_o\mu_r\omega\sigma\, h^2q^2p^2)$

$C = o$ for the x-component of the MVP

$C = q^2p^2h^2\mu_o\mu_r\, V\sigma\, \psi$ for the z-component of the MVP

$\psi = \frac{\partial Ax}{\partial z}$ which is obtained after solving the x-component of the MVP

$\bar{A} = \hat{x}\, Ax + \hat{y}\, 0 + \hat{Z}\, Az$

$\bar{J} = \hat{x}\, Jx + \hat{y}\, 0 + \hat{Z}\, Jz$

$s3 = \mu_x/\mu_y$

$$\bar{A}_o = \bar{A}(i, j, k)$$

$$\bar{A}_1 = \bar{A}(i, j + 1, k) \quad , \quad \bar{A}_3 = \bar{A}(i, j - 1, k)$$

$$\bar{A}_2 = \bar{A}(i + 1, j, k) \quad , \quad \bar{A}_4 = \bar{A}(i - 1, j, k)$$

$$\bar{A}_5 = \bar{A}(i, j, k-1) \quad , \quad \bar{A}_6 = \bar{A}(i, j, k+1)$$

The above finite-difference equations are derived for the three-dimensional problem. In sections 3.7 and 3.8 finite difference equations for two and one dimensions are presented respectively. In each of them the two models of the primary winding are examined.

3.4 Boundary Conditions

It is often found that electrical or magnetic properties change significantly over distances which are infinitesimal with respect to the significant dimensions of an electromechanical system. Such changes usually occur at the surface of a medium or at an interface between media. In such cases the abrupt changes can be represented mathematically as a spatial discontunuity which produces boundary conditions on the electromagnetic variables.

In regions away from any surfaces, the usual finite difference approximations are both simple and accurate, even with comparatively large distances between nodes. But the principal reason for adopting a numerical formulation is to take into account the conditions imposed by boundaries and interfaces at which the material properties change and it is these which impose the main limitations, particularly in accuracy.

The four general boundary conditions to be satisfied at the interfaces of dissimilar media (see Figs. 3.2 and 3.3) may be derived from the electromagnetic equation given by eqs. (3.1) to (3.4) and these are given below:

For a stationary boundary, as well as for a moving boundary, the normal component of the flux density vector $\overline{B}$ must be continuous at the boundary.

$$Bn)_I = Bn)_{II}$$

where (n) denotes the normal to the surface. I and II denotes the two sides of the interface.

The boundary condition of the tangential component of the magnetic field intensity vector $\overline{H}$ is given as

$$\overline{Ht})_I - \overline{Ht})_{II} = \overline{K}$$

where (t) denotes the tangent to the surface, and K is the surface current density on the interface which is normal to the magnetic field intensity vector $\overline{Ht}$ and located on the same plane.

If there is no real surface current density on the interface, the above boundary condition becomes

$$\overline{Ht})_I = \overline{Ht})_{II}$$

The first boundary condition is automatically satisfied if the tangential components of the MVP are continuous at the surface

i.e. $$\overline{At})_I = \overline{At})_{II}$$

The more significant condition is the second boundary condition which in terms of the MVP is given by

$$\left(\frac{\partial \overline{At}}{\partial n} - \frac{\partial An}{\partial t} \right)_I = \frac{\mu_I}{\mu_{II}} \left(\frac{\partial \overline{At}}{\partial n} - \frac{\partial An}{\partial t} \right)_{II}$$

The discontinuity required by the above equation must be met entirely by both the tangential components of $\overline{A}$. The effect

of An is to change its magnitude.[43]

The above equation gives two components of $\bar{A}t$, one in each of the two tangential directions, which are independent of each other but dependent on An.

For the case where the y-axis is normal to the interface, the tangential components of the MVP become completely uncoupled, as it is assumed that Ay does not exist.

$$\left.\frac{\partial \bar{A}t}{\partial n}\right|_{I} = \frac{\mu_I}{\mu_{II}} \left.\frac{\partial \bar{A}t}{\partial n}\right|_{II}$$

But, for the case where either the x- or z-axis is normal to the interfaces, the tangential boundary condition will lead to coupling equations, and it becomes necessary to make local studies and perhaps practical assumptions to meet the problem. For instance, in defining $\bar{A}$ such that

$$\nabla \cdot (\nu \bar{A}) = 0$$

thus,
$$An)_I = \frac{\mu_I}{\mu_{II}} An)_{II}$$

this gives an uncoupled tangential interface

$$\left.\frac{\partial \bar{A}t}{\partial n}\right|_{I} = \frac{\mu_I}{\mu_{II}} \left.\frac{\partial \bar{A}t}{\partial n}\right|_{II}$$

The last two boundary conditions are imposed on the MVP at the magnetic interfaces.

For the electric field problem, analogous boundary conditions exist and these are, first, that the normal component of electric current density vector ($\bar{J}$) must be continuous at the boundary

$$Jn)_I = Jn)_{II}$$

and secondly, the tangential components of the electric field intensity vector $\bar{E}$ are also equal on both sides of the boundary

surface

$$\overline{Et)}_I = \overline{Et)}_{II}$$

where the tangential components of the field intensity vector require that

$$\overline{At)}_I = \overline{At)}_{II}$$

and the continuity of the normal component of the electric current density vector requires that

$$\sigma_I \, An)_I = \sigma_{II} An)_{II}$$

or in general by defining $\overline{A}$ such that

$$\nabla.(\sigma\overline{A}) = 0$$

at the interface, the gradient of the magnetic scalar potential ($\nabla\phi$) of eq. (3.8) is eliminated, and since ($\nabla.\overline{J}$) is zero, the equation for ϕ is $\nabla.(\sigma\nabla\phi) = 0$

Further examination for these local studies are presented in the boundary equations section.

A good deal of studies have been made by Carpenter[43] to examine the ways in which the magnetic description of the problem can be generalized. This paper gives a lot of confidence and support for the above formulation.

The specific boundary conditions which should be satisfied on the models interface (Figs. 3.2 and 3.3) are given below:

A) Three dimensional current sheet model (3DCM). The interfaces which have their normal boundary condition in y-direction are:

1. Stator (current sheet)/Air-gap, (1/2) interface;

at $y = M$, $K<x<L$, and $IT<z\leqslant IH$

$$B_{y1} = B_{y2} \qquad \text{Normal Component}$$

$$\left.\begin{aligned} H_{x1} - H_{x2} &= -Kz \\ H_{z1} - H_{z2} &= Kx \end{aligned}\right\} \qquad \text{Tangential components}$$

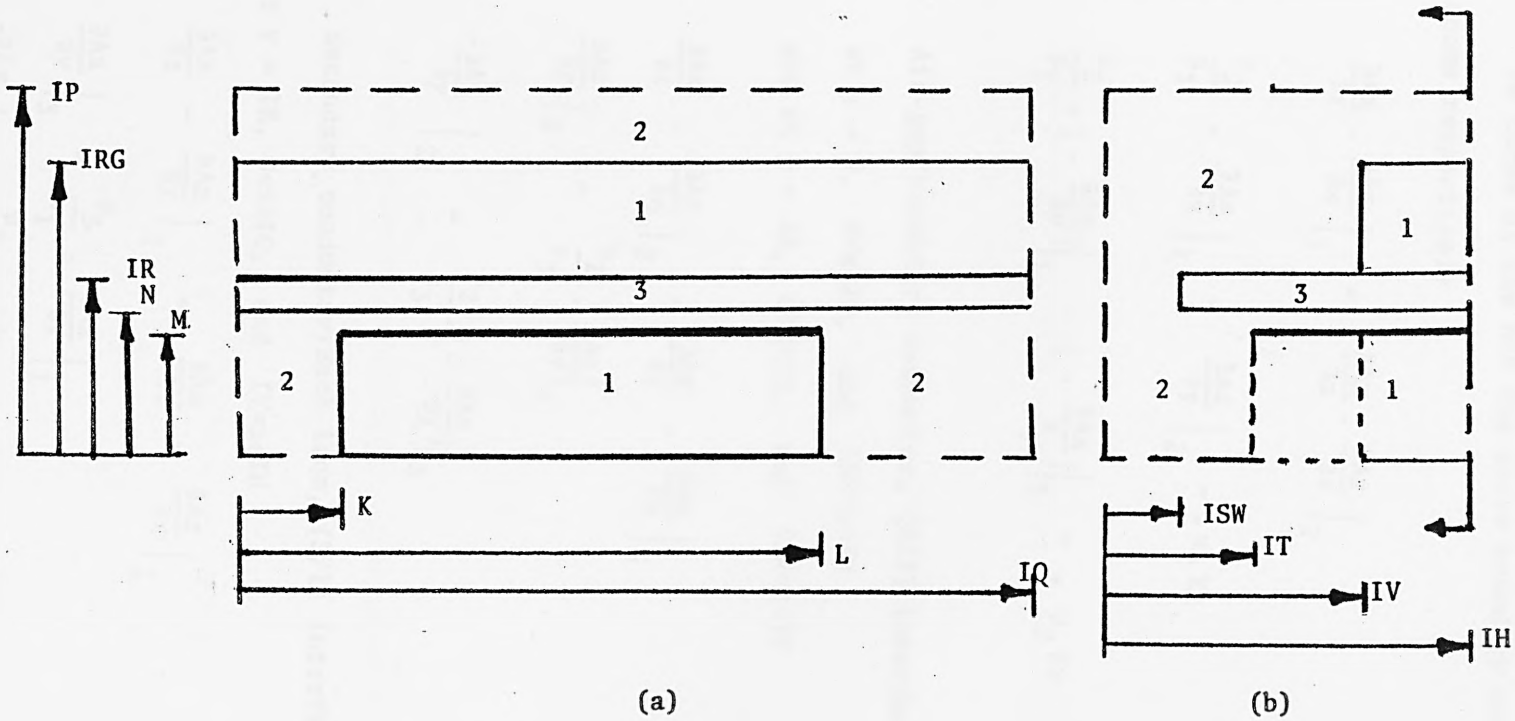

Fig. 3.2. Current sheet models of the LIM

In terms of the MVP the above boundary conditions become respectively

$$\frac{\partial Ax}{\partial z} - \frac{\partial Az}{\partial x}\bigg|_1 = \frac{\partial Ax}{\partial z} - \frac{\partial Az}{\partial z}\bigg|_2 \qquad (3.21a)$$

$$\frac{\mu_2}{\mu_1} \cdot \frac{\partial Az}{\partial y}\bigg|_1 - \frac{\partial Az}{\partial y}\bigg|_2 = -\mu_2 Kz \qquad (3.21b)$$

$$\frac{\mu_2}{\mu_1} \cdot \left[-\frac{\partial Ax}{\partial y}\right]\bigg|_1 - \left[-\frac{\partial Ax}{\partial y}\right]\bigg|_2 = +\mu_2 Kx \qquad (3.21c)$$

2. Air-gap/secondary conductor, (2/3) interface;

at y = N, $0<x<IQ$, and $ISW<z<IH$

and at y = IR, $0<x<IQ$, and $ISW<z<IV$

$$\frac{\partial Ax}{\partial z} - \frac{\partial Az}{\partial x}\bigg|_2 = \frac{\partial Ax}{\partial z} - \frac{\partial Az}{\partial x}\bigg|_3 \qquad (3.22a)$$

$$\frac{\partial Az}{\partial y}\bigg|_2 = \frac{\mu_2}{\mu_3} \cdot \frac{\partial Az}{\partial y}\bigg|_3 \qquad (3.22b)$$

$$-\frac{\partial Ax}{\partial y}\bigg|_2 = \frac{\mu_2}{\mu_3} \cdot \left[-\frac{\partial Ax}{\partial y}\right]\bigg|_3 \qquad (3.22c)$$

3. Secondary conductor/Back iron, (3/1) interface;

at y = IR, $0<x<IQ$, and $IV<z\leq IH$

$$\frac{\partial Ax}{\partial z} - \frac{\partial Az}{\partial x}\bigg|_3 = \frac{\partial Ax}{\partial z} - \frac{\partial Az}{\partial x}\bigg|_1 \qquad (3.22a)$$

$$\frac{\partial Az}{\partial y}\bigg|_3 = \frac{\mu_3}{\mu_1} \cdot \frac{\partial Az}{\partial y}\bigg|_1 \qquad (3.22b)$$

$$-\frac{\partial Ax}{\partial y}\bigg|_3 = \frac{\mu_3}{\mu_1} \cdot \left[-\frac{\partial Ax}{\partial y}\right]\bigg|_1 \qquad (3.22c)$$

The interfaces which have their normal boundary condition in x-direction are:

4. Air-gap/stator iron stack, (2/1) interface;

at x = K, or x = L, O<y<M, and IT<z<IH

$$\left.\frac{\partial Az}{\partial y}\right|_2 = \left.\frac{\partial Az}{\partial y}\right|_1 \tag{3.24a}$$

$$\left.\frac{\partial Ax}{\partial z} - \frac{\partial Az}{\partial x}\right|_2 = \frac{\mu_2}{\mu_1}\cdot\left.\left[\frac{\partial Ax}{\partial z} - \frac{\partial Az}{\partial x}\right]\right|_1 \tag{3.24b}$$

$$\left.-\frac{\partial Ax}{\partial y}\right|_2 = \frac{\mu_2}{\mu_1}\cdot\left.\left[-\frac{\partial Ax}{\partial y}\right]\right|_1 \tag{3.24c}$$

The interfaces which have their normal boundary condition in z-direction are:

5. Air-gap/Iron stack, (2/1) interface;

at z = IT, K<x<L, and O<y<M

and at z = IV, O<x<IQ, and IR<y<IRG

$$\left.-\frac{\partial Ax}{\partial y}\right|_2 = \left.-\frac{\partial Ax}{\partial y}\right|_1 \tag{3.25a}$$

$$\left.\frac{\partial Az}{\partial y}\right|_2 = \frac{\mu_2}{\mu_1}\left.\frac{\partial Az}{\partial y}\right|_1 \tag{3.25b}$$

$$\left.\frac{\partial Ax}{\partial z} - \frac{\partial Az}{\partial x}\right|_2 = \frac{\mu_2}{\mu_1}\left.\left[\frac{\partial Ax}{\partial z} - \frac{\partial Az}{\partial x}\right]\right|_1 \tag{3.25c}$$

6. Air-gap/secondary conductor, (2/3) interface;

at Z=ISW, O<x<IQ, and N<y<IR

$$\left.-\frac{\partial Ax}{\partial y}\right|_2 = \left.\frac{\partial Ax}{\partial y}\right|_3 \tag{3.26a}$$

$$\left.\frac{\partial Az}{\partial y}\right|_2 = \frac{\mu_2}{\mu_3}\cdot\left.\frac{\partial Az}{\partial y}\right|_3 \tag{3.26b}$$

$$\left.\frac{\partial Ax}{\partial z} - \frac{\partial Az}{\partial x}\right|_2 = \frac{\mu_2}{\mu_3}\cdot\left.\left[\frac{\partial Ax}{\partial z} - \frac{\partial Az}{\partial x}\right]\right|_3 \tag{3.26c}$$

B. Three-dimensional homogenous-anisotropic model (3DHM).

The same boundary conditions of the 3DCM are applied to 3DHM except the one concerning the current sheet, which is replaced by the following boundary conditions see Fig. 3.3. The interfaces which have their normal boundary condition in y-direction are:

7. Overhang zone/air-gap, (2/5) interface;

at y = M, K<x<L, and IT<z<IV

and at y = IS, K<x<L, and IT<z<IV

$$\frac{\partial Ax}{\partial z} - \frac{\partial Az}{\partial x}\Big|_2 = \frac{\partial Ax}{\partial z} - \frac{\partial Az}{\partial x}\Big|_5 \tag{3.27a}$$

$$\frac{\partial Az}{\partial y}\Big|_2 = \frac{\mu_2}{\mu_5} \cdot \frac{\partial Az}{\partial y}\Big|_5 \tag{3.27b}$$

$$-\frac{\partial Ax}{\partial y}\Big|_2 = \frac{\mu_2}{\mu_5} \cdot \left[-\frac{\partial Ax}{\partial y}\right]\Big|_5 \tag{3.27c}$$

8. Active zone/stator iron stack, (1/6) interface;

at y = M, K<x<L, and IV<z≤IH

$$\frac{\partial Ax}{\partial z} - \frac{\partial Az}{\partial x}\Big|_1 = \frac{\partial Ax}{\partial z} - \frac{\partial Az}{\partial x}\Big|_6 \tag{3.28a}$$

$$\frac{\partial Az}{\partial y}\Big|_1 = \frac{\mu_1}{\mu_{x6}} \cdot \frac{\partial Az}{\partial y}\Big|_6 \tag{3.28b}$$

$$-\frac{\partial Ax}{\partial y}\Big|_1 = \frac{\mu_1}{\mu_{z6}} \cdot \left[-\frac{\partial Ax}{\partial y}\right]\Big|_6 \tag{3.28c}$$

9. Active zone/air-gap, 2/6 interface;

at y = IS, K<x<L, and IV<z≤IH

$$\frac{\partial Ax}{\partial z} - \frac{\partial Az}{\partial x}\Big|_2 = \frac{\partial Ax}{\partial z} - \frac{\partial Az}{\partial x}\Big|_6 \tag{3.29a}$$

$$\frac{\partial Az}{\partial y}\Big|_2 = \frac{\mu_2}{\mu_{x6}} \cdot \frac{\partial Az}{\partial y}\Big|_6 \tag{3.29b}$$

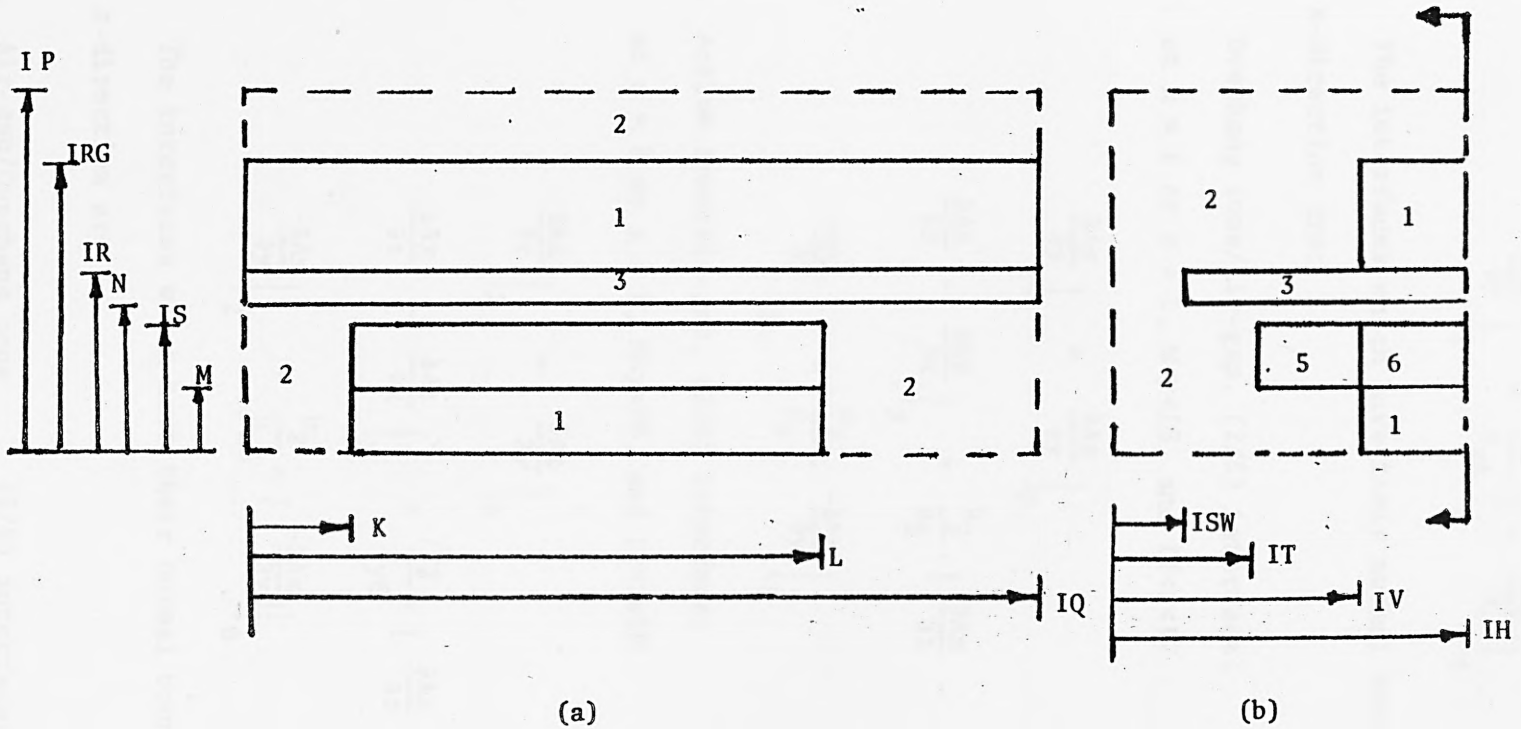

Fig. 3.3. Homogenous anisotropic models of the LIM

$$-\frac{\partial Ax}{\partial y}\Big|_2 = \frac{\mu_2}{\mu_{z6}} \cdot \left[-\frac{\partial Ax}{\partial y} \right]\Big|_6 \qquad (3.29c)$$

The interfaces which have their normal boundary condition in x-direction are:

10. Overhang zone/Air-gap, (2/5) interface;

at x = K or x = L, M<y<IS, and IT<z<IV

$$\frac{\partial Az}{\partial y}\Big|_2 = \frac{\partial Az}{\partial y}\Big|_5 \qquad (3.30a)$$

$$\frac{\partial Ax}{\partial z} - \frac{\partial Az}{\partial x}\Big|_2 = \frac{\mu_2}{\mu_5} \cdot \left[\frac{\partial Ax}{\partial z} - \frac{\partial Az}{\partial x} \right]\Big|_5 \qquad (3.30b)$$

$$\frac{-\partial Ax}{\partial y}\Big|_2 = \frac{\mu_2}{\mu_5} \cdot \frac{-\partial Ax}{\partial y}\Big|_5 \qquad (3.30c)$$

11. Active zone/Air-gap, (2/6) interface;

at x = K or x = L, M<y<IS, and IV<z≤IH

$$\frac{\partial Az}{\partial y}\Big|_2 = \frac{\partial Az}{\partial y}\Big|_6 \qquad (3.31a)$$

$$\frac{\partial Ax}{\partial z} - \frac{\partial Az}{\partial x}\Big|_2 = \frac{\mu_2}{\mu_{y6}} \cdot \left[\frac{\partial Ax}{\partial z} - \frac{\partial Az}{\partial x} \right]\Big|_6 \qquad (3.31b)$$

$$\frac{-\partial Ax}{\partial y}\Big|_2 = \frac{\mu_2}{\mu_{z6}} \cdot \left[\frac{-\partial Ax}{\partial y} \right]\Big|_6 \qquad (3.31c)$$

The interfaces which have their normal boundary condition in z-direction are:

12. Air-gap/Overhang zone (2/5) interface;

at z = IT, K<x<L, and M<y<IS

$$\frac{-\partial Ax}{\partial y}\Big|_2 = \frac{-\partial Ax}{\partial y}\Big|_5 \qquad (3.32a)$$

$$\frac{\partial Ax}{\partial z} - \frac{\partial Az}{\partial x}\Big|_2 = \frac{\mu_2}{\mu_5} \cdot \left[\frac{\partial Ax}{\partial z} - \frac{\partial Az}{\partial x} \right]\Big|_5 \qquad (3.32b)$$

$$\frac{\partial Az}{\partial y}\Big|_2 = \frac{\mu_2}{\mu_5} \cdot \frac{\partial Az}{\partial y}\Big|_5 \qquad (3.32c)$$

13. Active zone/Overhang zone, (6/5) interface;

at z = IV, K<x<L, and M<y<IS

The normal boundary condition of the current density is given by

$$J_{6z} = J_{5z}$$

and the tangential boundary condition of the field intensity is given by

$$E_{6x} = E_{5x}$$

which requires that

$$Ax_6 = Ax_5$$

At this interface the magnetic vector potential should satisfy the electric, as well as magnetic, requirements. These magnetic requirements are

$$\frac{-\partial Ax}{\partial y}\Big|_5 = \frac{-\partial Ax}{\partial y}\Big|_6$$

$$\frac{\partial Az}{\partial y}\Big|_5 = \frac{\mu_5}{\mu_{x6}} \cdot \frac{\partial Az}{\partial y}\Big|_6$$

$$\frac{\partial Ax}{\partial z} - \frac{\partial Az}{\partial x}\Big|_5 = \frac{\mu_5}{\mu_{y6}} \cdot \left[\frac{\partial Ax}{\partial z} - \frac{\partial Az}{\partial x} \right]\Big|_6$$

3.5 Boundary Equations

The models shown in Figs. 3.2 and 3.3 do not have curved boundaries. Therefore it is convenient, first of all, to select a grid structure parallel to the boundaries and choose a mesh spacing in which the nodes coincide with the boundaries. The above requirements can be met with a simplified computational molecule. The most critical spacing is that in the z and y directions; sufficient flexibility is achieved by letting $h_5 = h_6 = ph$, $h_2 = h_4 = qh$ or $h_2 = rh$ and $h_4 = qh$, and $h_1 = h_3 = h$ as shown in Fig. 3.1 .

All boundary conditions at the interfaces are of Neumann type (where the potentials of the interfaces are not specified). However, those at the periphery of the model are called Dirichlet boundary conditions (which specified the values of potentials at all points or along any numbers of segments of the boundary).

In order to derive the equation at the interface where no exciting current sheet is present, the following steps are taken: consider the interface between regions 2 and 3 at y = N, O<x<IQ, and ISW<z<IH

For the continuity of the magnetic vector potential between two regions, the normal boundary conditions may lead to:

$$Az\ (i, j, k)_2 = Az\ (i, j, k)_3$$

$$Ax\ (i, j, k)_2 = Ax\ (i, j, k)_3$$

The numerical forms of the tangential boundary conditions are given by

$$Az\ (i+1, j, K)_2 - Az\ (i-1, j, K)_2 = \frac{\mu_2}{\mu_3}\ [Az\ (i+1, j, k)_3 - Az\ (i-1, j, k)_3]$$

and

$$Ax\ (i+1,\ j,\ k)_2 - Ax\ (i-1,\ j,\ k)_2 = \frac{\mu_2}{\mu_3}\ [Ax\ (i+1,\ j,\ k)_3 - Ax\ (i-1,\ j,\ k)_3]$$

$Az\ (i-1,\ j,\ k)_2$, $Az\ (i+1,\ j,\ k)_3$, $Ax\ (i-1,\ j,\ k)_2$ and $Ax\ (i+1,\ j,\ k)_3$ have no physical meaning because they lie outside the region defined by labels 2 and 3. However, they can be used as mathematical quantities for the purpose of deriving the equation for the interface nodes[44]. These nodes are called fictitious nodes. The values of the fictitious nodes can be replaced by their equivalents in the region where they referred, eg. the value of $Az\ (i-1,\ j,\ k)_2$ can be determined from equation 3.19 and similarly $Ax\ (i-1,\ j,\ k)_2$ from the x-component version of eq. 3.19 . While $Az\ (i+1,\ j,\ k)_3$ and $Ax\ (i+1,\ j,\ k)_3$ from eq. (3.17).

Therefore from the above two tangential boundary conditions the z and x components of vector potential at node (i, j,k) on the interface of the two regions 2 and 3 are given by:

$$Az\ (i,j,k) = \frac{1}{2(q^2p^2+q^2+p^2) + \gamma}\ ((q^2p^2 + \alpha).Az\ (i,j+1,k) +$$

$$(q^2p^2 + \beta).Az(i,j-1,k) + 2p^2.(Az(i+1,j,k) + Az(i-1,j,k)) +$$

$$2q^2.(Az(i,j,k+1) + Az(i,j,k-1)) + C)$$

and

$$Ax(i,j,k) = \frac{1}{2(q^2p^2+q^2+p^2) + \gamma}\ ((q^2p^2+\alpha).Ax(i,j+1,k) +$$

$$(q^2p^2+\beta).Ax(i,j-1,k) + 2p^2.(Ax(i+1,j,k) + Ax(i-1,j,k))$$

$$+ 2q^2.(Ax(i,j,k-1) + Ax(i,j,k+1)))$$

where $\mu_2/\mu_3 = 1$

*For better presentation for the equation, the label of the nodes will be written hereafter by the number of the nodes

rather than the dimemsion arrays, eg. (0/(i,j,k), 1/(i,j+1,k), 2/(i+1,j,k), ...etc.).

Similarly the equations for the MVP at the other interfaces can be determined, except for stator current sheet/air boundary as it has no fictitious nodes.

The above procedure is applied directly to the boundaries where the y-axis is normal to the interfaces, since the y-component of the MVP is negligible. Thus the boundary conditions are uncoupled in terms of the MVP components. The situation for the boundaries where the z-or x-axis is normal to the interface is rather different, owing to the high coupling boundary condition due to the discountinuity of the tangential components of the boundary condition by the amount of the gradient of the normal component of the MVP. Therefore as mentioned earlier local studies should be made to uncouple the boundary equations before applying the procedure mentioned earlier:e.g. the boundary in which the x-axis is normal to the interface has the following boundary condition, see eq. (3.24).

$$\left.\frac{\partial Az}{\partial y}\right|_2 = \left.\frac{\partial Az}{\partial y}\right|_1 \tag{3.24a}$$

$$\left.\frac{\partial Ax}{\partial z} - \frac{\partial Az}{\partial x}\right|_2 = \frac{\mu_2}{\mu_1}\cdot\left.\left[\frac{\partial Ax}{\partial z} - \frac{\partial Az}{\partial x}\right]\right|_1 \tag{3.24b}$$

$$\left.-\frac{\partial Ax}{\partial y}\right|_2 = \frac{\mu_2}{\mu_1}\cdot\left.\left[-\frac{\partial Ax}{\partial y}\right]\right|_1 \tag{3.24c}$$

Eq. (3.24a) represents the normal components of flux density, while eqs. (3.24b) and (3.24c) represent the two tangential component of the magnetic field intensity.

The abrupt change in the tangential component of the magnetic field intensity at the interfaces suggest that the coupling which this imposes on the MVP components, as seen from eq. (3.24b), may be removed by defining an A function such that

$$\nabla . (\nu A) = 0$$

then
$$\frac{1}{\mu_2} Ax)_2 = \frac{1}{\mu_1} Ax)_1 \qquad (3.24I)$$

The above requirement is already satisfied by eq. (3.24c). Thus it is practical to split eq. (3.24b) into two parts to meet the new requirements and to discouple the MVP components, and these are

$$\left.\frac{\partial Ax}{\partial z}\right|_2 = \frac{\mu_2}{\mu_1} \cdot \left.\frac{\partial Ax}{\partial z}\right|_1$$

and

$$\left.\frac{\partial Az}{\partial x}\right|_2 = \frac{\mu_2}{\mu_1} \cdot \left.\frac{\partial Az}{\partial x}\right|_1 \qquad (3.24II)$$

Therefore the z-component of the MVP can be obtained from eqs. (3.24II) and (3.24a) using the procedure mentioned earlier which is concerned with the fictitious nodes, while eq. (3.24I) is used to determine the x-component of the MVP at the boundary.

Similarly for the interfaces which have their normal boundary condition in z-direction. The two boundary conditions which are used to determine the z and x component of the MVP are respectively

$$\frac{1}{\mu_2} \cdot Az)_2 = \frac{1}{\mu_1} \cdot Az_1)_1$$

$$\left.\frac{\partial Ax}{\partial z}\right|_2 = \frac{\mu_2}{\mu_1} \cdot \left.\frac{\partial Ax}{\partial z}\right|_1$$

The specific boundary equation which should be applied to the appropriate boundaries of the models are given below

A. 3DCM Boundary Equations

The boundary equations of the interfaces which have their normal boundary condition in y-direction are:

1. Stator (current sheet)/Air-gap, (1/2) interface; at y=M, K<x<L, and IT<z≤IH

$$\bar{A}_o = \frac{1}{(1+sl)} \quad (sl\bar{A}_4 + \bar{A}_2 + qh\mu_o\bar{K}) \tag{3.34}$$

2. Air-gap/secondary conductor, (2/3) interface; at y=N, O<x<IQ, and ISW<z<IH and at y = IR, O<x<IQ, and ISW<z<IV

$$\bar{A}_o = \frac{1}{2(q^2p^2+q^2+p^2) + \gamma} \quad [(q^2p^2 + \alpha).\bar{A}_1 + (q^2p^2+\beta).\bar{A}_3 + 2p^2.(\bar{A}_2 + \bar{A}_4) + 2q^2.(\bar{A}_5 + \bar{A}_6) + C] \tag{3.35}$$

3. Secondary conductor/Back iron, (3/1) interface; at y=IR, O<x<IQ, and IV<z≤IH

$$\bar{A}_o = \frac{1}{2(q^2p^2+q^2+p^2) + \gamma} \quad [(sl\,q^2p^2 + \alpha).\bar{A}_1 + (sl\,q^2p^2+\beta).\bar{A}_3 + 2p^2.(sl\,\bar{A}_2 + \bar{A}_4) + q^2.(1 + sl).(\bar{A}_5 + \bar{A}_6) + C] \tag{3.36}$$

as written in eq. 3.37

where $sl = \frac{1}{\mu_i}$

$\bar{K}$, $\bar{A}$ are either the z-or the x-components of the phasor value of the current sheet density and the magnetic vector potential respectively.

α, β, γ, and C are the constants defined by eq. (3.19).

The boundary equation of the interfaces which have their normal boundary condition in x-direction are:

4. Air-gap/stator iron stack, (2/1) interface; at

$x=k$, $0<y<M$, and $IT<z\leq IH$

$$Az_o = \frac{1}{2(q^2p^2+q^2+p^2)\cdot(1+s1)} [\, 2q^2p^2\cdot(s1\, Az_1 + Az_3) +$$

$$p^2\cdot(1+s1)\cdot(Az_2 + Az_4) + q^2\cdot(1+s1)\cdot(Az_5 + Az_6)] \qquad (3.37)$$

and at $x = L$, $0<y<M$, and $IT<z\leq IH$

$$Az_o = \frac{1}{2(q^2p^2+q^2+p^2)\cdot(1+s1)} [\, 2q^2p^2\cdot(Az_1 + s1\, Az_3) +$$

$$p^2\cdot(1+s1)\cdot(Az_2 + Az_4) + q^2\cdot(1+s1)\cdot(Az_5 + Az_6)] \qquad (3.38)$$

As mentioned earlier the x-component of the MVP at such interfaces are obtained by making use of the constraint given by eq. (3.24I). The x-component of the MVP at node (0) of (2/1) interface is defined by

$$Ax_{o/2} = s1\, Ax_{o/1}$$

But the above expression causes abrupt change in the magnitude of the MVP at the interfaces, and consequently the rate of convergence of the system may reduce considerably, and even goes to the opposite extreme with a large number of such nodes. However, the sensitivity of the finite difference techniques to the discontinuity of these nodes can be reduced by smoothing these values so that only a unique value at these nodes is considered, which is the average of the above two values.

i.e. $Ax_o = (Ax_{o/2} + Ax_{o/1})/2$

Hence $$Ax_o = \frac{1+s1}{2}\cdot Ax_{o/1} \qquad (3.39a)$$

or $$Ax_o = \frac{1+s1}{2s1}\cdot Ax_{o/2} \qquad (3.39b)$$

In the case where the system (the convergence rate) is still sensitive with these values, more approximation could be made to overcome the divergence of the system, and this could be done by replacing $Ax_{0/2}$ by Ax_3 and $Ax_{0/1}$ by Ax_1, where medium 2 is on the left hand side of medium 1.

Hence $Ax_o = (Ax_1 + Ax_3)/2$ (3.39c)

The boundary equation of the interfaces which have their normal boundary condition in z-direction are:

5. Air-gap/Iron stack, (2/1) interface; at

z = IT, K<x<L, and O<y<M and at z = IV, O<x<IQ and IR<y<IRG

$$Ax_o = \frac{1}{2(q^2p^2 + q^2 + p^2)\cdot(1+s1)} [q^2p^2\cdot(1+s1)\cdot(Ax_1+Ax_3) +$$

$$p^2\cdot(1+s1)\cdot(Ax_2+Ax_4) + 2q^2\cdot(s1\ Ax_5 + Ax_6)] \quad (3.40)$$

One the basis of the last argument the z-component of the MVP at the interface could be any of the following expressions, depending on the sensitivity of the system.

$$Az_o = \frac{1+s1}{2}\cdot Az_{o/1} \quad (3.41a)$$

$$Az_o = \frac{1+s1}{2s1}\cdot Az_{o/2} \quad (3.41b)$$

$$Az_o = (Az_5 + Az_6)/2 \quad (3.41c)$$

6. Air-gap/secondary conductor, (2/3) interface;

at z = ISW, O<x<IQ, and N<y<IR

$$Ax_o = \frac{1}{2(q^2p^2 + q^2 + p^2) + \gamma} [(q^2p^2 + \alpha)\cdot Ax_1 + (q^2p^2 + \beta)\cdot Ax_3$$

$$+ 2p^2\cdot(Ax_2 + Ax_4) + 2q^2\cdot(Ax_5 + Ax_6) + C] \quad (3.42a)$$

and $Az_o = (Az_5 + Az_6)/2$ (3.42b)

B. 3DHM Boundary Equations

The same boundary equations derived earlier may apply to the 3DHM wherever appropriate, and the same procedure is used to deduce

the rest of boundary equation of the boundaries shown in Fig. 3.3.

The boundary equations of the interfaces which have their normal boundary condition in y-direction are:

7. Overhang zone/Air-gap, (2/5) interface; at

y = M, K<x<L and IT<z<IV and at y = IS, K<x<L, and IT<z<IV

$$\bar{A}_o = \frac{1}{2(q^2p^2+q^2+p^2)} [q^2p^2.(\bar{A}_1+\bar{A}_3) + p^2.(\bar{A}_2+\bar{A}_4) + q^2.(\bar{A}_5 + \bar{A}_6) + 0.5\ \mu_o q^2p^2h^2\ \bar{J}o] \quad (3.43)$$

where $\bar{J}o$ = Joz for the z-component of the magnetic vector potential, while for the determination of the x-component of the MVP $\bar{J}o$ = Jox. $\bar{J}o$ is the overhang current density vector (A/m^2).

8. Active zone/stator iron stack, (1/6) interface; at

y = M, K<x<L, and IV<z≤IH

$$\bar{A}_o = \frac{1}{2((q^2p^2+q^2)s3+p^2) + 2(q^2p^2+q^2+p^2)s6} [q^2p^2.(s3+s6).(\bar{A}_1+\bar{A}_3) + 2p^2.(s6\ \bar{A}_4+\bar{A}_2)+q^2.(s3+s6).(\bar{A}_5+\bar{A}_6) + \mu_o\mu_r\ q^2p^2h^2\ \bar{J}a] \quad (3.44)$$

where for the z-component of the MVP

$$s3 = \frac{\mu_x}{\mu_y}\ ,\quad s6 = \frac{\mu_x}{\mu_i}\ ,\quad \mu_r = \mu_x$$

and $\bar{J}a$ = Jaz

while for x-comp. of the MVP

$$s3 = 1.0\ ,\ s6 = \frac{\mu_y}{\mu_i}\ ,\quad \mu_r = \mu_y,$$

and $\bar{J}a$ = Jax = 0

Ja is the active zone current density vector (A/m^2)

9. Active zone/Airgap, (2/6) interface; at

y = IS, K<x<L, and IV<z≤IH

$$\bar{A}_o = \frac{1}{2(s3(q^2p^2+q^2) + p^2) + 2(q^2p^2+q^2+p^2)\ s2} [q^2p^2\cdot(s3+s2)\cdot$$

$$(\bar{A}_1 + \bar{A}_3) + 2p^2\cdot(\bar{A}_4 + s2\bar{A}_2) + q^2\cdot(s3 + s2)\cdot(\bar{A}_5 + \bar{A}_6)$$

$$+ \mu_o\mu_r\ q^2p^2h^2\ \bar{Ja}] \qquad (3.45)$$

where for z-component of the MVP

$$s3 = \frac{\mu_x}{\mu_y}\ ,\quad s2 = \frac{\mu_x}{\mu_x}\ ,\quad \mu_r = \mu_x, \text{ and}$$

$$\bar{Ja} = Jaz$$

while for the x-component of the MVP

$$s3 = 1.0,\ s2 = \mu_y\ ,\ \mu_r = \mu_y$$

and $\bar{Ja} = Jax$

The boundary equations of the interfaces which have their normal boundary condition in x-direction are:

10 Overhang zone/Air-gap, (2/5) interfaces; at

x=K or x=L, M<y<IS, and IT<z<IV

$$Az_o = \frac{1}{2(q^2p^2+q^2+p^2)} [q^2p^2\cdot(Az_1 + Az_3) + p^2\cdot$$

$$(Az_2 + Az_4) + q^2\cdot(Az_5 + Az_6) + 0.5\mu_o\ q^2p^2h^2\ Joz] \qquad (3.46)$$

and the x-component of the MVP at the above interface is given by

$$Ax_o = (Ax_1 + Ax_3)/2 \qquad (3.47)$$

11. Active zone/Airgap, (2/6) interface; at

x = K, M<y<IS, and IV<z≤IH

$$Az_o = \frac{1}{2((q^2p^2+q^2)s3+p^2) + 2(q^2p^2+q^2+p^2)s2} [q^2p^2\cdot(s3\ Az_1 +$$

$$s2\ Az_3) + p^2\cdot(1+s2)\cdot(Az_2 + Az_4) + q^2\cdot(s3 + s2)\cdot$$

$$(Az_5 + Az_6) + \mu_o\mu_r q^2p^2h^2\ Jaz] \qquad (3.48)$$

where $s3 = \mu_x/\mu_y,\ s2 = \mu_x,\ \mu_r = \mu_x$

while the x-component of the MVP at the above interface is given by

$$Ax_o = (Ax_1 + Ax_3)/2 \qquad (3.49)$$

at x=L, M<y<IS, and IV<z<IH

$$Az_o = \frac{1}{2((q^2p^2+q^2)s3+p^2) + 2(q^2p^2+q^2+p^2)s2} [q^2p^2.(s2Az_1 + s3Az_3) + p^2.(1+s2).(Az_2+Az_4) + q^2.(s3 + s2).(Az_5+Az_6) + \mu_o\mu_r q^2p^2h^2 \, Jaz] \quad (3.50)$$

while the x-component of the MVP at the above interface is given by

$$Ax_o = (Ax_1 + Ax_3)/2 \quad (3.51)$$

The boundary equations of the interfaces which have their normal boundary condition in z-direction are:

12. Overhang/Airgap, (2/5) interface; at

z = IT, M<y<IS, and K<x<L

$$Ax_o = \frac{1}{2(q^2p^2+q^2+p^2)} [q^2p^2.(Ax_1 + Ax_3) + p^2.(Ax_2 + Ax_4) + q^2.(Ax_5 + Ax_6) + .5\mu_o q^2p^2h^2 \, Jox] \quad (3.52)$$

while the z-component of the MVP at the above interface is given by

$$Az_o = (Az_5 + Az_6)/2 \quad (3.53)$$

13. Active zone/overhang zone boundary; at

z = IV, K<x<L and M<y<IS

From the boundary conditions, it can be seen that the tangential component of the electric requirement and the normal component of the magnetic requirement are automatically satisfied if the tangential component of A is continuous:

$$Ax_5 = Ax_6$$

Therefore, by considering the same procedure described earlier in this section, the tangential component of the magnetic requirement reduces to

$$\left.\frac{\partial Ax}{\partial z}\right|_5 = \frac{\mu_5}{\mu_{y6}} \cdot \left.\frac{\partial Ax}{\partial z}\right|_6$$

thus the tangential component of the magnetic vector potential is obtained

$$Ax_o = \frac{1}{2(q^2p^2 + q^2 + p^2)\cdot(1 + s2)} [q^2p^2\cdot(1+s2)\cdot(Ax_1 + Ax_3) + p^2\cdot(1 + s2)\cdot(Ax_2+Ax_4) + 2q^2\cdot(s2\ Ax_5+Ax_6) + \mu_o\mu_x q^2p^2h^2\cdot(Jax + Jox)] \quad (3.54)$$

where $s2 = \mu_y$

For the z component of the magnetic vector potential, it is found that a satisfactory result is obtained in using the average expression given by

$$Az_o = (Az_5 + Az_6)/2 \quad (3.55)$$

However, the analytical argument of this component is different than the one which involves in the other boundaries, where the electric requirement is not considered.

3.6 Line-and dot-corners of the three-dimensional models

The other two classes of nodes which exists in the 3-D models are shown in Fig.3.4. The first one is the line-corner nodes which represents the nodes lying at a straight boundary line formed by the intersection of two surfaces (planes) and coincide with/or parallel to a mesh line. The second class is the dot-corner nodes, which represents the nodes lying at vertices of the block with their boundaries parallel to the mesh lines.

Making use of a method already described recently in literature[45],

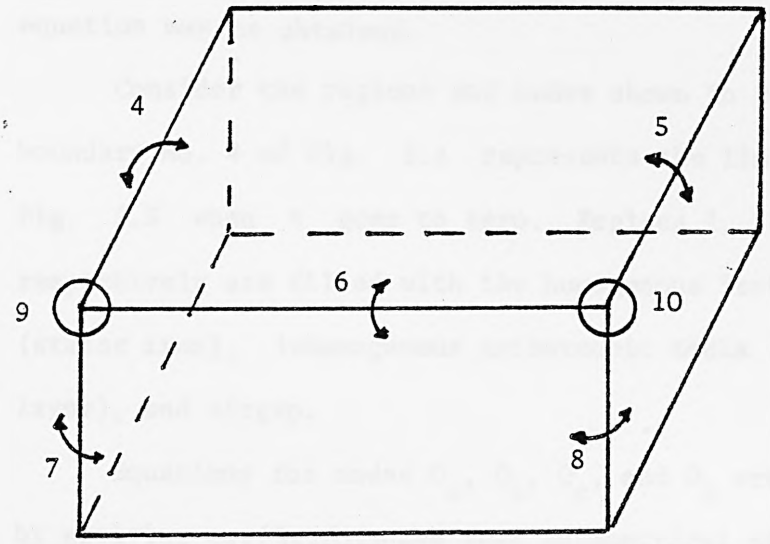

Fig. 3.4. The line- and dot-corners of the stator core

the finite difference expression of these nodes may be deduced. However, the approach presented in the paper is for two-dimensional problem. Further work is done here to extend the approach to determine the three-dimensional line and dot corners.

In this approach the interface is replaced by a transition layer of thickness t, within which the components of the relative permeability vary continuously from their values in one region to their values in the other. Consequently by applying the appropriate finite difference equation to the nodes lying at the surface of the layer and taking the limit of the transition layer thickness to zero, the desired finite-difference equation may be obtained.

Consider the regions and nodes shown in Fig. 3.5 where boundary No. 4 of Fig. 3.4 represents the limiting case of Fig. 3.5 when t goes to zero. Regions I, II, and III, respectively are filled with the homogenous isotropic media (stator iron), inhomogenous anisotropic media (transition layer), and airgap.

Equations for nodes O_a, O_b, O_c, and O_d are deduced by applying eq.(3.16) to the four asymmetrical stars centered at these nodes, as follows

$$B_{oa}A_{oa} = B_{1a}A_{1a} + B_{2d}A_{2d} + B_{3b}A_{3b} + B_{4a}A_{4a} + B_{5a}A_{5a} + B_{6c}A_{6c}$$

$$B_{ob}A_{ob} = B_{1a}A_{1a} + B_{2c}A_{2c} + B_{3b}A_{3b} + B_{4b}A_{4b} + B_{5b}A_{5b} + B_{6b}A_{6b}$$

$$B_{oc}A_{oc} = B_{1d}A_{1d} + B_{2c}A_{2c} + B_{3c}A_{3c} + B_{4b}A_{4b} + B_{5c}A_{5c} + B_{6c}A_{6c}$$

$$B_{od}A_{od} = B_{1d}A_{1d} + B_{2d}A_{2d} + B_{3c}A_{3c} + B_{4a}A_{4a} + B_{5d}A_{5d} + B_{6d}A_{6d}$$

When the limit ($t \to 0$) is taken the coefficients B_{ij} ($i=0,1,2,\ldots 6$, $j= a,b,c,d$) are expressed by the equation (3.16). Adding the last four equations result in

$$(B_{oa} + B_{ob} + B_{oc} + B_{od})A_o = (2B_{1a} + 2B_{1d})A_1 + (2B_{2d} + 2B_{2c})A_2 +$$
$$(2B_{3b} + 2B_{3c})A_3 + (2B_{4a} + 2B_{4b})A_4 +$$
$$(B_{5a} + B_{5b} + B_{5c} + B_{5d})A_5 +$$
$$(B_{6a} + B_{6b} + B_{6c} + B_{6d})A_6$$
$$= \frac{2}{h_1(h_1 + h_3)} \cdot (2\nu_i + 2\nu_a) \cdot A_1 +$$
$$\frac{2}{h_3(h_1 + h_3)} \cdot (2\nu_a + 2\nu_a) \cdot A_3 +$$
$$\frac{2}{h_2(h_2 + h_4)} \cdot (2\nu_a + 2\nu_a) \cdot A_2 +$$
$$\frac{2}{h_4(h_2 + h_4)} \cdot (2\nu_i + 2\nu_a) \cdot A_4 +$$
$$\frac{2}{h_5(h_5 + h_6)} \cdot (\nu_i + 3\nu_a) \cdot A_5 +$$
$$\frac{2}{h_6(h_5 + h_6)} \cdot (\nu_i + 3\nu_a) \cdot A_6$$

where $\nu_i = \frac{1}{\mu_o \mu_i}$ (iron reluctivity)

and $\nu_a = \frac{1}{\mu_o}$ (airgap reluctivity)

μ_i = iron relative permeability

Let $h_1 = h_3 = h$, $h_2 = h_4 = qh$, and $h_5 = h_6 = ph$

as used for the formulation of the other field equations.

Hence

$$A_o = \frac{1}{2(q^2p^2 + p^2 + q^2) \cdot (3 + s1)} [q^2p^2 \cdot (4A_3 + (2 + 2s1)A_1) +$$
$$p^2 \cdot (4A_2 + (2 + 2s1)\ A_4) + q^2 \cdot (3 + s1) \cdot (A_5 + A_6)] \qquad (3.56)$$

where $s1 = \frac{\nu_i}{\nu_a} = \frac{1}{\mu_i}$

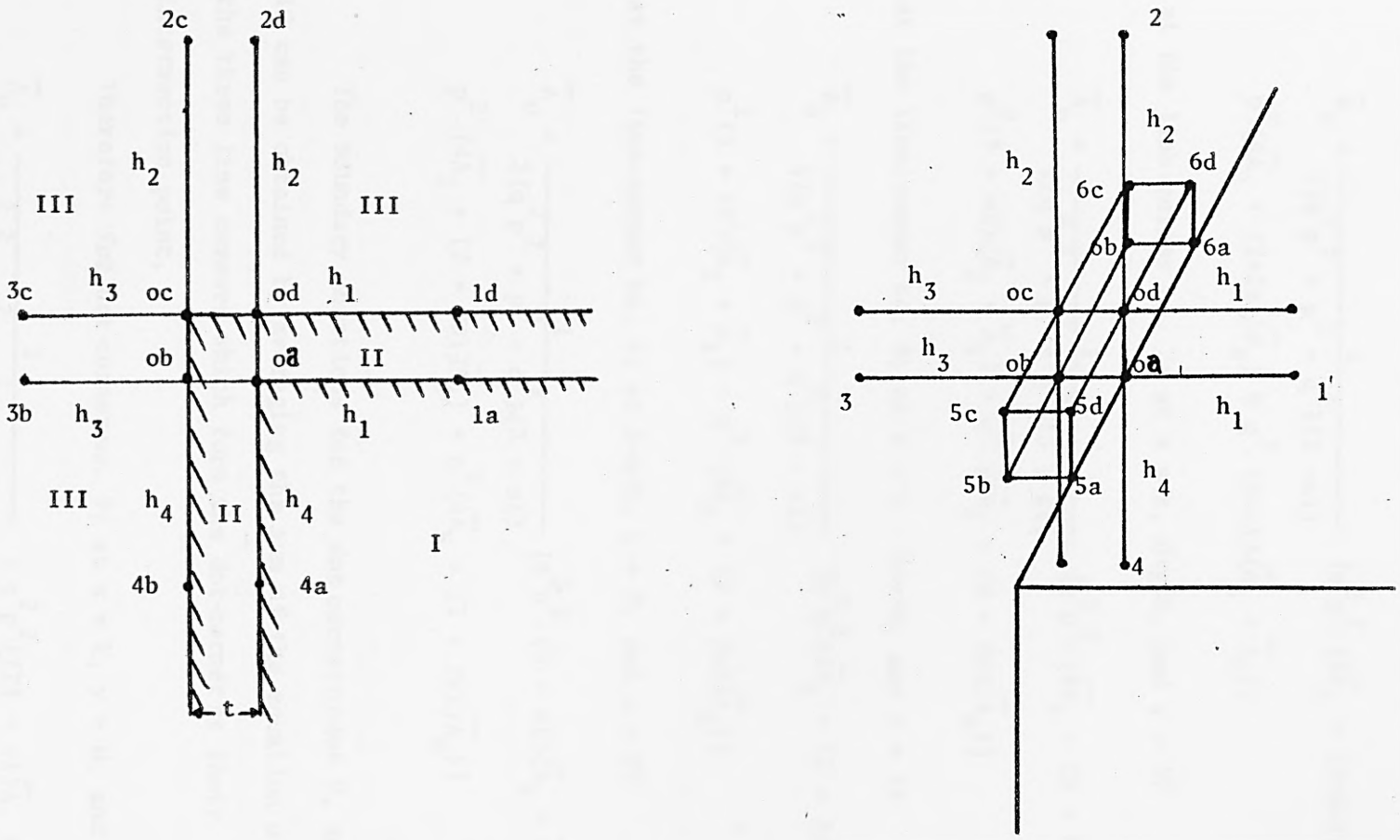

Fig. 3.5. Interface No. 4

Similarly;

at the line-corner no. 5; at x = L, y = M, and IT<z≤IH

$$\bar{A}_o = \frac{1}{2(q^2p^2 + p^2 + q^2)\cdot(3 + s1)} [q^2p^2\cdot(4\bar{A}_1 + (2+2s1)\bar{A}_3) +$$

$$p^2\cdot(4\bar{A}_2 + (2+2s1)\bar{A}_4) + q^2\cdot(3+s1)\cdot(\bar{A}_5 + \bar{A}_6)] \qquad (3.57)$$

at the line-corner no. 7; at x = k, 0<y<H, and z = IT

$$\bar{A}_o = \frac{1}{2(q^2p^2 + p^2 + q^2)\cdot(3 + s1)} [q^2p^2\cdot(4\bar{A}_3 + (2 + 2s1)\bar{A}_1) +$$

$$p^2\cdot(3 + s1)\cdot(\bar{A}_2 + \bar{A}_4) + q^2\cdot(4\bar{A}_5 + (2 + 2s1)\bar{A}_6)] \qquad (3.58)$$

at the line-corner no. 8; at x = L , 0<y<M, and z = IT

$$\bar{A}_o = \frac{1}{2(q^2p^2 + p^2 + q^2)\cdot(3 + s1)} [q^2p^2\cdot(4\bar{A}_1 + (2 + 2s1)\bar{A}_3) +$$

$$p^2\cdot(3 + s1)\cdot(\bar{A}_2 + \bar{A}_4) + q^2\cdot(4\bar{A}_5 + (2 + 2s1)\bar{A}_6)] \qquad (3.59)$$

at the line-corner no. 6; at k<x<L, y = M, and z = IT

$$\bar{A}_o = \frac{1}{2(q^2p^2 + p^2 + q^2)\cdot(3 + s1)} [q^2p^2\cdot(3 + s1)\cdot(\bar{A}_1 + \bar{A}_3) +$$

$$p^2\cdot(4\bar{A}_2 + (2 + 2s1)\bar{A}_4) + q^2\cdot(4\bar{A}_5 + (2 + 2s1)\bar{A}_6)] \qquad (3.60)$$

The boundary equations for the dot corner nodes 9, and 10 can be obtained by averaging the sum of the equation of the three line corners which form the dot-corner at their intersection point.

Therefore for dot-corner no. 9; at x = k, y = M, and z = IT

$$\bar{A}_o = \frac{1}{6(q^2p^2 + p^2 + q^2)\cdot(9 + 3s1)} [q^2p^2\cdot((11 + s1)\bar{A}_1 + (7 + 5s1)\cdot$$

$$\bar{A}_3) + p^2\cdot((11 + s1)\bar{A}_2 + (7 + 5s1)\bar{A}_4) + q^2\cdot((11 + s1)\bar{A}_5 +$$

$$(7 + 5s1)\bar{A}_6)] \qquad (3.61)$$

and for dot-corner no. 10; at x = L, y = M, and z = IT

$$\bar{A}_o = \frac{1}{6(q^2p^2 + p^2 + q^2)\cdot(9 + 3s1)} [q^2p^2.((11 + s1)\bar{A}_3 + (7 + 5s1)\bar{A}_1) + p^2.((11 + s1)\bar{A}_2 + (7 + 5s1)\bar{A}_4) + q^2.((11+s1)\bar{A}_5 + (7 + 5s1)\bar{A}_6)] \quad (3.62)$$

Following the same procedure, the boundary equation of the line-nodes corner between the back iron and secondary conductor (at O<x<IQ, y = IR, z = IV) is obtained, see Figs. 3.2 , 3.3 , and 3.6 .

$$\bar{A}_o = \frac{1}{(q^2p^2 + p^2 + q^2)\cdot(1 + s1) + 2\gamma} [(q^2p^2.(1 + s1) + 2\alpha)\bar{A}_1 + (q^2p^2.(1 + s1) + 2\beta)\bar{A}_3 + p^2.(2(1 + s1)\bar{A}_2 + 4\bar{A}_4) + q^2.(2(1 + s1)\bar{A}_6 + 4\bar{A}_5)] \quad (3.61)$$

The equation of the line corner at the intersection of the secondary conduction with the airgap, at z = ISW, o<x<IQ, and y = N, or y = IR is given by

$$\bar{A}_o = \frac{1}{6(q^2p^2 + q^2 + p^2) + \gamma} [(3q^2p^2 + \alpha)\bar{A}_1 + (3q^2p^2 + \beta)\bar{A}_3 + 4p^2.(\bar{A}_2 + \bar{A}_4) + 4q^2.(\bar{A}_5 + \bar{A}_6)] \quad (3.64)$$

In addition to the last line and dot-corners,the following boundary equations concerning the line- and dot-corners involved in the geometry of the primary winding-equivalent media of the 3DHM are used, where the same bases of the last precedure are applied, see Fig. 3.7 .

For the line-corners, 1, 4, and 5, and dot-corner no. 11;

$$\bar{A}_o = \frac{1}{2(q^2p^2 + q^2 + p^2)} [q^2p^2.(\bar{A}_1 + \bar{A}_3) + p^2.(\bar{A}_2 + \bar{A}_4) + q^2.(\bar{A}_5 + \bar{A}_6) + .25\,\mu_o\, q^2p^2h^2\,\bar{J}_o] \quad (3.65)$$

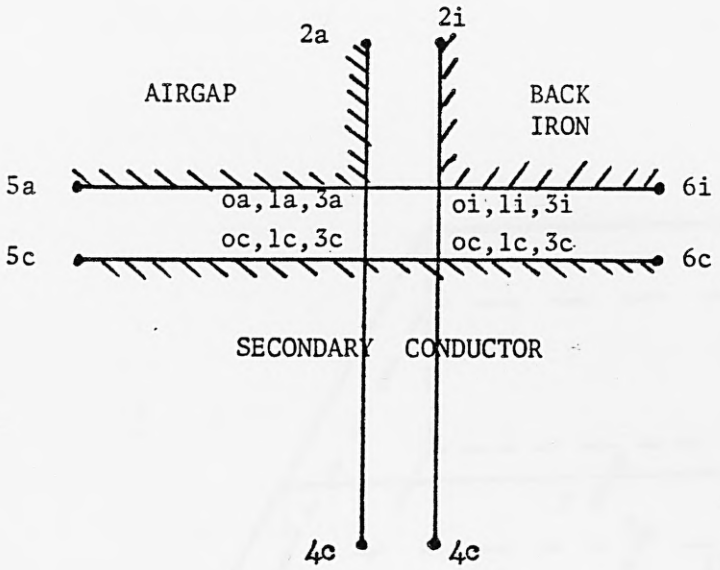

Fig. 3.6. Line-nodes corner; the back iron, airgap and secondary conductor are separated by a transition layer

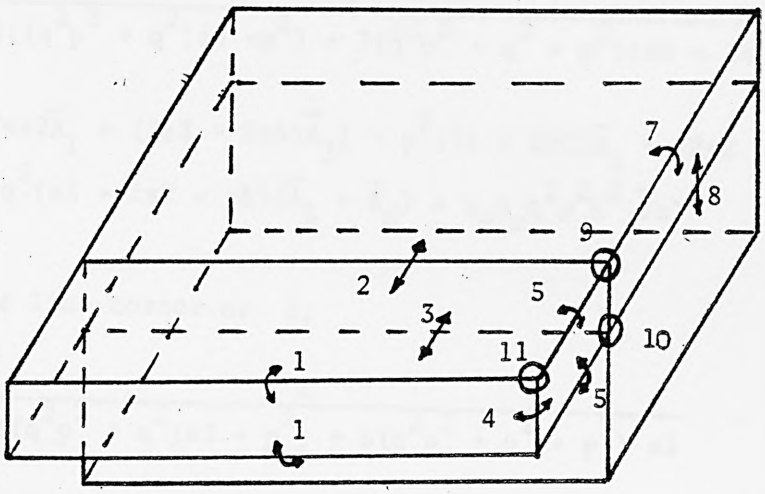

Fig. 3.7. The line- and dot-corners of the primary winding zones of 3DHM model

For the line-corner no. 7;

$$\bar{A}_o = \frac{1}{2((q^2p^2 + q^2)s3 + p^2) + 6(q^2p^2 + q^2 + p^2)s2} [q^2p^2(4s2\bar{A}_1$$

$$+ (2s2 + 2s3)\bar{A}_3) + p^2(4s2\bar{A}_2 + (2s2 + 2)\bar{A}_4) +$$

$$q^2(3s2 + s3)(\bar{A}_5 + \bar{A}_6) + \mu_o\mu_r q^2p^2h^2 \bar{J}a] \qquad (3.66)$$

For the line-corner no. 8;

$$\bar{A}_o = \frac{1}{2((q^2p^2 + q^2)s3 + p^2) + 2(q^2p^2 + q^2 + p^2)(s6 + 2s2)}$$

$$(q^2p^2(4s2\bar{A}_1 + (2s3 + 2s6)\bar{A}_3) + p^2((2 + 2s2)\bar{A}_2 + (2s2 + 2s6)\cdot$$

$$\bar{A}_4) + q^2(s3 + 2s2 + s6)(\bar{A}_5 + \bar{A}_6) + \mu_o\mu_r q^2p^2h^2 \bar{J}a) \qquad (3.67)$$

For the line-corner no. 2;

$$\bar{A}_o = \frac{1}{2((q^2p^2 + q^2)s3 + p^2) + 6(q^2p^2 + q^2 + p^2)\, s2}$$

$$[q^2p^2\cdot(s3 + 3s2)\cdot(\bar{A}_1 + \bar{A}_3) + p^2(4s2\bar{A}_2 + 2(s2 + 1)\bar{A}_4) + q^2\cdot$$

$$(4s2\bar{A}_5 + 2(s2 + s3)\bar{A}_6) + \mu_o\mu\, q^2p^2h^2(\bar{J}o + \mu_r \bar{J}a)] \qquad (3.68)$$

For line-corner no. 6;

$$\bar{A}_o = \frac{1}{2((q^2p^2 + q^2)s3 + p^2)\; 6(q^2p^2 + q^2 + p^2)\; s2} [q^2p^2(4s2\bar{A}_1$$

$$+2(s2 + s3)\bar{A}_3) + p^2(1 + 3s2)(\bar{A}_2 + \bar{A}_4) + q^2(4s2A_5 +$$

$$2(s2 + s3)\bar{A}_6) + \mu_o q^2p^2h^2\, (\bar{J}o + \mu_r \bar{J}a)] \qquad (3.69)$$

For line-corner no. 3;

$$\bar{A}_o = \frac{1}{2((q^2p^2 + q^2)s3 + p^2) + 2(q^2p^2 + q^2 + p^2)(s6 + 2s2)}$$

$$[q^2p^2(s3 + s6 + 2s2)(\bar{A}_1 + \bar{A}_3) + p^2((2 + 2s2)\bar{A}_2 + 2(s2 + 2s6)\cdot \bar{A}_4) + q^2((2s2 + 2s6)\bar{A}_6 + 4s2\bar{A}_5) + \mu_o q^2 p^2 h^2(\bar{J}o + \mu_r \bar{J}a)] \quad (3.70)$$

where for the determination of z-component of the MVP

$$s3 = \mu_x/\mu_y \quad , \quad s2 = \mu_x/\mu_o$$

$$s6 = \mu_x/\mu_i \quad , \quad \mu_r = \mu_x,$$

$$\bar{J}a = Jza \quad , \quad \text{and } \bar{J}o = Jzo$$

while for the calculation of x-component of the MVP

$$s3 = 1 \quad , \quad s2 = \mu_y/\mu_o$$

$$s6 = \mu_y/\mu_i \quad , \quad \mu_r = \mu_y$$

$$\bar{J}a = Jxa = 0$$

$$\bar{J}o = Jxo$$

For the dot-corner no. 9;

The boundary equation of this corner is obtained by averaging the sum of the finite difference equations at node (O) of the line-corners no. 2, 5, 6, and 7.

$$\bar{A}_o = \frac{1}{CA} [q^2p^2((s3 + 11s2 + 1)\bar{A}_1 + (1 + 5s3 + 7s2)\bar{A}_3) + p^2((11s2 + 2)\bar{A}_2 + (7s2 + 6)\bar{A}_4) + q^2((11s2 + s3 + 1)\cdot \bar{A}_5 + (7s2 + 5s3 + 1)\bar{A}_6) + \mu_o q^2 p^2 h^2(3\mu_r \bar{J}a + 2.25 \bar{J}o)] \quad (3.71)$$

For the dot-corner no. 10;

The boundary equation of the above corner is obtained by averaging the sum of the equation at node (0) of the line corners no. 6, 8, 5, and 3 of Fig. 3.7 and no. 8 of Fig. 3.4

$$\bar{A}_o = \frac{1}{CB} \; [q^2p^2.((5 + s3 + s6 + 10s2)\bar{A}_1 + (3 + 2s1 + 4s2 + 5s3 + 3s6)\bar{A}_3) + p^2.((9 + s1 + 7s2)\bar{A}_2 + (5 + s1 + 7s2 + 4s6)\bar{A}_4) + q^2.((5 + 10s2 + s3 + s6)\bar{A}_5 + (3 + 2s1 + 6s2 + 3s3 + 3s6)\bar{A}_6) + 3\,\mu_o q^2 p^2 h^2\,(\mu_r \bar{Ja} + \bar{Jo})] \qquad (3.72)$$

where $CA = (q^2p^2 + q^2).(6s3 + 18s2 + 2) + p^2.(18s2 + 8)$ and $CB = (q^2p^2 + q^2).(6s3 + 4s6 + 14s2 + 2s1 + 8) + p^2.(14 + 2s1 + 14s2 + 4s6)$

3.7 Finite Difference Representation of Two-Dimensional Models

As mentioned earlier, by reducing the current distribution from two- to one-dimension and the flux density distribution from three- to two-dimension, the analysis will be reduced from three- to two-dimensional. Thus the two-dimensional analysis could be considered as a particular case of the three-dimensional analysis.

Figs. 3.2a and 3.3a represents the two-dimensional current sheet model and the two-dimensional homogenous model respectively.

The boundary conditions of these two models are the same as that for the three dimensional model where the third-dimension of the members in z-axis is considered to be infinite.

Having used the procedures adapted earlier, the Laplace, Poisson and the boundary equations are obtained, where only the z-component of the magnetic vector potential exists. Typical rectangular mesh used for the nodes pattern is shown in Fig. (3.8)

The finite difference equations which apply to the two-dimensional models to determine the z-component of the MVP (Az) are:

For the non-conducting medium;

$$A_o = \frac{1}{2(q^2 + 1)} [q^2(A_1 + A_3) + (A_2 + A_4)] \qquad (3.73)$$

For the conducting medium moving in x-direction at constant speed.V.

$$A_o = \frac{1}{\gamma} [\alpha A_1 + \beta A_3 + (A_2 + A_4)] \qquad (3.74)$$

where $\gamma = 2(q^2 + 1) + j\omega\mu_o\mu_r\sigma q^2h^2$

$\alpha = q^2(1 - 0.5\ \mu_o\mu_r hV_x)$

$\beta = q^2(1 + 0.5\ \mu_o\mu_r hV_x)$

For the homogeneous isotropic conducting medium;

$$A_o = \frac{1}{2(q^2 + 1)} [q^2.(A_1 + A_3) + (A_2 + A_4) + \mu_o\mu_r q^2h^2J_z] \qquad (3.75)$$

For the homogeneous anisotropic conducting medium;

$$A_o = \frac{1}{2(q^2\mu_x + \mu_y)} [\mu_x q^2.(A_1 + A_3) + \mu_y.(A_2 + A_4) + \mu_o\mu_x\mu_y q^2h^2Jz] \qquad (3.76a)$$

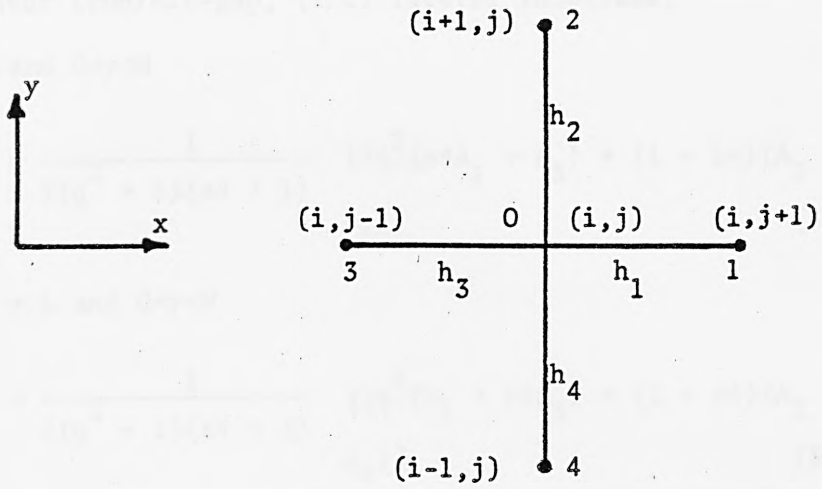

Fig. 3.8. Typical rectangular mesh

or $$A_o = \frac{1}{2(s2q^2 + 1)} [s2q^2(A_1 + A_3) + (A_2 + A_4) + \mu_o\mu_x q^2 h^2 Jz] \quad (3.76b)$$

and the common finite boundary equations of the two models are as follows;

Stator iron/Air-gap, (1/2) lateral interface;

at x = k and O<y<M

$$A_o = \frac{1}{2(q^2 + 1)\cdot(s4 + 1)} [2q^2(s4A_1 + A_3) + (1 + s4)\cdot(A_2 + A_4)] \quad (3.77)$$

and at x = L and O<y<M

$$A_o = \frac{1}{2(q^2 + 1)\cdot(s4 + 1)} [(q^2(A_1 + s4A_3) + (1 + s4)\cdot(A_2 + A_4)] \quad (3.78)$$

Air-gap/secondary conductor, (2/3) interface;

at y = N and O<x<IQ

$$A_o = \frac{1}{2(q^2 + 1) + \gamma} [(q^2 + \alpha)A_1 + (q^2 + \beta)A_3 + 2(A_2 + A_4)] \quad (3.79)$$

Secondary conductor/Laminated Back Iron, (3/1) interface

at y = IR and O<x<IQ

$$A_o = \frac{1}{2s1(q^2 + 1) + \gamma} [(s1q^2 + \alpha)A_1 + (s1q^2 + \beta)A_3 + 2(s1A_2 + A_4)] \quad (3.80)$$

For the current sheet-airgap interfaces in the 2DCM the following equation is used at

at y = M, and O<x<IQ

$$A_o = \frac{1}{(1 + s1)} (s1A_4 + A_2 + qh\mu_o Kz) \quad (3.81)$$

while for the 2DHM model eq. 3.81 is replaced by the set of equations given below:

Stator iron/primary winding, (1/5) interface;

at $y = M$ and $K<x<L$

$$A_o = \frac{1}{2(s2q^2 + 1) + 2s1(q^2 + 1)} [q^2.(s1 + s2).(A_1 + A_3) + 2(A_2 + s1A_4) + \mu_o\mu_x q^2h^2J] \quad (3.82)$$

and for the primary winding at $M<y<IS$, $k<x<L$ eq. 3.73 is applied.

Primary winding/Airgap, (5/2) interface;

at $y = IS$ and $K<x<L$

$$A_o = \frac{1}{2(q^2s2 + 1) + 2(q^2 + 1)s3)} [q^2.(s3 + s2).(A_1 + A_3) + 2(A_4 + s3\ A_2) + \mu_o\mu_x\ q^2h^2J] \quad (3.83)$$

Primary winding/Airgap, (5/2) lateral interface;

at $x = K$ and $M<y<IS$

$$A_o = \frac{1}{2(q^2s2 + 1) + 2(q^2 + 1)s3} [q^2.(2s3\ A_1 + 2s2\ A_3) + (1 + s3).(A_4 + A_2) + \mu_o\mu_x q^2h^2J] \quad (3.84)$$

and at $x = L$ and $M<y<IS$

$$A_o = \frac{1}{2(q^2s2 + 1) + 2(q^2 + 1)\ s3} [q^2.(2s3A_3 + 2s2A_1) + (1 + s3).(A_4 + A_2) + \mu_o\mu_x q^2h^2J] \quad (3.85)$$

For the 2DCM, the finite difference expression of the corners are given below;

at $x = k$ and $y = IS$.

$$A_o = \frac{1}{(q^2 + 1).(3 + s1)} [q^2.((1 + s1)A_1 + 2A_3) + (1 + s1).A_4 + 2A_2\ ] \quad (3.86)$$

at x = L, and y = IS

$$A_o = \frac{1}{(q^2 + 1)\cdot(3 + s1)} [q^2\cdot((1 + s1)A_3 + 2A_1) + (1 + s1)\cdot A_4 + 2A_2 \ ] \quad (3.87)$$

While the expression for the 2DHM corners which are obtained by applying the transition layer method mentioned earlier, are given below:

at x = K, y = IS

$$A_o = \frac{1}{2(q^2 s2 + 1) + 2(q^2 + 1)\cdot(3s3)} [q^2\cdot(2(s2 + s3)A_1 + 4s3\cdot A_3) + 4s3\ A_2 + 2(1 + s3)A_4 + \mu_o\mu_x q^2h^2J] \quad (3.88)$$

at x = L, y = IS

$$A_o = \frac{1}{2(q^2 s2 + 1) + 2(q^2 + 1)(3s3)} [q^2\cdot(4s3A_1 + 2(s2 + s3)\cdot A_1) + 4s3\ A_2 + 2(1 + s3)A_4 + \mu_o\mu_x q^2h^2J] \quad (3.89)$$

at x = k, y = M

$$A_o = \frac{1}{2(q^2(s2 + s3) + 2) + 2(q^2 + 1)\cdot(s1 + s3)} [q^2\cdot(2(s2 + s1)\cdot A_1 + 4s3A_3) + 2(1 + s3)A_2 + 2(1 + s1)A_4 + \mu_o\mu_x q^2h^2J] \quad (3.90)$$

at x = L, y = M

$$A_o = \frac{1}{2(q^2(s2 + s3)+2)+2(q^2+1)\cdot(s1 + s3)} [q^2\cdot(2(s2 + s1)\ A_3 + 4s3A_1) + 2(1 + s3)A_2 + 2(1 + s1)A_4 + \mu_o\mu_x q^2h^2J] \quad (3.91)$$

where $s1 = 1/\mu_i$, $s2 = \mu_x/\mu_y$

$s3 = \mu_x/1$, $s4 = \mu_x/\mu_i$

$A_1 = A(i,j+1)$, $A_3 = A(i,j-1)$

$A_2 = A(i+1,j)$, $A_4 = A(i-1,j)$

$A_o = A(i,j)$

3.8 Finite Difference Representation of One-Dimensional Models

In order to facilitate the analysis for the one-dimensional models, all the variables are considered to be varying sinusoidially with time and with the direction of motion, in addition to the assumptions made earlier for two dimensional model.

In these models, the longitudinal end effect is completely neglected. Both the transverse edge effect and skin effect can be considered as same as in the two dimensional model.

Figs. 3.9a and 3.9b show the current sheet representation and the homogenous anisotropic representation of the one-dimensional model respectively. The nodes at which the potential are calculated are distributed along the line YY only.

The field equations of this model are;

For non-conducting media

$$-k^2 Az + \frac{\partial^2 Az}{\partial y^2} = 0 \qquad (3.92)$$

For isotropic homogenous current source media

$$-k^2 Az + \frac{\partial^2 Az}{\partial y^2} = -\mu_o \mu_r Jz \qquad (3.93)$$

For anisotropic homogenous current source media,

$$-\frac{1}{\mu_y} k^2 Az + \frac{1}{\mu_x} \cdot \frac{\partial^2 Az}{\partial y^2} = -\mu_o Jz \qquad (3.94)$$

For conducting medium moving with velocity v in x-direction

$$-k^2 Az + \frac{\partial^2 Az}{\partial y^2} = +\mu_o \sigma s \omega Az \qquad (3.95)$$

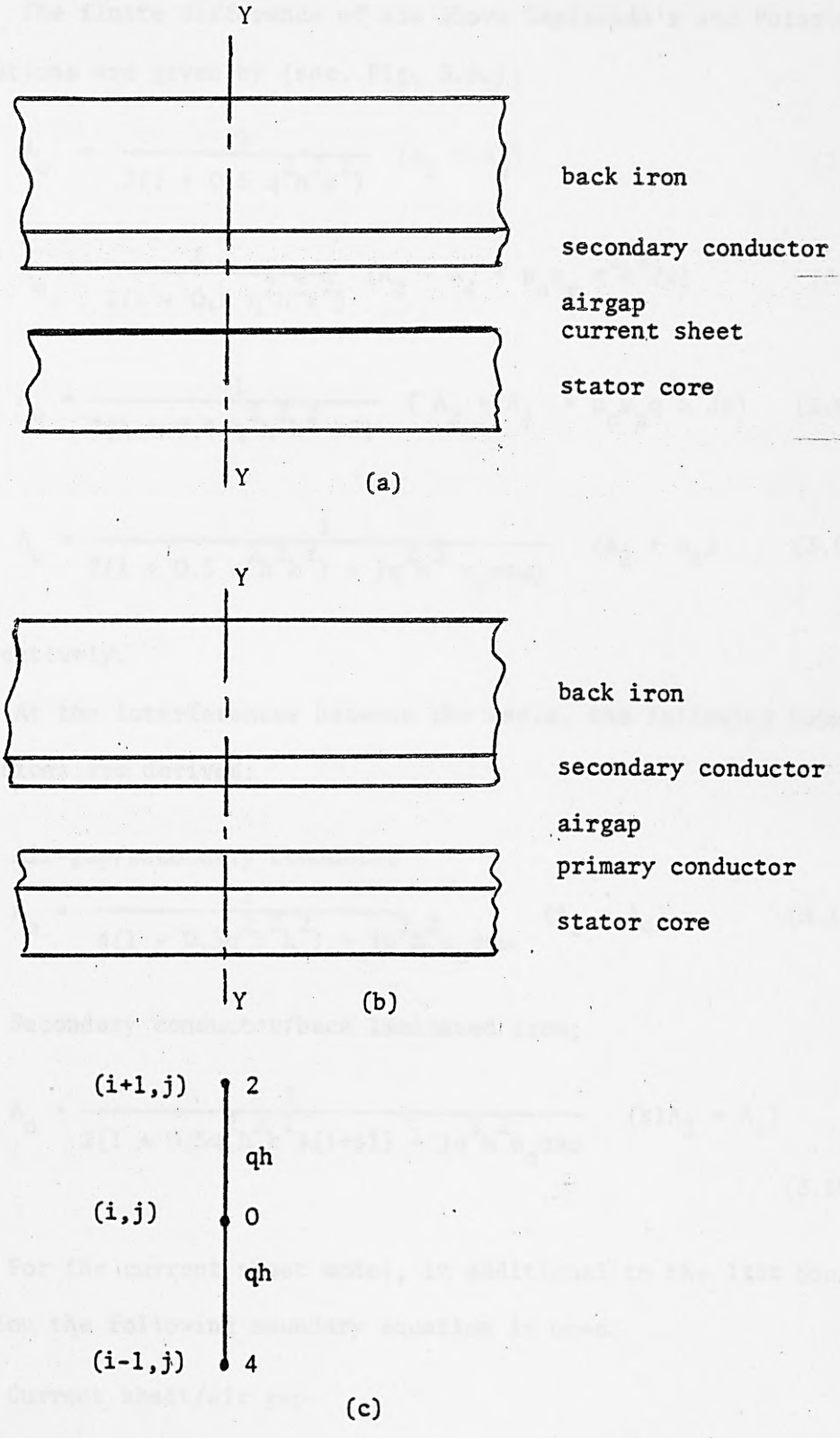

Fig. 3.9. The one-dimensional models of the LIM

The finite difference of the above Laplacian's and Poisson's equations are given by (see. Fig. 3.9c);

$$A_o = \frac{1}{2(1 + 0.5\, q^2h^2k^2)} (A_2 + A_4) \tag{3.96}$$

$$A_o = \frac{1}{2(1 + 0.5\, q^2h^2k^2)} (A_2 + A_4 + \mu_o\mu_r\, q^2h^2Jz) \tag{3.97}$$

$$A_o = \frac{1}{2(1 + 0.5\, q^2h^2k^2\, s3)} (A_2 + A_4 + \mu_o\mu_x q^2h^2Jz) \tag{3.98}$$

and $$A_o = \frac{1}{2(1 + 0.5\, q^2h^2k^2) + jq^2h^2\, \mu_o\sigma s\omega)} (A_2 + A_4) \tag{3.99}$$

respectively.

At the interferences between the media, the following boundary equations are derived;

Air-gap/secondary conductor

$$A_o = \frac{2}{4(1 + 0.5q^2h^2k^2) + jq^2h^2\mu_o\sigma s\omega} (A_2 + A_4) \tag{3.100}$$

Secondary conductor/back laminated iron;

$$A_o = \frac{2}{2(1 + 0.5q^2h^2k^2)\cdot(1+s1) + jq^2h^2\mu_o\sigma s\omega} (s1A_2 + A_4) \tag{3.101}$$

For the current sheet model, in additional to the last boundary equation the following boundary equation is used.

Current sheet/air gap

$$A_o = \frac{1}{1 + s1} (A_2 + s1A_4 + \mu_o qhKz) \tag{3.102}$$

Whilst for the homogenous anisotropic model, the last equation is replaced by;

at Stator iron/primary winding

$$A_o = \frac{2}{2(1 + 0.5q^2h^2k^2s3) + 2\ (1 + 0.5q^2h^2k^2)}\ (A_2 + s4\ A_4 + .5\ \mu_o\mu_x q^2h^2Jz) \qquad (3.103)$$

and at primary winding/air gap

$$A_o = \frac{2}{2(1 + 0.5q^2h^2k^2s3) + 2s2\ (1 + 0.5q^2h^2k^2)}\ (s2A_2 + A_4 + .5\ \mu_o\mu_x q^2h^2Jz) \qquad (3.104)$$

Where s1, s2, s3 and s4 are the permeability ratios as defined earlier in section 3.7.

CHAPTER 4

PERFORMANCE DERIVATION AND COMPUTER PROGRAMING

4.1 Introduction

The state variables of performance characteristics of the linear induction motor are derived in terms of the magnetic vector potentials which are formulated in discrete forms.

The state variables which are derived in this chapter include the flux density components, the current density components of the secondary member, 3-axis forces, terminal voltage, losses, input and output power.

The technique used to solve the problem specified in the models described in the previous chapter is discussed in section 4.3. In section 4.4 the flow chart and the basic considerations of the computer programmes developed to solve the three, two and one dimensional models are presented.

4.2 Performance Derivation

4.2.1 Magnetic and Electric Field Densities

The flux density components can be determined by making use of

$$\overline{B} = \nabla X \overline{A} = \begin{vmatrix} \hat{x} & \hat{y} & \hat{z} \\ \frac{\partial}{\partial x} & \frac{\partial}{\partial y} & \frac{\partial}{\partial z} \\ Ax & 0 & Az \end{vmatrix}$$

and these are

$$B_x = \frac{\partial Az}{\partial y} \tag{4.1a}$$

$$B_y = -\left(\frac{\partial Az}{\partial x} - \frac{\partial Ax}{\partial z}\right) \tag{4.1b}$$

$$B_z = -\frac{\partial Ax}{\partial y} \tag{4.1c}$$

where in terms of the MVP values at the lattice node (i, j, k), the flux density components maybe given by:

$$B_x(i, j, k) = \frac{Az(i+1, j, k) - Az(i-1, j, k)}{h_2 + h_4} \tag{4.2a}$$

$$B_y(i, j, k) = \frac{Ax(i, j, k-1) - Ax(i, j, k+1)}{h_5 + h_6} - \frac{Az(i, j+1, k) - Az(i, j-1, k)}{h_1 + h_3} \tag{4.2b}$$

$$B_z(i, j, k) = \frac{Ax(i-1, j, k) - Ax(i+1, j, k)}{h_2 + h_4} \tag{4.2c}$$

Inaccurracies may occur in the above formulation, since the calculations of gradient are based on a linear variation in potential, and the value of the gradient may be formed as the small difference between large numbers in which error is presented. To minimize both of these inaccuracies, it is therefore sometimes necessary to use rather more elaborate formulae of the evaluation of a gradient. Such expressions are derived by fitting a polynomial expansion to the values of potential at points lying on a straight line along which the gradient is required[44]. For example, in terms of potential at four points equally spaced the density components are obtained as below:

$$B_x(i,j,k) = \frac{1}{6qh} \cdot (Az(i-2,j,k) - 6\ Az(i-1,j,k) + 3\ Az(i,j,k) + 2\ Az(i+1,j,k) \quad (4.3a)$$

$$B_y(i,j,k) = \frac{1}{6ph} \cdot (Ax(i,j,k+2) - 6\ Ax(i,j,k+1) + 3\ Ax(i,j,k) + 2\ Ax(i,j,k-1)) - \frac{1}{6h} \cdot (Az(i,j-2,k) + 3\ Az(i,j,k) + 2\ Az(i,j+1,k) - 6\ Az(i,j-1,k)) \quad (4.3b)$$

$$B_z(i,j,k) = \frac{-1}{6qh} \cdot (Ax(i-2,j,k) - 6\ Ax(i-1,j,k) + 3\ Ax(i,j,k) + 2\ Ax(i+1,j,k)) \quad (4.3c)$$

The total flux density at node (i,j,k) is

$$B(i,j,k) = \hat{x}\ B_x(i,j,k) + \hat{y}\ B_y(i,j,k) + \hat{z}\ B_z(i,j,k)$$

The electric field components in the moving medium are obtained from

$$\overline{E} = -\frac{\partial \overline{A}}{\partial t} + V_x\ X\ \overline{B}$$

Hence for steady state system

$$E_z = -j\omega Az + V_x B_y$$

and $E_x = -j\omega Ax$

and the corresponding current density components of the moving medium at a discrete form are given by:

$$Jz(i,j,k) = -j\omega Az(i,j,k) + V_x \sigma B_y(i,j,k) \quad (4.4a)$$

and $$Jx(i,j,k) = -j\omega Ax(i,j,k) \quad (4.4b)$$

The total electric current density at node (i,j,k) is

$$\overline{J}(i,j,k) = \hat{x}Jx\ (i,j,k) + \hat{z}Jz(i,j,k)$$

4.2.2 Force Components

In the class of problem undertaken in this thesis, the force density, F (N/m^3) is calculated by making use of the Lorentz force equation:

$$\bar{f} = \mathrm{Re}\ (\bar{J} \times \bar{B}) = \mathrm{Re} \begin{vmatrix} \hat{x} & \hat{y} & \hat{z} \\ Jx & 0 & Jz \\ B_x & B_y & B_z \end{vmatrix}$$

$$\text{Thus } \bar{f} = \hat{x}\ \mathrm{Re}(-Jz \cdot B_y^*) + \hat{y}\ \mathrm{Re}\ (Jz \cdot B_x^* - Jx \cdot B_z^*) + \hat{z}\ \mathrm{Re}\ (Jx B_y^*)$$

where the x-component represents the propulsion force, the y-component represents the normal force, and the z-component represents the lateral force.

The time-average values of these three-axes force densities are given by:

$$f_x = -\frac{1}{2}\ \mathrm{Re}\ (Jz \cdot B_y^*)$$

$$f_y = \mathrm{Re}\ (Jz \cdot B_x^* - Jx \cdot B_z^*)$$

$$f_z = \mathrm{Re}\ (Jx \cdot B_y^*)$$

In discrete form, these components become

$$f_x(i,j,k) = -\frac{1}{2}\ \mathrm{Re}\ [(-j\omega\sigma Az(i,j,k) + \sigma V_x B_y(i,j,k)) \cdot B_y^*(i,j,k)] \qquad (4.5a)$$

$$f_y(i,j,k) = \frac{1}{2}\ \mathrm{Re}\ [(-j\omega\sigma A_z(i,j,k) + \sigma V_x B_y(i,j,k)) \cdot B_x^*(i,j,k) - ((-j\omega\sigma)Ax(i,j,k)) \cdot B_z(i,j,k)^*] \qquad (4.5b)$$

$$f_z(i,j,k) = \frac{1}{2}\ \mathrm{Re}\ [-j\omega\sigma Ax(i,j,k) \cdot B_y^*(i,j,k)] \qquad (4.5c)$$

where the MVP components and the flux density components are in complex form.

To find the total force components in the secondary, it is necessary to integrate over the volume of the secondary member as given below:

$$F_x = \int_{Z=ISW}^{2IH} \int_{y=N}^{IR} \int_{x=0}^{IQ} f_x \, dx \, dy \, dz$$

Since the model is considered symmetrical about the x-y plane at z=IH, the force equation becomes:

$$F_x = 2 \int_{ISW}^{IH} \int_{N}^{IR} \int_{0}^{IQ} f_x \, dx \, dy \, dz$$

and similarly

$$F_y = 2 \int_{ISW}^{IH} \int_{N}^{IR} \int_{0}^{IQ} f_y \, dx \, dy \, dz$$

The lateral force (F_z) vanishes at the normal condition of operation. In other words, when the secondary is entirely centralized with respect to the centre plane (x-y) of the primary member,

$$F_z = \int_{ISW}^{2IH} \int_{N}^{IR} \int_{0}^{IQ} f_z \, dx \, dy \, dz = 0$$

The attraction force density (N/m^2) between the secondary and primary is controlled by the normal component of the flux density. The time average of the attraction force is thus given by:

$$F_{ya}(i,j,k) = \frac{1}{2\mu_o} |B_y(i,j,k)|^2 \qquad (4.5d)$$

where B_y is evaluated at the surface of the back iron.

To determine the total attraction force, a surface numerical integration should be applied to the last equation. The numerical integration method which is used to determine the effective force is shown in appendix B.

4.2.3 Power and Efficiency

Several authors[46,47] have discussed the application of Poynting's theorem to the calculation of energy transfer between stator and rotor in electrical machines. They reveal that the radial component of the vector

$$\overline{P} = \overline{E} \times \overline{H} = \begin{vmatrix} \hat{x} & \hat{y} & \hat{z} \\ E_x & E_y & E_z \\ H_x & H_y & H_z \end{vmatrix}$$

integrated over the whole air-gap surface corresponds to the synchronous power of a conventional machine.

Consequently, in a three-dimensional field problem, the time-average air gap cross-power density in the y-direction is given by:

$$S_a = \frac{1}{2}(E_z H_x^* - E_x H_z^*) \qquad (4.6a)$$

The specific active air gap cross-power density in terms of the MVP becomes

$$P_a(i,j,k) = \frac{1}{2\mu_o} \cdot \mathrm{Re}\,(-j\omega A_z(i,j,k) B_x^*(i,j,k) + (j\omega A_x(i,j,k)) \cdot B_z(i,j,k)^*) \qquad (4.6b)$$

The specific air gap reactive power density which supplies the reactive power of both the magnetizing and secondary leakage reactances is given by:

$$Q_a(i,j,k) = \frac{1}{2\mu_o} \cdot \mathrm{Im}\ (-j\omega Az(i,j,k) B_x^*(i,j,k) + (j\omega Ax(i,j,k)) B_z(i,j,k)^*) \qquad (4.6c)$$

where $S_a = P_a + j\ Q_a$

The developed output-mechanical power is given by

$$P_o = V_x F_x$$

where P_o can be the specific (power per volume) or the total power produced by the secondary.

The time average ohmic losses per volume of the secondary conductor in discrete form is given by

$$P_L(i,j,k) = \frac{1}{2\sigma} \cdot \mathrm{Re}\ (J_s(i,j,k) J_s^*(i,j,k)) \qquad (4.7)$$

The input power to the secondary conductor is given by

$$P_i = P_o + P_L$$

which represents the air gap cross power as well.

Therefore the input power of the secondary may be determined by two alternatives as shown earlier, where the Poynting vector approach gives a satisfactory result for the steady state air gap field distribution.

The total values of the specific powers mentioned earlier are obtained by applying the numerical integration method shown in appendix B.

Having determined the primary impedance by the conventional method shown in the next section, the efficiency (η) and the power

factor (PF) of the LIM are obtained by making use of the following formulae.

$$\eta = \frac{P_o}{P_a + P_s} \tag{4.8}$$

$$PF = \frac{P_a + P_s}{S} \tag{4.9}$$

Also the power factor may be determined from the phase angle of the terminal voltage.

where $S = S_a + S_s$

$S_s = P_s + j\,Q_s$

4.2.4 Terminal Voltage

The primary phase voltage of the LIM is given by

$$V = R_1 \cdot I_1 + jX_1 \cdot I_1 - E_1 \tag{4.10}$$

the primary resistance is:

$$R_1 = \rho \frac{L_t N}{a}$$

where N = number of turns in series per phase.

L_t = mean length of the coil.

a = total copper area of the coil.

X_1 is the primary leakage reactance [48], which for both the 2DCM and 3DCM representation is given by:

$$X_1 = \omega \mu_o N_s^2 (\lambda L_i + 2\sqrt{q}\ (L_m - L_i))$$

while for 2DHM representation it is given by:

$$X_1 = \omega \mu_o N_s^2 (\lambda Li)$$

and for 3DHM representation it is:

$$X_1 = 0$$

Since the slot and overhang leakage have already been taken into account.

In the above expressions,

N_s = Number of turns per slot

L_i = Length of the conductor in the active zone

L_m = mean length of the half turn

q = number of slots/phase/pole

λ = slot permanence

The electric field intensity is defined by

$$\nabla X \overline{E} = - \frac{\partial \overline{B}}{\partial t}$$

Substituting of eq. (3.7) in the above equation gives the general form:

$$\overline{E} = - \frac{\partial \overline{A}}{\partial t} + E_s$$

The electromotive force induced in the closed stationary loop is given by

$$\overline{E}_c = - \int_c \frac{\partial \overline{A}}{\partial t} \, d\ell + \int_c E_s d\ell$$

where the term E_s is referred to the electrostatic field due to the changes on the conductor surface. However, the integral of this constant term around a closed loop is always zero[49], that is

$$\int_c E_s \, d\ell = 0$$

thus,

$$\overline{E}_c = - \int_c \frac{\partial \overline{A}}{\partial t} \, d\ell$$

In terms of the MVP component this becomes

$$E_c = - \int \frac{\partial Az}{\partial t} \, dz - \int \frac{\partial Ax}{\partial t} \, dx \qquad (4.11)$$

Therefore the induced phase voltage in the primary winding of the LIM is:

$$E_1 = -j\sqrt{2}\,\omega\, N_{eff}\left(\sum_{i=1}^{5} C_i Az_i\, Dz + \sum_{i=1}^{5} C_i Ax_i\, Dx\right) \qquad (4.12)$$

where N_{eff} = No. of coil sides in (q) slots of completely filled slots

i = the No. of poles

Az_i = the overall z-component of the MVP of each group of coils per phase per pole.

Ax_i = The overall x-component of the MVP of each group of coils per phase per pole.

C_i = a factor referring to either the completely filled slots ($C_i = 1$) or the half filled slots ($C_i = \frac{1}{2}$)

Dx, Dz = mesh interval in x and z direction respectively.

4.3 The Solution Technique

4.3.1 Basic Considerations

As mentioned earlier (Ch. 3), some form of iterative procedure is adopted to find out the solution of the field problem from the simple form of finite difference equations. Theoretically, these procedures could be applied using hand or machine computation. Such computation, when carried out by hand, has traditionally been termed "relaxation" and when the computation is carried out by machine, the procedure is usually referred to as "iteration".

In solving the finite-difference equations using machine computation, the technique, as with hand relaxation, is to modify continuously values of potential until all the equations are

satisfied to a sufficient degree of accuracy. All machine methods are characterized by two main features which distinguish them from hand methods. First, they are designed for use in a completely automatic cycle in which each of the equations (and so each node in the system) is considered in turn throughout the calculation. Secondly, improved values of potential are determined directly from the difference equations.

The Gauss-Seidel method is a common iterative technique for solving sets of simultaneous linear algebraic equations. It is marked by the simplicity and the ease with which it may be programmed for computer.

The potential at each node (n) and for each iteration (m) is calculated using eq. (3.16.)

$$A_n^m = \sum_{i=1}^{6} \beta_i A_i / \beta_o \qquad (4.13)$$

In order to test the convergence of the solution as the number of iterations is increased, the changes in the potential between successive iteration and for each node should be examined. A typical way of determining the difference is to let

$$\Delta A = A_n^{(m)} - A_n^{(m-1)} \qquad (4.14a)$$

Alternatively, the relative difference may be tested using the expression:

$$\Delta A = \frac{A_n^{(m)} - A_n^{(m-1)}}{A_n^{(m)}} \qquad (4.14b)$$

The process is iterated until all $A_n^{(m)}$ are sufficiently close to $A_n^{(m-1)}$ by a small positive tolerance ε. Thus if

$$\text{Max. } \Delta A < \varepsilon$$

where the maximum is taken over all n, the iteration process is stopped.

The choice of starting values for the potential does not normally affect whether the Gauss-Seidel process converges, and often has comparatively little effect on the number of iterations required.

4.3.2 The Successive Over-Relaxation Method

The main disadvantage of the Gauss-Seidel method is that it may require a large amount of computing time to achieve convergence. But it is often possible to improve the rate of convergence by a technique generally known as over-relaxation. The technique used in the developed programmes of this work is known as the "successive over-relaxation method" (SOR) or, sometimes the "extrapolated Liebmann Method". This is still regarded as supreme for general purpose application to practical problems because of its simplicity and rapid convergence.

The technique can be derived from the "Gauss-Seidel Method". Eq.(4.13) provides new estimates $A_n^{(m)}$ which are closer to the required solution than the $A_n^{(m-1)}$ provided that the process is converging. Over-relaxation applies a limited amount of extrapolation from these two sets of estimates towards the final solution. Thus, if $A_n^{(m)}$ are the values-obtained from eq.(4.13) the extrapolated values after the mth iteration are

$$A_n^{(m)} = A_n^{(m-1)} + \Gamma \cdot (A_n^{(m)} - A_n^{(m-1)}) \qquad (4.15)$$

where Γ is known as the "convergence" or "relaxation factor", which is the same for all the nodes. For a particular set of linear equations there is an optimum value of Γ, normally in the range $1 < \Gamma < 2$. When $\Gamma = 1$, the process reduces to the Gauss-Seidel method, whilst the use of too large a value of Γ can cause divergence.

The optimum relaxation factor can be determined by a number of equations using an iterative technique as well. Although some work[50] has been done for this purpose, certain precautions are necessary in applying the method and it becomes worth while only in the case of large and slowly converging problems.

According to the method described in the literature[51] the improved value of the relaxation factor is estimated by

$$\Gamma_i = 2\left[1+\left(1 - \frac{(C_1 + \Gamma - 1)^2}{C_1 \cdot \Gamma^2}\right)^{\frac{1}{2}}\right]^{-1} \qquad (4.16)$$

where C_1 is the ratio of the norm of the residuals of the last two successive iterations of each set.

$$C_1 = \frac{n^{(k)}}{n^{(k-1)}}$$

For example, if the number of iterations in each set is 12, then

$$n^{(k)} = \sum_{i=2}^{N-1} \Delta A \quad \text{at iteration No. 12}$$

$$n^{(k-1)} = \sum_{i=2}^{N-1} \Delta A \quad \text{at iteration No. 11}$$

The basic steps of the method for estimating the optimum relaxation factor are as follows:

1. Apply an initial value of relaxation factor
   eg. $\Gamma = 1.0$ for 1st set
   and $\Gamma = 1.35 + j0.01$ for the 2nd set

2. at the end of the 2nd set calculate the improved relaxation factor Γ_i from eq. (4.16)

3. In order to prevent Γ_i being greater than the optimum value, the real term of Γ_i can be modified to give a new estimated value of relaxation factor (Γ_e), by using either

$$\text{Re}\,(\Gamma_e) = \text{Re}\,(\Gamma_i) - F.(2-\text{Re}\,(\Gamma_i)) \qquad (4.17a)$$

where F usually lies between $0.2 \rightarrow 0.25$ [52], or [53]

$$\text{Re}\,(\Gamma_e) = 1 + F.(\text{Re}(\Gamma_i) - 1)/$$
$$[(5-\text{Re}(\Gamma_i)).(2+\text{Re}(\Gamma_i))] \qquad (4.17b)$$

where F may lie between 6 and 12.

4. Thus the complex relaxation factor introduced to the next iteration is:

$$\Gamma_e = \text{Re}\,(\Gamma_e) + \text{Im}\,(\Gamma_i) \qquad (4.18)$$

The process is repeated until the calculated value Γ_e converges to within a specified limit. Thus the optimum value of relaxation factor Γ_o is obtained. Γ_o is applied to the rest of the iteration until the convergence of the system is achieved.

However, the system may converge before reaching the optimum value of the relaxation factor.

4.4 Computer Program

4.4.1 Description of Computer Program

Six comprehensive programs are written and developed by the author to determine the performance characteristics of the LIM using the six models described earlier. The flow chart of the three-dimensional analysis is shown in Fig. 4.1, which described the four main processes of each of the six programs:

1) Calculates the magnetic vector potential components (A_x and A_z) in complex form at discrete points using the finite difference method and the iterative technique.
2) Checks after each iteration the state of convergence and modifies the acceleration factor to achieve the optimum value and consequently to accelerate the speed of the calculations.
3) After the values of the magnetic vector potential components are satisfied to a sufficient degree of accuracy, it calculates the components of the magnetic flux density (B_x, B_y, and B_z), induced voltages, and the performance state variables (3-axis forces, losses, output and airgap cross powers).
4) Obtains the total performance state variables of the machine by applying the numerical integration methods. Finally, it presents the results in the form of graphs, contours and tables.

4.4.2 Description of the Flow Chart

Box 1 ; Read input data: data of machine dimensions, source and boundary conditions, mesh intervals, number of nodes, properties of materials, maximum number of iteration and the required tolerance.

In this part of the program , the necessary constants which used in the later stage of the program , are calculated as well.

Box 2 ; Set the necessary conditions and constraints of calculating the x-component of the MVP; for instance the condition imposed on the symmetry plane, the boundary conditions, and the waveform of x-component of the current density.

Box 3 ; Set the initial value of the MVP component over all the nodes of the model. It is usually difficult to estimate a close value to the final value of the MVP component, unless a rough plotting for the flux has been done, therefore in this analysis the initial value of the MVP component is set to be equal to zero.

Preset condition for start of iteration (iteration count IT = 1). In here the cycles of the iteration are present to cooperate for finding out the optimum acceleration factor.

Set the maximum change in the MVP component to be equal to zero.

$$\text{Max } \Delta A^{IT} = 0$$

Then start scanning the nodes which are labelled by three-dimensions (i,j,k) where i is the row number, j is

the column number, and k is the layer number in z-direction.

Box 4 ; Calculate the new value of the MVP components at the interior nodes ($A^{IT+1}_{(i,j,k)}$) according to the appropriate equations. The magnetic vector potentials at the peripherial nodes are set equal to zero for the first iteration, and for subsequent iterations they are set equal to the nearest node value eg.

$$A(1,j,k) = A(2,j,k)$$

$$A(IP, j,k) = A(IP-1,j,k)$$

$$A(i,1,k) = A(i,2,k)$$

$$A(i,IQ,k) = A(i,IQ-1,k)$$

$$A(i,j,1) = A(i,j,2)$$

This procedure is repeated for about 80 of the total number of iterations. For subsequent iterations, the values at the peripheral nodes are assumed to remain constant. The above procedure has been followed instead of forcing the peripheral nodes to zero potential . This reduced the error which might be caused by insufficient length of the reaction rail beyond the entry and exit ends and the specific dimensions of the outer frame of the model.

Calculate the residual value of the MVP component at node (i,j,k).

$$\Delta A^{IT+1}_{(i,j,k)} = A^{IT+1}_{(i.j.k)} - A^{IT}_{(i,j,k)}$$

Then test the residual value of node (i,j,k) with the highest residual value in the model.

In some of the programmes, the relative residuals have been determined instead

$$\Delta A^{IT+1}_{(i,j,k)} = \frac{A^{IT+1}_{(i,j,k)} - A^{IT}_{(i,j,k)}}{A^{IT+1}_{(i,j,k)}}$$

which is used for testing the convergence only.

Box 5 ; Having calculated the MVP component and its residual value at node (i,j,k), the new value of the MVP is modified to be used in the next iteration by applying the SOR technique mentioned earlier.

$$A^{IT+1}_{(i,j,k)} = A^{IT}_{(i,j,k)} + \Gamma.(A^{IT+1}_{(i,j,k)} - A^{IT}_{(i,j,k)})$$

Γ is the convergence factor which will be modified until the optimum value is obtained as mentioned earlier.

Box 6 ; Test for convergence and termination of the programme. In this section the criterias used for the test of the computer programme are:

a) the highest residual is less than a pre-set value ε, (the system has converged).

b) the number of iterations is greater than the pre-set value; in this case the results are printed out and examined to see if they are meaningful, (the system may not fully converge and be considered to have taken too much time).

c) the highest residual is greater than a pre-set value R_{max}, (the system has diverged).

Box 7 ; If the values of the x-component of the MVP are satisfied to a sufficient degree of accuracy, store the potential values of the interested sections to be used later in the programme for the calculation of the state variables performance.

Box 8 ; Arrange the necessary conditions for the calculation of the z-component of the MVP. For instance the boundary conditions on the symmetry plane and the other interfaces, and the z-component of the current density. Repeat the same process mentioned in boxes 3, 4, 5 and 6.

Box 9 ; Calculate the flux density component, 3-axis forces, output, losses and airgap powers in discrete form. Then calculate the primary induced voltages per phase.

Box 10 ; Apply the numerical itergration method, which is based on Simpson's rule (Appendix B) to obtain the total effective forces and powers.

Box 11 ; Print output; the output contains the results in tabulated form, three and two dimensions graphs and flux contours.

The listing of the three-dimensional analysis of 3DHM model is presented in Appendix C.

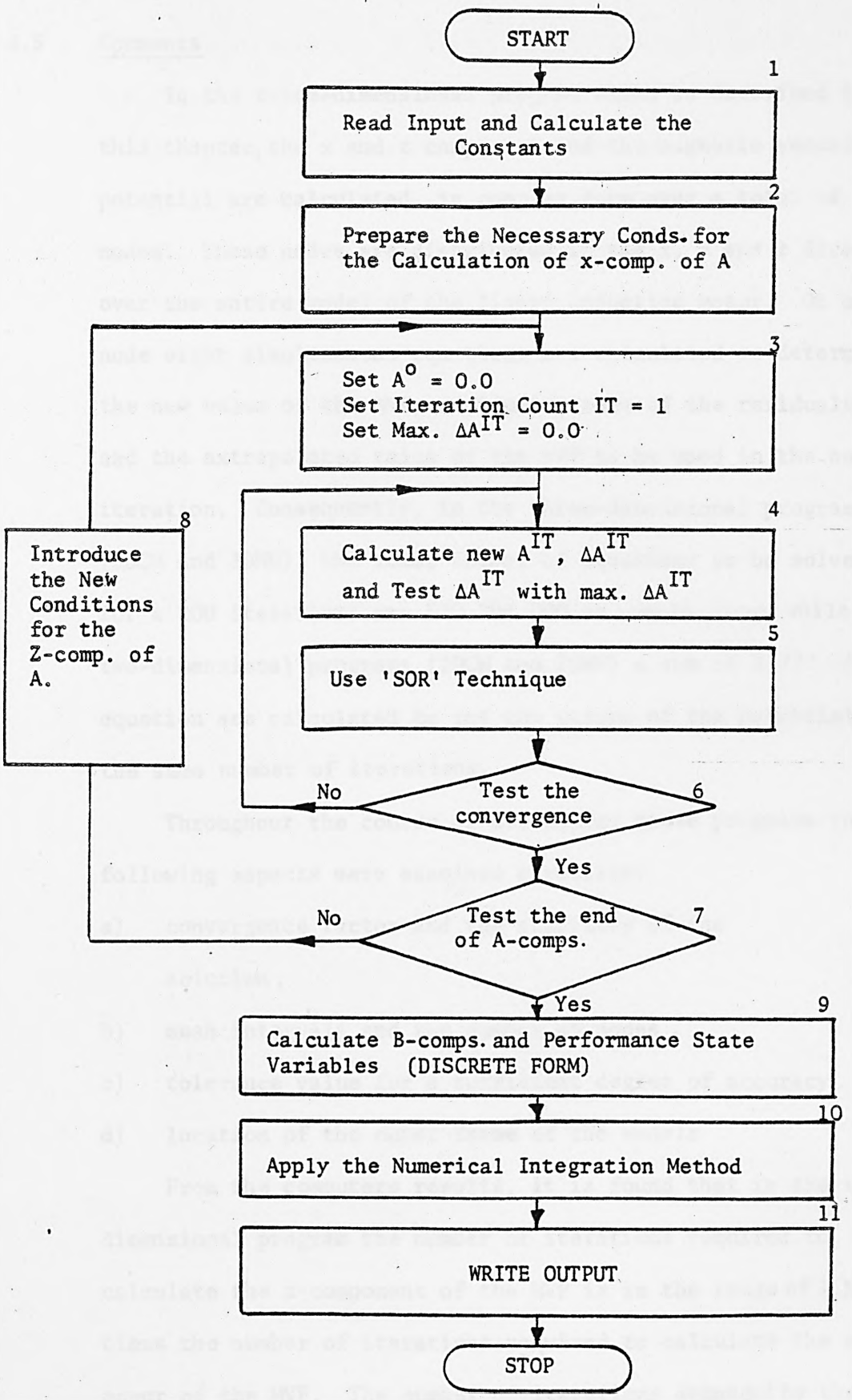

Fig. 4.1 Flow Chart of 3-Dimensional Numerical Analysis

4.5 Comments

In the three-dimensional program which is described in this chapter, the x and z components of the magnetic vector potential are calculated in complex form over a total of 30 176 nodes. These nodes are distributed in the x, y and z directions over the entire model of the linear induction motor. On each node eight simultaneous equations are calculated to determine the new value of the MVP, residuals, norm of the residuals, and the extrapolated value of the MVP to be used in the next iteration. Consequently, in the three-dimensional programs (3DCM and 3DHM), the total number of equations to be solved for a 200 iterations are 120 704 000 in complex form, while using the two-dimensional programs (2DCM and 2DHM) a sum of 3 772 000 equation are calculated to get the values of the potentials on the same number of iterations.

Throughout the course of developing these programs the following aspects were examined carefully:

a) convergence factor and the stability of the solution,

b) mesh intervals and the number of nodes,

c) tolerance value for a sufficient degree of accuracy,

d) location of the outer frame of the models.

From the computers results, it is found that in the three-dimensional program the number of iterations required to calculate the z-component of the MVP is in the range of 1.5 to 3 times the number of iterations required to calculate the x component of the MVP. The number of iterations demanded by the two-dimensional program is in the average of 2 to 3 times the number

of iteration required to calculate the z component of the MVP of the three-dimensional program.

It is found in general that the computations take more time at high frequency operations, low slips, and in machine with backing iron.

The convergence factor which satisfies the stability of the solutions is in the following range

1.4 < Real term of the convergence factor < 1.7

-.3 < Imaginary term of the convergence factor < 0.0

At high frequency a low real term is preferable with a high imaginary in the range specified above.

CHAPTER 5

TEST RIG

5.1 Introduction

In order to test a linear induction machine, it is not sufficient to examine the dynamic performance under static conditions because of the entry and exit edge effects, which can lead to a considerable performance modification.

With respect to high speed machines, the experimental results on the performance of the linear induction motor involve some difficulty because the dimensional needs of the linear motor are large compared with those of the rotating motors. In order to avoid these difficulties a rotating disc and a rotating drum are the most practical configuration which can be built to have an equivalent function to the reaction plate of the linear induction motor. However, each of these type has its own merits and demerits.

To choose the most appropriate configuration, the factors which effect the function of these two types should be considered and examined. The most important of these factors are the air-gap length and the rotor speed.

Changing the length of the air-gap between the stator and the rotor causes a non-uniform air-gap length over the length of the secondary sheet of the drum type, whilst the air-gap length remains uniform over the length of the secondary of the disc-type, see Fig. 5.1.

The ratio of the air gap length to the displacement at the centre along the length of the machine for the drum type is given by

$$\frac{R_1 - R}{d} = \frac{(d^2 + R^2 + 2Rd \cos \theta)^{\frac{1}{2}} - R}{d}$$

where R_1-R represents the distance in which the edge of the stator is displayed away from the drum surface due to the movement of the centre of the stator by d.

Practically $(R_1-R)/d$ should be as close as possible to unity, the smaller the value of the angle θ the closer (R_1-R) becomes to d. The angle θ is directly proportional to the total length of the stator and inversely proportional to the radius of the drum R. Therefore the selection of stator length and drum radius becomes a matter of compromise so as to minimise the angle θ as well as considering the other requirement concerning the machine performance.

Thus for a drum of 1500 mm diameter, the length of the stator ℓ should be 500 mm, in order to keep the difference between (R_1-R) and d within 5%.

For a constant rotating speed, the peripheral speed is constant over the width of the secondary conductor of the drum type, while the peripheral speed of the disc type is changing considerably over the secondary width, see Fig. 5.2.

Let the angular speed of the drum be ω rad/sec. Then the peripheral speed at radius r becomes $v = \omega r$ m/sec. Hence, the ratio of the peripheral speed at points a and b of the disc type is

$$\frac{V_a}{V_b} = \frac{r_a}{r_b}$$

To get a ratio as close to unity as possible, either the disc is of a very large radius, or the secondary conductor is of a very small width.

Using the same specifications given earlier and with secondary conductor of 240 mm width the ratio becomes

$$\frac{V_a}{V_b} = \frac{0.75 + 0.12}{0.75 - 0.12} = 1.38$$

which is somewhat large, and it means that the peripheral speed at a and b is changing by ±19% of the peripheral speed at the centre of the secondary sheet. In consequence, to keep the difference in these peripheral speeds within ±5% either the radius of the disc is increased to 4920 mm for a width of 240 mm, or the width of the secondary is reduced to 18.3 mm for a radius of 750 mm. Either of these alternatives are unpractical to construct, specially when the other requirements of the rig design and performance are considered.

The conclusion is that the change in peripheral speed over the width of the secondary conductor of the disc type is rather considerable, and can only be minimised either by using a very narrow secondary conductor sheet, or designing a disc with a large diameter. The change in the airgap length over the peripheral surface of the drum type is however rather small. Moreover the stator of the drum type could be designed to keep the change in the airgap length over the surface of the drum to a minimum.

However it is worth stating that the stator is not being displaced relative to the surface of the drum during operating conditions, whilst the peripheral speed is the significant factor of the dynamic test.

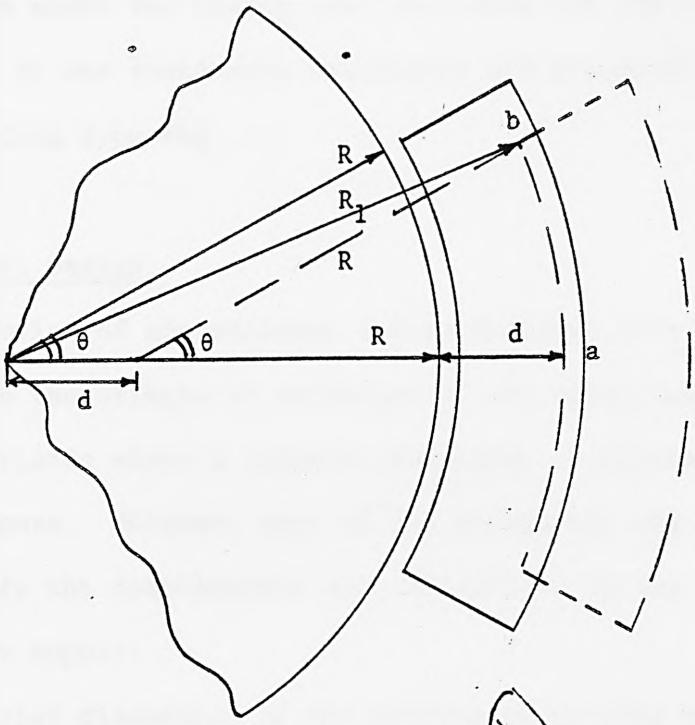

Fig. 5.1.
Drum Type

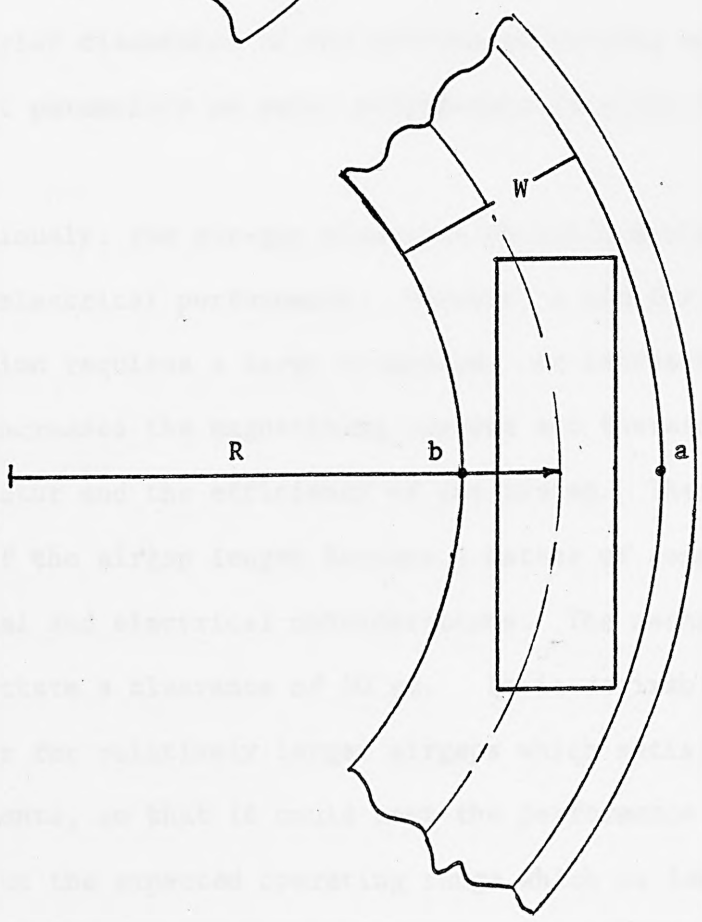

Fig. 5.2
Disc Type

From above and taking into consideration the other technical aspects, it was found more reasonable and practical to choose and build a drum type rig.

5.2 Electrical Design

A series of conventional design formulae have been used to establish the effects of variation of the linear motor parameters characteristic where a computer programme is developed to serve this purpose. However, some of the parameters are already specified to satisfy the requirements and limitations of the drum design and power supply.

A brief discussion of the effects of varying some of the more important parameters on motor performance is given below:

Air gap;

Obviously, the air-gap clearance should be minimised for optimum electrical performance. However, a LIM for a high speed application requires a large clearance. An increase in air-gap length increases the magnetizing current and therefore lowers the power factor and the efficiency of the system. Therefore a selection of the airgap length becomes a matter of compromise between mechanical and electrical considerations. The mechanical limitations dictate a clearance of 10 mm. It is desirable to design the motor for relatively larger airgaps which satisfy the mechanical requirements, so that it could meet the performance requirement throughout the expected operating range which is lower than the airgap design point.

Frequency and Pole Pitch;

The pole pitch is dependent upon the operating speed and the frequency of the power supply, since they are tied together in a definite manner. The speed of the vehicle is given by

$$V = 2 \tau f$$

For a maximum speed of 78.4 m/sec (282.24 km/h) a pole pitch τ of 112 mm was found most convenient to meet the limitation of the stator total length and the frequency of the power supply. The 350 Hz system, is therefore, chosen as the maximum operating frequency and the motor could be operated at frequencies of 50, 150, and 250 Hz.

Number of Poles;

The primary of the motor should contain at least ten or more poles to minimise the longitudinal end effects on the motor performance, but because of the limitation in the total length of the machine, a five pole half-filled end slot primary winding was found just practicable to serve the purpose.

Other Parameters;

Generally speaking, the evaluation of design parameters of the motor stator are obtained for a LIM backed by laminated iron. The drum was, however, designed and constructed without backing iron.

A thicker secondary conductor gives a lower resistance which leads to less secondary copper losses. However, the thicker secondary conductor increases the effective airgap which requires high magnetising current. Therefore the selection of the secondary thickness is a matter of compromise between these two constraints and to meet the requirements concerning the strength and rolling resistivity. A pure aluminimum (1C) half hard grain sheet of $\frac{1}{8}$" (3.175 mm) thickness was used as a track of the LIM.

The number of slots per phase per pole and the coil span of the primary winding affect the winding reactance, harmonic content, and winding factor. The considerations which are used in choosing the most efficient of these parameters for conventional machines are still applicable to longitudinal linear induction motors. Thus two slots per pole per phase and a coil span equal to 5/6 of the pole pitch were found the most convenient figures to choose.

In a LIM, since the airgap is relatively large, the airgap flux density is relatively low. The low air-gap flux density permits wider slots and narrower teeth to be used in the primary member. In order to obtain a reasonable ratio of useful current to the magnetizing current, the Ampere-conductor per meter of motor length should be considerably higher than that which is used for a smaller airgap length. A 3-phase winding of a double layer and 50 turns per coil of lap-connection is used in the stator. This requires a deep slot, in order to provide a low current density in the primary winding which reduces the heat loss per unit area. The size of the wire is 16 SWG for a rated current of 7 A.

The thermal performances of a LIM is better than a rotating machine because the heat losses in one of the members are left behind as the motor proceeds.

The machine data of the test model are shown in table 5.1

5.3 Mechanical Design

In this section the design and process of construction of the drum as well as the stator structure and its frame are described.

Table 5.1

MACHINE DATA

Number of poles	4(5,when half end slots are used)
Number of phases	3
Power frequency	50, 150, 250, 350 Hz
STATOR:	
Stator length	547 mm
Stator depth	76 mm
Stator width	80 mm
(Stator and overhang winding) width	160 mm
Pole pitch	112 mm
Slot pitch	18.7 mm
Slot width	13 mm
Slot depth	38 mm
Number of turns per slot (double layer)	100
Number of slots per pole per phase	2
Winding distribution	Half-end slots, with chorded coil = $\frac{5}{6}$ pole pitch
Size of the wire	16 SWG
ROTOR:	
Type of the rotor	Pure aluminium (1C - $\frac{1}{2}$ hard)
Thickness of the conductor	3.175 mm
Width of the conductor	240 mm
Conductivity of the conductor	59.9% I.A.C.
Outer diameter of the rotor	1554 mm

Stator;

As the stator core of the LIM used in this research is made from laminated iron, it was found to be impractical to manufacture a slotted lamination of iron in the form of an arch with a large radius owing to the high tool costs involved. It was decided as a fairly accurate solution to form the arch of the stator core by using six linear sections bolted together with two steel plates. The radius of the curvature of the stator core becomes equal to 790 mm with a tolerance of ± .7 mm. Obviously, if the number of the linear sections increased, the arch form will be more close to the exact curvature required, 790 mm, and by calucation it was found that a number of 10 sections gives a tolerance of ± .25 mm, but the amount of work required for the second configuration makes the one with six sectors more practical (see Fig. 5.3 and 5.4).

The sections were obtained by chopping a standard linear motor slotted lamination. The laminations were obtained from Linear Machines Limited, U.K., being "Standard A LAM 65 mm NEWCOR" type. 126 laminations are used in each sector, stacked to form an overall width of 80 mm. The sections were bolted together with two steel plates of arch shape along the stator length by 12 bolts, each bolt being insulated from the steel plates by bakelite sleeves. The edges of the sections were coated with varnish to avoid any conduction which may lead to an increase in the circulated eddy current.

The total number of slots of the stator is 29, which are filled by a two-layer lap-winding of 5/6 coil span, with the exception of the first and last pole pitchers where they are filled by a one-layer winding. Two search coils are located around each tooth, one at the top and the other at the bottom.

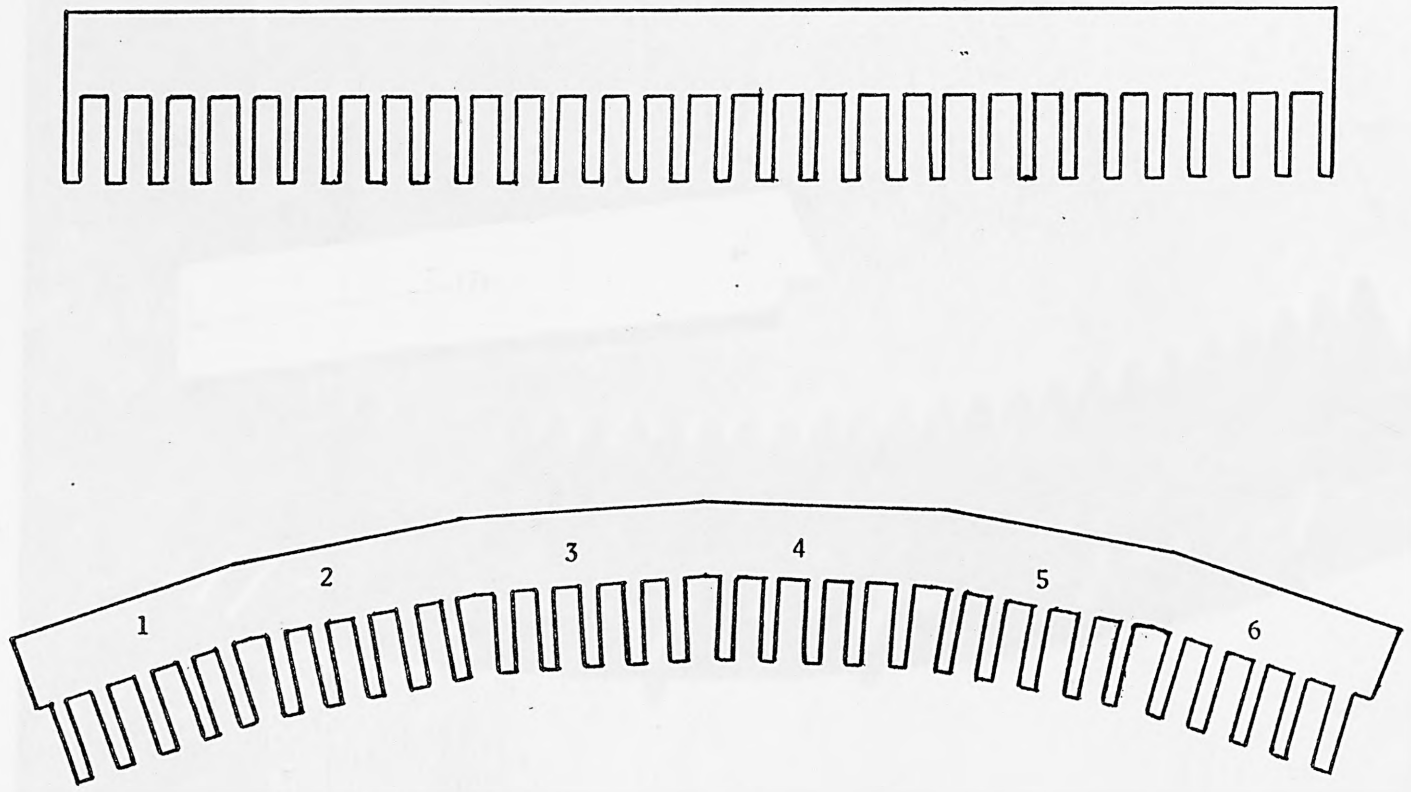

Fig. 5.3. The linear and curvature versions of the stator core of the linear induction motor

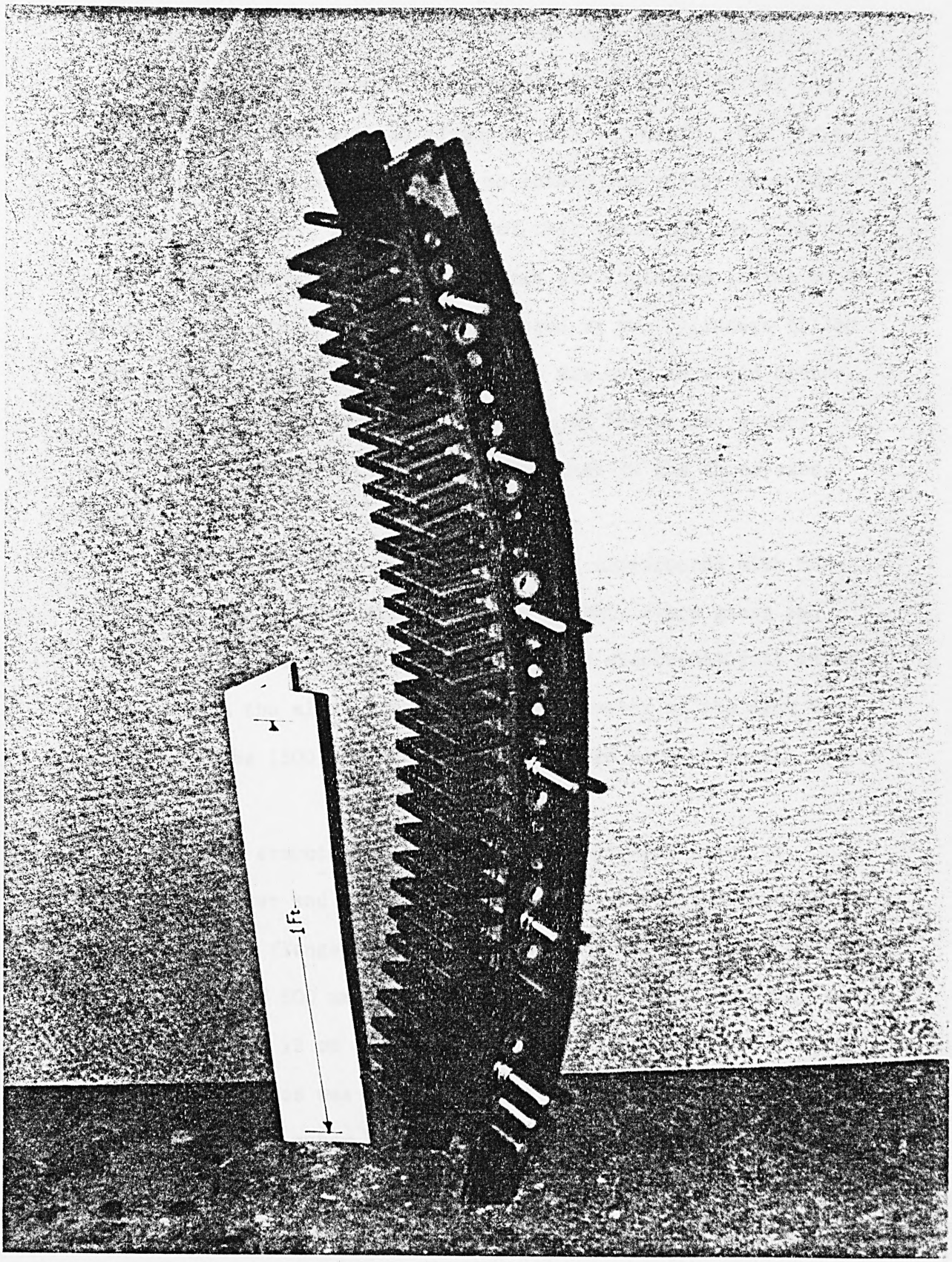

Fig. 5.4. Stator core of the LIM

A few search coils are wound around the core of the stator.

The stator is mounted on the side of the drum, facing the surface of the drum with an airgap of 9.5 mm length. The frame shown in Fig. 5.5 is constructed to locate the stator into the required position. The mechanism of this frame and the technique used for the measurement of the forces are explained in the next section. The stator is counter-balanced by two cylinders filled with a lead shot. The counter-balance was used to avoid distortion which may be caused by pre-loading of the strain gauges which are concerned with the induced forces in the three-axes.

Rotor;

The rotating drum of the test rig is constructed with non-conducting and non-magnetic materials (mainly fibre glass and wood) in order to minimize any unnecessary electromagnetic interference with the aluminium track. The diameter of the drum was designed to be 1500 mm for the reason stated earlier in the introduction.

The drum structure consists of three plywood discs of 1500 mm diameter and 18 mm thickness; they are bolted together with two steel flanges of 228 mm diameter and 100 mm long and six steel plates of 500 mm diameter and 10 mm thickness by using six master bolts of 12 mm diameter and 320 mm long. The whole structure of the three discs was installed on a shaft of 100 mm diameter and locked with each other by two long grip taper keys (see Fig. 5.6)

The stresses on the plywood discs and the shaft were calculated up to a speed of 150% of the maximum speed; the dimensions of the shaft and the other parts of the structure are thus obtained. The torsional and shearing stresses on the shaft were investigated, in order to choose the bearings required. The additional force

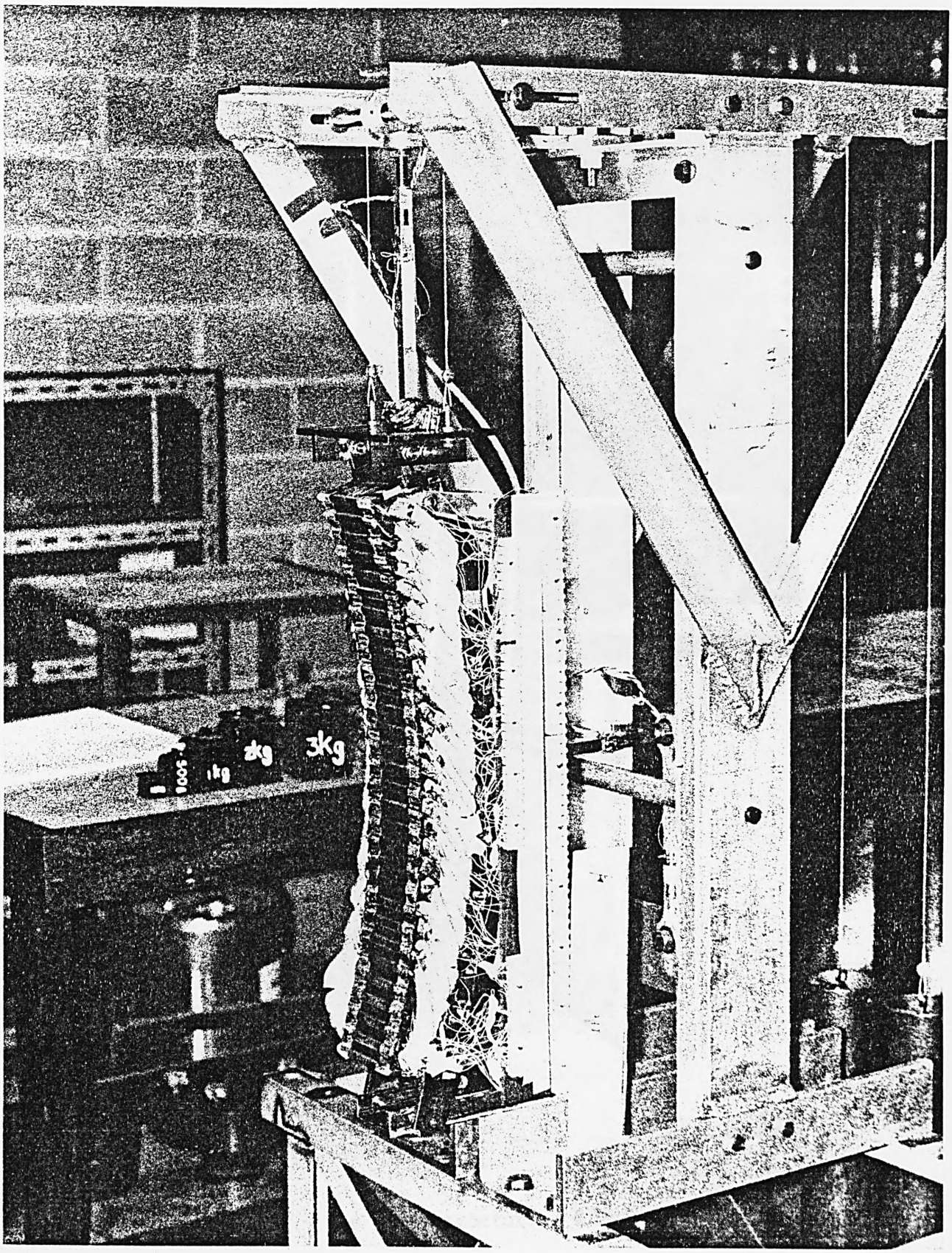

Fig. 5.5. Stator frame

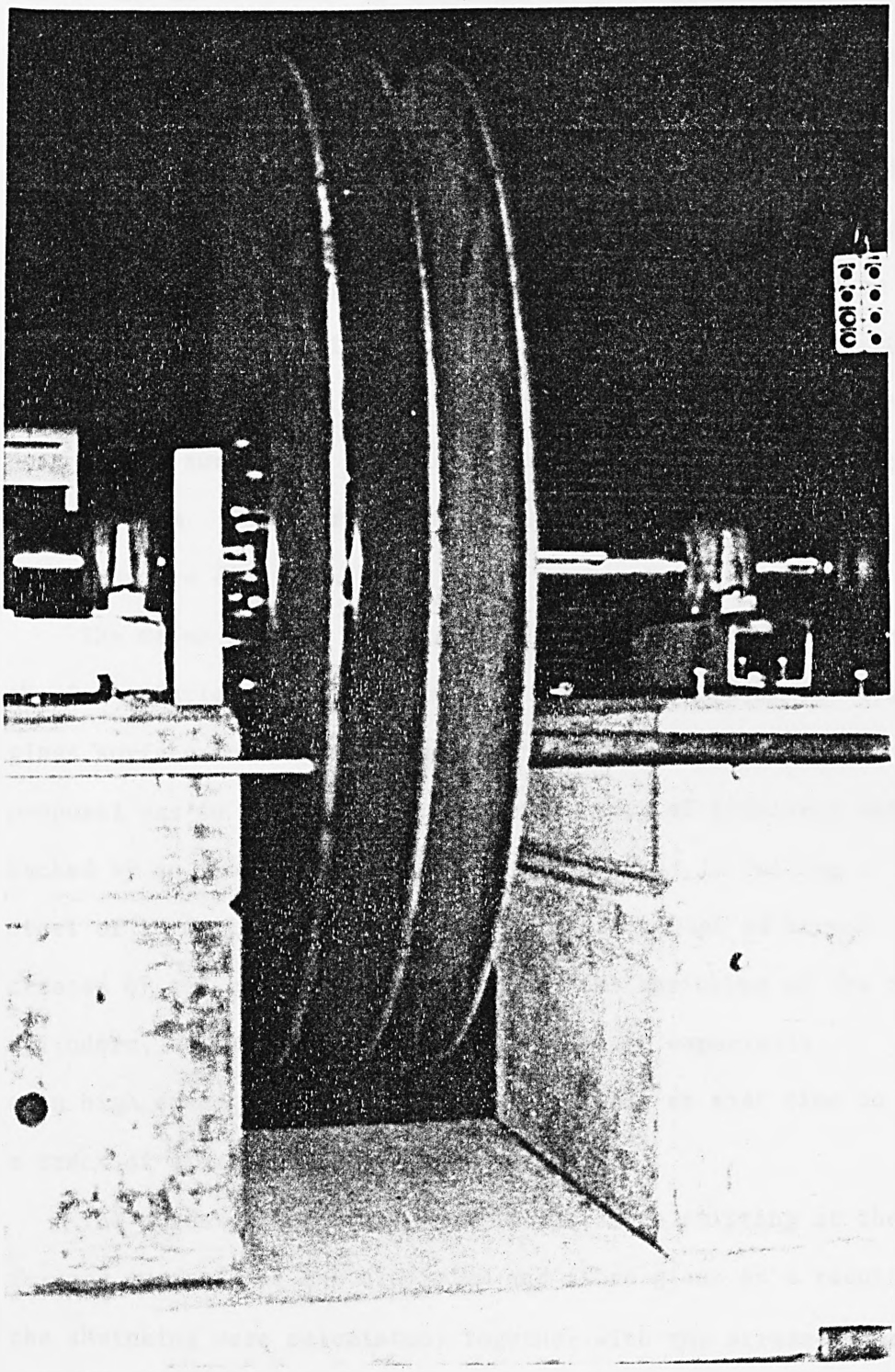

Fig. 5.6. The drum structure - First stage

due to the misalignment of the drum was also considered.

A concrete plinth was constructed especially by the Concrete Laboratory of the Civil Engineering Department. The 10 h.p. driving motor and the bearings were aligned with each other on the plinth.

A thin sheet of plywood of 4 mm thickness and 300 mm width was attached to the edges of the three plywood discs to form the surface of the drum. Layers of fibre glass were bonded on the surface of the drum to cover the whole surface of the drum and down to the surface of the lateral plywood discs to a depth of about 200 mm. The fibre glass was machined down to about 10 mm thickness see Fig. 5.7.

The major and the most critical part of the construction was the installation of the aluminium sheet on the top of the fibre glass surface to form the track of the LIM. Initially, the proposal was to construct a track consisting of aluminium sheet backed by an iron, but because of limitations in rolling steel of 10 mm thickness, the considerable amount of stress created by the contact pressure due to the shrinking of the two cylinders, and the large centrifugal forces, especially at a high speed, it was found more practical at that time to use a track of aluminium sheet only.

The stresses due to the contact pressure existing at the interference surfaces of the aluminium and fibre glass as a result of the shrinking were calculated, together with the stresses due to the centrifugal forces at a speed of 120% of the maximum speed. However, it was found more secure to bond the aluminium on the surface of the fibre glass with epoxy resin adhesive in addition to the shrinking process.

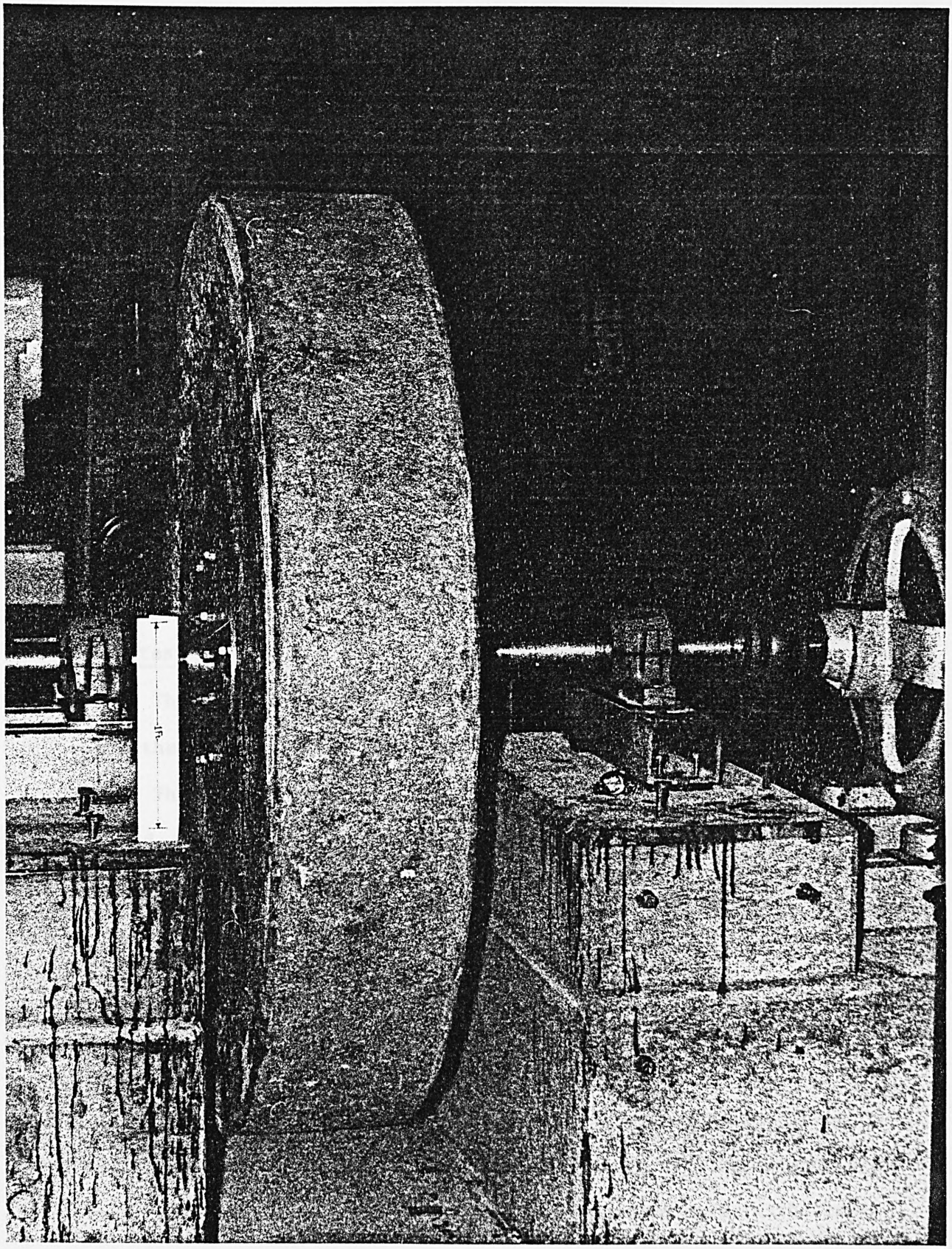

Fig. 5.7. The drum structure - Second stage

The aluminium track was made by welding two strips of aluminium of 3.175 mm thickness and 240 mm wide; the whole sheet was then rolled to the required diameter of about 1500 mm and finally welded at the other ends in order to give an interference of 1 mm in radius with respect to the radius of the fibre glass, see Fig. 5.8 and 5.9.

During the construction of the drum, some tests were carried out to measure the strength of the plywood for different grain distribution, welding strength of aluminium, the level of vibration of the rig and the balance of the drum. All these tests were supervised by the Mechanical Engineering Department of the City University.

The drum data of the test model are shown in table 5.2.

The test Rig

The whole rig shown in Figs. 5.10 and 5.11 comprises the drum and the stator supported by the frame.

The drum is driven by a d.c. motor of 10 hp to the required speed. Variable speed is obtained using thyristor control; the maximum speed is 1200 RPH. This control system is described in Appendix D.

5.4 Instrumentation and Measurement Technique

The success of any tests does not depend only on the design plan but also on the technique and method of measurement.

The design of the test rig on a linear electric machine gives rise to problems which are not normally present in a corresponding rotating machine. Moreover to facilitate measurements in the case of a linear machine one requires very sensitive devices which must be carefully calibrated, in particular for force measurements. The instrumentation and the technique of measurements for forces and

Table 5.2

DRUM DATA

Outer diameter of the drum	1554 mm
Thickness of the aluminium ring	3.715 mm
Width of the aluminium ring	240 mm
Width of the drum	300 mm
Maximum peripheral speed, V_s	78.4 m/sec (282.24 km/h)
Maximum angular velocity, w	100.9 rad/sec
Maximum rotational speed	963.63 R.P.M.
Drum weight	335 kgm
Moment of inertia	55.372 kg-m^2
Maximum kinetic energy	281.87 KJoul
Natural frequency	25 Hz

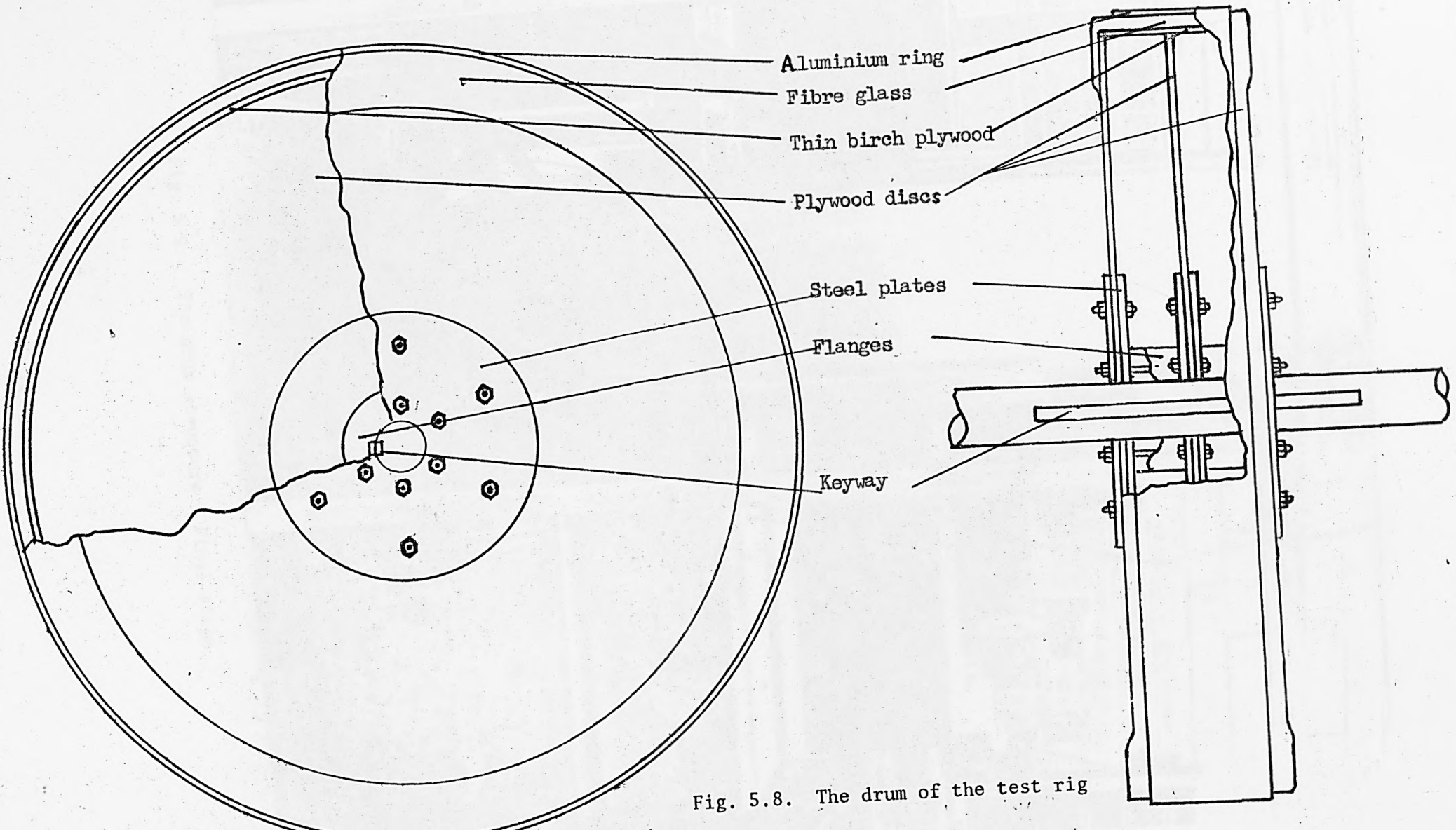

Fig. 5.8. The drum of the test rig

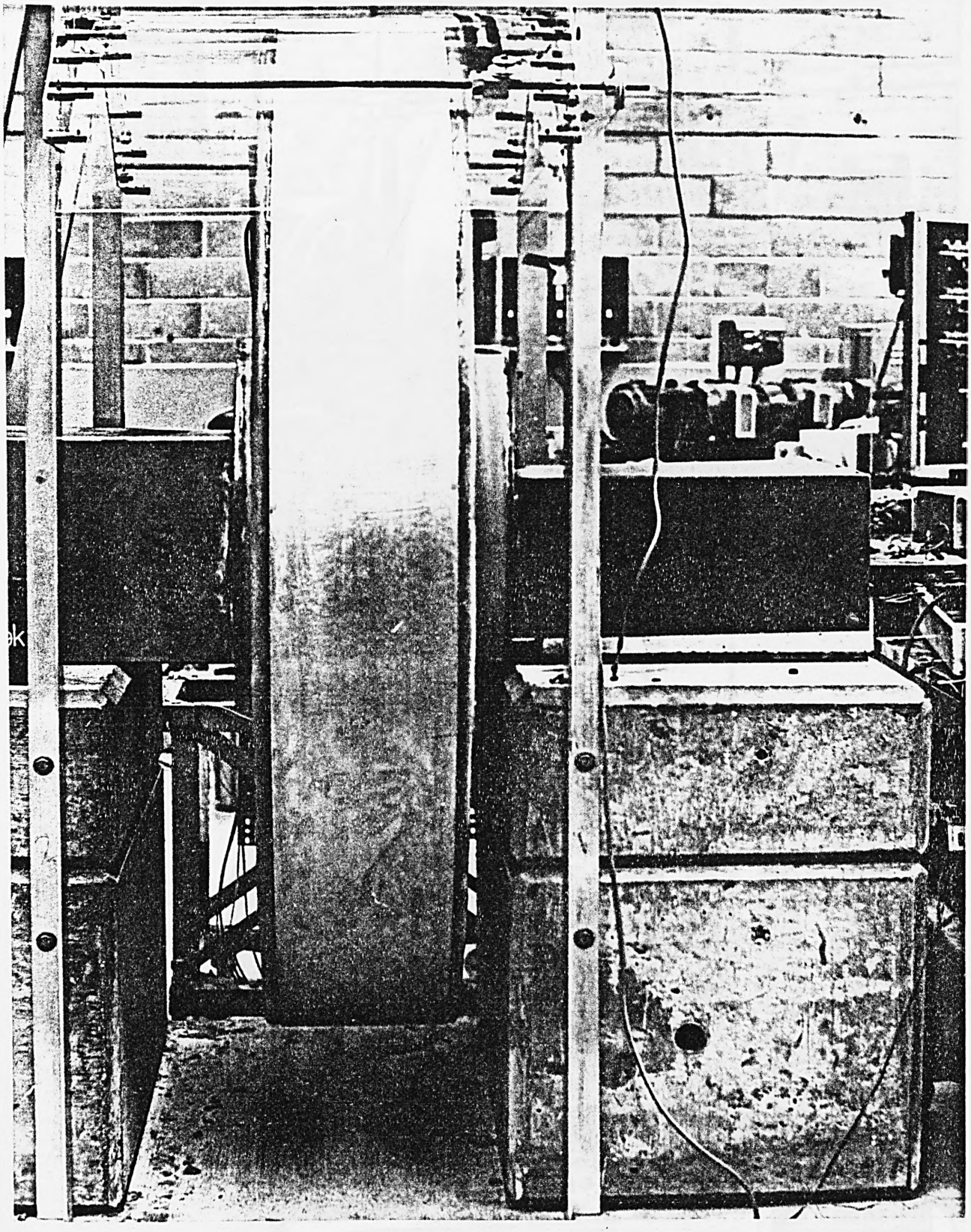

Fig. 5.9. The drum structure - Final stage

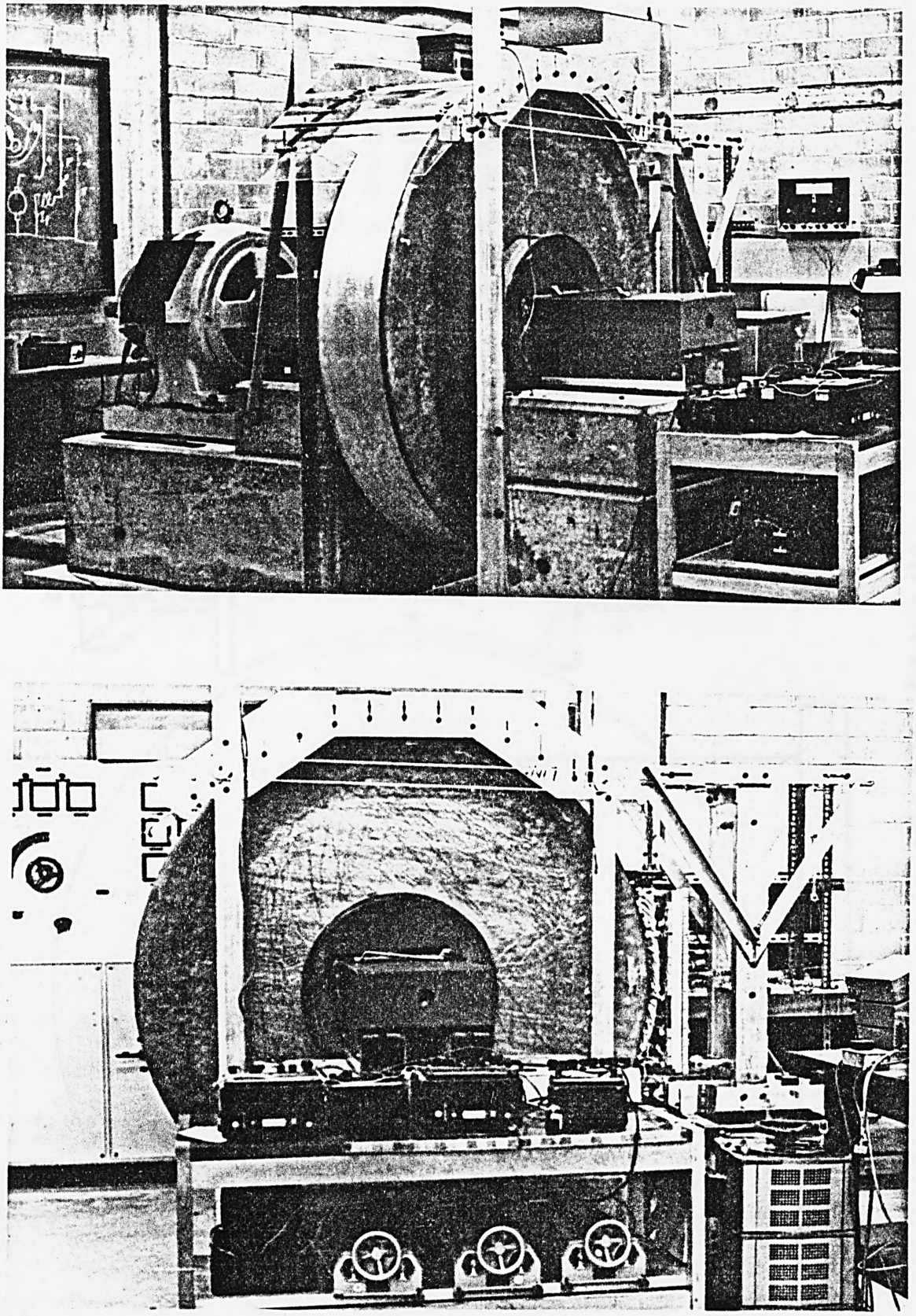

Fig. 5.10. The test rig

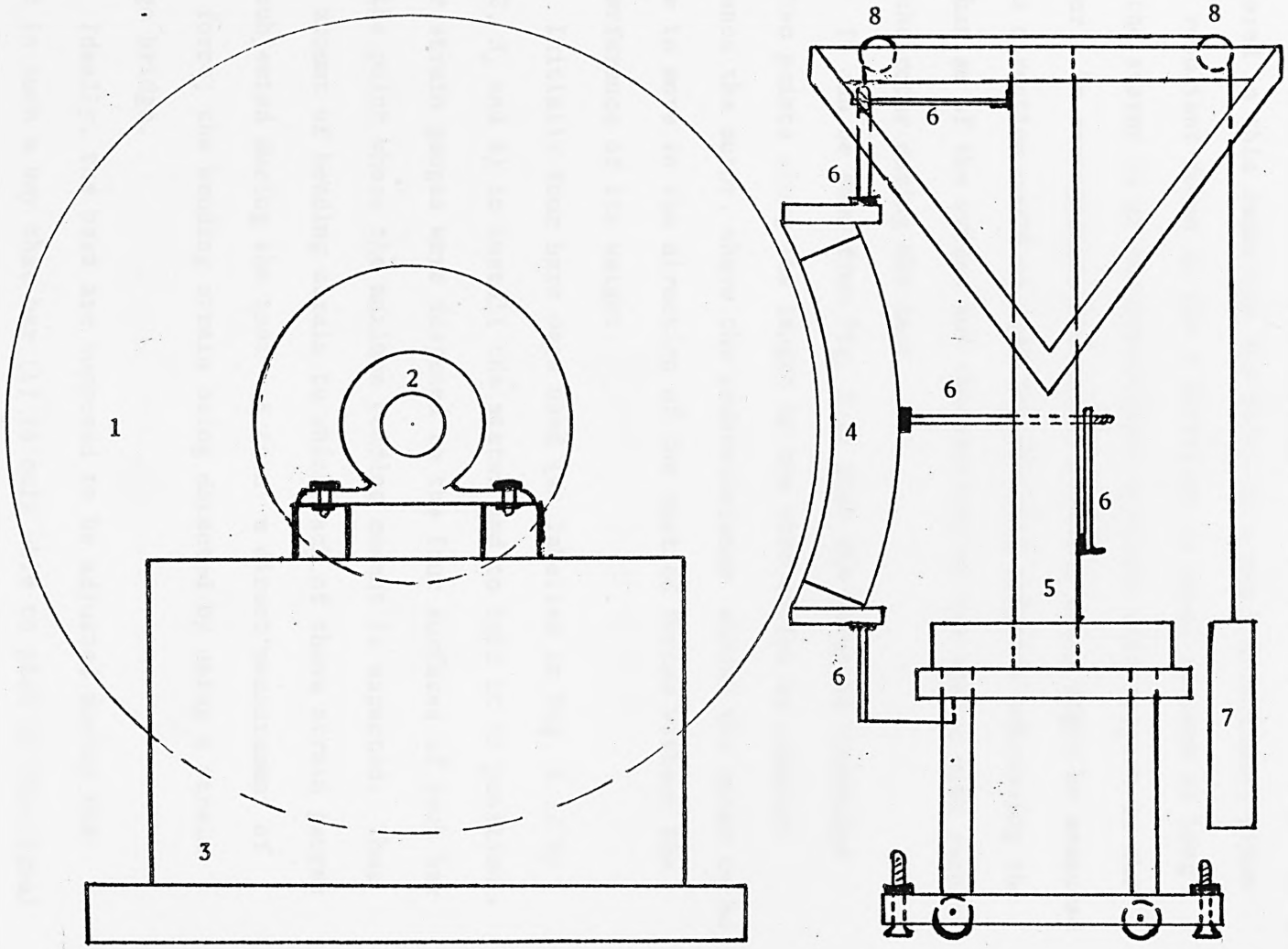

1. Rotating drum
2. Bearing
3. Concrete table
4. Stator
5. Stator Frame
6. Bars (force measurement)
7. Counter balance
8. Pulley

Fig. 5.11. The test rig

flux density are both mentioned in the next sections.

5.4.1. Force Measurements

The three force components applied to the stator in x, y, and z direction can be measured by using the technique shown in Fig. 5.11 and 5.12. However, the most important axes to be considered in this technique are those in x and y directions, since the resultant force in the z direction is equal to zero as long as the stator is at the centralized position with respect to the rotor. In consequence, the amount of force which might be measured in z direction could be used for checking purposes concerning the mechanism of the system and the position of the stator with respect to the rotor during the test.

It can be seen from Fig. 5.11 that the motor is suspended at two points along its length by two wire cables to counterbalance the motor, where the counterbalance allows the motor to be free to move in the direction of the applied forces without the interference of its weight.

Initially four bars were used (as labelled in Fig. 5.12 by 1, 2, 3, and 4) to install the stator and to hold it in position. Four strain gauges were fastened to the four surfaces of each bar at the point where the maximum bending moment is expected. Thus the amount of bending strain to which each of these strain gauges is subjected during the test is then a direct measurement of the force; the bending strain being detected by using a strain gauge bridge.

Ideally, the bars are supposed to be adjusted during the test in such a way that bar (1) is only able to pick up the signal of the force acting in x direction, while bar (4) is to pick up the signal of the force acting in y direction. One way of achieving

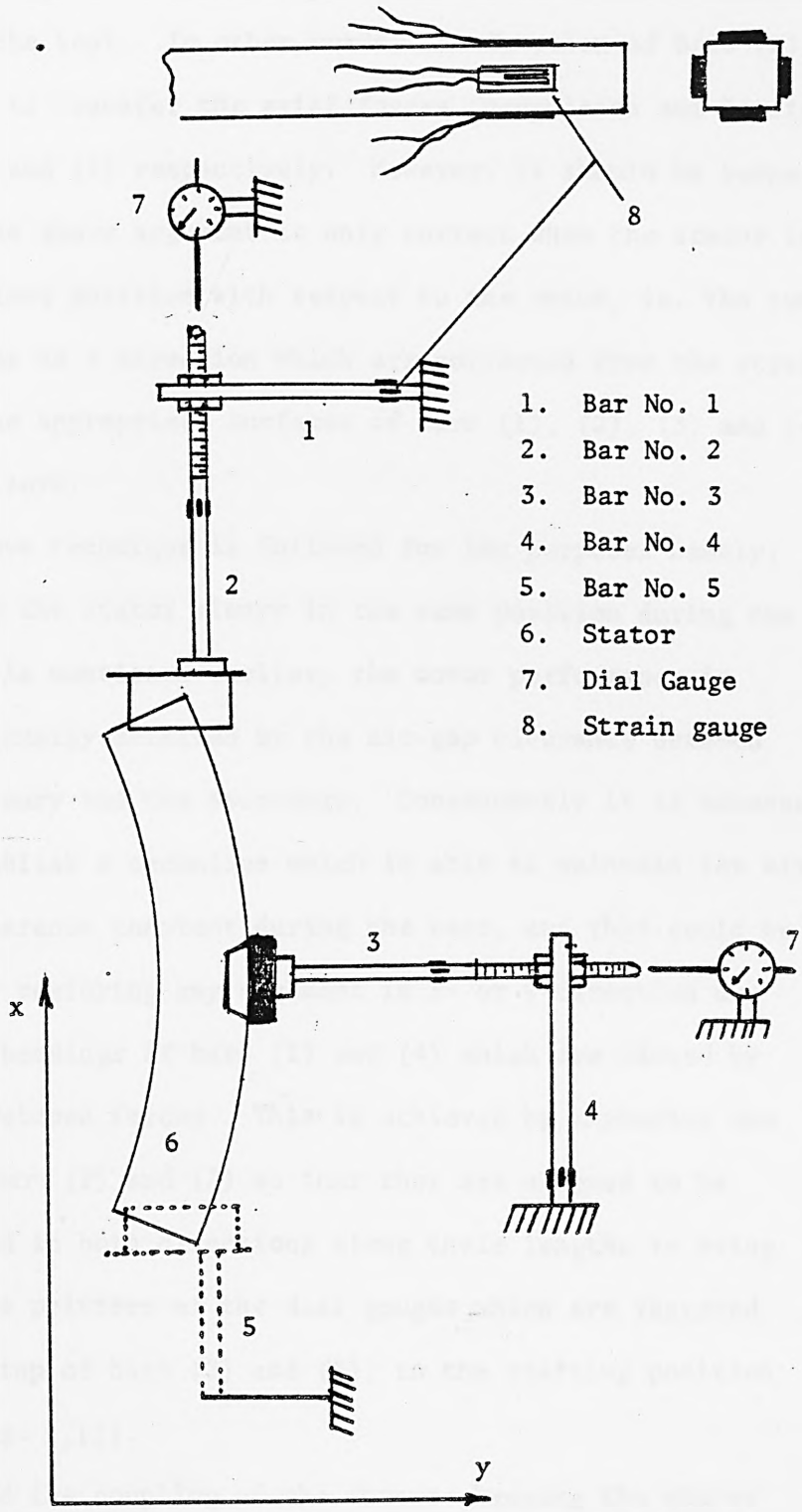

Fig. 5.12. Force measurement technique

this is to keep bars (2) and (3) always at the same position before and during the test. In other words, the function of bars (2) and (3) is only to transfer the axial forces (propulsion and levitation) to bars (1) and (4) respectively. However, it should be borne in mind that the above argument is only correct when the stator is at the centralised position with respect to the rotor, ie. the sum of the forces in z direction which are collected from the strain gauges on the appropriate surfaces of bars (1), (2), (3) and (4) is equal to zero.

The above technique is followed for two purposes namely:

(1) To keep the stator always in the same position during the test: As mentioned earlier, the motor performance is significantly effected by the air-gap clearance between the primary and the secondary. Consequently it is necessary to establish a technique which is able to maintain the air-gap clearance constant during the test, and this could be done by restoring any movement in x- or y-direction due to the bendings of bars (1) and (4) which are caused by the developed forces. This is achieved by threading one end of bars (2) and (3) so that they are allowed to be adjusted in both directions along their lengths to bring back the pointers of the dial gauges which are fastened at the top of bars (2) and (3), to the starting position (see Fig. 5.12).

2) To avoid the coupling of the forces: keeping the stator and bars (2) and (3) at the same position before and during the test will let both bars (2) and (3) carry no forces in the y and x direction respectively. In other words, bar (1) and (4) will act in such a way that each

one of them does not know what the other bar is doing.

However, during the calibration it was found that:

a) the position of the stator is not significantly effected by the developed forces.

b) the adjustment of bars (2) and (3) to bring back the pointers of the dial gauges to its starting position is impractical.

c) the measurement of the forces should be taken at once, otherwise the speed of the drum at the time of the measurement will be different because of the developed forces.

d) a single-value calibration curve for Fy forces cannot be obtained as the bending moment at bar (4) is effected by the Fy force distribution along the length of the stator.

Because of the above limitations and constraints, bar (5) is introduced to the system, (see Fig. 5.12), in order

a) to make the system rather more rigid, and symmetrically balanced in the y direction without obstruction of the force developed in x direction

b) to get single-value calibration curve of Fy force, independent of the Fy force distribution.

In consequence, it was found practical and fairly satisfactory for the calibration system to use bar (1) for thrust measurement, and both bars (4) and (5) for levitation force, where the magnification factor of the signal from bars (4) and (5) are adjusted in such a way to get a single-value calibration curve of Fy force.

For a number of reasons most strain gauge measurements require an instrumentation system. These systems vary widely in complexity and flexibility with the type of the strain gauge, frequency and amplitude of the strain gauge signal. In this project a bridge circuit was used.

The bridge consisted of two strain gauges, one fastened to the one surface and the other to the opposite surface of the bar, together with two other resistors. The resistance of each gauge will change in proportion to the bending strain induced in the bar. The changes will be of opposite sign due to the contraction of one face of the bar and the extension of the other. The output voltage will be a function of this change and the input voltage, and it is evident that a regulated power supply must be used if the input voltage is to be equated with the measurement.

One of the advantages of using a bridge as connected in Fig. 5.13 is heat compensation. A single gauge cemented to one surface of the bar would give an erroneous strain reading if there is a change in temperature. However, when two gauges are used no change in voltage is apparent at the output terminal.

With the strain gauge bridge, a d.c. amplifier was built as shown in Fig. 5.13 A number of signals can be added, allowing not only one bar to pick up the total force, but also any other, in case of any contribution.

Since the stator is in the form of an arch, the measured forces, should be transformed to the axes at which the real LIM is acting and developing forces.

From Fig. 5.14 the transformation formula are given below:

$$Fx_m(\theta) = F_t(\Theta) \cos \theta - F_n(\Theta) \sin \theta \quad -\delta < \theta < \delta$$

and $$Fy_m(\theta) = F_t(\theta) \sin \theta + F_n(\theta) \cos \theta \quad -\delta < \theta < \delta$$

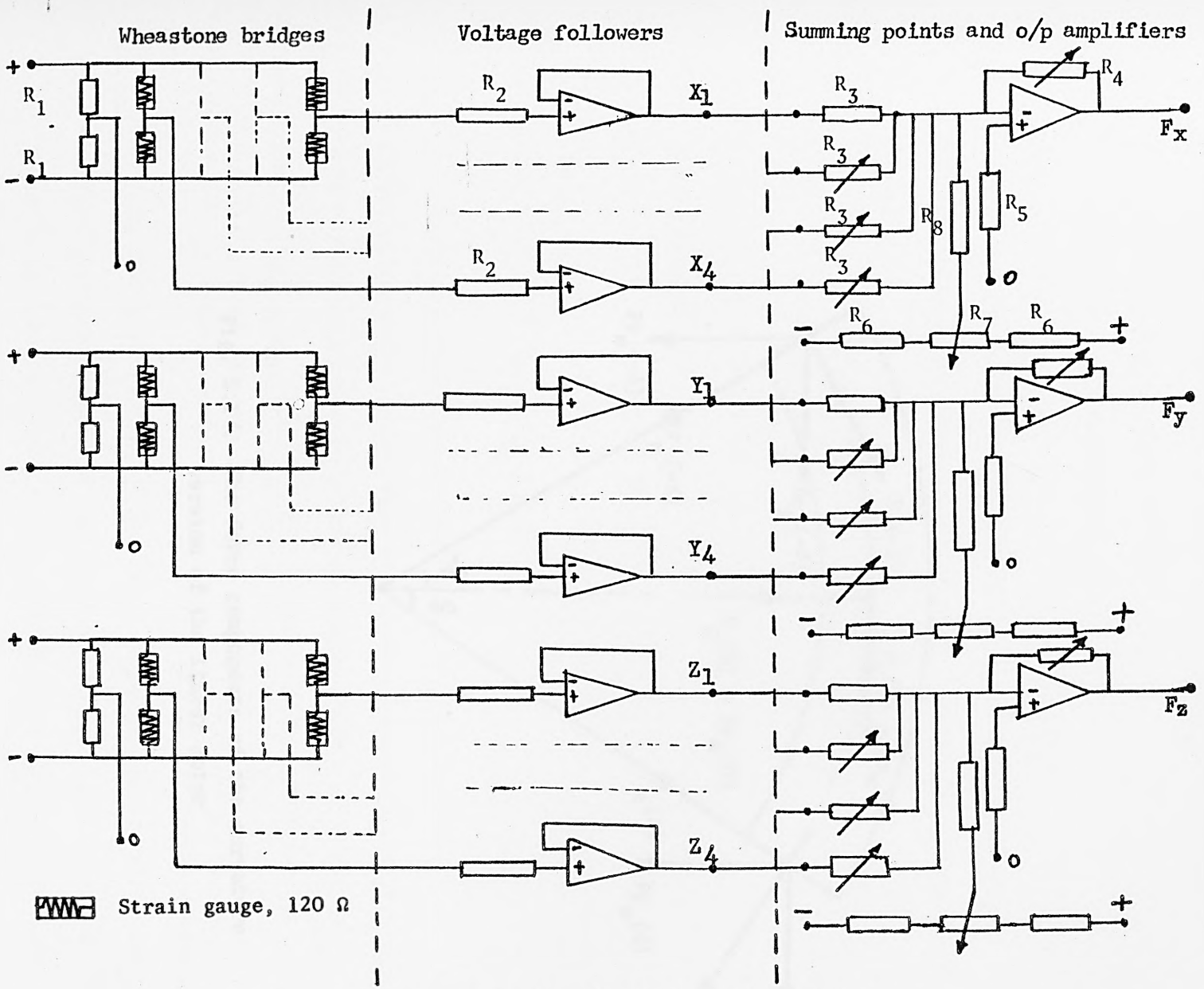

Fig. 5.13. The Electronic Circuit of Force Measurements

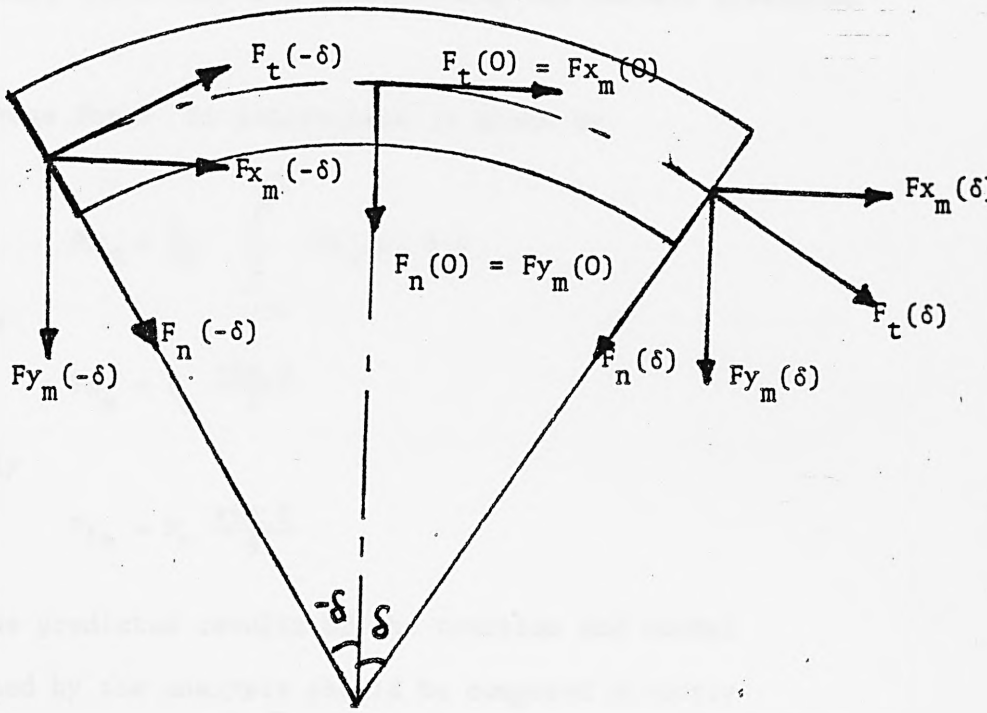

Fig. 5.14. The force components of the curvature version of the linear motor

where $Fx_m(\theta)$ = the measured force in x-direction at angle θ

$Fy_m(\theta)$ = the measured force in y-direction at angle θ

$F_t(\theta)$ = the traction force at angle θ

$F_n(\theta)$ = the normal force at angle θ

$Ft(\theta)$ and $Fn(\theta)$ could be replaced by their average value Ft and Fn respectively, which they are representing the overall developed forces.

The average force in x-direction is given by

$$Fx_m = \frac{1}{2\delta} \int_{-\delta}^{\delta} Fx_m(\theta)\, d\,\theta$$

which becomes

$$Fx_m = F_t \frac{\sin \delta}{\delta}$$

and similiarly

$$Fy_m = F_n \frac{\sin \delta}{\delta}$$

Since the predicted results of the traction and normal forces obtained by the analysis should be compared directly with the developed forces Ft and Fn respectively, the measured forces Fx_m and Fy_m should be multiplied by a factor $(\delta/\sin \delta)$ before any sort of comparisons are made.

In the above derivation the force distribution is considered uniform along the length of the machine. Precautions should be taken in applying the last factor at high speed operation because of the entry and exit end effects.

However, for the designed stator used in this work the force factor is rather close to unity (1.086).

5.4.2. Flux Density Measurement

The airgap flux densities were measured by means of search coils. Three search coils were used which wound on a perspex block, such that their axes are mutually perendicular to each other. These search coils were used to measure the flux density components in x, y and z directions.

Fig. 5.15 shows the mechanism of the search coils used in the dynamic test. A 3 mm perspex was used to eliminate any aerodynamic drag effect and to isolate the search coil mechanism from the rotating drum. The search coil set which was mounted at the top of the perspex was adjusted by pulleys mounted on the side and the top of the perspex to move the search coil set in the z and x directions respectively.

The search coils were calibrated against a known uniform flux in the three axes.

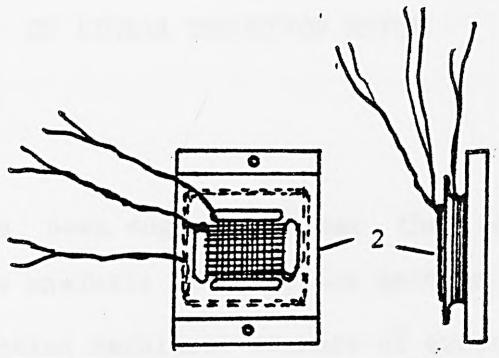

1. Stator
2. Search coil
3. Top pulleys
4. Side pulleys
5. Perpex

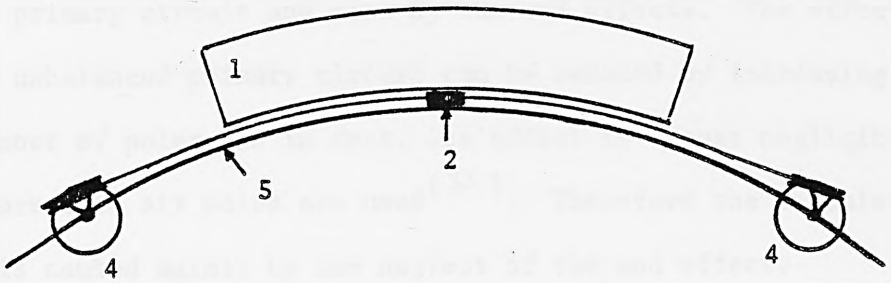

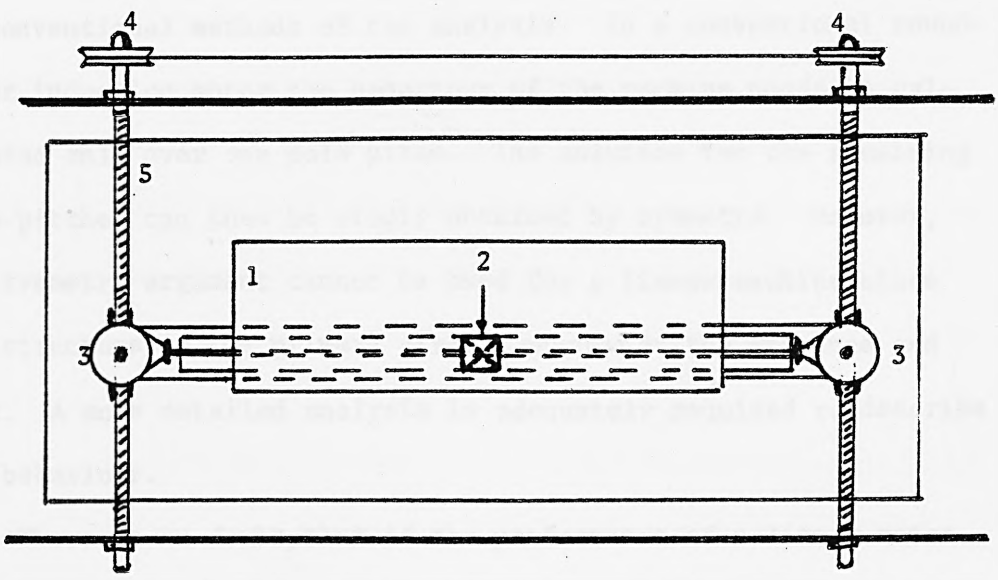

Fig. 5.15. Mechanism of flux density measurements

CHAPTER 6

POLE-BY-POLE EQUIVALENT CIRCUIT OF LINEAR INDUCTION MOTOR

6.1 Introduction

It has been suggested that the conventional methods for the analysis of induction machines are not applicable to linear induction machines, because of error caused by the negative phase driving force produced by the unbalanced structure of the primary circuit and also by the end effects. The effect of the unbalanced primary circuit can be reduced by increasing the number of poles and in fact, its effect is almost negligible when more than six poles are used[33]. Therefore the calculation error is caused mainly by the neglect of the end effect.

Another point, perhaps worth mentioning here with regard to conventional methods of the analysis. In a conventional round-rotor induction motor the behaviour of the machine needs be calculated only over one pole pitch. The solution for the remaining pole-pitches can then be simply obtained by symmetry. However, the symmetry argument cannot be used for a linear machine since the structure of the primary circuit changes at the entrance and exit. A more detailed analysis is adequately required to describe its behaviour.

There is no doubt, that if the performance of a linear motor can be represented by an equivalent circuit, this is likely to lend itself more readily to the process of computation than is, for example, the process of solving simultaneous partial differential

equations. However, that set of partial differential equations may in the first instance be used to derive the concept of any equivalent circuit.

Prominent among the numerous paper devoted to the equivalent circuit of linear induction machines are the works of Freeman[54], Ooi and White[55], Matsumija and Takagi[33] and Lipo and Nondah[34].

Using the concept of surface impedance and the transmission line analogy, Freeman has derived an equivalent circuit. His model is subjected to a travelling field produced by an applied current sheet, at the interface between two layers, distributed sinusoidally along the plane of laminations and flowing normally to the direction of motion. The procedure for systematically setting up his equivalent circuit is as follows; the cross-section through the machine is divided into a number of regions which have their boundaries parallel to the current sheet. The device is then thought of as two transmission lines comprising a number of sections in tandem, each section (representing a region) being replacable by a T or π network. The sections can then be joined together in the appropriate order to make one equivalent circuit which represents the whole machine. The impedance which the equivalent circuit presents at the current sheet is then referred to the phase terminals to give the input terminal impedance. In this model all end effects are neglected.

The analysis done by Ooi to derive the equivalent circuit of the LIM consists of applying the quasi-static approximation of Maxwell's electromagnetic equations to an idealised basis model of the linear machine. In this model the rotor conductor is represented as an infinitsimally thin conducting sheet. The longitudinal end effects as well as the skin and the transverse edge

effects are not considered in this analysis.

Matsumyi has developed a"per phase" equivalent circuit similar to those used for round rotor machines but which takes into account the end effects. However, the distribution of the air-gap flux density is approximated by a piece - straight line and the mmf induced by the end effect current flowing through the secondary conductor has been neglected. It also assumes that the skin and transverse edge effects are negligible.

The concept of d-q coupled circuit representing stator and rotor magnetic poles has been used by Lipo, and it is extended to the analysis of linear induction motor. In this paper the classical rotor winding is retained in the analysis. The developed model has been shown to predict the performance of a LIM in an acceptable fashion by using only conventional machine parameters, and machine equations are developed assuming that the rotor currents under each pole are independent on each other. The machine airgap fluxes and rotor currents are then solved on a pole-by-pole basis rather than a per-phase basis as commonly done for conventional cylindrical machines. The system of differential equations are of low order that their transient solution is entirely feasible on an analog or digital computer. The main assumption in this analysis is that the airgap flux density is confined to the area of the active winding at all speeds.

In this chapter a new equivalent circuit is set for a linear induction motor which is based on both the magnetic field and electric circuit theory. The flux density distribution of the machine is calculated using one-dimensional analysis, where the longitudinal ends effect are considered.

6.2 The Mathematical Model and its Analysis

The approach of deriving the equivalent circuit of the linear induction motor deals with the one-dimensional solution which takes into account one-dimensional field variation of the airgap in the direction of motion of the motor. Therefore all the necessary assumptions to present the one-dimensional model of the LIM shown in Fig. 6.1 are adopted. However, the longitudinal end effects are taken into account, while the skin effect, airgap leakage, the effect of slotting, and the transverse edge effects may consider by introducing their corresponding coefficients.

Referring to Fig.6.1 and applying Amperes law to the loop located at x and Δx wide yields

$$\frac{g}{\mu_o} \frac{\partial \overline{B}}{\partial x} = \overline{K} + \overline{J}.d \qquad (6.1)$$

The Maxwell-Faraday equation for a moving medium (secondary) is given by

$$\nabla \times \overline{E} = - \frac{\partial \overline{B}}{\partial t} - \nabla \times (\overline{V} \times \overline{B}) \qquad (6.2)$$

On the basis of the assumptions of the one-dimensional analysis, the following constraints are applied.

$$\overline{K} = Kz \ , \quad \overline{E} = E_x, \quad \overline{J} = Jz, \quad \text{and} \quad \overline{B} = \overline{B}_y$$

Therefore eq.(6.2) becomes

$$\frac{\partial E_z}{\partial x} = \frac{\partial B_y}{\partial t} + V_x . \frac{\partial B_y}{\partial x} \qquad (6.3)$$

Hence
$$\frac{\partial Jz}{\partial x} = \sigma \cdot \left(\frac{\partial B_y}{\partial t} + V_x \frac{\partial B_y}{\partial x}\right) \qquad (6.4)$$

where
$$J_z = \sigma E_z \qquad (6.5)$$

From eqs. (6.1) and (6.4) the characteristic equations of the one-dimensional analysis of the LIM is obtained.

$$\frac{\partial Kz}{\partial x} = + \frac{g}{\mu_o} \cdot \frac{\partial^2 B_y}{\partial x^2} - d.\sigma \cdot \left(\frac{\partial B_y}{\partial t} + V_x \frac{\partial B_y}{\partial x}\right) \qquad (6.6)$$

The primary excitation is given by

$$Kz = K_a \cdot e^{j(\omega t - kx)}$$

and it is assumed that all variables are vary sinusiodally with the time.

The general solution of equation(6.6)on the active zone may be given by

$$B_y = B_s \cdot e^{-jkx} + B_1 \cdot e^{\beta_1 x} + B_2 \cdot e^{\beta_2 x} \qquad (6.7)$$

where B_s is obtained from the steady state solution of the characteristic equation and given by

$$B_s = \frac{K_a}{C1} = \frac{K_a}{|C1|} \cdot e^{j\delta s} \qquad (6.8)$$

where $C1 = s\nu_s \sigma d - j \frac{gk}{\mu_o}$

$$\delta s = \tan^{-1} \left(\frac{gk}{sV_s \sigma \mu_o d}\right)$$

β_1 and β_2 are the roots of the auxiliary equation

$$\frac{g}{\mu_o} \cdot \beta^2 - d\sigma V.\beta - j\omega\sigma d = 0 \qquad (6.9)$$

whose solution is

$$\beta = \frac{\sigma v \mu_o d}{2g} \pm \frac{1}{2}\sqrt{\left(\frac{\sigma v \mu_o d}{g}\right)^2 + j\frac{4\omega\sigma\mu_o d}{g}}$$

Hence $$\beta_1 = \frac{\sigma v \mu_o d}{2g} - \frac{1}{2}\sqrt{\left(\frac{\sigma v \mu_o d}{g}\right)^2 + j\frac{4\omega\sigma\mu_o d}{g}} = -\frac{1}{\alpha} - j\,k_1$$

$$\beta_2 = \frac{\sigma v \mu_o d}{2g} + \frac{1}{2}\sqrt{\left(\frac{\sigma v \mu_o d}{g}\right)^2 + j\frac{4\omega\sigma\mu_o d}{g}} = \frac{1}{\alpha_2} + jk_2$$

and B_1, B_2 are found from the boundary conditions as descriped later on.

Therefore the airgap flux density equation becomes

$$B_y = B_s.e^{-jkx} + B_1.e^{\frac{-x}{\alpha 1}}.e^{-jk_1x} + B_2.e^{\frac{x}{\alpha 2}}.e^{+jk_2x}$$

and as all variables vary as $e^{j\omega t}$ it becomes

$$B_y = B_s.e^{j(\omega t - kx)} + B_1.e^{\frac{-x}{\alpha 1}}.e^{j(\omega t - k_1x)} + B_2.e^{\frac{x}{\alpha 2}}.e^{j(\omega t + k_2x)}$$

The first term of the above equation represents the "normal wave" which is the steady-state sinusoidal wave travelling at synchronous speed. The second term represents the "forward wave" travelling in the same direction as the normal wave, having a pole pitch (π/k_1) and attenuating while travelling by the factor (α_1). The third wave represents the "backward wave" travelling in the opposite direction to that of the normal wave, having a pole pitch (π/k_2) and attenuating while travelling by the factor (α_2).

It is believed that the third wave has no significant effect on the performance of the machine [17,36], since it is attenuating very rapidly with respect to the second wave, therefore the equation of the airgap flux density which is considered in this work will be

$$B_y = B_s.e^{j(\omega t - kx)} + B_1.e^{\frac{-x}{\alpha 1}}.e^{j(\omega t - k_1x)} \qquad (6.11)$$

Generally speaking, B_1 may be related to B_s by the expression

$$B_1 = T \cdot B_s \tag{6.12}$$

where T is determined by using the appropriate boundary conditions, as will be shown later in this chapter.

Therefore the airgap flux density equation becomes

$$B_y = (1 + T \cdot e^{\frac{-x}{\alpha 1}} \cdot e^{j(k-k_1)x}) \cdot B_s \cdot e^{j(\omega t - kx)} \tag{6.13}$$

6.3 The Deriviation of the Equivalent Circuit Elements

6.3.1 Constant-Current Drive

For the case of series connected-primary winding, the primary line current density is specified as being sinusoidally distributed, as mentioned earlier.

Having found the value of the normal flux density (B_s) the secondary current density can be obtained from eqs. (6.1), (6.8), (6.11), and (6.12).

$$Js = (C2 + C3 \cdot e^{\frac{-x}{\alpha 1}} \cdot e^{j(k-k_1)x}) \cdot B_s \cdot e^{j(\omega t - kx)} \tag{6.14}$$

$$Js = M1 \cdot B_s \cdot e^{j(\omega t - kx)}$$

where

$$C2 = - \sigma s v_s$$

$$C3 = \frac{g}{\mu_o} \cdot (\frac{-1}{\alpha 1} - jk_1)$$

$$M1 = C2 + C3 \cdot e^{\frac{-x}{\alpha 1}} \cdot e^{j(k-k_1)x}$$

Making use of Lorentz force-equation the time average thrust force of the LIM in x-direction is given by

$$F_x = \frac{-hd}{2} \cdot \mathrm{Re}\left[\int_0^L B_y . J_s^* \, dx\right] \tag{6.15}$$

and the time average ohmic losses of the secondary is

$$P_L = \frac{hd}{2} \cdot \mathrm{Re}\left[\int_0^L E_s . J_s^* \, dx\right] \tag{6.16}$$

The output power is

$$P_o = F_x . V_x \tag{6.17}$$

The input power is

$$P_i = W_o + W_L$$

As the airgap field density, is changing while travelling in x-direction due to the end-effects and consequently the secondary current density, the equivalent circuit for the LIM should be formulated on the basis of pole by pole.

Therefore the elements of the equivalent circuit shown in Fig. (6.2) are determined per pole as follows:

Substituting of eqs.(6.13) to (6.15) in eq.(6.17) gives

$$P_o = \frac{-hdV_x}{2} \cdot \mathrm{Re}\left[\int_{x_1}^{x_2} B_y J_s^* \, dx\right]$$

$$P_o = \frac{-hdV_x |B_s^2|}{2} \cdot \mathrm{Re}\,(C4 + C5 + C6 + C7) \tag{6.18}$$

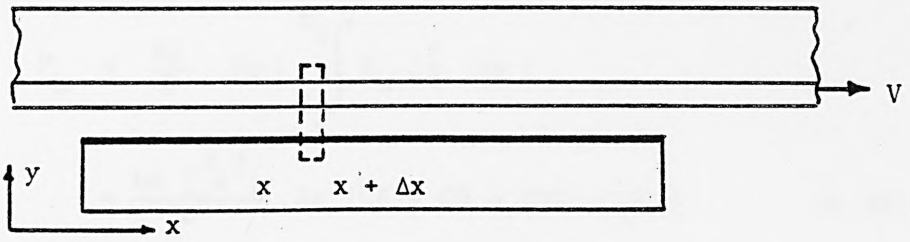

Fig. 6.1. Model of a LIM for the equivalent circuit approach

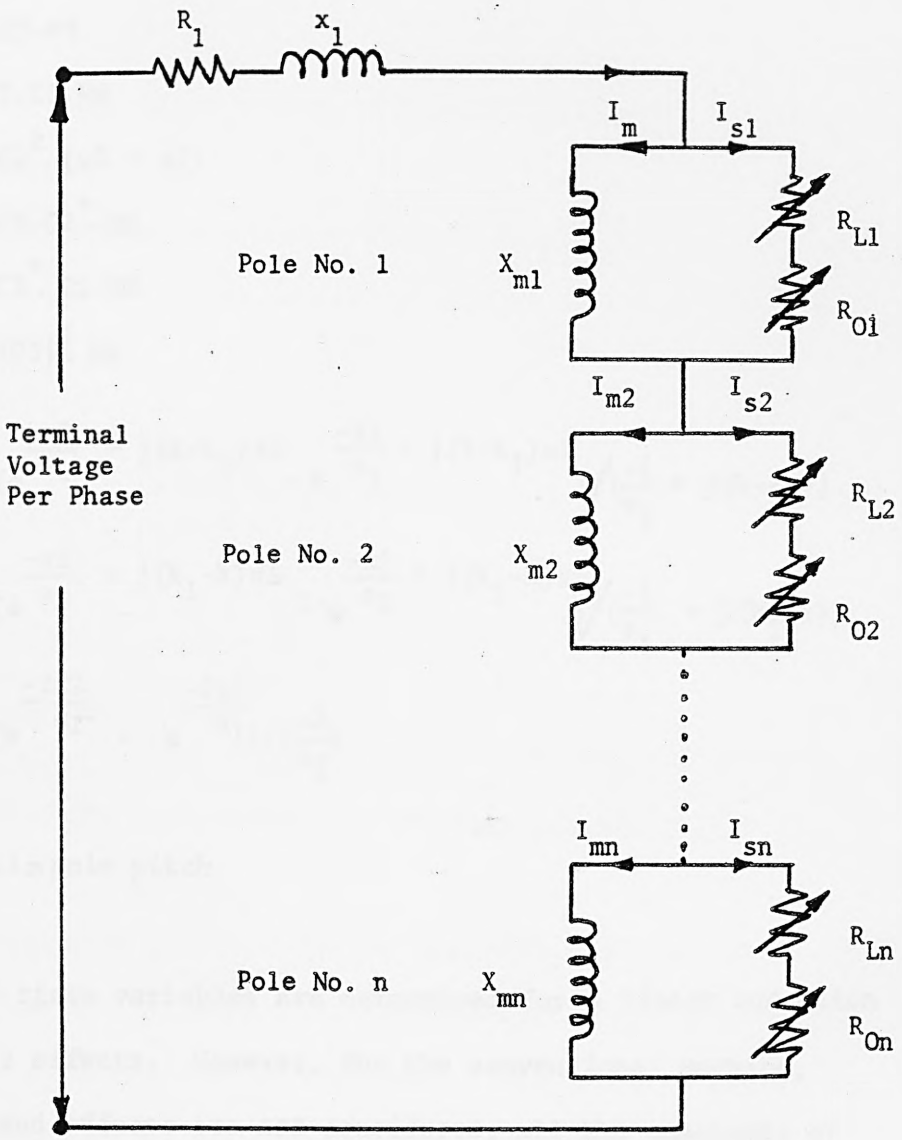

Fig. 6.2. The equivalent circuit of a LIM of series - connected primary winding

and substituting eqs. (6.5) and (6.14) in eq. (6.16) yields

$$P_L = \frac{hd}{2} \cdot \mathrm{Re}\left[\int_{x_1}^{x_2} E_s \cdot J_s^* \, dx\right]$$

$$= \frac{hd\,|B_s^2|}{2\sigma} \cdot \mathrm{Re}\,(C8 + C9 + C10 + C11) \qquad (6.19)$$

where $C4 = C2 \cdot (x2 - x1)$

$C5 = T \cdot C2 \cdot M2$

$C6 = C3 \cdot M3$

$C7 = T \cdot C3 \cdot M4$

$C8 = C2^2 \cdot (x2 - x1)$

$C9 = C3 \cdot C2^* \cdot M2$

$C10 = C3^* \cdot C2 \cdot M3$

$C11 = |C3|^2 \cdot M4$

$$M2 = \left(e^{\frac{-x2}{\alpha_1} + j(k-k_1)x2} - e^{\frac{-x1}{\alpha_1} + j(k-k_1)x1}\right) \Big/ \left(\frac{-1}{\alpha_1} + j(k-k_1)\right)$$

$$M3 = \left(e^{\frac{-x2}{\alpha_1} + j(k_1-k)x2} - e^{\frac{-x1}{\alpha_1} + j(k_1-k)x1}\right) \Big/ \left(\frac{-1}{\alpha_1} + j(k_1-k)\right)$$

$$M4 = \left(e^{\frac{-2x2}{\alpha_1}} - e^{\frac{-2x1}{\alpha_1}}\right) / \left(\frac{-2}{\alpha_1}\right)$$

$x2 - x1 =$ pole pitch

The above state variables are determined for a linear induction motor with ends effects. However, for the conventional machine, i.e. when the end effects are not considered, all the constants of eqs. (6.18) and (6.19) except C4 and C8 become zero.

By making use of eqs. (6.18) and (6.19), the rotor elements of the equivalent circuit shown in Fig. 6.2 may be determined.

$$R_o = \frac{P_o}{3|I_2|^2} \tag{6.20}$$

$$R_L = \frac{P_L}{3|I_2|^2} \tag{6.21}$$

where $I_2 = \frac{Js.d}{Q}$ (6.22)

where Q is a constant which relates the phase current to the primary line current density.

I_2 is calculated at the centre of each pole, i.e. at $x = \frac{x2 + x1}{2}$

Then from eqs. (6.18) to (6.22) the values of the elements of Fig. 6.2 per poles are

$$R_o = \frac{-hvQ^2d}{6|M_1|^2} \cdot \mathrm{Re}\ (C4 + C5 + C6 + C7) \tag{6.23}$$

and

$$R_L = \frac{hQ^2d}{6\sigma|M_1|^2} \cdot \mathrm{Re}\ (C8 + C9 + C10 + C11) \tag{6.24}$$

R_1 and X_1 are obtained by using the conventional expressions. The secondary leakage reactance X_2 is neglected at the primitive studying.

Having determined the flux density components at the centre of each pole, the secondary current and in consequence the magnetizing current of each pole referred to the primary are obtained using Kirchoff's current law.

The magnetizing reactance is either obtained by the conventional method using machine parameters, or from the equivalent circuit of each pole as follows

$$(jX_m).I_m = (R_o + R_L + jX_2).I_2$$

Let $I_m = a + jb$

$I_2 = c + jd$

Therefore

$$X_m = \frac{(R_o + R_L).(c^2 + d^2)}{(ad - cb)} \qquad (6.25)$$

and

$$X_2 = \frac{(R_o + R_L).(ac + bd)}{ad - cb} \qquad (6.26)$$

or

$$X_2 = X_m.\frac{(ac + bd)}{(c^2 + d^2)}$$

It was found, without end effect, that Xm which is calculated by the above expression is equal to that given by the conventional method, and the secondary leakage reactance X_2 is equal to zero.

The voltage induced across the pole pitch i is obtained from Faraday's Law.

$$\nabla \times \overline{E} = -\frac{\partial \overline{B}}{\partial t}$$

Thus

$$E_i = \left[\left(-V_s + \frac{-j\omega T}{\frac{1}{\alpha_1} + jK_1} \cdot e^{\frac{-x}{\alpha_1}} \cdot e^{j(k-k_1)x}\right).B_s.e^{j(\omega t - kx)} + Ec\right].D \qquad (6.27)$$

where D is a constant to relate the induced voltage E_i to the electric

field intensity E.

Ec is a constant can be determined by making use of the appropriate boundary condition which has been choosen to calculate the factor T of the entry end wave of the flux density and as described in the next section.

However, the induced voltage per pole may be obtained as well from the equivalent circuit as

$$E_i = I_{mi} \cdot (jX_{mi})$$

The resultant terminal voltage per phase is given by

$$V = I_1 . Z_1 - \sum_{i=1}^{i=n} E_i \qquad (6.28)$$

where n : total number of poles

I_1 : RMS of the primary current

Z_1 : primary impedance

The total losses, output power and the propulsion force of the linear induction motor are obtained by adding up the contributions of all the poles on these state variables.

In consequence, the power factor and the efficiency of the machine are obtained

6.3.2. Constant Voltage Drive

The equivalent circuits of the constant voltage drive and constant current drive are the same as shown in Fig. 6.2.

The same derivation is adopted for both supply systems. However, for a constant voltage drive, the normal flux density B_s is related to the terminal voltage rather than the primary current density.

Thus the characteristic equation (6.6) becomes

$$\frac{Q}{Z_1} \cdot \frac{dV}{dx} = \frac{g}{\mu_o} \cdot \frac{\partial^2 B}{\partial x^2} - d\sigma . V \cdot \frac{\partial B}{\partial x} - (d\sigma + \frac{Q}{Z_1} \cdot D) \cdot \frac{\partial B}{\partial t}$$

where B_s is obtained from the steady state solution of the characteristic equation and given by

$$B_s = \frac{V}{\frac{Cl . Z_1}{Q} + V_s . D}$$

and the roots of the characteristic equation become

$$\beta = \frac{\sigma v \mu_o d}{2g} \pm \frac{1}{2} \sqrt{(\frac{\sigma v \mu_o d}{g})^2 + j \frac{4\omega \mu_o (\sigma d + \frac{Q}{Z_1} D)}{g}}$$

6.4 Boundary Conditions

The influences of the end effects on the performance characteristics of the linear induction motor at high speed and low speed drives are quite different.[17] Therefore, certain precautions should be taken in choosing the appropriate boundary conditions.

In this analysis two boundary conditions are examined as follows:

1) Due to the end effects, a considerable value of the secondary current at x = 0 is induced, thus the magnetizing current becomes negligible, in particular for series-connected primary windings. From the above fact the following constraints may obtain

$$\frac{g}{\mu_o} \cdot \frac{\partial B}{\partial x} = 0 \qquad \text{at } x = 0$$

thus $$|B_1| . e^{j\delta 1} = T . |B_s| . e^{j\delta s}$$

where $$T = \frac{-jk}{\frac{1}{\alpha_1} + jk_1} \tag{6.34}$$

Thus equation (6.1) becomes

$$Js = - \frac{Kz}{d}$$

and from eqs. (6.5) and (6.27)

$$Ec = + [V_s . (1 + \frac{k^2}{(\frac{1}{\alpha} + jk_1)^2}) - \frac{C1}{d\sigma}] . B_s \tag{6.35}$$

where the secondary leakage reactance is neglected.

2) At the entry end of a high speed machine the magnetic field is built up very steeply, and the speed term $(\frac{\partial B_y}{\partial x})$ of equation (6.4) is much larger than the transformer term $(\frac{\partial B_y}{\partial t})$

$$V \frac{\partial B_y}{\partial x} >> \frac{\partial B_y}{\partial t}$$

And if there is no fringing of magnetic flux, then eq.(6.4) becomes;

$$Js = \sigma v_x B_y \qquad \text{at } x = 0$$

By making use of eq.(6.1) T is given by

$$T = \frac{-\sigma d V_s}{\sigma v_x d + \frac{g}{\mu_o}(\frac{1}{\alpha_1} + jk_1))} \tag{6.36}$$

Eq.(6.4) together with eqs.(6.5) and (6.27) gives

$$E_c = [-V_x(1 + T) + (V_s + \frac{j\omega T}{\frac{1}{\alpha_1} + jK_1})] B_s \tag{6.37}$$

Fig. 6.3. shows the performance of the LIM under a constant current drive by implementing the two boundary conditions mentioned earlier.

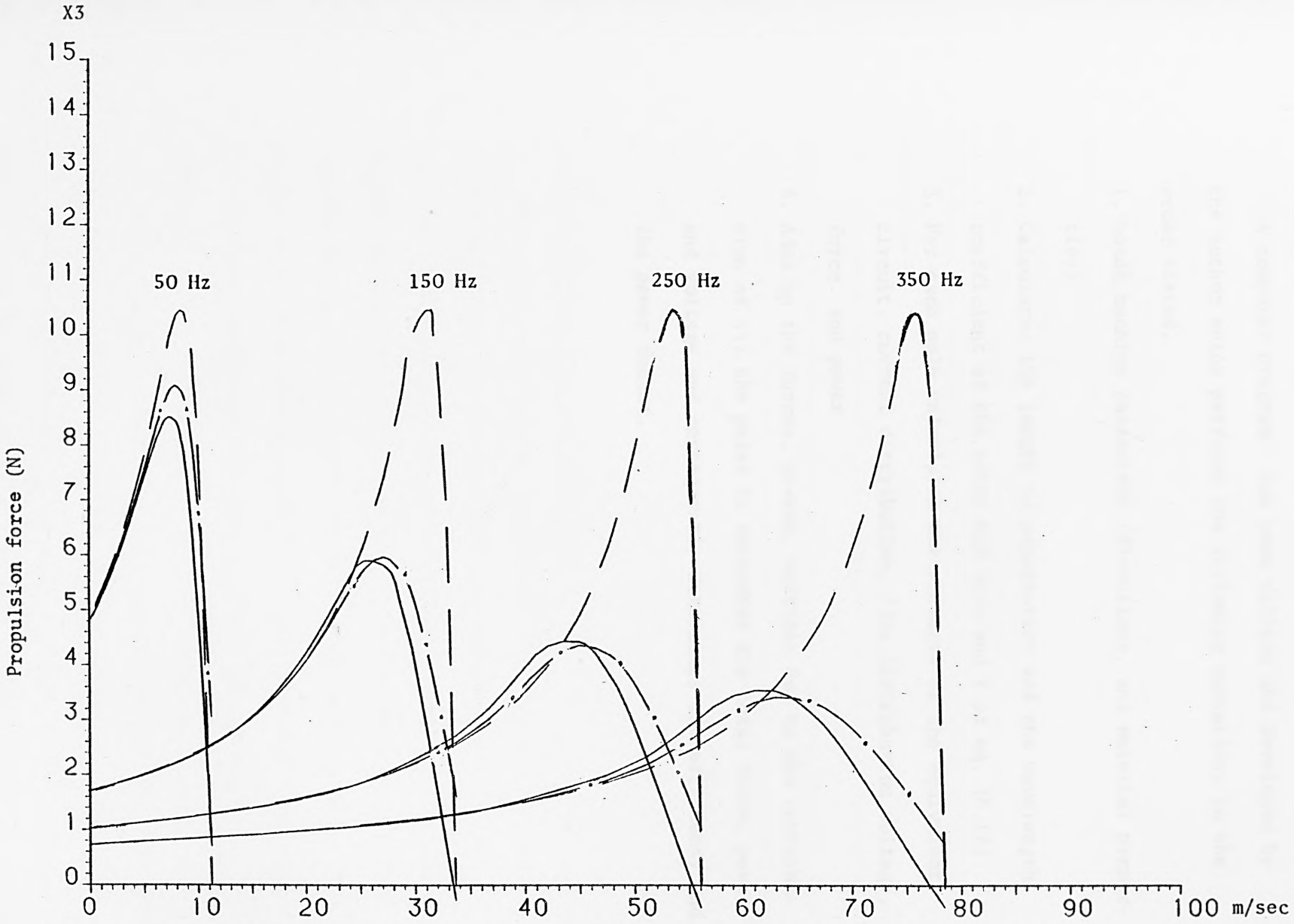

Fig. 6.3. Propulsion speed characteristics of the LIM using different boundary conditions
-- without end effects, -·- with end effects using boundary condition No. 1,
— with end effects using boundary condition No. 2

6.5 Computer Program

A computer program has been written and developed by the author which performs the following operations in the order stated.

1. Reads machine parameters (dimensions, and material properties)
2. Calculates the length of penetration and the wavelength coefficient of the entry end wave and T of eq. (6.12)
3. For each pole calculates the elements of the equivalent circuit, current distribution, flux distribution, voltage, force and power
4. Adds up the forces, powers, voltages due to the contribution of all the poles to determine the total force, power and voltage and consequently determines the efficiency and the power factor.

CHAPTER 7

COMPARISON OF THE RESULTS WITHOUT BACKING IRON

7.1 Introduction

The objective of this chapter is to present and compare the predicted and experimental results of the performance characteristics of the linear induction motor.

The linear motor is of half-filled end slots, with an airgap of 9.5 mm; the secondary consists of a pure aluminium sheet unbacked by iron.

The predicted results were computed by the numerical solution method using the models described earlier. The measurements and the predicted results were obtained at a constant current drive of 5A phase current (35.34 kA/m) and at supply frequencies of 50, 150, 250 and 350 Hz.

7.2 Flux Density and Flux Distributions

The airgap flux density components were measured by means of search coils. The measured and the predicted results were obtained on a plane 3.17 mm above the stator surface. The values of the flux density along the x-direction are taken on the line passing through the centre of the machine along its length. The values of the flux density along the z-direction are taken on the line passing through the centre of the machine along its width.

Figs. 7.1 to 7.4 show the x and y components of the flux density along the z axis for f = 50, 150, 250 and 350 Hz at stand still.

Figs. 7.5 to 7.8 show the x and y components of the flux density along the x axis for f = 50, 150, 250 and 350 Hz at stand still.

Figs 7.9 and 7.10 show the z component of the flux density along the z axis for f = 50, 150, 250 and 350 Hz.

Figs. 7.11 and 7.12 show the x and y components of the flux density along the z and x axis for a frequency = 250 Hz and at a slip of 0.6.

Figs. 7.13 and 7.14 show the x and y components of the flux density along the z and x axis for f = 350 Hz and at a slip of 0.6.

Figs. 7.15 and 7.16 show the predicted results of the x and y components of the flux density along the z axis for different slips and at supply frequencies of 150 and 350 Hz

Figs. 7.17 and 7.18 show the predicted results of the x and y components of the flux density along the x axis for different slips and at supply frequencies of 150 and 350 Hz.

The results shown in Figs. 7.15 to 7.18 were obtained from the three dimensional homogenous anisotropic model 3DHM. The results of one dimensional model 1DHM are plotted so that to illustrate the significance of the end effects on the flux density distribution with the speed of the linear motor.

Generally, it is found from the above results that the x-component of the flux density B_x increases slightly with frequency, while the y-component B_y is inversely proportional to the frequency. Also B_x decreases slightly, with the slip, while B_y increases at a higher rate.

From Fig. 7.18, the end effects due to the entry and exit ends of the linear motor can be recognised from the redistribution of the y component of the flux density along the x direction for different slips. The value of B_y is reduced at the entry end, and as the end effects attenuate along the length of the machine,

the flux will build itself to the normal value.

It can be seen as well from the margin between the 3DHM and 1DHM results that the end effects become more significant at high speed.

So far, the predicted results are satisfactory in general with the experimental results, as they are fall between the measured values which were obtained above the teeth and slots. However, the predicted results, as expected, are not close enough to each other. The divergences in the results of the two dimensional models (2DHM and 2DCM) and the three dimensional models (3DHM and 3DCM) can be related to the assumptions made. The differences in the results of the models represented by the current sheet (3DCM, and 2DCM) and the corresponding homogenous anisotropic models (3DHM and 2DHM) are related directly to the way in which the primary winding is represented. In homogenous anisotropic models the slot leakage of the stator is already considered; thus part of the winding m.m.f. is consumed by the leakage reluctance and the rest of it by the main magnetic path. In the case of current sheet models the winding mmf is consumed only by the main magnetic path.

From the graphs of the y and z components of the flux density along the z axis it can be seen that there are some differences between the results of the 3DCM and 3DHM. These disagreements may be due to first, the assumption of extending the iron of the stator of the 3DCM up to the end of the overhang winding, which cannot be avoided with a current sheet representation. Secondly, the shape of the overhang conductor of the 3DHM which is mounted in air at an angle of 90 degrees with the stator core. The first assumption is rather over estimating the overhang topology, while

in the second configuration the overhang is under estimated which leads to a small value of the x component of the magnetic vector potential (Ax). The z-component of the flux density is depending only on Ax, while the y-component of the flux density is significantly effected by Ax.

In figs. 7.19 to 7.26 the contours of the flux on a plane along the machine are presented. These obtained by the two dimensional models 2DHM and 2DCM for supply frequencies of 50, 150, 250, and 350 Hz at different slips.

From these contours the end effects could be seen clearly in redistributing the flux contours along the machine in the direction of motion of the secondary.

It can be observed that the flux contours at the top of the stator (on the airgap and the secondary) are almost identical for both 2DHM and 2DCM models. However, they are rather different through the stator core due to the consideration of the slots flux leakage in the configuration of the 2DHM.

For better understanding of the flux distribution and for further examination of the flux density distribution along the x and z directions, three dimensional plot for the three components of the flux density are presented in Figs. 7.27 to 7.30. These plots were obtained from 3DHM and 3DCM for supply frequencies of 150 and 350 Hz and at a slip of 0.3.

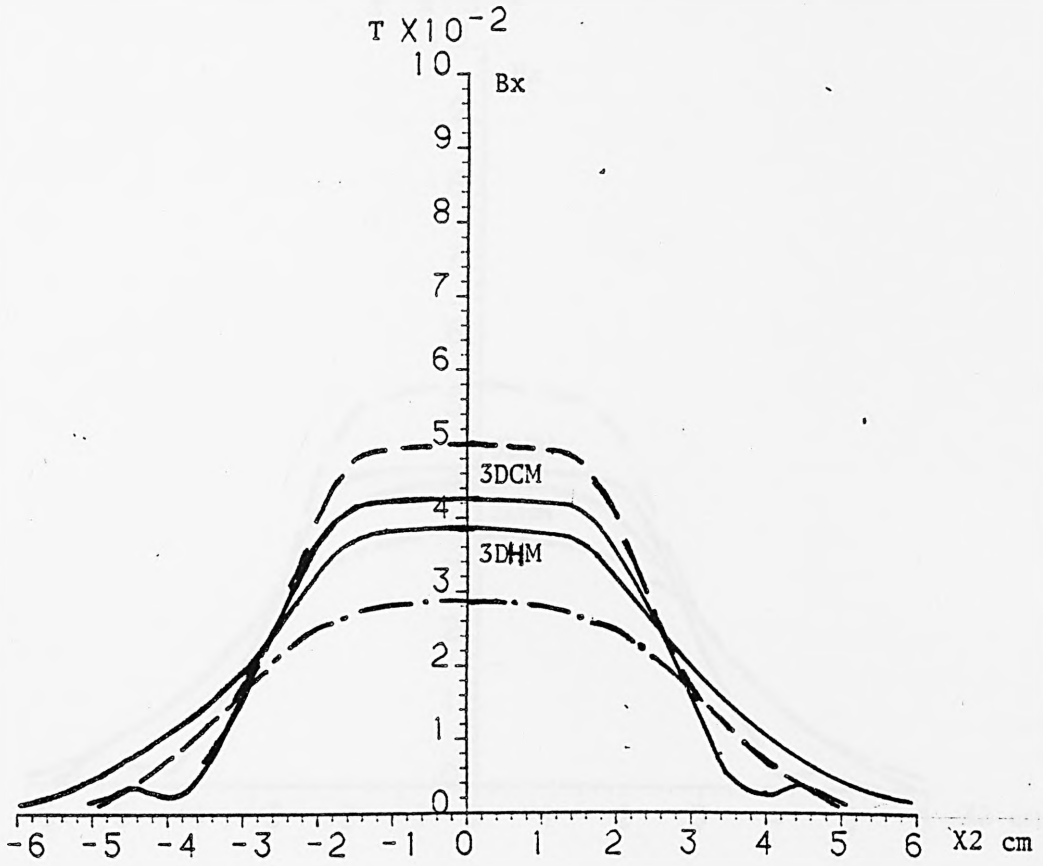

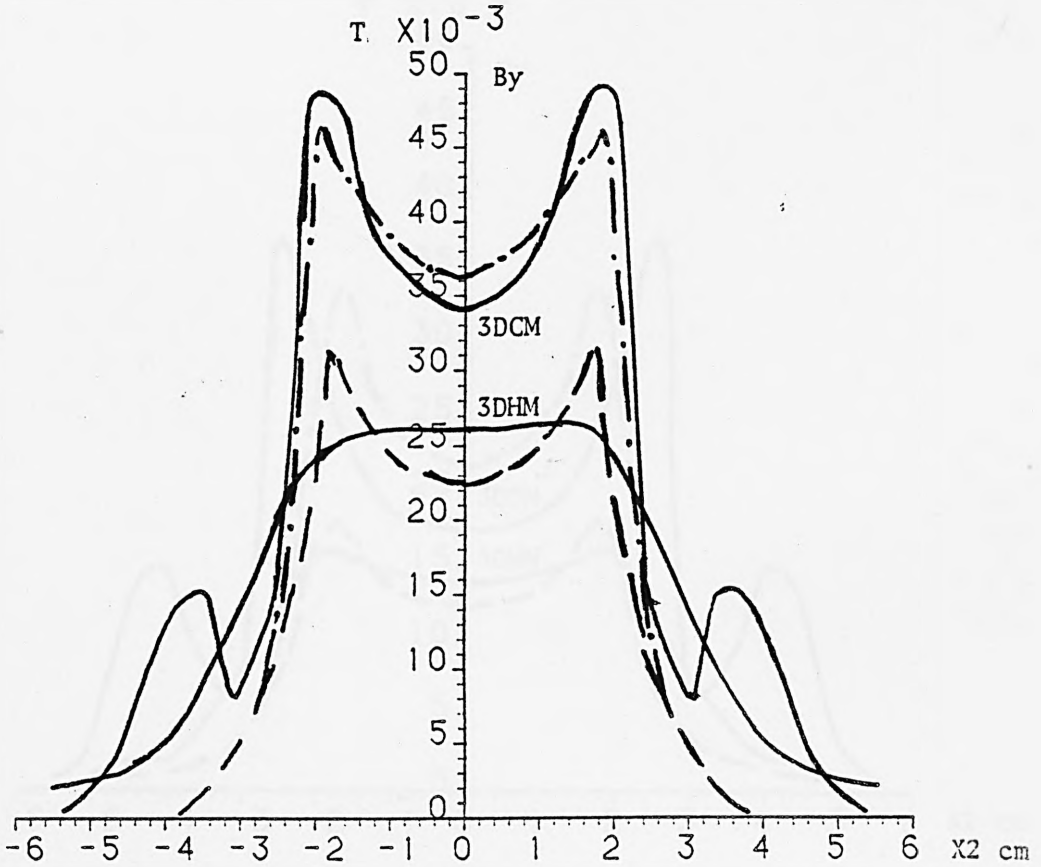

Fig. 7.1. Airgap Flux Density Components along the z-direction at I = 5A, g = 9.5 mm, F = 50 Hz S = 1.0.

— computed, -- measured above slots, -·- measured above teeth

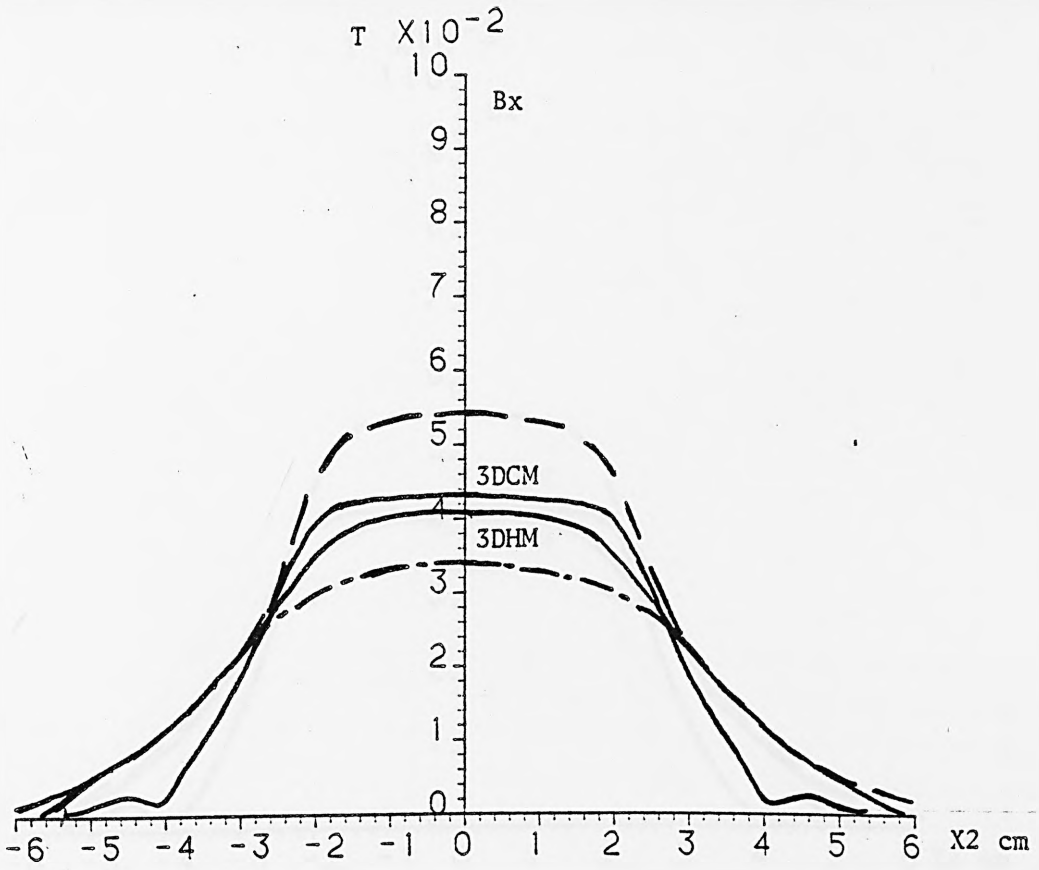

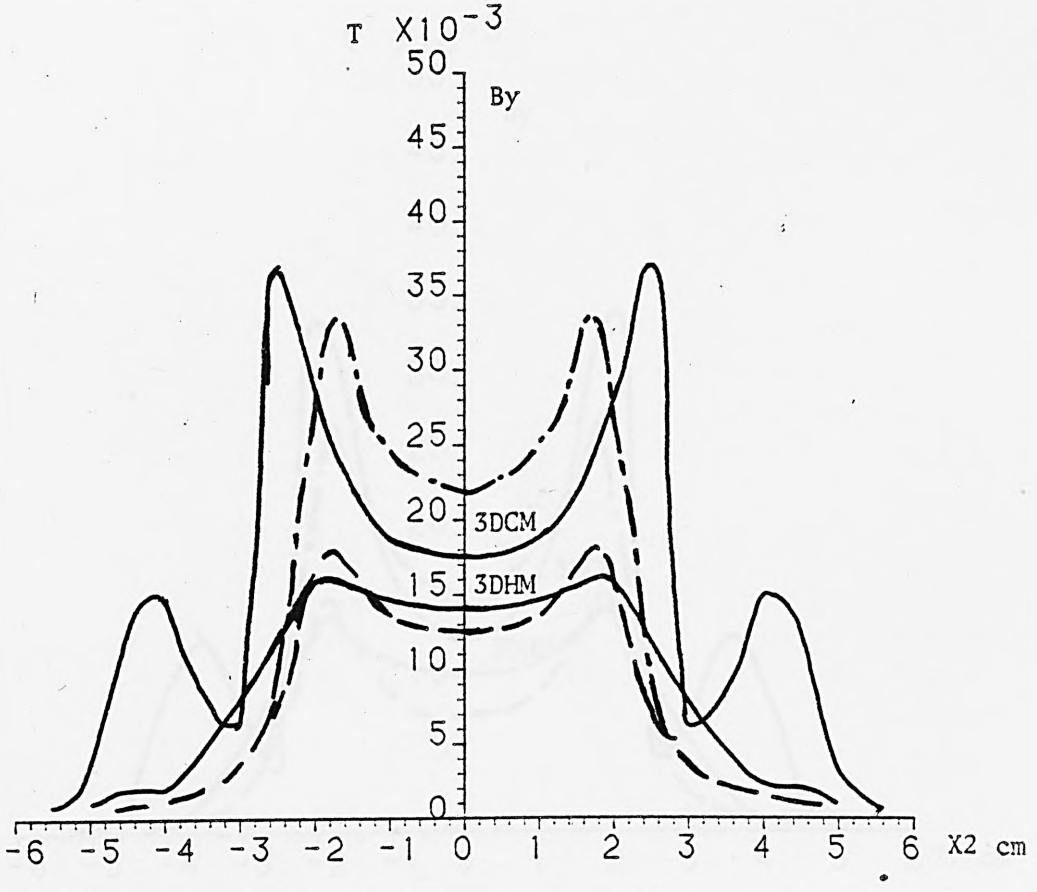

Fig. 7.2. Airgap Flux Density Components along the z-direction at I = 5A, g = 9.5 mm, f = 150 Hz, S = 1

— computed, -- measured above slots, -·- measured above teeth

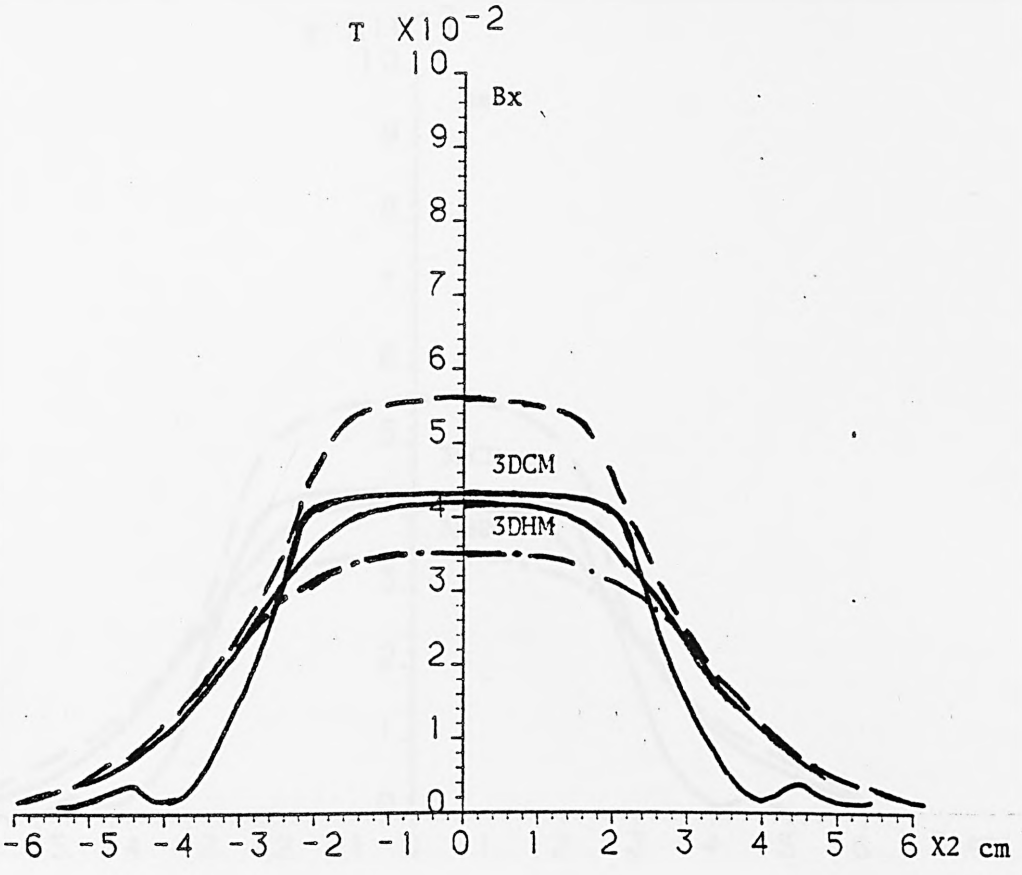

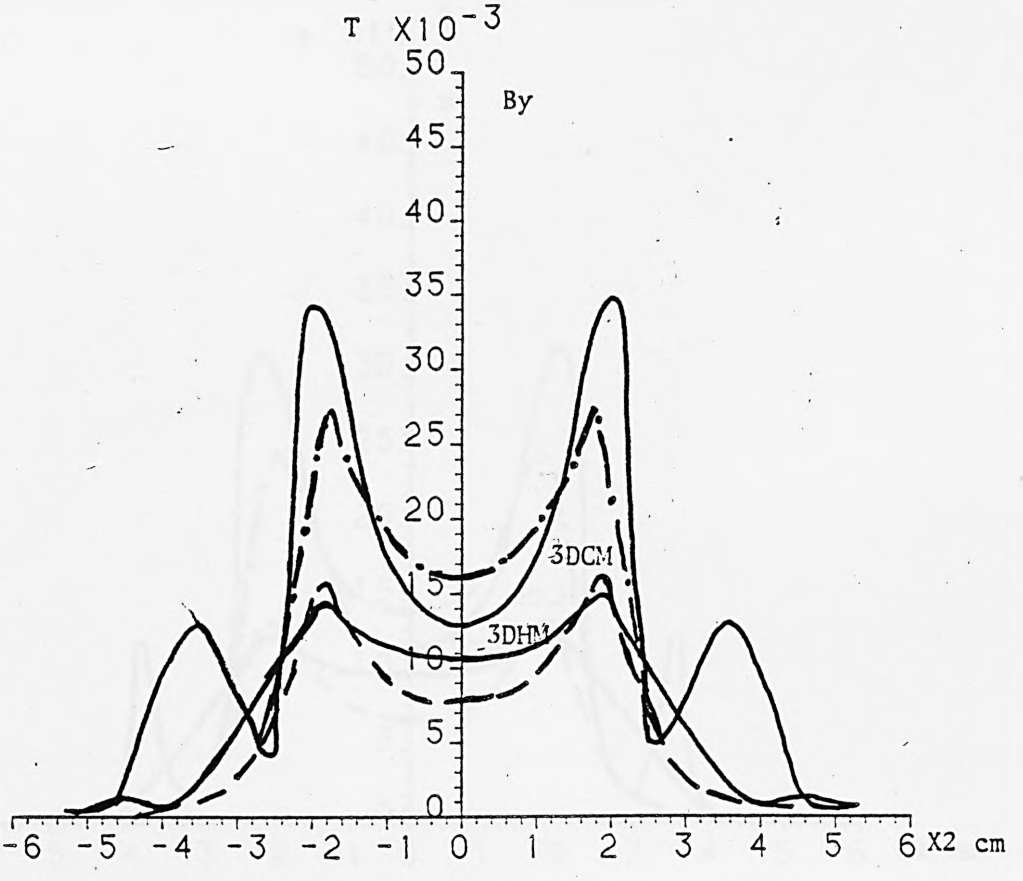

Fig. 7.3. Airgap Flux Density Components along the z-direction at I = 5A, g = 9.5 mm, f = 250 Hz, S = 1

— computed, -- measured above slots, -·- measured above teeth

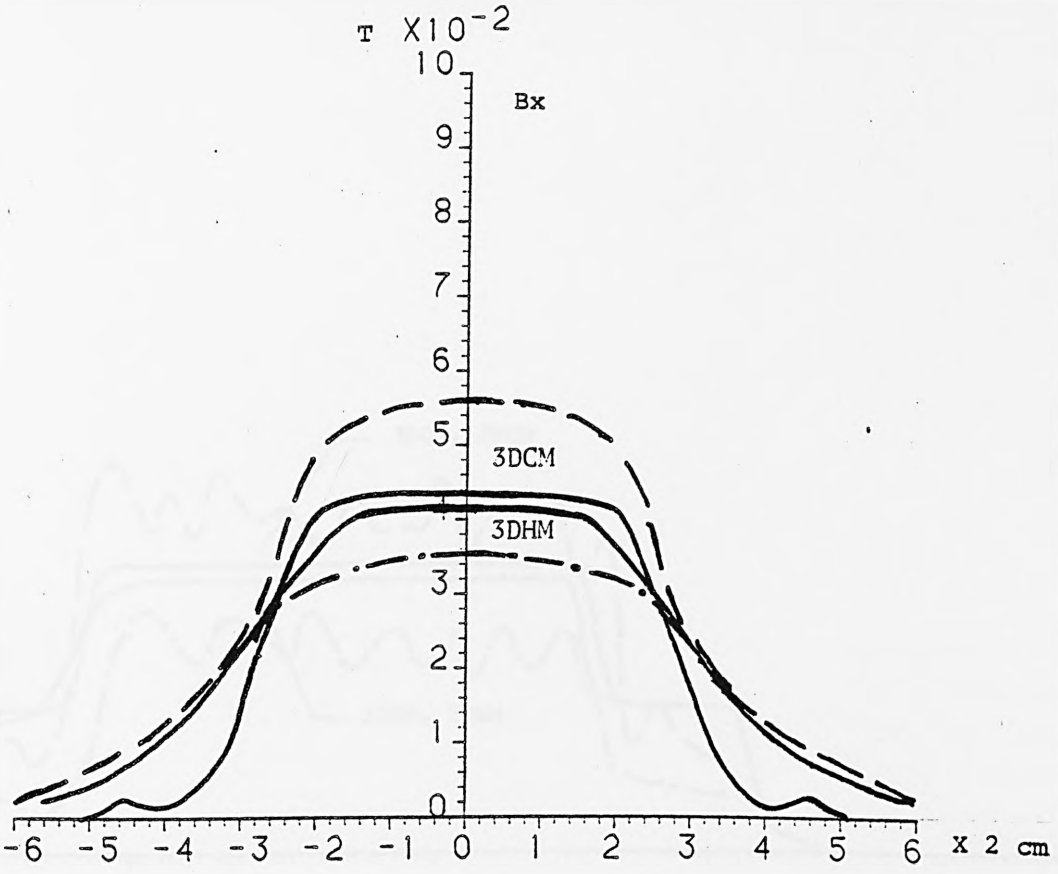

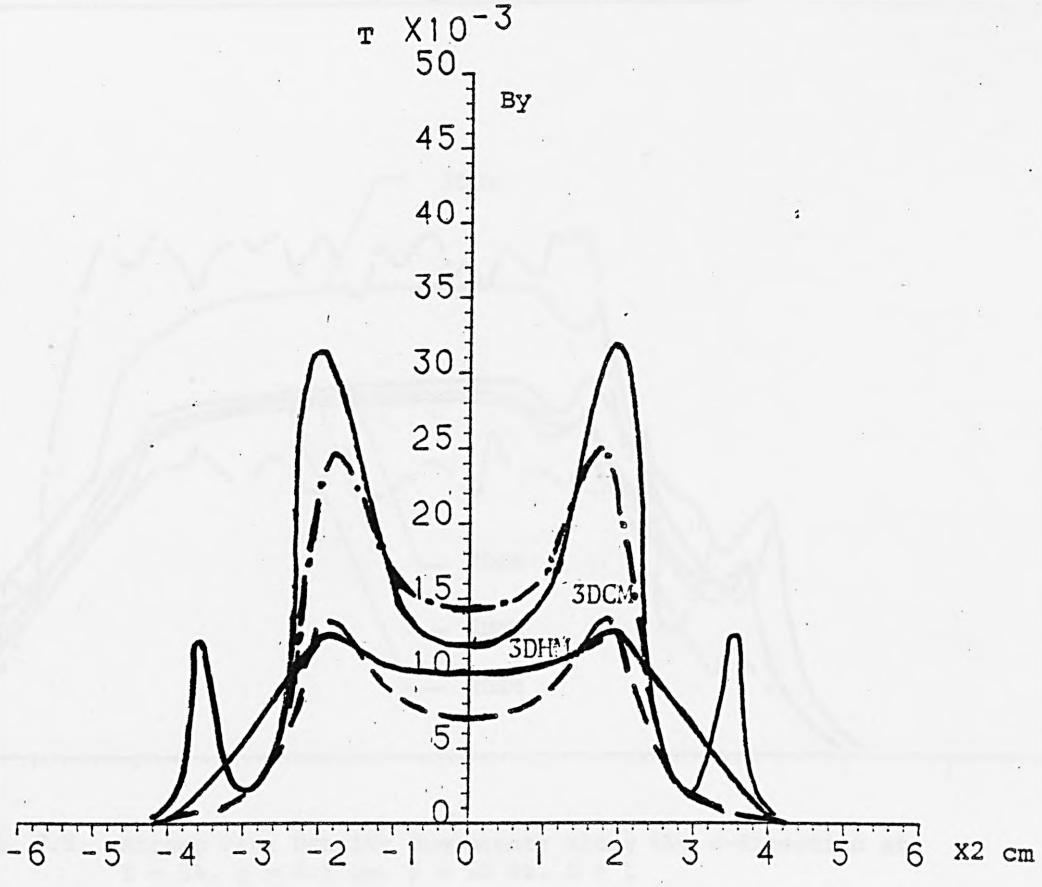

Fig. 7.4. Airgap Flux Density Components along the z-direction at I = 5A, g = 9.5 mm, f = 350Hz, S = 1

— computed, -- measured above slots, -·- measured above teeth

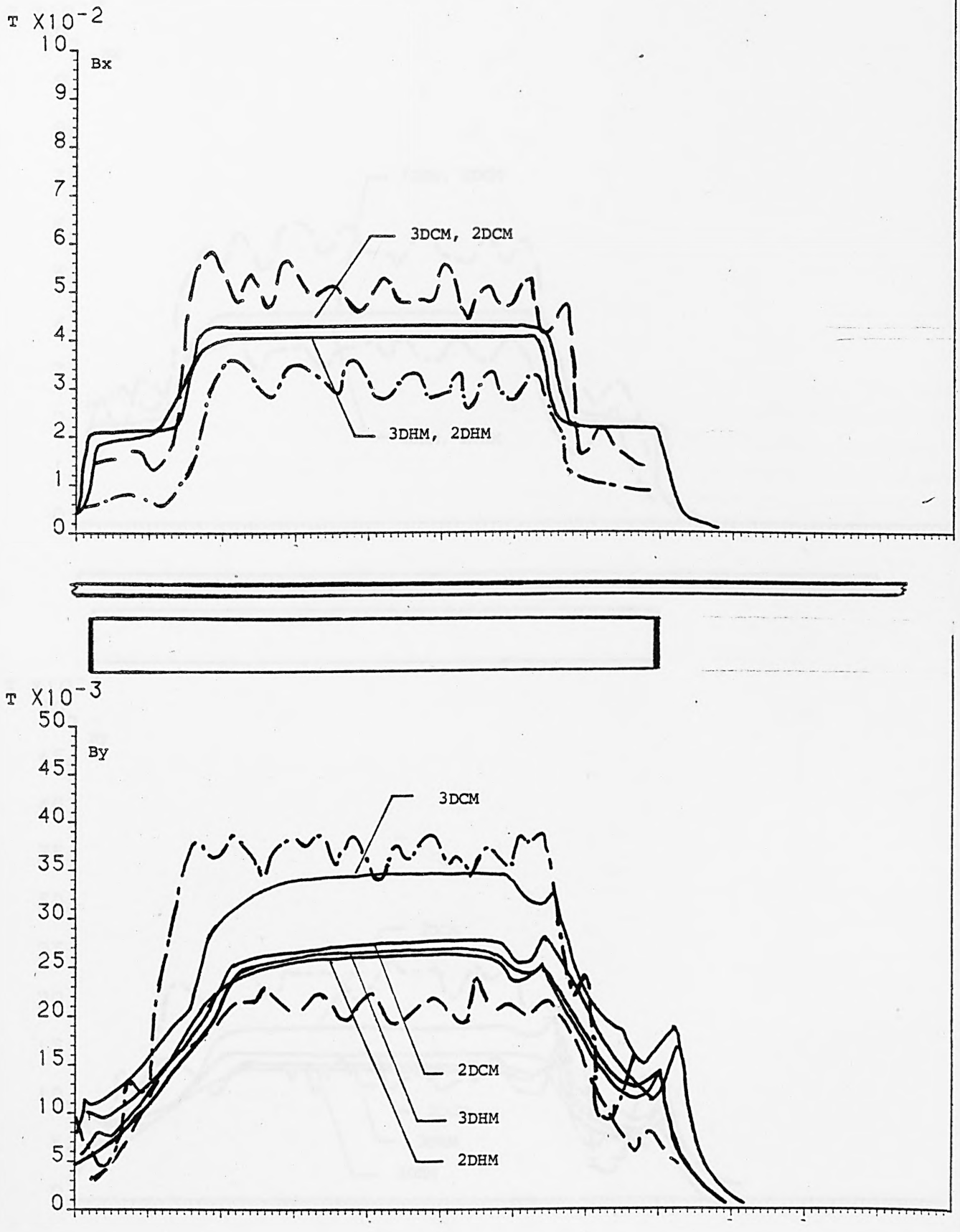

Fig. 7.5. Airgap Flux Density Components along the x-direction at I = 5A, g = 9.5 mm, f = 50 Hz, S = 1

— computed, -- measured above slots, -·- measured above teeth

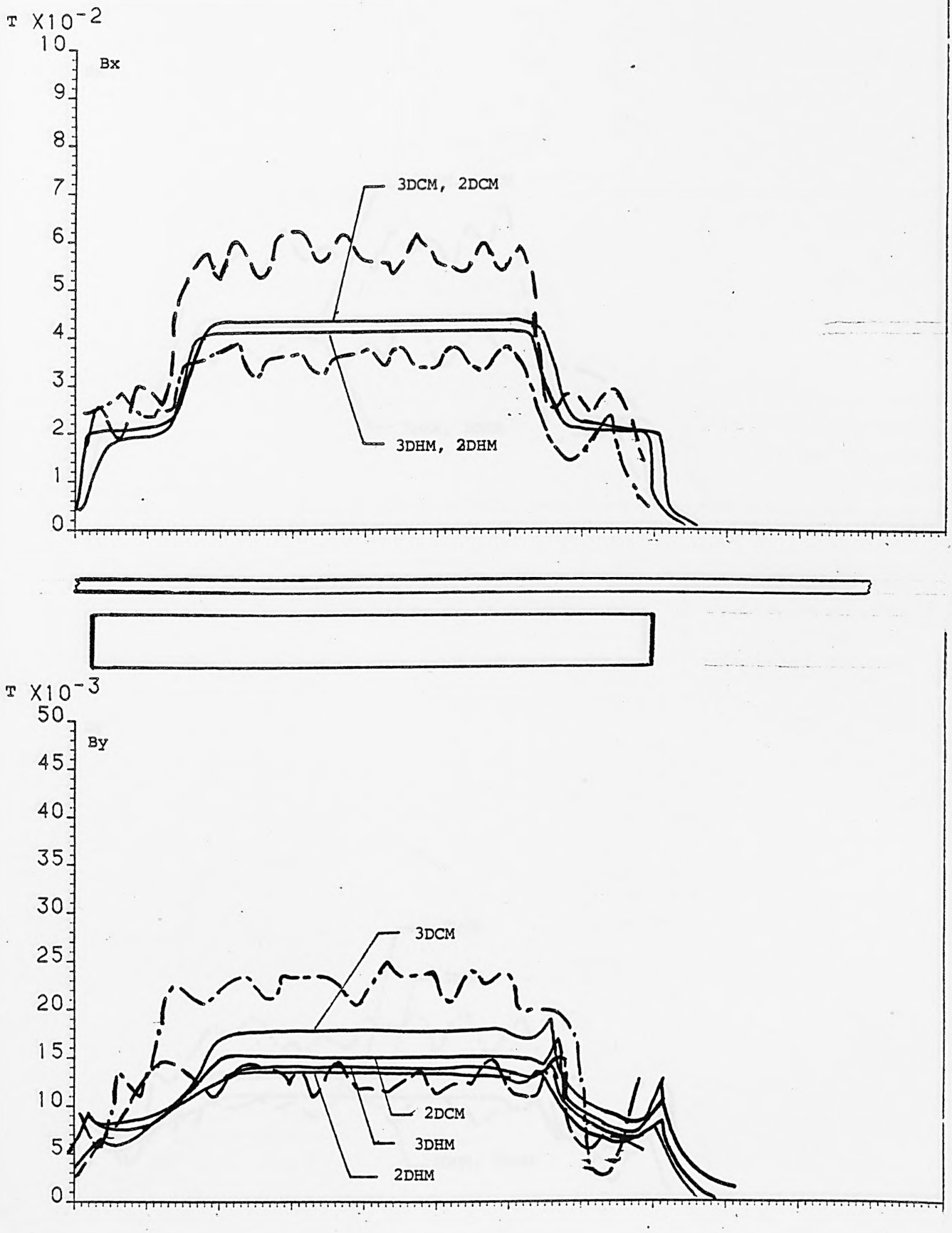

Fig. 7.6. Airgap Flux Density Components along the x-direction at I = 5A, g = 9.5 mm, f = 15OHz, S = 1

— computed, - - measured above slots, -.- measured above teeth

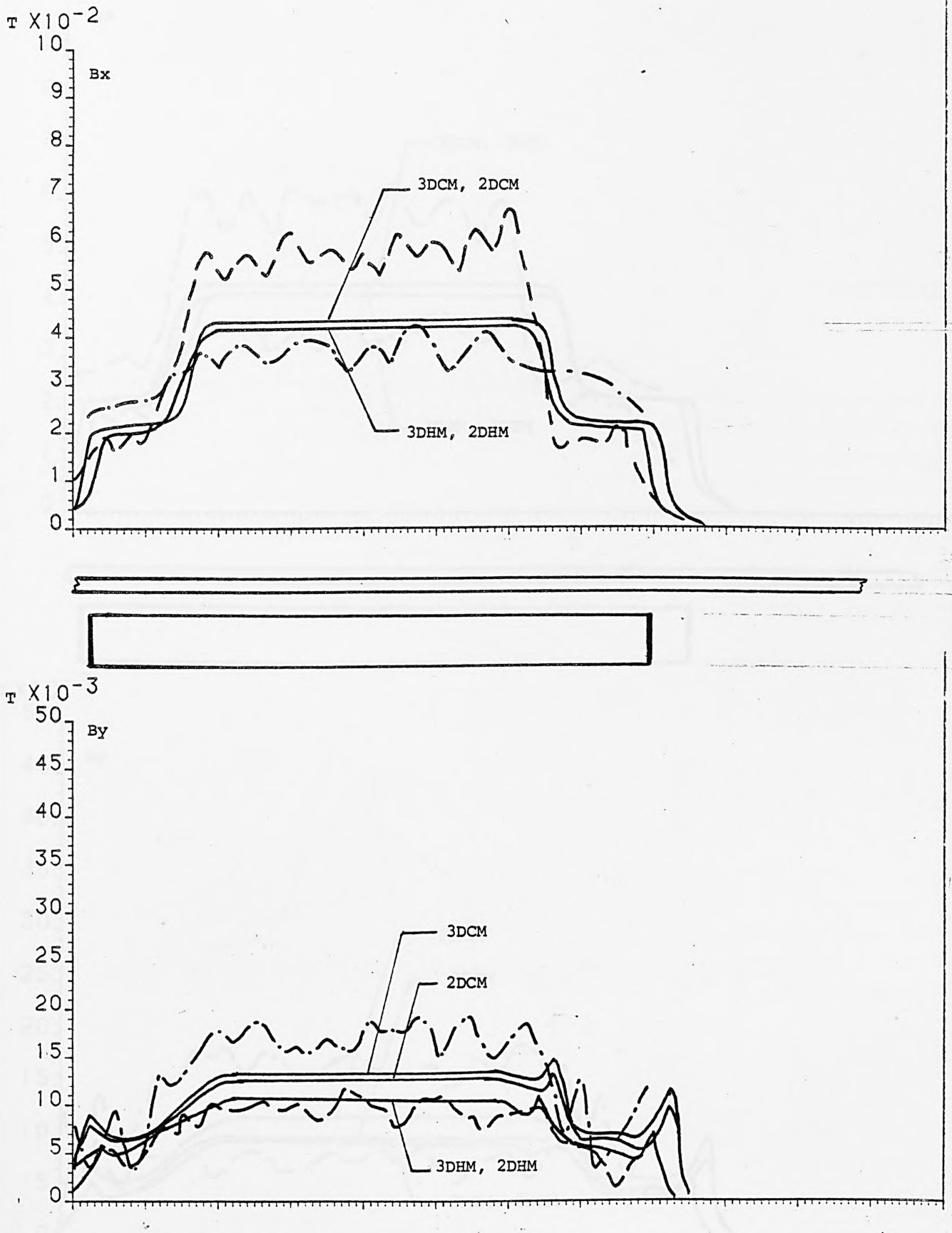

Fig. 7.7. Airgap Flux Density Components along the x-direction at I = 5A, g = 9.5 mm, f = 25OHz, S = 1

— computed, --measured above slots, -·- measured above teeth

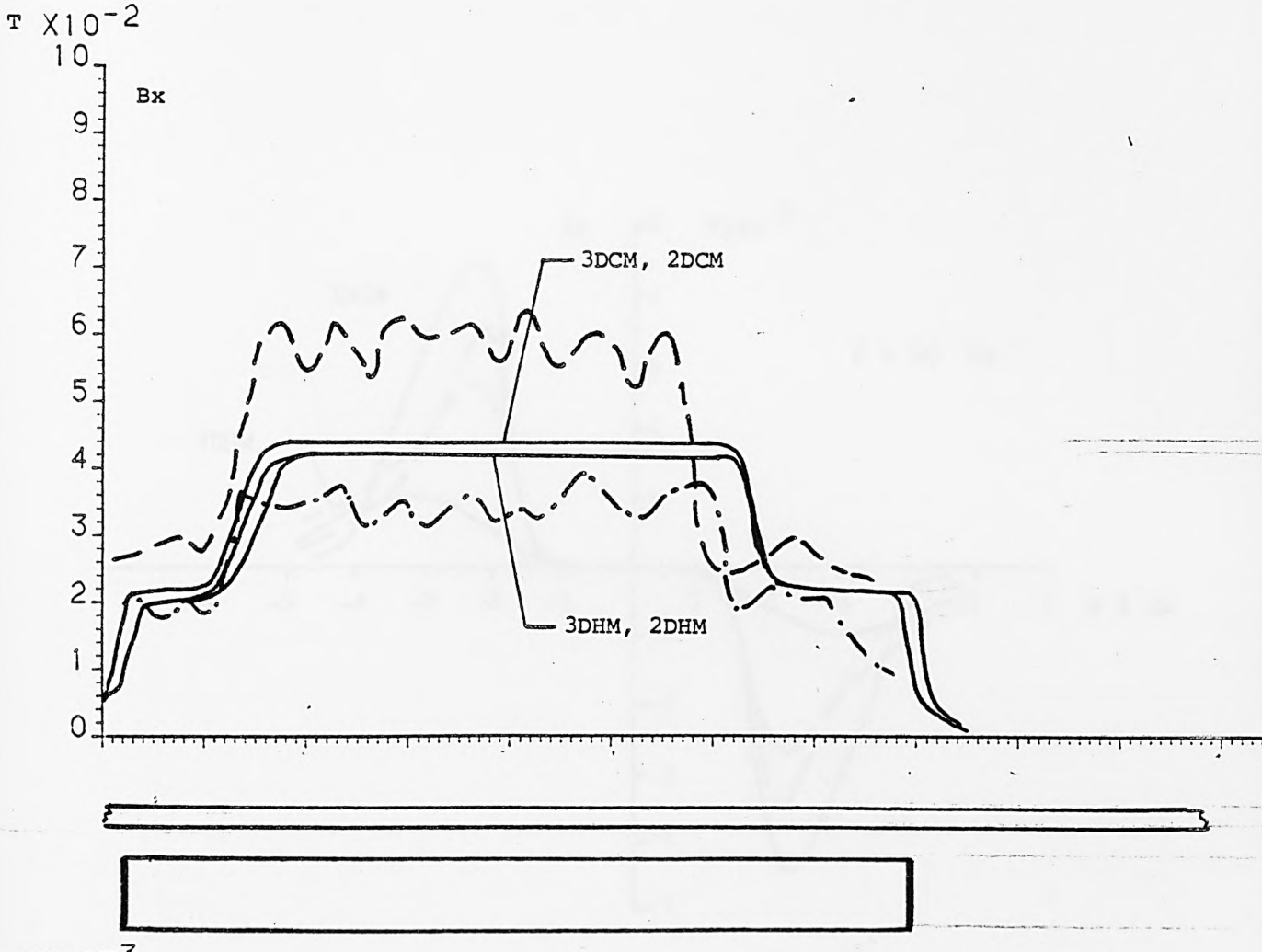

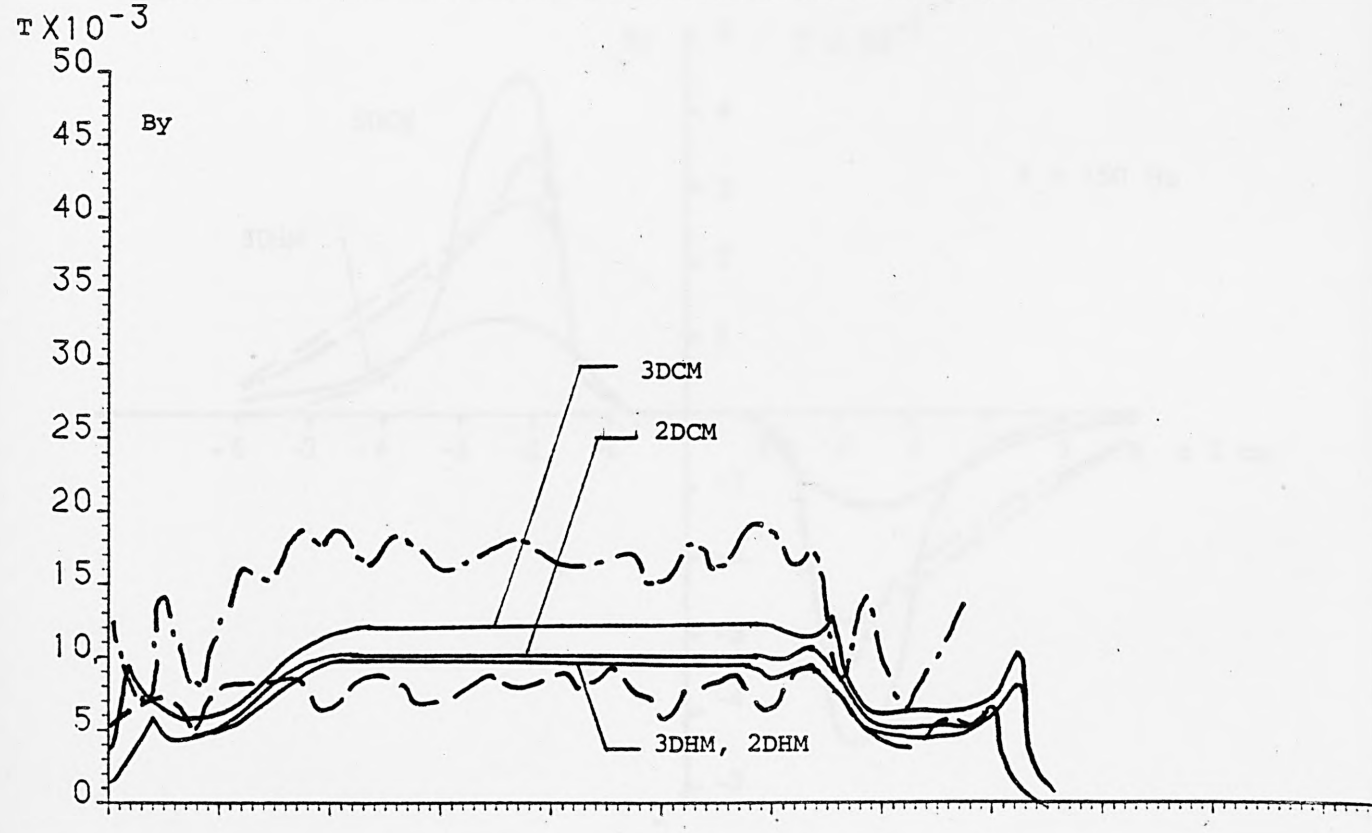

Fig. 7.8. Airgap Flux Density Components along the x-direction at I = 5A, g = 9.5 mm, f = 350 Hz, S = 1

— computed, -- measured above slots, -·- measured above teeth

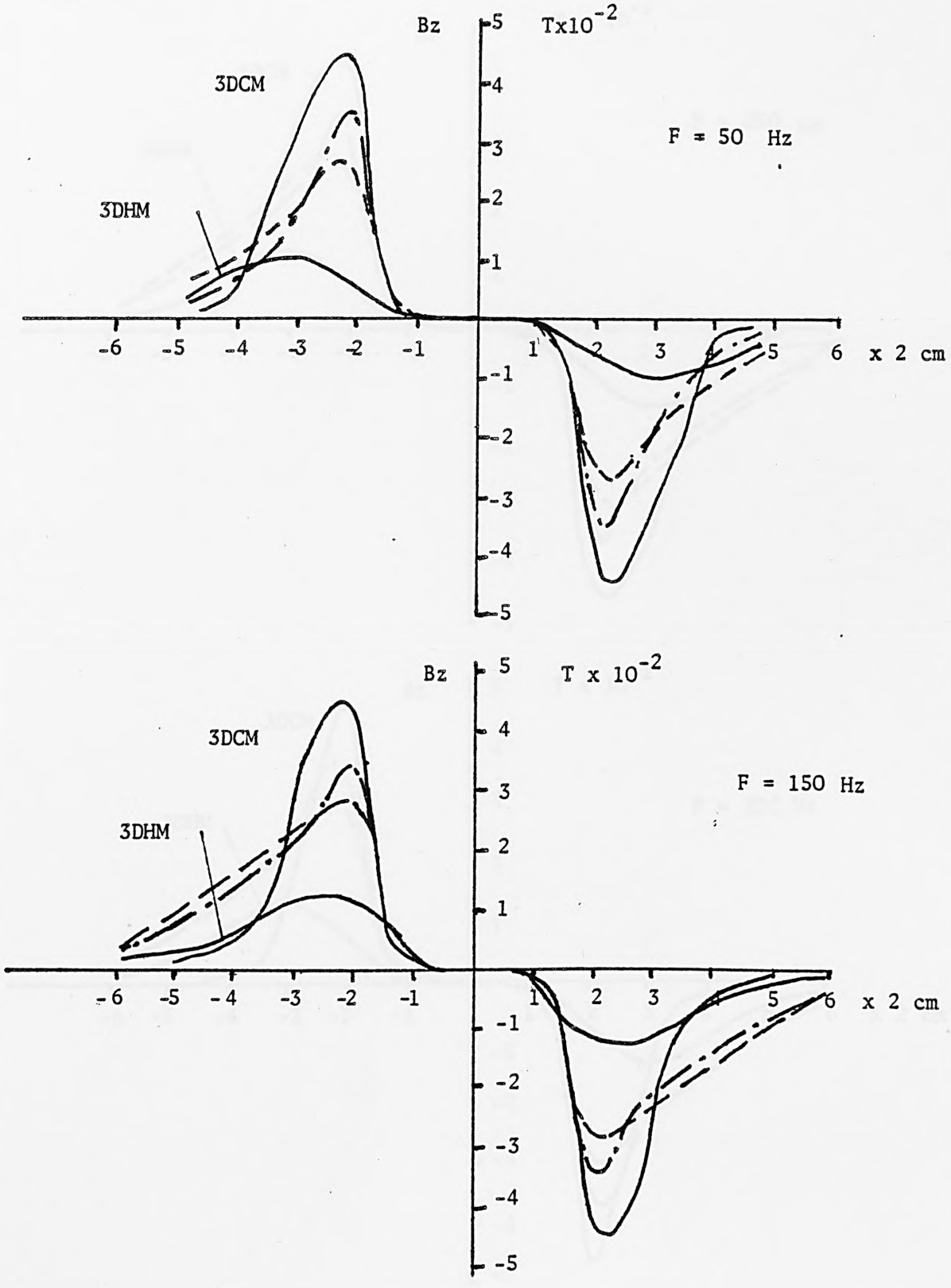

Fig. 7.9. z-component of Airgap Flux Density along the z-direction at stand still, I = 5A, g = 9.5 mm

—— computed, --measured above slots, ·-· measured above teeth

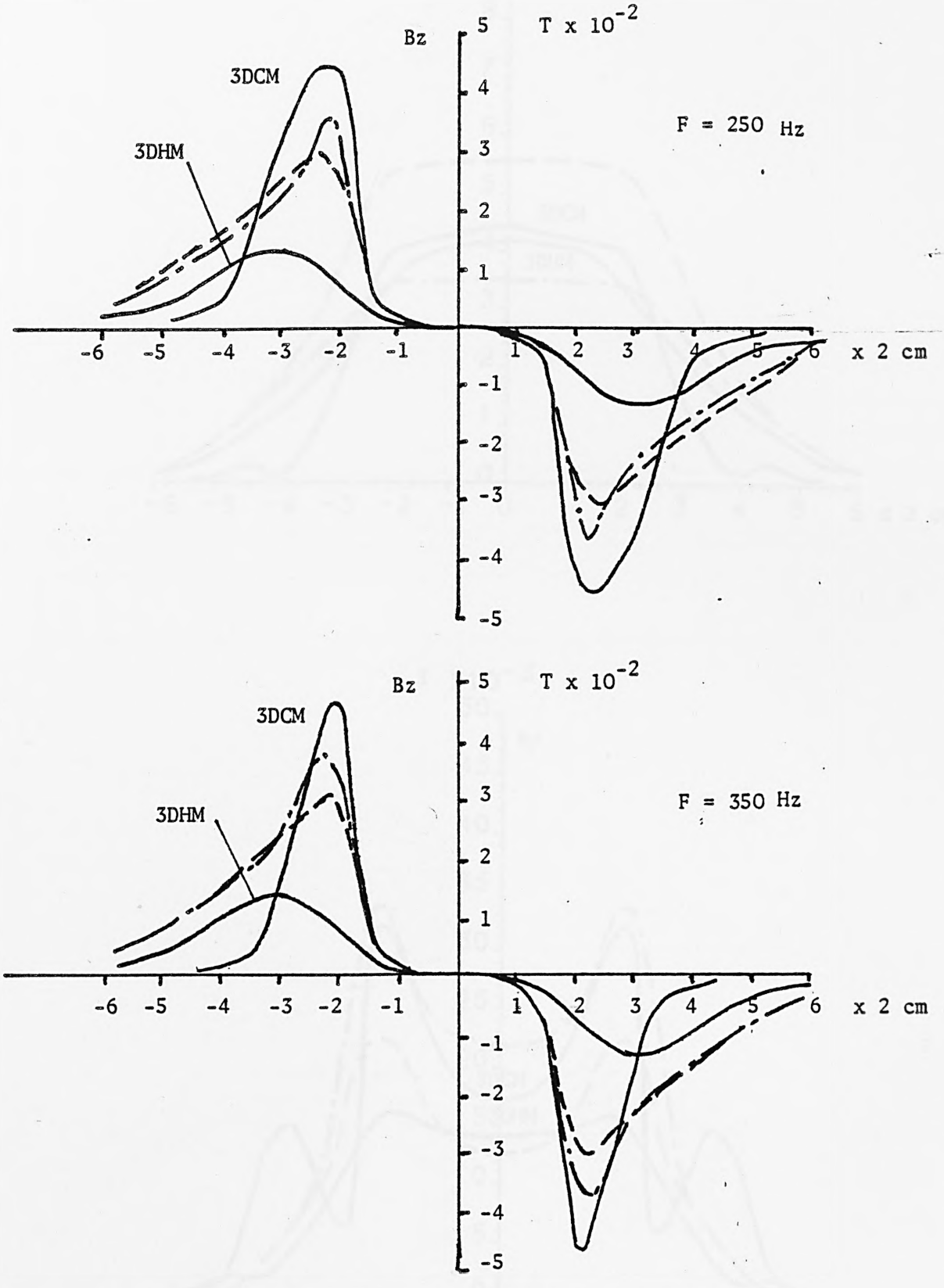

Fig. 7.10. z-component of Airgap Flux Density along the z-direction at stand still, I = 5A, g = 9.5 mm.

—— computed, -- measured above slots, -·- measured above teeth

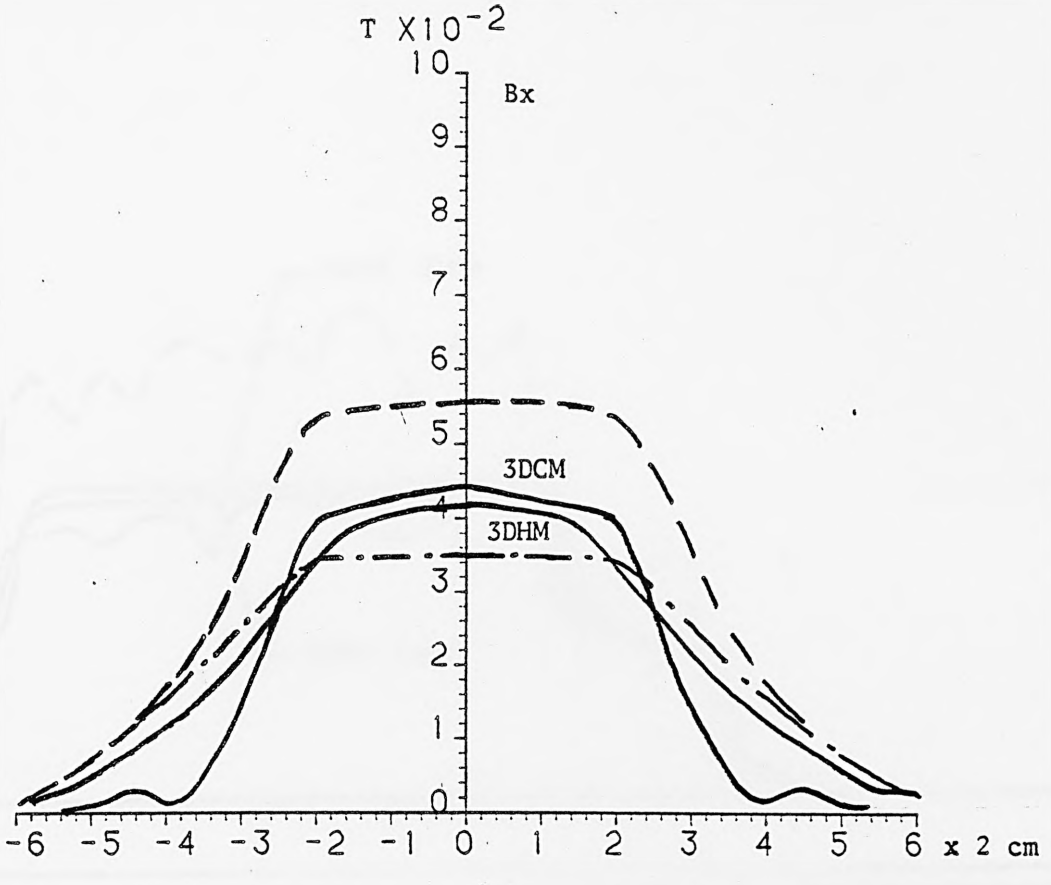

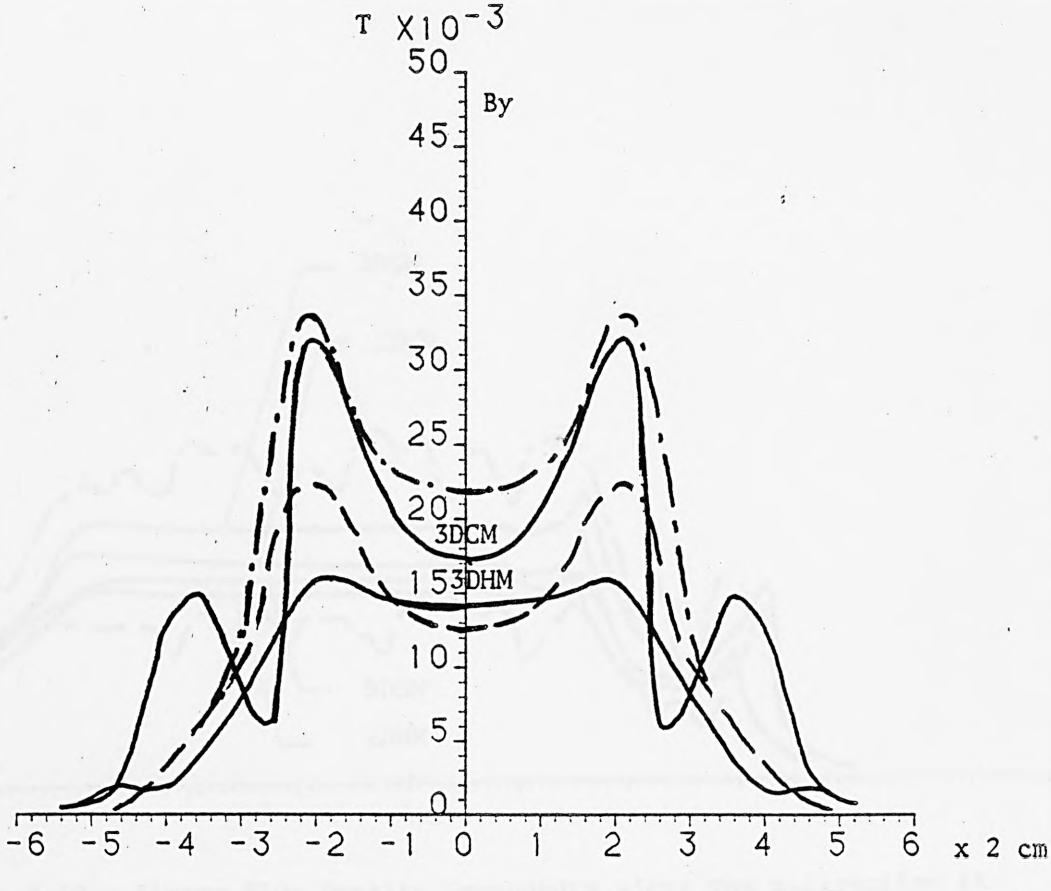

Fig. 7.11. Airgap Flux Density Components along the z-direction at I = 5A, g = 9.5 mm, f = 250 Hz, S =.6

—— computed, -- measured above slots, -.- measured above teeth

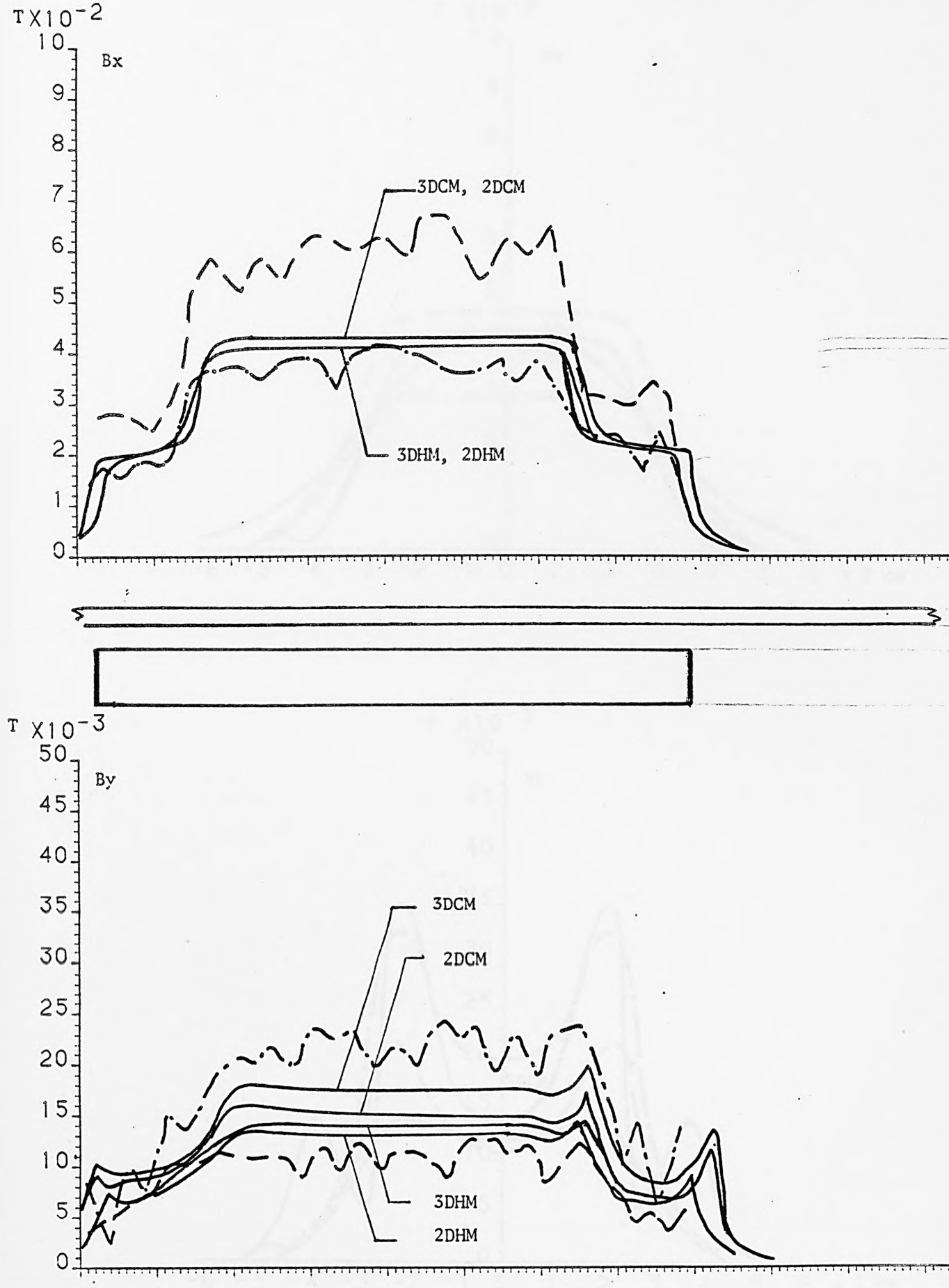

Fig. 7.12. Airgap Flux Density Components along the x-direction at I = 5A, g = 9.5 mm, f = 250 Hz, S =.6

— computed, --measured above slots, -·- measured above teeth

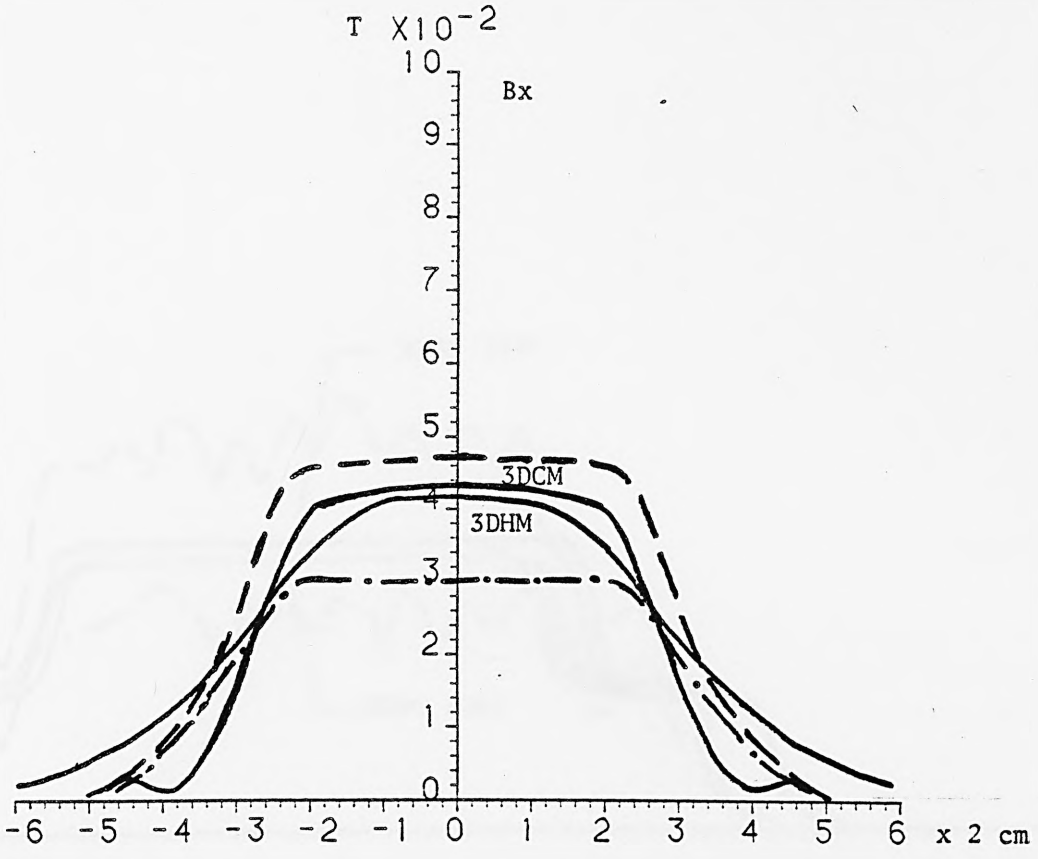

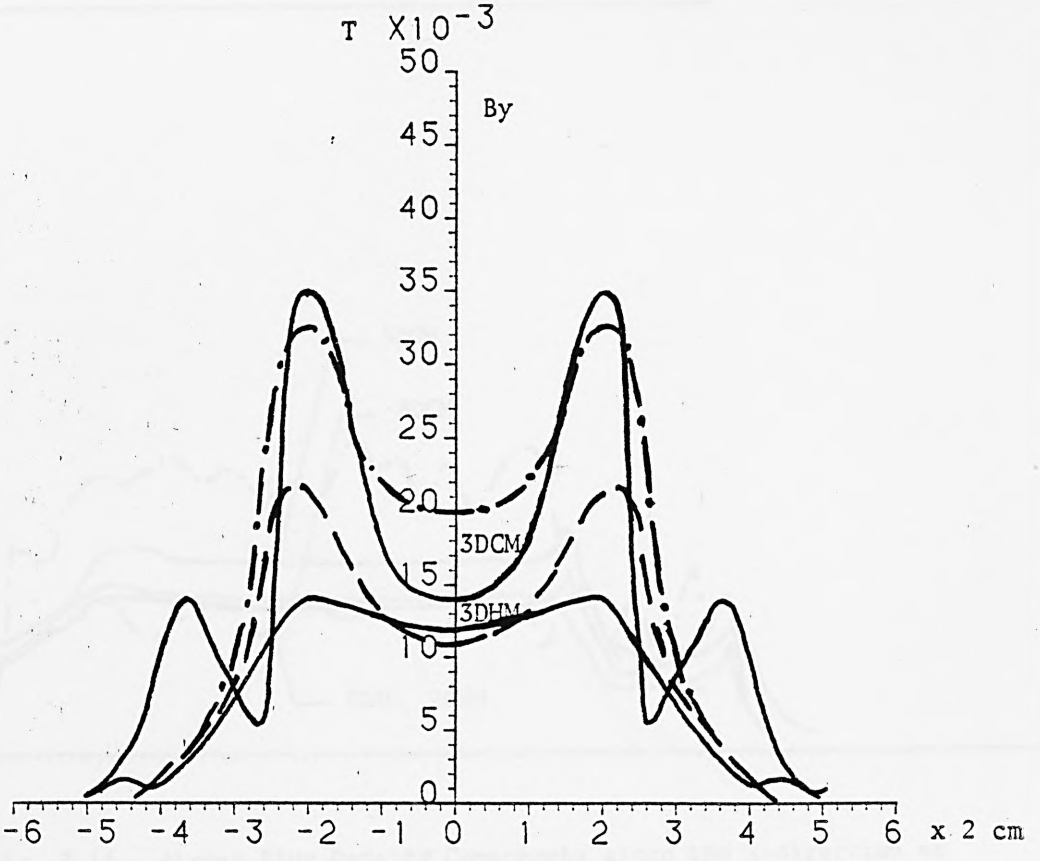

Fig. 7.13. Airgap Flux Density Components along the z-direction at I = 5A, g = 9.5 mm, f = 350 Hz, S = 6

—— computed, --measured above slots, -·- measured above teeth

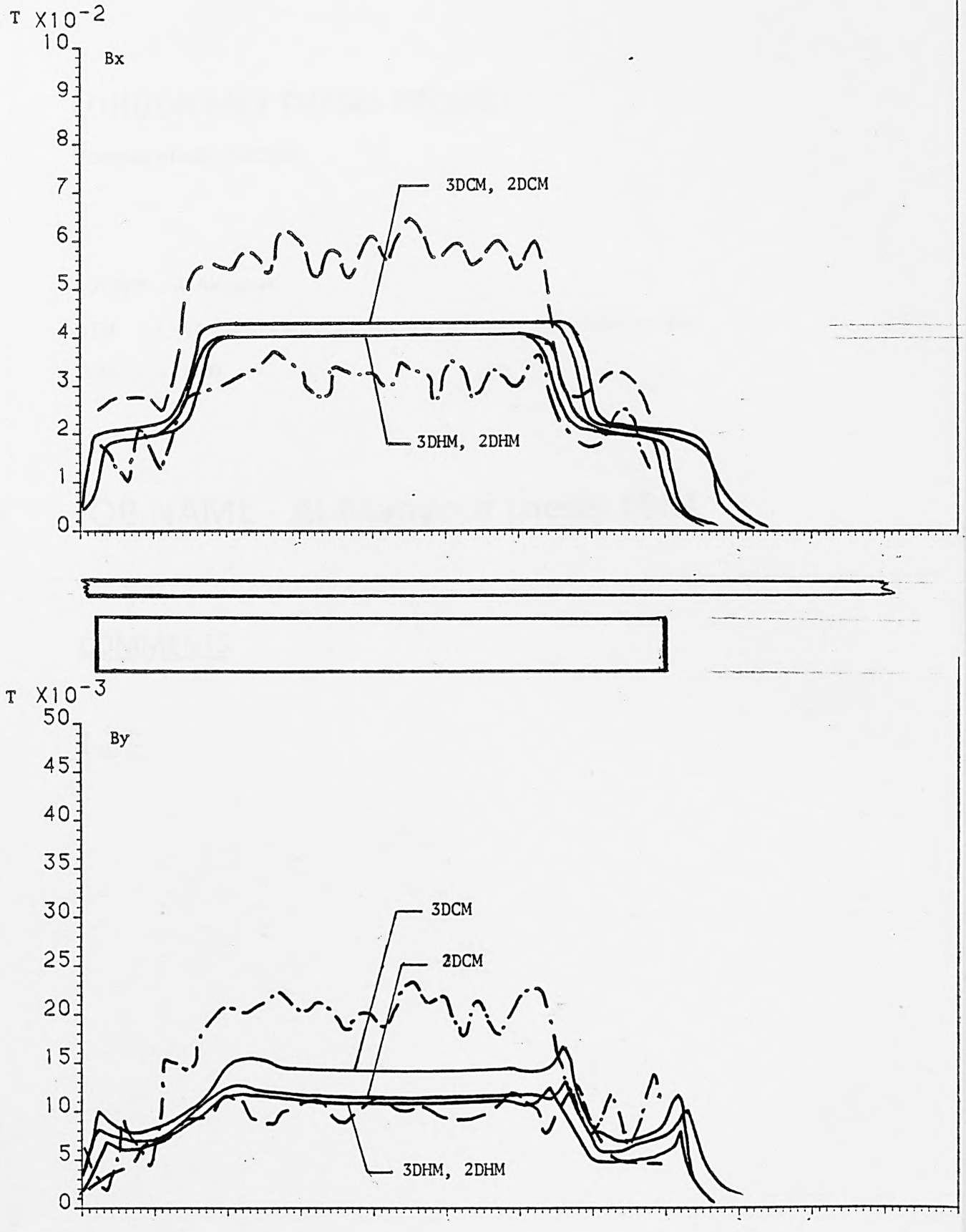

Fig. 7.14. Airgap Flux Density Components along the x-direction at I = 5A, g = 9.5 mm, f = 350 Hz, S = 6

—— computed, -- measured above slots, -·- measured above teeth

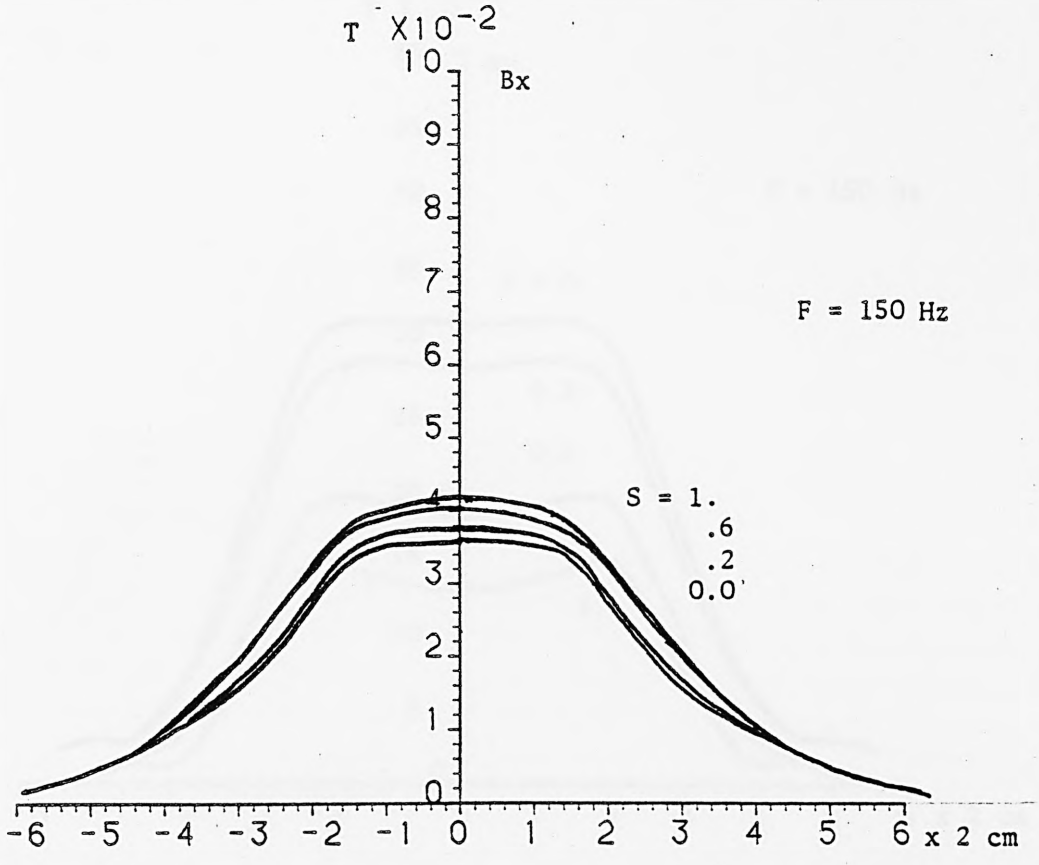

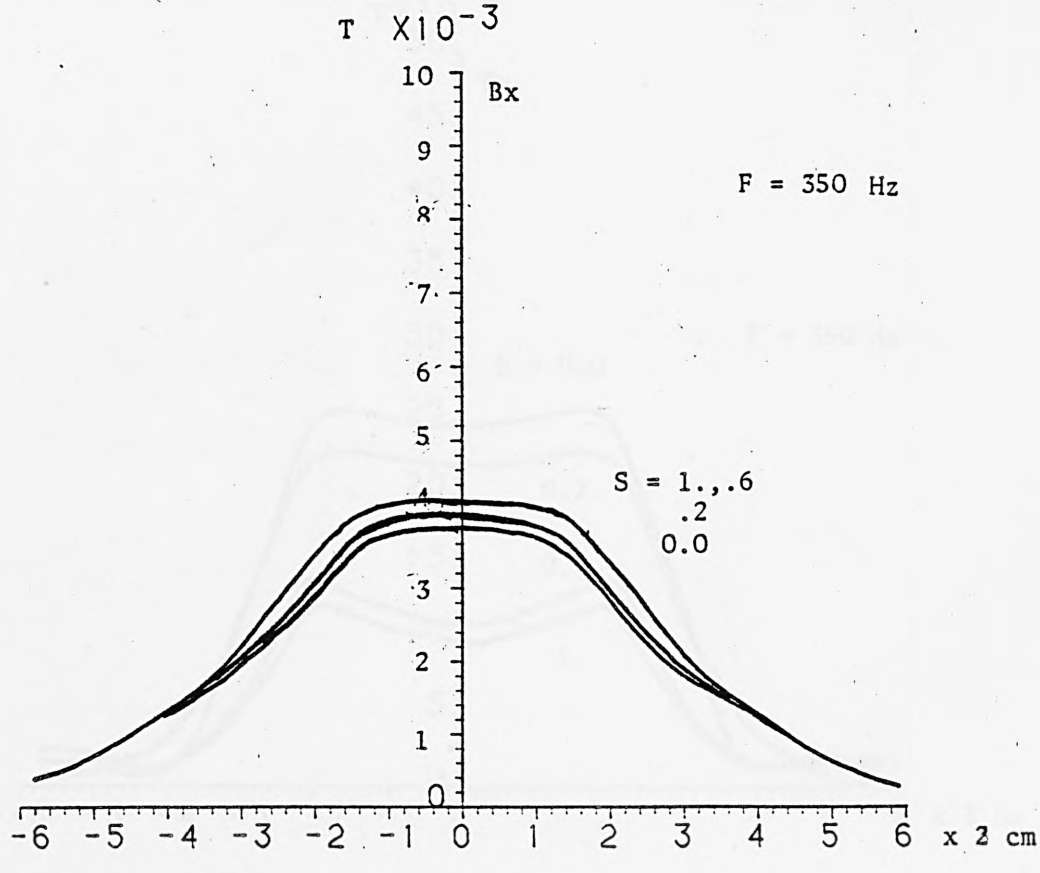

Fig. 7.15. x-component of Flux Density along the z-direction using 3DHM

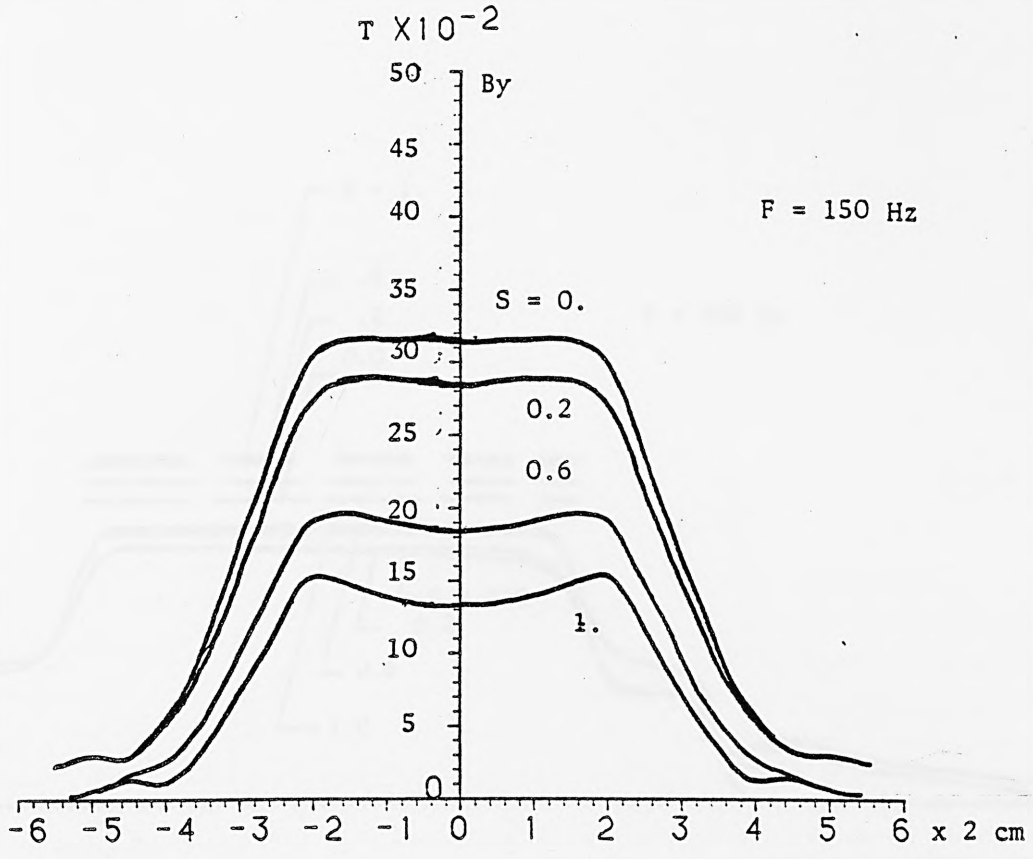

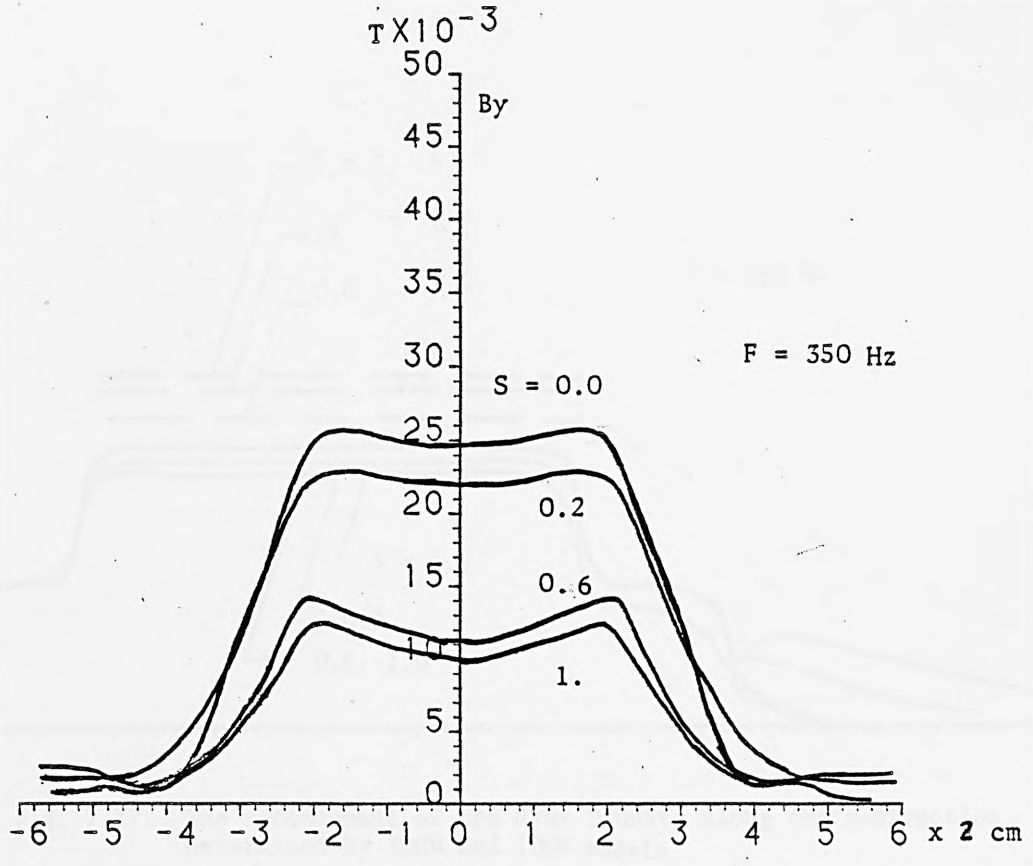

Fig. 7.16. y-component of Flux Density along the z-direction using 3DHM

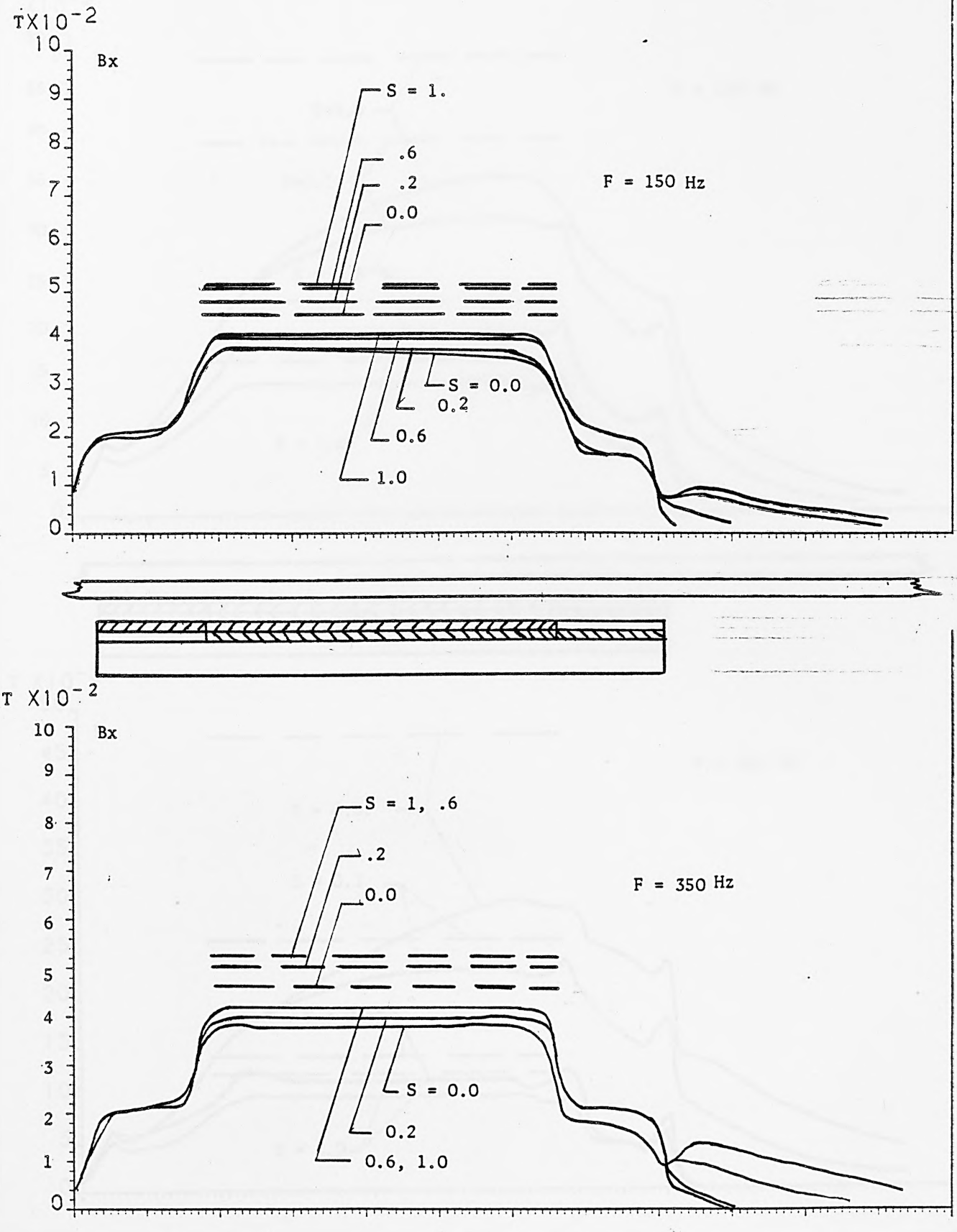

Fig. 7.17. The x-component of the Flux Density along the x-direction determined by 3DHM and 1DHM models

— 3DHM , -- 1DHM

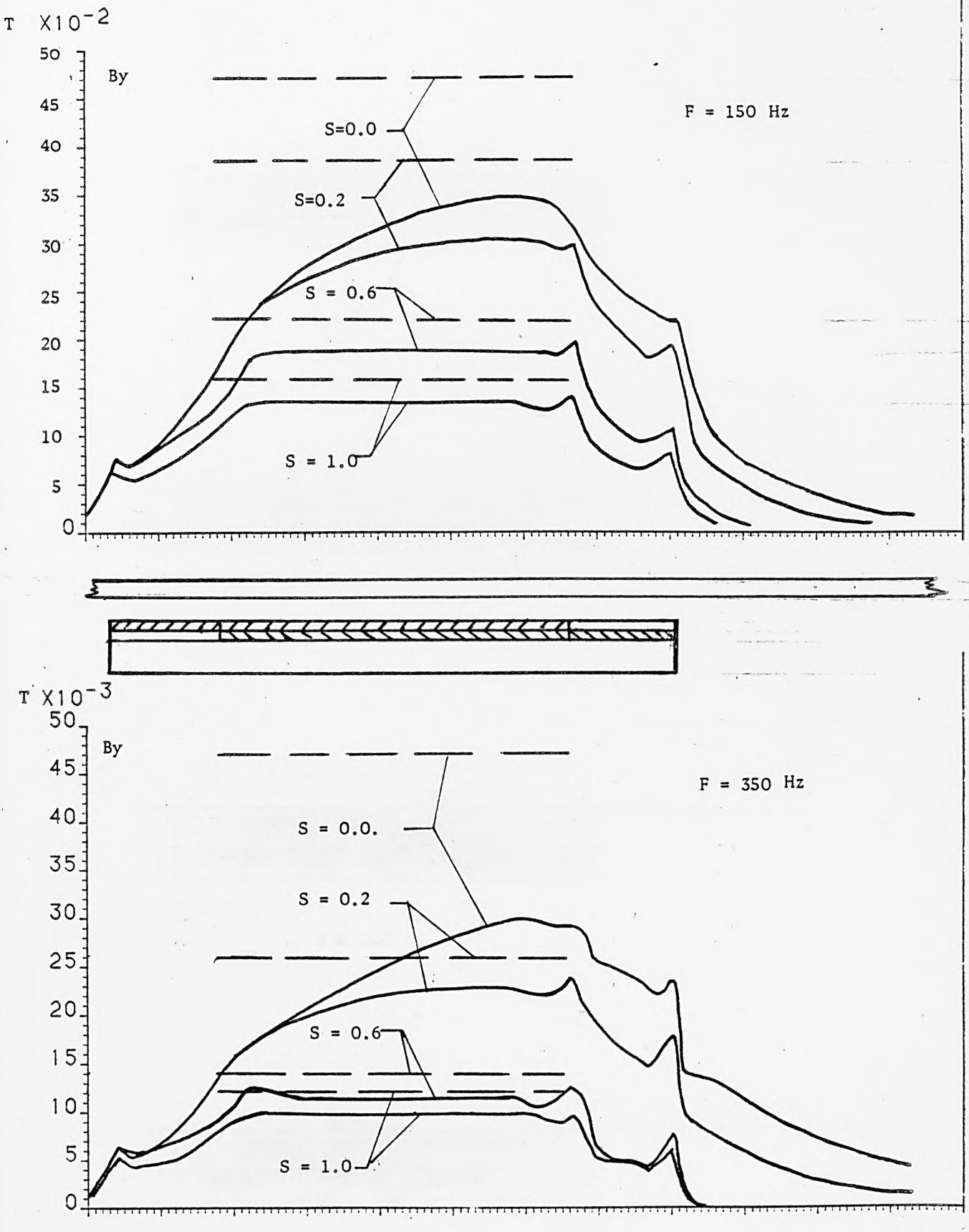

Fig. 7.18. The y-component of the Flux Density along the x-direction determined by 3DHM and 1DHM

— 3DHM , -- 1DHM

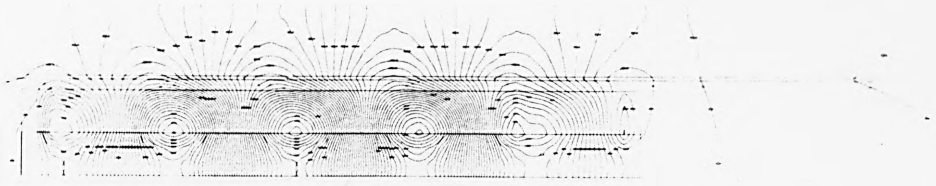

s = 1.

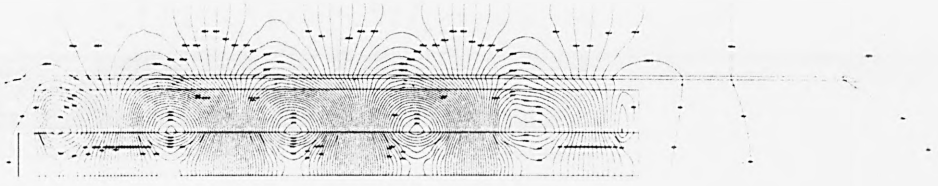

s = 0.6

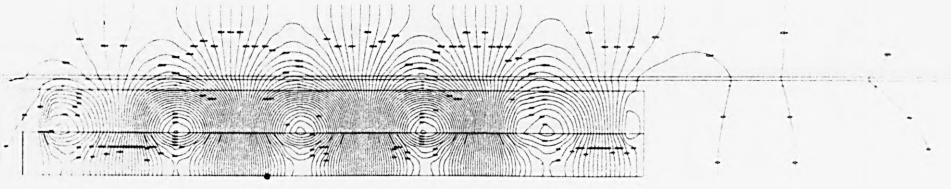

s = 0.2

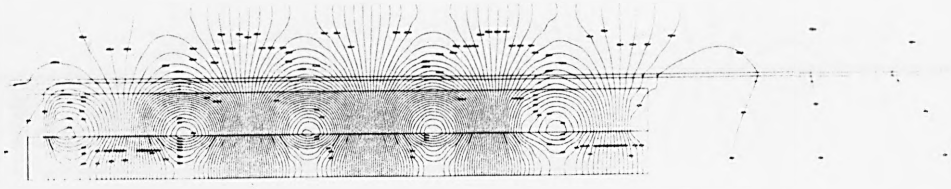

s = 0.0

Fig. 7.19. Flux distribution of 2DHM model at f = 50 Hz

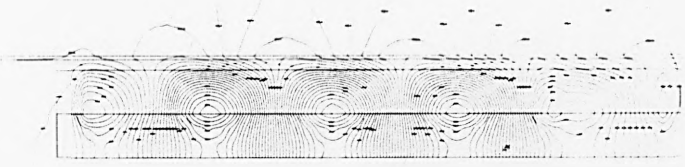

s = 1.

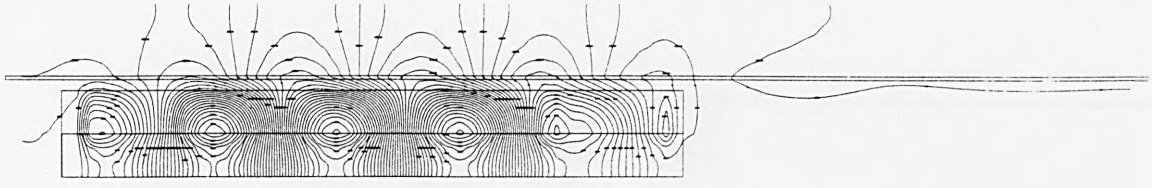

s = 0.6

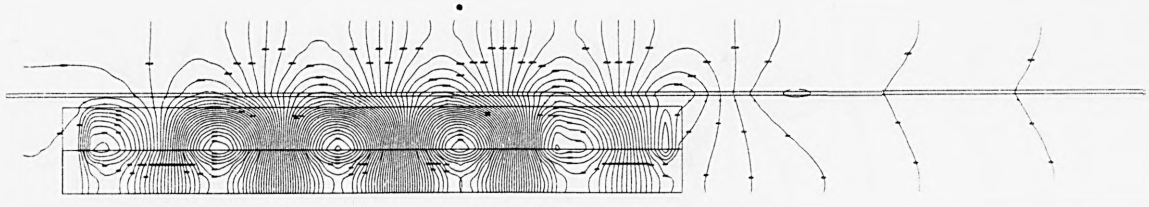

s = 0.2

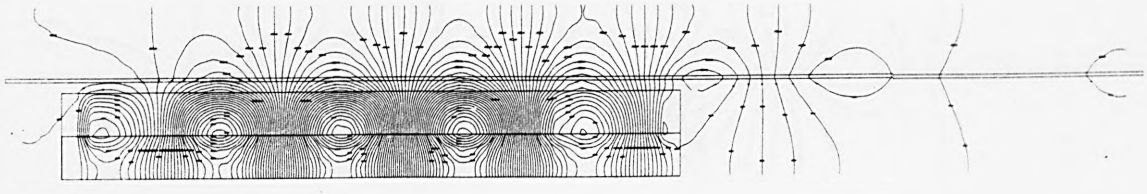

s = 0.0

Fig. 7.20. Flux distribution of 2DHM model at f = 150 Hz

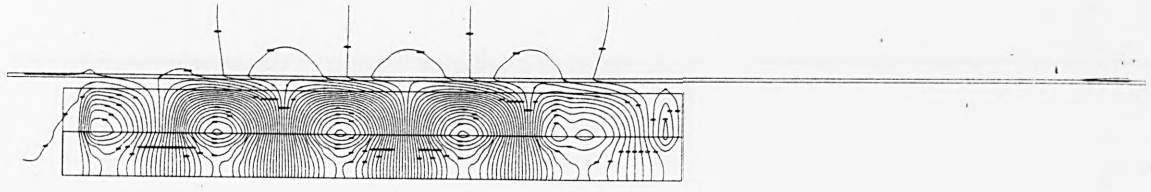

s = 1.

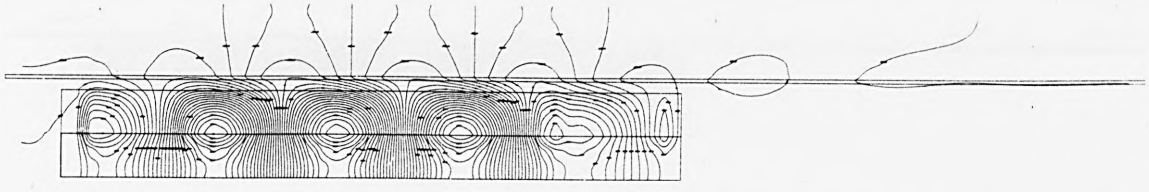

s = 0.6

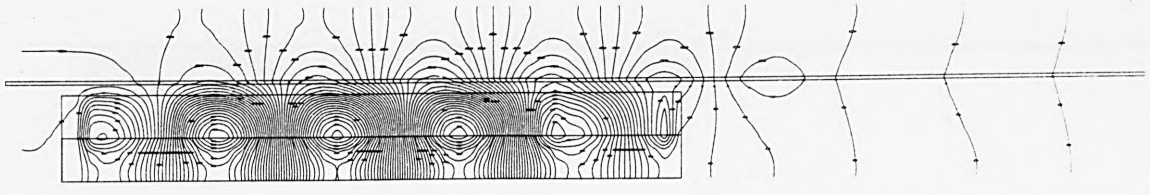

s = 0.2

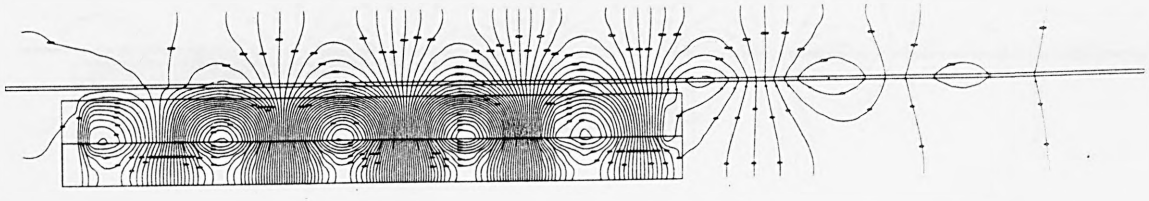

s = 0.0

Fig. 7.21. Flux distribution of 2DHM model at f = 250 Hz

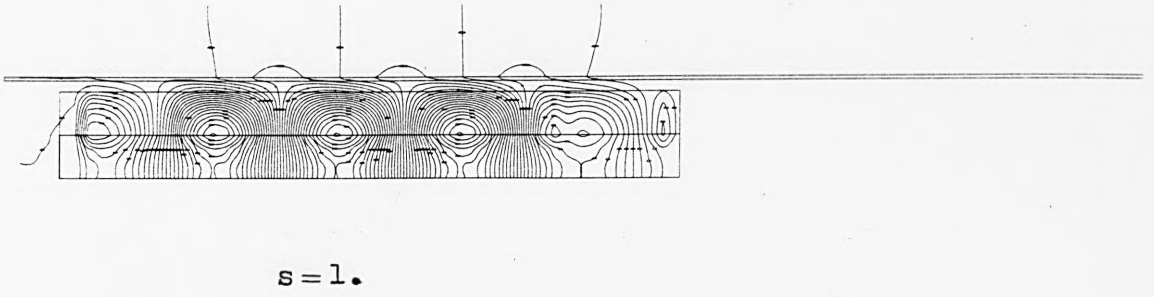

s = 1.

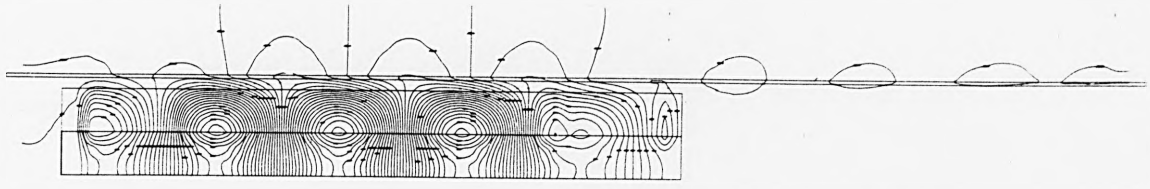

s = 0.6

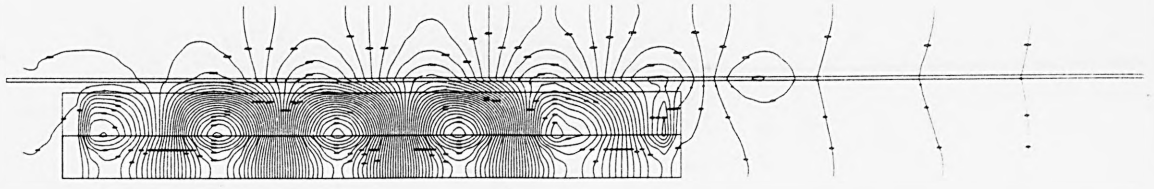

s = 0.2

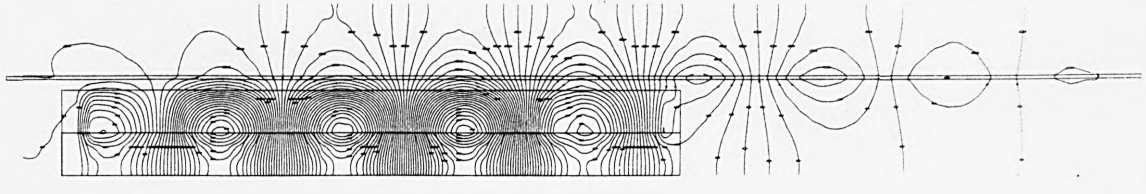

s = 0.0

Fig. 7.22. Flux distribution of 2DHM model at f = 350 Hz

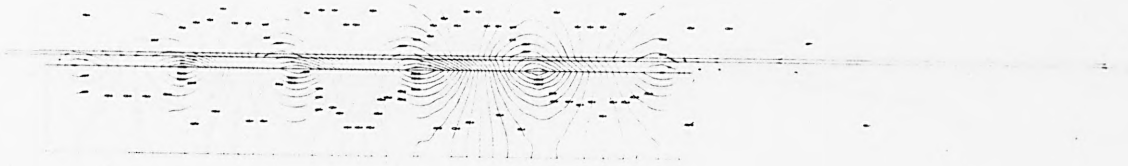

s = 1.

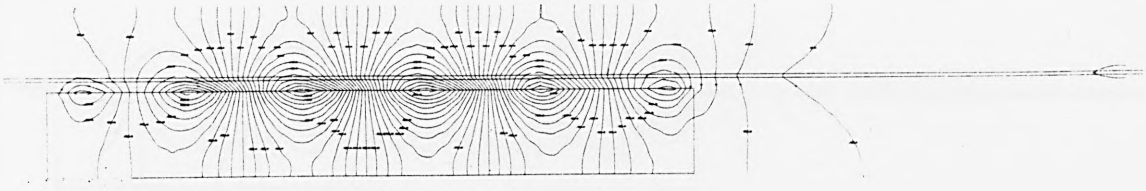

s = 0.6

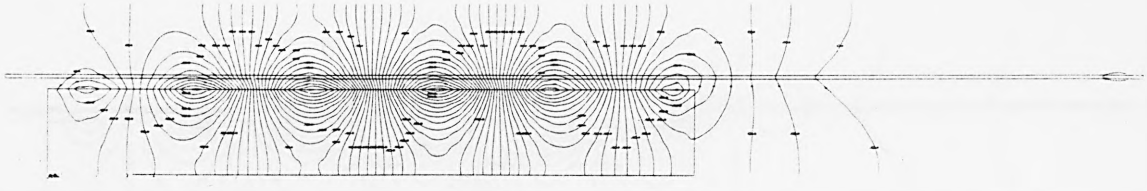

s = 0.2

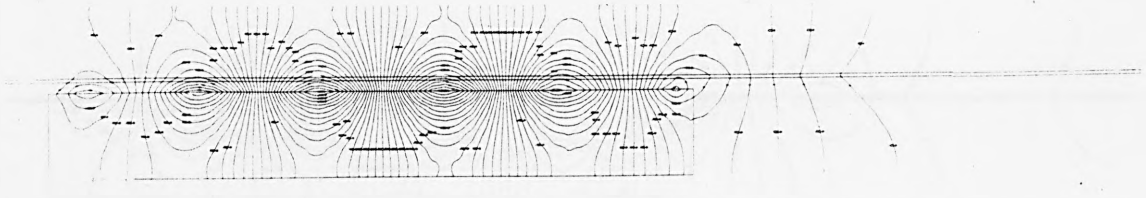

s = 0.0

Fig. 7.23. Flux distribution of 2DCM model at f = 50 Hz

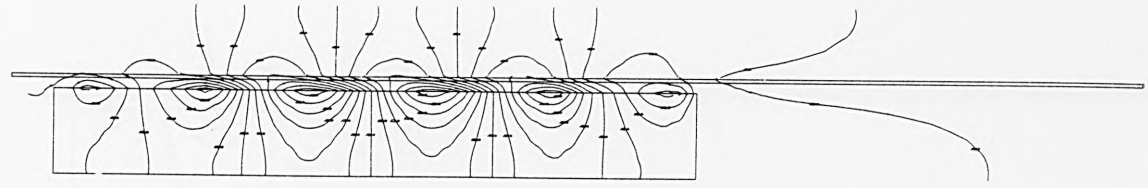

s = 1.

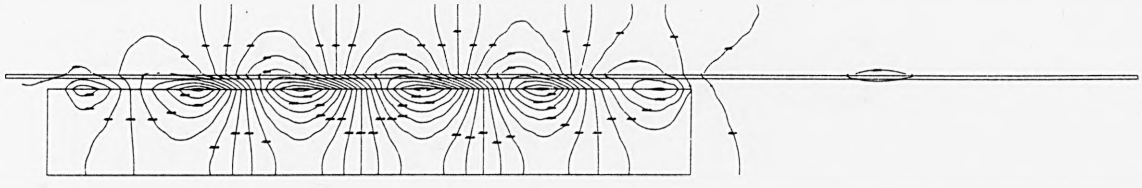

s = 0.6

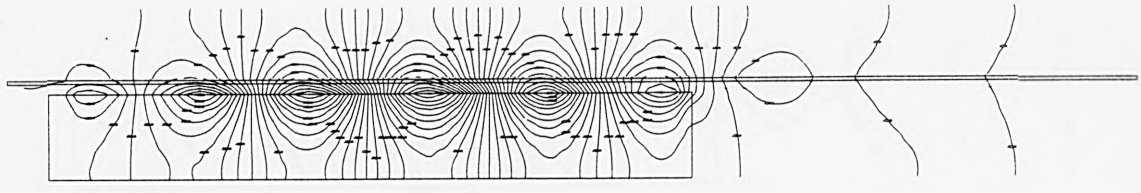

s = 0.2

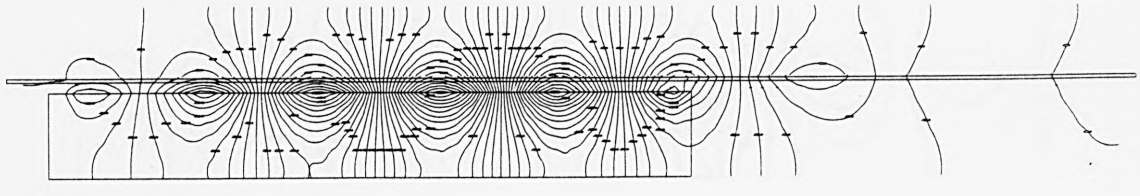

s = 0.0

Fig. 7.24. Flux distribution of 2DCM model at f = 150 Hz

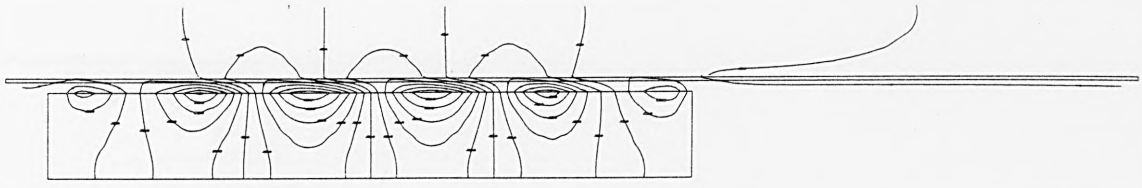

s = 1.

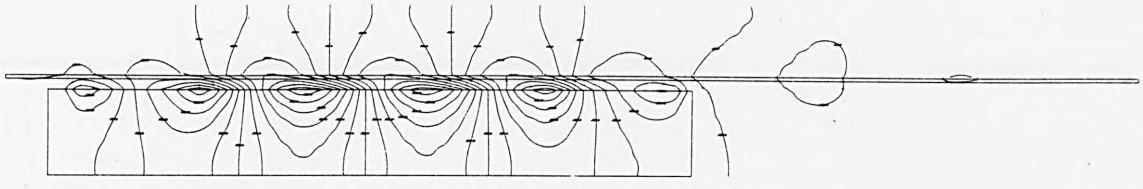

s = 0.6

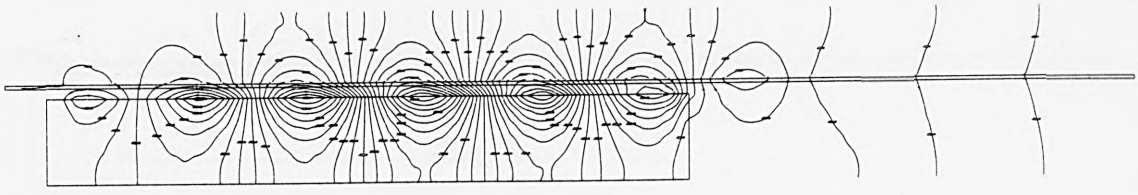

s = 0.2

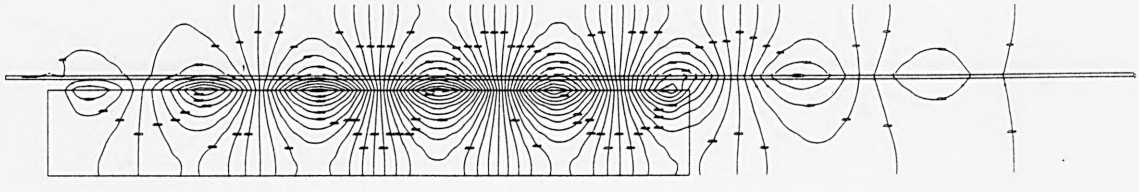

s = 0.0

Fig. 7.25. Flux distribution of 2DCM model at f = 250 Hz

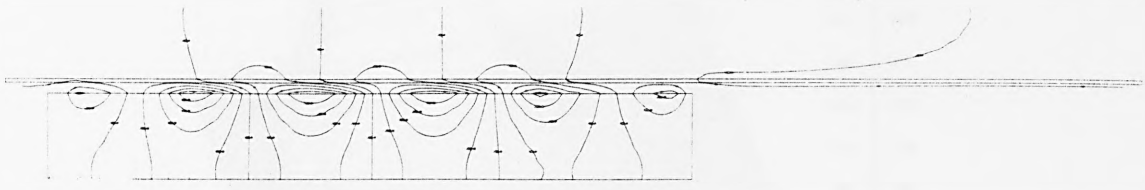

s = 1.

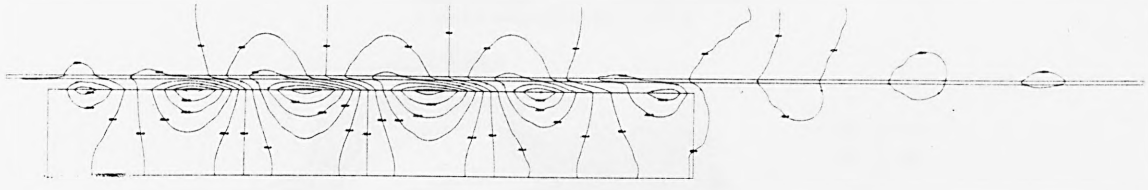

s = 0.6

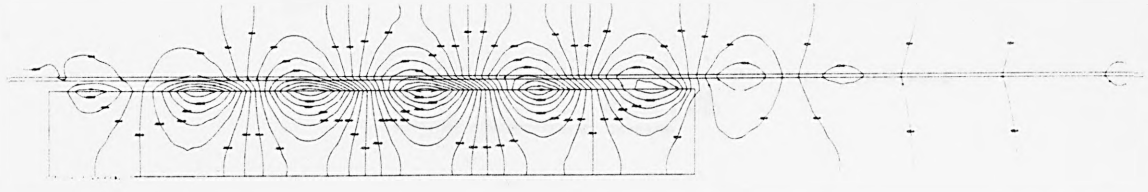

s = 0.2

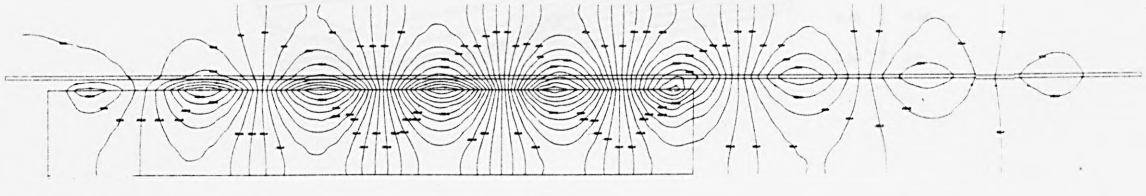

s = 0.0

Fig. 7.26. Flux distribution of 2DCM model at f = 350 Hz

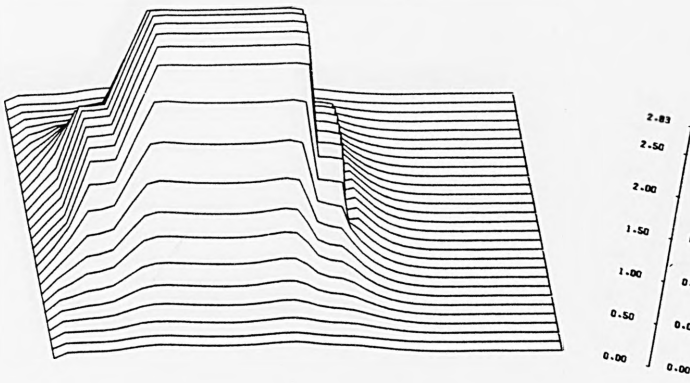

X-COMP. OF FLUX DENSITY OF THE LIM-3DHMA.AT S=.3.I=5A.F=150.
AZIMUTH = 15 ALTITUDE = 45
*WIDTH = 6.00 *HEIGHT = 4.00
* BEFORE FORESHORTENING 16/09/81

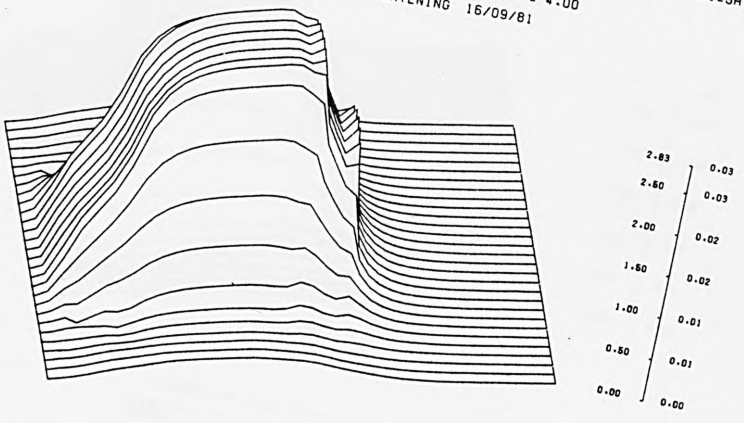

Y-COMP. OF FLUX DENSITY OF THE LIM-3DHMA.AT S=.3.I=5A.F=150.0
AZIMUTH = 15 ALTITUDE = 45
*WIDTH = 6.00 *HEIGHT = 4.00
* BEFORE FORESHORTENING 16/09/81

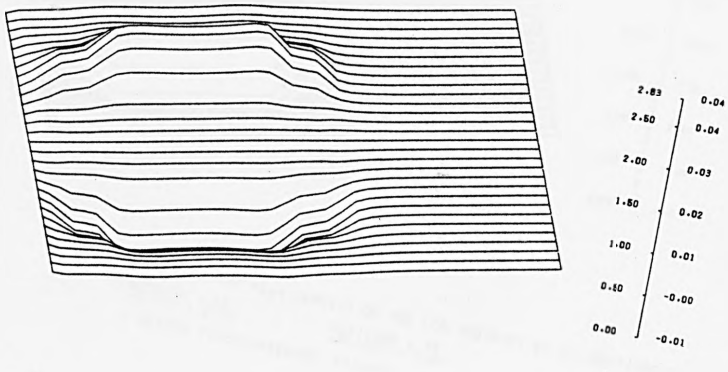

Z-COMP. OF FLUX DENSITY OF THE LIM-3DHMA.AT S=.3.I=5A.F=150.0
AZIMUTH = 15 ALTITUDE = 45
*WIDTH = 6.00 *HEIGHT = 4.00
* BEFORE FORESHORTENING 16/09/81

Fig. 7.27. Flux density distribution of 3DHM model at f = 150 Hz and S = 0.3

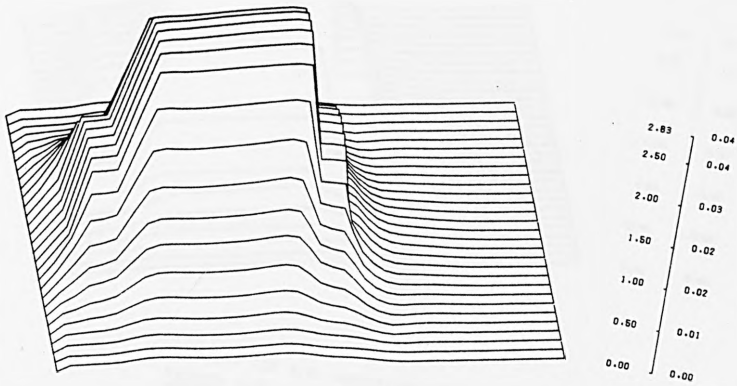

X-COMP. OF FLUX DENSITY OF THE LIM-3DHMA.AT S=.3.I=5A.F=350.0
AZIMUTH = 15 ALTITUDE = 45
*WIDTH = 6.00 *HEIGHT = 4.00
* BEFORE FORESHORTENING 14/09/81

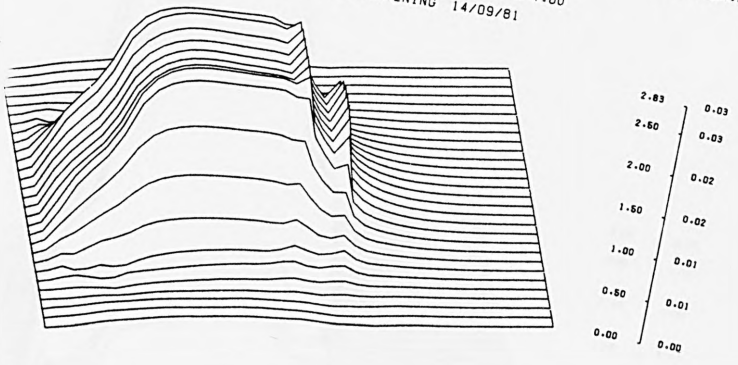

Y-COMP. OF FLUX DENSITY OF THE LIM-3DHMA.AT S=.3.I=5A.F=350.0
AZIMUTH = 15 ALTITUDE = 45
*WIDTH = 6.00 *HEIGHT = 4.00
* BEFORE FORESHORTENING 14/09/81

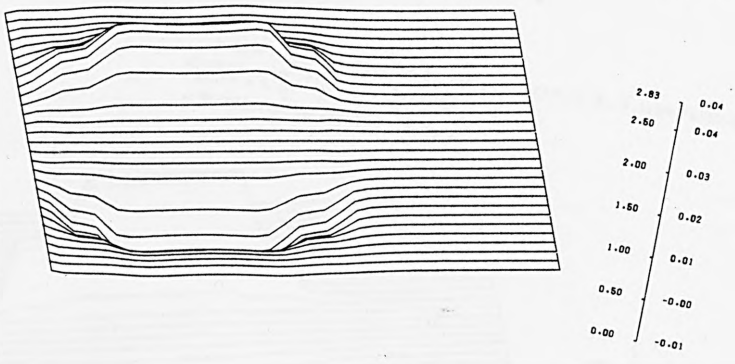

Z-COMP. OF FLUX DENSITY OF THE LIM-3DHMA.AT S=.3.I=5A.F=350.0
AZIMUTH = 15 ALTITUDE = 45
*WIDTH = 6.00 *HEIGHT = 4.00
* BEFORE FORESHORTENING 14/09/81

Fig. 7.28. Flux density distribution of 3DHM model at f = 350 Hz and S = 0.3

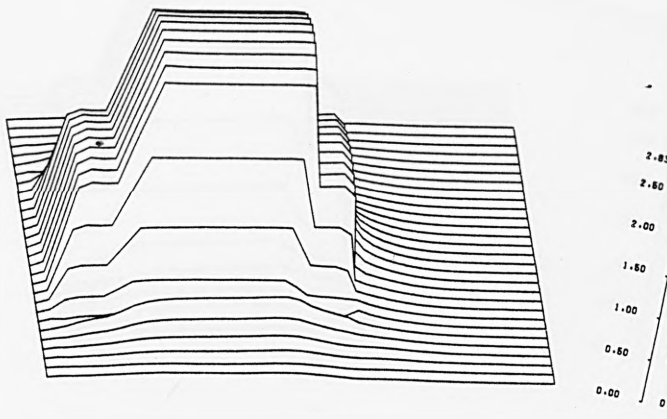

X-COMP. OF FLUX DENSITY OF THE LIM-3DCMA.AT S=.3,I=5A,F=150
AZIMUTH = 15 ALTITUDE = 45
*WIDTH = 6.00 *HEIGHT = 4.00
* BEFORE FORESHORTENING 18/09/81

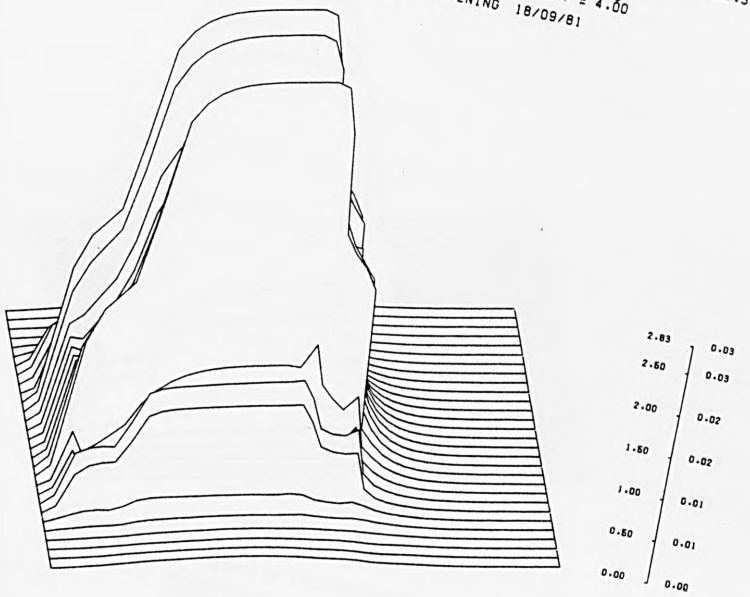

Y-COMP. OF FLUX DENSITY OF THE LIM-3DCMA.AT S=.3,I=5A,F=150.0
AZIMUTH = 15 ALTITUDE = 45
*WIDTH = 6.00 *HEIGHT = 4.00
* BEFORE FORESHORTENING 18/09/81

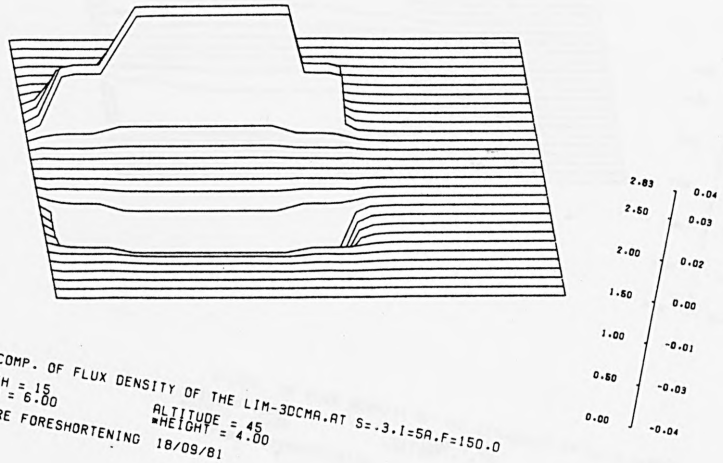

Z-COMP. OF FLUX DENSITY OF THE LIM-3DCMA.AT S=.3,I=5A,F=150.0
AZIMUTH = 15 ALTITUDE = 45
*WIDTH = 6.00 *HEIGHT = 4.00
* BEFORE FORESHORTENING 18/09/81

Fig. 7.29. Flux density distribution of 3DCM model
f = 150 Hz and S = 0.3

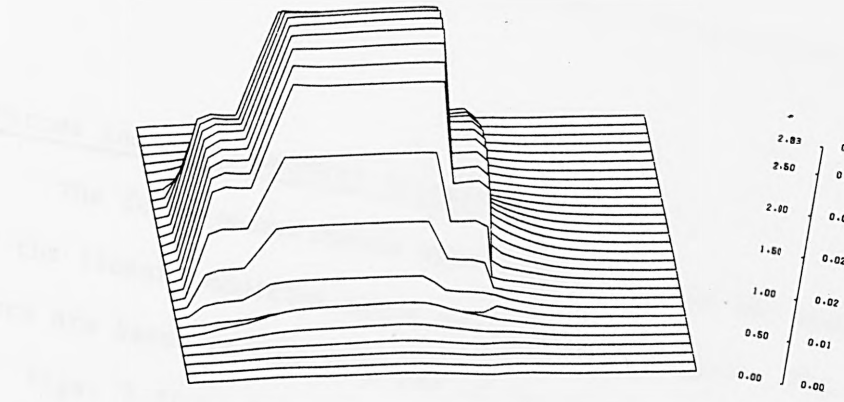

X-COMP. OF FLUX DENSITY OF THE LIM-3DCMA.AT S=.3,I=5A,F=350.0
AZIMUTH = 15
*WIDTH = 6.00
ALTITUDE = 45
*HEIGHT = 4.00
* BEFORE FORESHORTENING 17/09/81

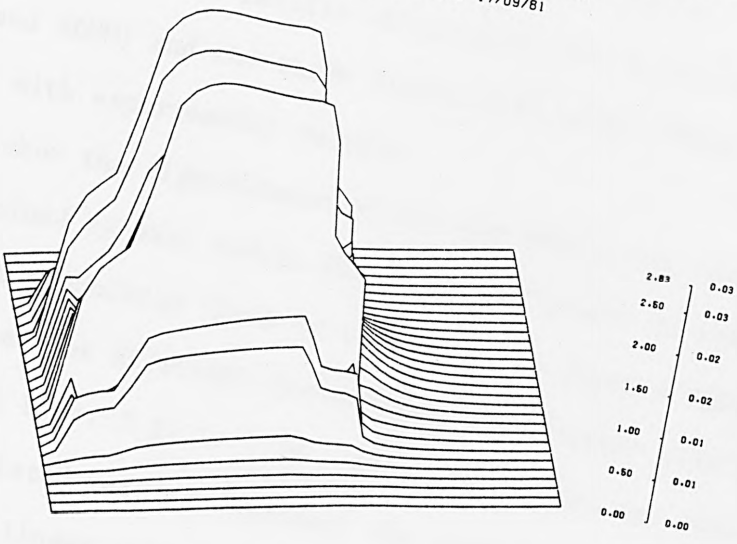

Y-COMP. OF FLUX DENSITY OF THE LIM-3DCMA.AT S=.3,I=5A,F=350.0
AZIMUTH = 15
*WIDTH = 6.00
ALTITUDE = 45
*HEIGHT = 4.00
* BEFORE FORESHORTENING 17/09/81

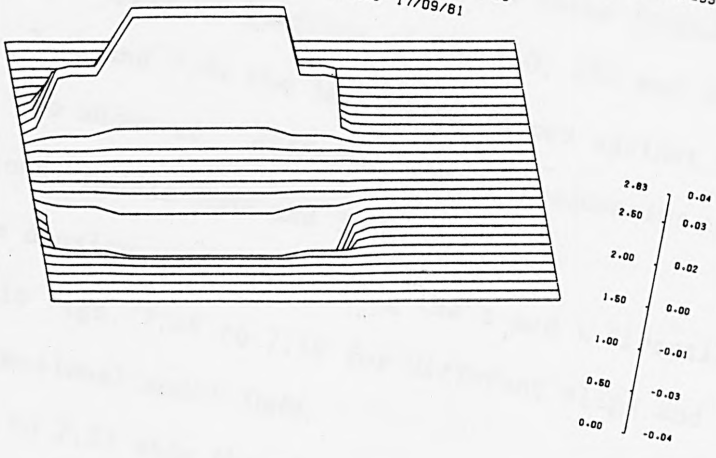

Z-COMP. OF FLUX DENSITY OF THE LIM-3DCMA.AT S=.3,I=5A,F=350.0
AZIMUTH = 15
*WIDTH = 6.00
ALTITUDE = 45
*HEIGHT = 4.00
* BEFORE FORESHORTENING 17/09/81

Fig. 7.30. Flux density distribution of 3DCM model at f = 350 Hz and S = 0.3

7.3 Forces and Force Density Distributions

The force measurements were carried out on the stator member of the linear induction motor using strain gauges. The measurements are based on Newton's law of the action and reaction forces.

Figs. 7.31 to 7.34 show the propulsion force against slip at supply frequencies of 50, 150, 250 and 350 Hz. In each figure the predicted results obtained by the two dimensional models (2DHM and 3DHM) and the three dimensional model (3DHm and 3DCM) were plotted with experimental results.

To show the significance of the end effects on the performance obtained by each models for different levels of synchronous speed, the propulsion force of each model is plotted against the linear speed for different frequencies and constant pole pitch as shown in Figs. 7.35 to 7.38. In these figures the one-dimensional predicted results represent the propulsion-speed performance of the linear induction motor without end effects.

Figs. 7.39 to 7.42 show the levitation force (repulsion) against slip at supply frequencies of 50, 150, 250 and 350 Hz.

In Fig. 7.43 and 7.44 the levitation forces against the linear speed are shown at different supply frequencies using three dimensional models 3DHM and 3DCM.

The force density components along the z and x directions are presented in Figs. 7.45 to 7.49 for different slips and using three dimensional model 3DHM.

Figs. 7.50 to 7.53 show the three dimensional plots of the force density component at supply frequencies of 150 and 350 Hz and a slip of 0.3 using 3DHM and 3DCM models.

Generally, it can be seen that the form of the propulsion speed characteristics of the linear induction motor is identical with the conventional speed torque characteristic of the induction rotating motor. However, because of the end effects the performance of the linear motor is adversely effected and the maximum propulsion force and its location with respect to slip are altered.

In linear induction motors the value of the maximum propulsion force decreases as the synchronous speed of the motor increases, while in a conventional motor it remains constant and its location with respect to slip moves toward zero.

It is also found that the propulsion force of the linear induction motor at synchronous speed is not zero. It is positive for a low synchronous speed motor which may be an advantage, and negative for a high synchronous speed motor which acts as a drag force.

It can be observed from the last results that there are some differences in the predicted results and in particular in the levitation speed characteristics. These differences may be related to the same argument stated in the last section. In the three dimensional models the overhang zone of the primary winding provides a considerable contribution to the magnitude of the levitation force, and because of the differences in the configuration of the three dimensional models concerning the overhang zone, it is found that the levitation force obtained by 3DCM is over-estimated, while the results obtained by the 3DHM is under-estimated.

It has been common in previous work for the two-dimensional approach to multiply the force density per width by the width of the stator to obtain the effective forces. This assumption is unjustified, because the force density distribution along the

z-direction.is changing with different slips as shown in Figs. 7.45 and 7.46. Thus, a factor in which the secondary width, stator width, and the distribution form of the current density components all involved is the most appropriate assumption.

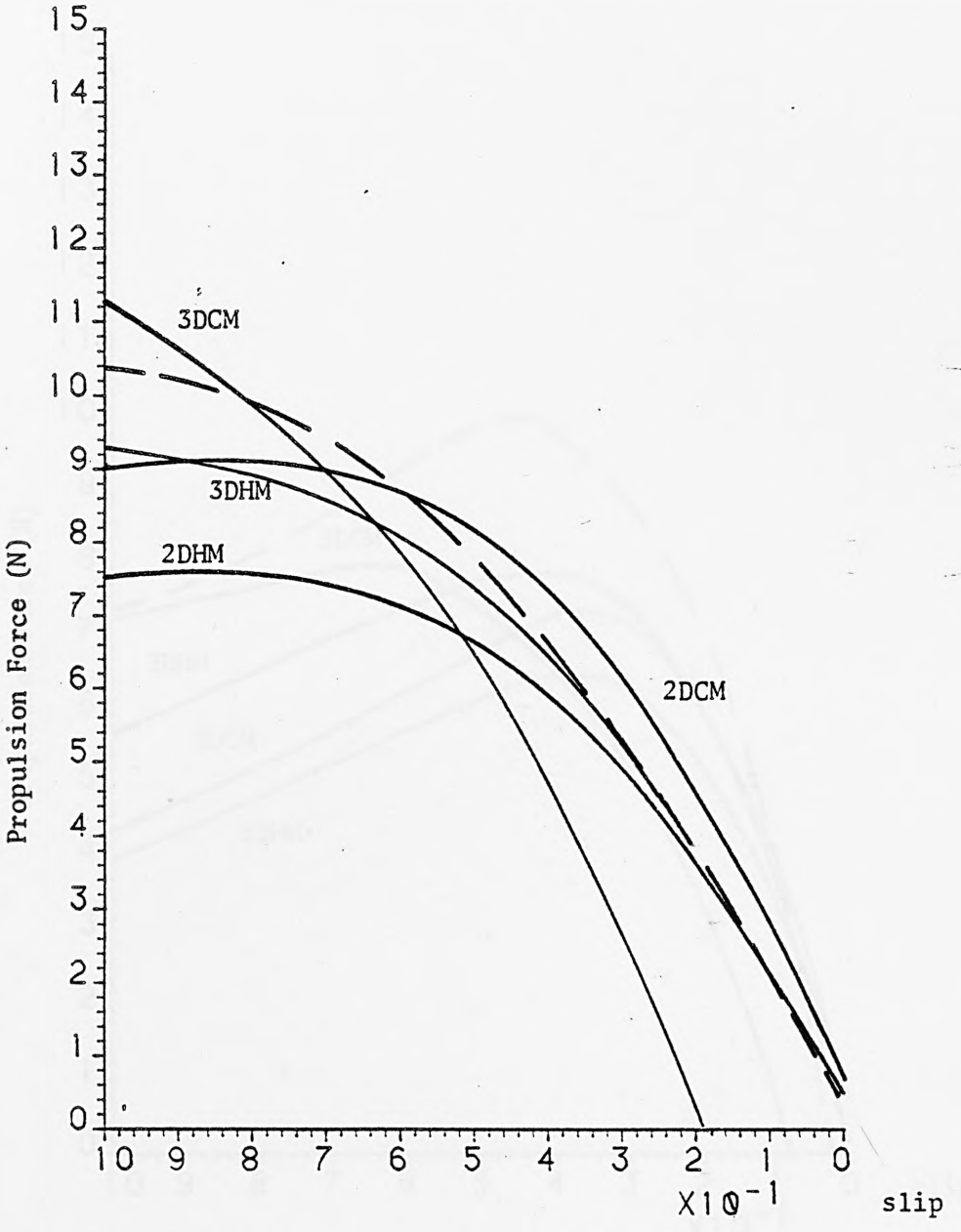

Fig. 7.31. Propulsion force against slip at f = 50 Hz

– – measured, — computed

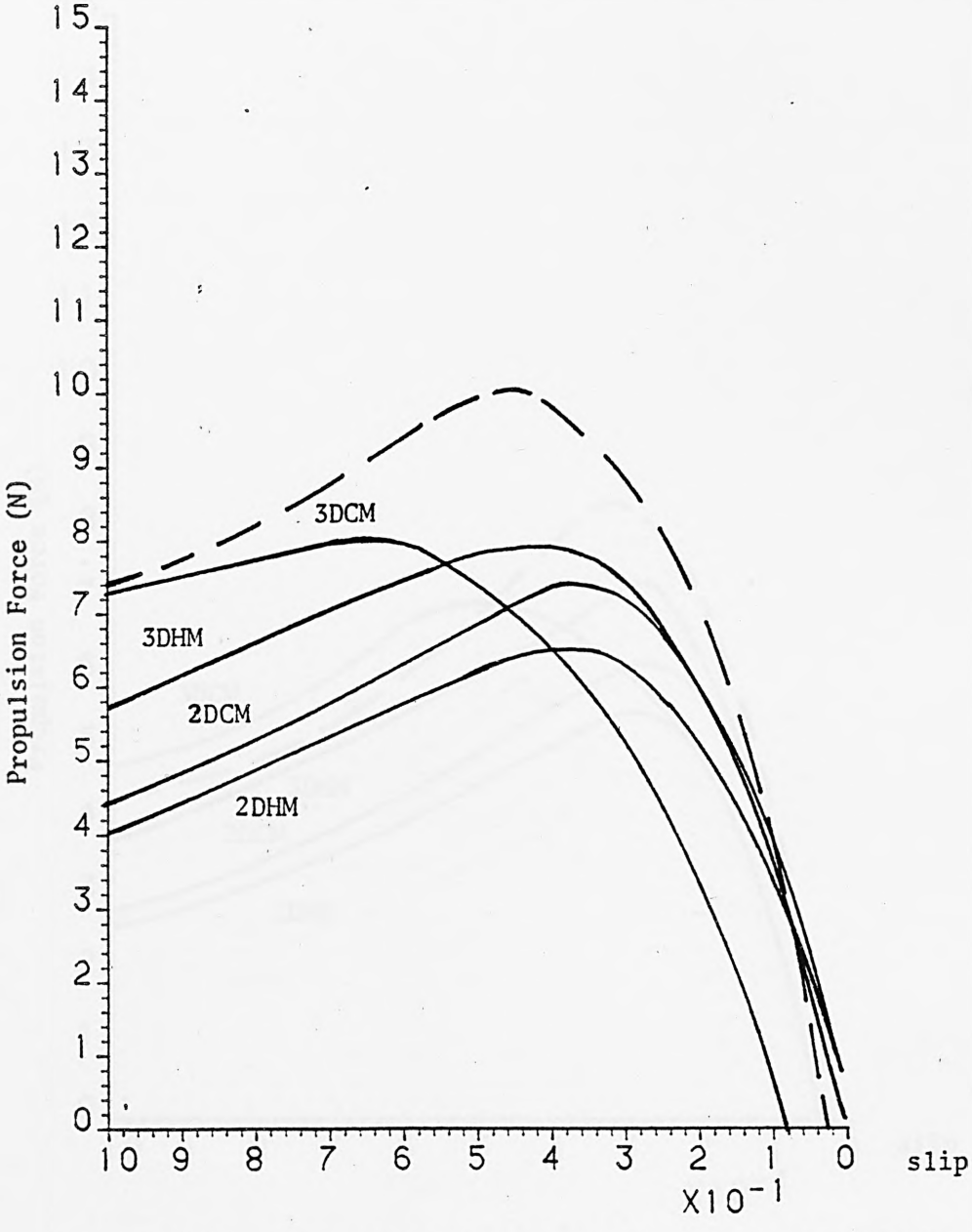

Fig. 7.32. Propulsion force against slip at f = 150 Hz

-- measured, — computed

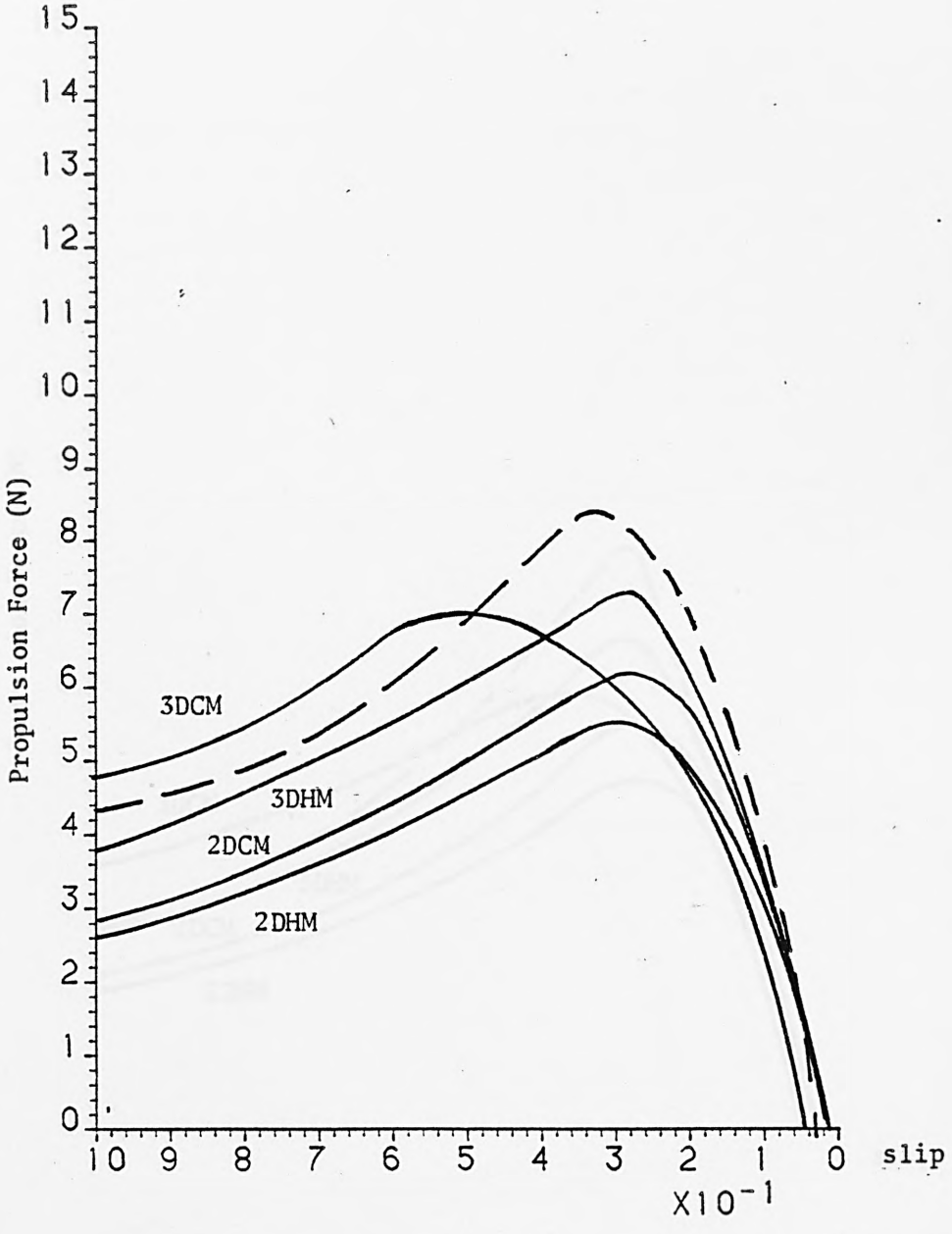

Fig. 7.33. Propulsion force against slip at f = 250 Hz

— computed, -- measured

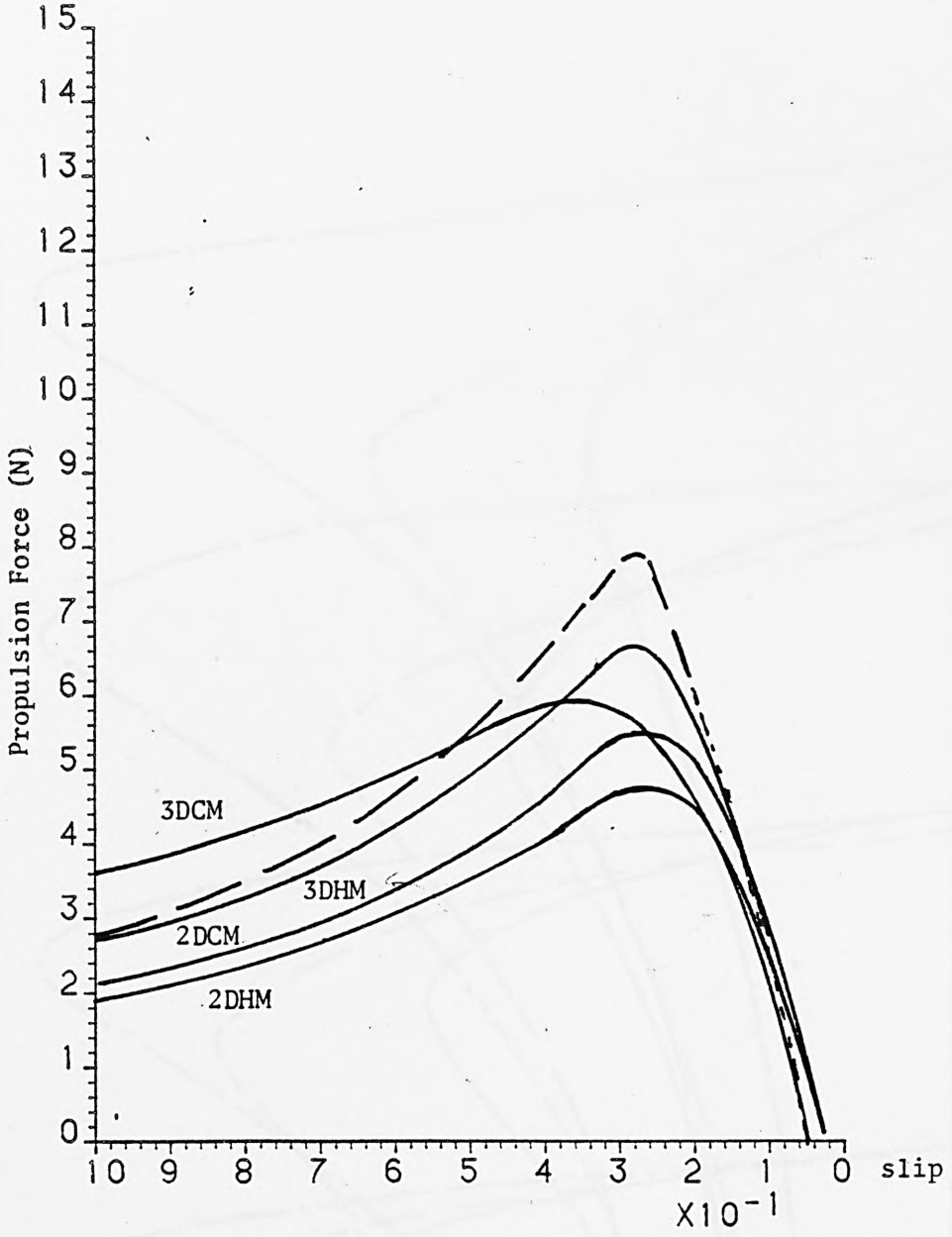

Fig. 7.34. Propulsion force against slip at f = 350 Hz

- - measured, — computed

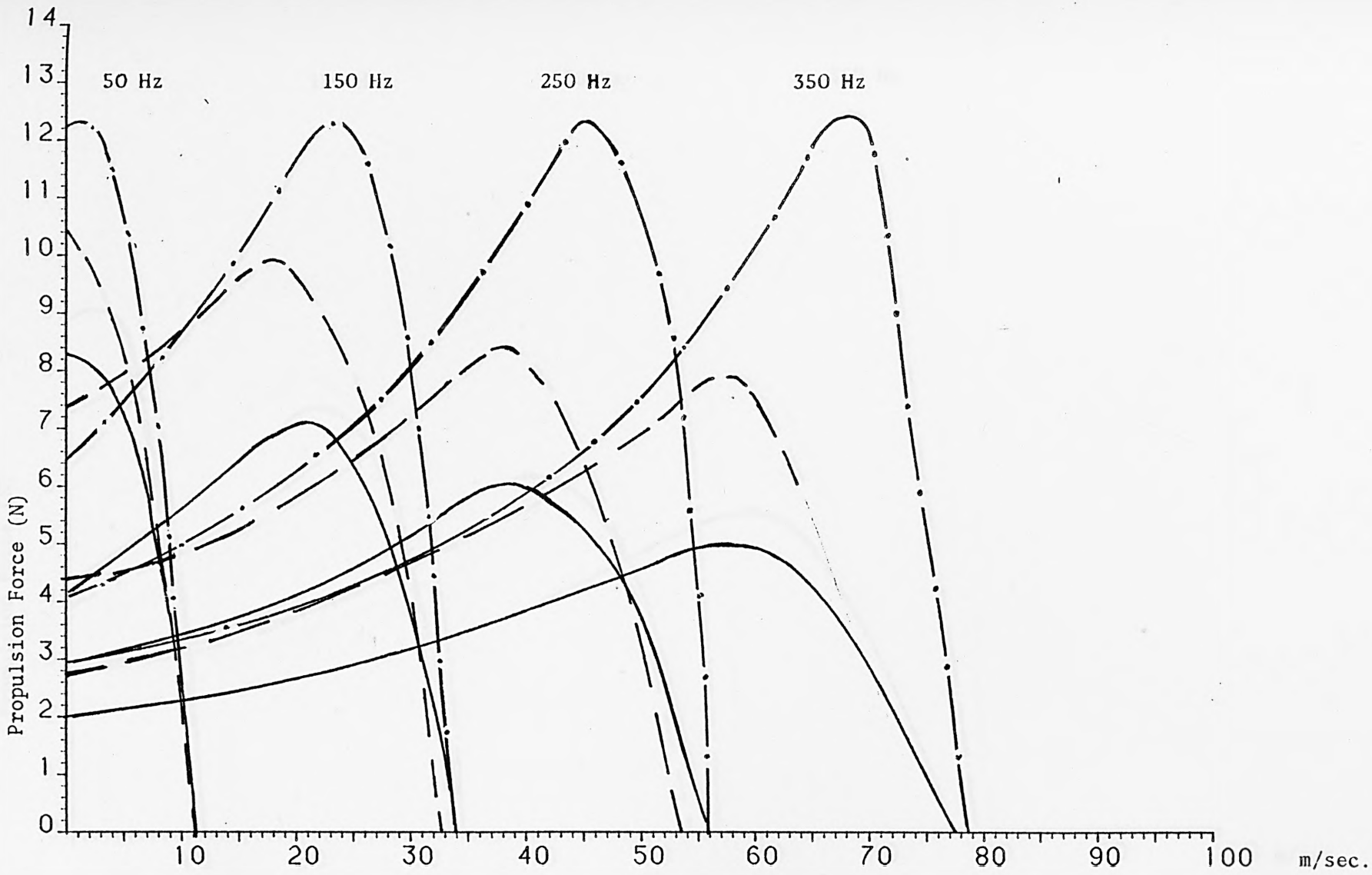

Fig. 7.35. Propulsion force against speed of 2DHM

-- Measured, —computed 2DHM, --- computed without end effects

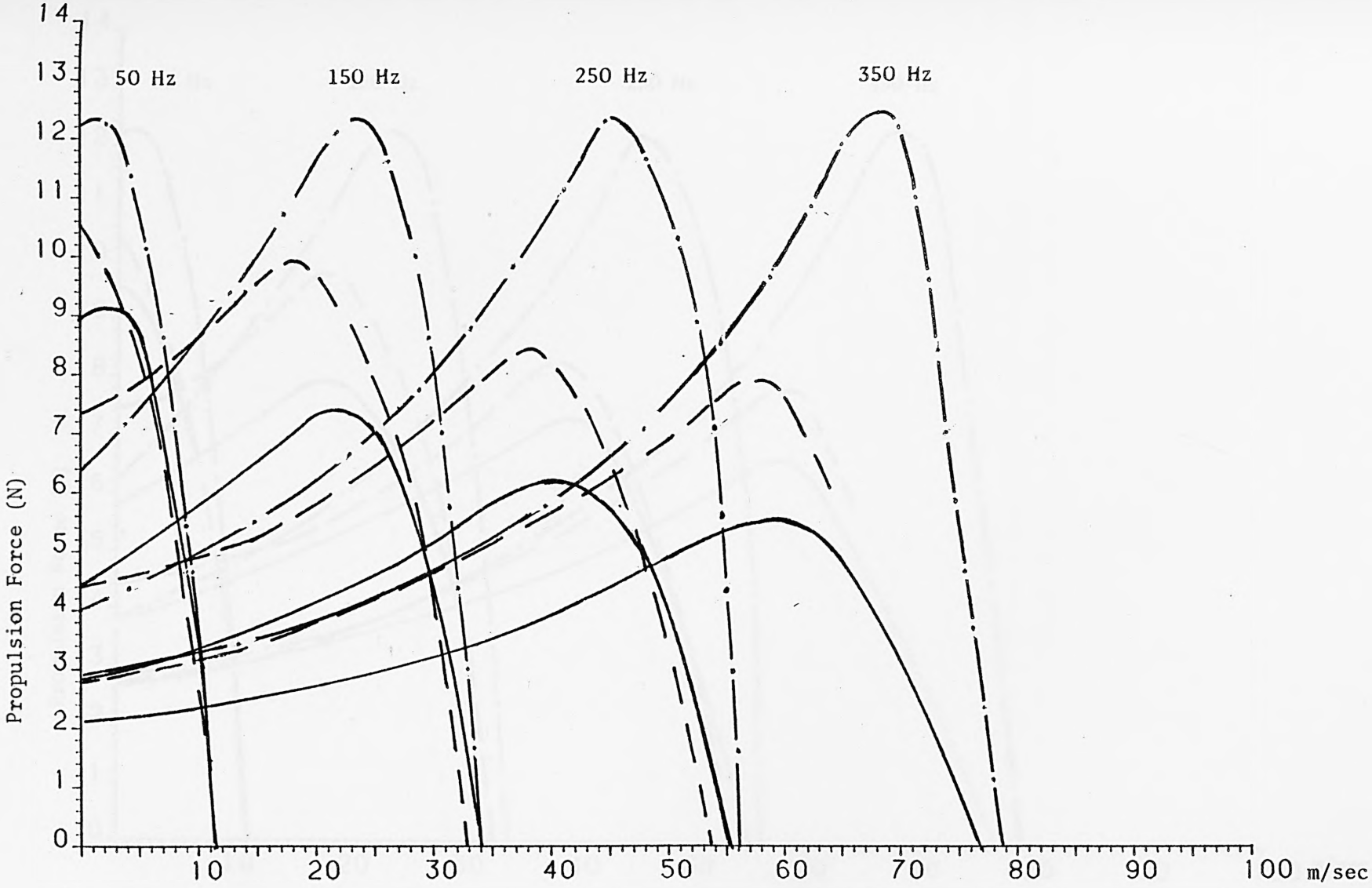

Fig. 7.36. Propulsion force against speed of 2DCM.

-- measured, — computed 2DCM, -·- computed without end effects

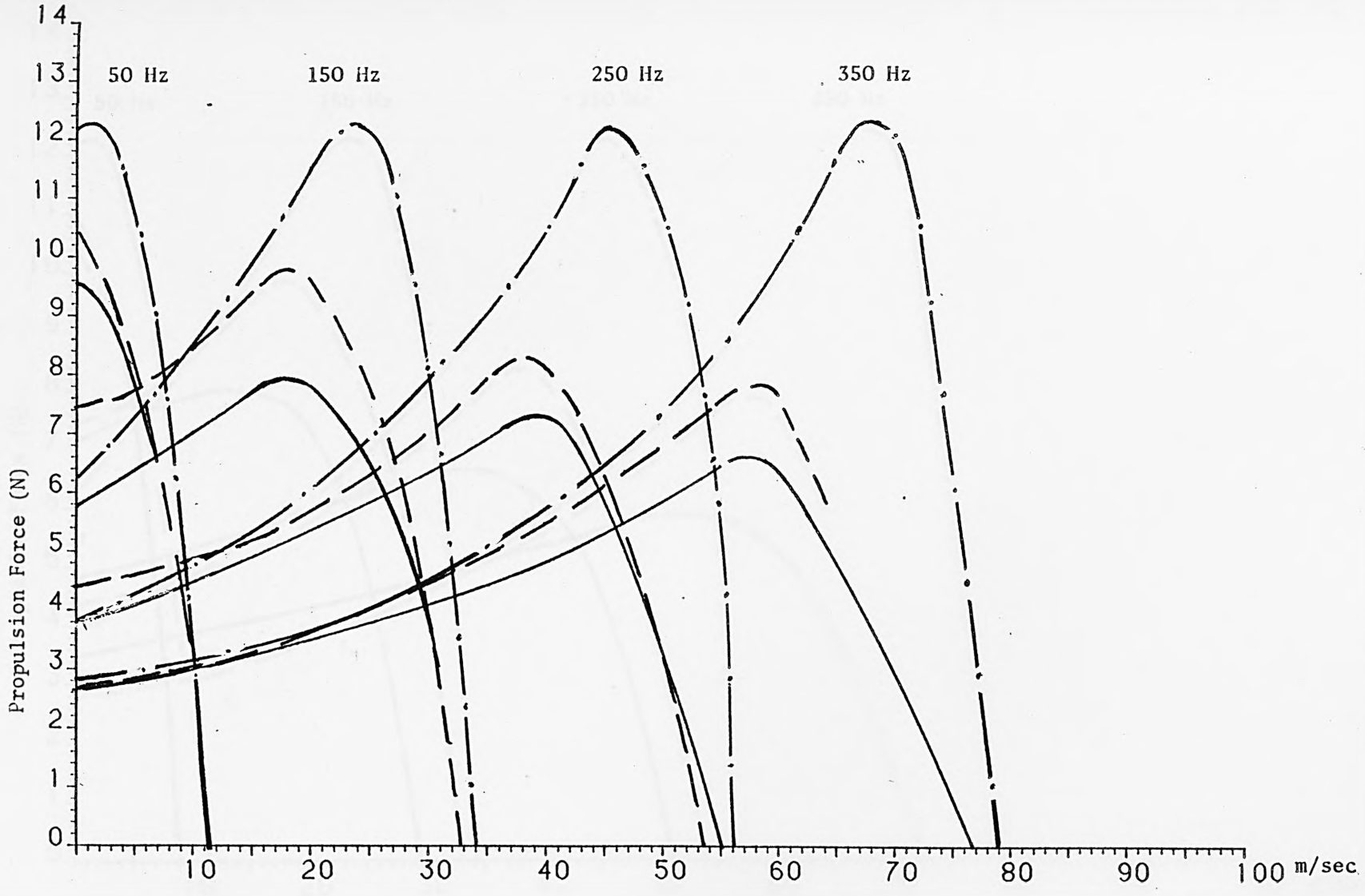

Fig. 7.37. Propulsion force against speed of 3DHM

-- measured, — computed 3DHM, --- computed without end effects

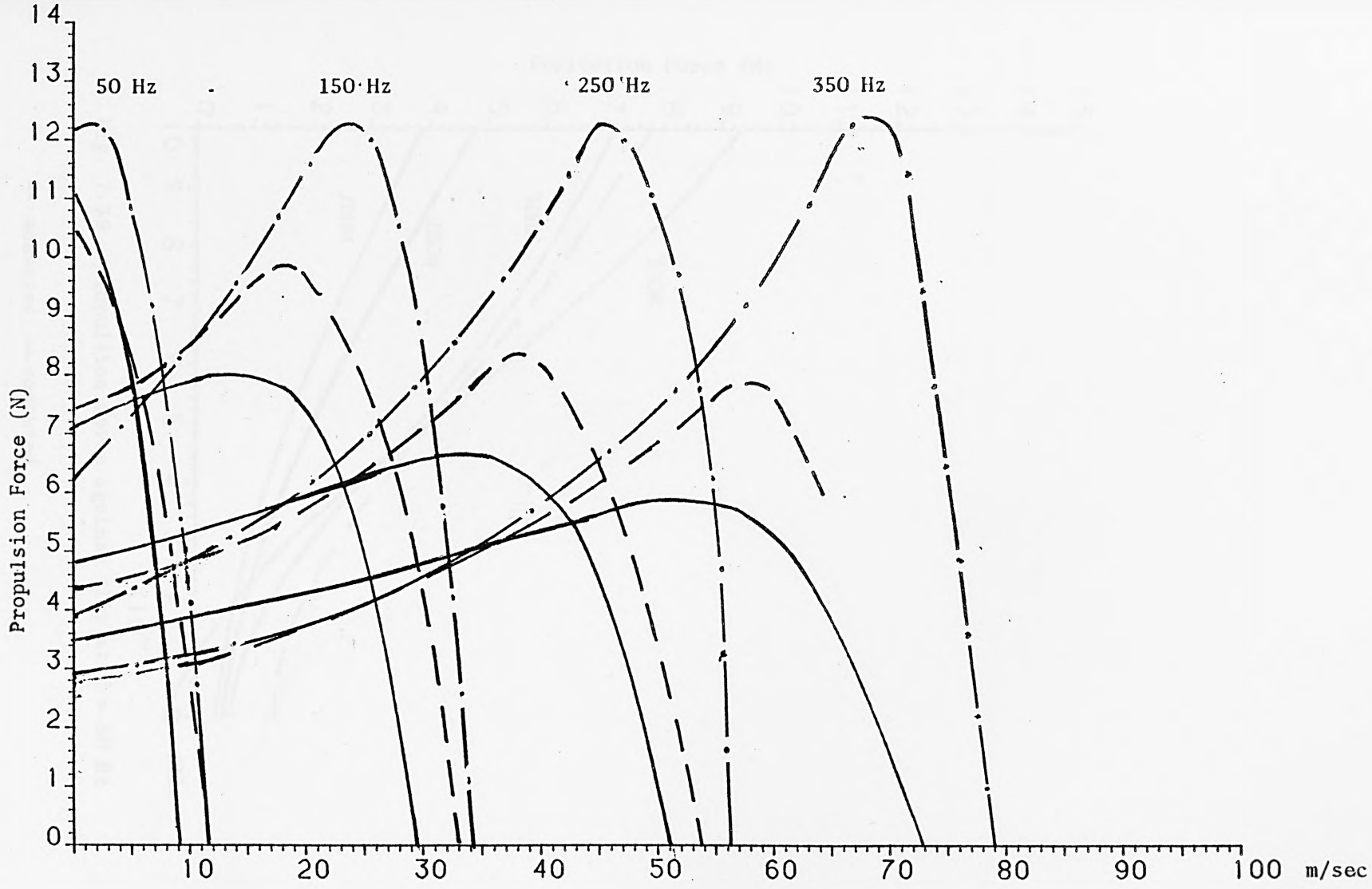

Fig. 7.38. Propulsion force against speed of 3DCM

-- measured, — computed 3DCM, -·- computed without end effects

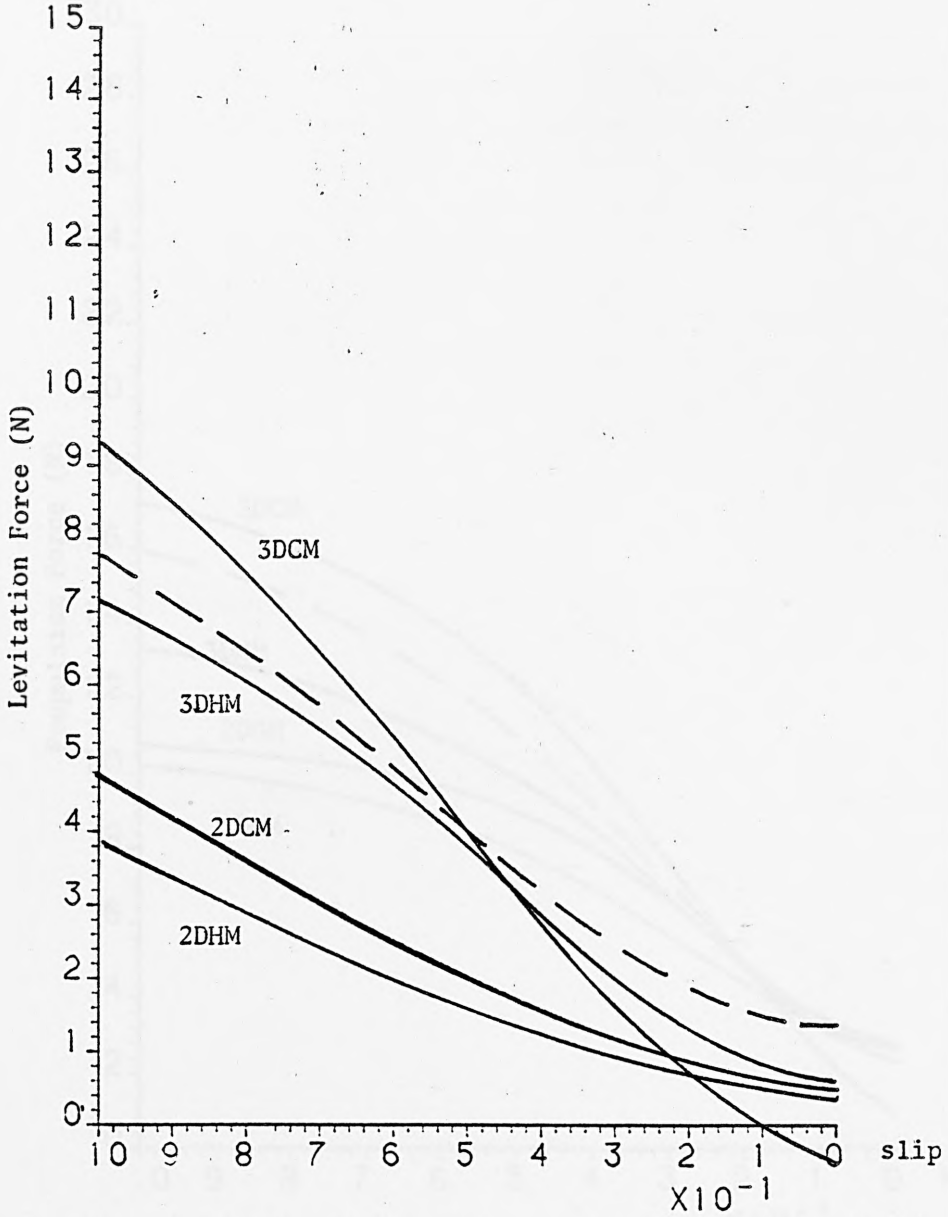

Fig. 7.39. Propulsion force against slip at f = 50 Hz

-- measured, — computed

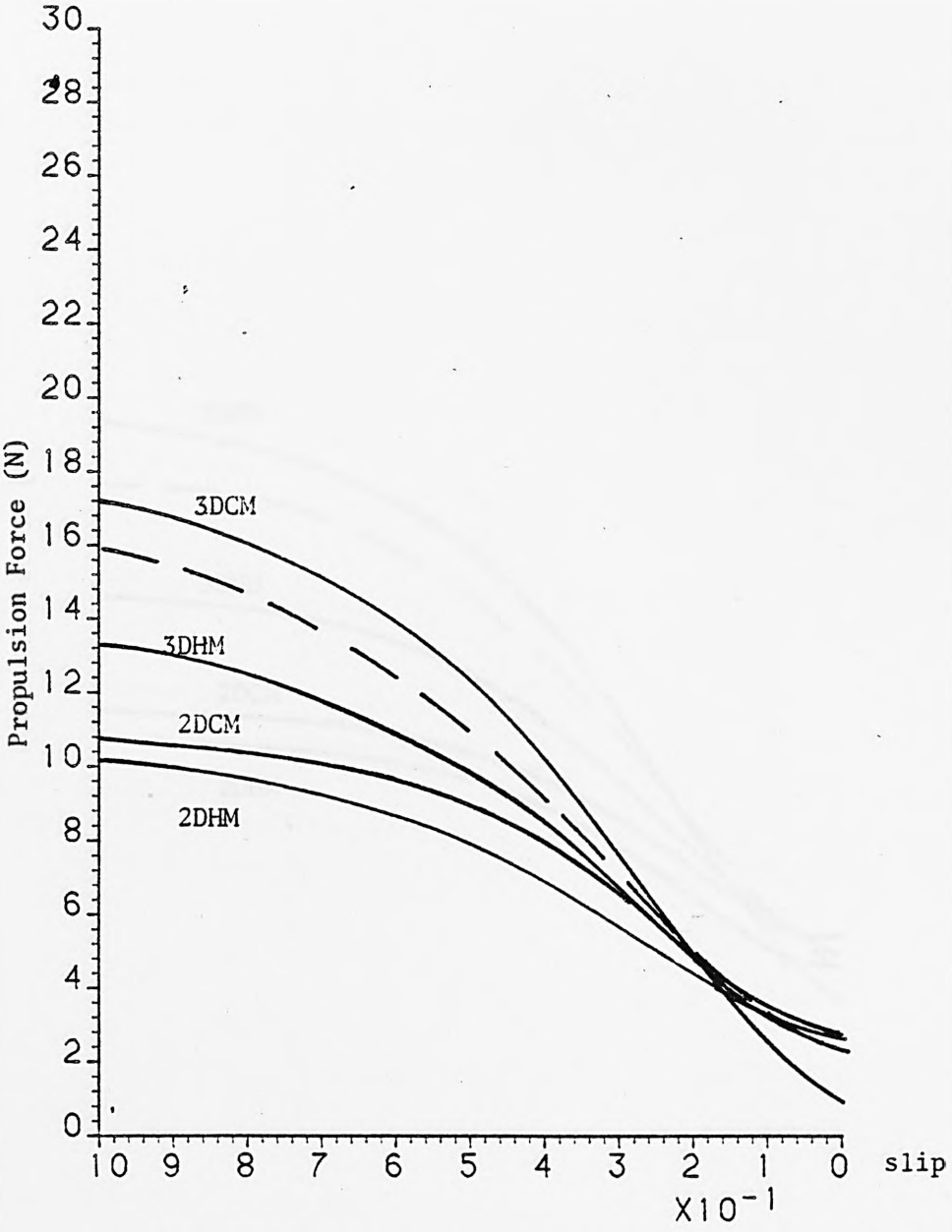

Fig. 7.40. Levitation force against slip at f = 150 Hz

- - measured, — computed

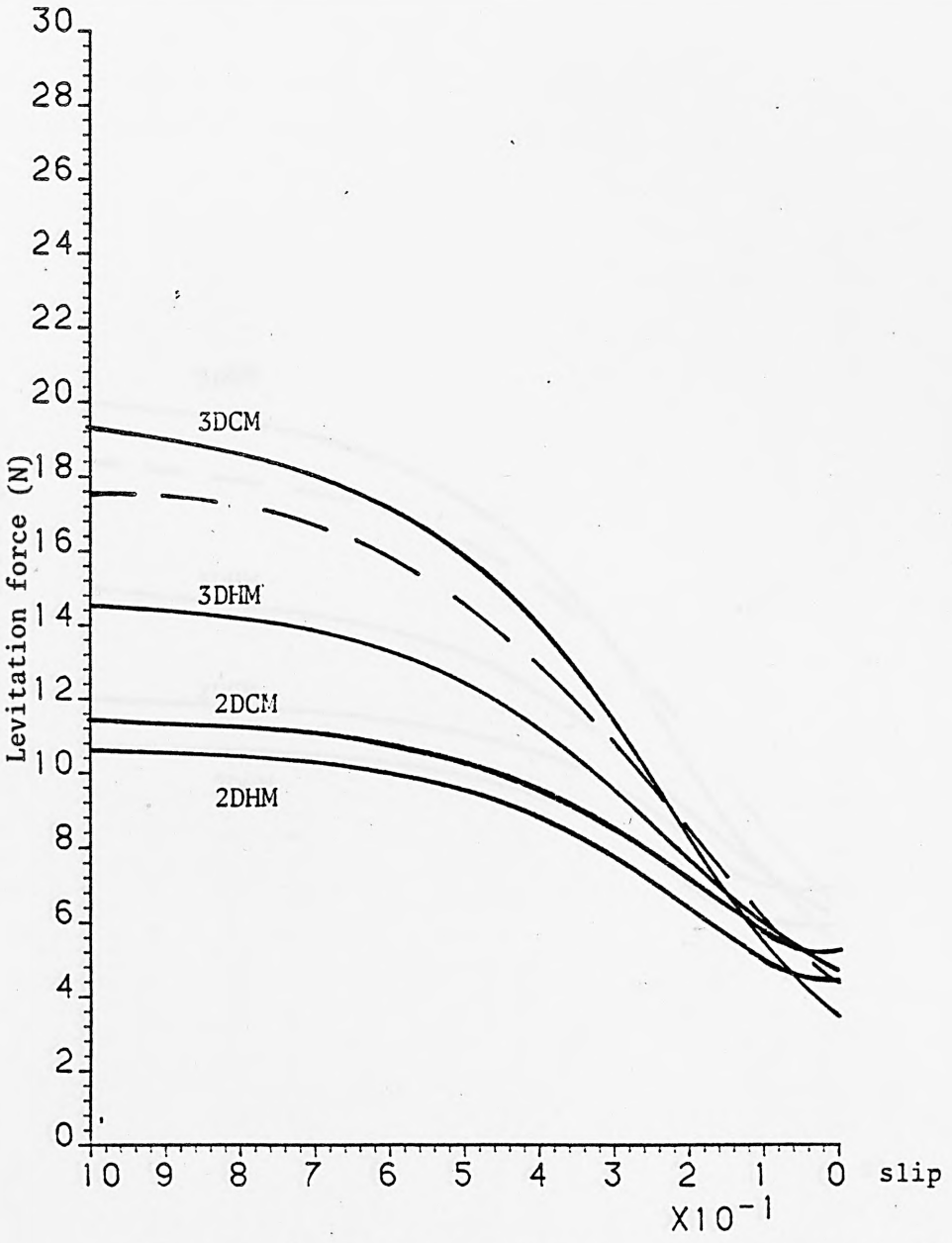

Fig. 7.41. Levitation force against slip at f = 250 Hz

-- measured, — computed

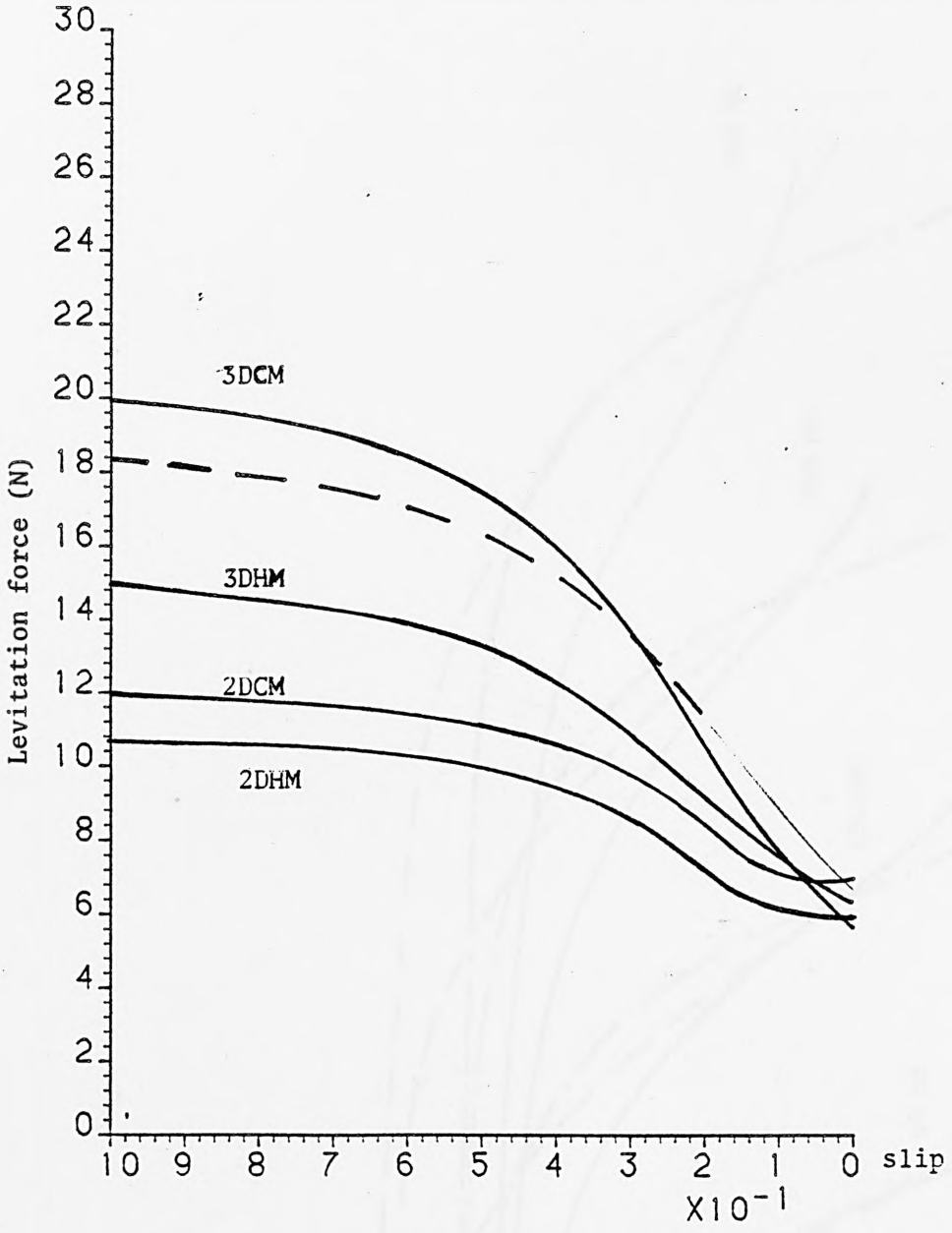

Fig. 7.42. Levitation force against slip at f =350 Hz

- - measured, — computed

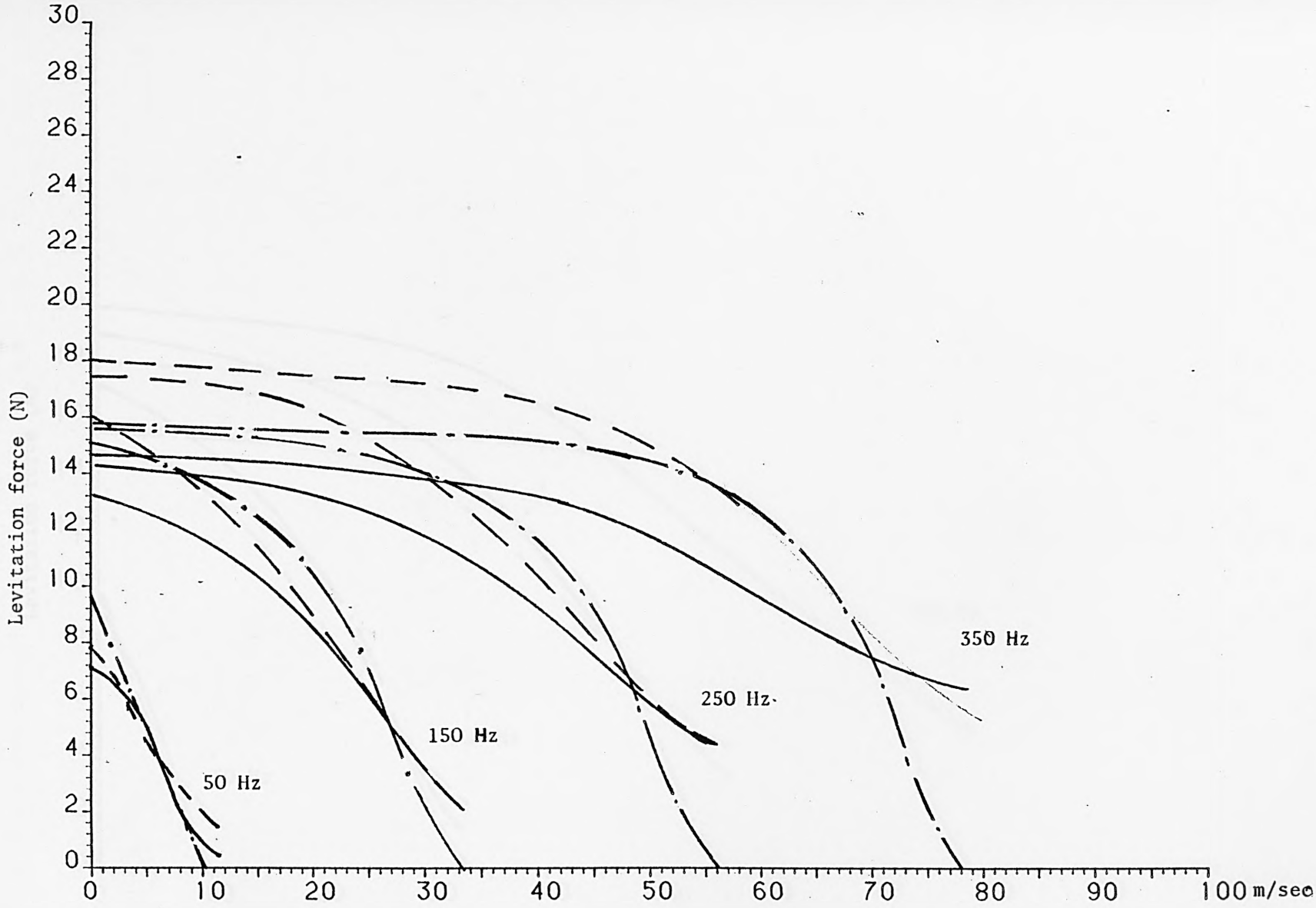

Fig. 7.43. Levitation force against speed of 3DHM

-- measured, — computed 3DHM, -·- computed without end effect

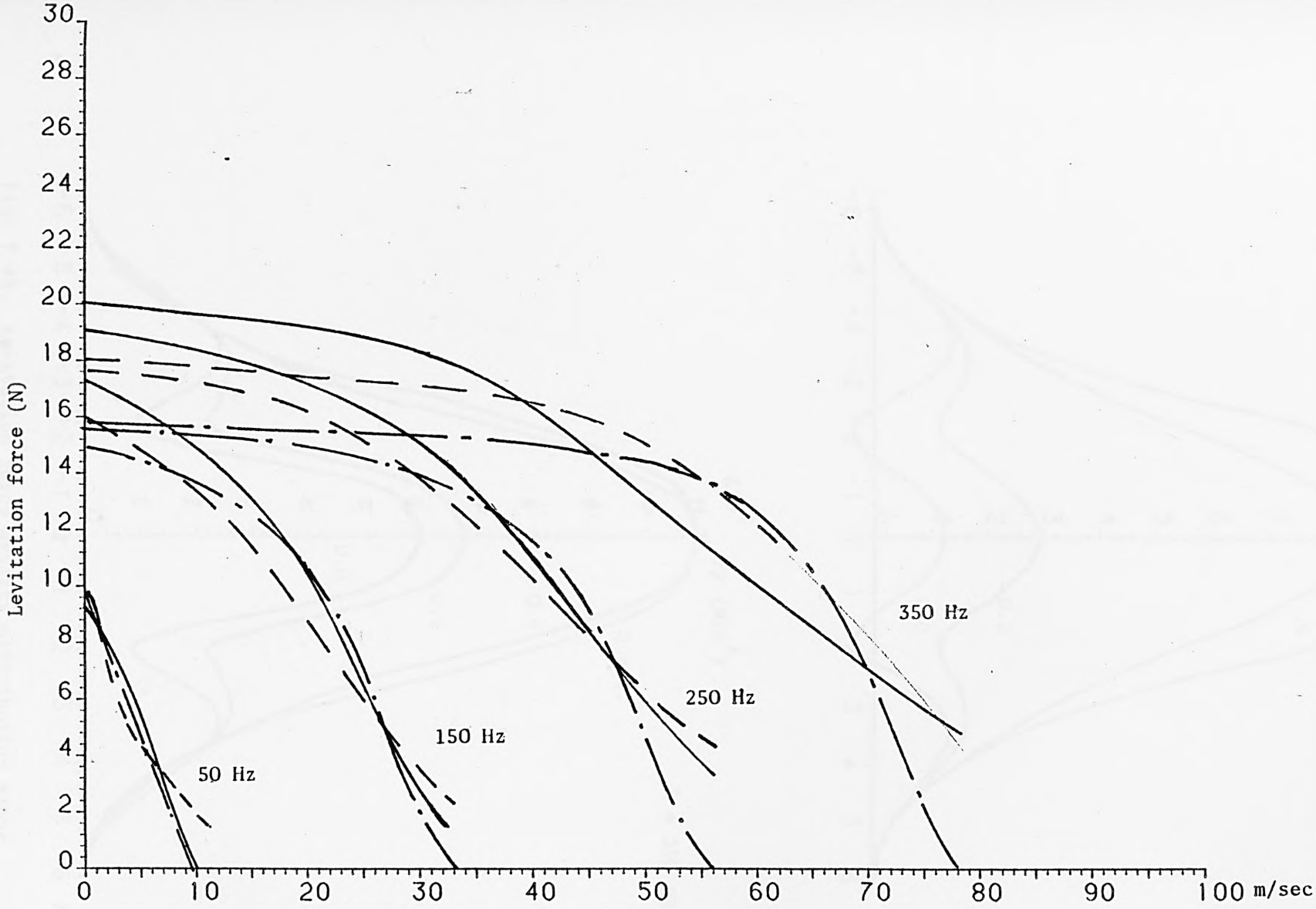

Fig. 7.44. Levitation force against speed of 3DCM

-- measured, — computed 3DCM, -·- computed without end effect

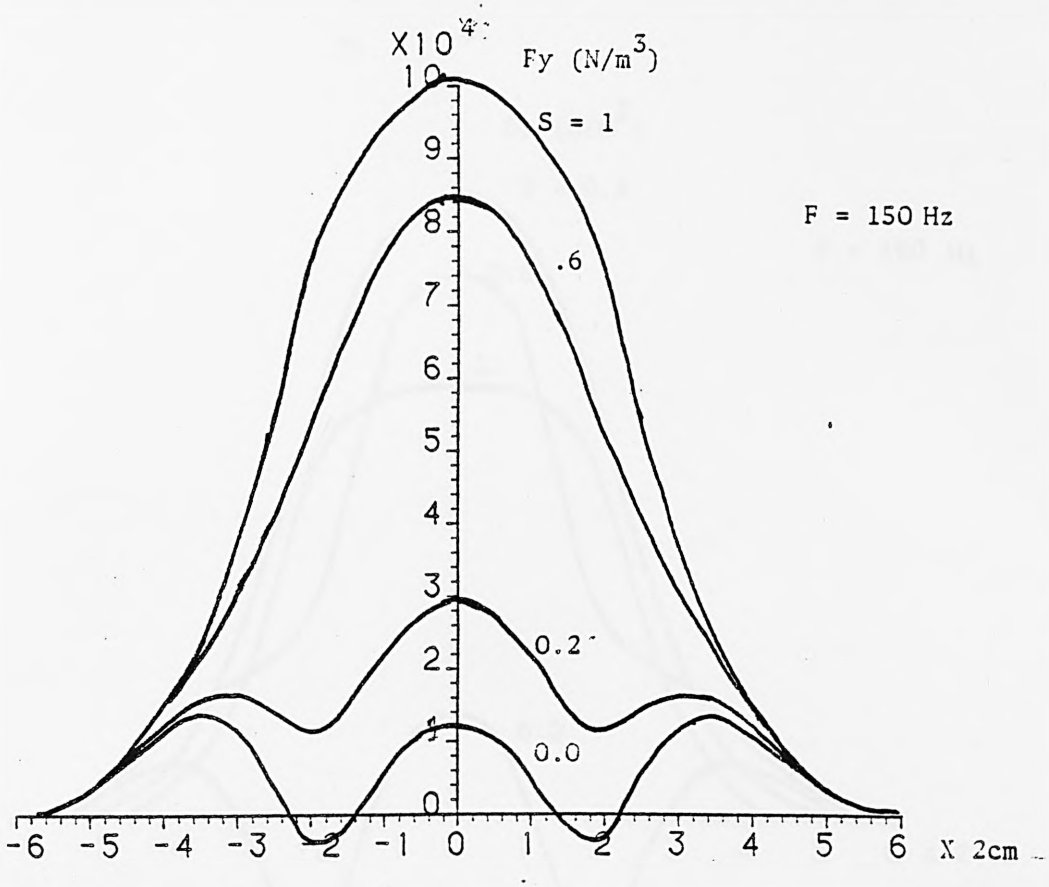

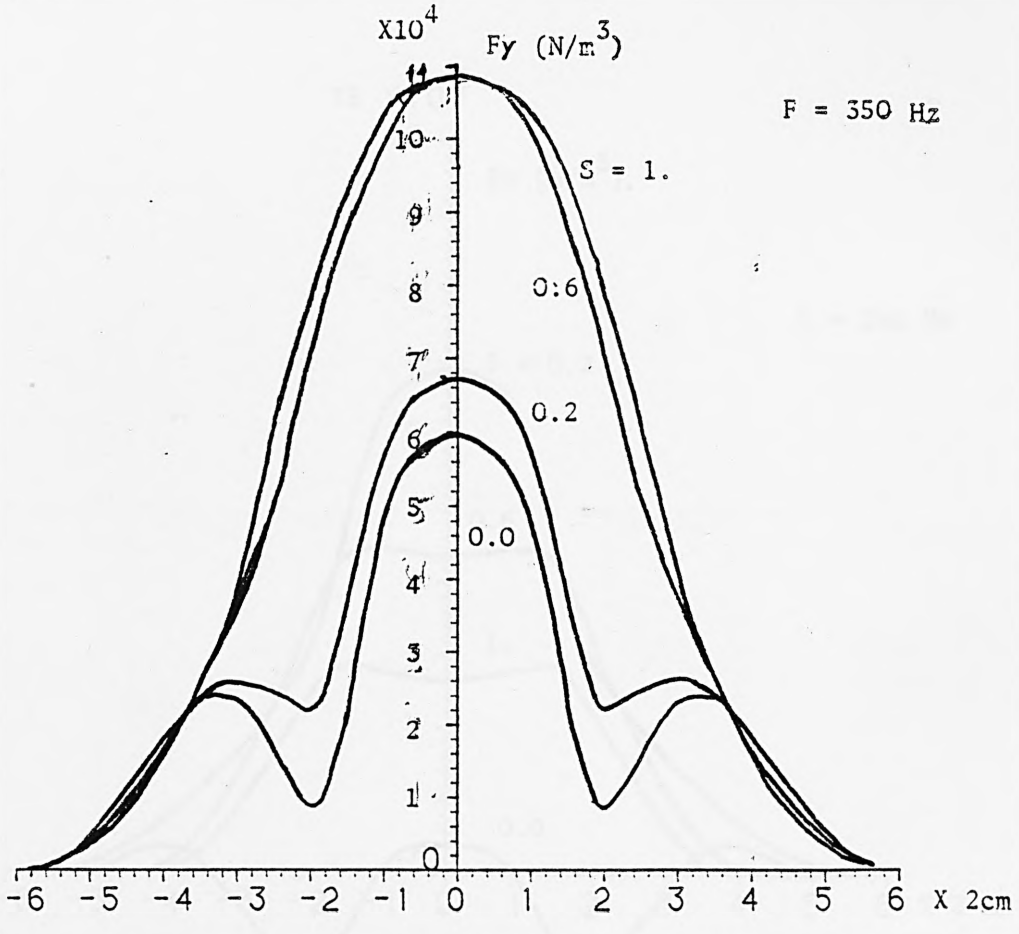

Fig. 7.45. Levitation force density distribution along z-direction of 3DHM

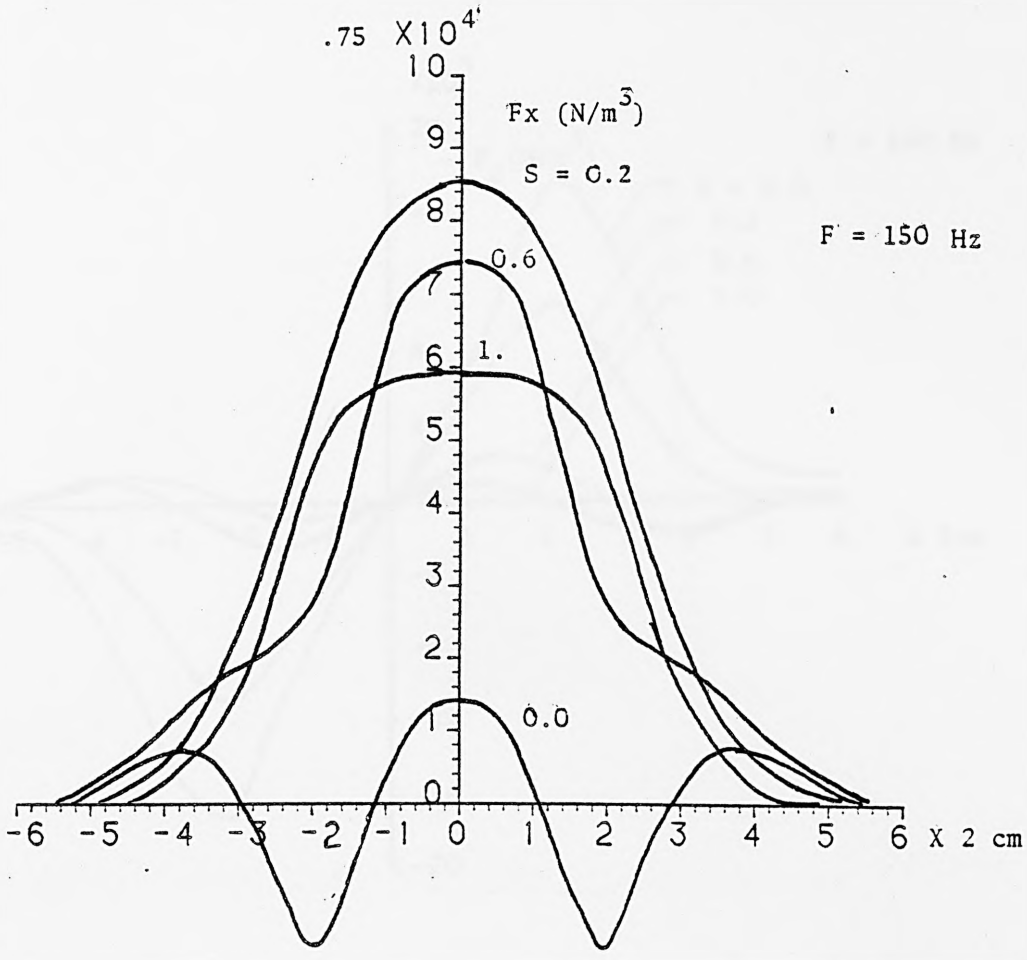

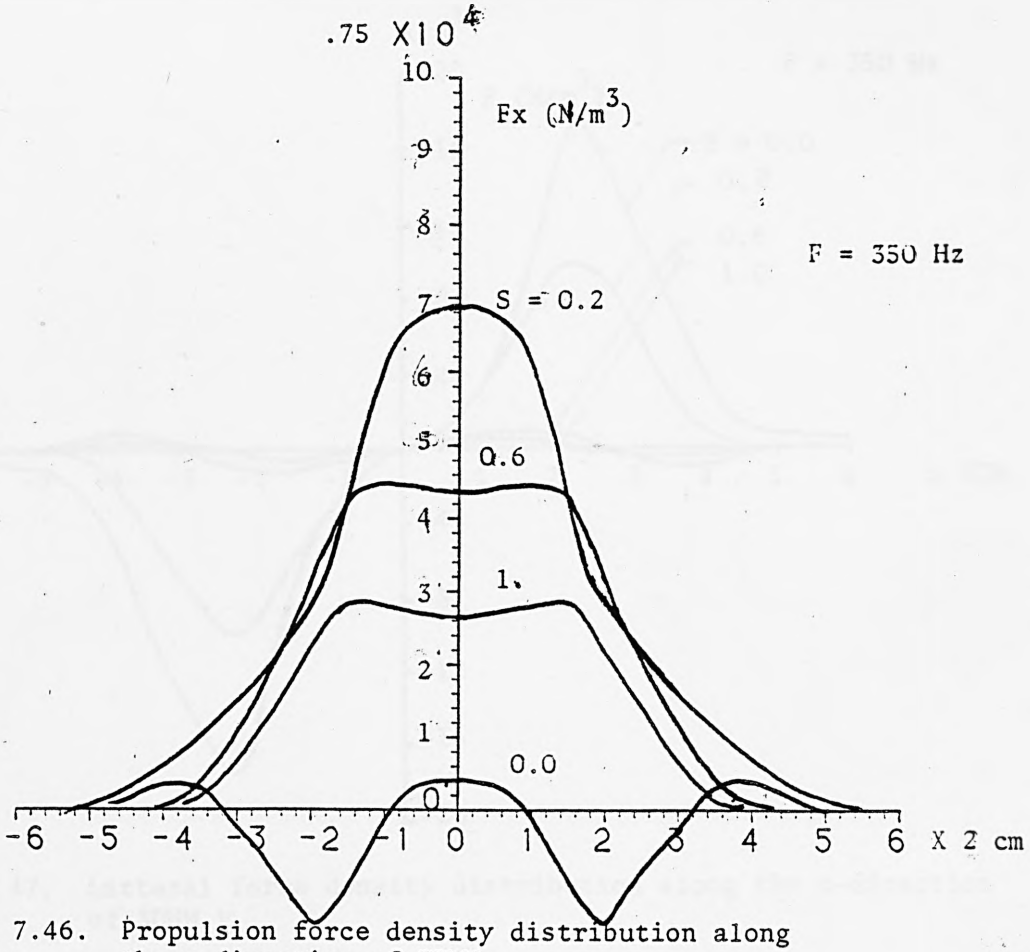

Fig. 7.46. Propulsion force density distribution along the z-direction of 3DHM

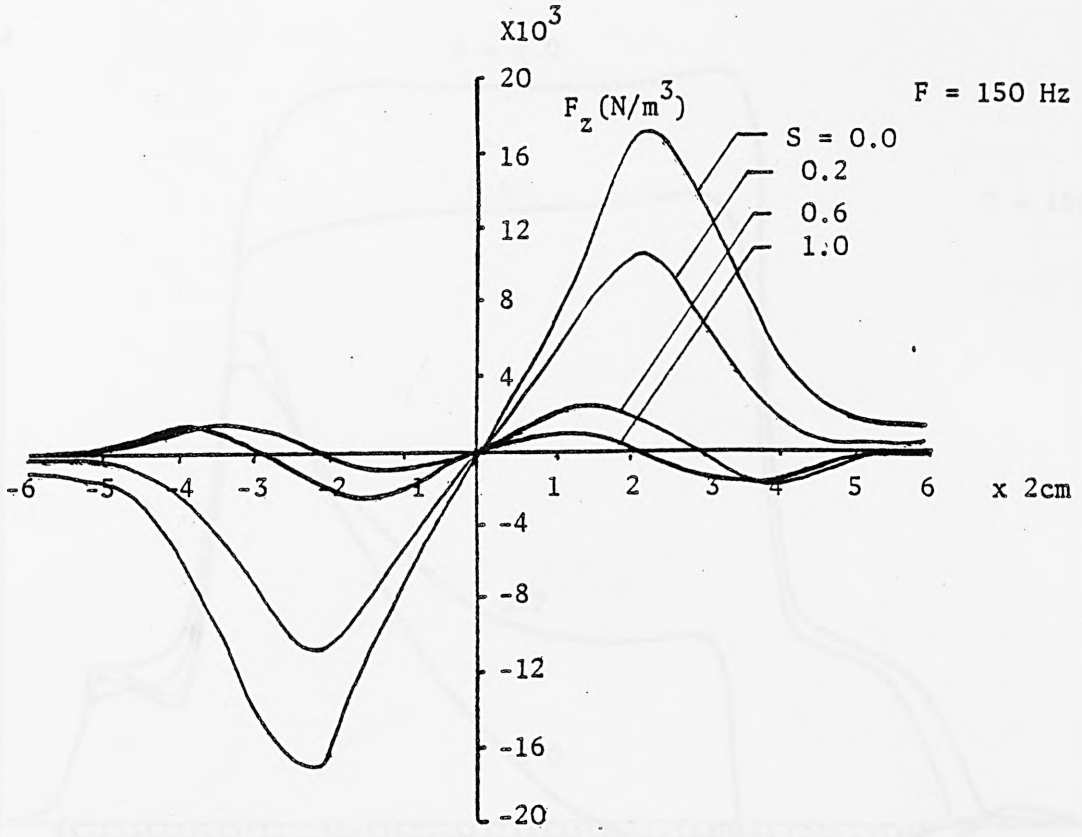

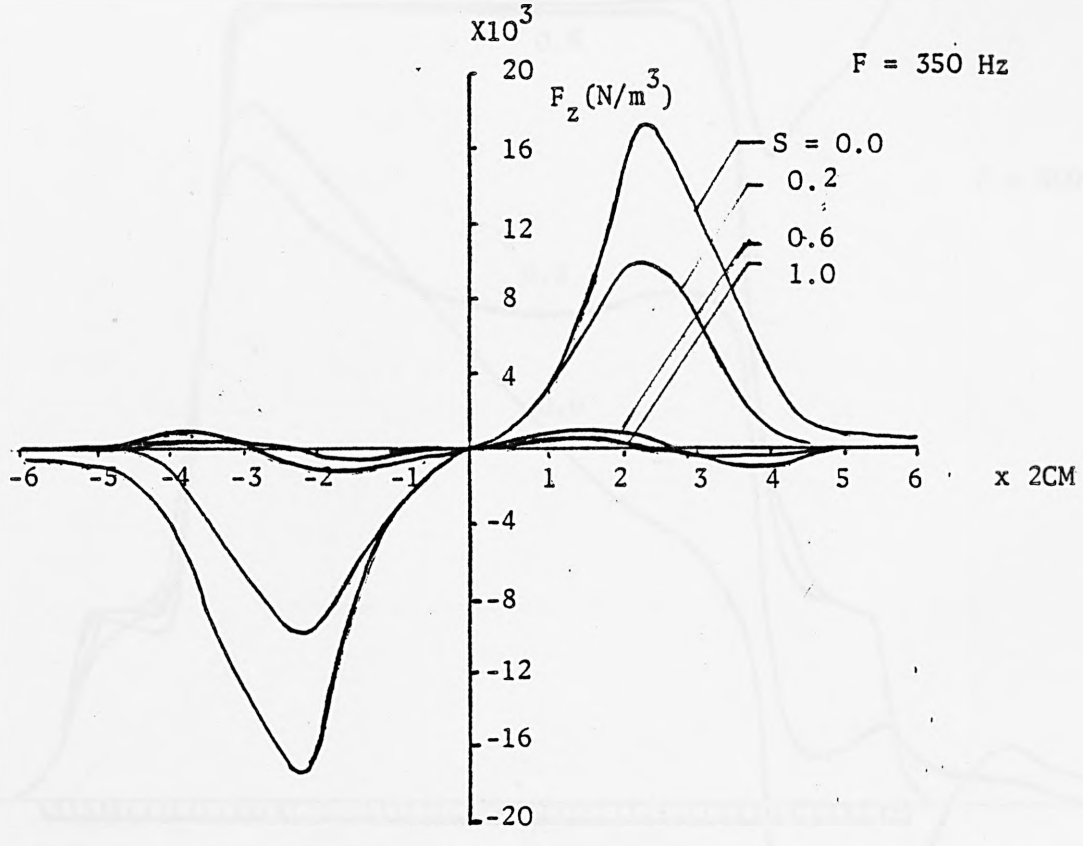

Fig. 7.47. Latteral force density distribution along the z-direction of 3DHM

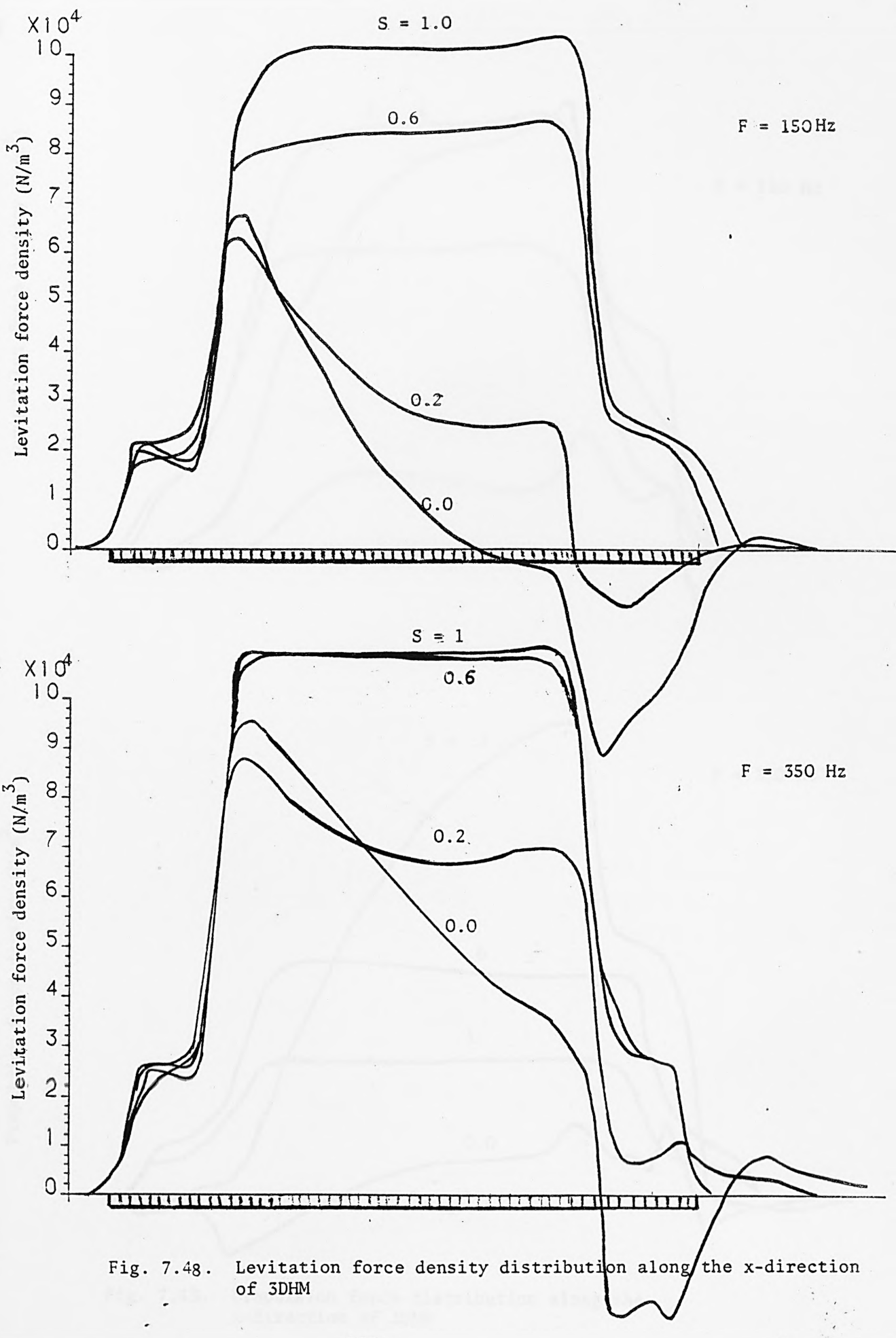

Fig. 7.48. Levitation force density distribution along the x-direction of 3DHM

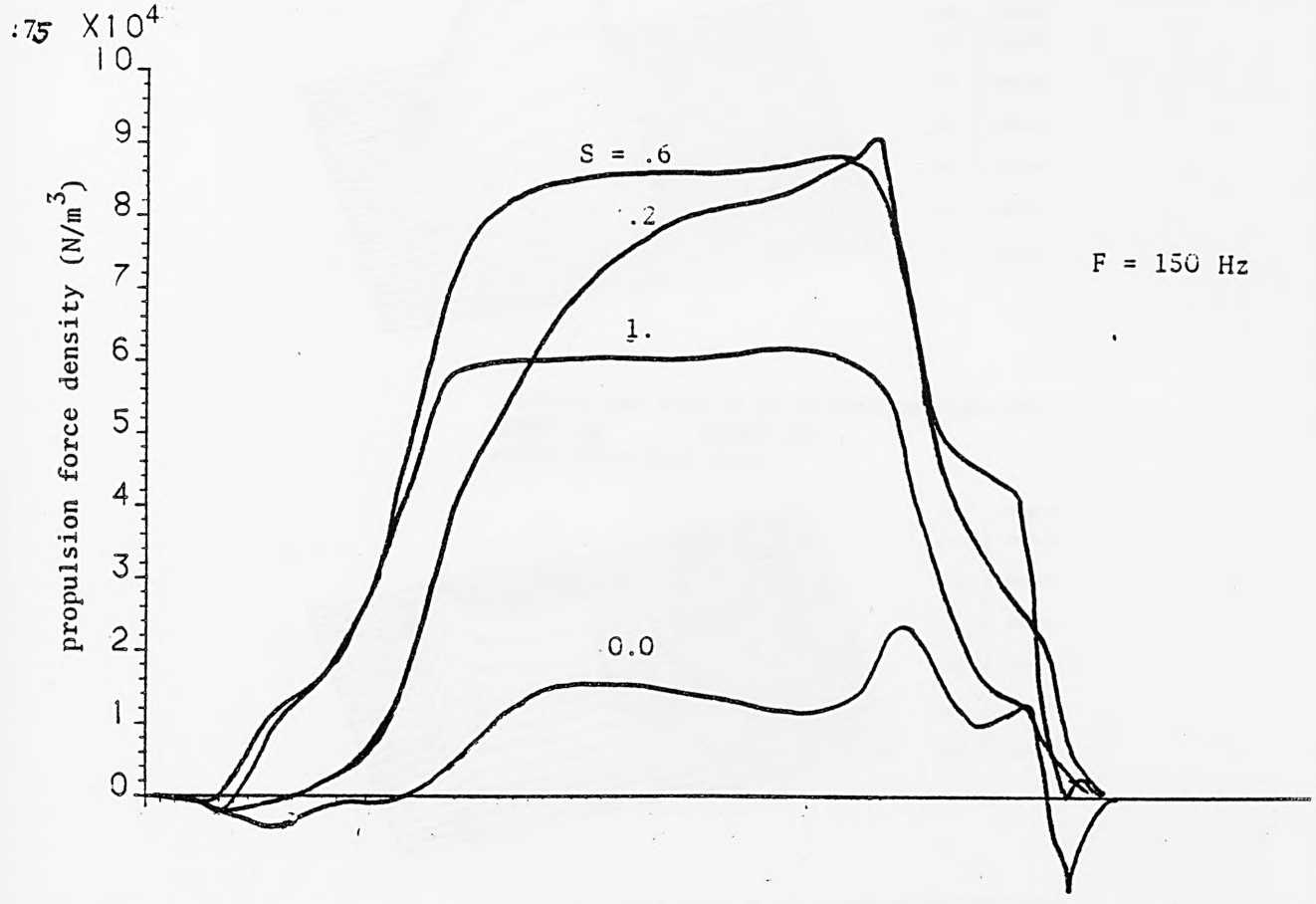

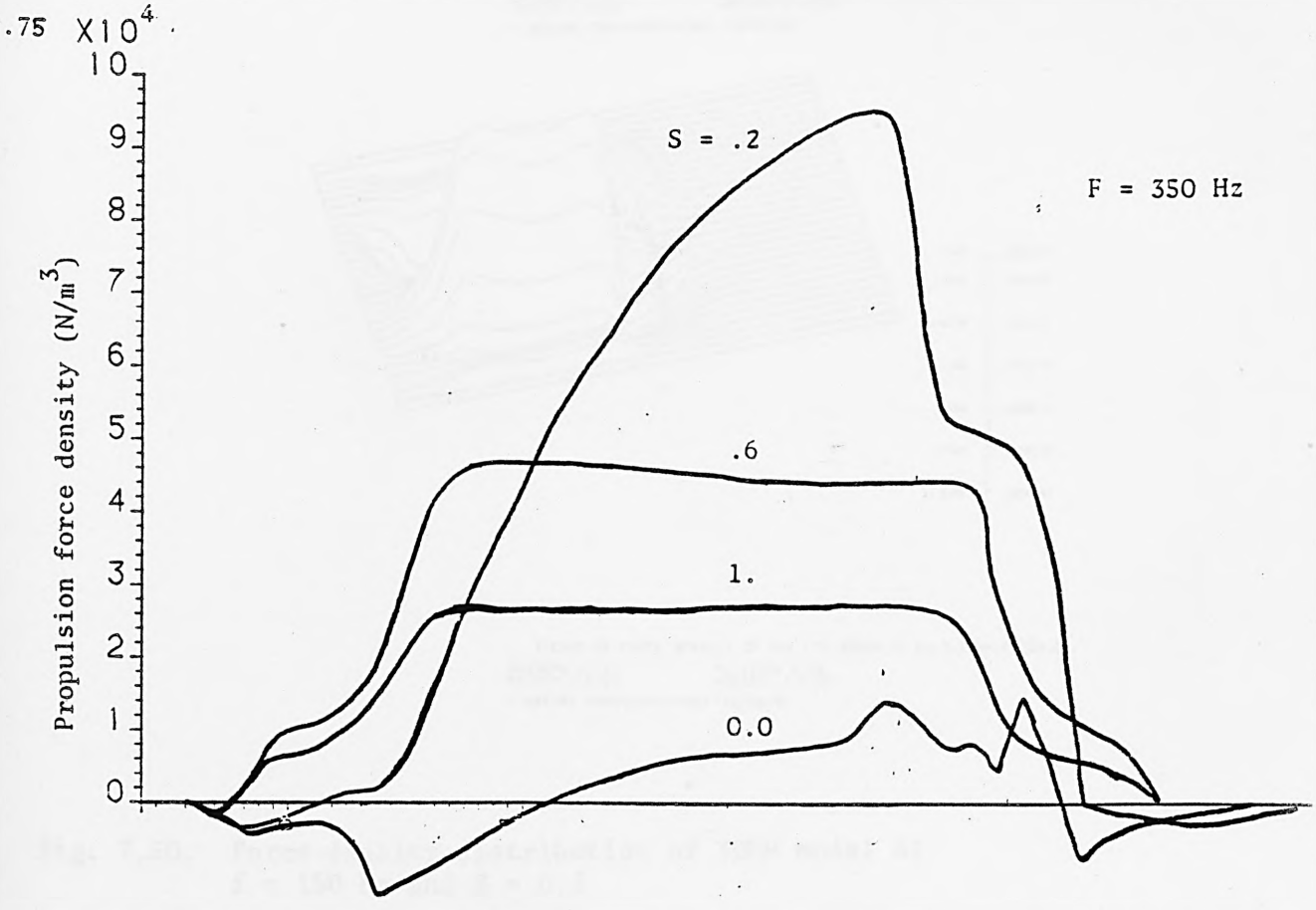

Fig. 7.49. Propulsion force distribution along the x-direction of 3DHM

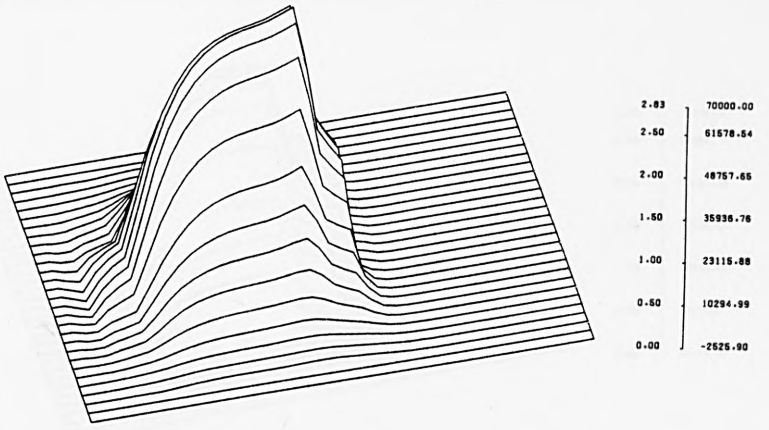

X-COMP.OF FORCE DENSITY OF THE LIM-3DHMA.AT S=.3.I=5A.F=150.0
AZIMUTH = 15 ALTITUDE = 45
*WIDTH = 6.00 *HEIGHT = 4.00
* BEFORE FORESHORTENING 16/09/81

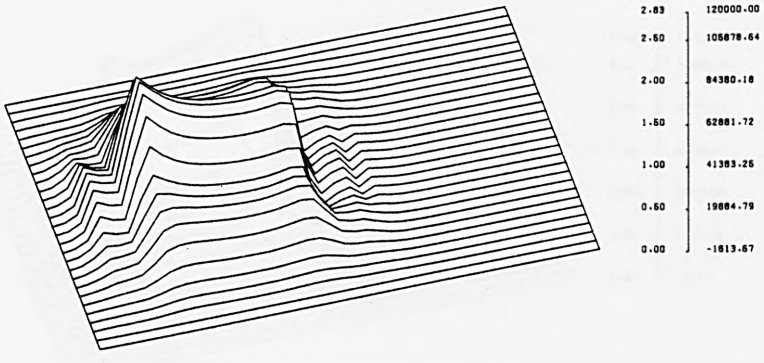

Y-COMP.OF FORCE DENSITY OF THE LIM-3DHMA.AT S=.3.I=5A.F=150.0
AZIMUTH = 15 ALTITUDE = 45
*WIDTH = 6.00 *HEIGHT = 4.00
* BEFORE FORESHORTENING 16/09/81

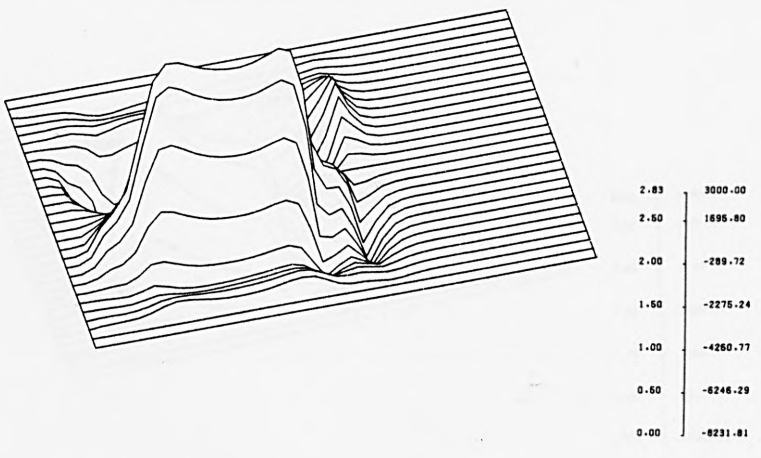

Z-COMP.OF FORCE DENSITY OF THE LIM-3DHMA.AT S=.3.I=5A.F=150.0
AZIMUTH = 15 ALTITUDE = 45
*WIDTH = 6.00 *HEIGHT = 4.00
* BEFORE FORESHORTENING 16/09/81

Fig. 7.50. Force density distribution of 3DHM model at f = 150 Hz and S = 0.3

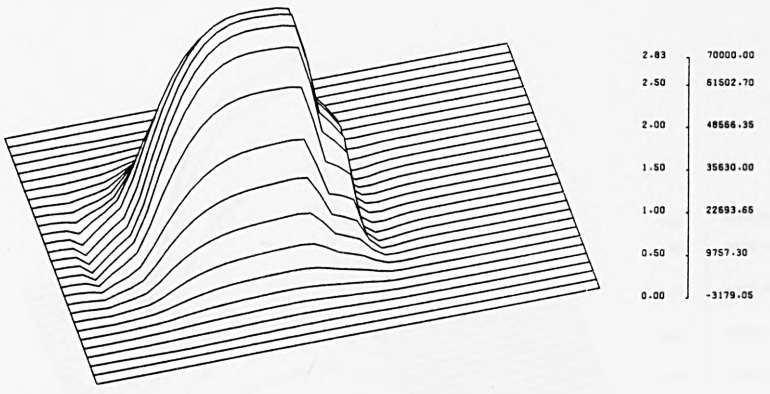

X-COMP.OF FORCE DENSITY OF THE LIM-3DHMA.AT S=.3.I=5A.F=350.0
AZIMUTH = 15 ALTITUDE = 45
*WIDTH = 6.00 *HEIGHT = 4.00
* BEFORE FORESHORTENING 14/09/81

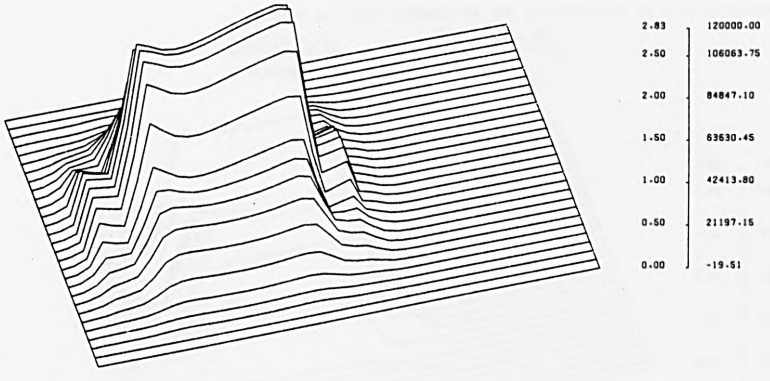

Y-COMP.OF FORCE DENSITY OF THE LIM-3DHMA.AT S=.3.I=5A.F=350.0
AZIMUTH = 15 ALTITUDE = 45
*WIDTH = 6.00 *HEIGHT = 4.00
* BEFORE FORESHORTENING 14/09/81

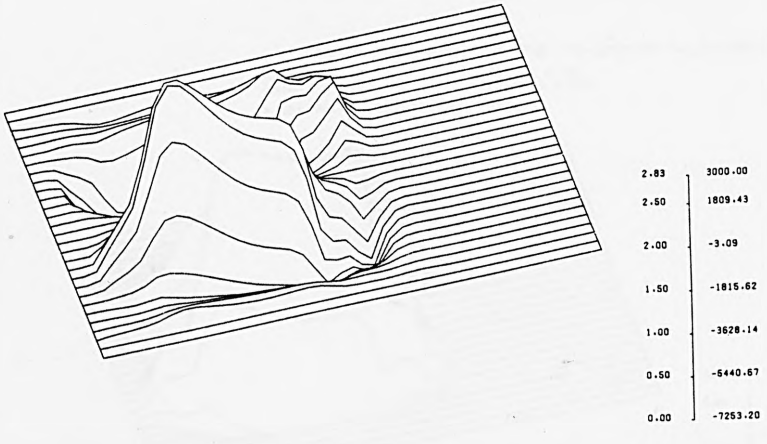

Z-COMP.OF FORCE DENSITY OF THE LIM-3DHMA.AT S=.3.I=5A.F=350.0
AZIMUTH = 15 ALTITUDE = 45
*WIDTH = 6.00 *HEIGHT = 4.00
* BEFORE FORESHORTENING 14/09/81

Fig. 7.51. Force density distribution of 3DHM model at f = 350 Hz and S = 0.3

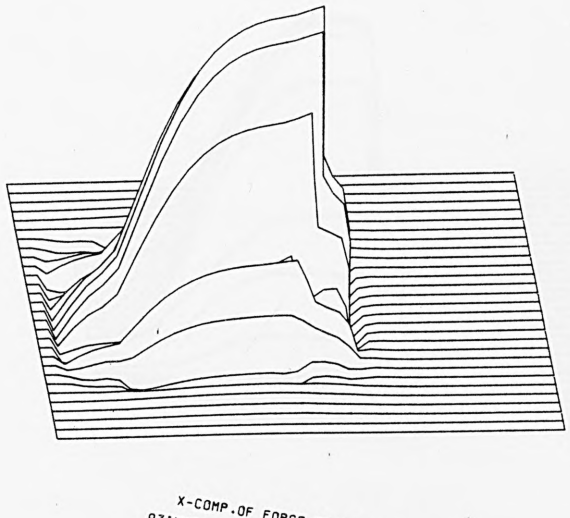

X-COMP.OF FORCE DENSITY OF THE LIM-3DCMA,AT S=.3,I=5A,F=150.0
AZIMUTH = 15 ALTITUDE = 45
*WIDTH = 6.00 *HEIGHT = 4.00
* BEFORE FORESHORTENING 18/09/81

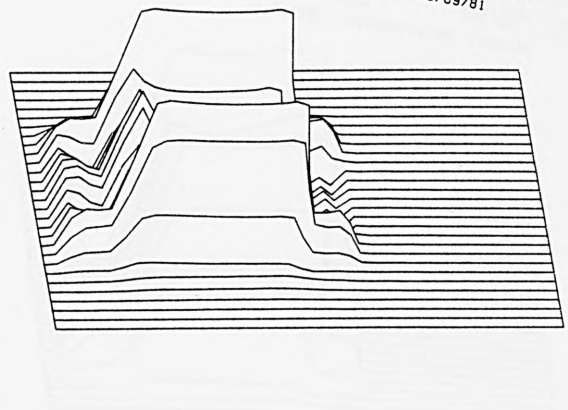

Y-COMP.OF FORCE DENSITY OF THE LIM-3DCMA,AT S=.3,I=5A,F=150.0
AZIMUTH = 15 ALTITUDE = 45
*WIDTH = 6.00 *HEIGHT = 4.00
* BEFORE FORESHORTENING 18/09/81

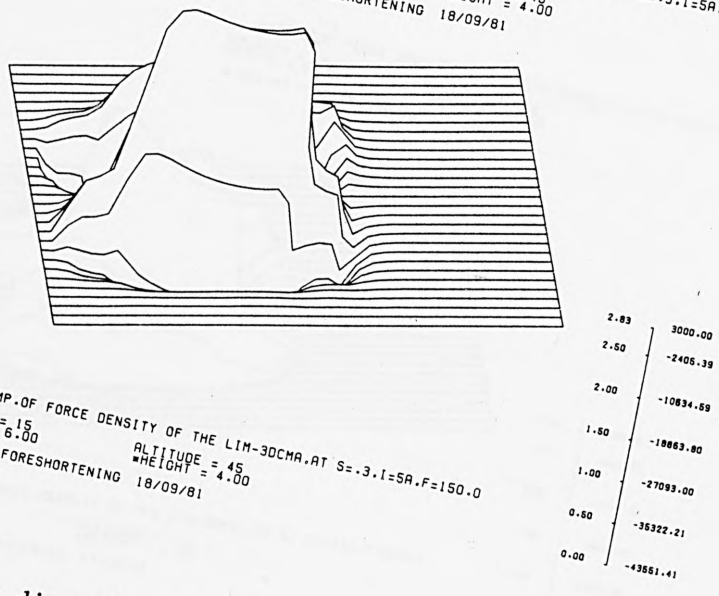

Z-COMP.OF FORCE DENSITY OF THE LIM-3DCMA,AT S=.3,I=5A,F=150.0
AZIMUTH = 15 ALTITUDE = 45
*WIDTH = 6.00 *HEIGHT = 4.00
* BEFORE FORESHORTENING 18/09/81

Fig. 7.52. Force density distribution of 3DCM model at f = 150 Hz and S = 0.3

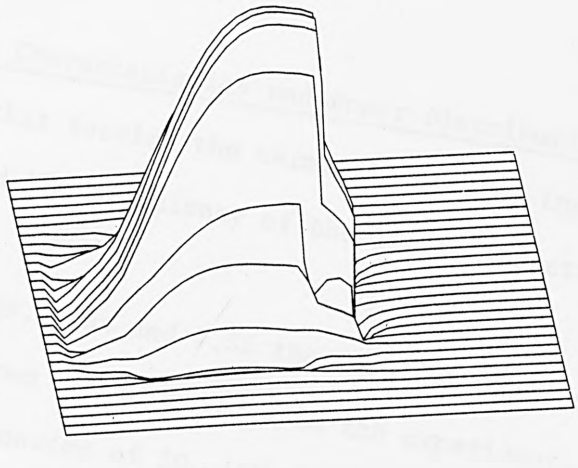

X-COMP.OF FORCE DENSITY OF THE LIM-3DCMA.AT S=.3.I=5A.F=350.0
AZIMUTH = 15 ALTITUDE = 45
■WIDTH = 6.00 ■HEIGHT = 4.00
■ BEFORE FORESHORTENING 17/09/81

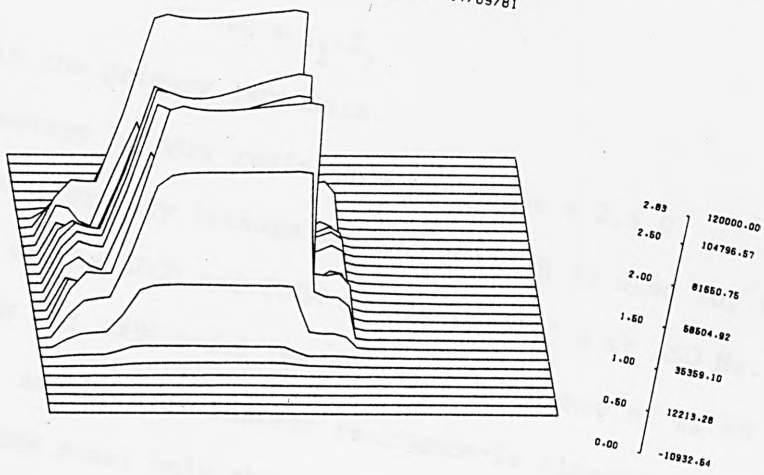

Y-COMP.OF FORCE DENSITY OF THE LIM-3DCMA.AT S=.3.I=5A.F=350.0
AZIMUTH = 15 ALTITUDE = 45
■WIDTH = 6.00 ■HEIGHT = 4.00
■ BEFORE FORESHORTENING 17/09/81

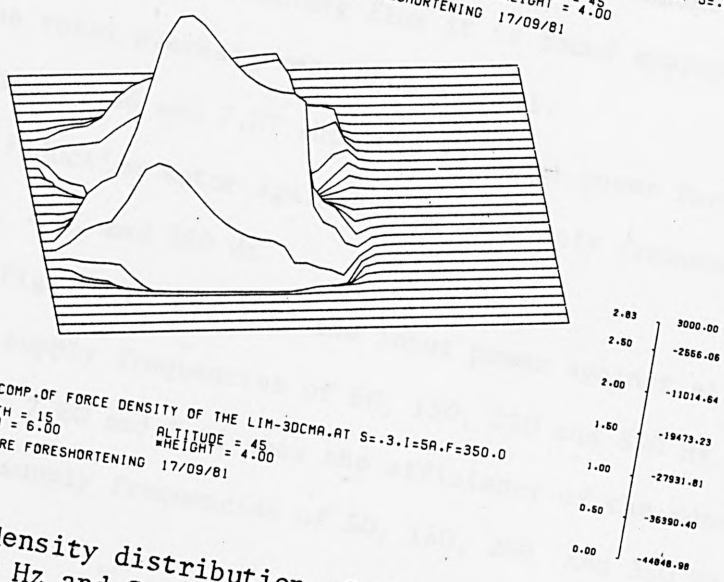

Z-COMP.OF FORCE DENSITY OF THE LIM-3DCMA.AT S=.3.I=5A.F=350.0
AZIMUTH = 15 ALTITUDE = 45
■WIDTH = 6.00 ■HEIGHT = 4.00
■ BEFORE FORESHORTENING 17/09/81

Fig. 7.53. Force density distribution of 3DCM model at f = 350 Hz and S = 0.3

7.4 Terminal Characteristics and Power Distribution

In this section the terminal voltage, input power, power factor and the efficiency of the linear induction motor are presented.

In Figs. 7.54 and 7.55 the terminal phase voltage against slip are shown and compared with the experimental results at supply frequencies of 50, 150, 250 and 350 Hz.

The terminal voltage is obtained by using the conventional formula:

$$V = -E + I_1 \cdot Z_1$$

where Z_1 is the primary impedance.

The average primary resistance per phase = 2.4 Ω

The total primary leakage reactance which is used for the calculation of the 3DCM and 2DCM models is 31.2 Ω at 350 Hz.

For 3DHM and 2DHM model the overhang reactance of 21.5Ω only is used, as the slot leakage reactance is already considered. However for 3DHM model only the primary resistance should be considered as stated in section 4.2.4, but because of the under-estimation for the overhang flux it is found appropriate to add the total overhang reactance as well.

Figs. 7.56 and 7.57 show the terminal power factor of the linear induction motor against slip at supply frequencies of 50, 150, 250, and 350 Hz.

In Figs. 7.58 and 7.59 the input power against slip is shown at supply frequencies of 50, 150, 250 and 350 Hz.

Figs. 7.60 and 7.61 show the efficiency of the motor against slip at supply frequencies of 50, 150, 250 and 350 Hz.

In Figs. 7.62 to 7.65 the active and reactive power cross air gap distributions are shown in three dimensional plot using 3DHM and 3DCM models at a slip of 0.3 and supply frequencies of 150 and 350 Hz. These plots are presented here to show the form in which the airgap-cross powers may take.

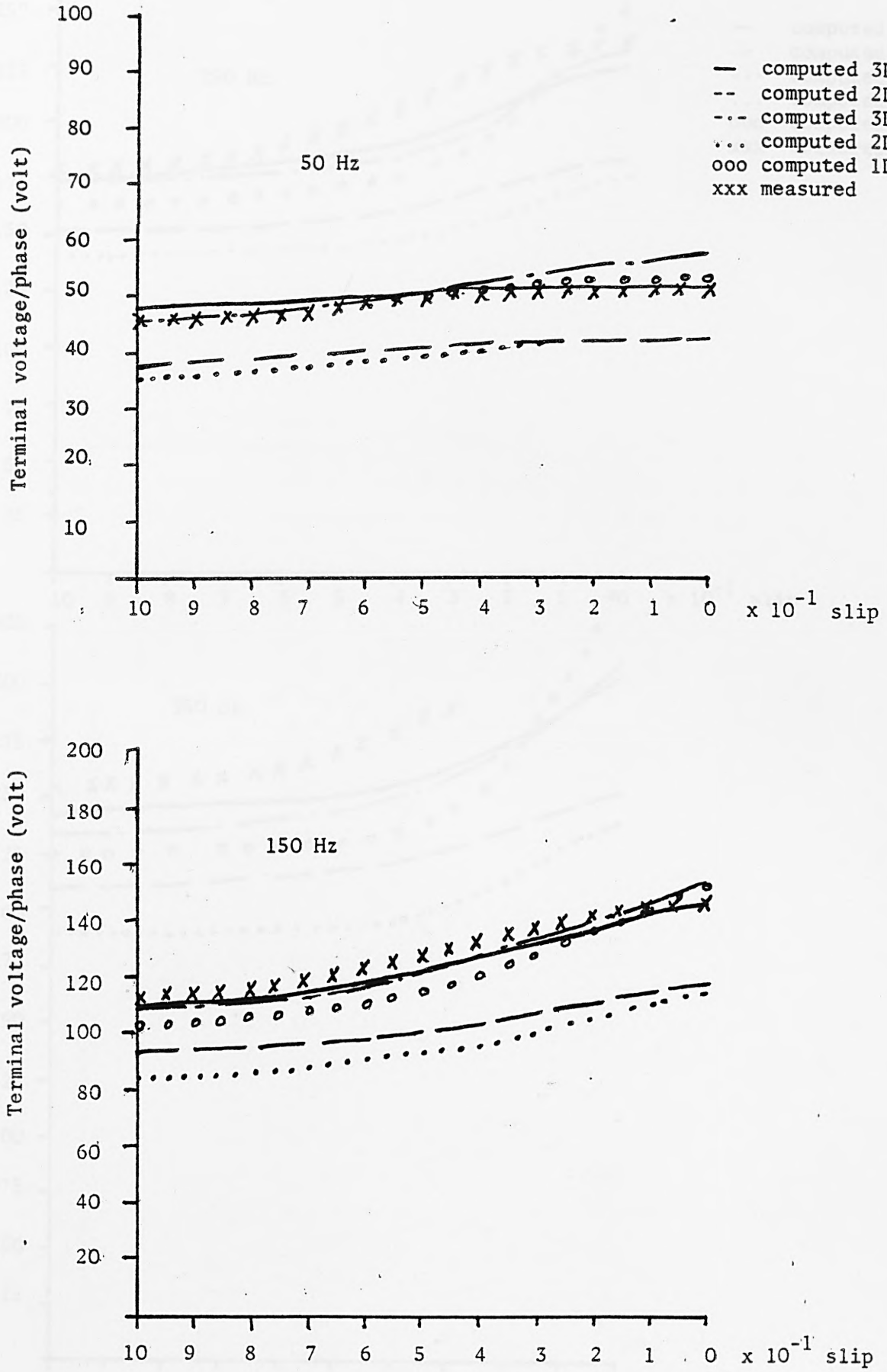

Fig. 7.54. Terminal voltage/phase against slip

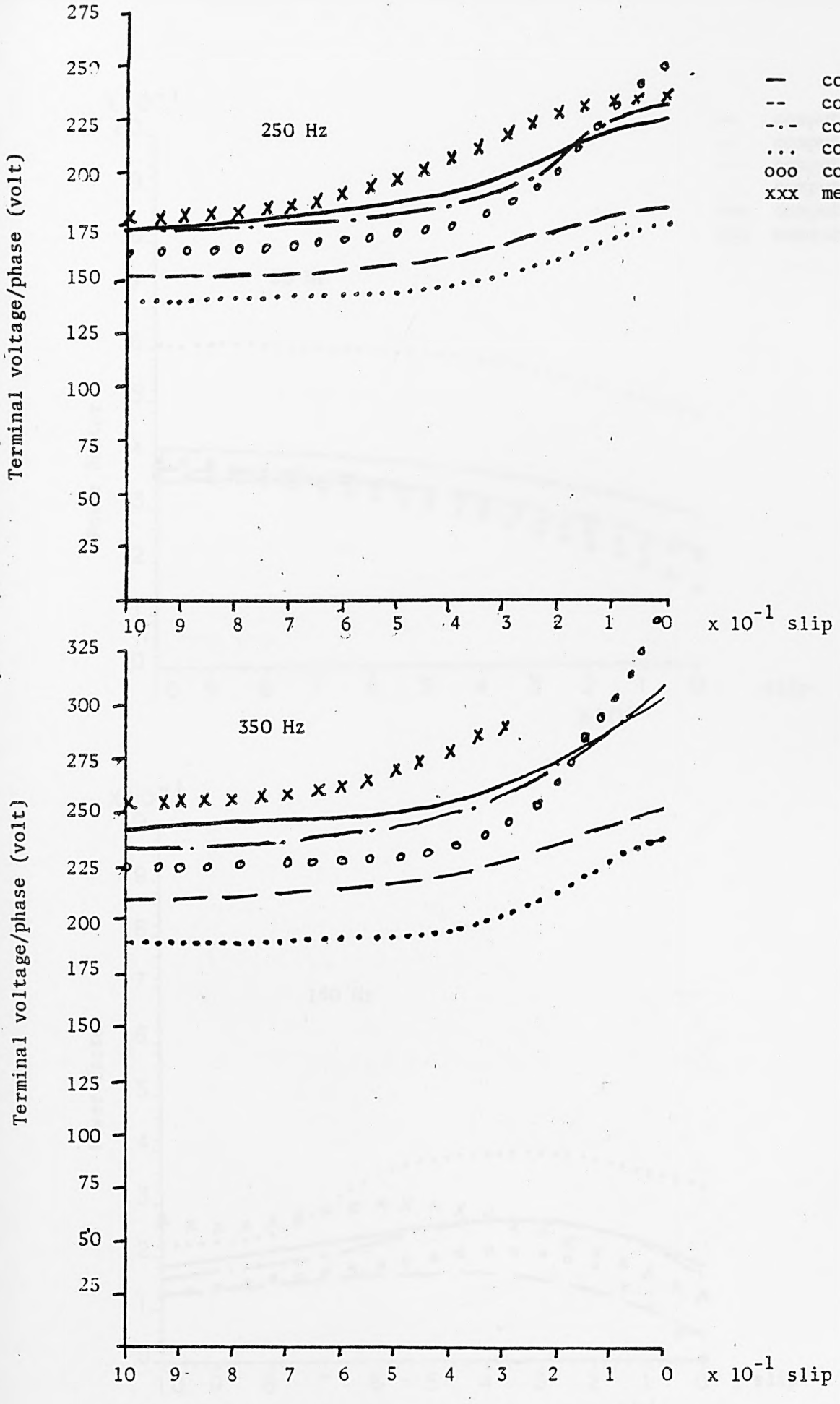

Fig. 7.55. Terminal voltage/phase against slip

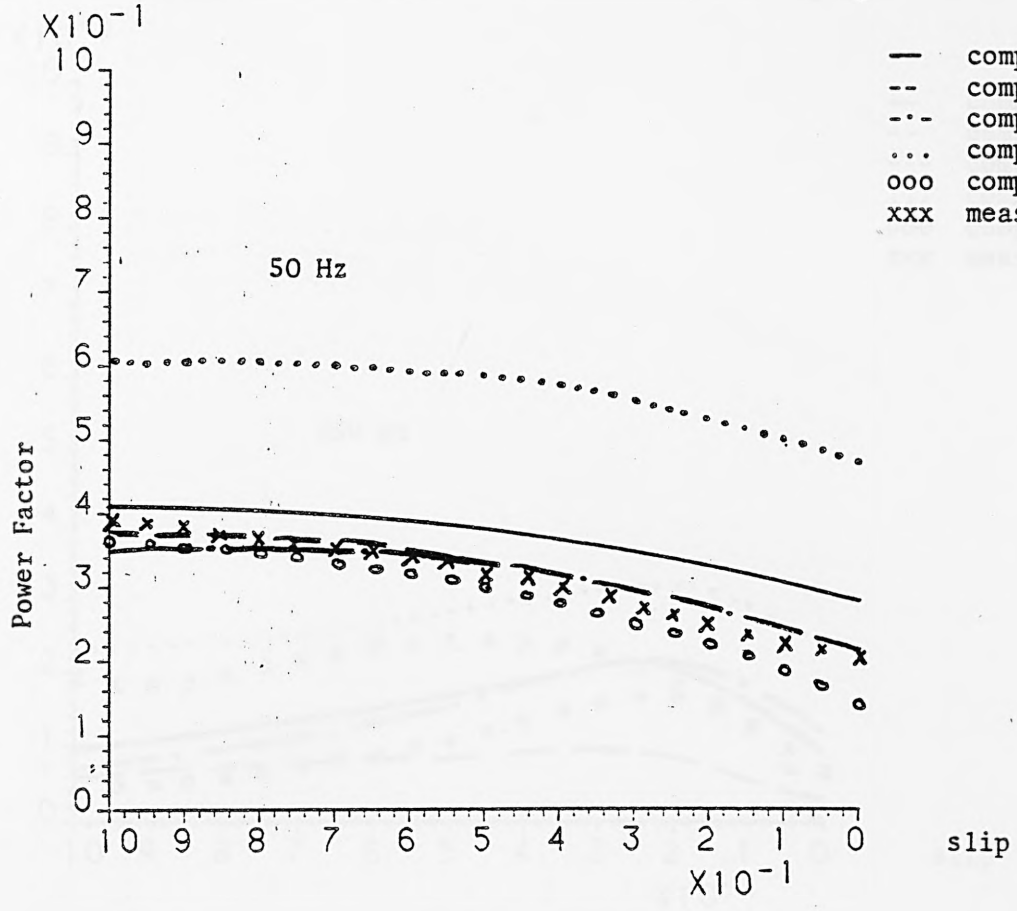

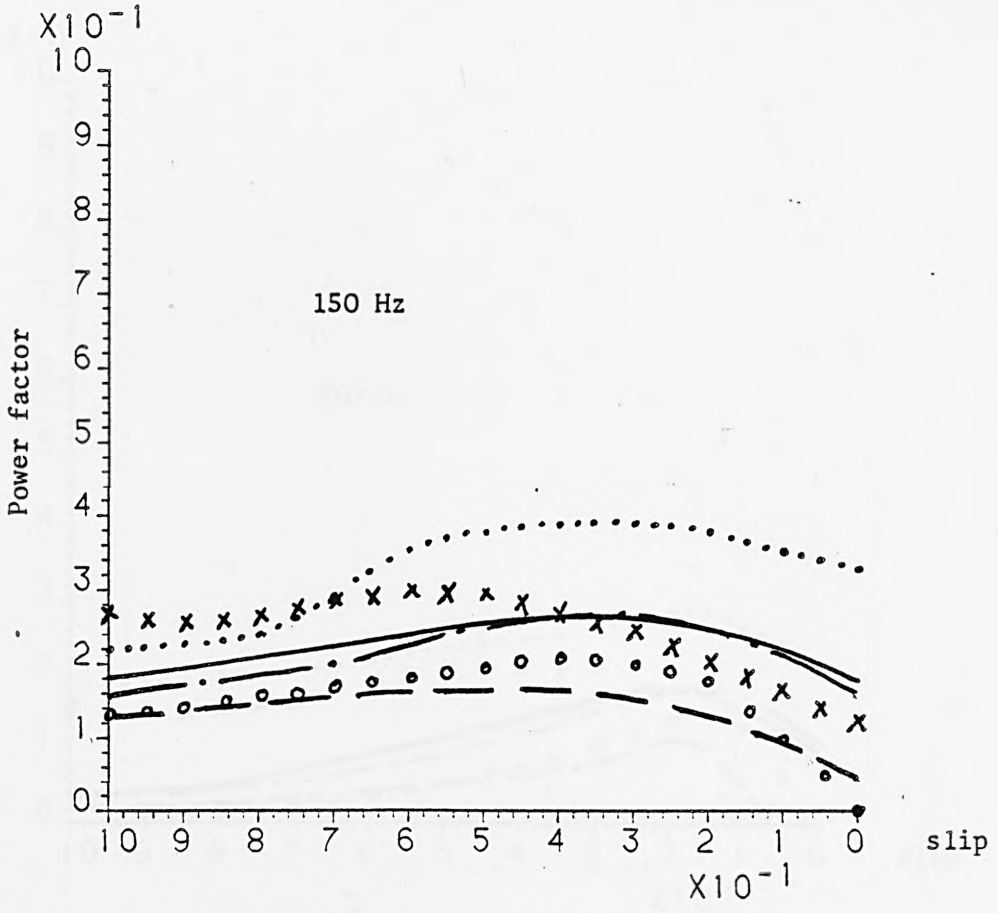

Fig. 7.56. Power factor against slip

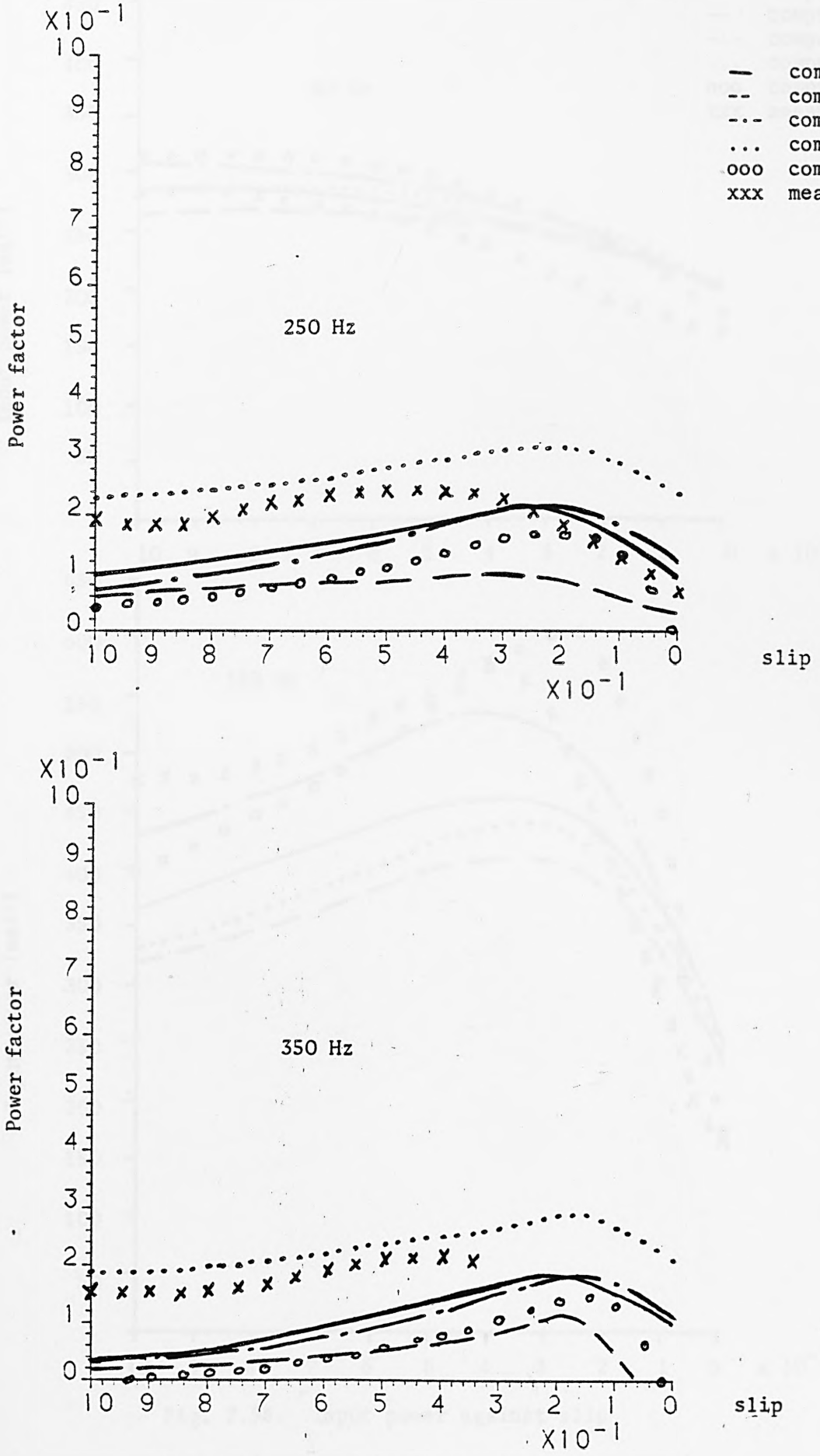

Fig. 7.57. Power-factor against slip

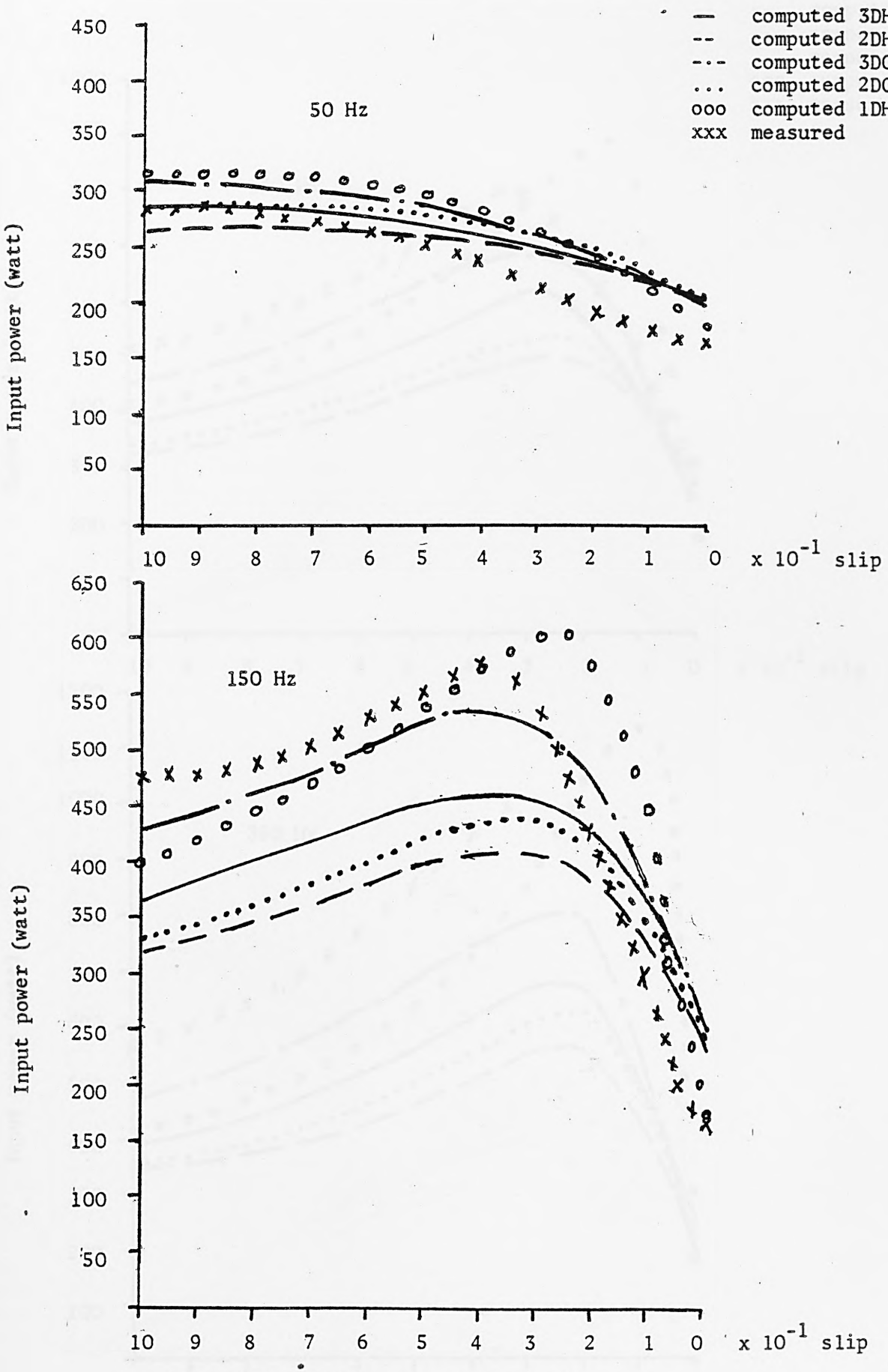

Fig. 7.58. Input power against slip

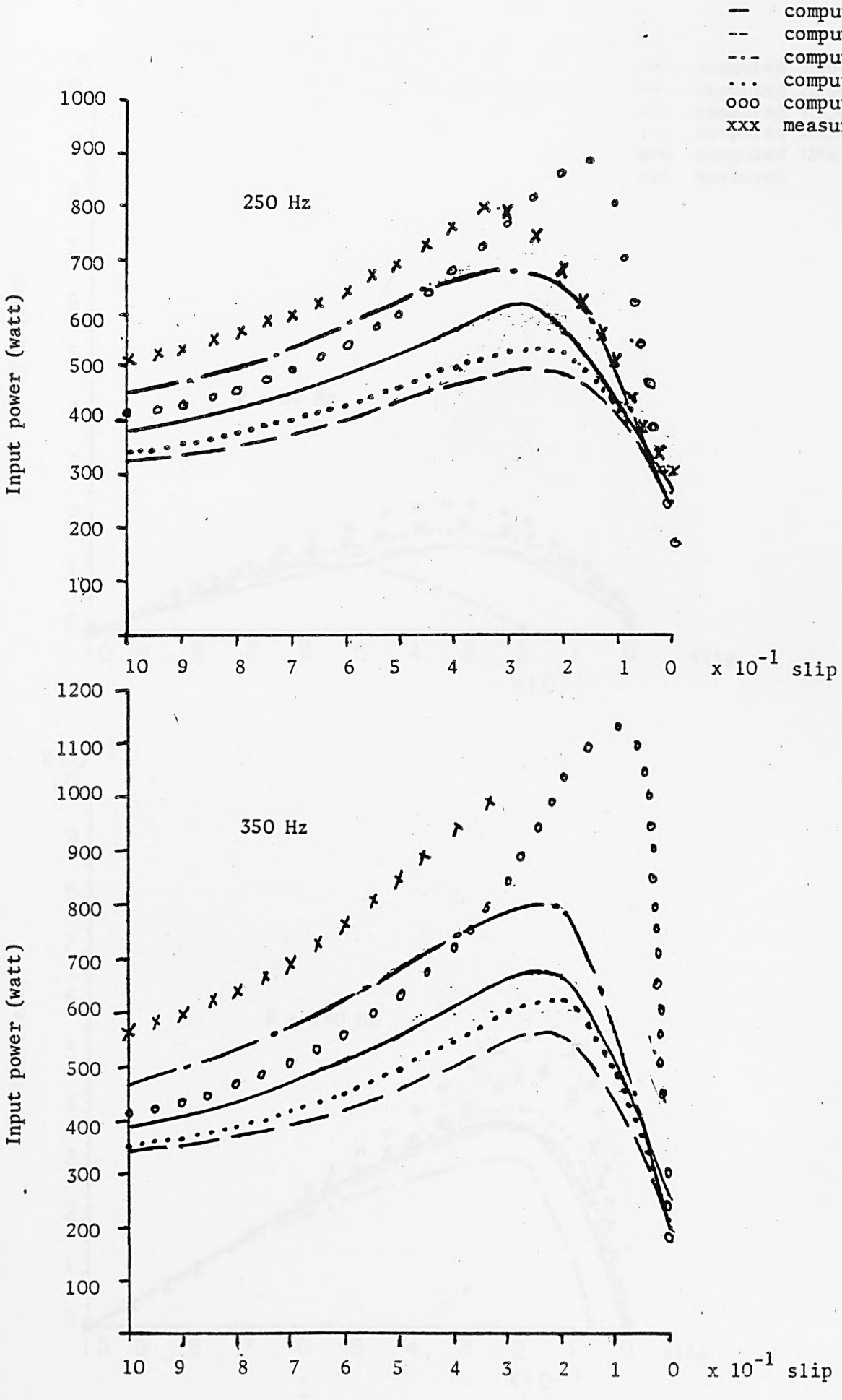

Fig. 7.59. Input power against slip

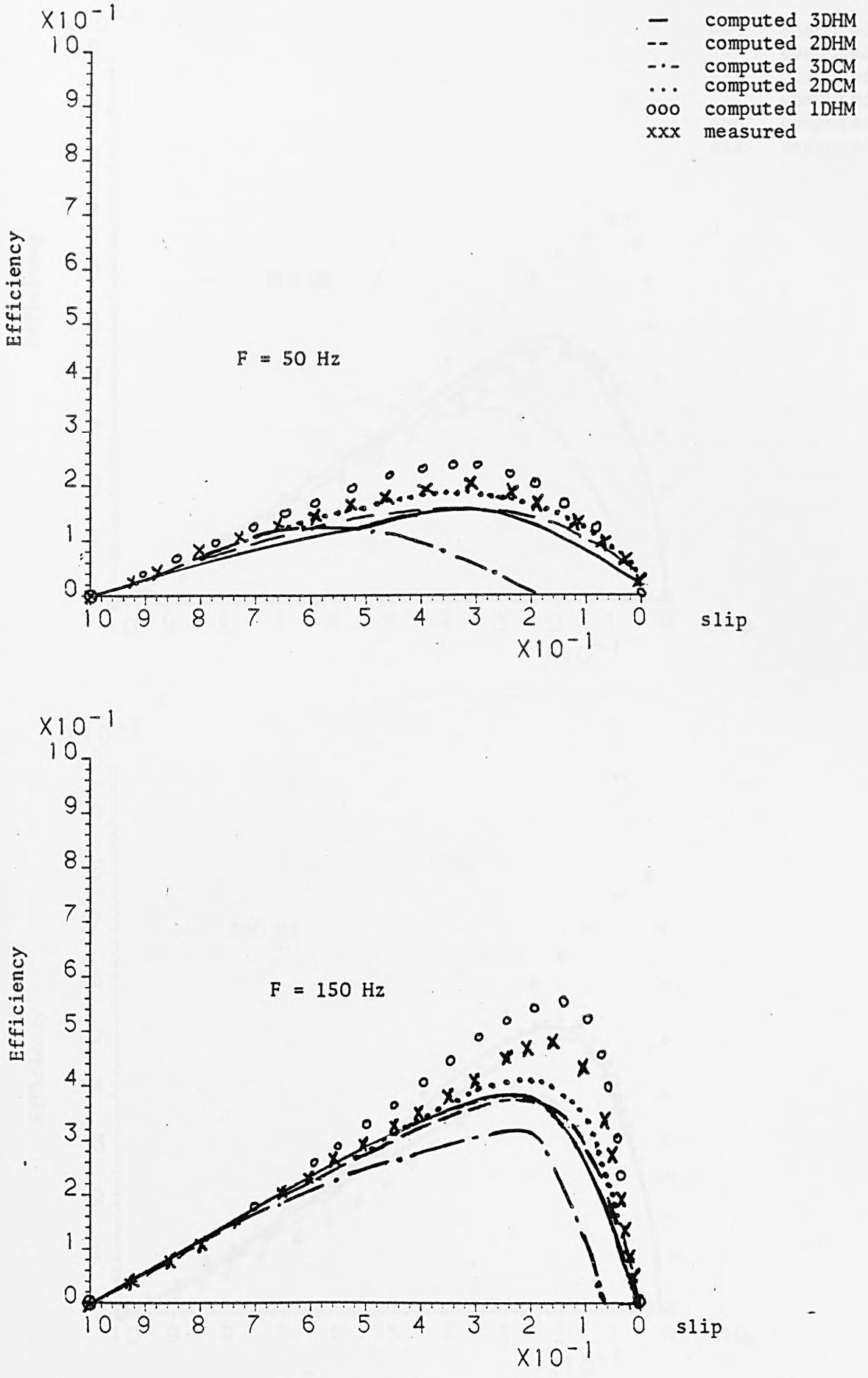

Fig. 7.60. Efficiency against slip

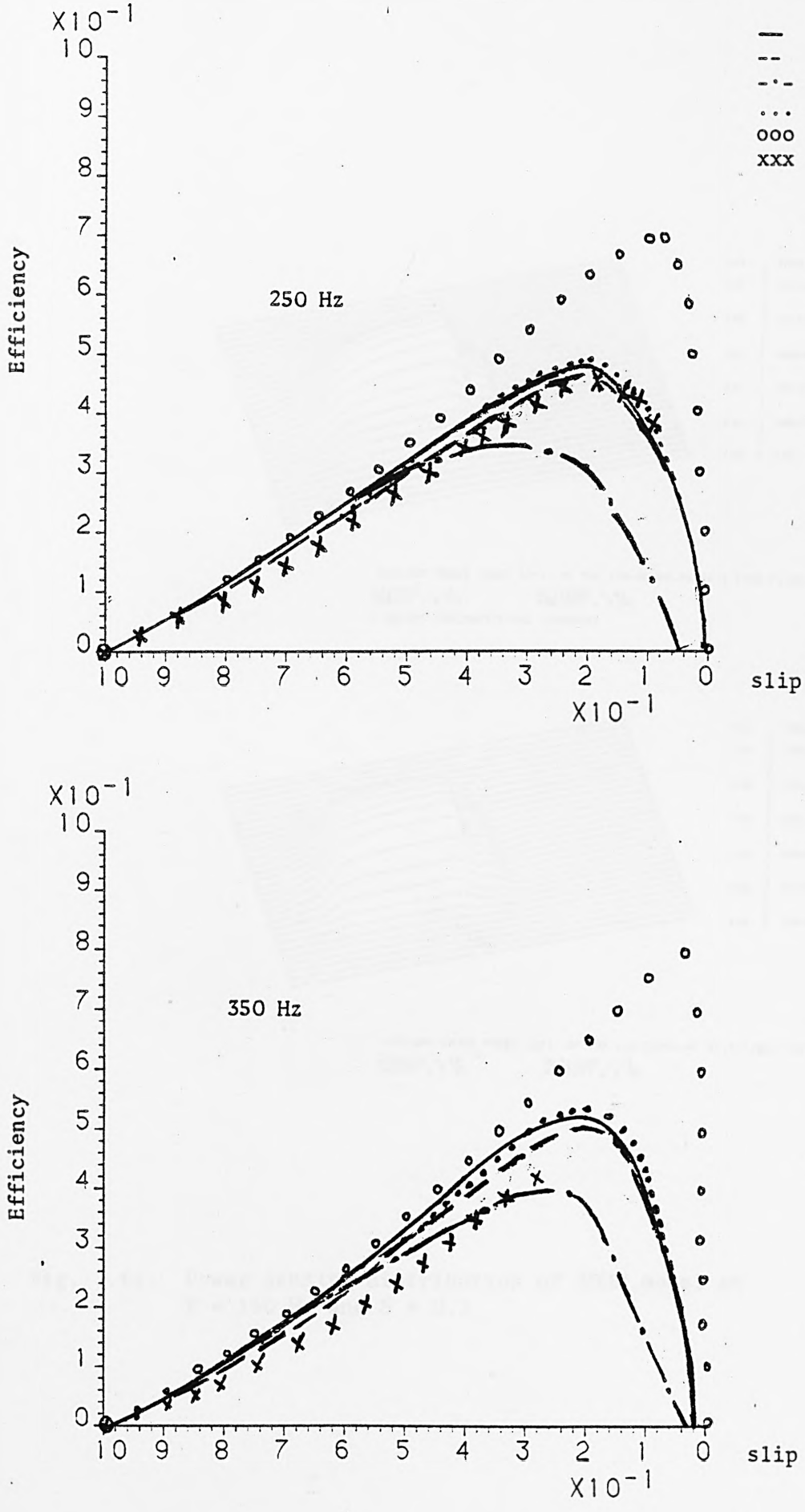

Fig. 7.61. Efficiency against slip

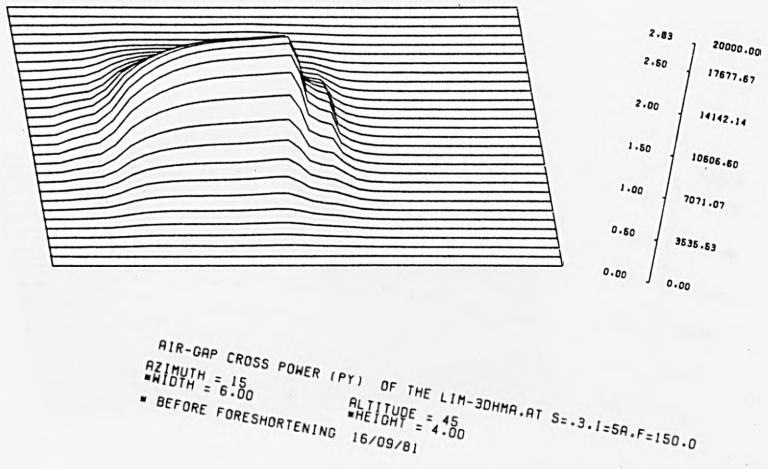

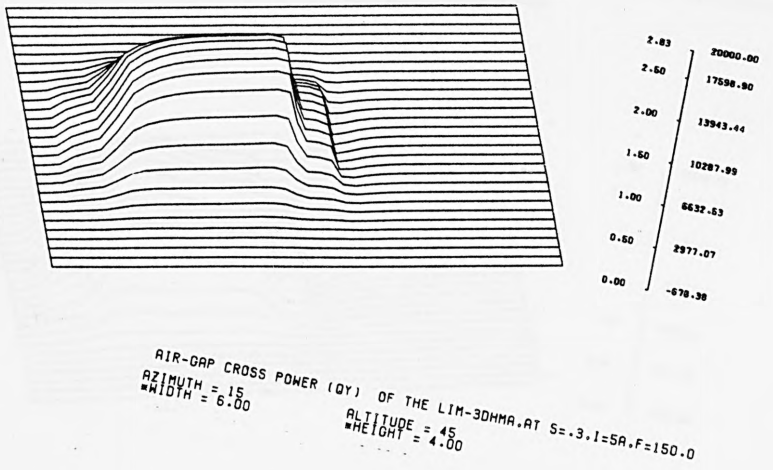

Fig. 7.62. Power density distribution of 3DHM model at f = 150 Hz and S = 0.3

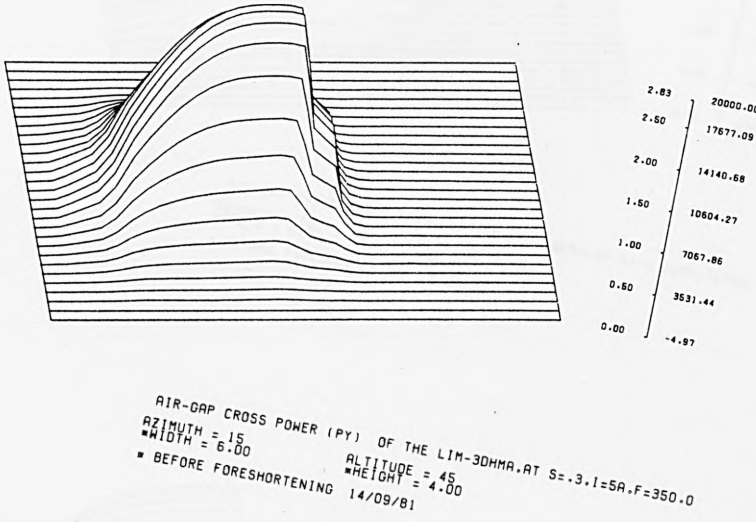

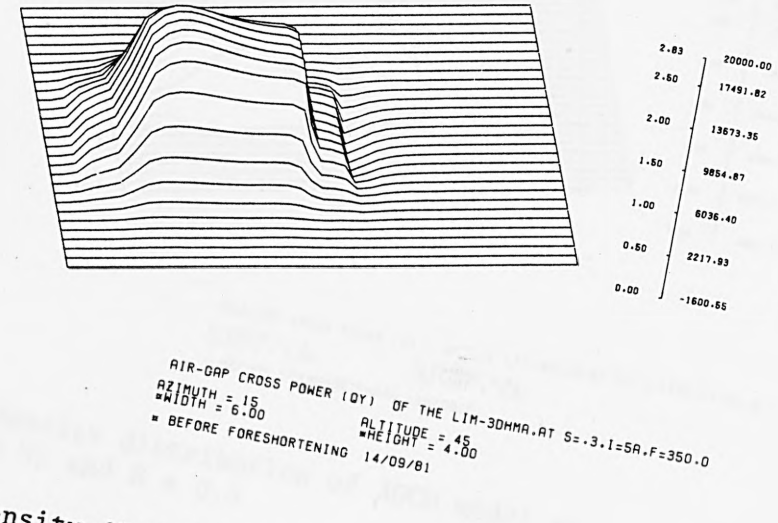

Fig. 7.63. Power density distribution of 3DHM model at f = 350 Hz and S = 0.3

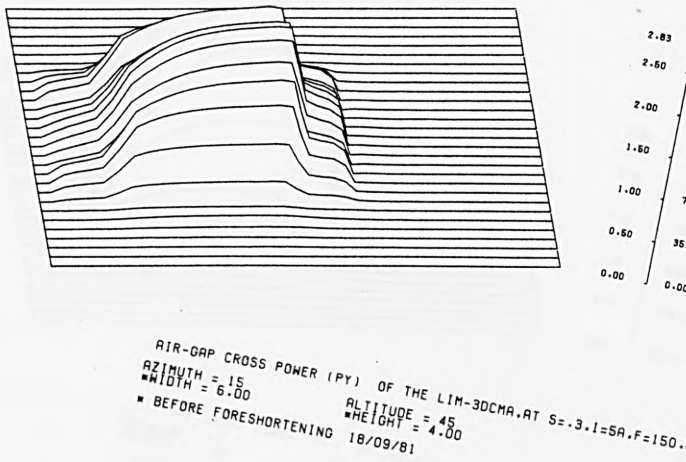

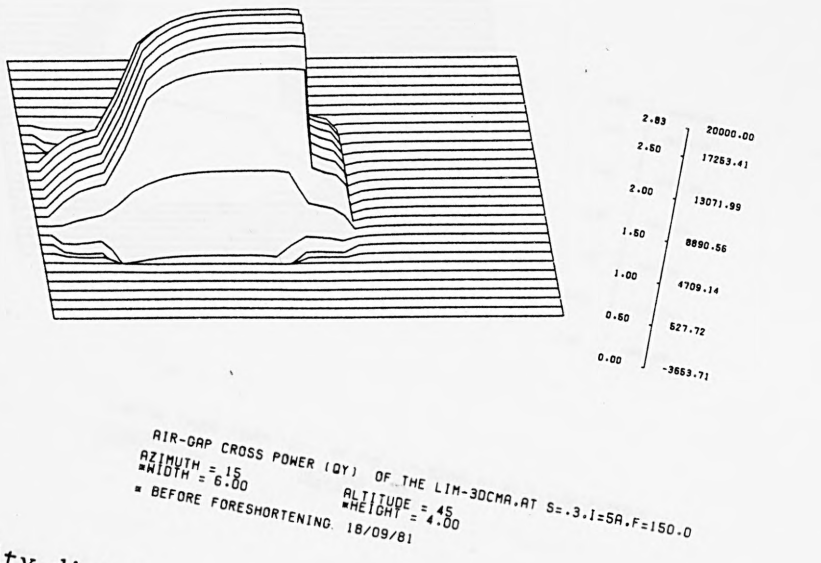

Fig. 7.64. Power density distribution of 3DCM model at f = 150 Hz and S = 0.3

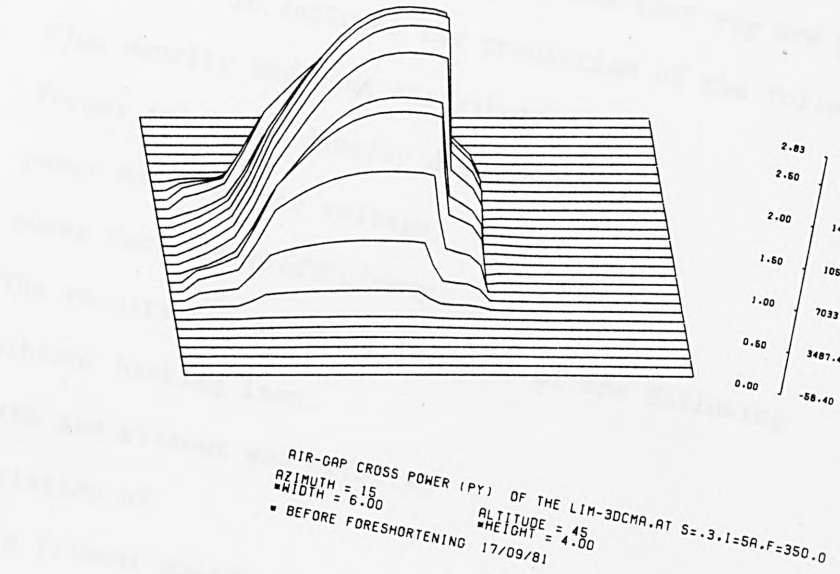

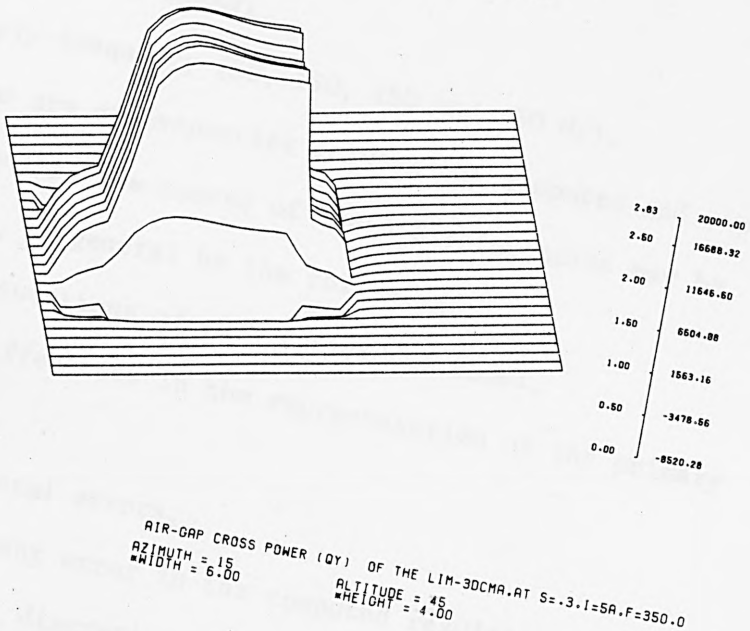

Fig. 7.65. Power density distribution of 3DCM model at f = 350 Hz and S = 0.3

7.5 Comments

In this chapter the performance characteristics which are obtained from the field approach and the test rig are presented and compared. It includes the prediction of the following:

a) flux density and flux distributions,

b) forces and force density distributions,

c) power and terminal voltage,

d) power factor and efficiency.

The results are obtained for each of the following

i) wihtout backing iron,

ii) with and without end effects,

with variation of

1) slip (linear speed),

2) supply frequency (50, 150, 250 and 350 Hz).

There are discrepancies between the computed and experimental results, the causes of these discrepancies may be summarized, in general by the following:

1) the assumptions of each individual model,

2) the differences in the representation of the primary winding,

3) experimental errors,

4) the inherent error in the computed results, namely: truncation, discretization and round-off errors.

From these results it is concluded, that the main reason for the discrepancies between the 3DCM and 3DHM is the representation of the overhang configuration. This part of primary winding is over estimated in 3DCM model by extending the stator iron to back the overhang winding. In 3DHM model better representation for the stator of the motor is made. However, the

overhang mass is assumed to be perpendicular to the lateral side of the stator core. It is found that this supposition under estimates the overhang behaviour which needs more real representation.

CHAPTER 8

COMPARISON OF THE RESULTS - WITH BACKING IRON

8.1 Introduction

In this chapter the predicted results obtained by the numerical solutions and the equivalent circuit are presented and compared with each others.

The performances of the linear motor without end effects are obtained from the one dimensional model and the equivalent circuit. The end effects are considered with different degree of accuracy in the three-and two-dimensional models and the equivalent circuit.

These models have the same specifications as the motor examined in the last chapter, except the secondary is backed by a laminated iron as wide as the secondary and a thickness equal to the stator core. The backing iron which extends as long as the secondary is considered to be of zero conductivity. Thus the forces which are developed in these models are due to the secondary conductor only. However in these models attraction forces are created due to the existance of the backing iron which oppose the repulsion forces due to the secondary conductor.

The results of these models are displayed in the same order as in the last chapter to ease the comparison of the performance for both motors.

The performances of the linear induction motor with backing iron are presented at different supply frequencies with a constant current drive of 5A phase current (35.34 KA/m).

8.2 Flux Density and Flux Distribution

The predicted results of the airgap flux density components were obtained on a phase 3.17 mm above the stator surface. The values of the flux density along the x-direction are taken on the line passing through the centre of the machine along its length. The values of the flux density along the z-direction are taken on the line passing through the centre of the machine along its width.

Figs. 8.1 and 8.2 show the x and y components of the flux density along the z axis for frequency = 150 and 350 Hz at stand still.

Figs. 8.3 and 8.4 show the x and y components of the flux density along the x axis for frequency = 150 and 350 Hz at stand still.

Figs. 8.5 and 8.6 show the z components of the flux density along the z axis for supply frequencies of 50, 150, 250 and 350 Hz.

Figs. 8.7 to 8.10 show the x and y components of the flux density along the z and x axis at a slip of 0.2 and at supply frequencies of 150 and 350 Hz.

Using the three dimensional model 3DHM, the flux density components for different slips and frequencies were plotted along the z and x axis as shown in Figs. 8.11 tp 8.14.

In Figs. 8.15 to 8.18 the contours of the flux on a plane along the machine passing through its centre are presented. These were obtained by the two dimensional models 2DHM and 2DCM for supply frequencies of 150 and 350 Hz at different slips.

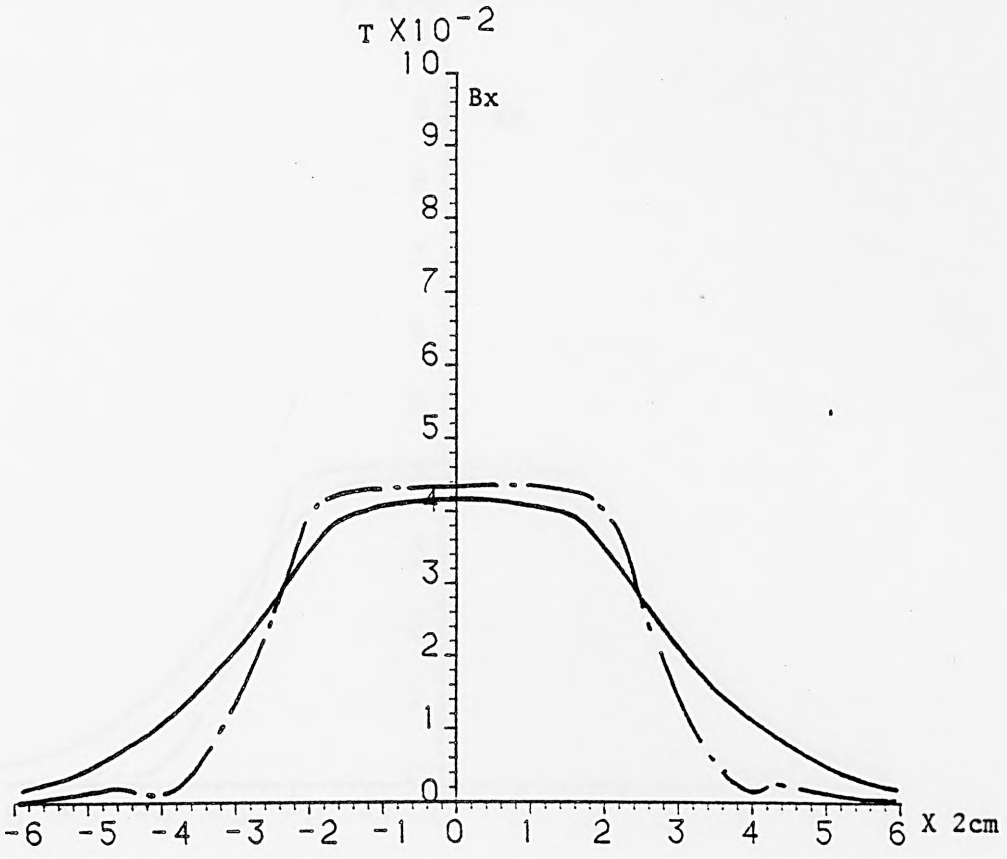

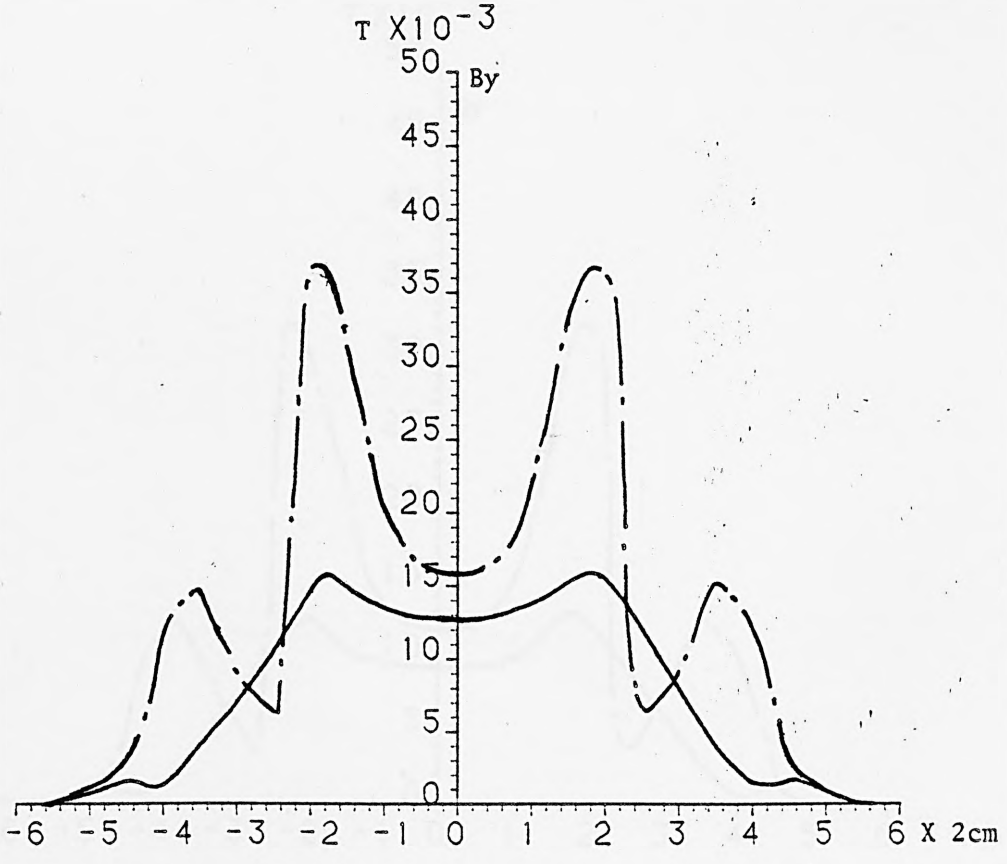

Fig. 8.1. Airgap Flux Density components along the z-direction at I = 5A, g = 9.5 mm, F = 150 Hz, S = 1.0

—3DHM, -·- 3DCM

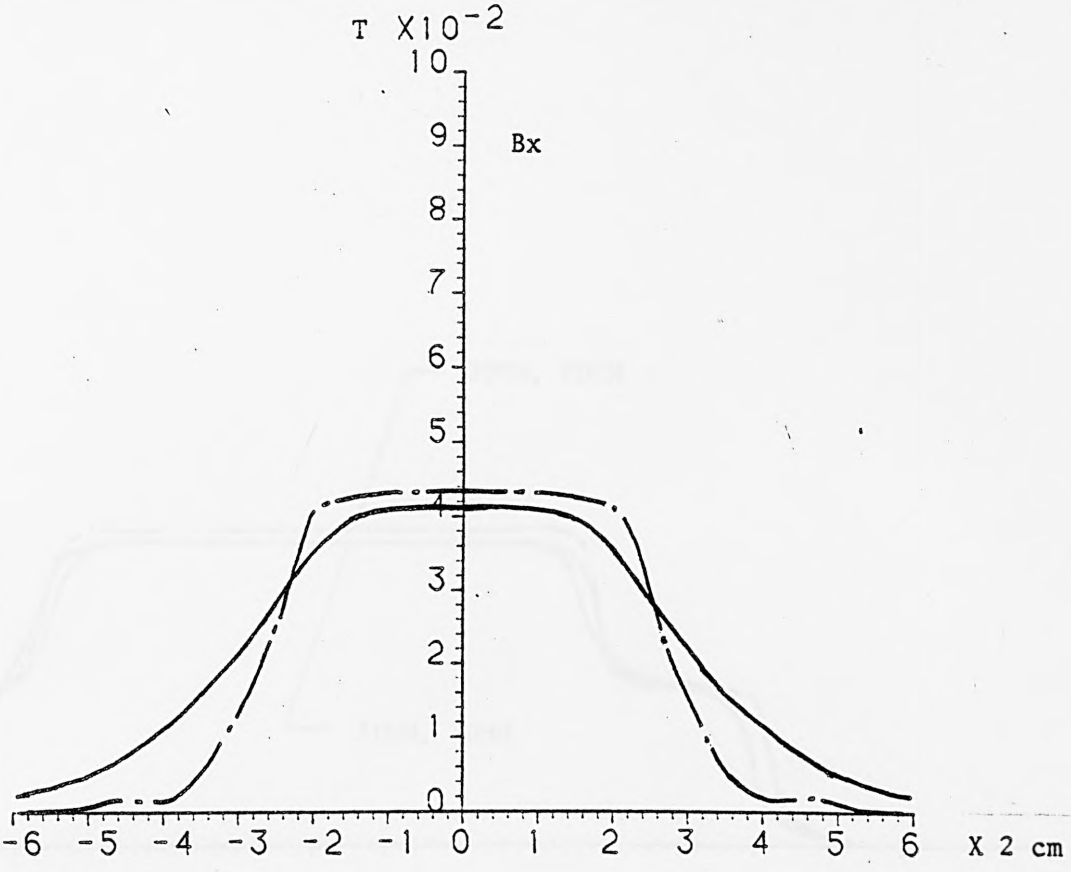

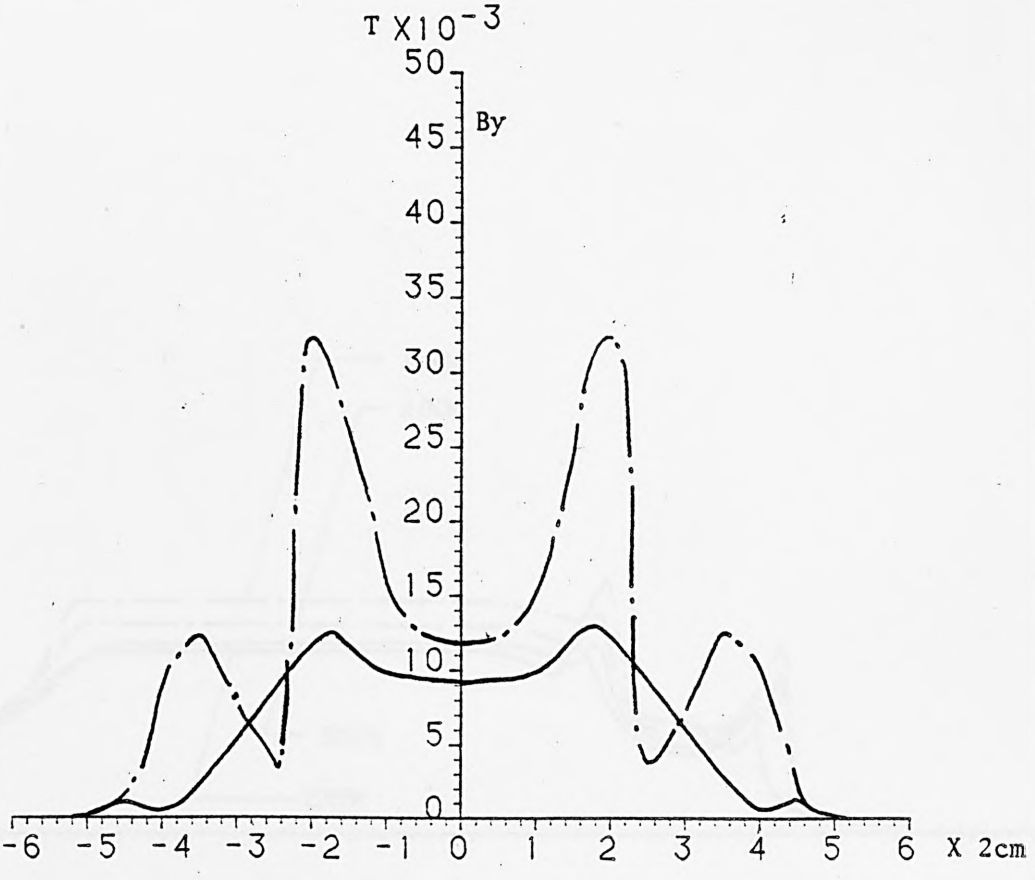

Fig. 8.2. Airgap Flux Density Components along the z-direction at I = 5A, g = 9.5 mm, F = 350 Hz, S = 1.0

—3DHM, -·- 3DCM

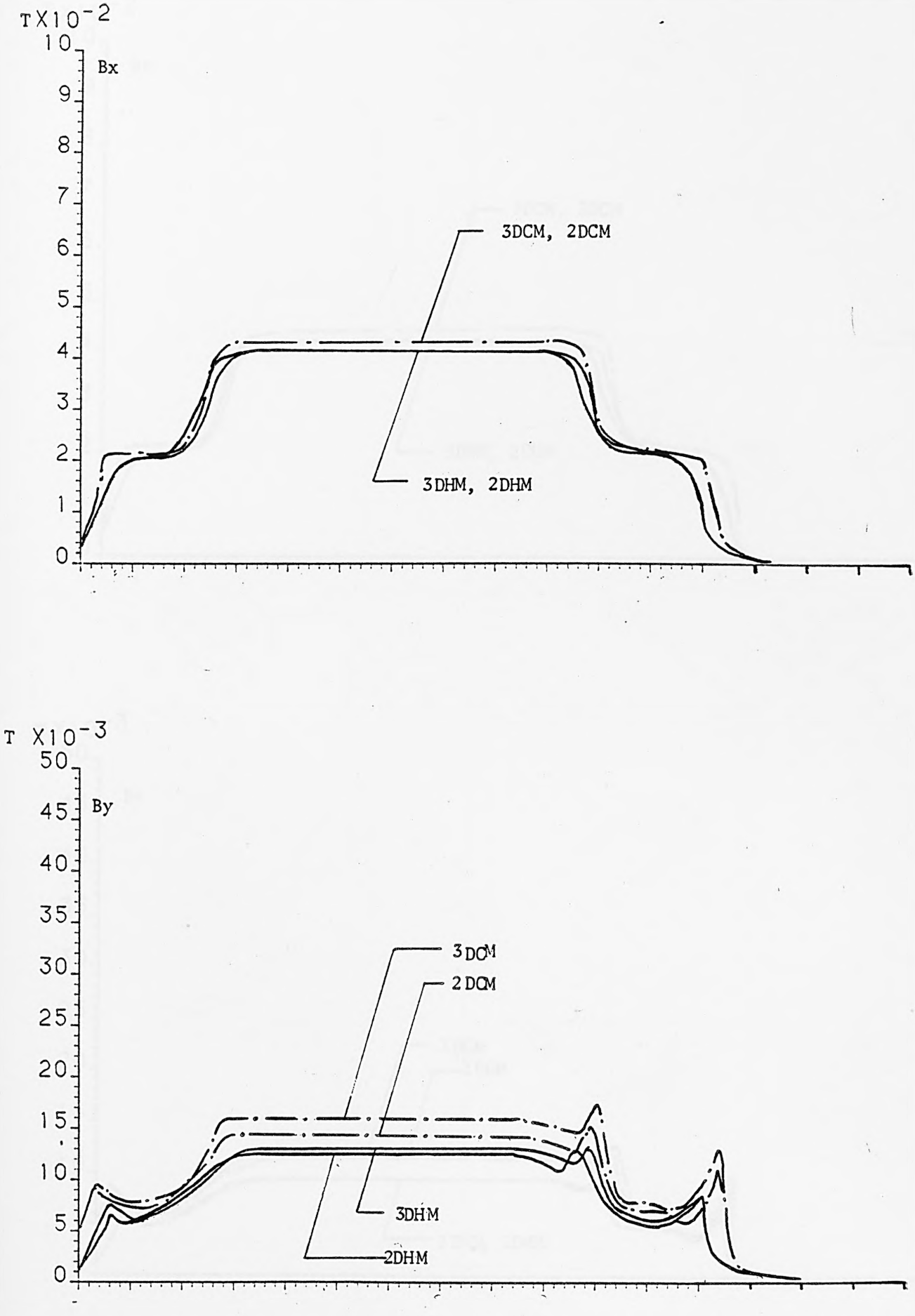

Fig. 8.3. Airgap Flux Density conponents along the x-direction at I = 5A, g = 9.5 mm, F = 150 Hz, S = 1.0

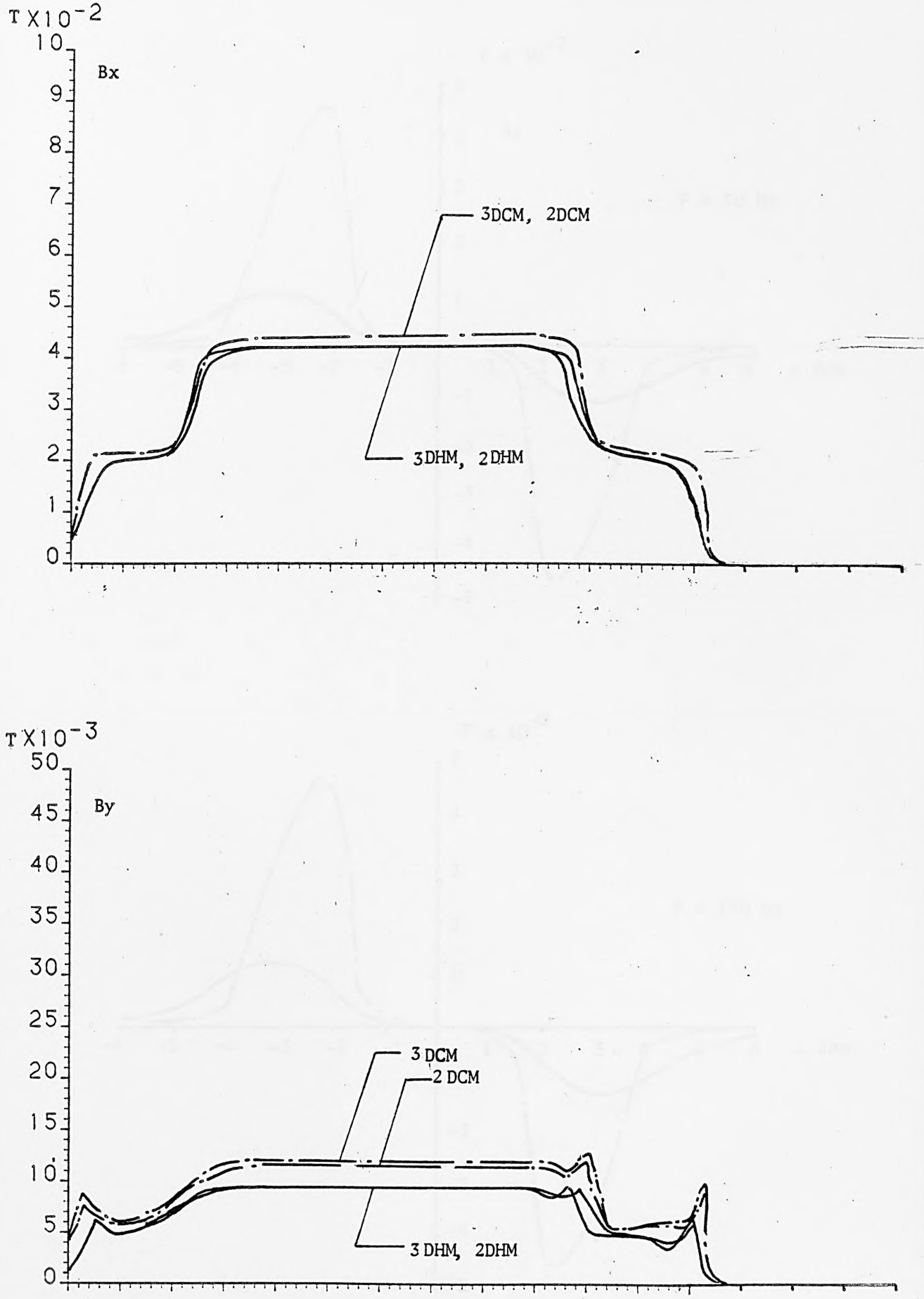

Fig. 8. 4. Airgap Flux Density components along the x-direction at I = 5A, g = 9.5 mm, F = 350 Hz, S = 1.0

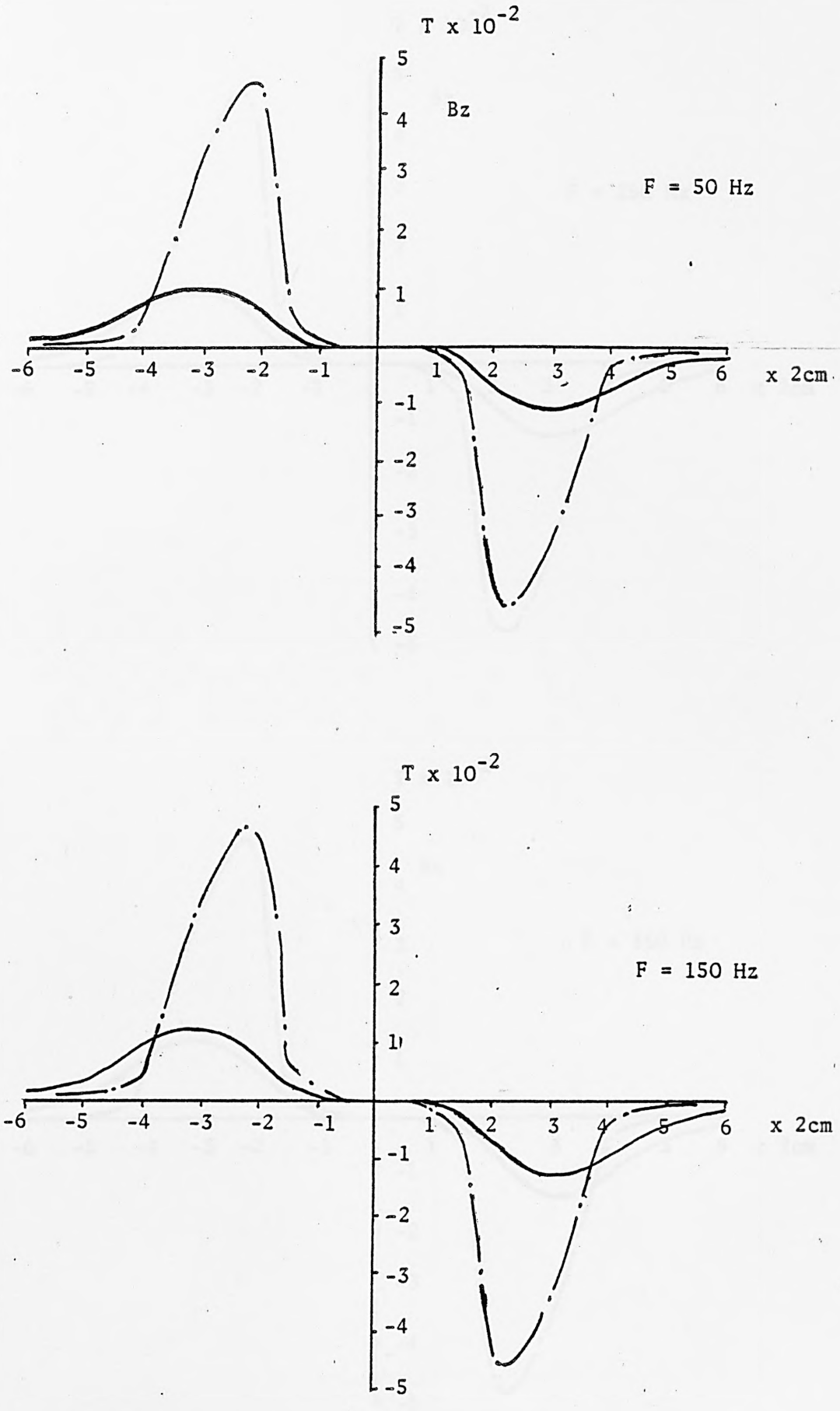

Fig. 8.5. Z-component of Airgap Flux Density along the z-direction at stand still, I = 5A, g = 9.5 mm

- 3DHM, --- 3DCM

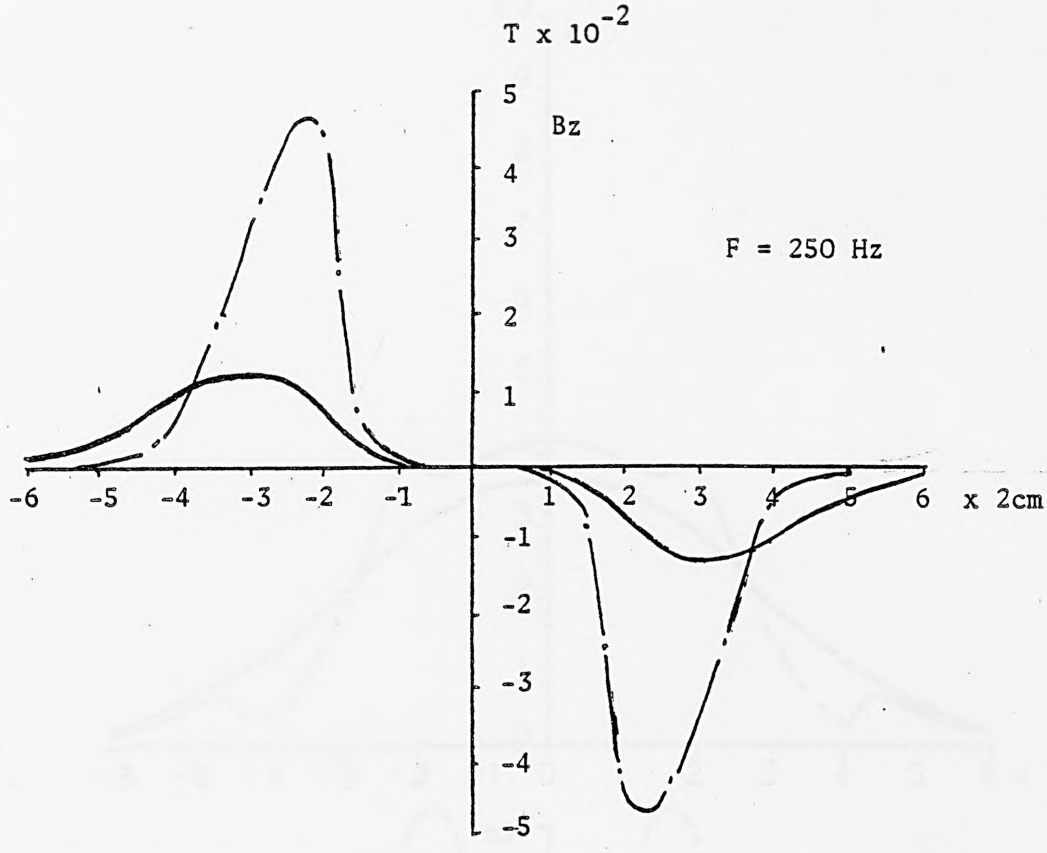

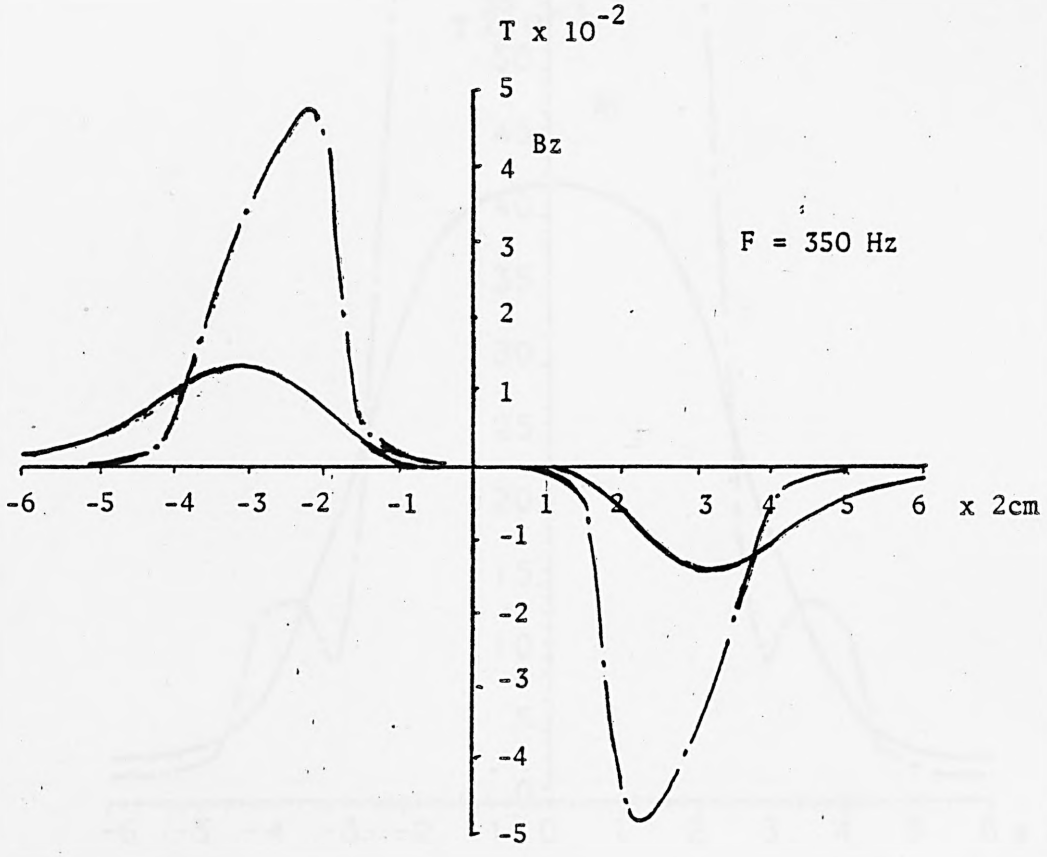

Fig. 8.6. Z-component of Airgap Flux Density along the z-direction at stand still, I = 5A, g = 9.5 mm

- 3DHM, --- 3DCM

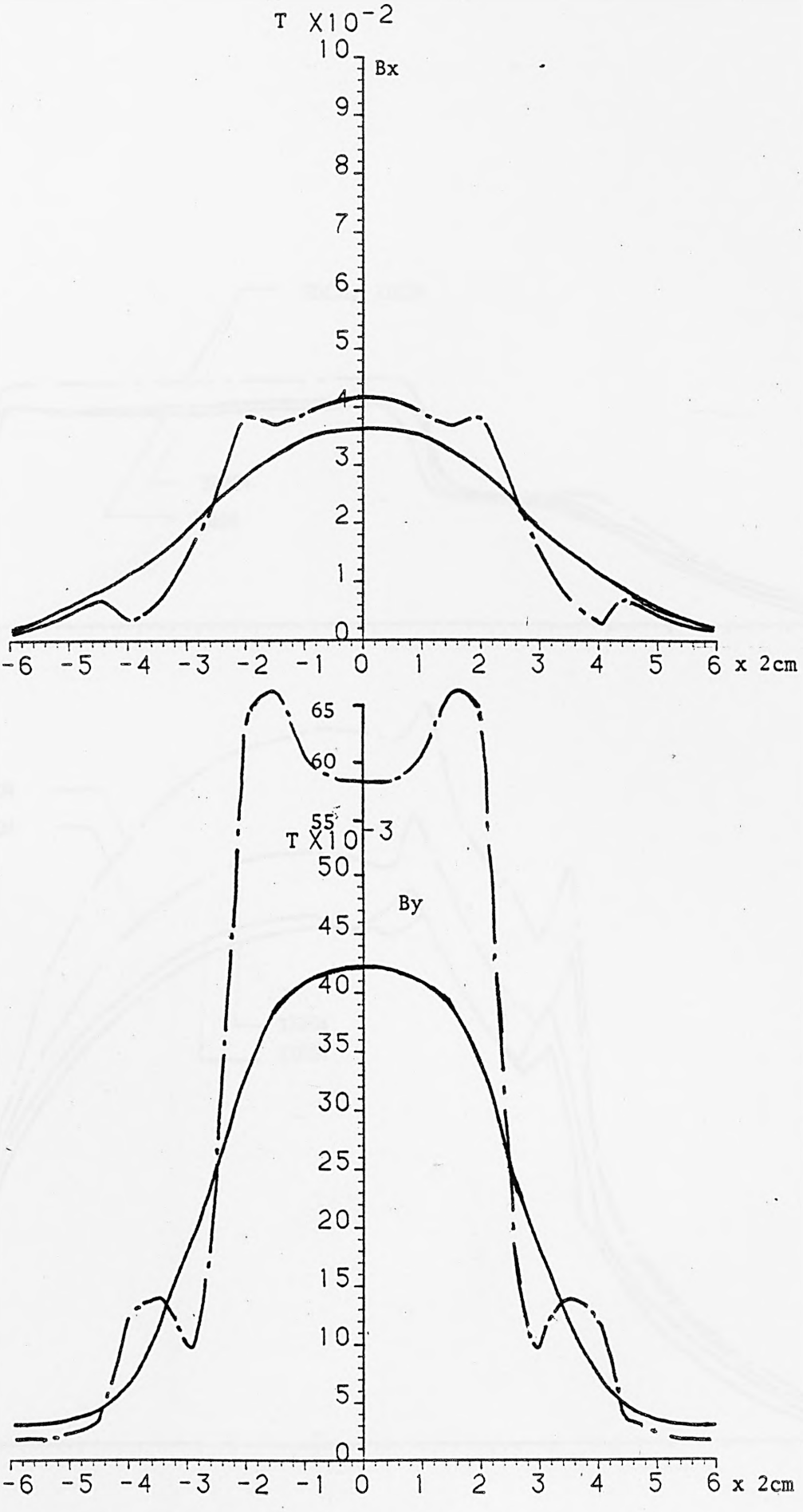

Fig. 8.7. Airgap Flux Density Component along the z-direction at I = 5A, g = 9.5 mm, f = 150 Hz, S = 0.2

—3DHM, -·- 3DCM

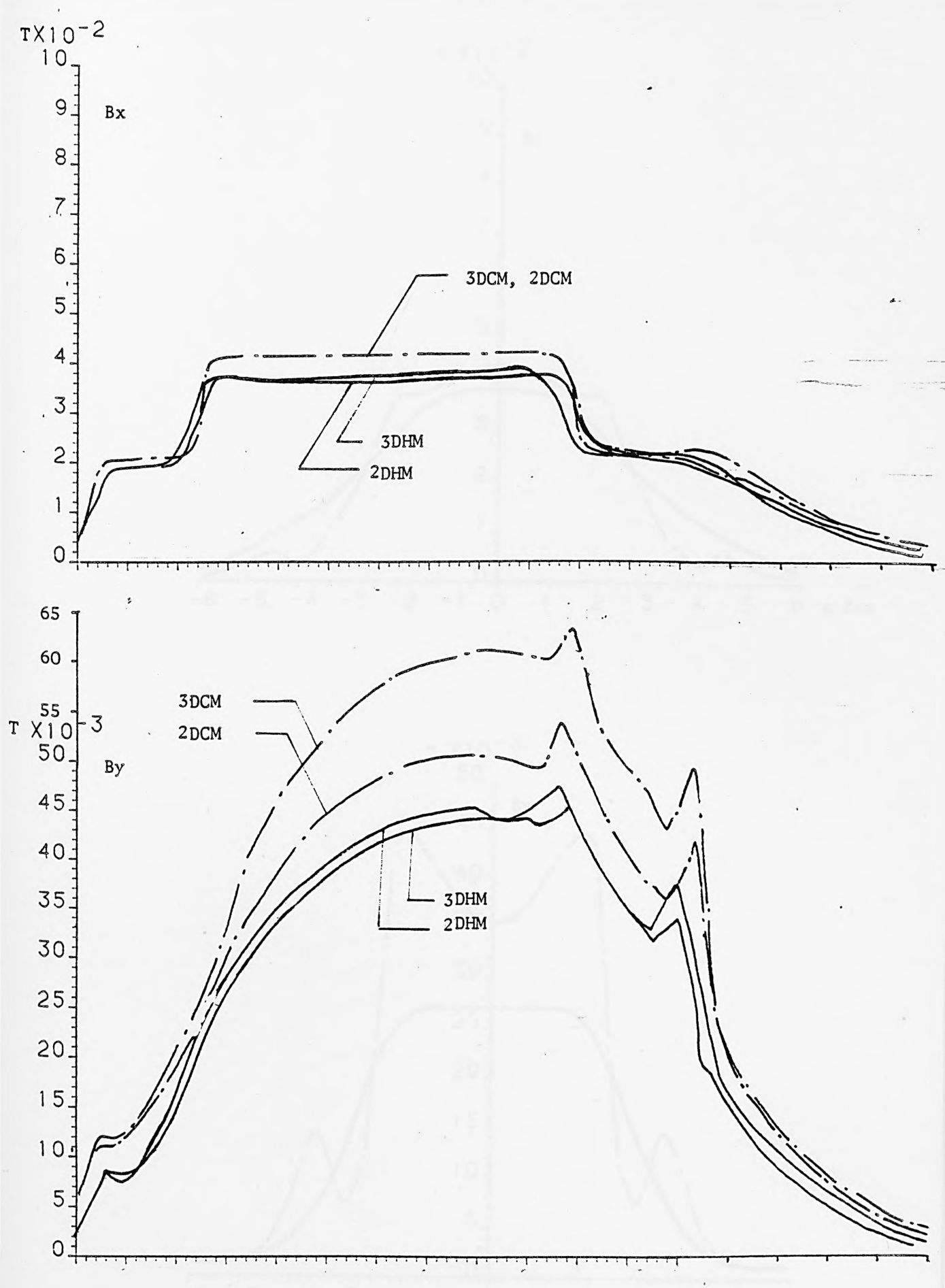

Fig. 8.8 . Airgap Flux Density Components along the x-direction at I = 5A, g = 9.5 mm, f = 150 Hz, S = 0.2

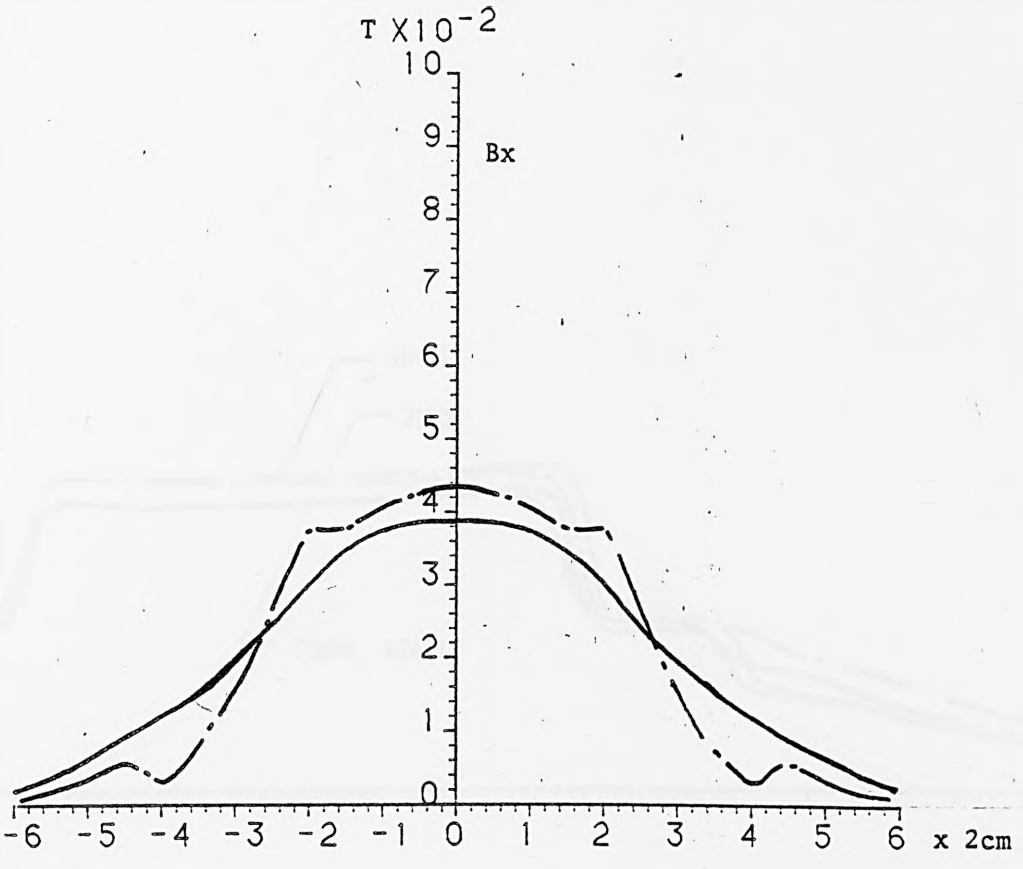

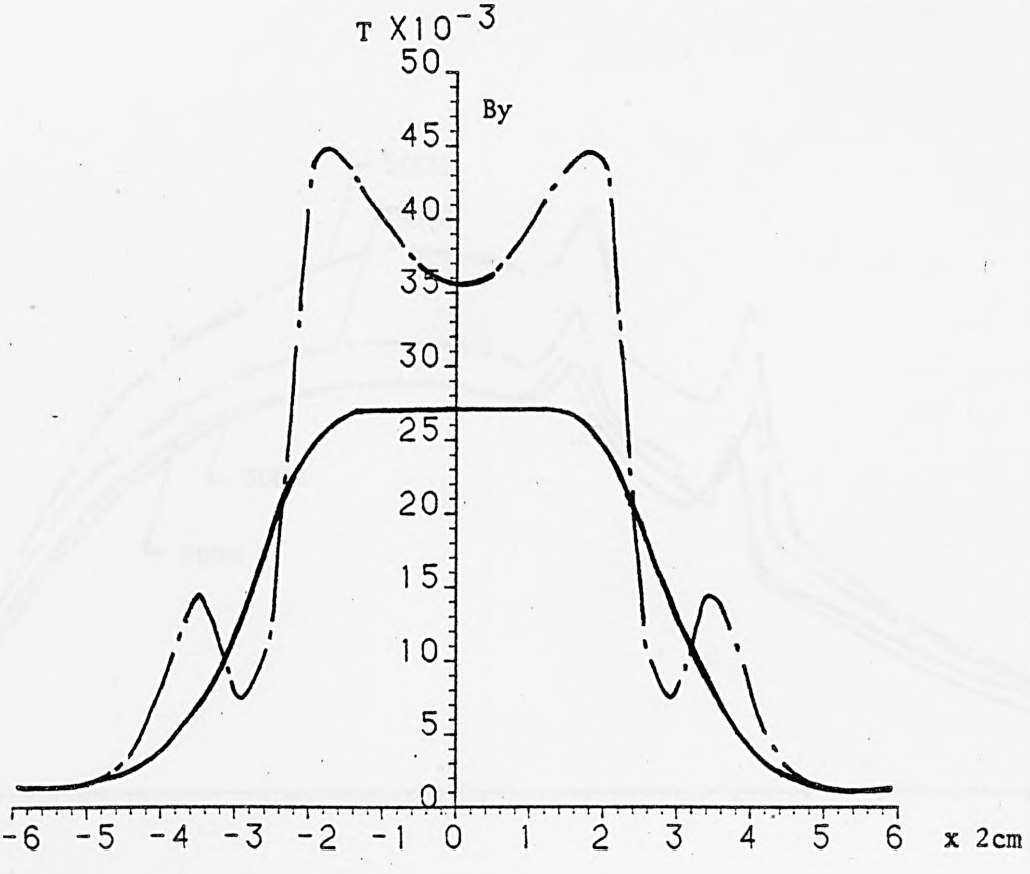

Fig. 8.9. Airgap Flux Density components along the z-direction at I = 5A, g = 9.5 mm, f = 350 Hz, S = 0.2

— 3DHM, --- 3DCM

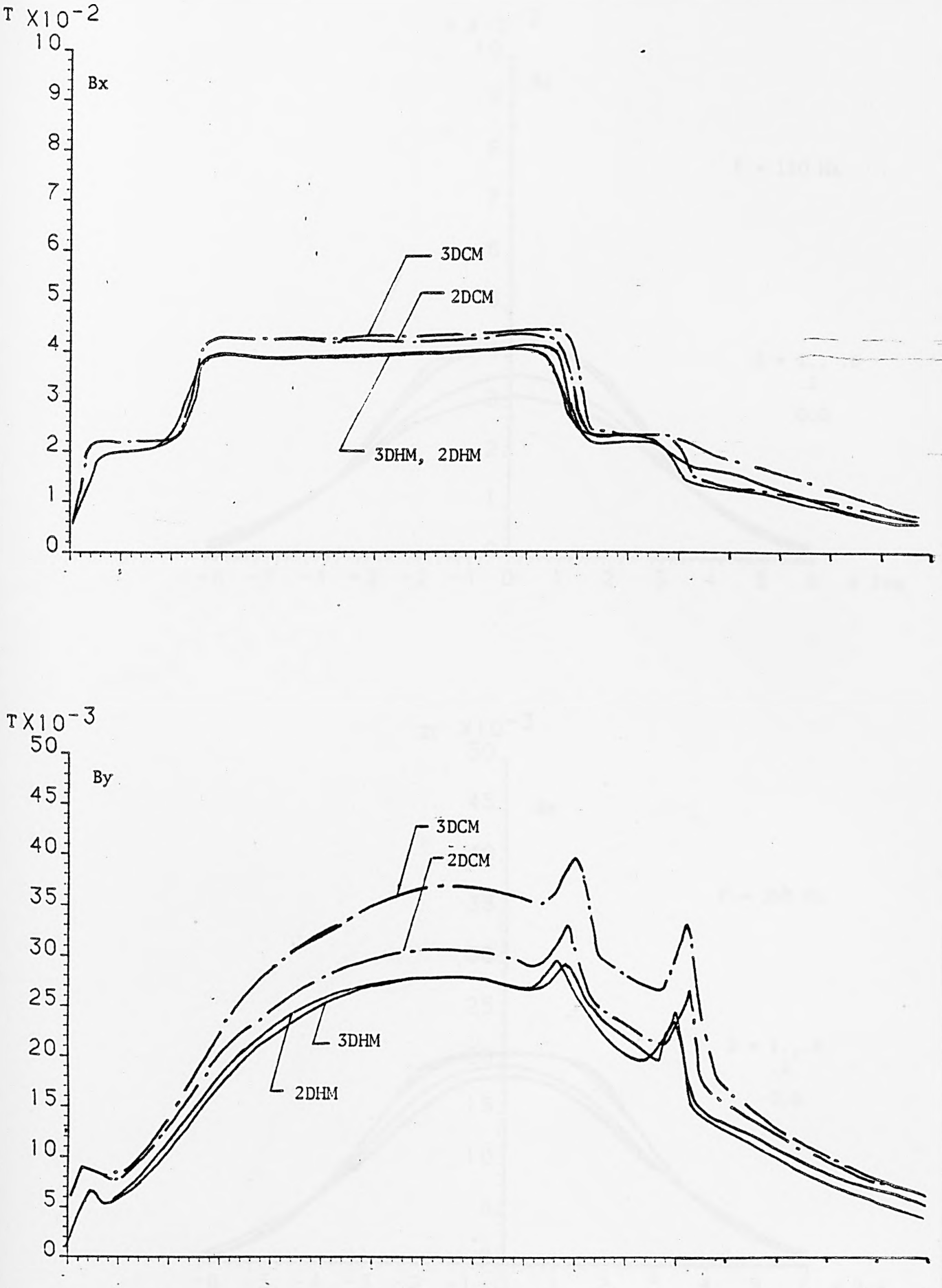

Fig. 8.10. Airgap Flux Density Components along the x-direction at I = 5A, g = 9.5 mm, f = 350 Hz, S = 0.2

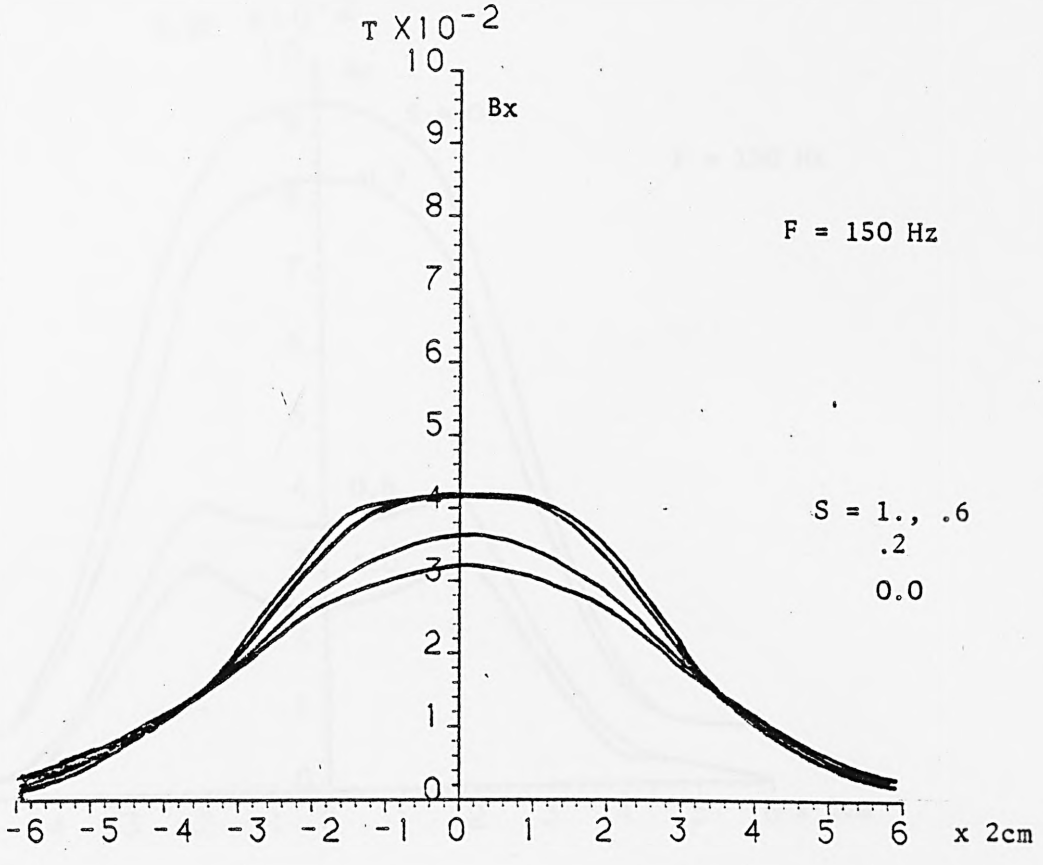

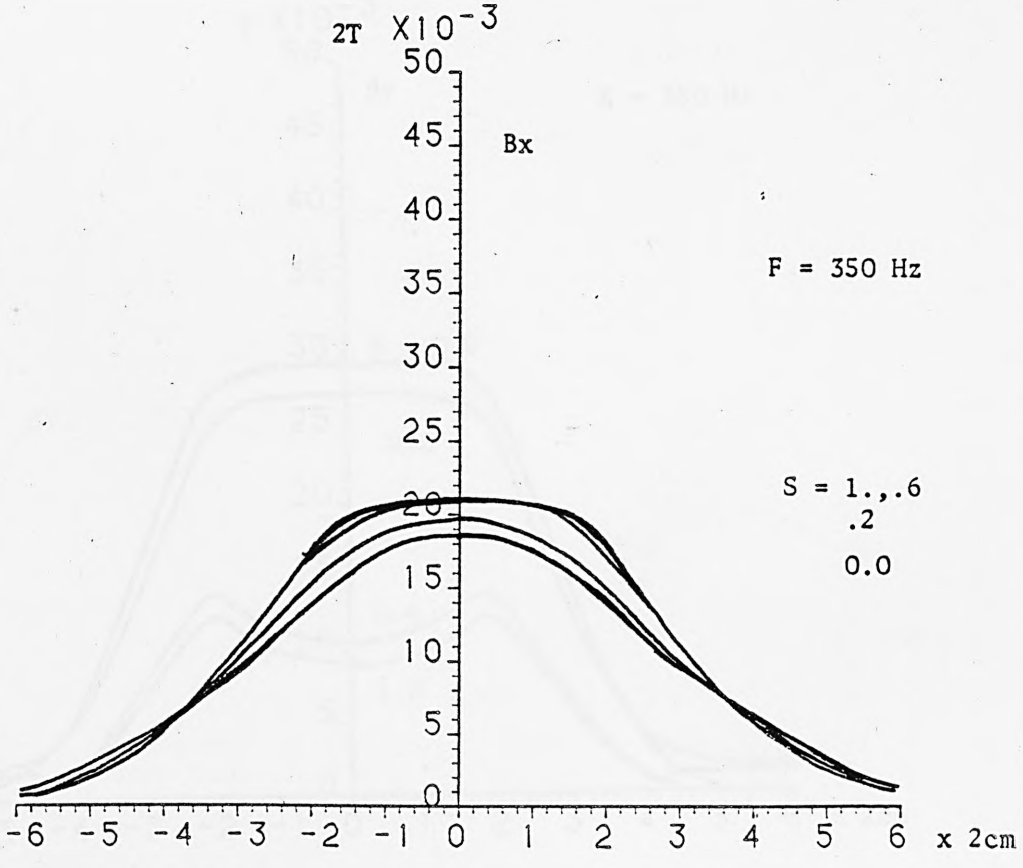

Fig. 8.11. x-component of Flux Density along the z-direction using 3DHM

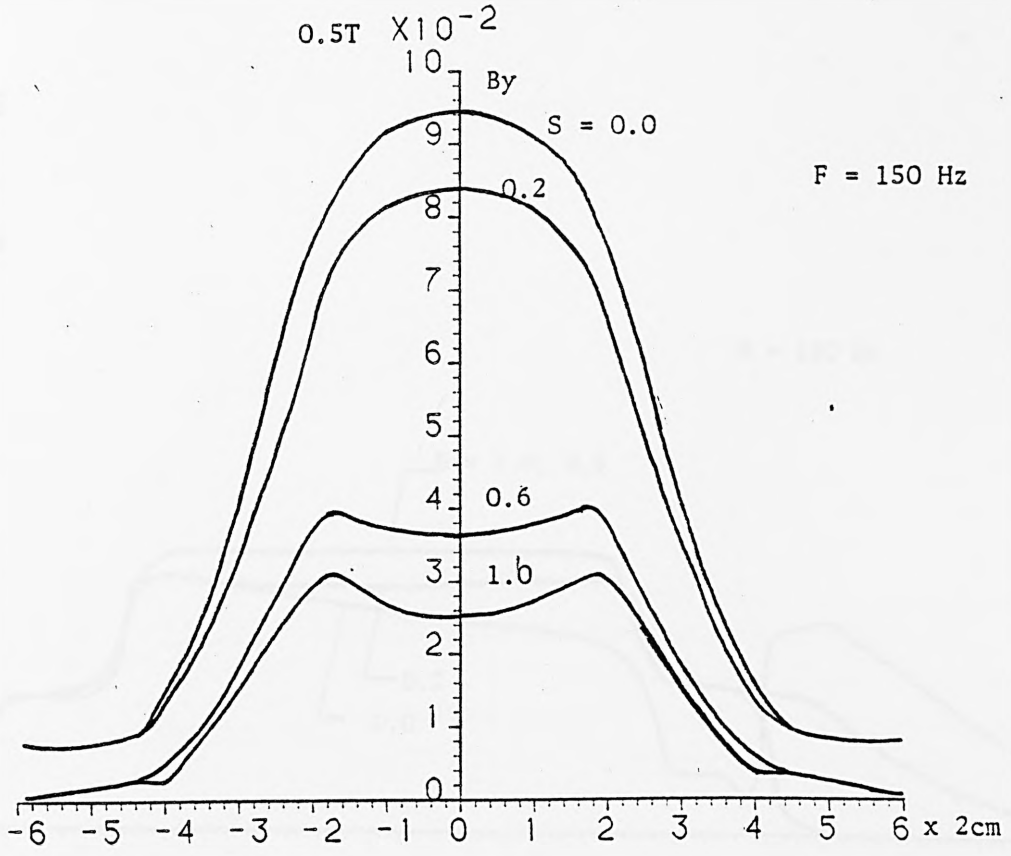

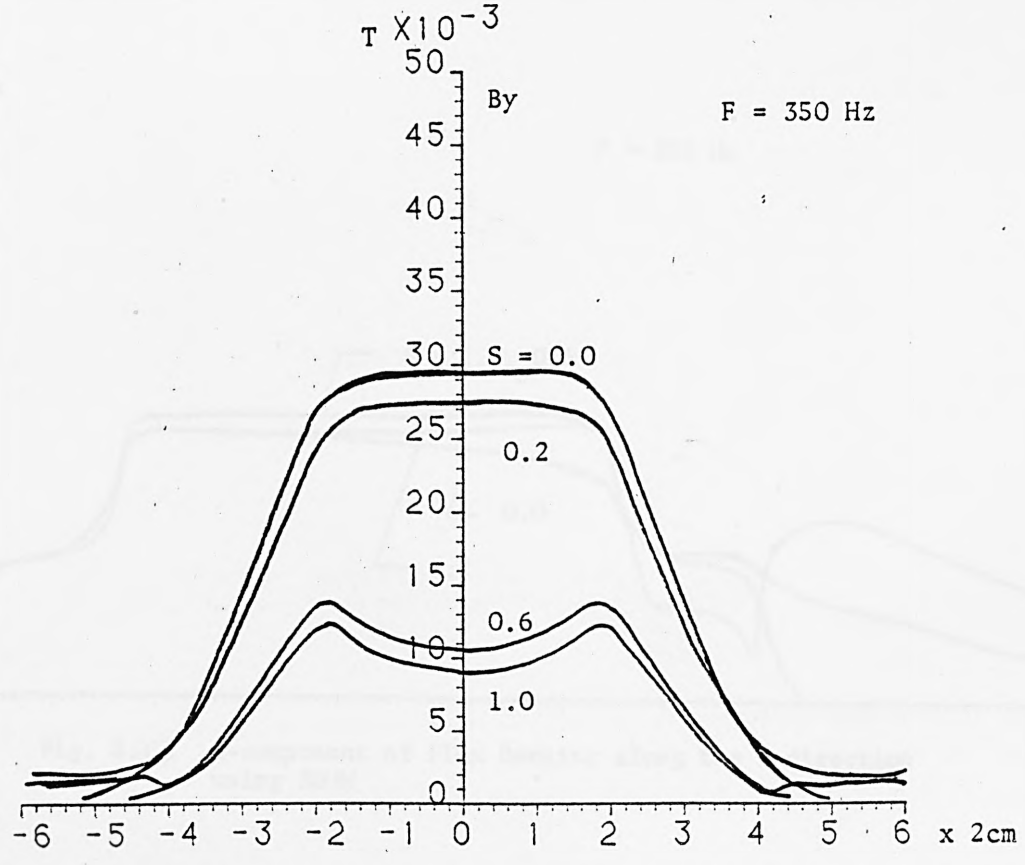

Fig. 8.12. y-component of Flux Density along the z-direction using 3DHM

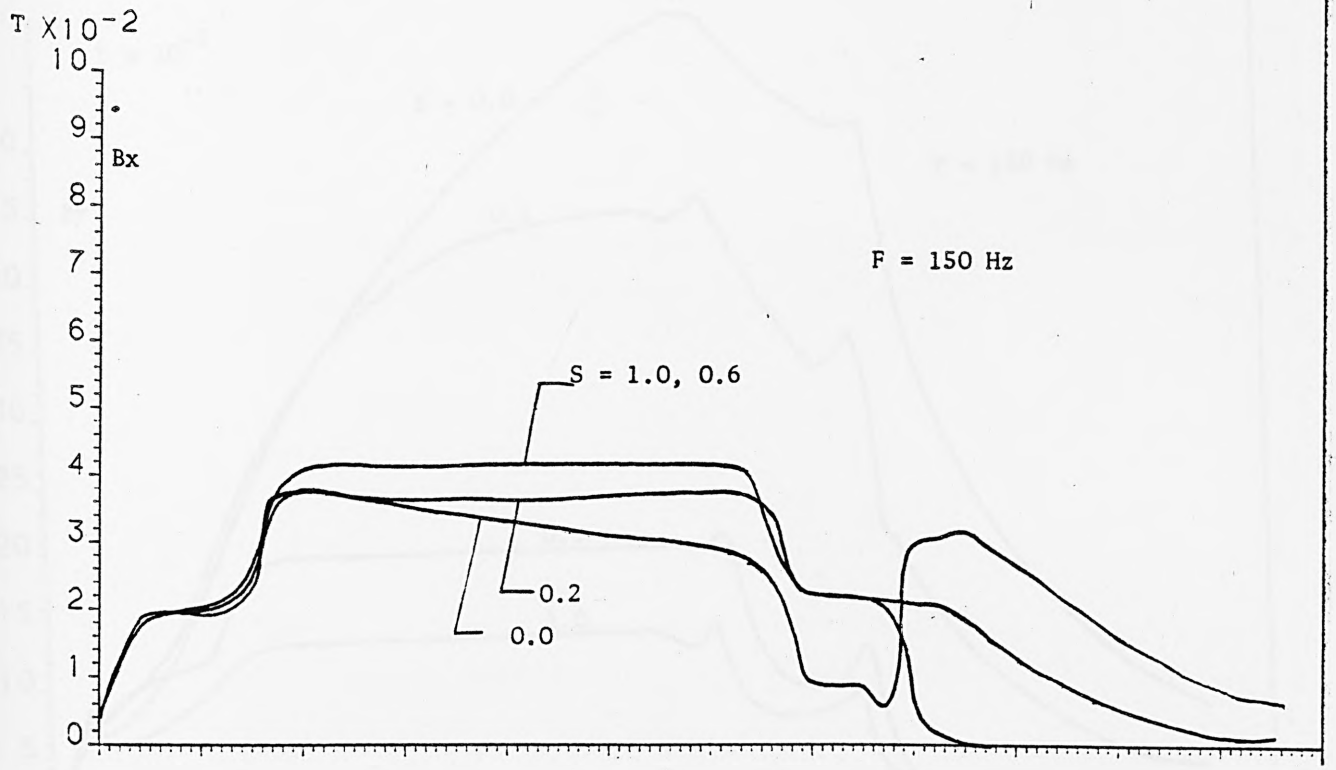

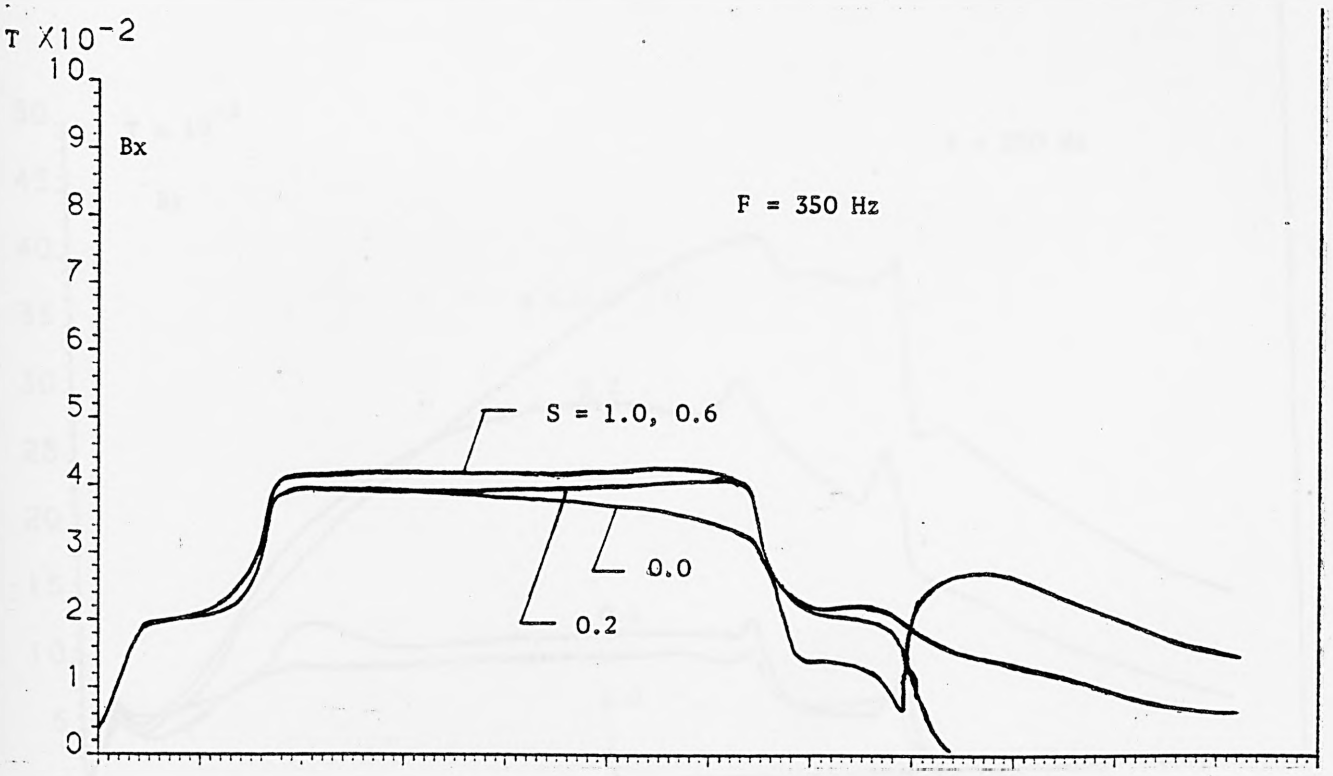

Fig. 8.13. x-component of Flux Density along the x-direction using 3DHM

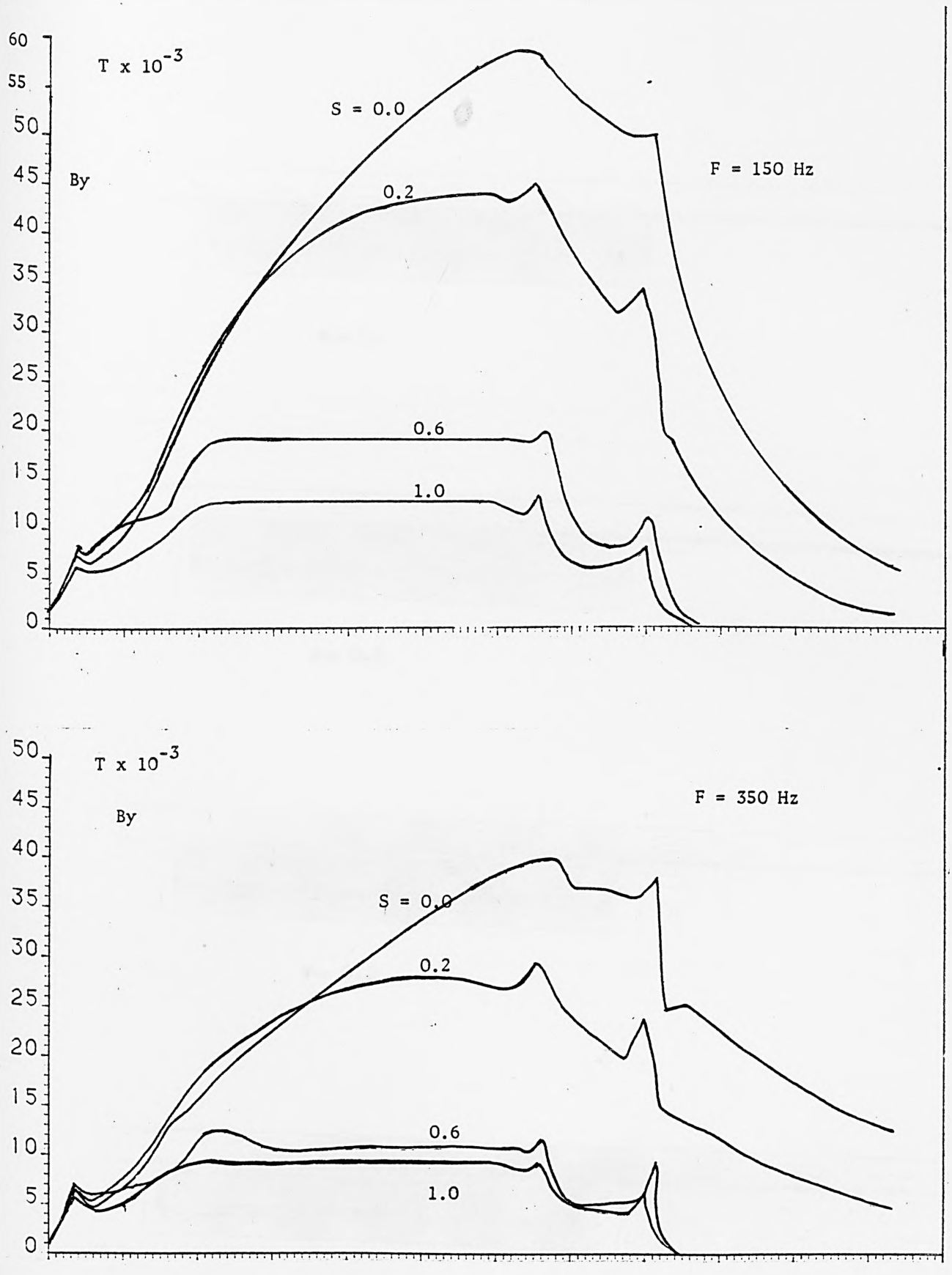

Fig. 8.14. y-component of Flux Density along the x-direction using 3DHM

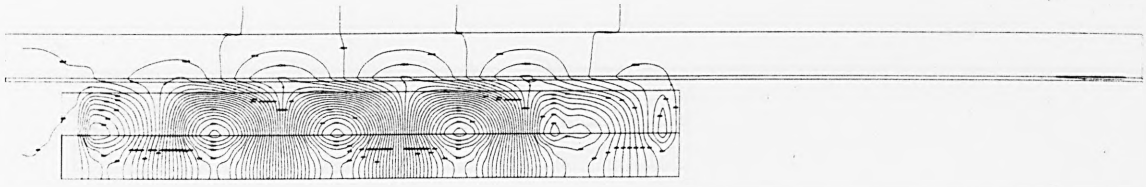

s = 1.

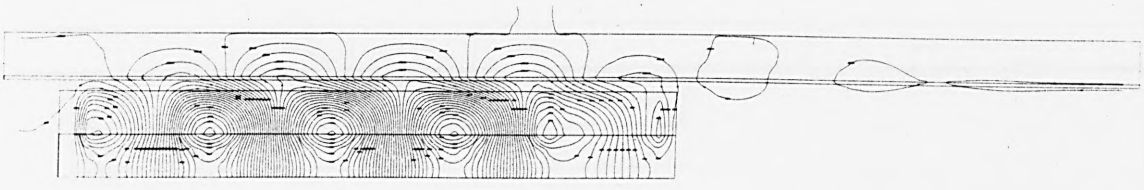

s = 0.6

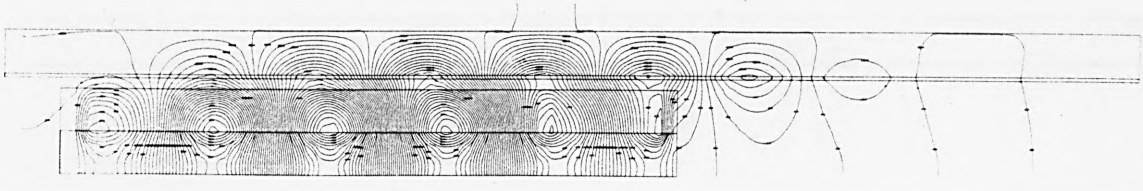

s = 0.2

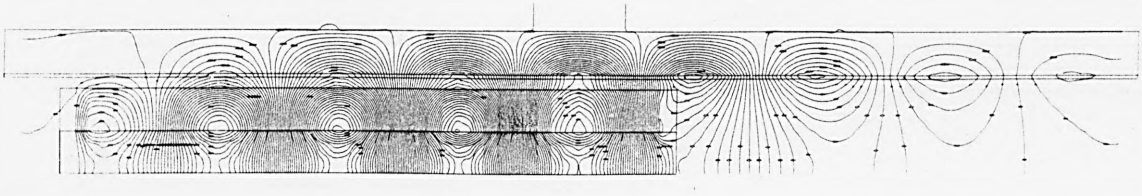

s = 0.0

Fig. 8.15. Flux distribution of 2DHM model at f = 150 Hz

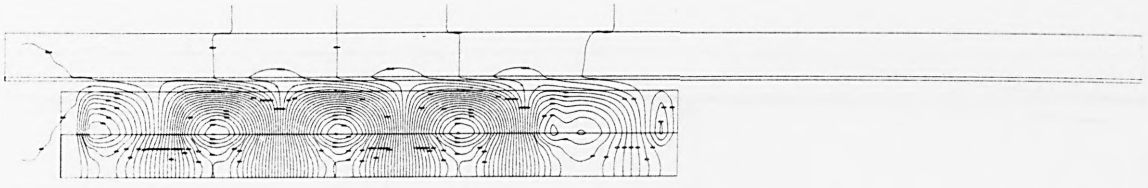

s = 1.

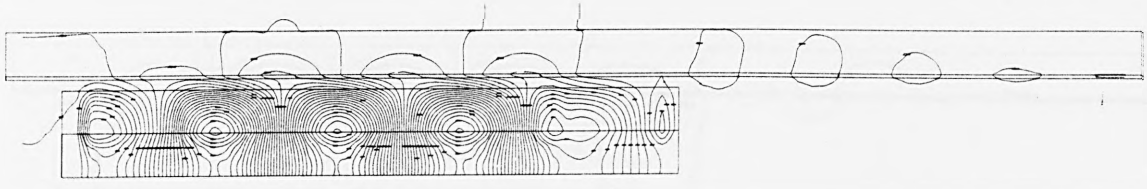

s = 0.6

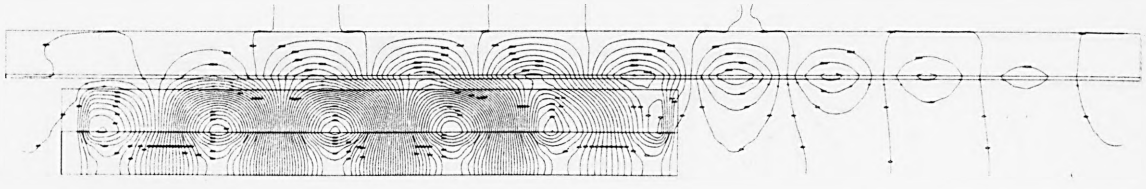

s = 0.2

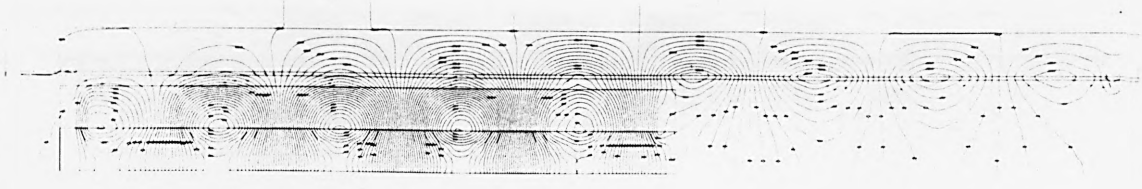

s = 0.0

Fig. 8.16. Flux distribution of 2DHM model at f = 350 Hz

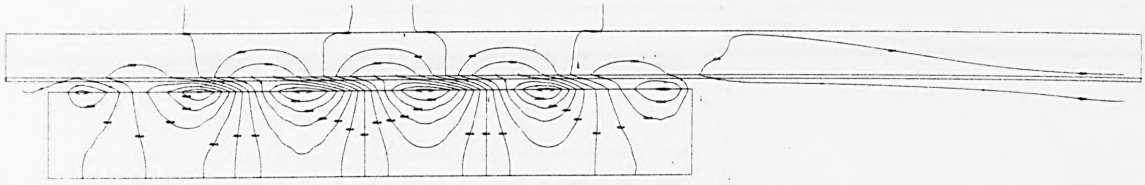

s = 1.

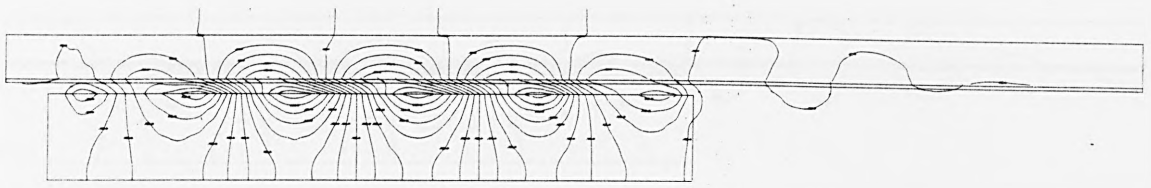

s = 0.6

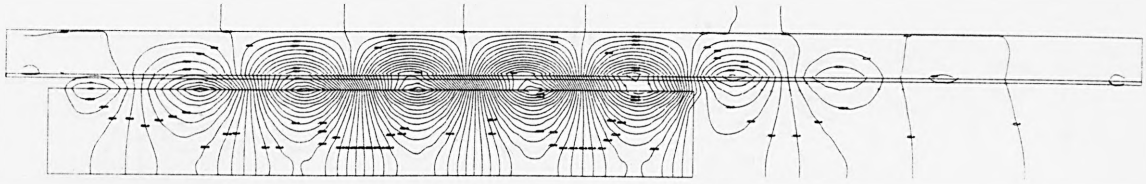

s = 0.2

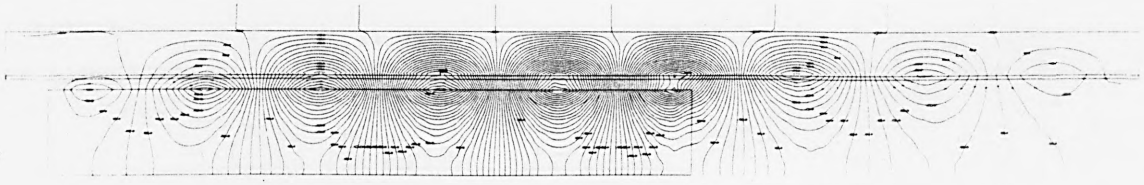

s = 0.0

Fig. 8.17. Flux distribution of 2DCM model at f = 150 Hz

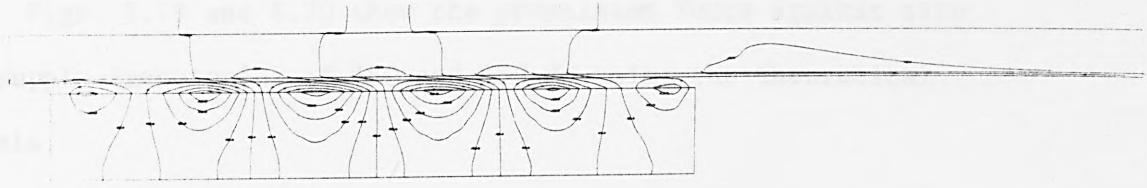

s = 1.

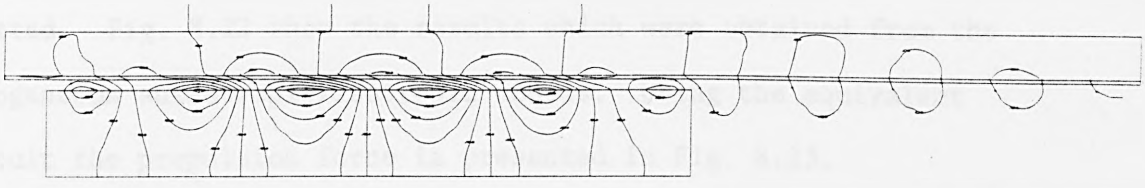

s = 0.6

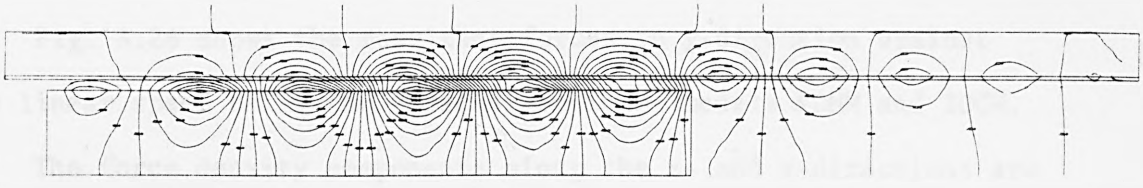

s = 0.2

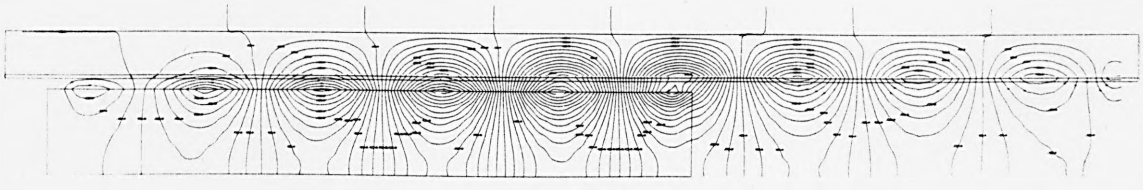

s = 0.0

Fig. 8.18. Flux distribution of 2DCM model at f = 350 Hz

8.3 Forces and Force Density Distributions

Figs. 8.19 and 8.20 show the propulsion force against slip at supply frequencies of 150 and 350 Hz using the theoretical models.

To show the significance of the end effects on the performance of the motor. The porpulsion force of each model is plotted against the linear speed for different synchronous speeds. In Fig. 8.21 the results obtained from the current sheet models were plotted. Fig. 8.22 show the results which were obtained from the homogeneous anisotropic/isotropic models. Using the equivalent circuit the propulsion force is presented in Fig. 8.23.

The resultant forces in y-direction (which is the sum of the levitation and attraction forces) are shown in Figs. 8.24 and 8.25 against slips for differend supply frequencies and from different models.

Fig. 8.26 shows the resultant forces in y-direction against the linear speed using the three-dimensional models 3DHM and 3DCM.

The force density components along the z- and x-directions are presented in Figs. 8.27 to 8.33 for different slips and frequencies. These plots were obtained from the three dimensional model 3DHM.

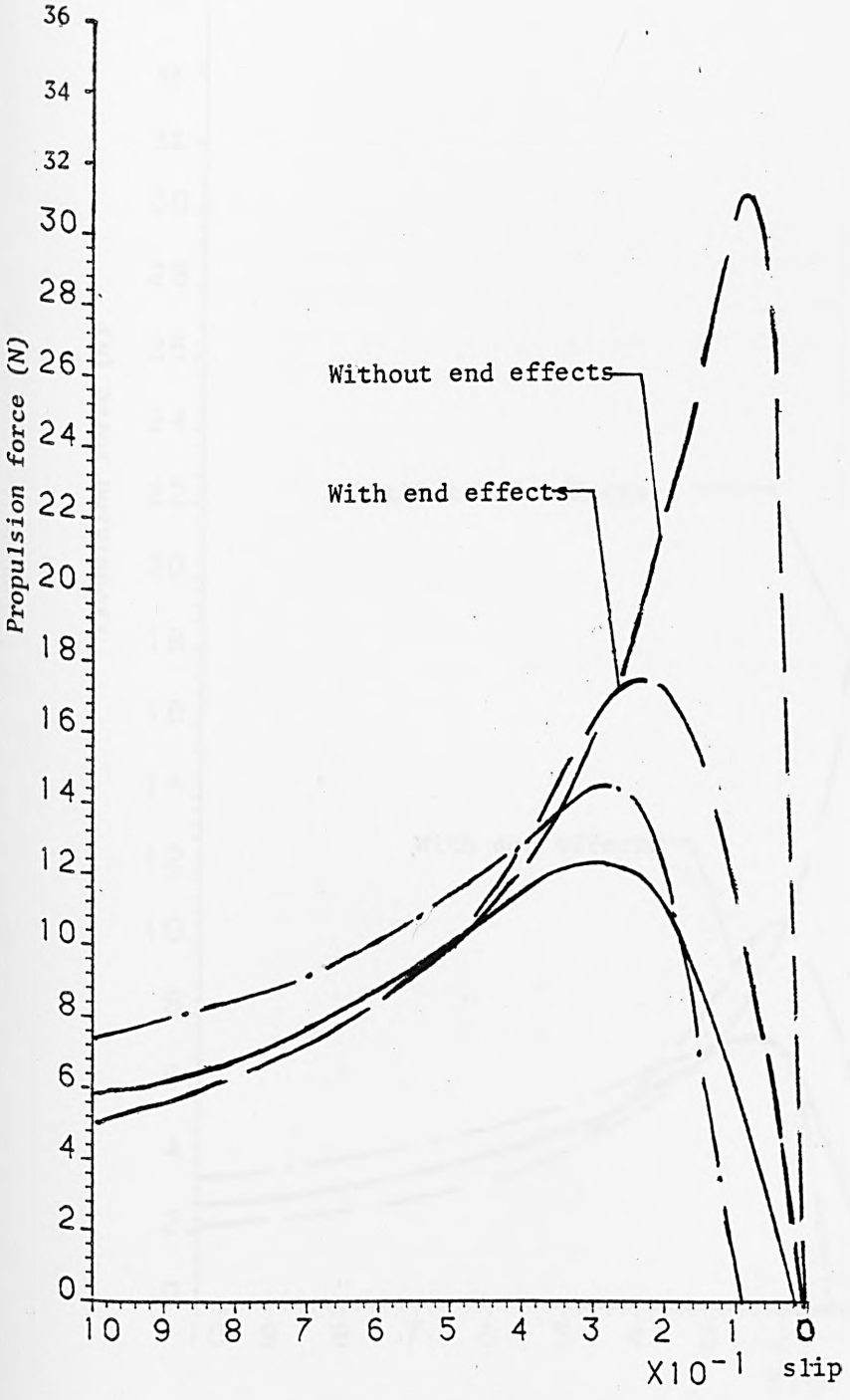

Fig. 8.19. Propulsion force against slip at f = 150 Hz

—3DHM, -·- 3DCM, -- equivalent circuit

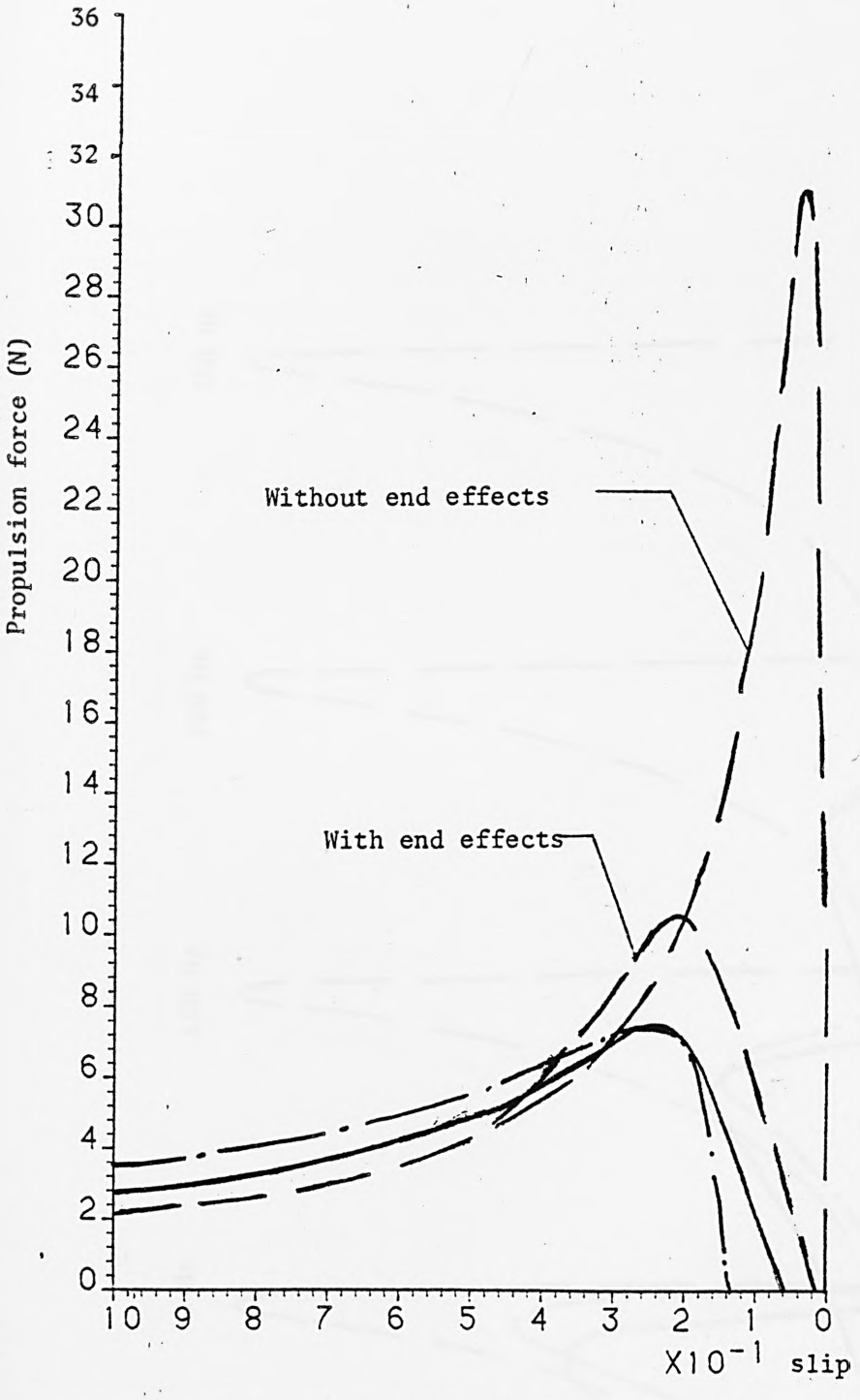

Fig. 8.20. Propulsion force against slip of f = 350 Hz

— 3DHM, -·- 3DCM, --equivalent circuit

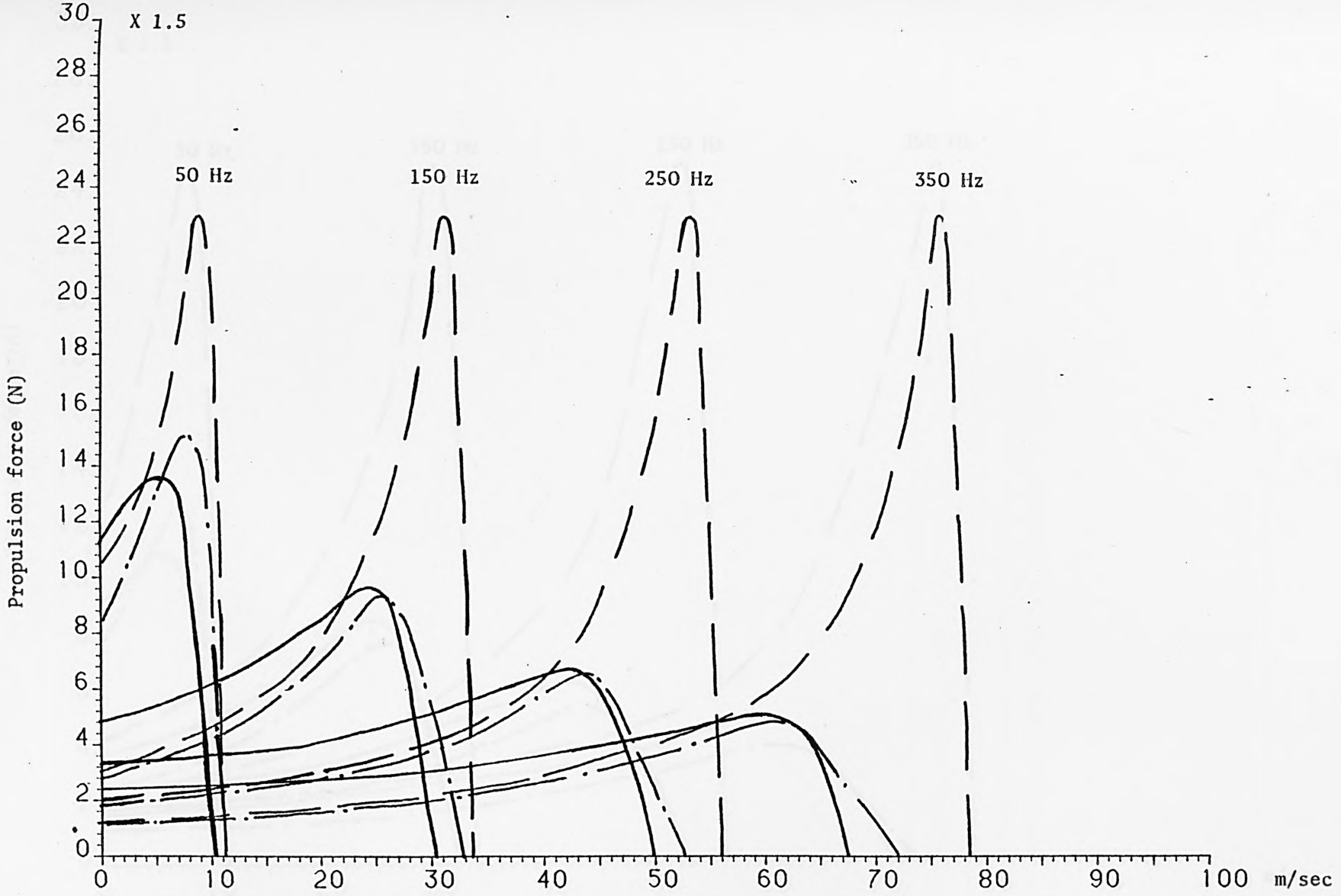

Fig. 8.21. Propulsion force against the linear speed using the current sheet models

-- 1DCM, -·- 2DCM, —3DCM

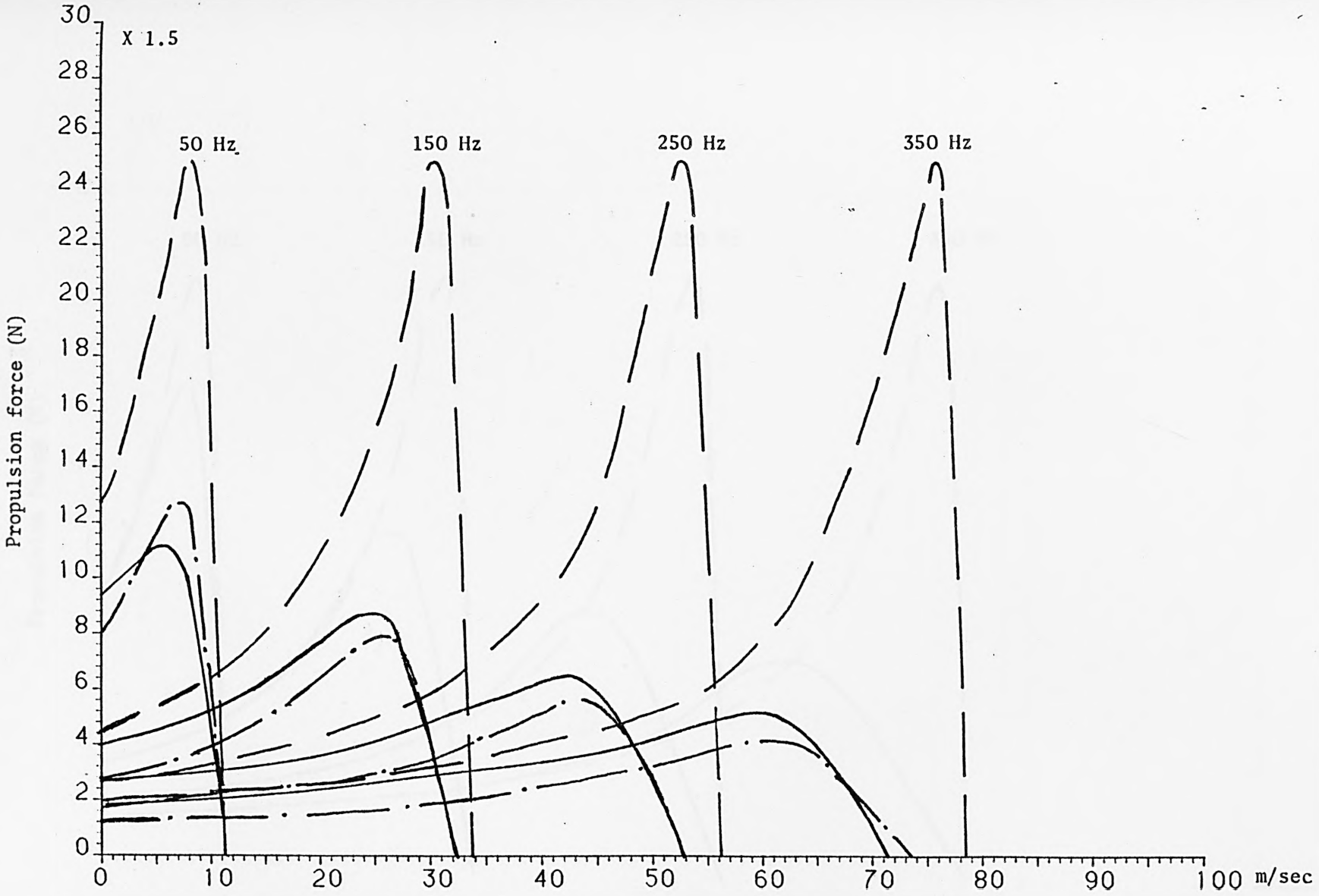

Fig. 8.22. Propulsion force against the linear speed using the homogenous anisotropic/isotropic
-- 1DHM, -·- 2DHM, — 3DHM

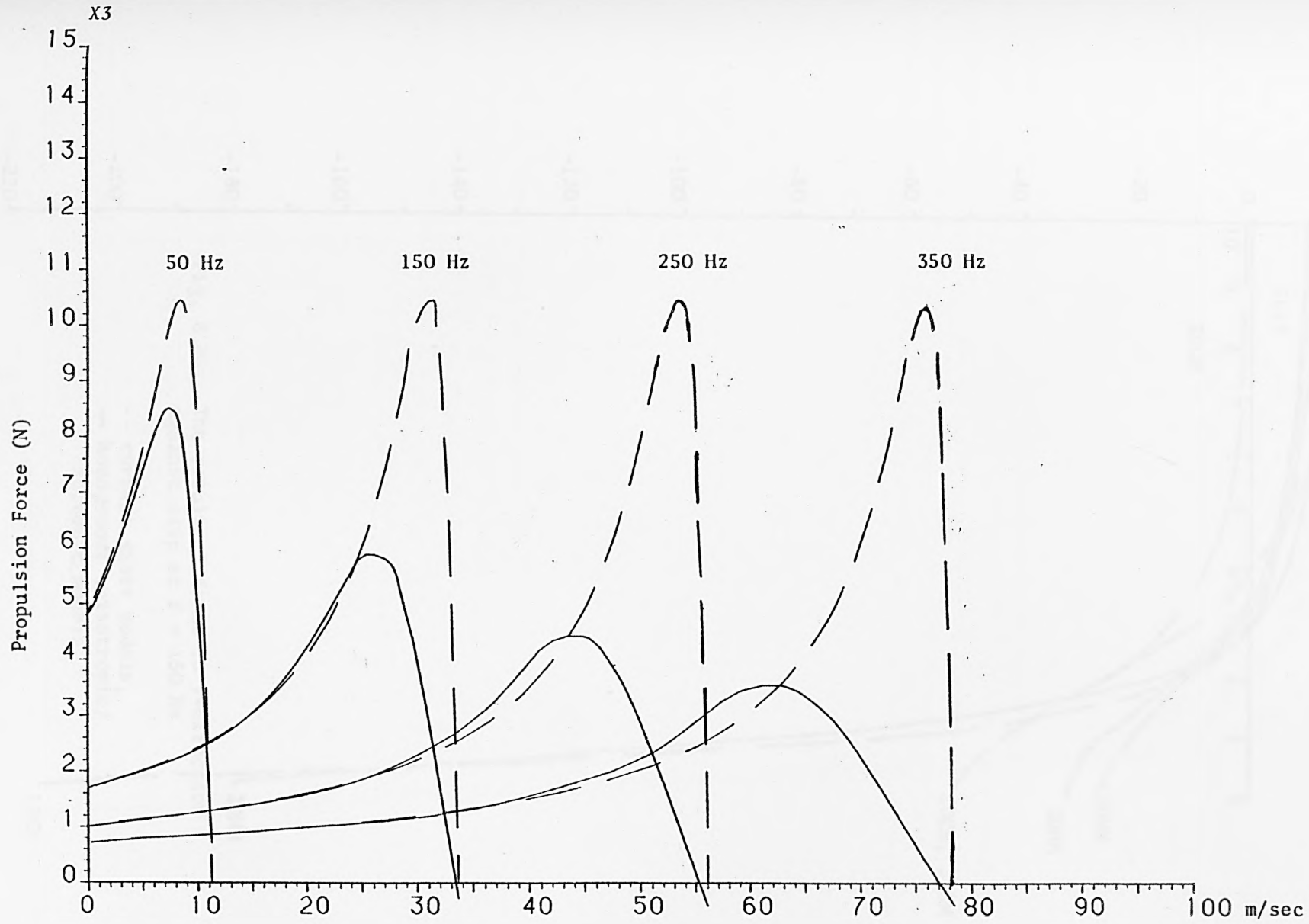

Fig. 8.23. Propulsion force against the linear speed using the equivalent circuit approach
-- without end effects, — with end effects

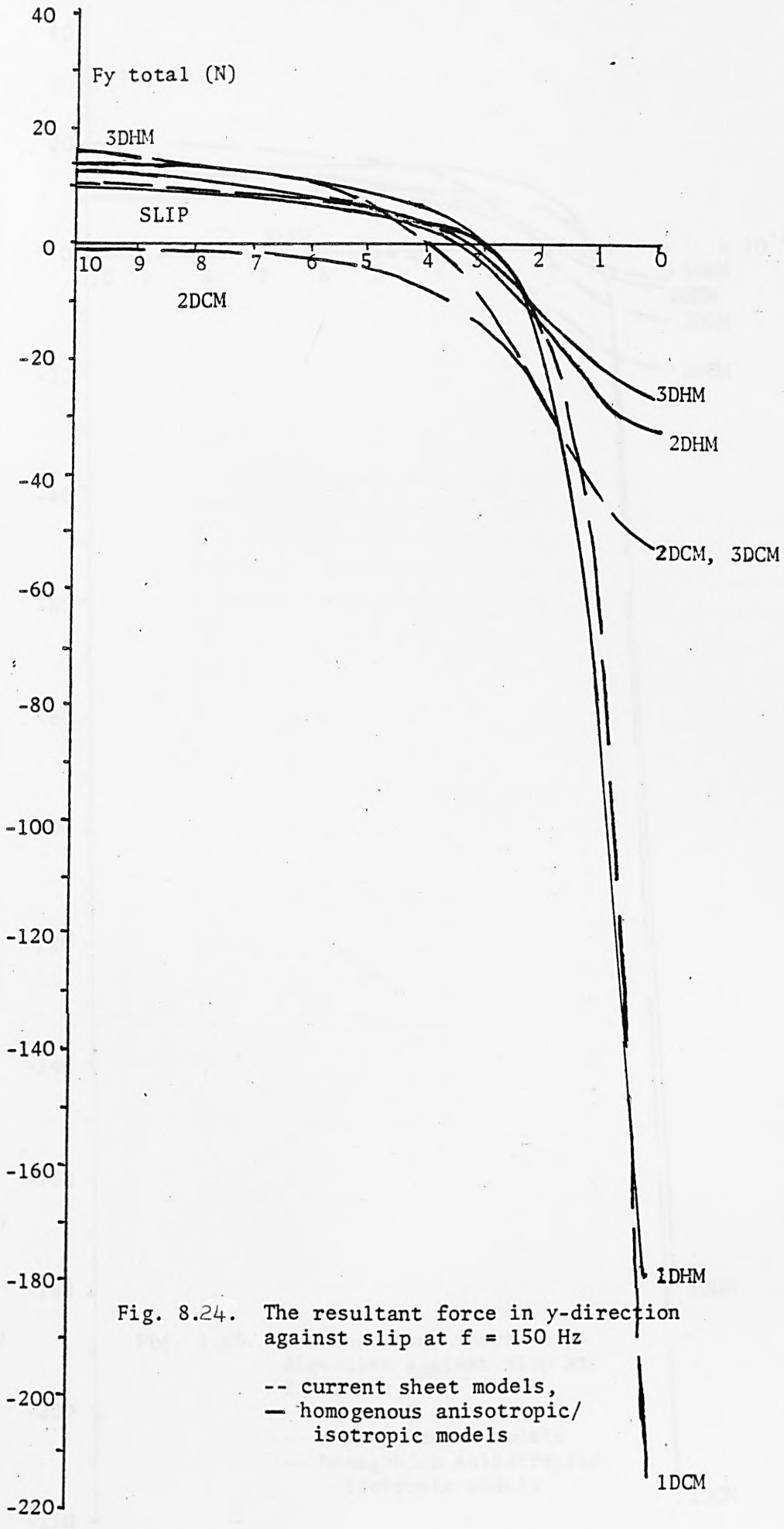

Fig. 8.24. The resultant force in y-direction against slip at f = 150 Hz

-- current sheet models,
— homogenous anisotropic/ isotropic models

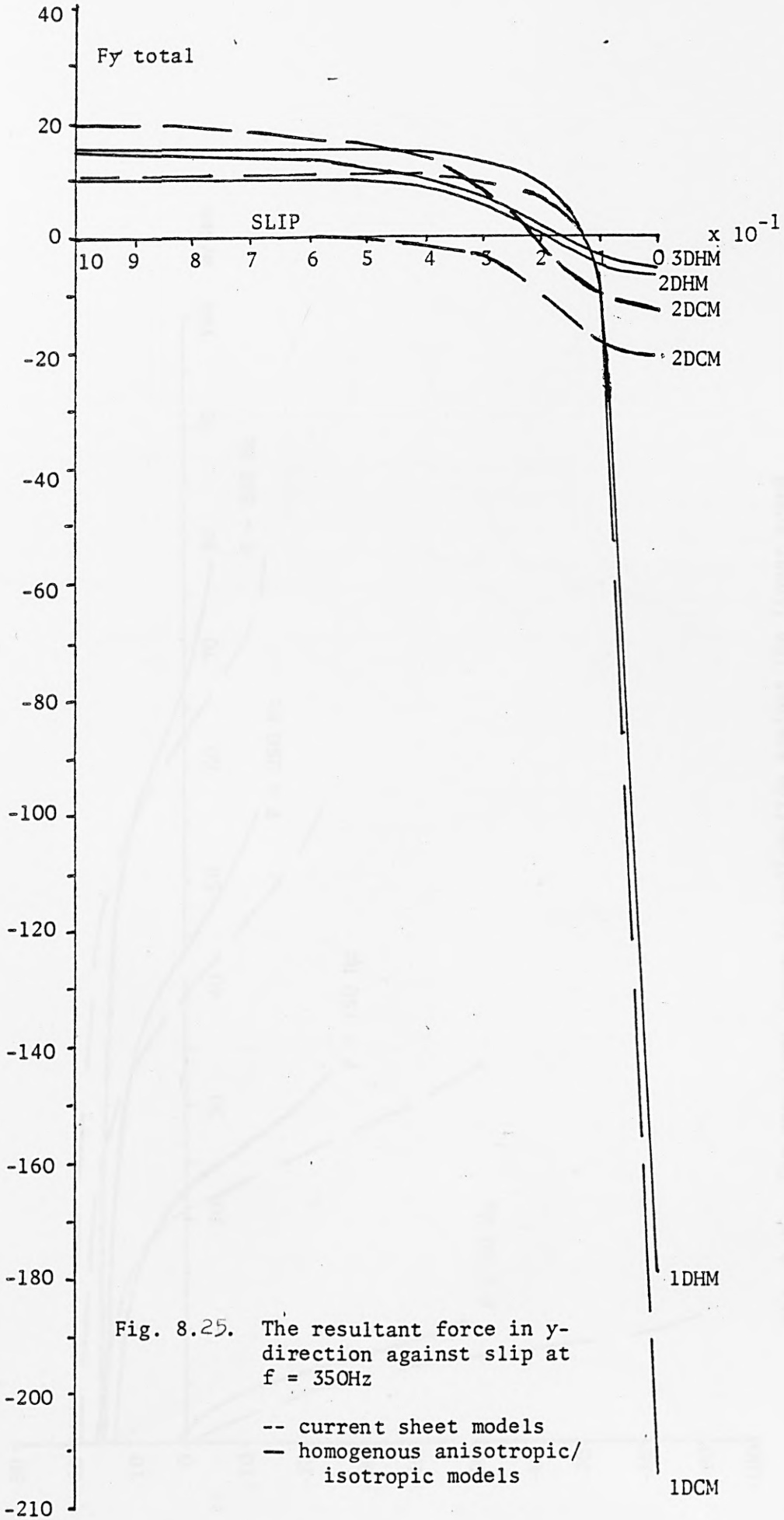

Fig. 8.25. The resultant force in y-direction against slip at f = 350Hz

-- current sheet models
— homogenous anisotropic/ isotropic models

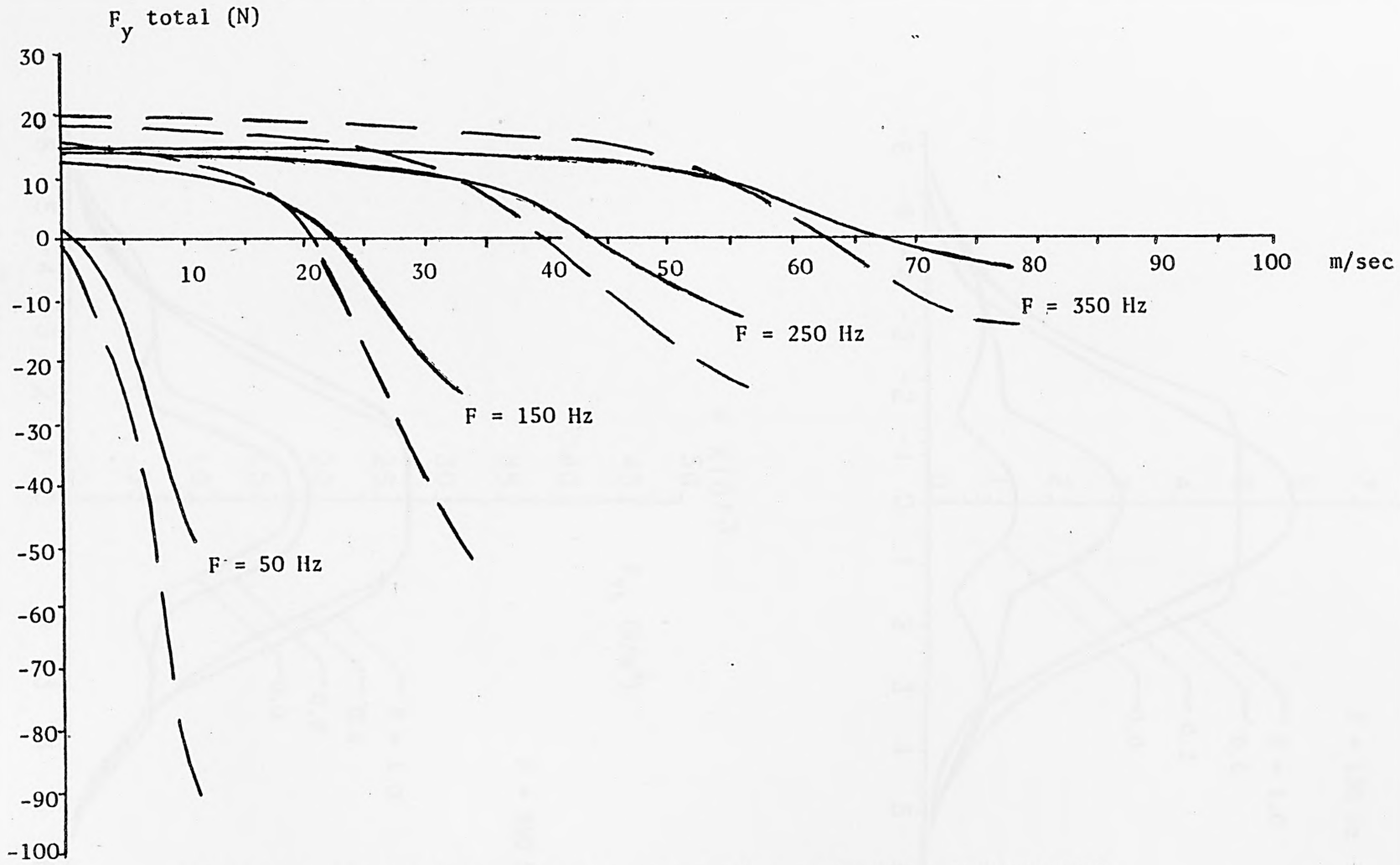

Fig. 8.26. The resultant force in y-direction against the linear speed

-- 3DCM, — 3DHM

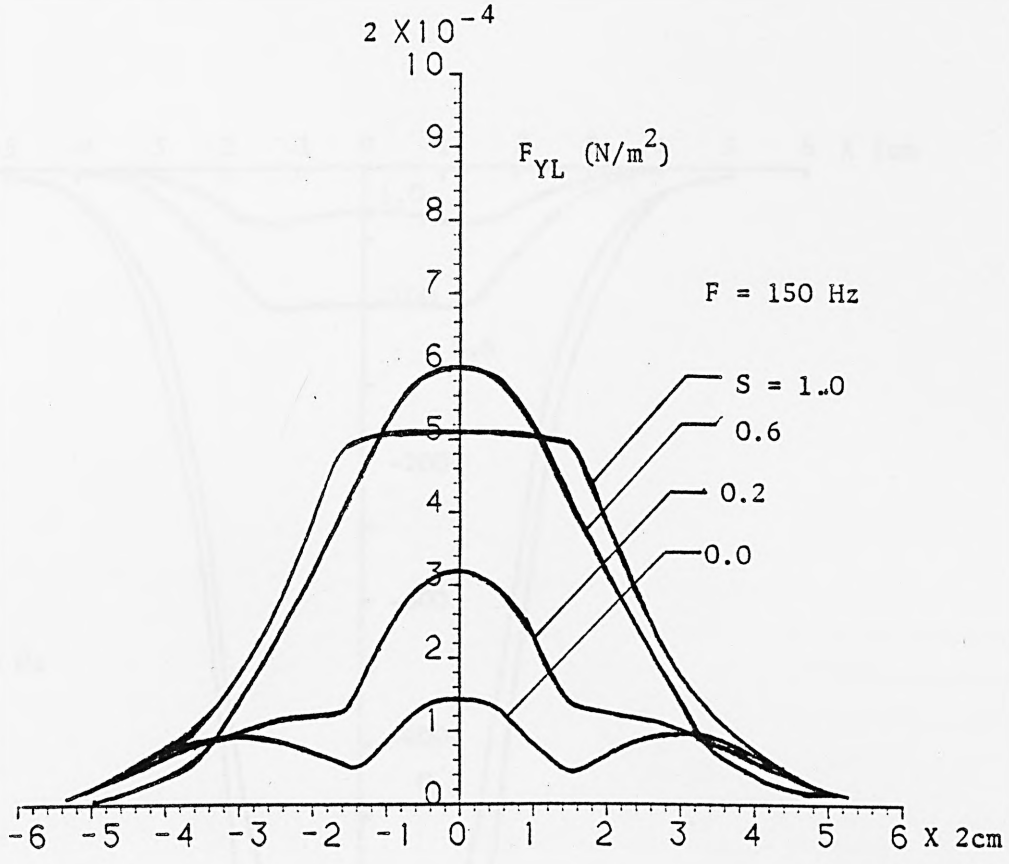

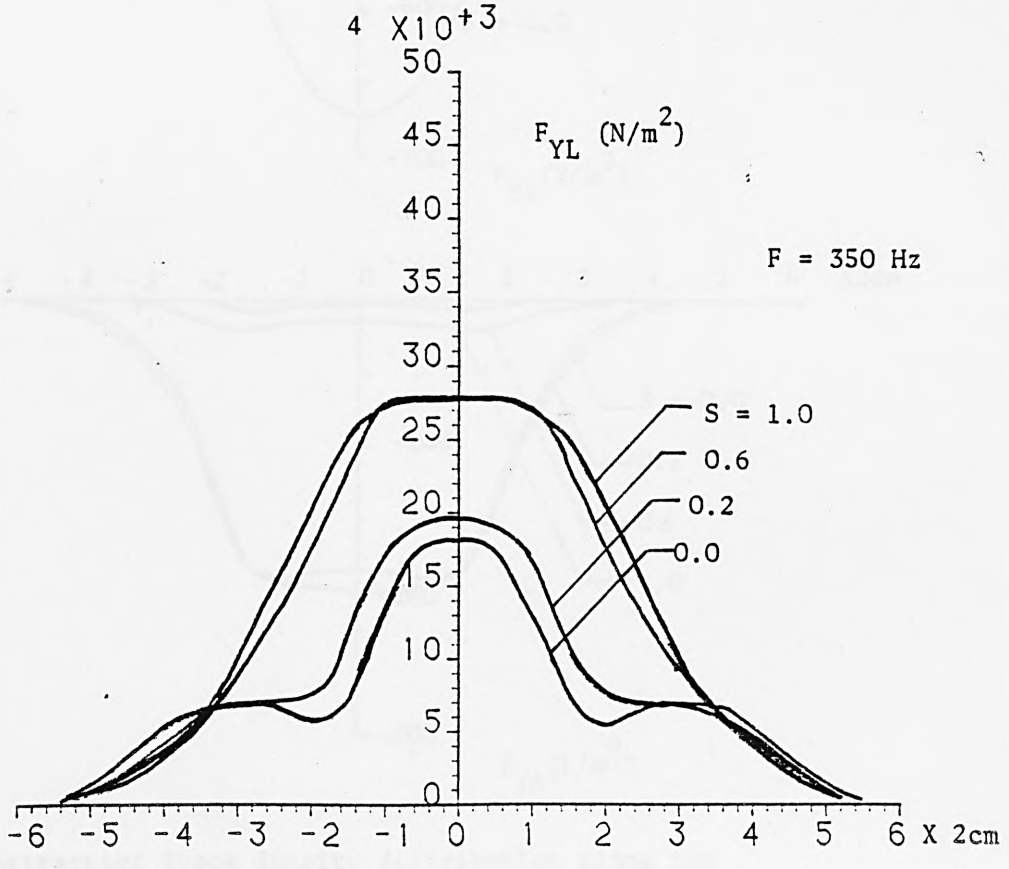

Fig. 8.27. Levitation force density distribution (repulsion) along the z-direction of 3DHM

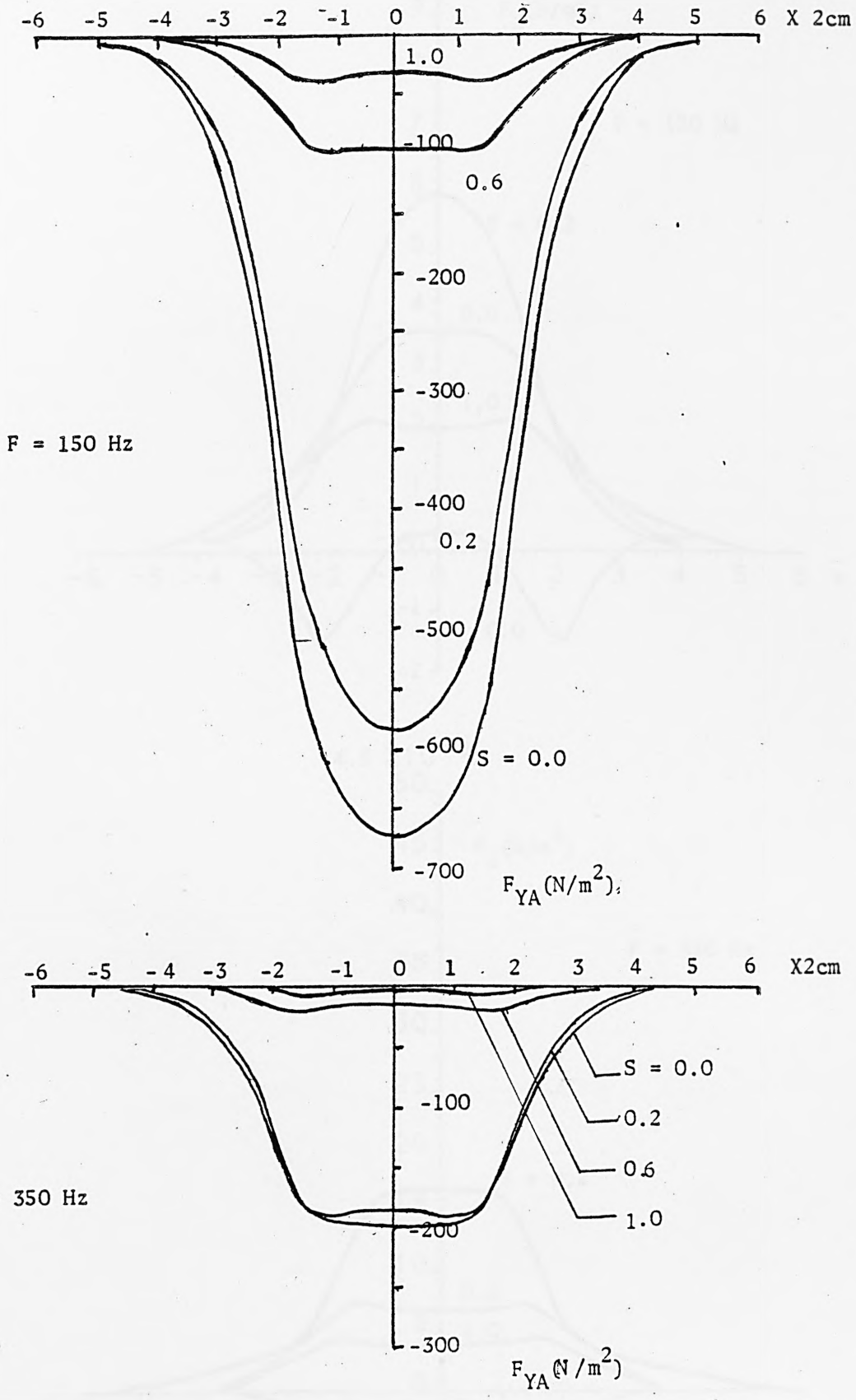

Fig. 8.28. Attraction force density distribution along the z-direction of 3DHM

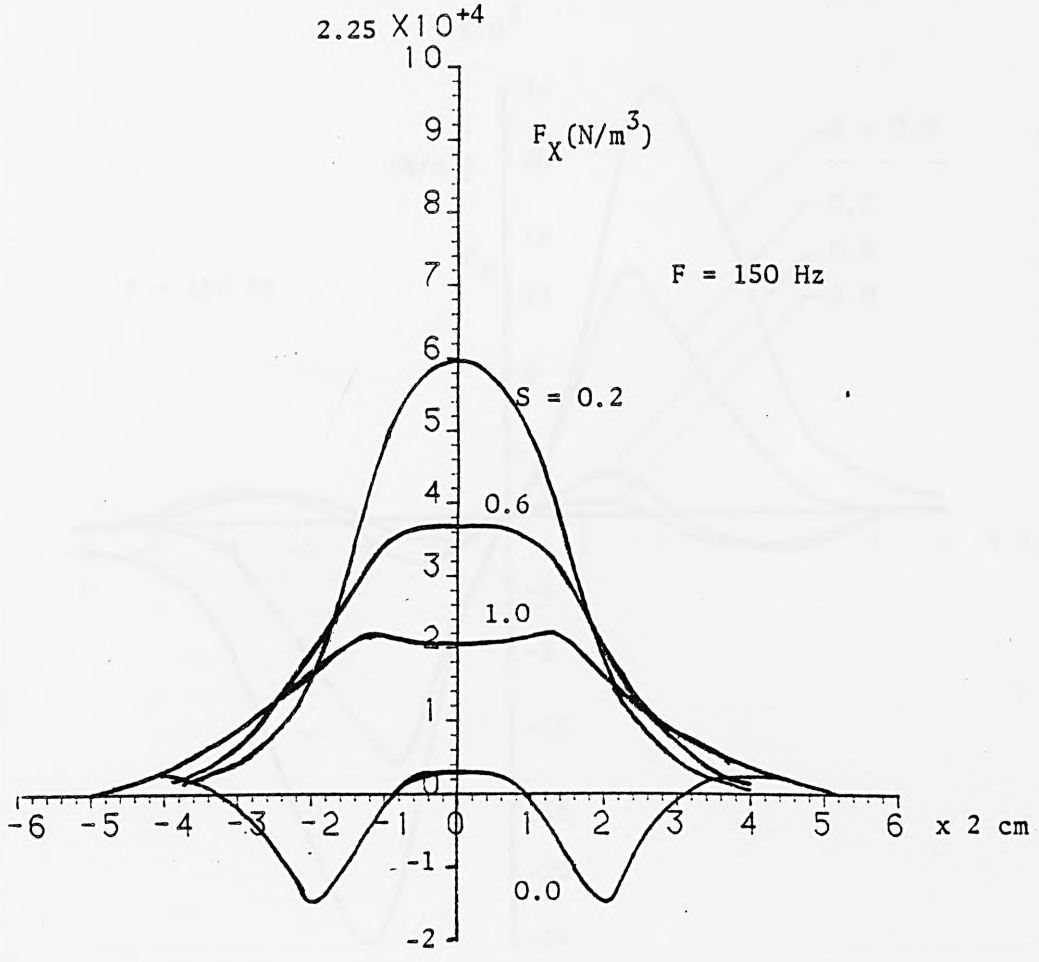

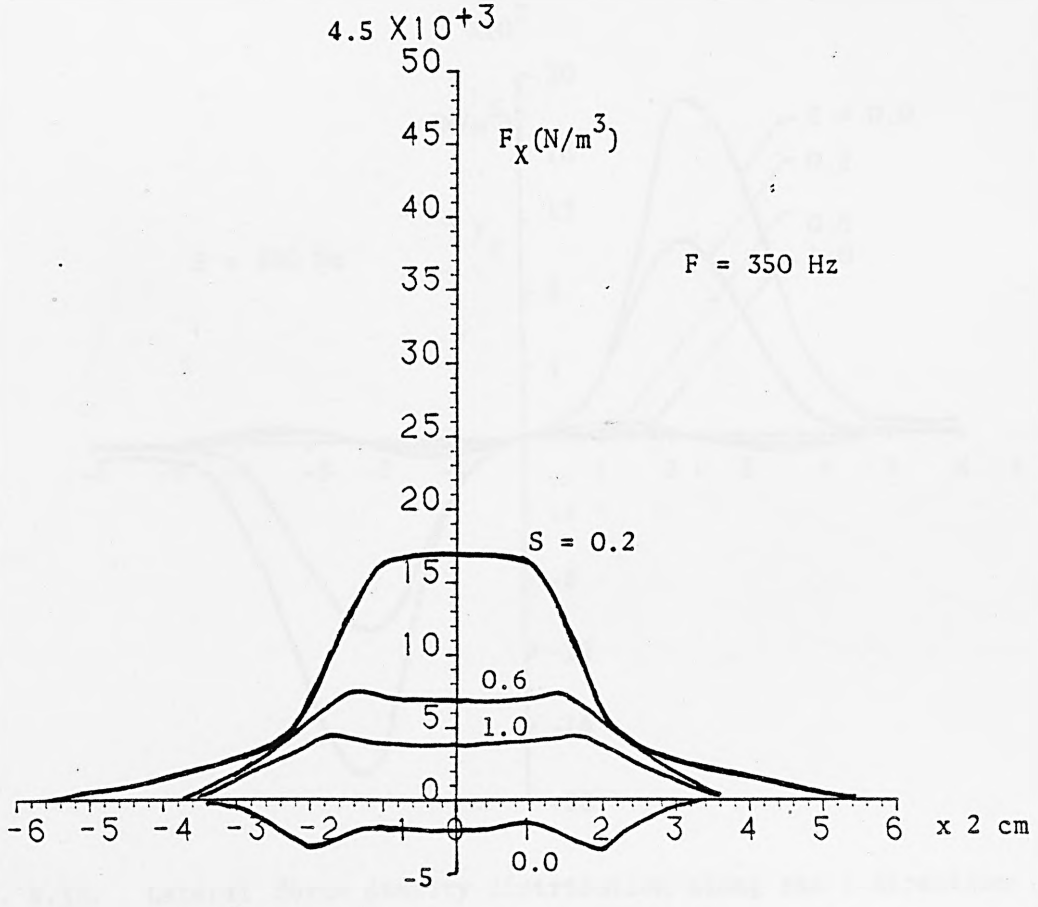

Fig. 8.29.Propulsion force density distribution along the z-direction of 3DHM

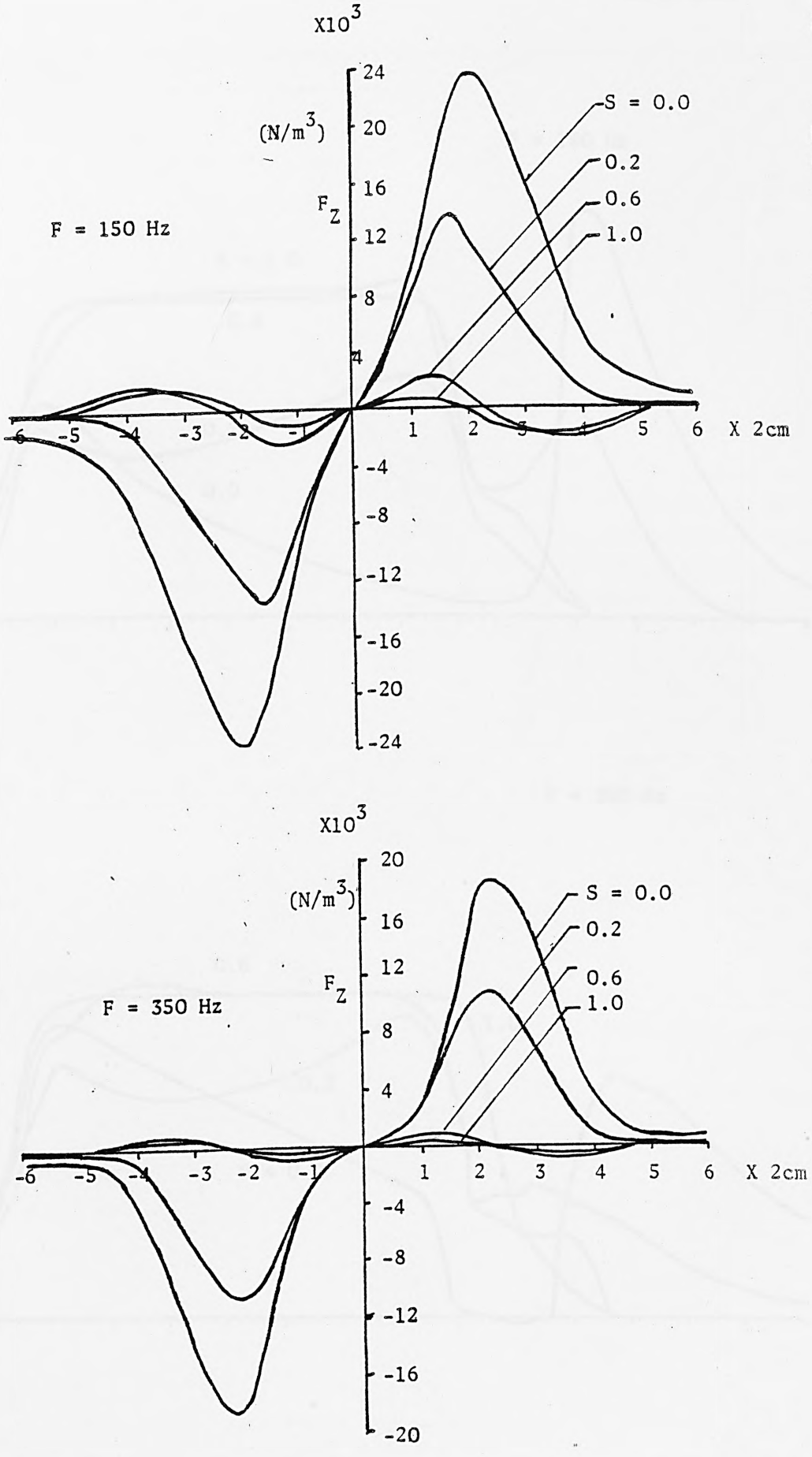

Fig. 8.30. Lateral force density distribution along the z-direction of 3DHM

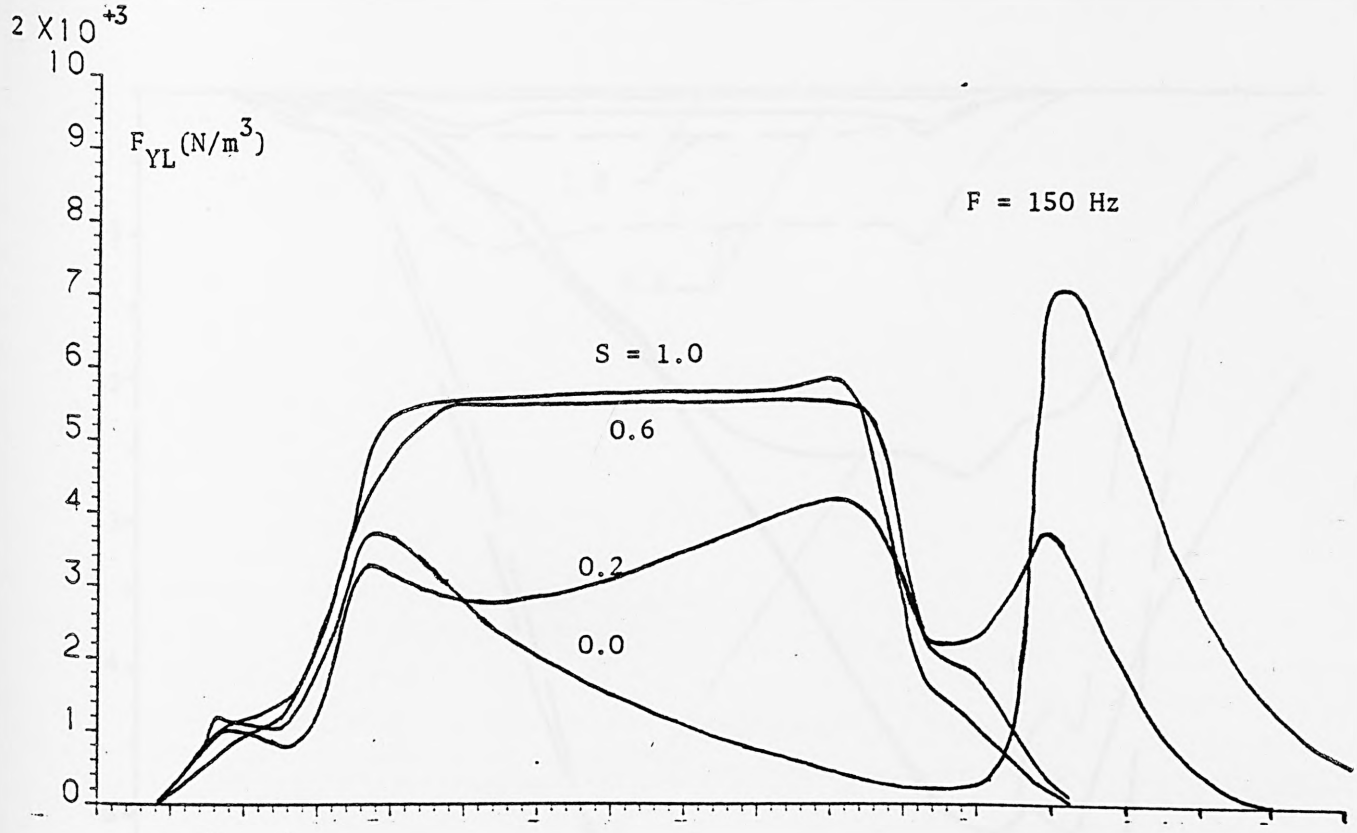

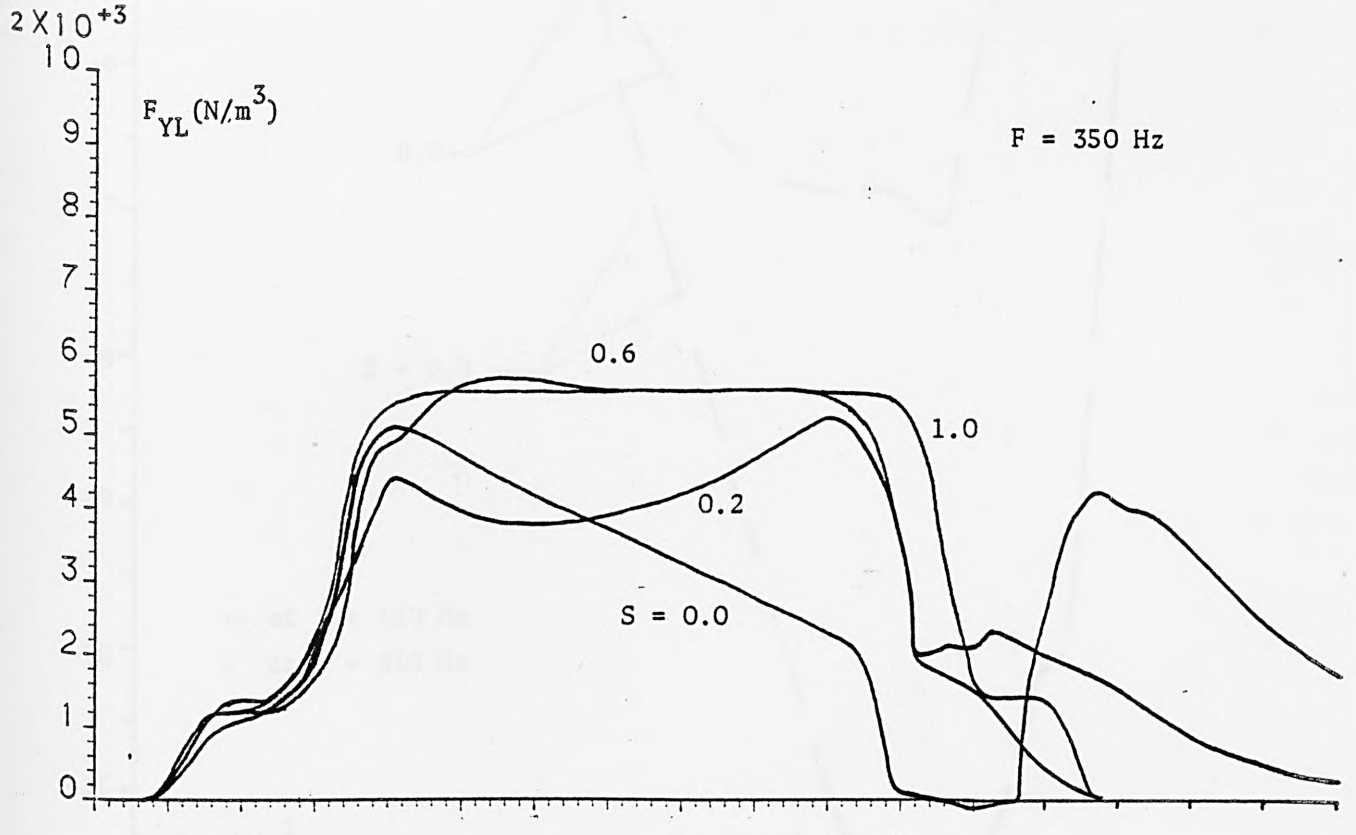

Fig. 8.31. Levitation force density distribution (repulsion) along the x-direction of 3DHM

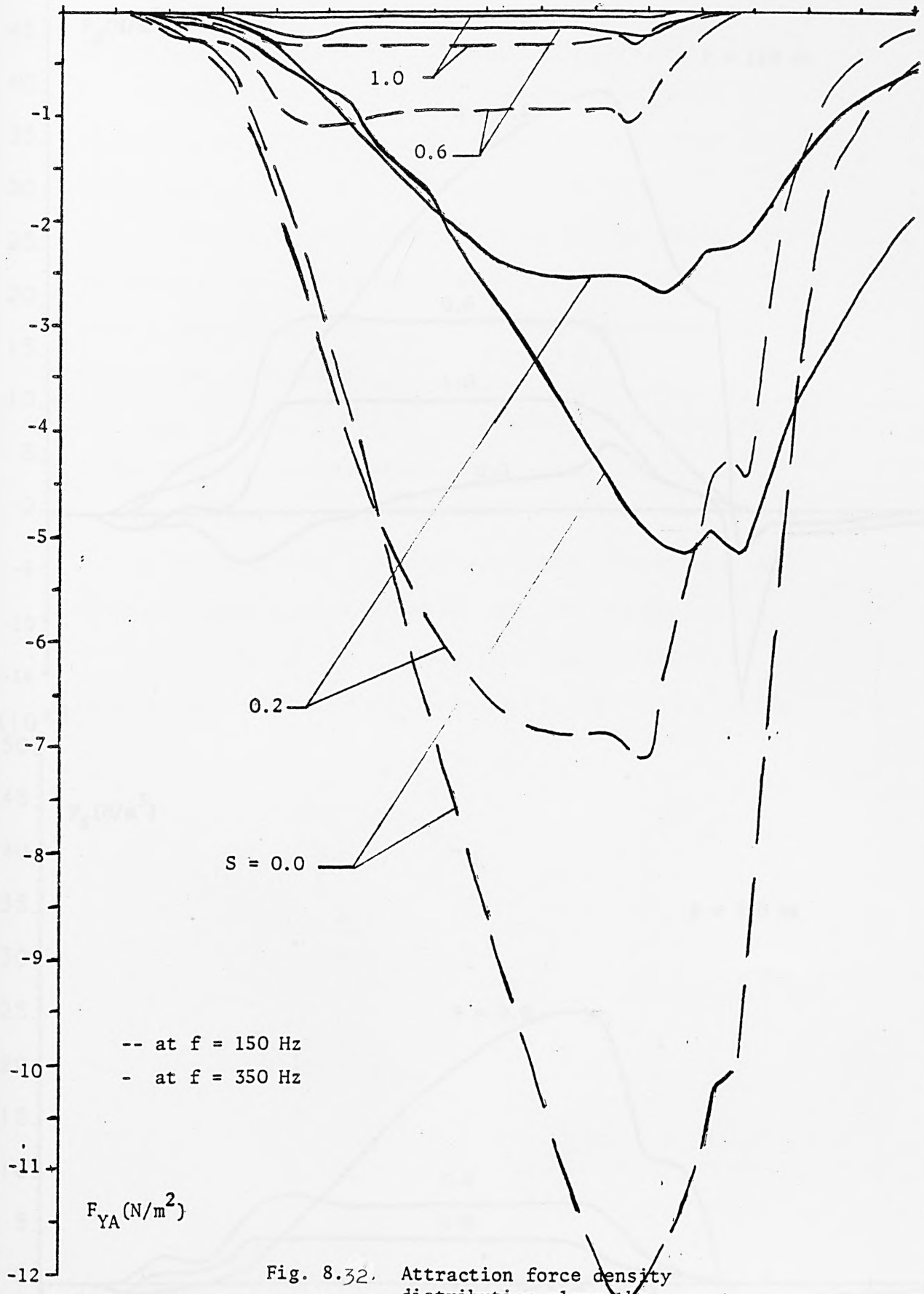

Fig. 8.32. Attraction force density distribution along the x-direction of 3DHM

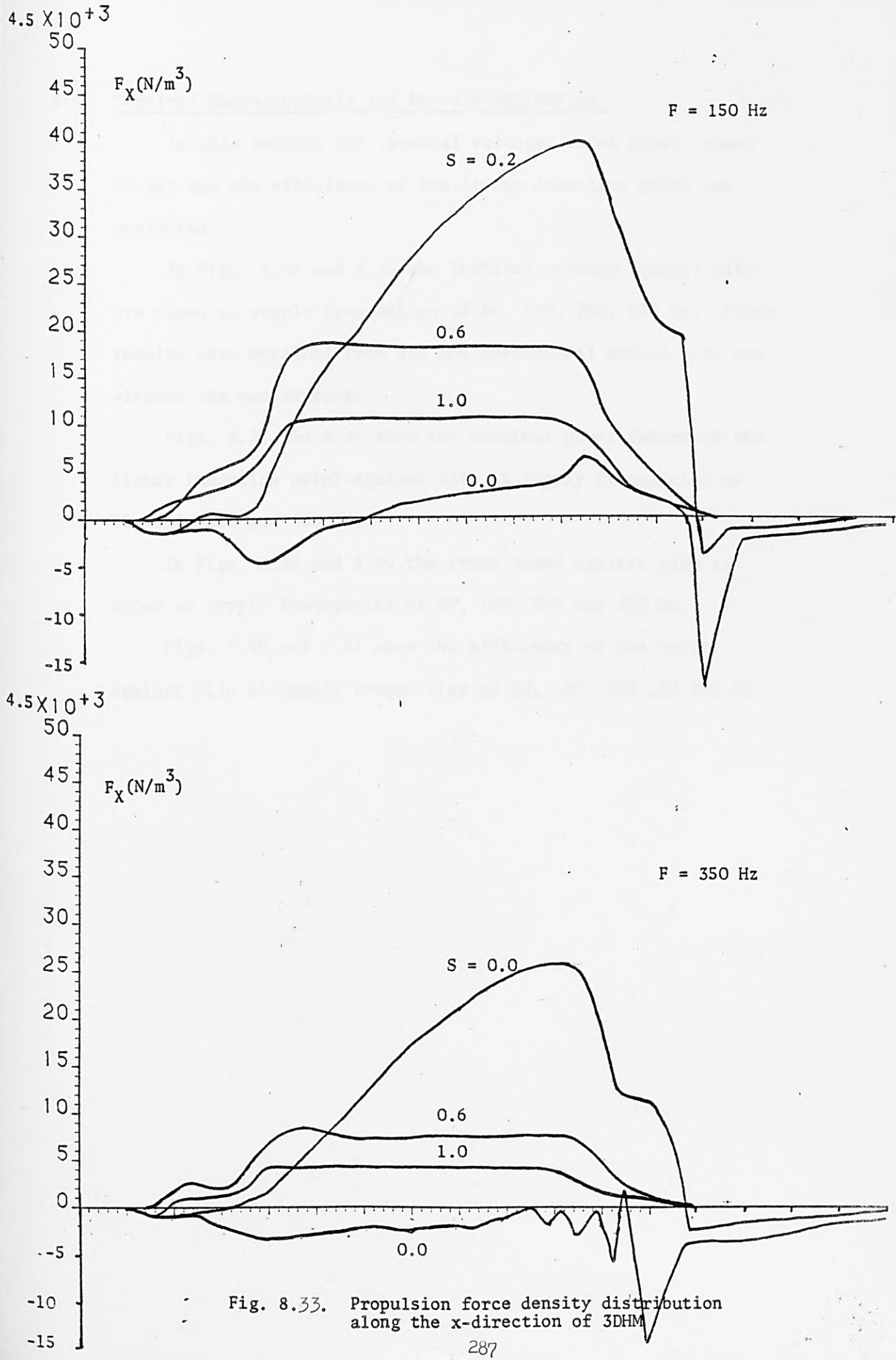

Fig. 8.33. Propulsion force density distribution along the x-direction of 3DHM

8.4 Terminal Characteristic and Power Distributions

In this section the terminal voltage, input power, power factor and the efficiency of the linear induction motor are presented.

In Figs. 8.34 and 8.35 the terminal voltage against slip are shown at supply frequencies of 50, 150, 250, 350 Hz. These results were obtained from all the theoretical models with and without the end effects.

Figs. 8.36 and 8.37 show the terminal power factor of the linear induction motor against slip at supply frequencies of 50, 150, 250 and 350 Hz.

In Figs. 8.38 and 8.39 the input power against slip is shown at supply frequencies of 50, 150, 250 and 350 Hz.

Figs. 7.40 and 7.41 show the efficiency of the motor against slip at supply frequencies of 50, 150, 250 and 350 Hz.

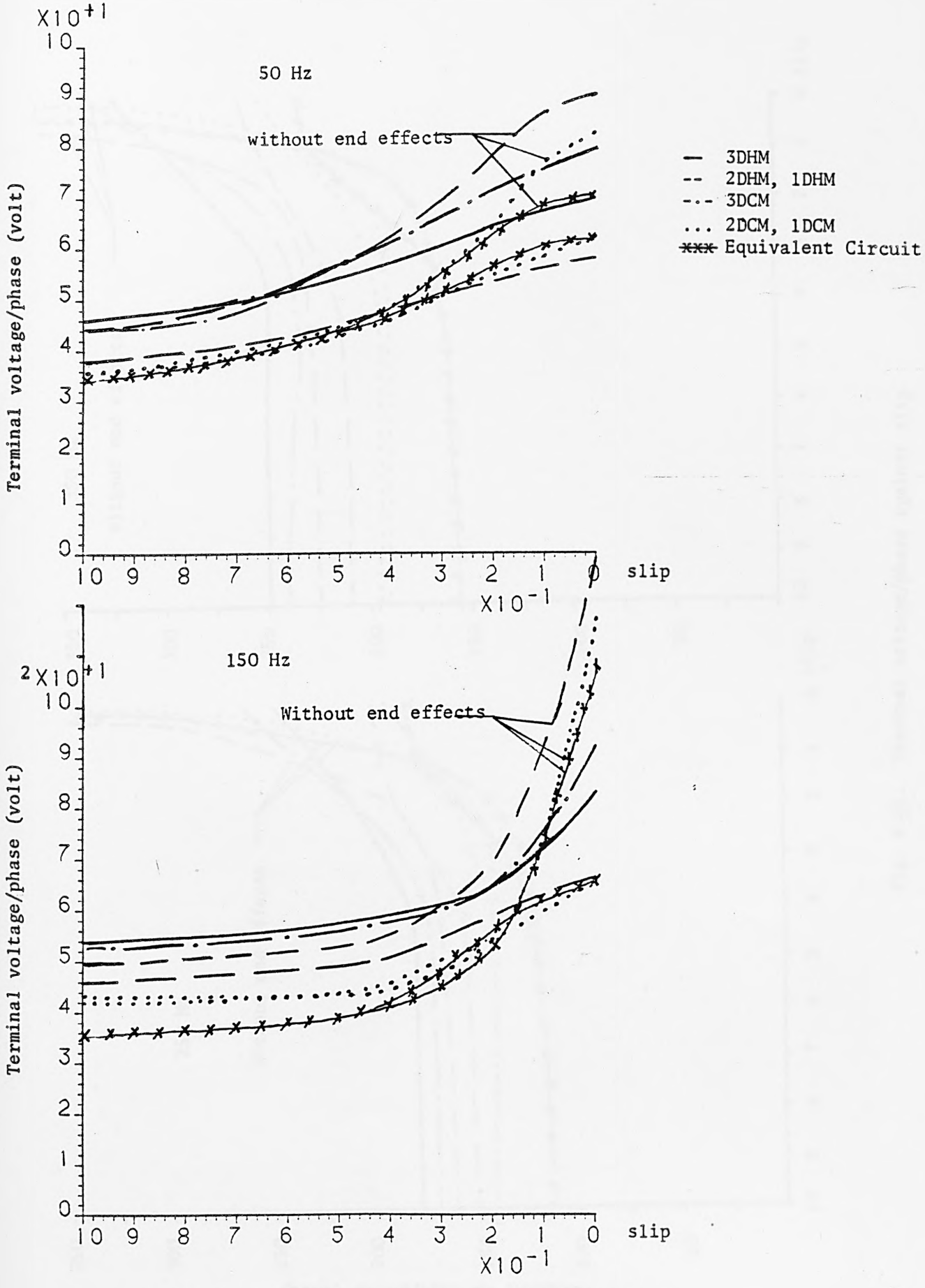

Fig. 8.34. Terminal voltage/phase against slip

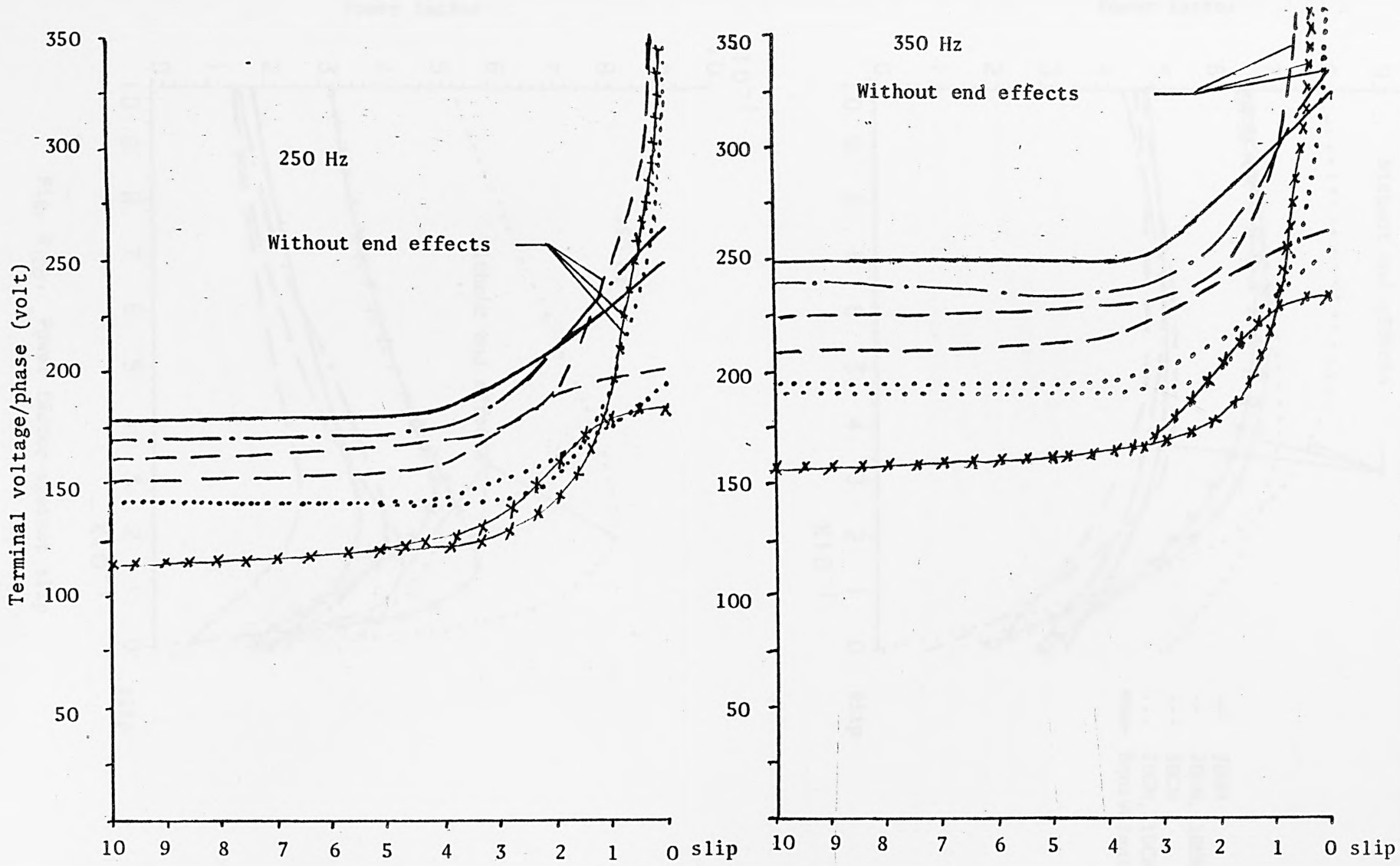

Fig. 8.35. Terminal voltage/phase against slip

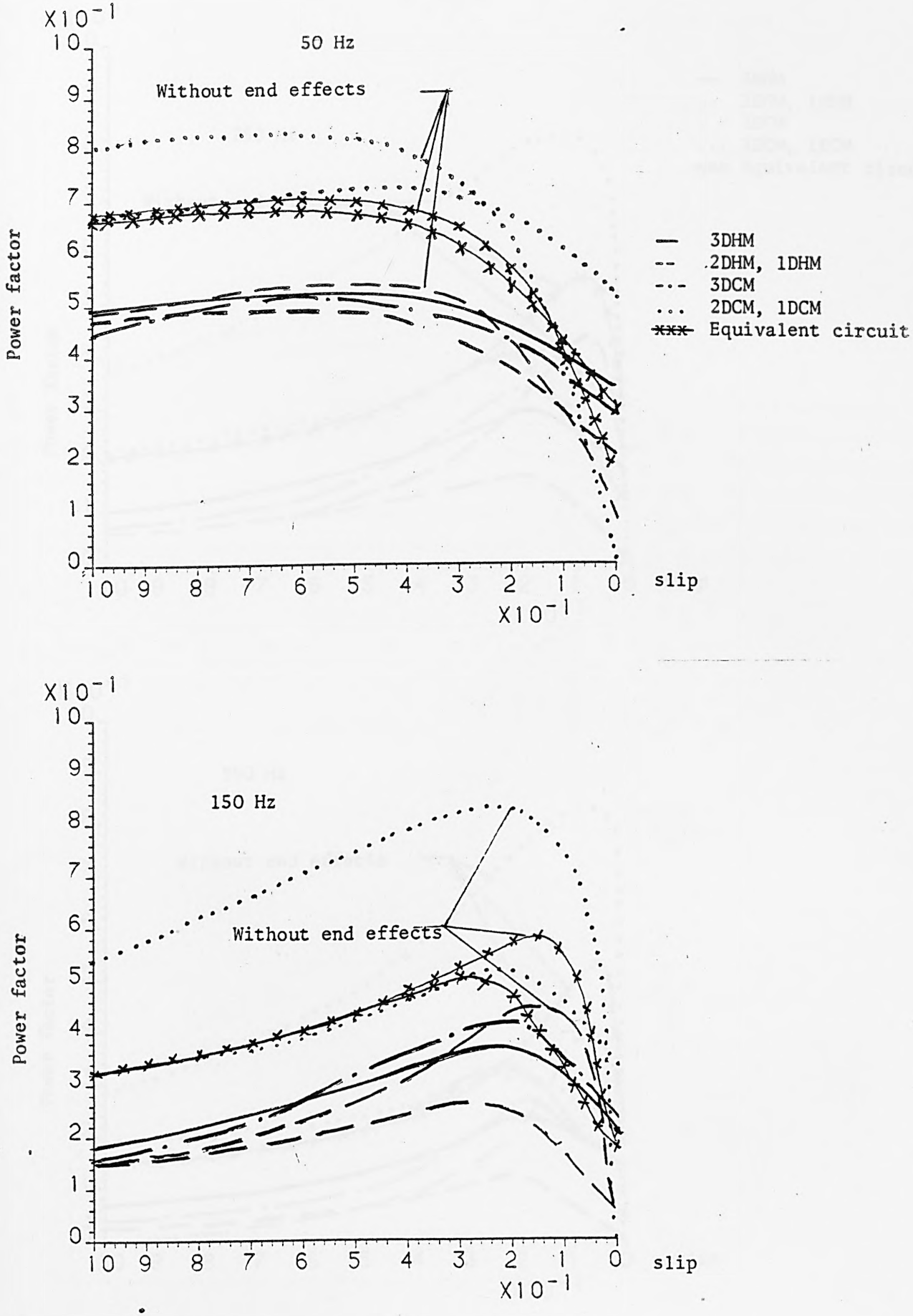

Fig. 8.36. Power factor against slip

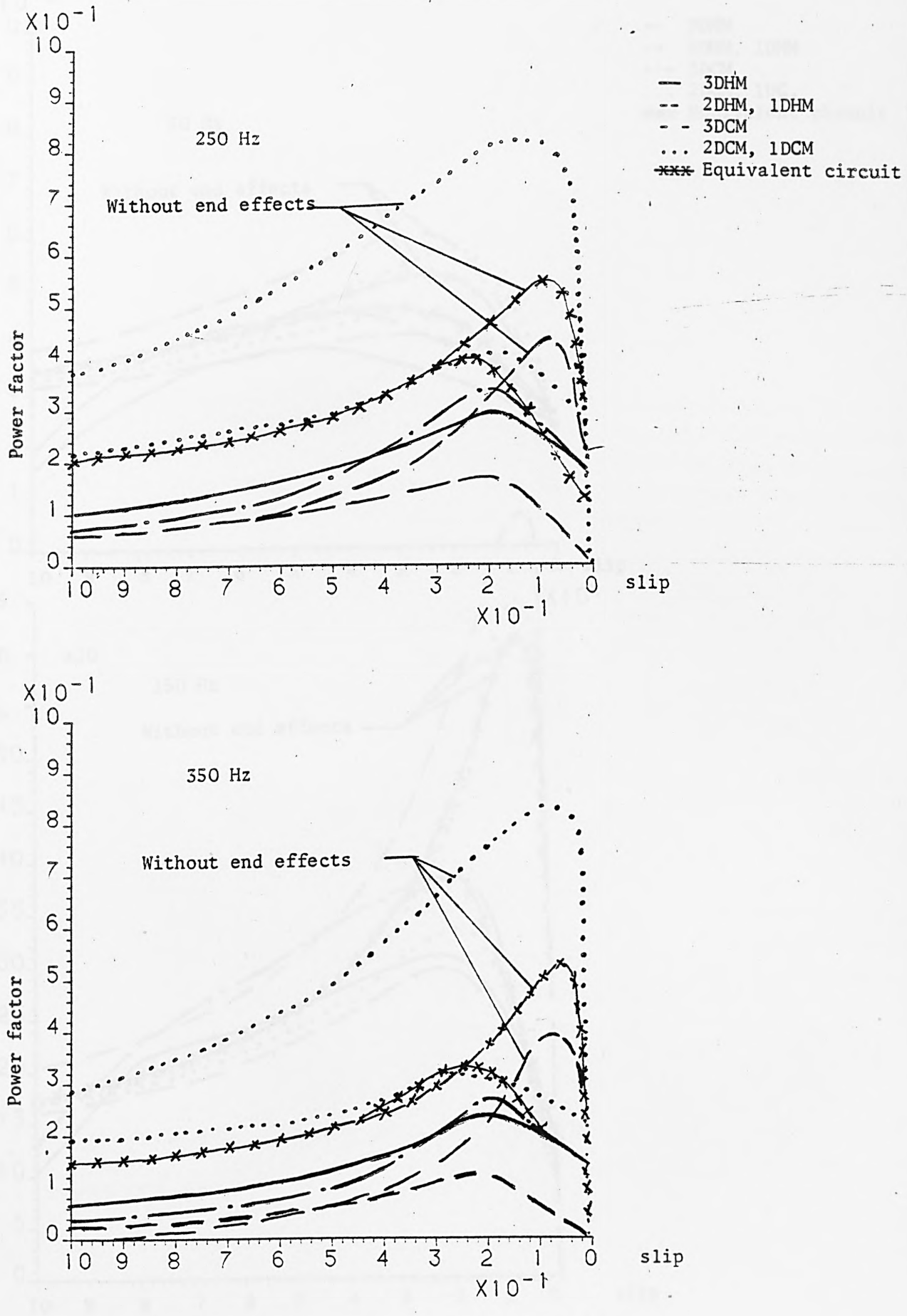

Fig. 8.37. Power factor against slip

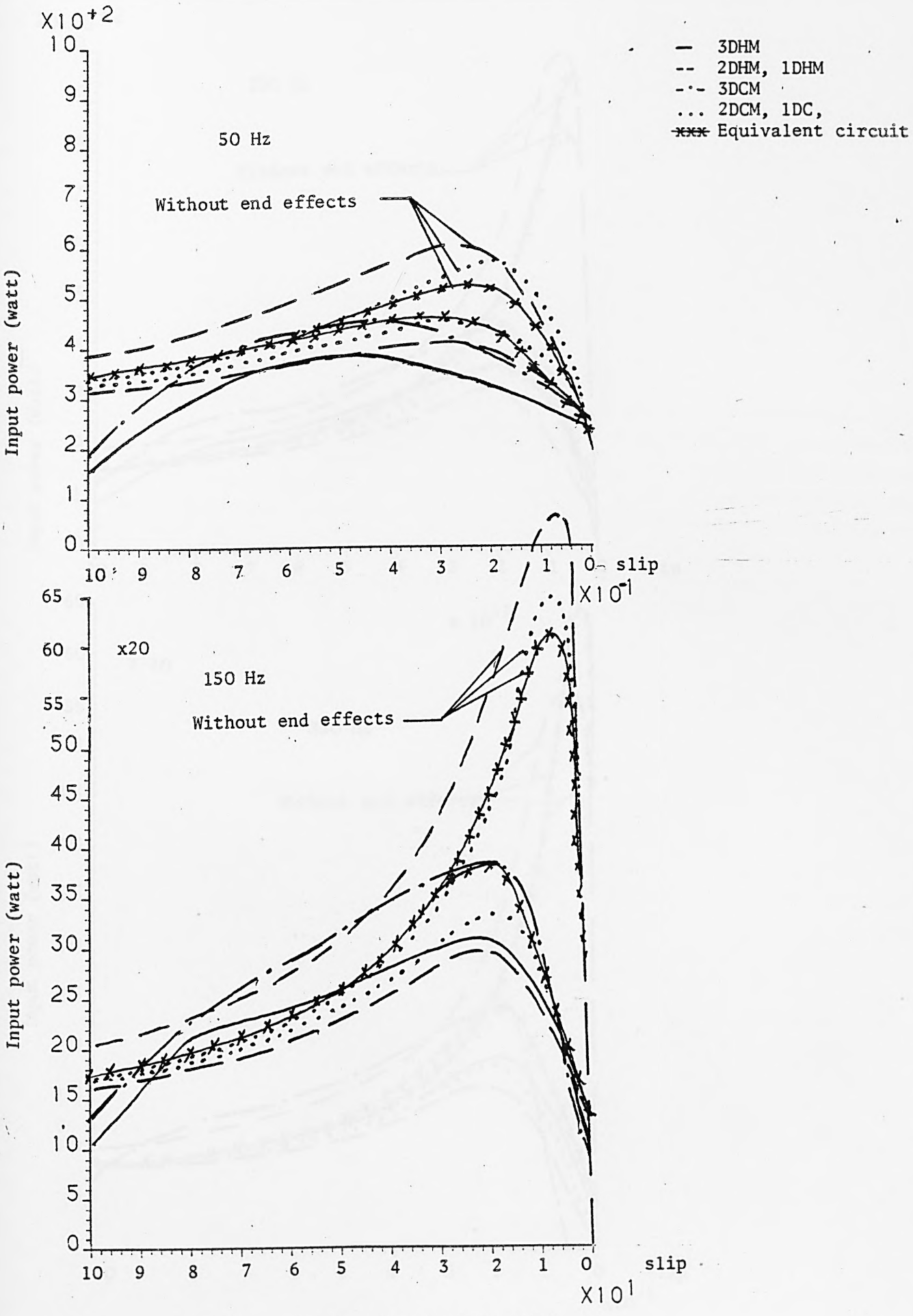

Fig. 8.38. Input power against slip

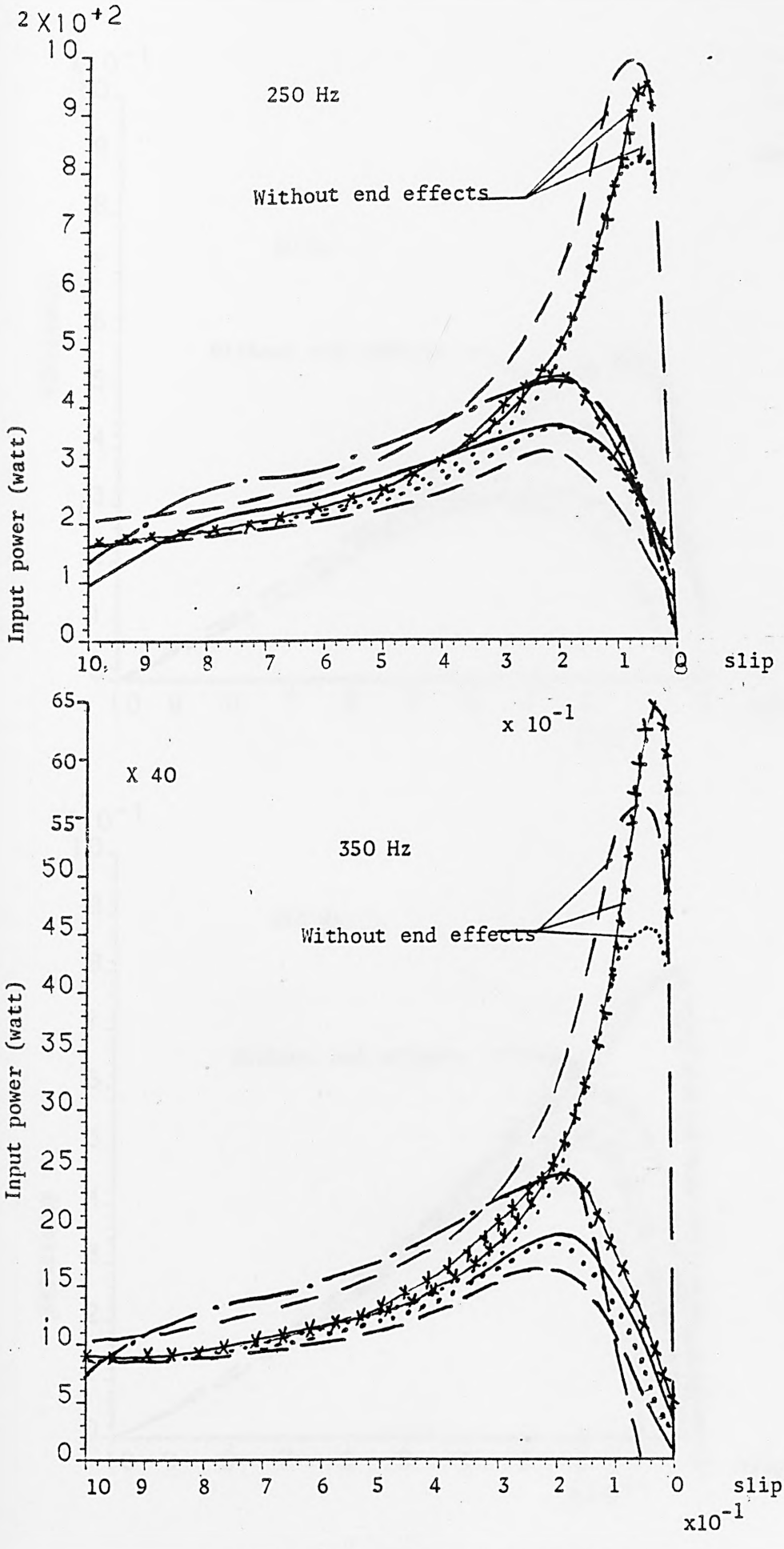

Fig. 8.39. Input power against slip

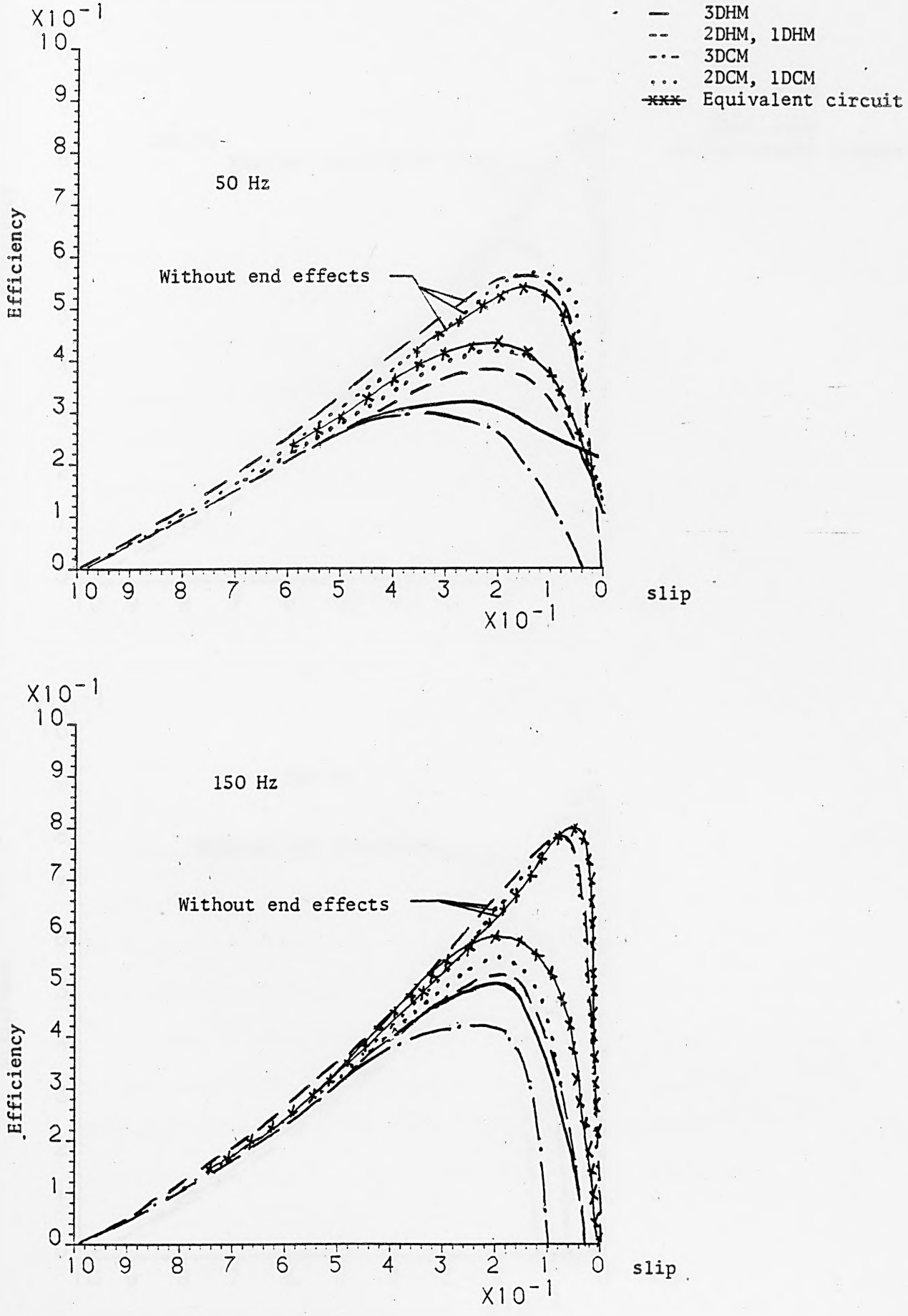

Fig. 8.40. Efficiency against slip

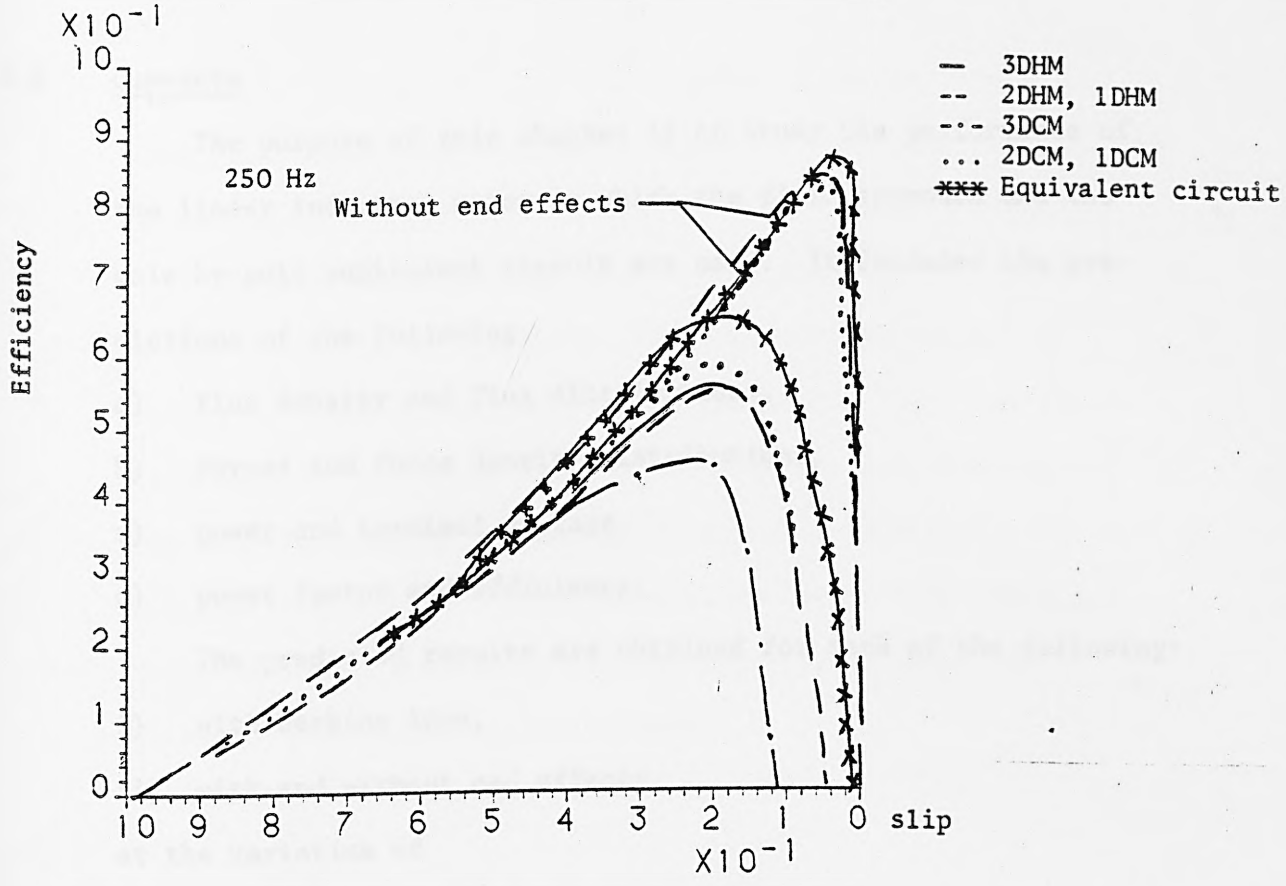

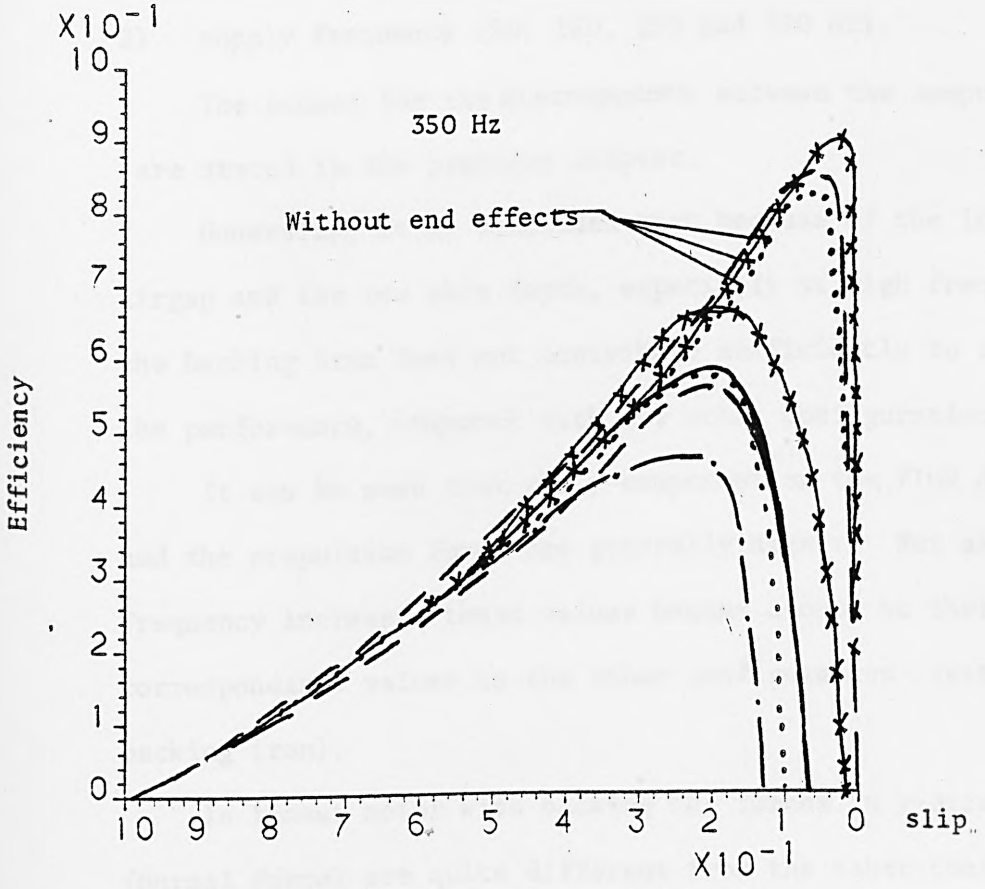

Fig. 8.41. Efficiency against slip

8.5 Comments

The purpose of this chapter is to study the performance of the linear induction motor in which the field approach and the pole-by-pole equivalent circuit are used. It includes the predictions of the following:

a) flux density and flux distributions,

b) forces and force density distributions,

c) power and terminal voltage,

d) power factor and efficiency.

The predicted results are obtained for each of the following:

i) with backing iron,

ii) with and without end effects,

at the variation of

1) slip (linear speed),

2) supply frequency (50, 150, 250 and 350 Hz).

The causes for the discrepances between the computed results are stated in the previous chapter.

Generally, it is concluded that because of the large airgap and the low skin depth, especially at high frequencies, the backing iron does not contribute sufficiently to improve the performance, compared with the other configuration .

It can be seen that the y-component of the flux density and the propulsion force are generally higher. But as the frequency increases these values become closer to their correspondance values in the other configuration (without backing iron).

In linear motor with backing the forces in y-direction (normal force) are quite different from the other configuration.

It is seen in the previous chapter, that the primary, under most operating conditions, exerts a repulsion force on the secondary.

However, with backing iron, the primary winding exerts either repulsion or attraction force on the secondary. At standstill, the linear motor may experience a repulsion force; this depends on factors such as conductivity and thickness of the secondary and on the supply frequency. As the slip is reduced or the speed of the machine increases, this repulsion force falls and eventually becomes negative in which the primary is attracted to the secondary.

CHAPTER 9

STUDY OF FURTHER CASES

9.1 Introduction

This chapter includes studies on certain aspects of the linear induction motor which are outside the scope of the results presented in chapters seven and eight.

These studies include:

a) change in the secondary topology

b) composite reaction plate

c) skin and transverse edge effects

d) longitudinal end effects

e) constant current and voltage drives

The linear motor which used in these studies is of the same specifications as the one examined in the previous chapters. Unless otherwise stated, the predicted results were obtained for a LIM of a constant current drive of 5A per phase (35.34 kA/m), with a series connected primary winding, half-filled end slots, an air gap length of 9.5 mm and a secondary conductor of pure aluminium of 3.17 mm thickness and a conductivity of 3.54×10^7 Ω/m.

9.2 Change in the Topology of the Secondary

The cases which are examined in this section are:

a) change in the conductivity of the secondary conductor,

b) change in the thickness of the secondary conductor,

c) change in the air gap length,

d) change in the medium backing the secondary conductor

In conventional induction motors, a high starting torque demands correspondingly larger rotor resistance, and the maximum torque that a motor can develop is independent of the secondary resistance. However, the maximum torque occurs at a slip which is directly proportional to the secondary resistance. This behaviour can be seen in Fig. 9.1 for a performance without end effects.

The propulsion force-speed characteristice of a linear induction motor are affected significantly by the changes in the conductivity of the secondary (see Fig. 9.1). The propulsion force including its peak value is increased by using a low conductivity material for the reaction plate, because the degree of penetration of the main flux into the secondary conductor is better with a low conductivity plate.

Similar results are obtained when the thickness of the secondary conductor is varied . Fig. 9.2 shows the propulsion force-speed characteristics for different thicknesses of the secondary conductor. These results are explained by the fact that the performance of the motor can be improved as the thickness of the secondary conductor is less than the skin depth of the flux penetration.

The effect of air gap length on the propulsion force-speed characteristics is shown in Fig. 9.3. An increase in air gap length increases the magnetizing current which results in a poorer performance.

The characteristics presented in Figs. 9.1 to 9.3 were obtained from the equivalent circuit approach for both with and without end effects.

Fig. 9.4. shows the propulsion force-speed characteristics obtained from the homogeneous anisotropic/isotropic models 1DHM and 3DHM. The results are presented again in this chapter in order to show the change in the performance of a linear motor with backing iron on the secondary conductor for both with and without end effects. It is seen from the figure that the thrust without end effects is considerably increased by the use of backing iron. However, with end effects the response of the propulsion force-speed characteristics to the backing iron is rather different. Fig. 9.5 shows the ratio of the maximum propulsion force with and without backing iron against the frequency. It can be seen that the ratio remains constant for a conventional characteristic (without end effects), while with end effects, the ratio reduces as the frequency increases. These results conclude that the existence of the backing iron for a high speed linear motor is less effective, especially for a large air gap and a low skin depth.

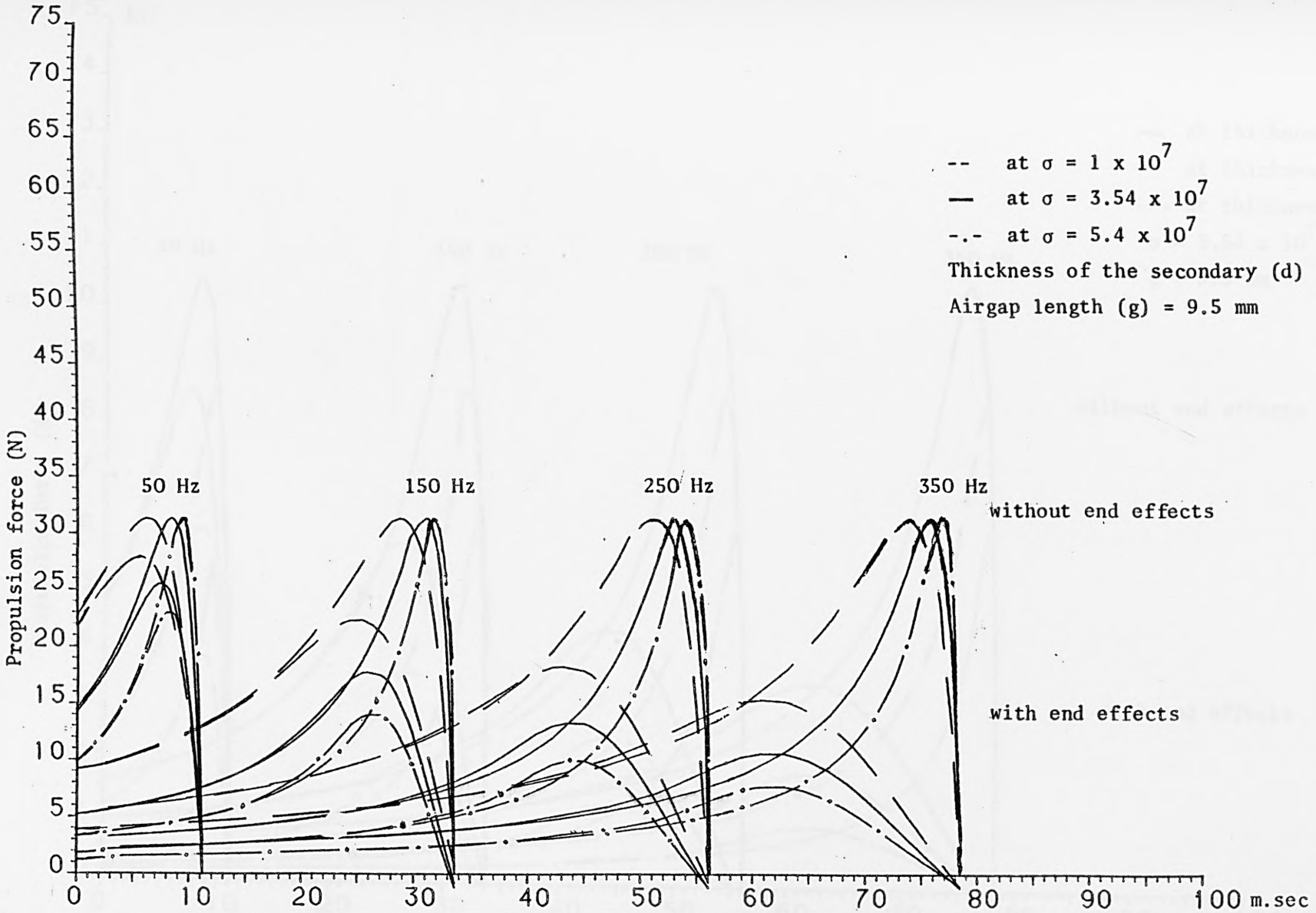

Fig. 9.1. Propulsion force-speed characteristics of the LIM for different conductivities of secondary conductor

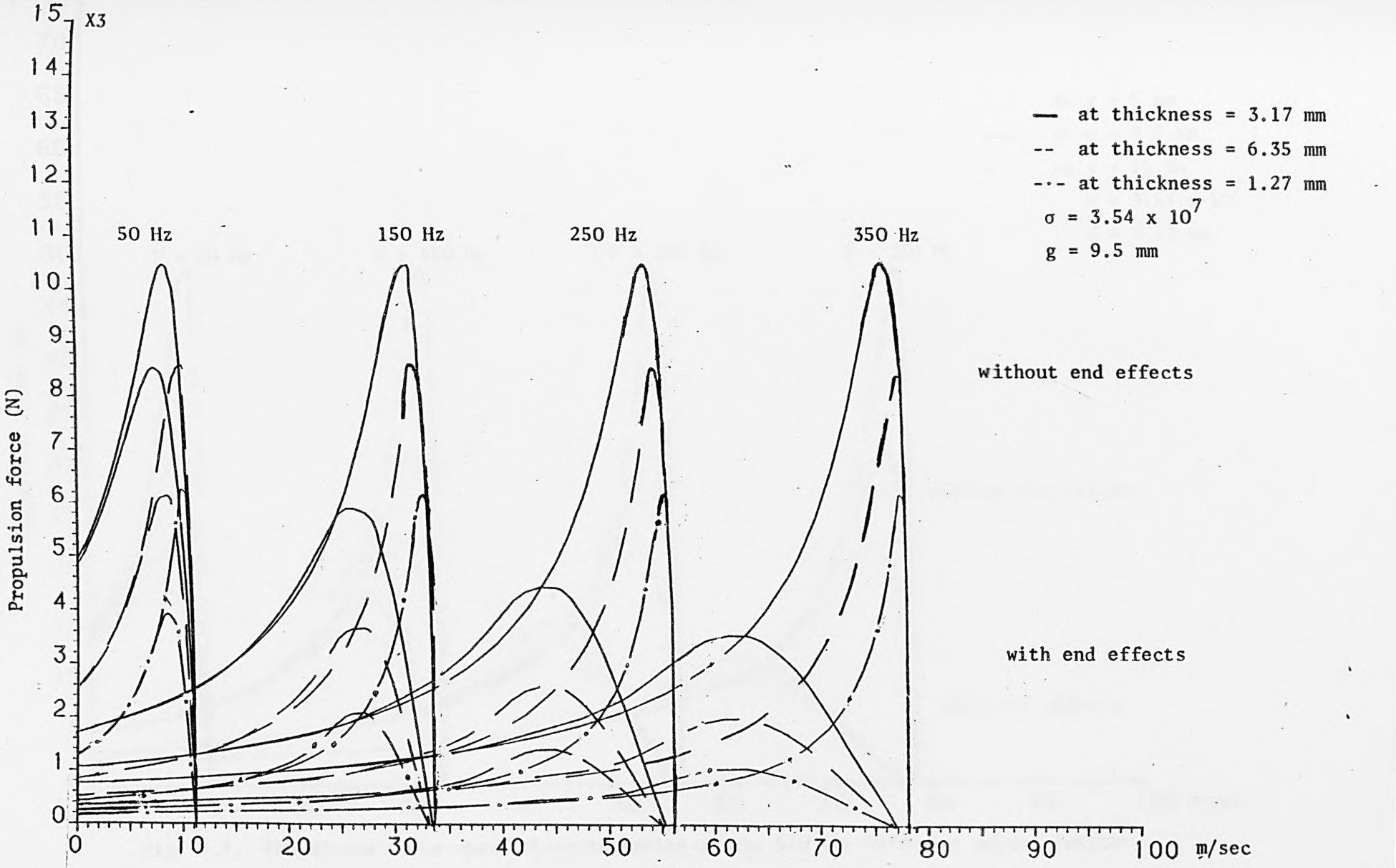

Fig. 9.2. Propulsion force-speed characteristics of the LIM for different thicknesses of secondary conductor

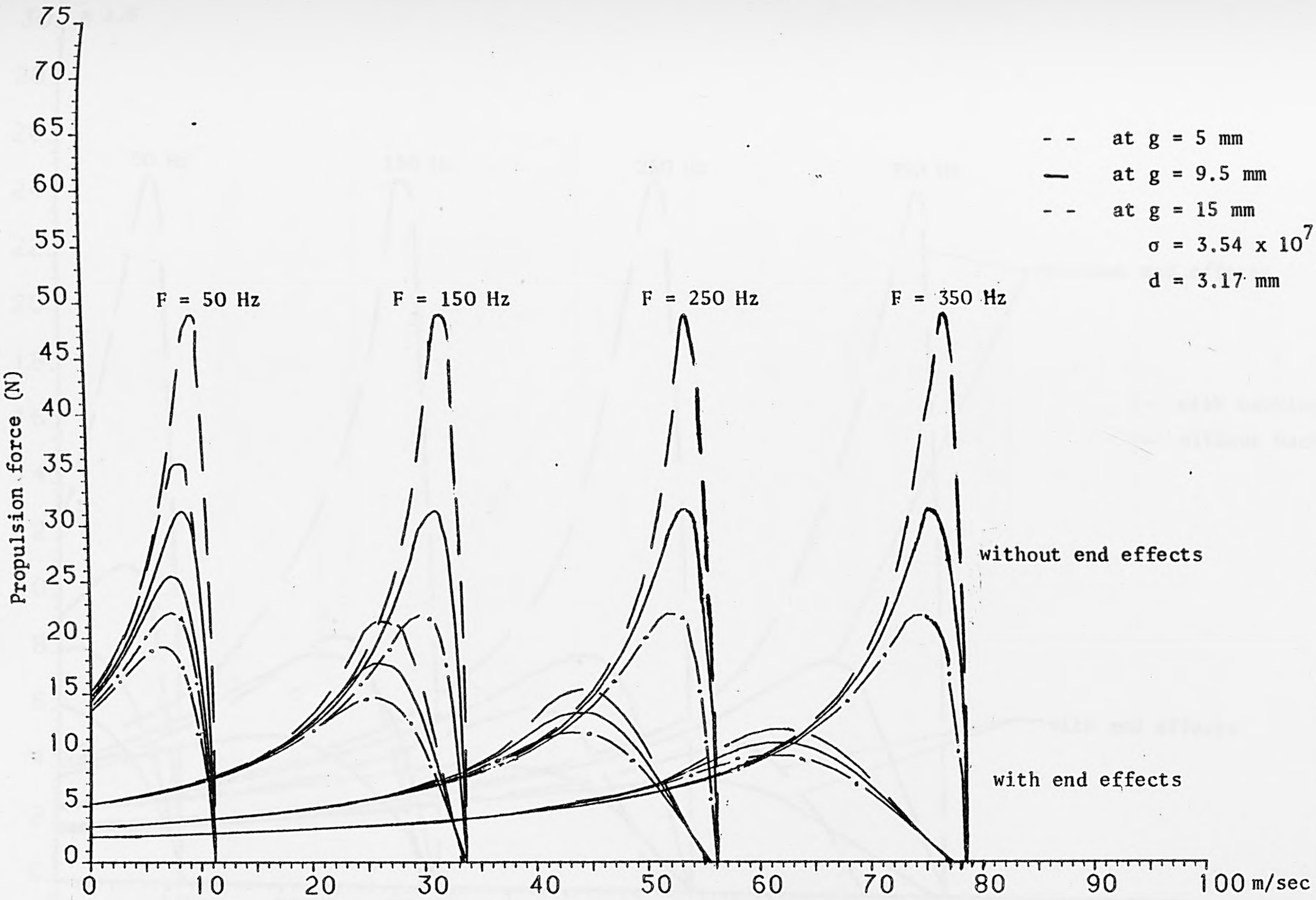

Fig. 9.3. Propulsion force-speef characteristics of the LIM for different airgap lengths

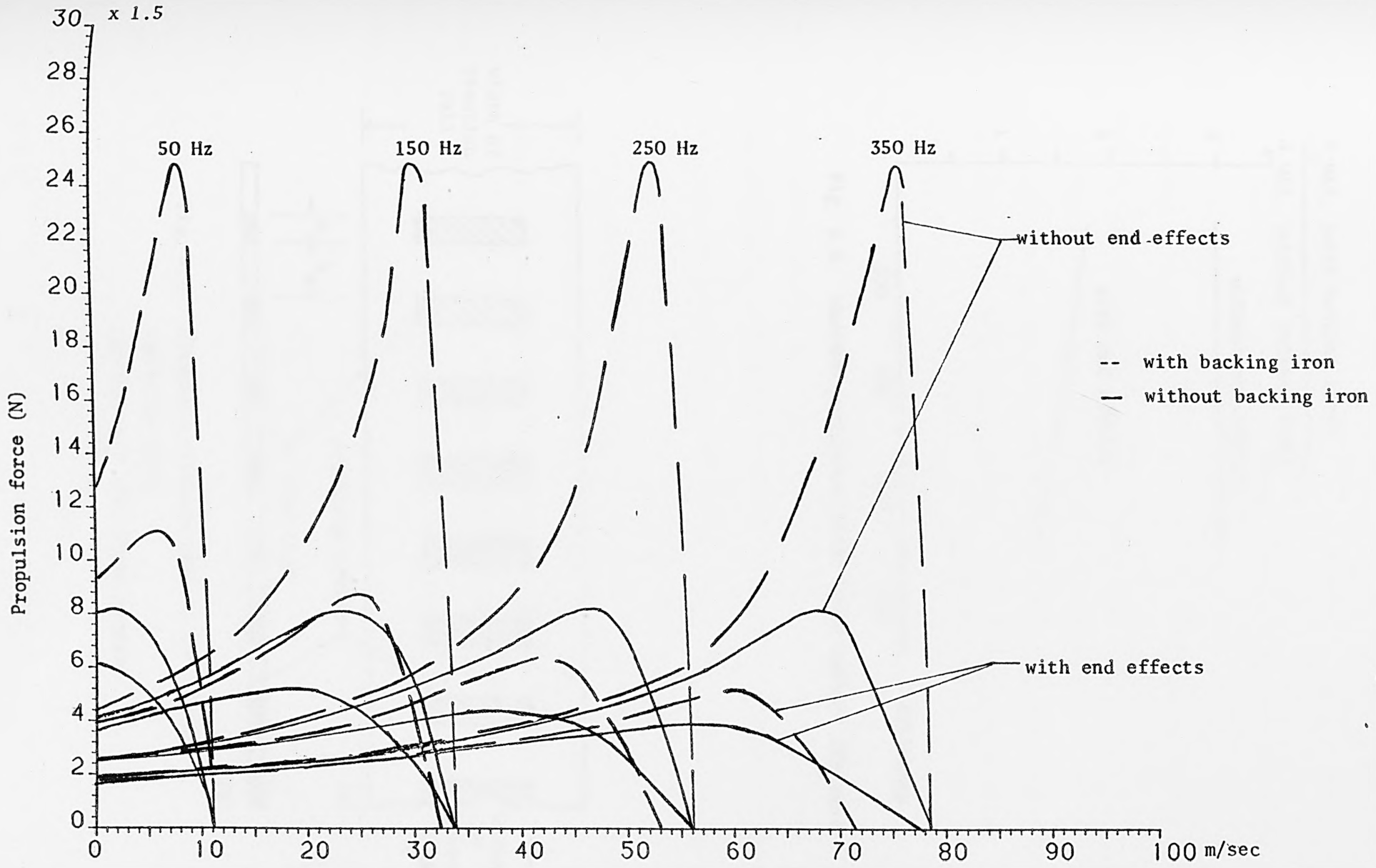

Fig. 9.4. Propulsion force-speed characteristics of the LIM with and without backing iron, using the 1DHM and 3DHM models

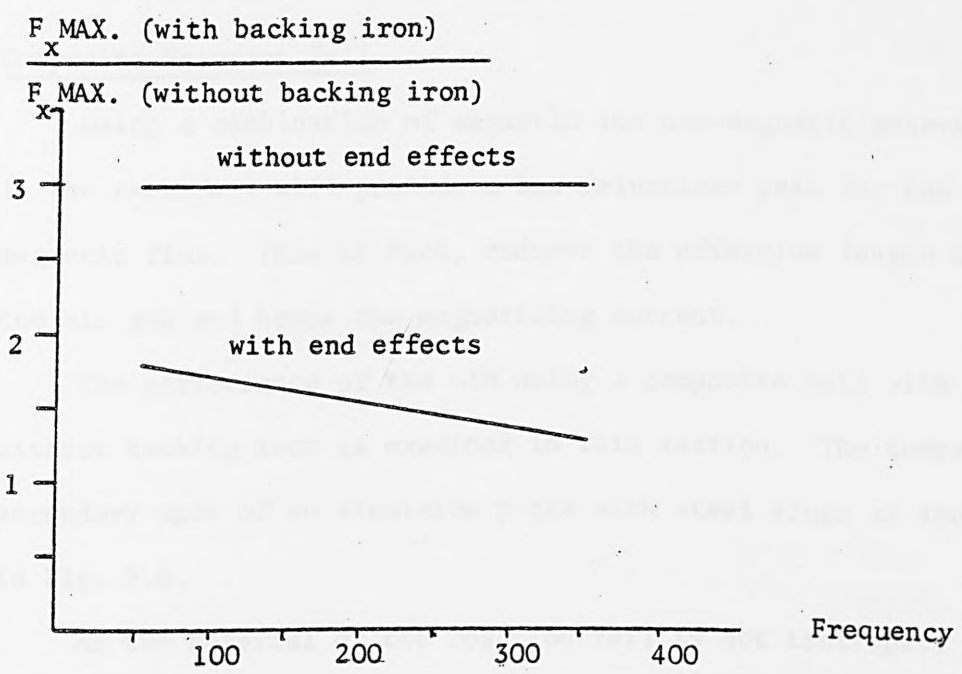

Fig. 9.5. Maximum propulsion force ratio against frequency

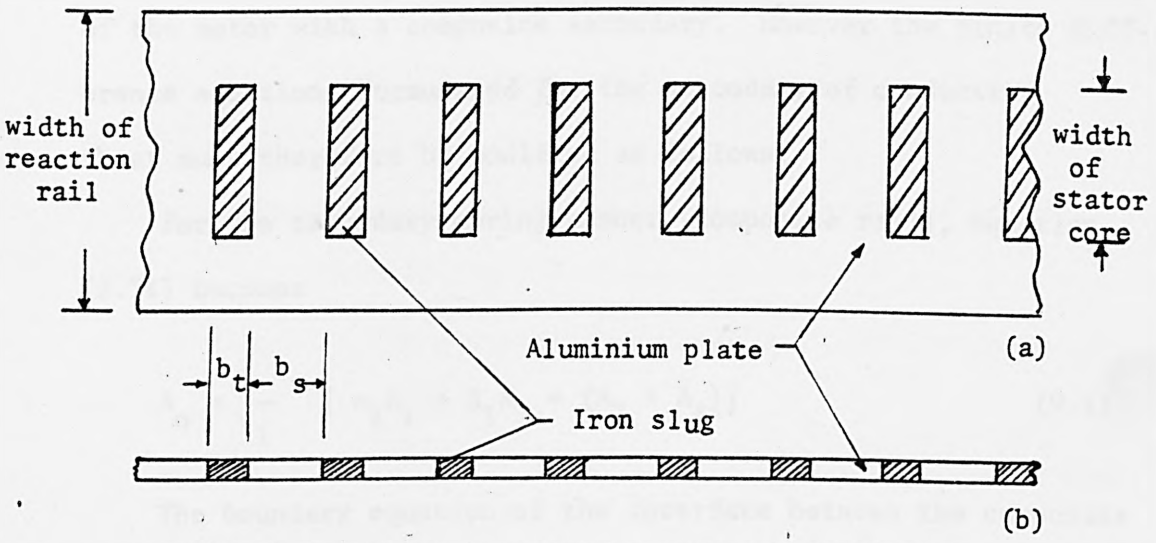

Fig. 9.6. Composite reaction rail of the linear induction motor
(a) Top view (b) Cross section

9.3 Composite Reaction Rail

Using a combination of magnetic and non-magnetic materials in the secondary will provide a low reluctance path for the magnetic flux. This in fact, reduces the effective length of the air gap and hence the magnetizing current.

The performance of the LIM using a composite rail with and without backing iron is examined in this section. The composite secondary made of an aluminium plate with steel slugs as shown in Fig. 9.6.

As the material of the reaction rail is not isotropic, it has different magnetic reluctance in both x and y directions. The permeabilities and the conductivity of the composite secondary are determined by the same expressions stated in chapter two which are used for the homogeneous anisotropic mass of the primary windings.

A two-dimensional model 2DHM is used to study the performance of the motor with a composite secondary. However the finite difference equations formulated for the secondary of conducting sheet must therefore be modified as follows:

For the secondary moving member (composite rail), equation (3.74) becomes

$$A_o = \frac{1}{\gamma_1} \left[\alpha_1 A_1 + \beta_1 A_3 + (A_2 + A_4) \right] \qquad (9.1)$$

The boundary equation of the interface between the composite rail and the air gap becomes

$$A_o = \frac{1}{\gamma_1 + 2S5(q^2+1)} \left[(q^2 S5 + \alpha_1) A_1 + (q^2 S5 + \beta_1) A_3 + 2 (\mu_{sy} A_2 + S5 A_4) \right] \qquad (9.2)$$

and the boundary equation of the interface between the composite rail and the backing iron becomes:

$$A_o = \frac{1}{\gamma_1 + 2S6(q^2+1)} [(q^2 S6 + \alpha_1)\cdot A_1 + (q^2 S6 + \beta_1)\cdot A_3 + 2\cdot(\mu_{sy} A_4 + S6 A_2)]$$

where $S5 = \mu_{sx}\,\mu_{sy}$

$S6 = \mu_{sx}\,\mu_{sy}/\mu_i$

$\gamma_1 = (2(q^2\mu_{sx} + \mu_{sy}) + j\omega\sigma_z q^2 h^2 \mu_o \mu_{sx} \mu_{sy})$

$\alpha_1 = q^2\mu_{sx}(1. - 0.5\ \mu_o\mu_{sy}\sigma_z\ hV_x)$

$\beta_1 = q^2\mu_{sx}\ (1. + 0.5\ \mu_o\mu_{sy}\sigma_z\ hV_x)$

σ_z = conductivity of the composite rail

μ_{sx} and μ_{sy} = permeabilities of the composite rail in the x and y directions respectively

The propulsion force-speed characteristics of the LIM using a composite secondary are shown in Figs. 9.7 and 9.8 with and without backing iron respectively.

In Figs. 9.9 and 9.10 the resultant force in y-direction at the above conditions are shown.

The terminal characteristics of the motor using a composite secondary are shown in Figs. 9.11 and 9.12.

In Fig. 9.13 the magnitude and phase shift of the induced emf of each phase are presented.

It can be concluded from the last results that with the composite rail the performance of the linear induction motor with and without end effects is improving significantly.

The efficiency and the power factor of the two configurations of the linear motor (with and without backing iron) are increasing almost for all level of speeds when the composite rail is used.

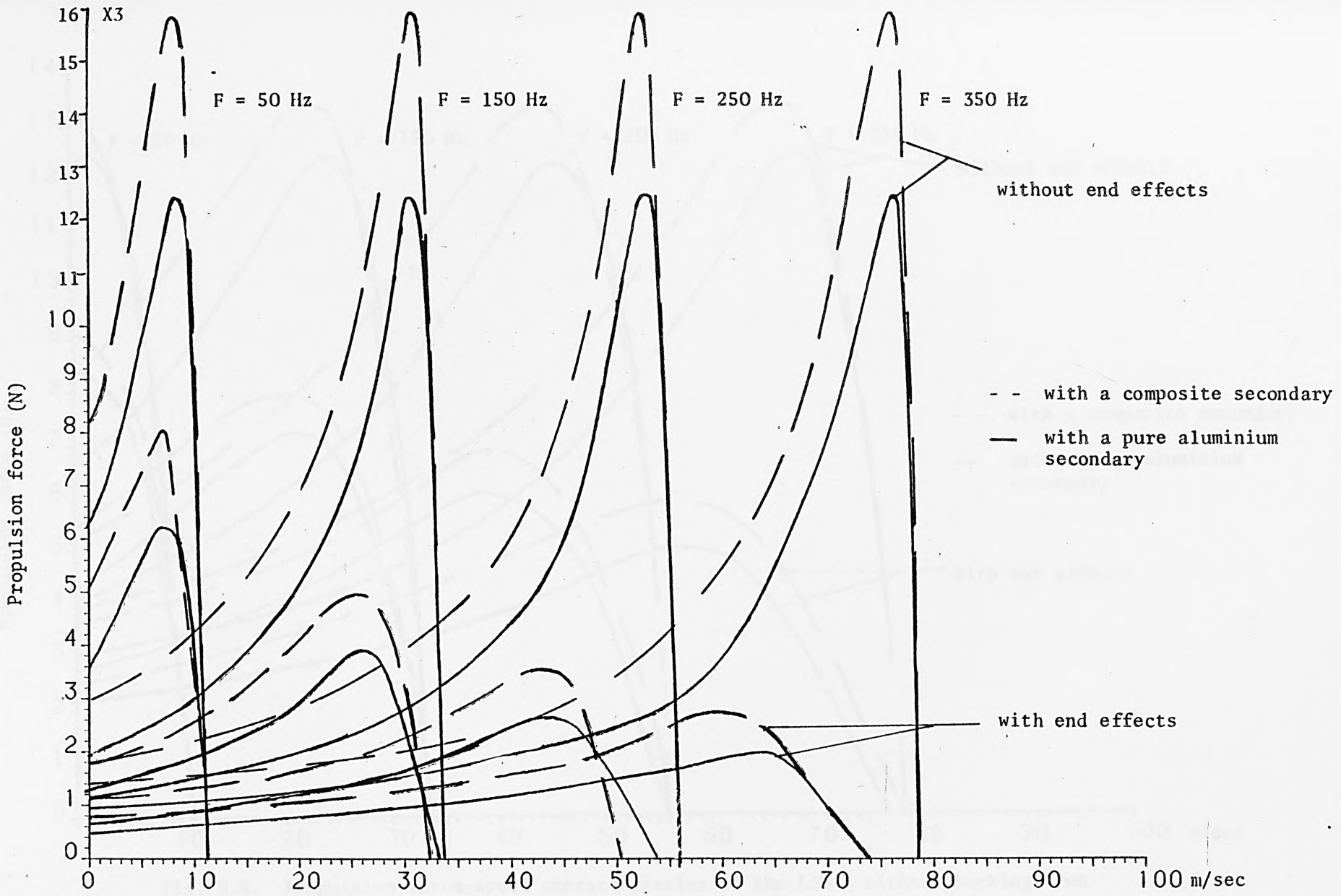

Fig. 9.7. Propulsion force-speed characteristics of the LIM - with backing iron

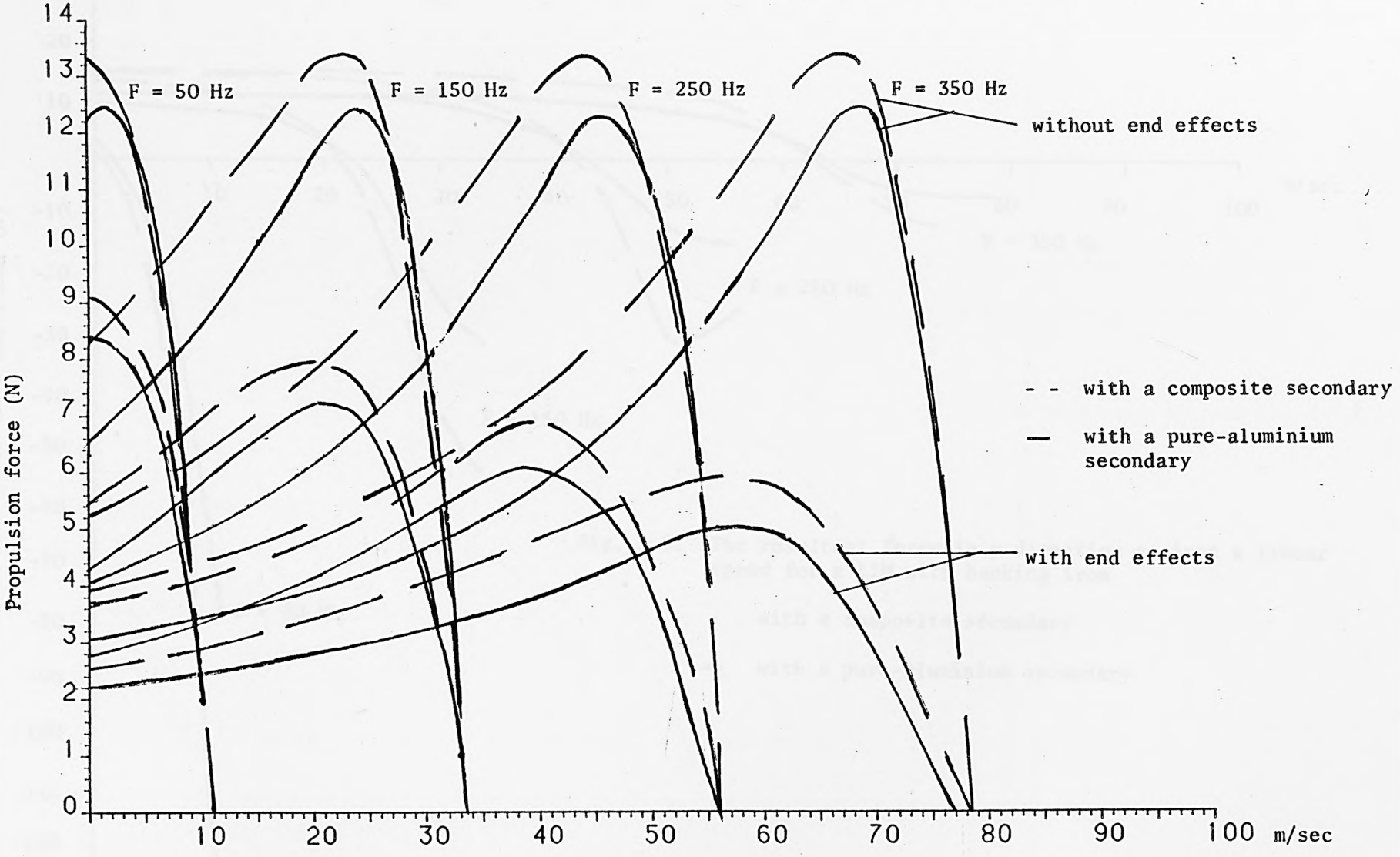

Fig. 9.8. Propulsion force-speed characteristics of the LIM - without backing iron

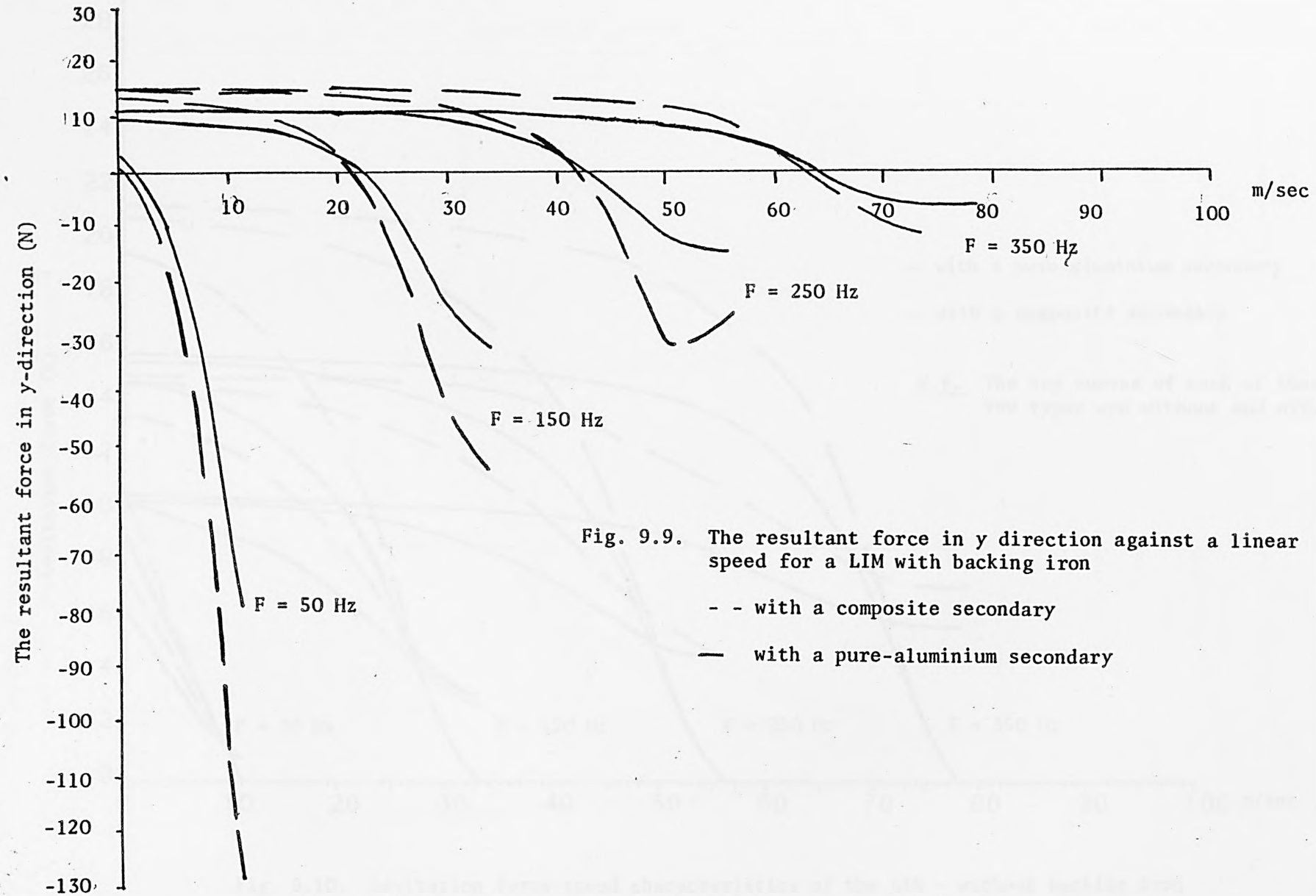

Fig. 9.9. The resultant force in y direction against a linear speed for a LIM with backing iron

- - with a composite secondary

— with a pure-aluminium secondary

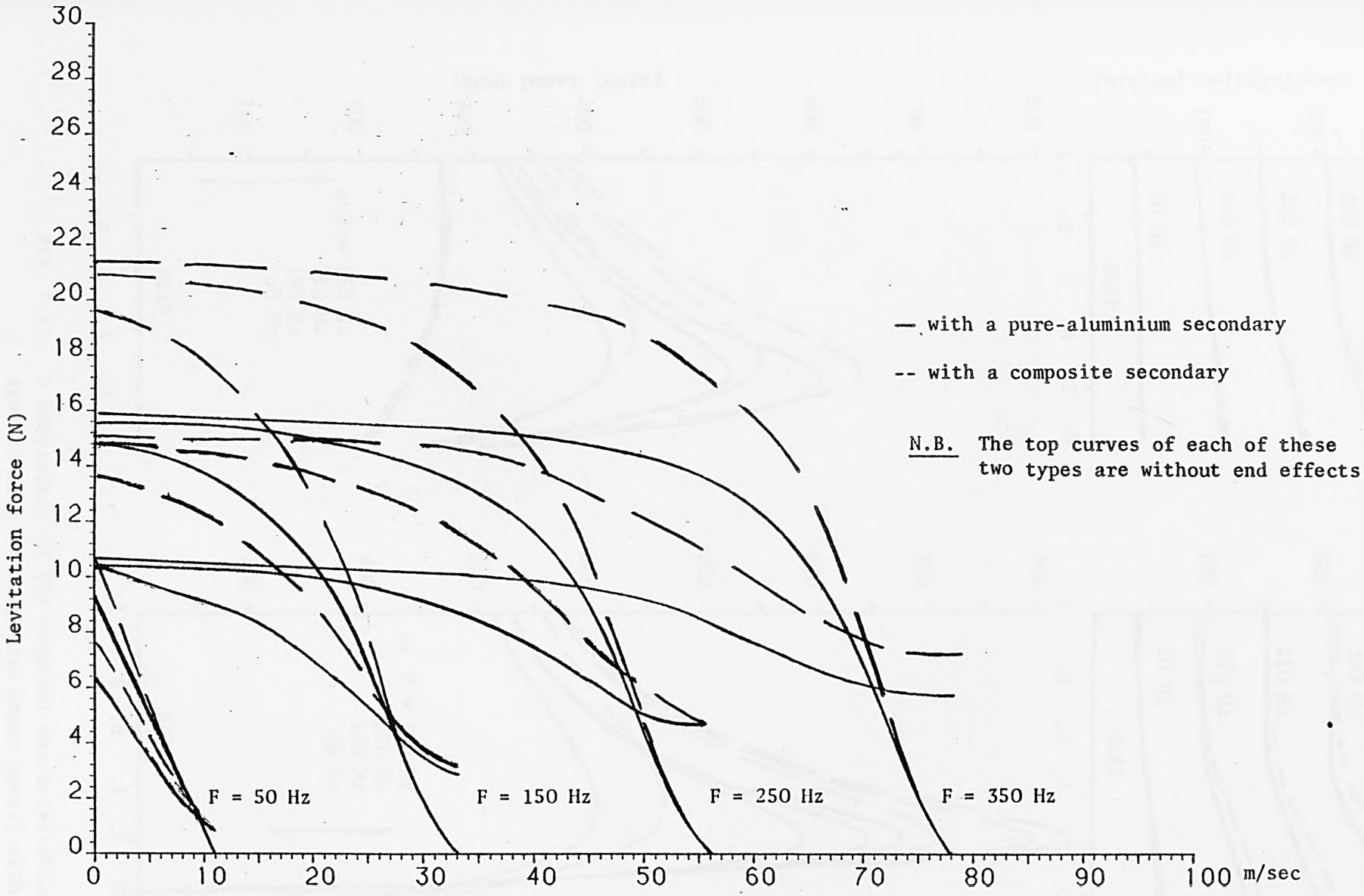

Fig. 9.10. Levitation force-speed characteristics of the LIM - without backing iron

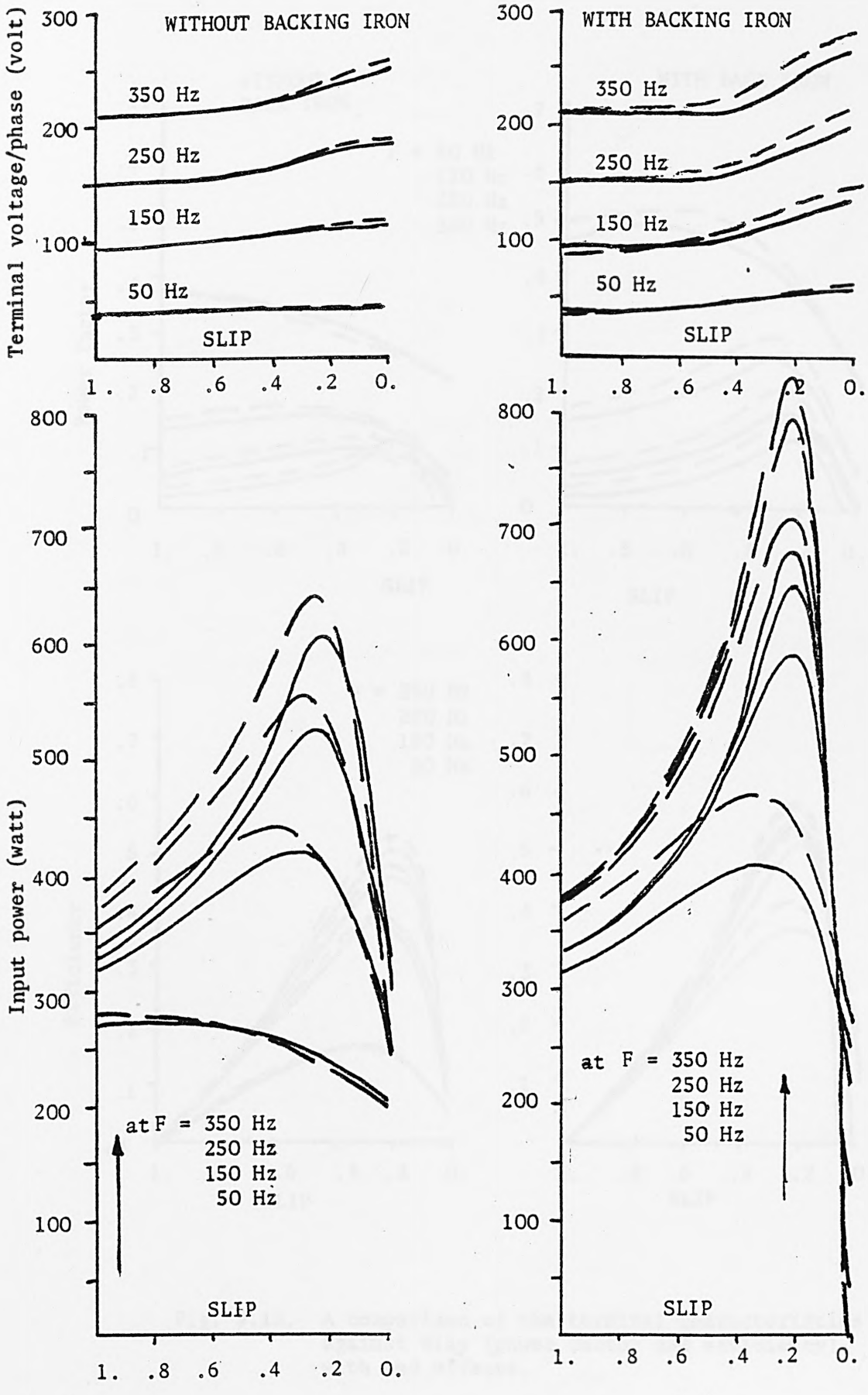

Fig. 9.11. A comparison of the terminal characteristics against slip (voltage and input power) with end effects. -- with a composite
— with a pure aluminum

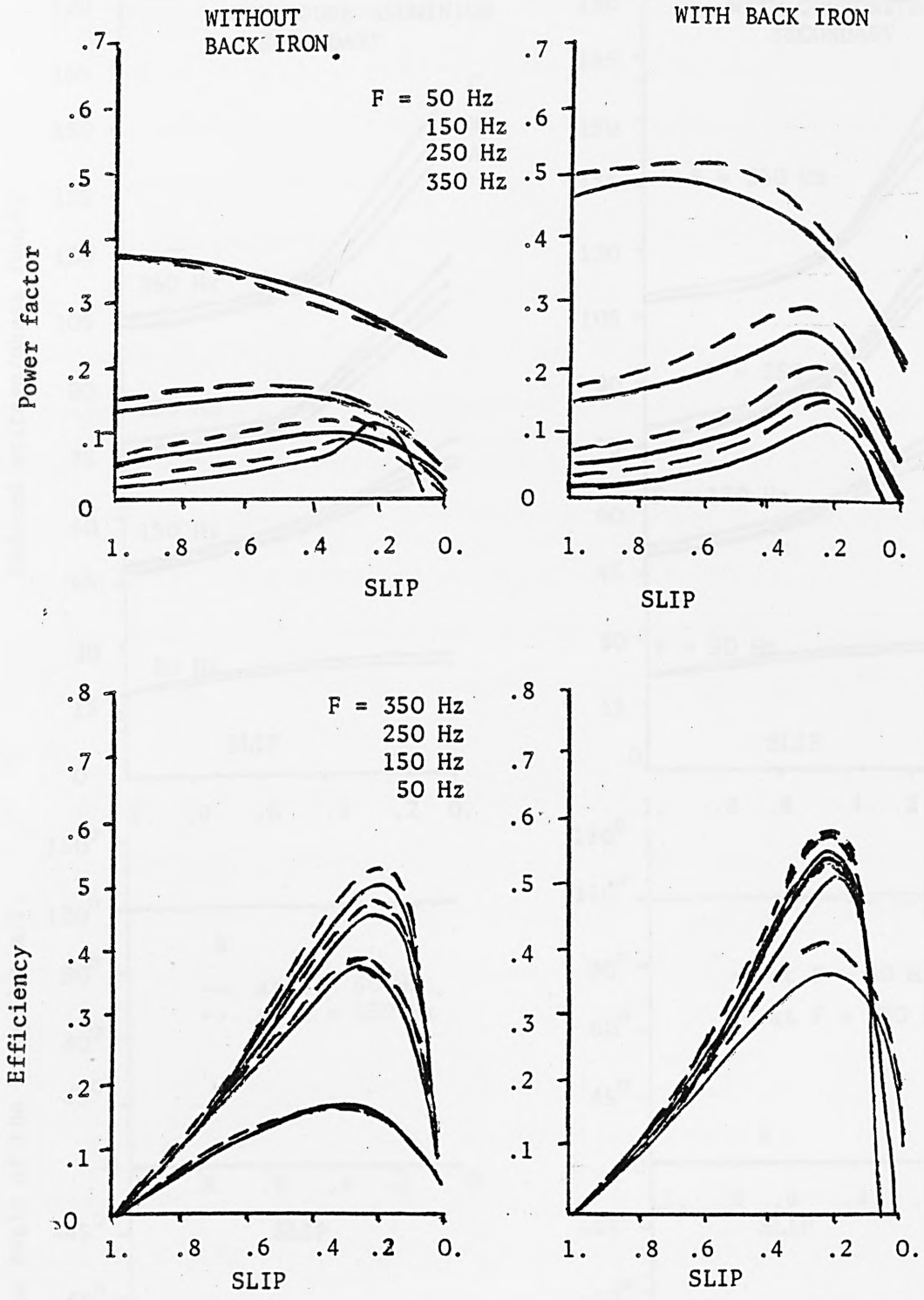

Fig. 9.12. A comparison of the terminal characteristics against slip (power factor and efficiency), with end effects.

- - with a composite, — with a pure aluminium

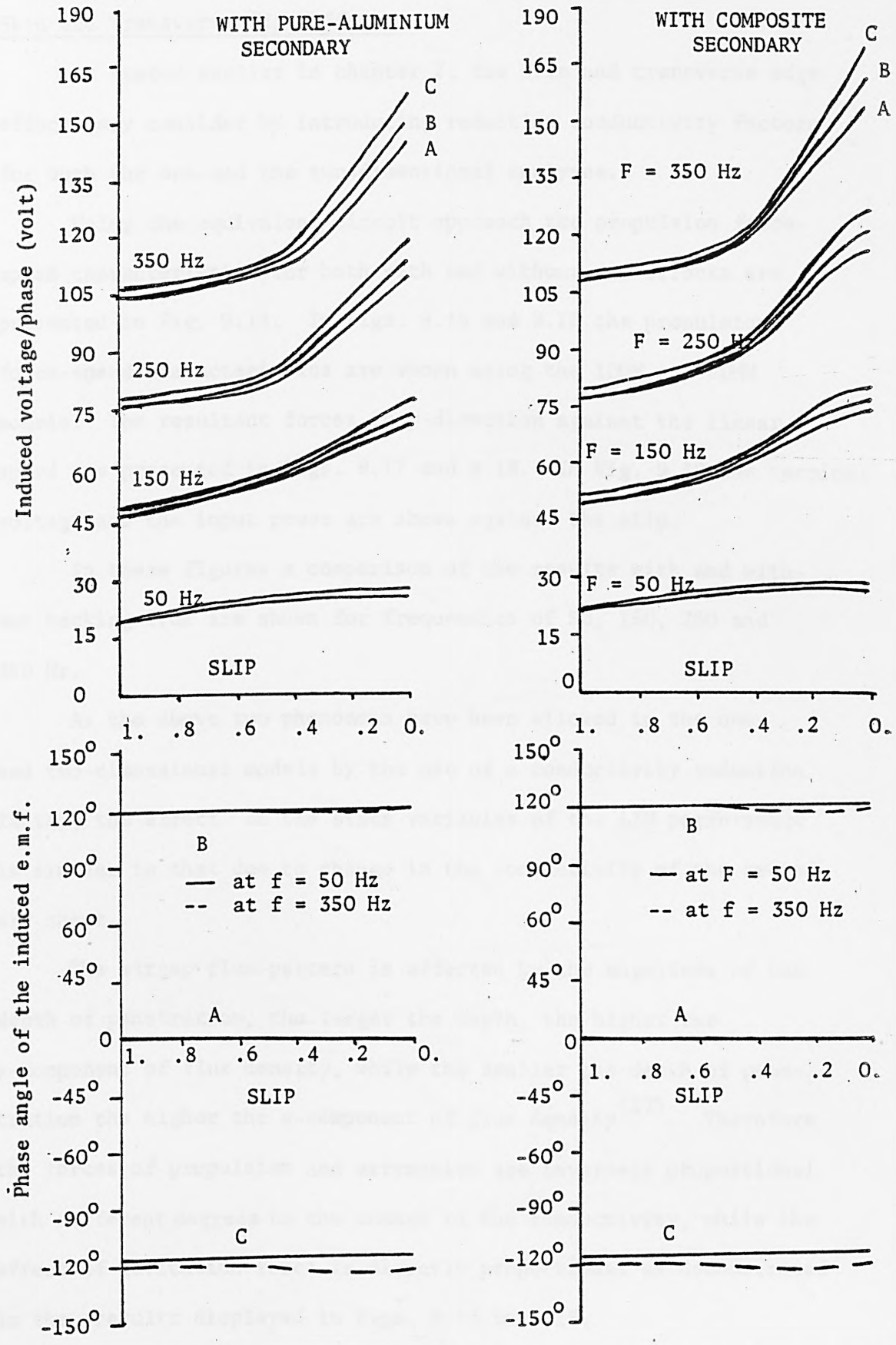

Fig. 9.13. The magnitude and phase shift of the induced e.m.f. per phase of each phase, with end effects

9.4 Skin and Transverse Edge Effects

As stated earlier in chapter 2, the skin and transverse edge effects may consider by introducing reduction conductivity factors for both the one-and the two-dimensional analyses.

Using the equivalent circuit approach the propulsion force-speed characteristics for both with and without end effects are presented in Fig. 9.14. In Figs. 9.15 and 9.16 the propulsion force-speed characteristics are shown using the 1DHM and 2DHM models. The resultant forces in y-direction against the linear speed are presented in Figs. 9.17 and 9.18. In Fig. 9.19 the terminal voltage and the input power are shown against the slip.

In these figures a comparison of the results with and without backing iron are shown for frequencies of 50, 150, 250 and 350 Hz.

As the above two phenomena have been allowed in the one- and two-dimensional models by the use of a conductivity reduction factor, the effect on the state variables of the LIM performance is similar to that due to change in the conductivity of the secondary sheet.

The airgap flux pattern is affected by the magnitude of the depth of penetration, the larger the depth, the higher the y-component of flux density, while the smaller the depth of penetration the higher the x-component of flux density[27]. Therefore the forces of propulsion and attraction are inversely proportional with different degrees to the change in the conductivity, while the effect of levitation force is directly proportional as demonstrated in the results displayed in Figs. 9.14 to 9.18.

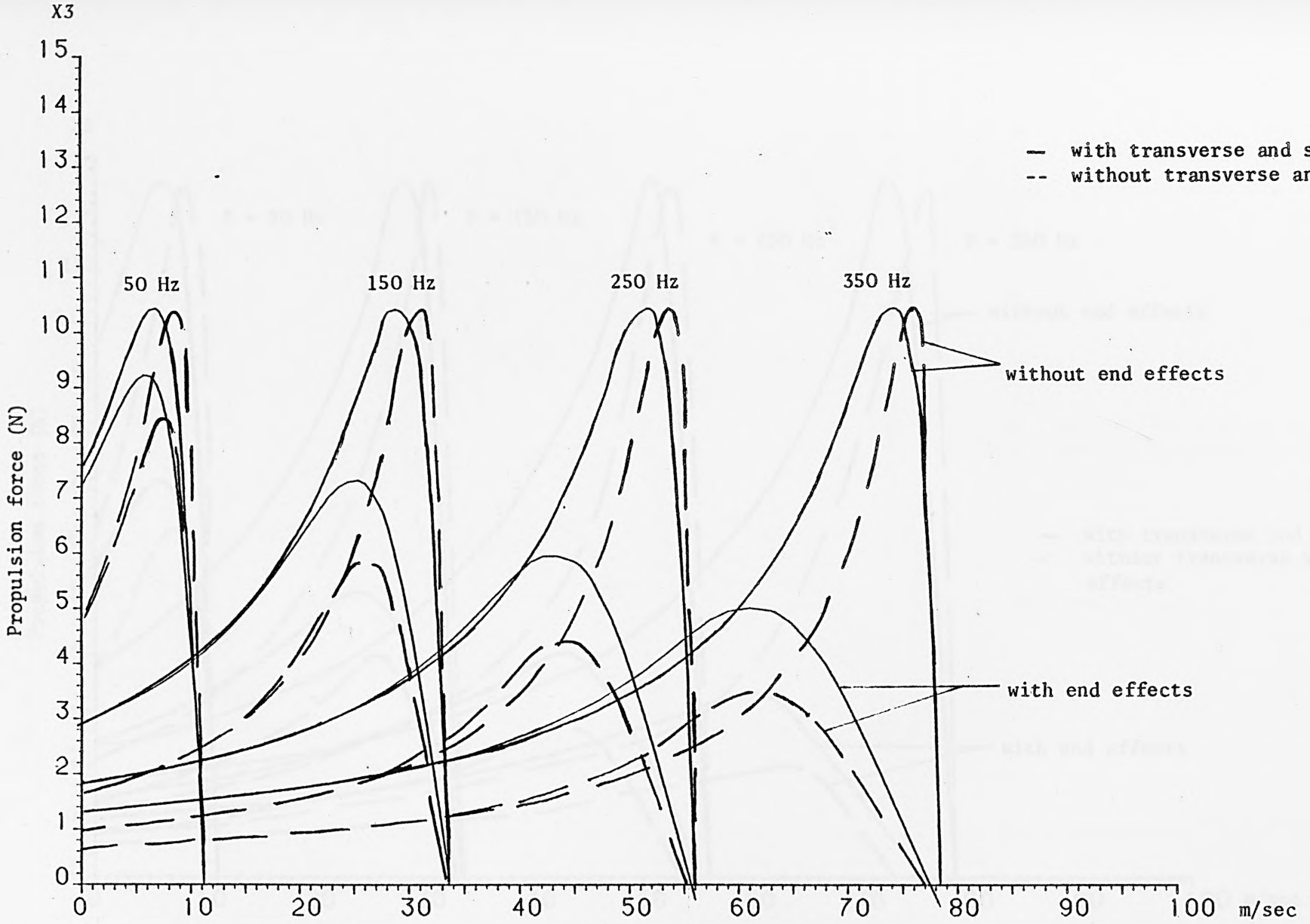

Fig. 9.14. Propulsion force-speed characteristics of the LIM with and without transverse and skin effects

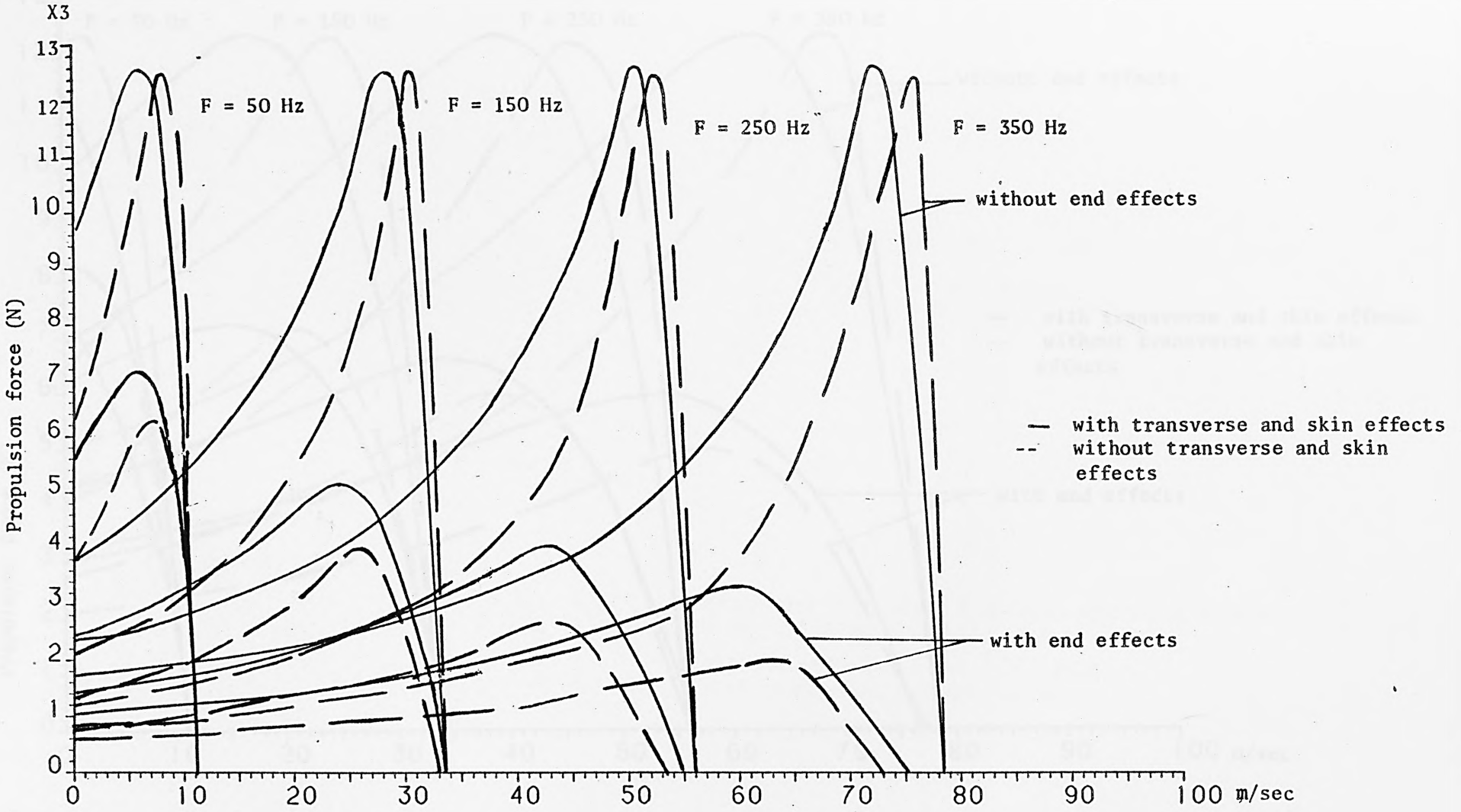

Fig. 9.15. Propulsion force-speed characteristics of the LIM - with backing iron

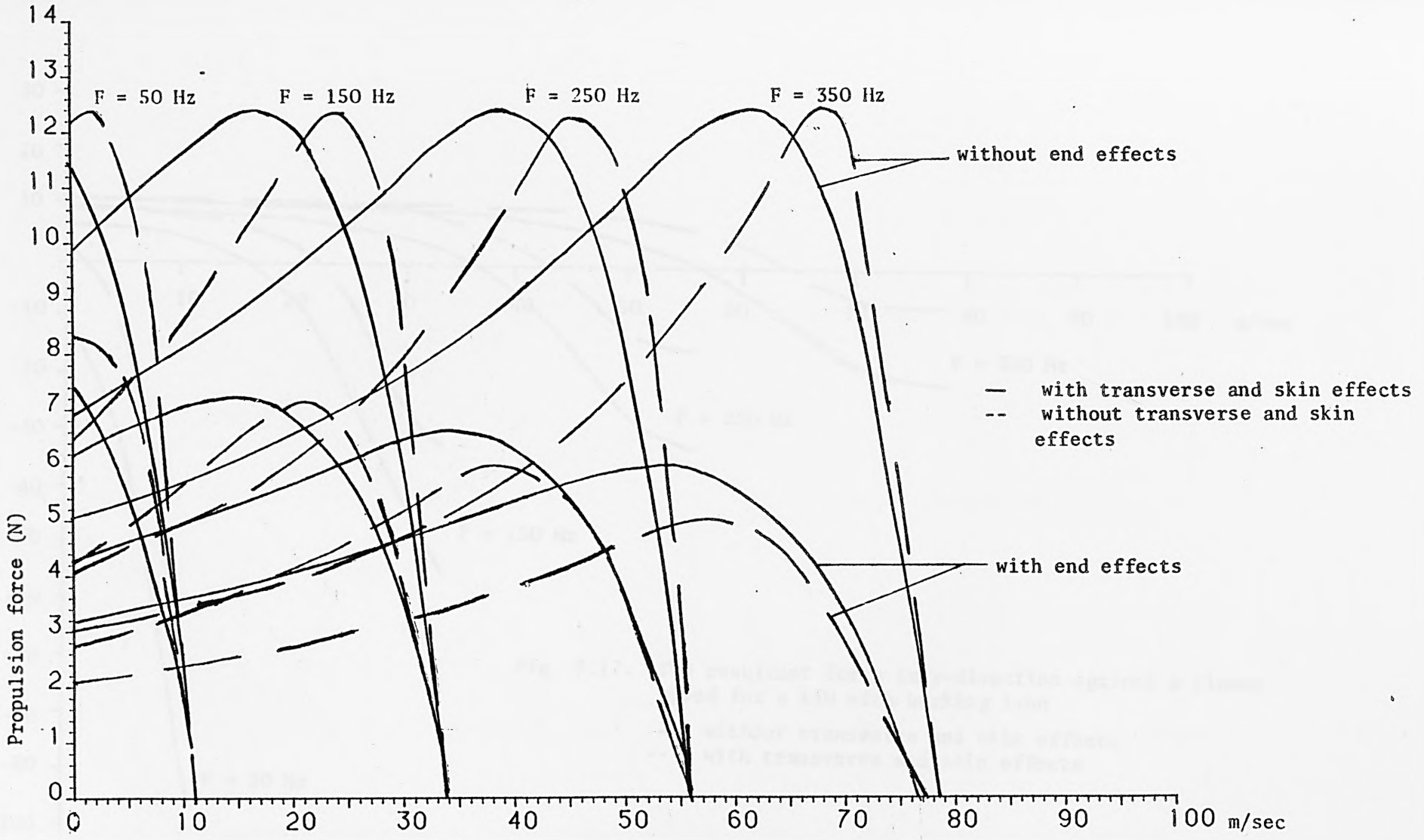

Fig. 9.16. Propulsion force-speed characteristics of the LIM - without backing iron

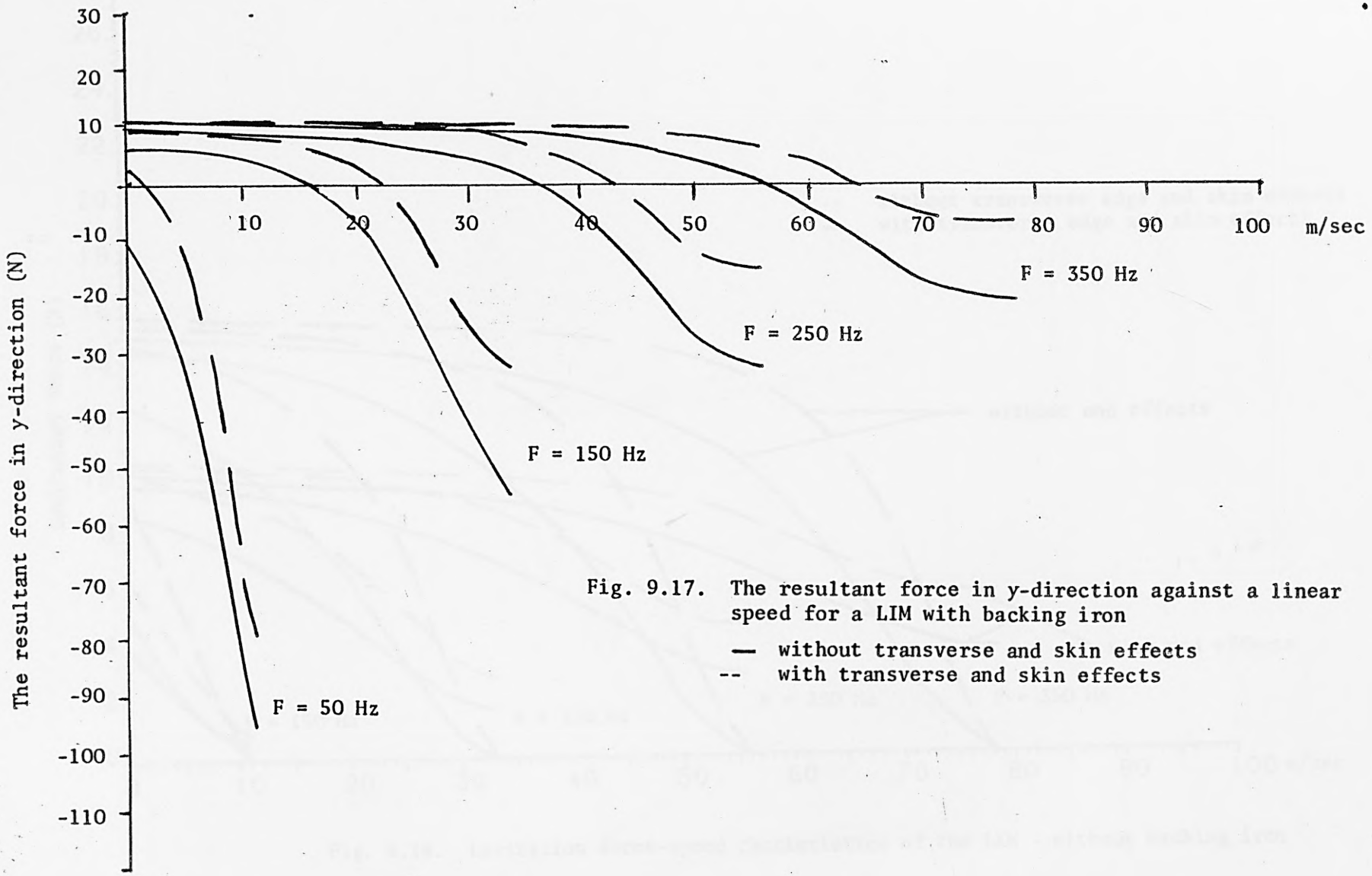

Fig. 9.17. The resultant force in y-direction against a linear speed for a LIM with backing iron

— without transverse and skin effects
-- with transverse and skin effects

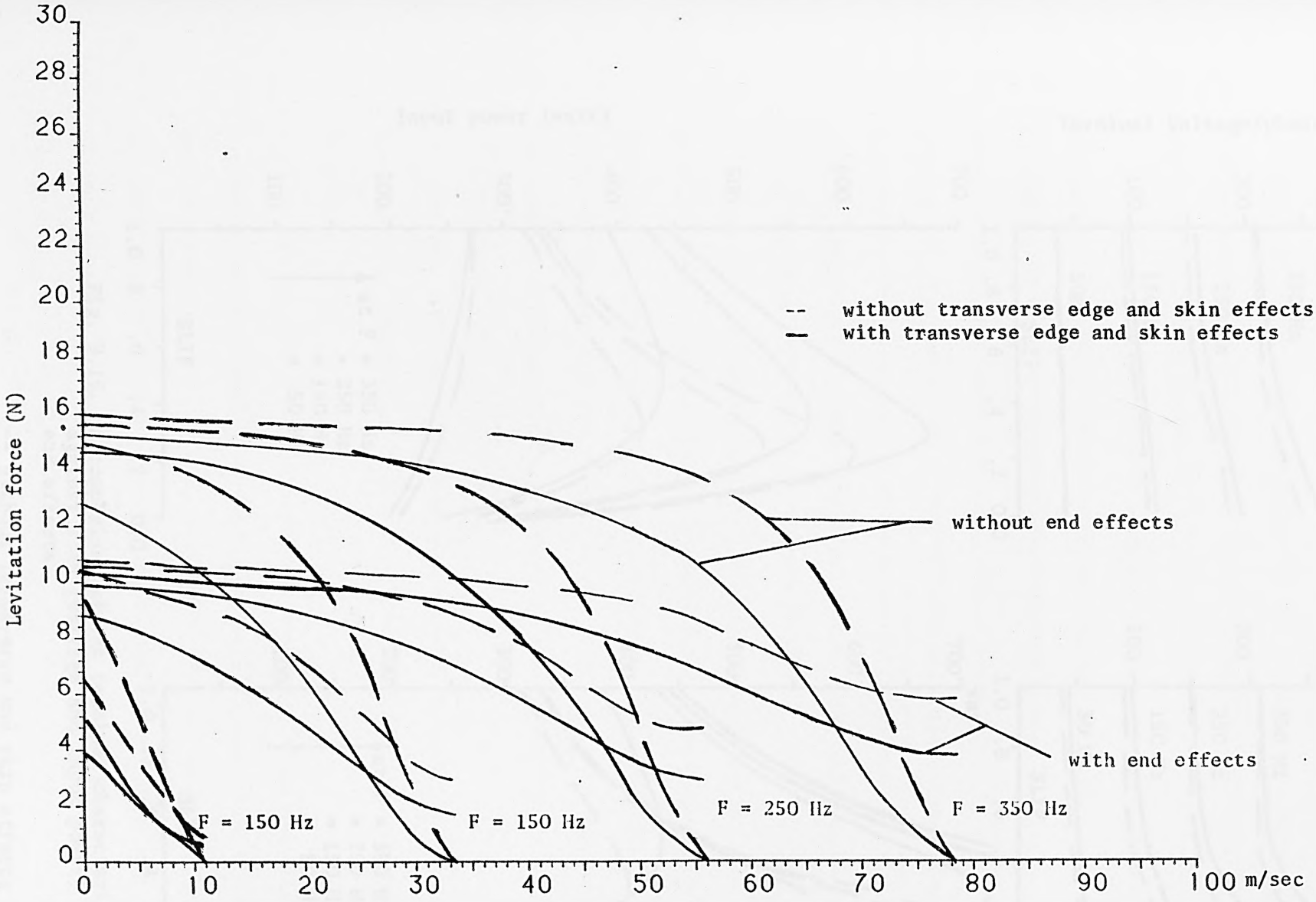

Fig. 9.18. Levitation force-speed chacteristics of the LIM - without backing iron

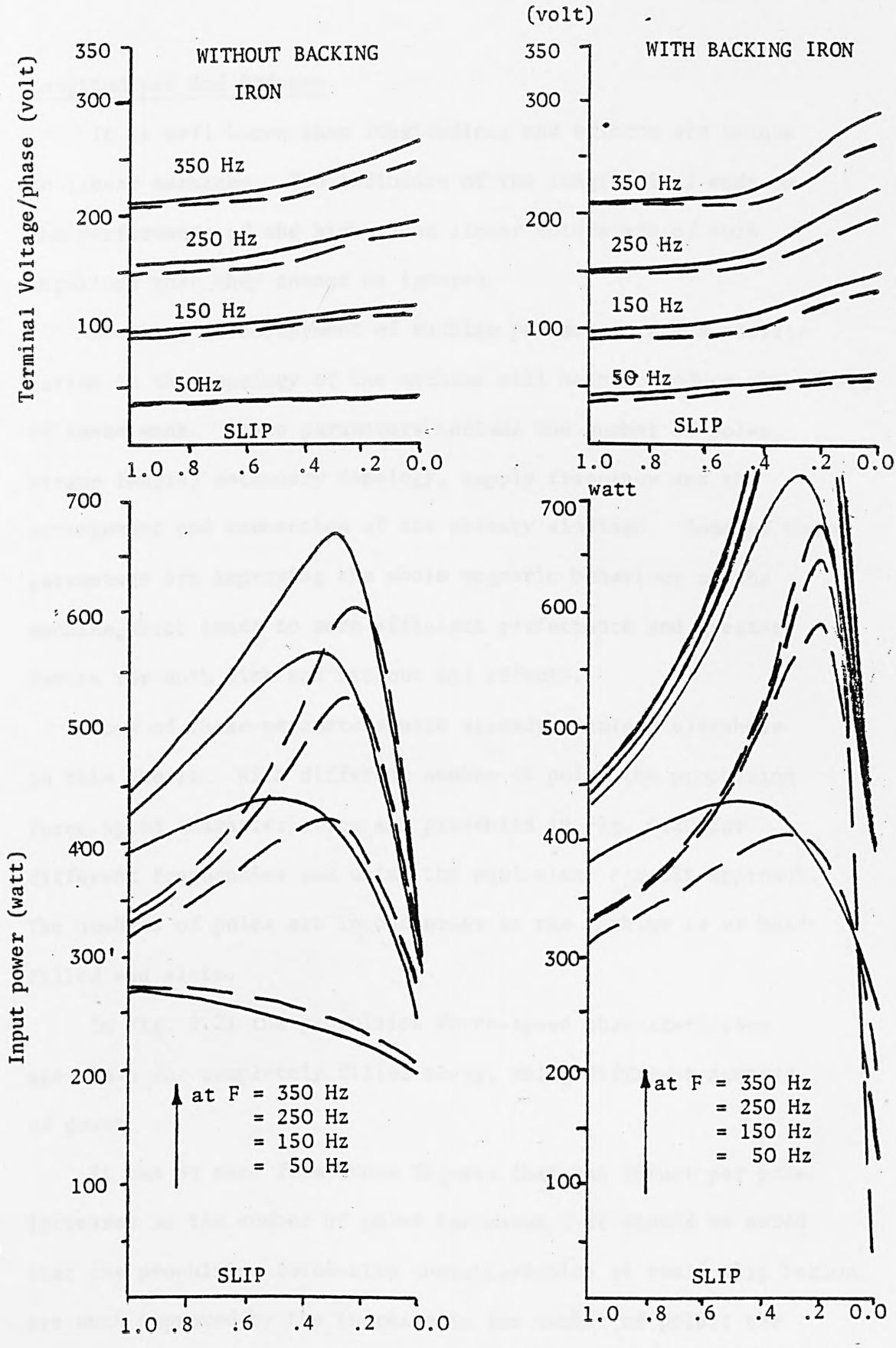

Fig. 9.19. A comparison of the terminal characteristics against slip (voltage and input power) with end effects

-- without transverse and skin effects
— with transverse and skin effects

9.5 Longitudinal End Effects

It is well known that longitudinal end effects are unique to linear machines. The influence of the longitudinal ends on the performance of the high speed linear motors are of such magnitude that they cannot be ignored.

However, an adjustment of machine parameters and a modification in the topology of the machine will help to reduce the effect of these ends. these parameters include the number of poles, airgap length, secondary topology, supply frequency and the arrangement and connection of the primary windings. Some of these parameters are improving the whole magnetic behaviour of the machine,which leads to more efficient performance and greater forces for both with and without end effects.

Some of these parameters were already examined elsewhere in this thesis. With different number of poles the propulsion force-speed characteristics are presented in Fig. 9.20 for different frequencies and using the equivalent circuit approach. The numbers of poles are in odd order as the machine is of half-filled end slots.

In Fig. 9.21 the propulsion force-speed characteristics are shown for completely filled slots, using different numbers of poles.

It can be seen from these figures that the thrust per pole increases as the number of poles increases. It should be noted that the propulsion force-slip characteristics at small slip region are much improved by the increase in the number of poles; the maximum values of propulsion force per pole are found to increase non linearly with the number of poles.

A comparison of the performances due to different arrangements of primary winding can be drawn from the last figures. The propulsion force of a completely-filled slots machine is higher than the values obtained by the half-filled end slots machine when the influence of the end effects is neglected. However, the propulsion force of half-filled end slot machine is less effected by the end effects. This may be explained by the arrangement of the winding which builds up the current at the entry end in two steps.

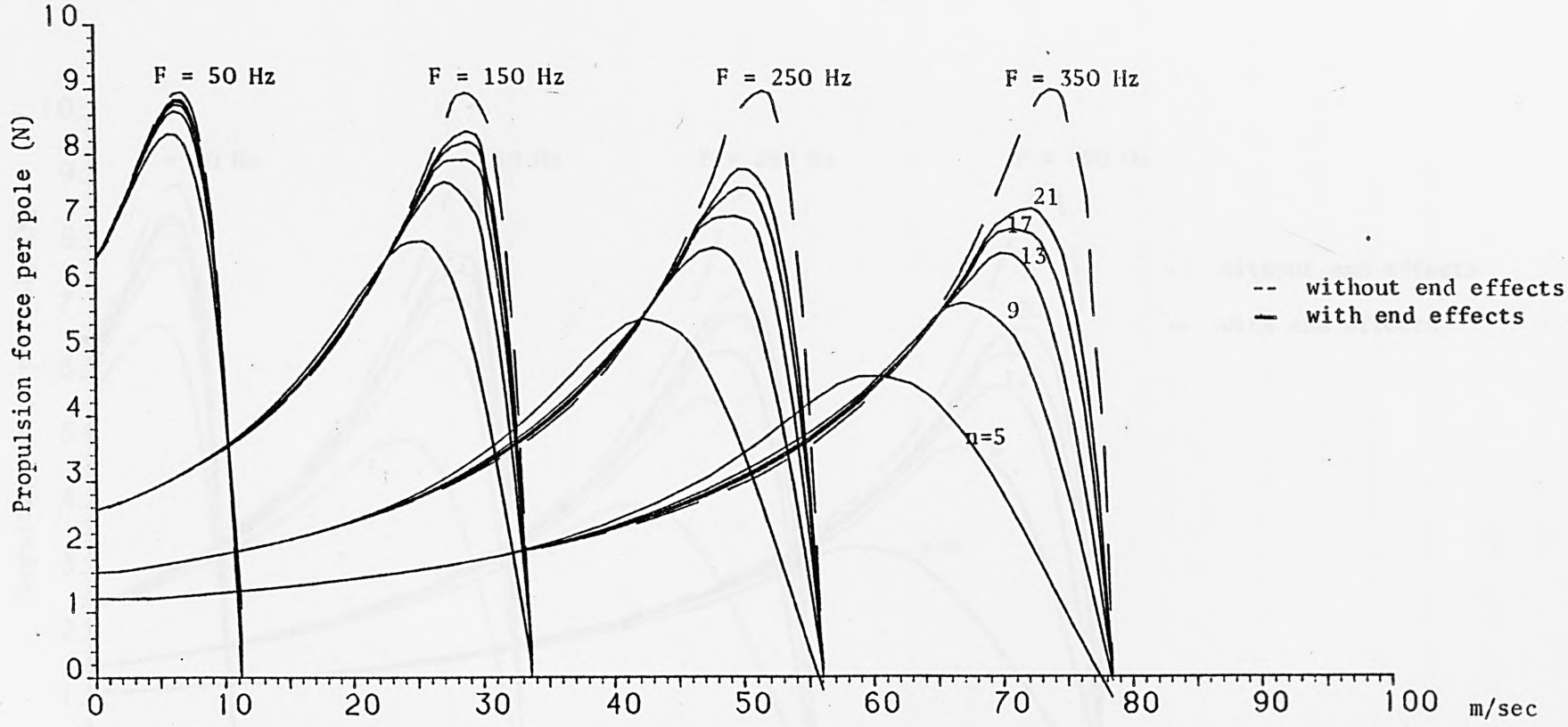

Fig. 9.20. Propulsion force-speed characteristics with different number of poles ; Half-filled end slots

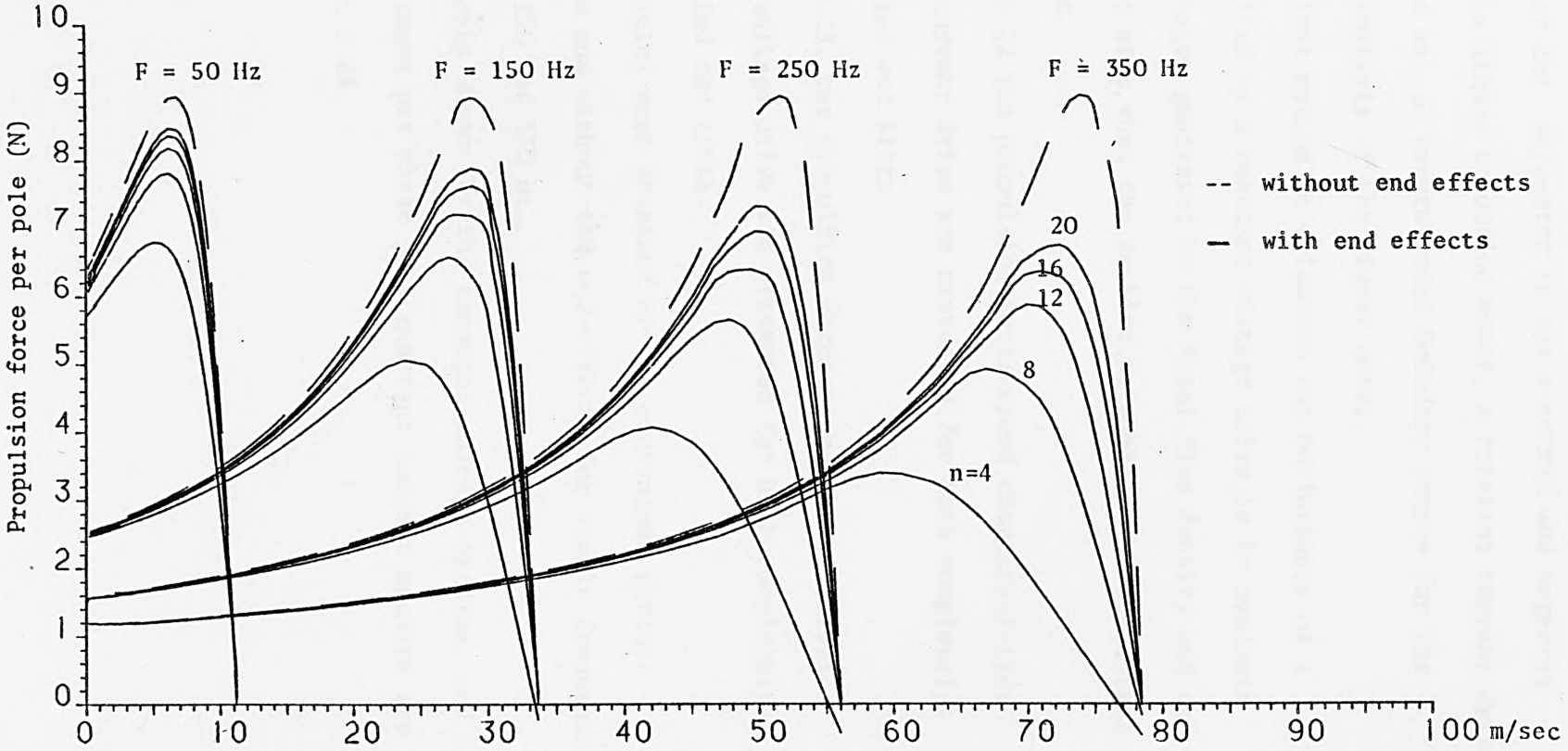

Fig. 9.21. Propulsion force-speed characteristics with different number of poles ; completely-filled slots

9.6 Constant Current and Constant Voltage Drives

Because of the asymmetry in the electric and magnetic circuit of the linear induction motor, a constant current drive is considered as a conventional boundary source for the performance analysis of the linear motor.

The simplest method to calculate the performance of a machine, supplied by a constant voltage drive, is to evaluate the back voltages generated by the total flux density and as a function of slip, when the machine is operated at a constant current drive.

In Fig. 9.22 the propulsion force-speed characteristics of constant current drive are presented for both completely- and half-filled end slots.

In Fig 9.23. the propulsion force-speed characteristics of constant voltage drive are presented for both completely- and half-filled end slots.

These results were obtained by the equivalent circuit approach with and without the end-effects for supply frequencies of 50, 150, 250 and 350 Hz.

The currents drawn by the constant voltage machine, and the treminal voltages per phase of a constant current machine are shown in Fig. 9.24.

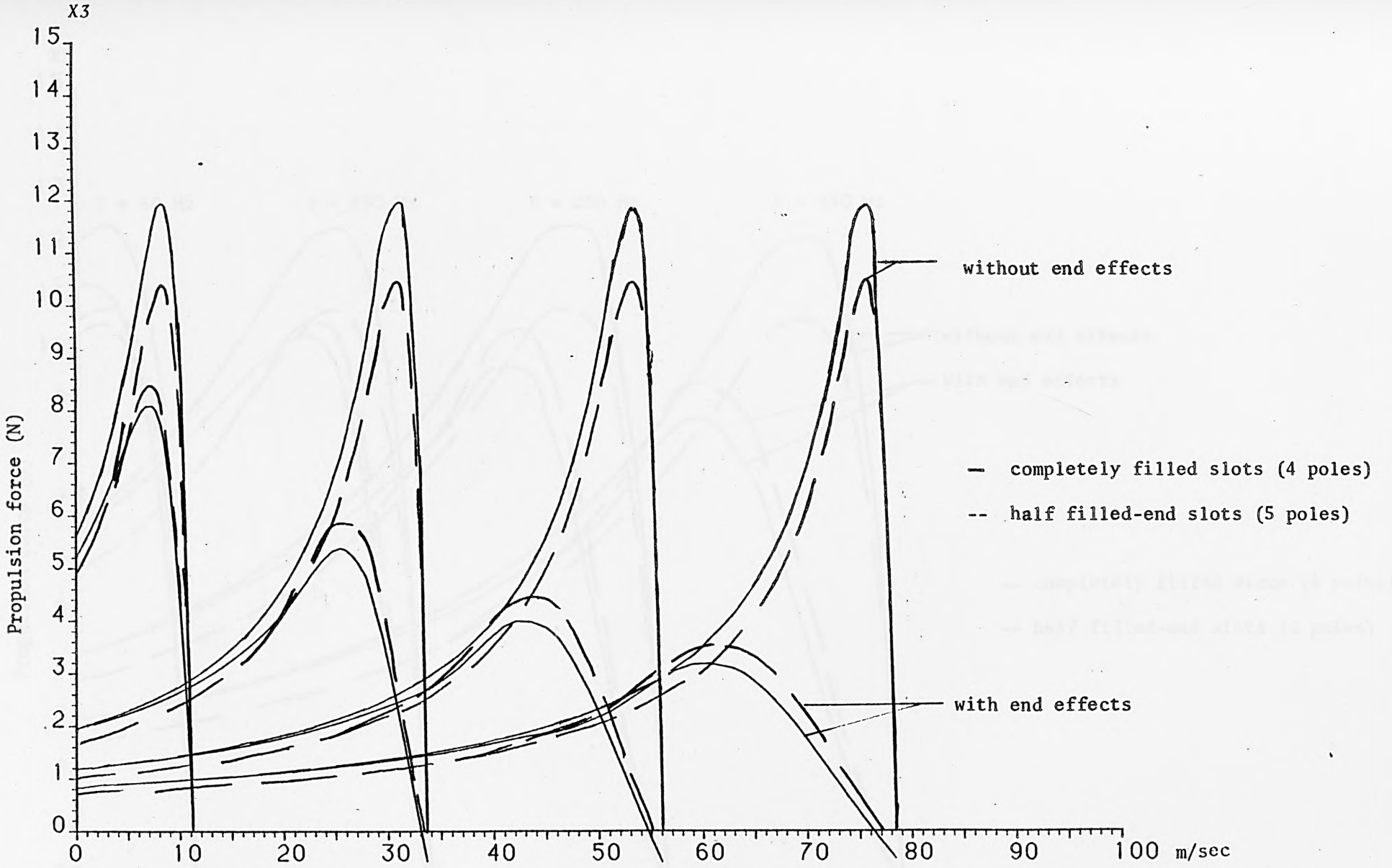

Fig. 9.22. Propulsion force-speed characteristics for a LIM of constant current drive

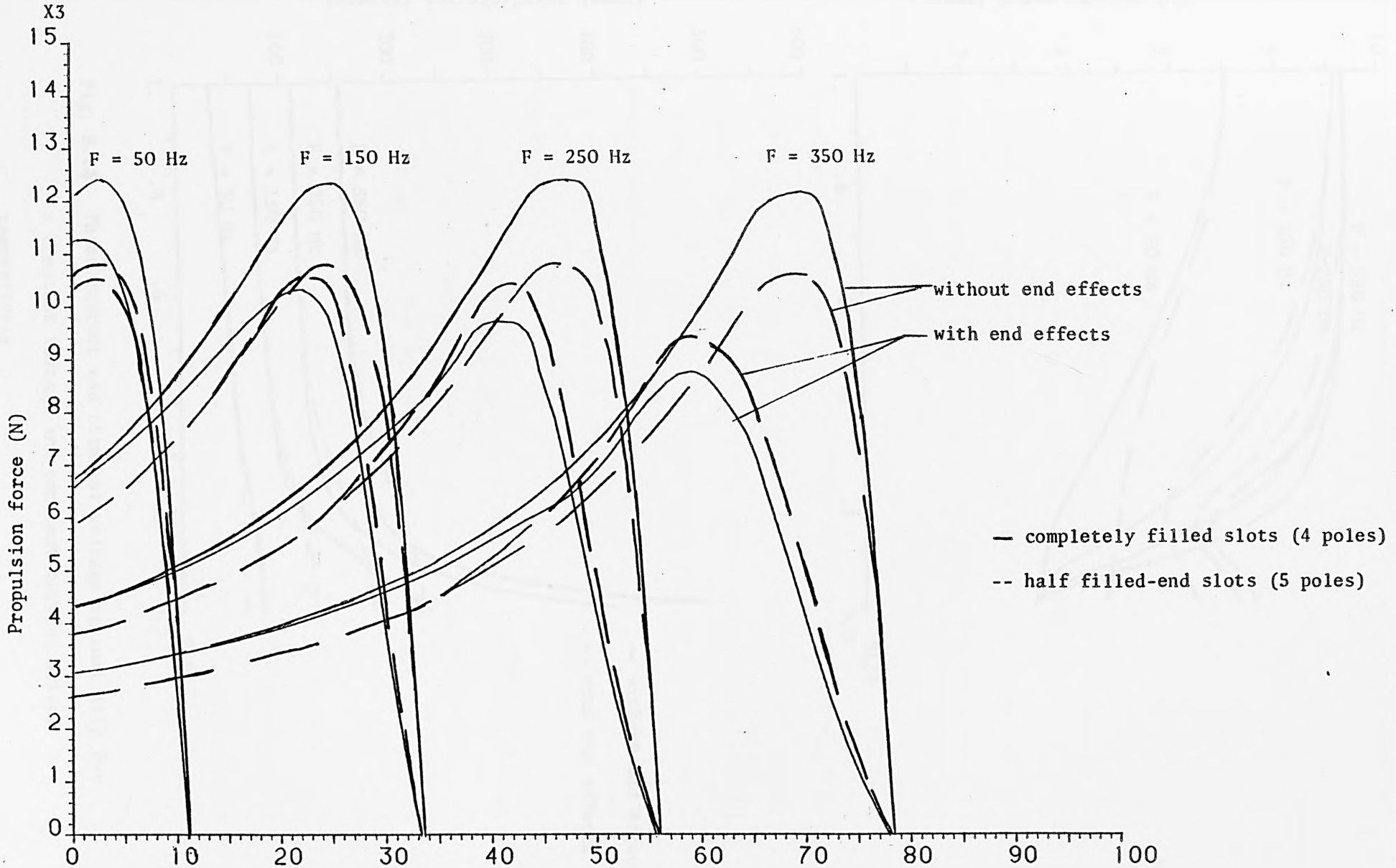

Fig. 9.23. Propulsion force-speed characteristics for a LIM of constant voltage drive.

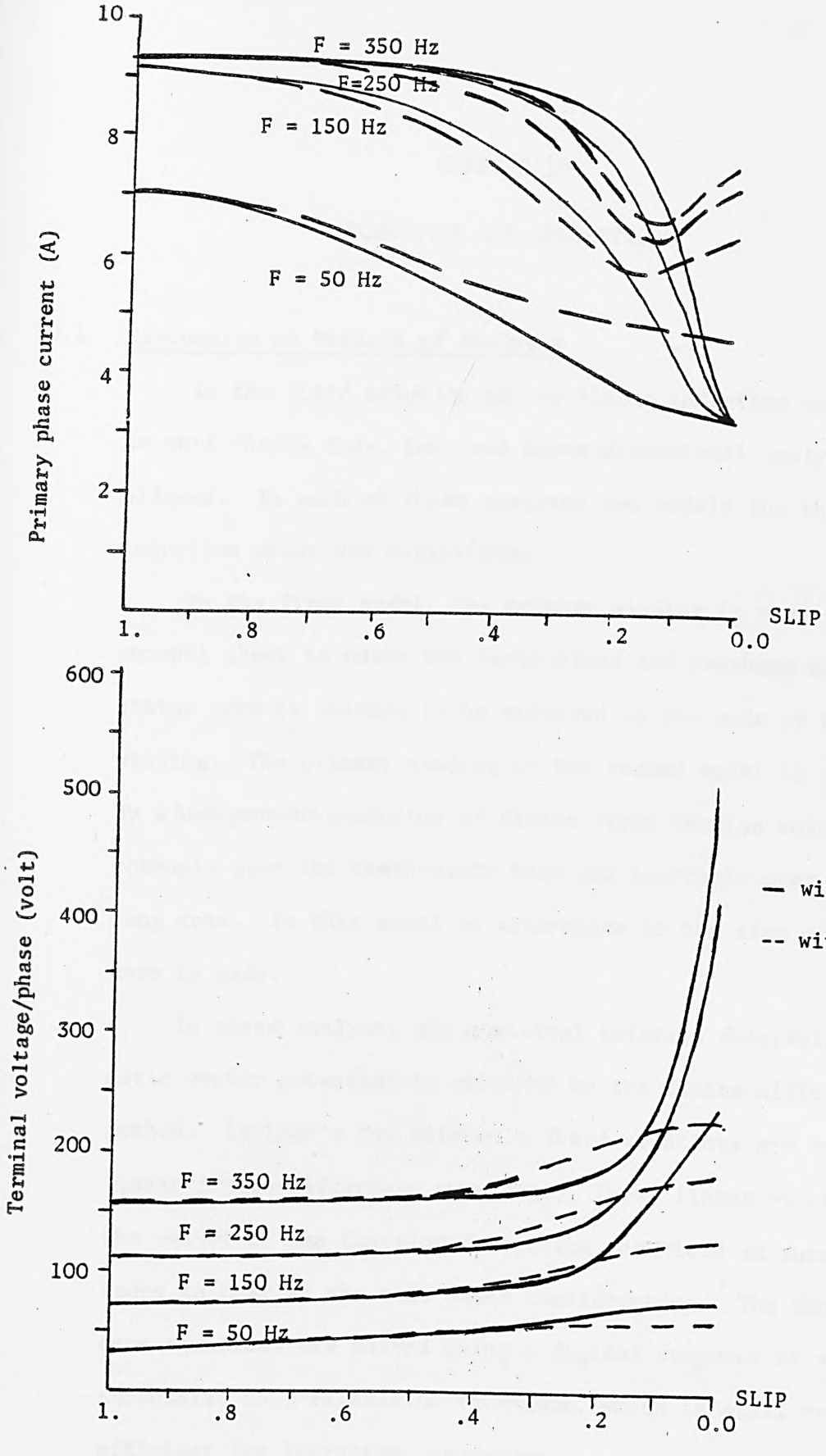

Fig. 9.24. Phase current and terminal voltage against slip for a constant voltage and constant current drives respectively

CHAPTER 10

DISCUSSIONS AND SUGGESTIONS

10.1 Discussion on Methods of Analysis

In the field solution of the linear induction motor described in this thesis one-, two- and three-dimensional analyses are considered. In each of these analyses two models for the linear induction motor are established.

In the first model, the primary winding is represented by a current sheet to cover the teeth-slots and overhang zones. The stator core is assumed to be extended to the ends of the overhang winding. The primary winding of the second model is represented by a homogeneous conductor of finite cross section which is anisotropic over the teeth-slots zone and isotropic over the overhang zone. In this model no alteration in the size of the stator core is made.

In these analyses the numerical solution describing the magnetic vector potential is obtained by the finite-difference method. Laplace's and Poisson's field equations are replaced by linear finite-difference equations. These linear equations connect the values of the function describing the field at surrounding nodes to that at the node under consideration. The finite-difference equations are solved using a digital computer by applying a successive over-relaxation technique, which is still regarded as efficient for iterative procedure.

The state variables of machine performance are formulated in discrete forms in terms of the magnetic vector potential components. By applying the numerical integration method the effective state

variables are obtained.

In considering these alternative models, some assumptions are made. Common assumptions among these models are that the current density is varying sinusoidally with time and direction of motion and that the machine is operating in the linear region of the B-H curve.

To facilitate the analysis for the three-dimensional models, only the transverse and longitudinal components of the current density are considered. Further assumptions are made for two- and one-dimensional models.

In the three-dimensional analysis the solution is established for two components of the magnetic vector potential which considers all the boundaries and discontinuties of the linear motor. At the interfaces which have their normal component in the transverse and longitudinal directions, the tangential components of the boundary condition lead to coupling the components of the magnetic vector potentials. It is, therefore, found necessary to make local studies at these interfaces, to uncouple the magnetic vector potential components.

The line and dot-corner nodes of these models are treated by replacing the interfaces at these locations by a transition layer, within which the components of the relative permeability vary continuously from their value in one region to their value in another. The equations of these nodes are obtained by taking the limit of the transition layer thickness to zero. Thus the equation of each corner becomes equivalent to the averaging equation of the boundary equations of the intersected surfaces.

Further couplings in the z and x components of the magnetic vector potential, exist in the Poissons equation (3.11a) of the

secondary conductor due to the induced voltage of the speed term. To uncouple these equations, the x-component term is replaced by its final value, which is developed from the solution of the x-component of the magnetic vector potential, using the iterative procedure.

The electric scalar potential is not considered in this analysis due to the necessities and constraints stated in chapter three.

The solution of two-dimensional models are derived from the three-dimensional analysis after applying the assumptions which reduce the analysis to two-dimensions. These solutions are presented for comparison purposes.

In the numerical solution of one-dimensional models, the magnetic vector potential is calculated on nodes which are distributed along a line passing through the cross section of the machine. In this analysis a conventional study of the linear induction motor is obtained which does not consider the influence of the end effects.

A program is written and developed by the author to determine the performance characteristics of the linear induction motor for each of six models.

The main process of each program is to

a) calculate the magnetic vector potential over the distributed nodes, using the iterative technique

b) check the convergence and accuracy of the solution

c) calculate the state variable performance in specific and effective values

Throughout the course of developing these programs, the convergence factor, mesh intervals, tolerance, and the location of the

outer frame are continuously investigated.

In each of these programs, the single-sided linear induction motor is examined with and without backing iron for differents speeds up to 282 Km/h using supply frequencies of 50, 150, 250, and 350 Hz.

The predicted results of the analytical models without backing iron are compared with the experimental results obtained from the test rig which is constructed to verify the dynamic performance of the motor. The test rig design processes are described in chapter six, and the comparison of the computed and measured results without backing iron are presented in chapter seven.

The experimental results provide good data to understand the efficient of the models investigated in this thesis.

The results of the field solution of the analytical models with backing iron are presented and compared with the results of the hybrid approach. The hybrid approach develops a pole-by-pole equivalent circuit based on a one-dimensional analysis which considers longitudinal end effects.

There are other studies which are considered in this thesis such as:

a) changes in the topology of the secondary
b) a composite secondary
c) the parameters and factors which compensate the end effects
d) skin and transverse edge effects
e) comparison of the results due to constant current and voltage drives.

10.2 Discussion on LIM Performance

The thesis is concerned with the prediction and study of the performance of the longitudinal single-sided linear induction motor. This study is carried out by using

1) a field approach,
2) a hybrid approach,
3) a test rig.

The state variables of the performance include

a) flux and flux density,
b) force and force density,
c) power and terminal voltage,
d) power factor and efficiency.

The predicted results are obtained for each of the following

i) with and without backing iron,
ii) with and without end effects,

with variation of

1) slip (linear speed),
2) supply frequency (50, 150, 250, and 350 Hz),
3) energy source (constant current and constant voltage drives),
4) topology of the machine (conductivity, thickness of secondary conductor, number of poles, airgap, winding arrangement and composite reaction rail).

Chapter seven considers the test rig and the field approach of the LIM without backing iron, while in chapter eight the field and hybrid approaches are presented for the LIM with backing iron. The main observations and conclusions deduced from these results can be summarized as follows.

Flux Density

From the airgap flux density distribution along the x and z directions, it can be seen that the y-component is generally higher in backing iron configuration. However, as the frequency increases, the values of the flux density in the y-direction of the two configurations become closer to each other. A slight change is noticed in the x and z components due to the change in the medium backing the secondary.

This insignificant change in the flux density components, can be explained by the fact, that the airgap length is relatively large and as the frequency increases the skin depth of flux penetration decreases.

The flux density measurement results show that there are large differences between the values above the teeth and above the slots. Therefore, in order to obtain an accurate prediction of the flux density, the slot leakage cannot be neglected. These effects are taken into account in the homogenous anisotropic models (3DHM and 2DHM).

The flux distributions in various parts of the motor without and with backing iron are shown in Figs. 7.19 to 7.26 and Figs. 8.19 to 8.26 respectively. These flux contours provide an easy insight of the flux pattern at different slips and frequencies. It can be observed that the flux penetrates gradually through the secondary conductor and its backing medium as the motor approaches synchronous speed and as the frequency decreases. At a particular value of slip and frequency the flux contours above the stator surface are almost identical in both 2DHM and 2DCM models. However, they are different through the stator core due to the

consideration of slot leakages in the configuration of 2DHM model

From these contours, the longitudinal end effects can be seen clearly in redistributing the flux (more condense at the exit end) along the machine in the direction of motion, especially at high speeds.

Forces

In general, it is found that the propulsion force is higher for a linear motor with backing iron. But, because of the end effects which become more severe at high speeds, the rate of change in the propulsion force becomes less at high frequency.

Without end effects, the rate of change in the maximum value of the propulsion force due to the backing iron, remains constant for all levels of frequencies.

In linear motors the value of the maximum propulsion force decreases as the synchronous speed increases, while in a conventional motor (without end effects) it remains constant.

It is also found that the propulsion force of the linear induction motor at synchronous speed is not zero. It is positive for low speed motors which may be considered as an advantage, and negative for high speed motors which acts as a drag force.

The forces in y-direction (normal force) are quite different in both configurations.

Without backing iron, the primary will, under most operating conditions, exert a repulsion force on the secondary. This force is directly proportional to the frequency, and it is higher at standstill.

In the other configuration, i.e. that of a secondary backed by a laminated iron, the primary exerts either a repulsion or an attraction force on the secondary. At standstill, the linear motor may experience a repulsion force; this depends on factors such as conductivity and thickness of the secondary and on the supply frequency. As speed increases, this repulsion force gradually reduces until it becomes negative and the primary is attracted to the secondary.

In addition to this overall variation in the normal force with speed, there are also additional variations, due to the longitudinal ends which redistribute the airgap flux for different slips.

The variation of normal force with speed has shown that it is highly dependent on the operating conditions such as supply frequency and secondary conductivity.

In most applications of the linear induction motor, with backing iron, a normal force which is less effected by the speed is preferable. Therefore it may be possible to use some form of secondary which enables it to produce a constant normal force with respect to speed.

Terminal Characteristics

The terminal voltage generally increases as the slip decreases, while the input power is more likely to be similar to the form of the propulsion force-speed characteristics. At standstill both the terminal voltage and the input power are roughly equal in both configurations. However these values become higher at high speed in the backing iron configuration.

The power factor and the efficiency of the motor are higher in backing iron configuration. The efficiency is directly proportional to the frequency while the power factor is inversely proportional.

Without end effects the values of the state variables of the terminal characteristics become larger.

From these results, it can be observed that with backing iron configuration there is no significant change in the values of the flux density components and consequently the propulsion forces. These results conclude that the existence of the backing iron for high speed motors operating at high frequency is less effective, especially in a machine with large airgap and a low skin depth.

The behaviour of the linear induction motor for other aspects and configurations are described in chapter nine. It is worth to mention again that the performance is improved significantly when a composite rail is used.

Most large linear machines have been built with the propulsion force as the main design factor, because the behaviour of the normal force is rather complicated, especially in backing iron configuration. This is due to the redistribution of the normal force density, because of end effects and the movements of either the stator or the secondary in the three directions. This force, then, may cause the motor to experience electromagnetic couplings.

It should be emphasized that the airgap of the motor for high speed applications should be mechanically safe enough and as small as possible to reach optimum performance. This actually requires a high electric source to maintain a reliable flux in the airgap and a magnetic circuit path which minimises the resultant reluctance.

10.3 Suggestions for Further Work

In this thesis a three-dimensional field theory has been used to study the performance of the longitudinal single-sided linear induction motor using two alternative models 3DCM and 3DHM. The overhang configurations of the primary winding are different in these two models. From the predicted results presented in chapters seven and eight, it can be seen that in 3DCM model the overhang performance is over-estimated. It is believed that the over-estimation is due to the extension of the stator iron up to the end of the overhang winding. This cannot be compensated for by any of the three current density waves presented in appendix A, unless further assumptions are made.

But in the 3DHM model, both the winding confuguration and the current density distribution are more realistic. The stator iron extends only over its width and the real size of the primary winding is considered. The model makes possible an adequate consideration of slot leakages. However, the overhang

equivalent mass is assumed to be perpendicular to the lateral surface of stator core, which is not the real case. Consequently, it would be useful to consider the realistic shape of the overhang winding with respect to the stator lateral surface. A possible alternative to the overhang conductor is shown in Fig. 10.1. Using the finite difference method, a node distribution on either side of the overhang mass is recommended. (Fig. 10.1).

Obviously, the three-dimensional analysis is not limited to the linear motor with a secondary sheet. It could be developed and used to consider the composite reaction rail which is examined in chapter nine. Consequently it would be useful to extend the analysis to include the effects of non-linearity due to saturation.

With the advent of large-storage digital computer, consideration of dynamic movements in the lateral and vertical directions has become possible, (limitations are due to large number of nodes distributed up to the symmetry plane of the machine in the lateral direction). In high speed linear motors, consideration of these displacements make studies on electro-mechanical stiffness and damping behaviour and vibration and stability vitally important.

The longitudinal end-effect in linear induction motors is an important phenomenon for any study of linear motor performance, especially in high speed applications. In this research, adjustment of machine parameters and modifications in topology have shown a significant influence in reducing longitudinal end effects and in improving performance in general. Study of this phenomenon can be extended to examine the influence of a compensating winding which may be located in front of or directly at

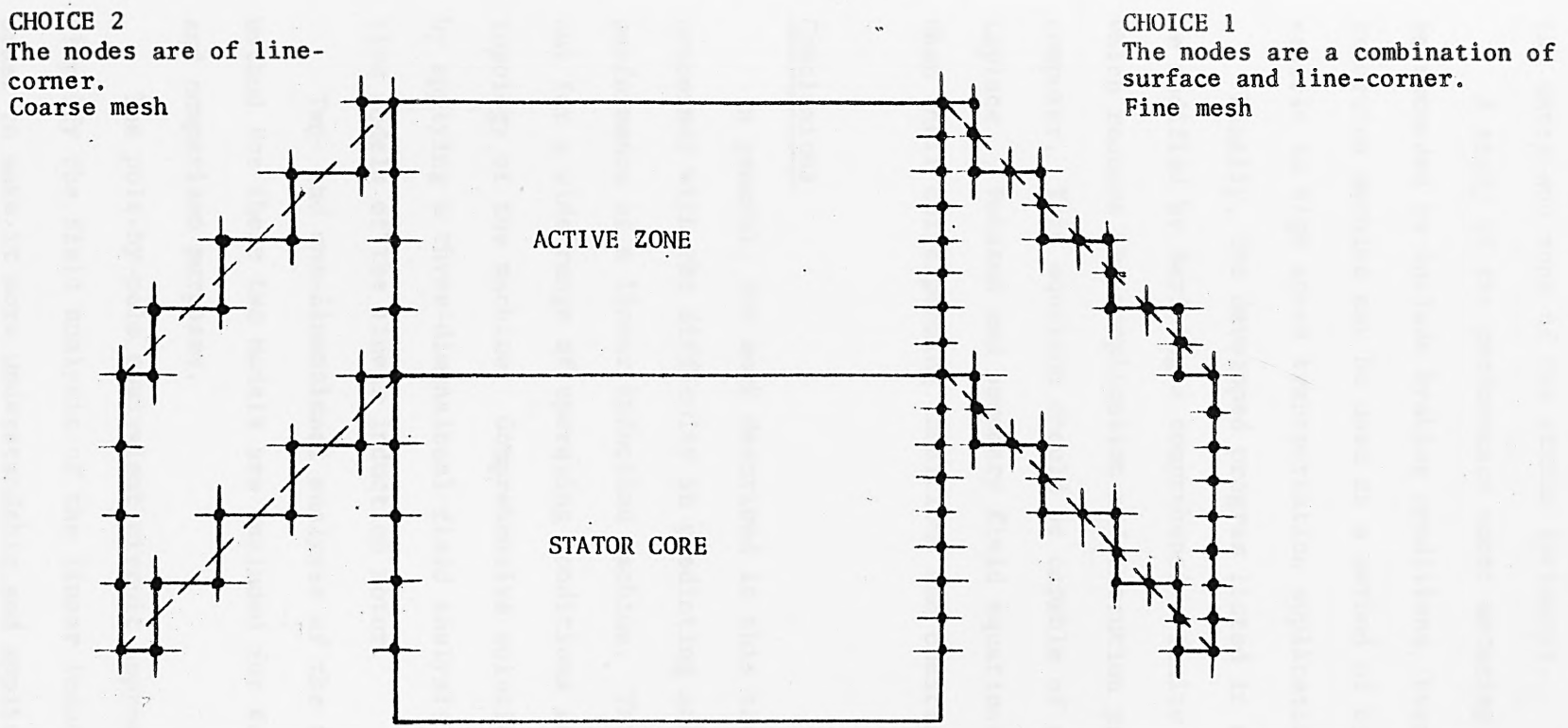

Fig. 10.1. A possible alternative for the overhang configuration in 3DHM model

the entry-end zone of the stator (primary).

A study of the performance under motoring conditions can be extended to include braking conditions, because the linear induction machine may be used as a method of braking the vehicle in high speed transportation applications.

Finally, the developed program listed in appendix C, can be modified by deriving a comprehensive finite difference equation which reduces the complication and execution process of the digital computer. This equation should be capable of satisfying the Laplace , Poisson and boundary field equations of the model when their corresponding conditions and constraints are imposed.

10.4 Conclusions

In general, the work described in this thesis has been concerned with the difficulty in predicting analytically the performance of a linear induction machine. This work is carried out for a wide range of operating conditions and changes in topology of the machine. Comprehensive solutions are obtained by applying a three-dimensional field analysis on two alternative models of the linear induction motor.

Two- and one-dimensional analyses of the finite-difference method for these two models are included for further studies and comparison purposes.

The pole-by-pole equivalent circuit approach is used to simplify the field analysis of the linear induction motor in order to make it more understandable and applicable for design processes.

It is hoped that approaches and techniques developed in this thesis will aid and increase the understanding of those concerned with linear machines and provide an introduction for further studies of the three-dimensional analysis and methods of designing.

APPENDIX A

CURRENT DENSITY DISTRIBUTION IN THE Z-DIRECTION

The waveforms shown in Fig. 2.5 represents a generalized current density distribution of the primary winding of a moving machine. However, due to the assumption of the artificial extension in the stator iron over the overhang region (as in the case of 3DCM model) both Oberretl[22] and Preston and Reece[21] have suggested an alternative waveform.

Fig. A.1 shows a three alternatives which are examined for a better response.

Fig. A.2 shows the flux density distributions along the z-direction using these three waves.

It is found, however, that waveforms No. 3 of Fig. A.1 are more practical to compensate the extension of the iron and to get results as close as possible to the experimental measurements.

The mathematical expressions of the waves shown in Fig. A.1 are as follows:

Waveforms No. 1;

over the active zone

$$Kz = \frac{K_a}{2} \cdot e^{j(\omega t - kx)} \cdot (1 - e^{jp\pi})$$

and $$Kx = 0$$

over the overhang zone

$$Kz = \frac{K_a}{2} \cdot e^{j(\omega t - kx)} \cdot (e^{j\theta} - e^{j(p\pi-\theta)})$$

and $$Kx = \frac{K_a}{2} \cdot e^{j(\omega t - kx)} \cdot (e^{j\theta} + e^{j(p\pi-\theta)})$$

Waveforms No. 2;

over the active zone

$$Kz = K_a \cdot e^{j(\omega t - kx)}$$

and $Kx = 0$

over the overhang zone

$$Kz = K_a \cdot e^{j(\omega t - kx)} \cdot \cos \theta$$

and $$Kx = K_a \cdot e^{j(\omega t - kx)} \cdot \sin \theta \cdot \cot \xi$$

Waveforms No. 3;

over the active zone

$$Kz = K_a \cdot e^{j(\omega t - kx)}$$

and $Kx = 0$

over the overhang zone

$$Kz = K_a \cdot e^{j(\omega t - kx)} \cdot (1 - \sin \theta)$$

and $$Kx = K_a \cdot e^{j(\omega t - kx)} \cdot \cos \theta \cdot \cot \xi$$

where $K_a = 6 \sqrt{2}\ I\ N\ K_p\ K_b / 4\tau$

$K_p = 1$ for waveforms No. 1

and $K_p = \cos \frac{\delta}{2}$ for waveforms No. 2 and 3

All the parameters stated in this appendix are defined in chapter 3 and the list of symbols.

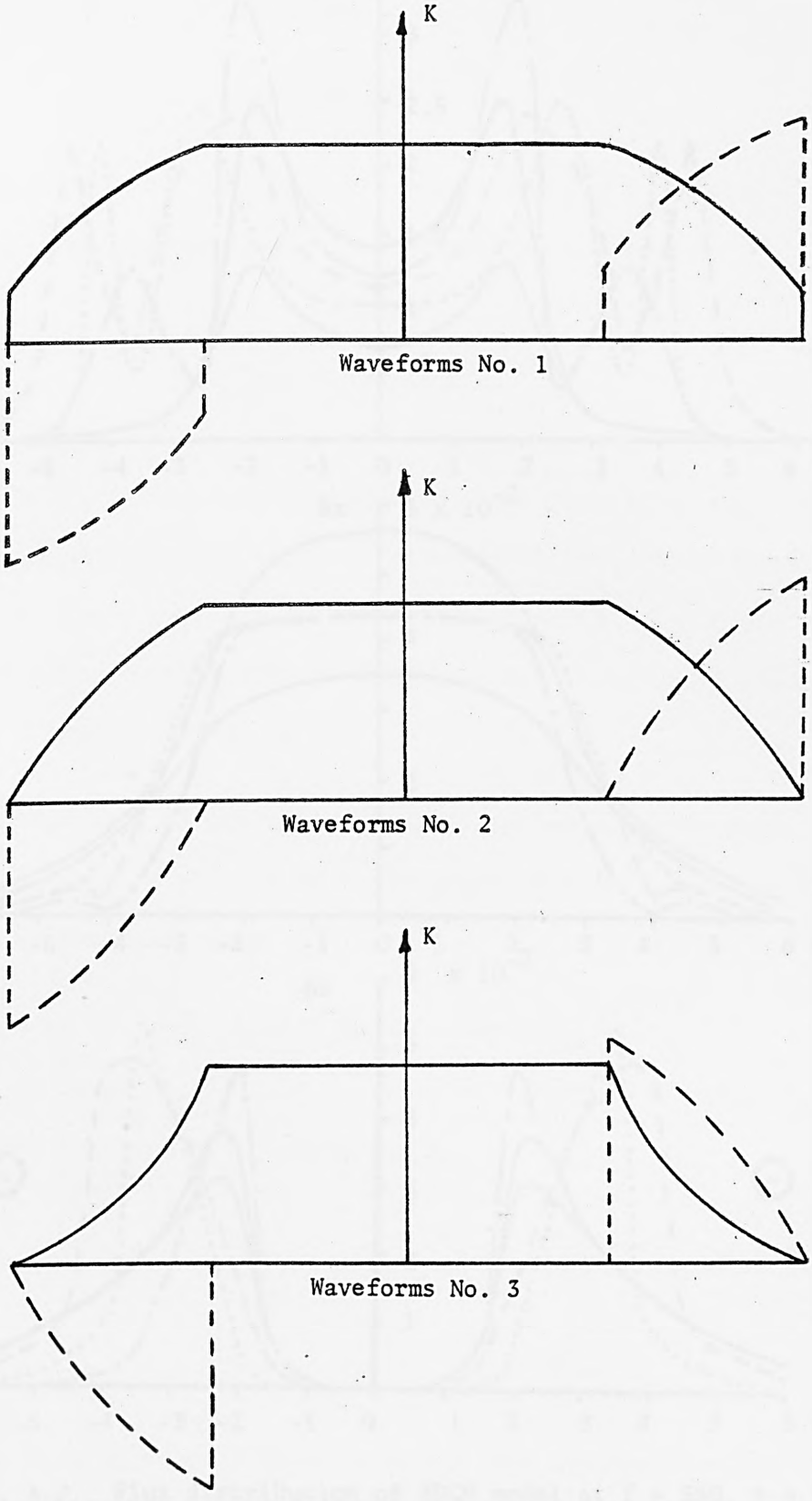

Fig. A.1. Current distribution of the primary winding

— Kz, --- Kx

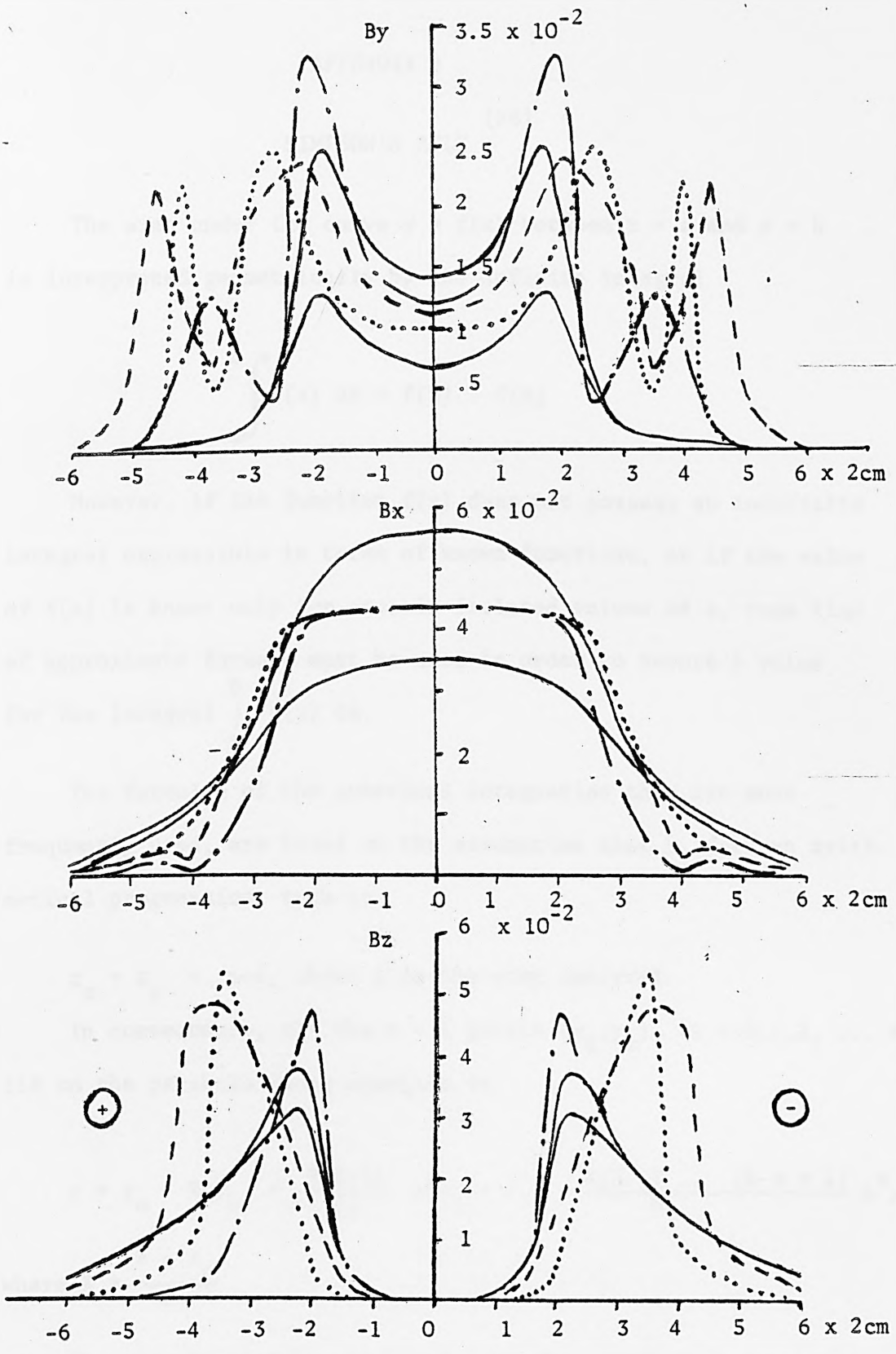

Fig. A.2. Flux distribution of 3DCM model at f = 350, s = 1.0

— measured, --- computed using waveforms No. 1 ... computed using waveforms No. 2, -·- computed using waveforms No. 3.

APPENDIX B

(56)

SIMPSON'S RULE

The area under the curve $y = f(x)$ between $x = a$ and $x = b$ is interpreted geometrically by the definite integral

$$\int_a^b f(x)\,dx = f(b) - f(a)$$

However, if the function $f(x)$ does not possess an indefinite integral expressible in terms of known functions, or if the value of $f(x)$ is known only for certain isolated values of x, some kind of approximate formula must be used in order to secure a value for the integral $\int_a^b f(x)\,dx$.

The formulae of the numerical integration that are most frequently used, are based on the assumption that x_i form an arithmetical progression, such as

$x_m = x_o + m.d$, where d is the step interval.

In consequence, all the $m + 1$ points (x_i, y_i), $(i = 0,1,2, \ldots m)$ lie on the parabola whose equation is

$$y = y_o + X\Delta y_o + \frac{X(X-1)}{2!}\Delta^2 y_o + \ldots + \frac{X(X-1)\ldots(X-m+1)}{m!}\Delta^m y_o$$

where $X = \dfrac{x - x_o}{d}$

The area bounded by the x-axis and this prarbola between $x = x_o$ and $x = x_m$ is an approximation to the value of

$$\int_{x_o}^{x_m} f(x)\,dx$$

It follows that if m = 1, the integral becomes

$$\int_0^1 ydX = y_o + \frac{\Delta y_o}{2}, \quad \Delta y_o = y_1 - y_o$$

and as $dX = \frac{dx}{d}$

The integral becomes

$$\int_{x_o}^{x_1} ydx = \frac{d}{2} \cdot (y_o + y_1)$$

If n+1 pairs of values are given, the above equation can be applied successively to the first two pairs, the second and third pairs, the third and fourth pairs, etc.

$$\int_{x_o}^{x_n} ydx = \frac{d}{2} \cdot (y_o + y_n + 2(y_1 + y_2 + ... + y_{n-1}))$$

The above formula is known as the trapezoidal rule.

Following the same precedure,

if m = 2

$$\int_{x_1}^{x_n} ydx = \frac{d}{3} \cdot (y_o + y_n + 4(y_1 + y_3 + ... + y_{n-1}) + 2(y_2 + y_4 + ... + y_{n-2}))$$

and if m = 3

$$\int_{x_o}^{x_n} ydx = \frac{3d}{8} \cdot (y_o + y_n + 3(y_1+y_2+y_4+y_5+ \ldots +y_{n-2} + y_{n-1}) + 2(y_3 + y_6 + \ldots + y_{n-3}))$$

The last two formulae are known as Simpson's rule, with m = 2 and m = 3 respectively.

Using the same procedure, Simpson's rule with m = 4, 5, etc. can be derived. However, the equations derived above are commonly used with satisfactory accuracy.

APPENDIX C
LISTING OF THE PROGRAM OF 3DHM MODEL

```
C ££------££------££------££------££------££------££------££
C ££  THIS IS A THREE-DIMENSIONAL ANALYSIS OF THE LINEAR  ££
C ££  INDUCTION MOTOR USING THE HOMOGENOUS ANISOTROPIC-   ££
C ££  ISOTROPIC MODEL ((3DHM)) .                          ££
C ££------££------££------££------££------££------££------££
C ££  TO MATCH THE PROGRAM WITH THE DIMENSIONS STATED IN  ££
C ££  CHAPTER THREE USE THE FOLLOWING TRANSFORMATIONS ;   ££
C ££  X-AXIS ; K=IR,L=IS,IQ=IQ                           ££
C ££  Z-AXIS ; ISW=ISW,IT=IT,IV=IV,IH=IH                 ££
C ££  Y-AXIS ;M=LL,IS=L,N=M,IR,N,IRG=IRG,IP=IP           ££
C ££  IU IS THE NO. OF NODES UP TO THE SECOND POLE       ££
C ££  IW IS THE NO. OF NODES UP TO THE FIFTH POLE        ££
C ££------££------££------££------££------££------££------££
      PROGRAM SEPT(INPUT,OUTPUT,TAPE5=INPUT,TAPE6=OUTPUT)
      COMPLEX AZ,BZ,AL,RR,ALO,ALM,CB,CBB,CZ,CZ1,CZ2,CZ3,CZ4,CZ5,CJ
      COMPLEX BX,BY,BY1,BY2,BZ1,AL1,AZS,DAMAX1,DAMAX2,AZ1,AZ2
      COMPLEX EE,EEX,EEZ,CEVEN,CODD,SUM1,SUM2
      COMPLEX EE1,EE2,EE3,EEX1,EEX2,EEX3,EEZ1,EEZ2,EEZ3
      DIMENSION AZ(23,82,16),AZS(3,82,16),BY(5,82,16),FX(3,82,16)
      DIMENSION FYL(3,82,16),FZ(3,82,16),FYA(82,16),PY(2,82,16)
      DIMENSION QY(2,82,16),PL(3,82,16),FR(3,82,16),SUM2(60)
      DIMENSION AB1(82,5),AB2(82,5),AB3(82,10),AB4(82,6)
      DIMENSION BXM(2,82),BYM(2,82),BZM(2,82),BXT(2,15),BYT(2,15)
      DIMENSION SUM3(3,14),SUM4(3),BZT(2,15),X(82),ZZ(25)
      COMMON//BXM,BYM,BZM,BXT,BYT,BZT
      COMMON//FR,FYL,QY,PY,AZS,FZ,BY,FX,AZ1,AZ2
      COMMON//AZ,FYA,PL
      LEVEL 2,BXM
      LEVEL 2,FR
      LEVEL 2,AZ
C   READ MACHINE DIMENSIONS,CONSTANTS OF THE MATERIALS AND
C                    NODES DISTRIBUTION
      READ(5,20) L,M,N,IR,IS,IT,IU,IP,IQ,IH,IV,IW,MITER,LL
   20 FORMAT(14I5)
      READ(5,21) H,WL,CM,CS
   21 FORMAT(4F15.5)
      WRITE(6,63)LL,L,M,N,IR,IS,IT,IU,IW,IV,IH,IP,IQ,MITER
   63 FORMAT(//2X,14(2X,I5))
      WRITE(6,73) H,WL,F,S
   73 FORMAT(//2X,4(2X,F12.6))
      WRITE(6,83) CM,CS
   83 FORMAT(//2X,2(2X,F16.6))
      ISW=3
      IRG=21
      IHH=IH+1
      IPP=IP+1
      IQQ=IQ+1
      TT=8.*ATAN(1.0)
      PRO=2.*TT/10000000.0
      S1=1./2000.
      PRI=2000.
      BT=0.0057
      BS=0.013
      PRX=(BS+BT)/(BS+BT/PRI)
```

```
      PRY=(BS+BT*PRI)/(BS+BT)
C ---------------  FREQUENCY CONTROL  ---------------
      F=-50.00
      DO 5000IFI=1,4
      F=F+100.00
      CALL CAM35MM
C ---------------  SLIP AND SPEED CONTROL  -----------
      S=1.1
      DO 3000MI3=1,11
      S=S-.100
      W=TT*F
      V=F*WL*(1.0-S)
C   START CALCULATION OF THE FIRST COMPONENT OF THE MAGNETIC
C   VECTOR POTENTIAL,AND INTRODUCE THE COMPONENTS CONSTRAINTS
      MNI=1
      DO 2000JIJ=MNI,2
      V=F*WL*(1.-S)
C  ---------  SET ALL POTENTIALS TO ZERO  -------
      DO 10K=1,IHH
      DO 10I=1,IPP
      DO 10J=1,IQQ
   10 AZ(I,J,K)=CMPLX(0.0,0.0)
C   CALCULATE THE FACTORS OF THE FINITE-DIFFERENCE EQUATIONS
      RA=1.0000
      IF(JIJ.EQ.1) V=0.0
      S2=PRX/1.
      S3=PRX/PRY
      IF(JIJ.EQ.1) S3=1.0
      IF(JIJ.EQ.1) S2=PRY/1.0
      S4=S2
      S5=PRX/PRI
      IF(JIJ.EQ.1) S5=PRY/PRI
      PE=.50
      PD=.250
      P=1.0/1.244444444
      Q=1.018
      R=.6107
      PP1=P*P
      QQ1=Q*Q
      QP1=QQ1*PP1
      CA1=2.*(QP1+QQ1+PP1)
      CC1=CA1*(1.5+.5*S1)
      PP2=2.*PP1/(Q+R)
      S6=(PRX/PRI)*(R/Q)
      IF(JIJ.EQ.1) S6=(PRY/PRI)*(R/Q)
      QQ2=Q*R
      QP2=QQ2*PP1
      PE1=Q/(Q+R)
      CA2=2.*(QP2+QQ2+PP1)
      CA5=2.*(S3*(QP2+QQ2)+PP1)
      CA11=2.*(QP2+QQ2)*(4.+S1+2.*S5+7.*S2+3.*S3)+PP2*(Q*(9.+S1+7.*S2
     1)+R*(5.+S1+7.*S2+4.*S5))
      CA12=2.*          (S3+S5+2.*S2)*(QP2+QQ2)+PP2*(Q*2.*(S2+1.)
     1+R*2.*(S2+S5))
      Q=.6107
      R=.1275
      QQ3=Q*Q
      QP3=QQ3*PP1
      CA3=2.*(QP3+QQ3+PP1)
```

```
      CA8=2.*(S3*(QP3+QQ3)+PP1)
      PP6=2.*PP1/(Q+R)
      QQ6=Q*R
      QP6=QQ6*PP1
      PE2=R/(Q+R)
      S7=S2*Q/R
      CA6=2.*(QP6+QQ6+PP1)
      CA4=2.*(S3*(QP6+QQ6)+PP1)
      CA13=2.*(QP6+QQ6)*(3.*S3+9.*S2+1.)+PP6*(Q*(11.*S2+2.)+R*(7.*S2+
     16.))
      CA14=2.*(QP6+QQ6)*(3.*S2+S3)+PP6*(Q*4.*S2+2.*R*(S2+1.))
      Q=.1275
      R=1.0
      QQ7=Q*Q
      QP7=QQ7*PP1
      CA7=2.*(QP7+QQ7+PP1)
      PR=PP1/(Q+R)
      QR1=Q*R
      QR=QR1*PP1
      CAA=2.*(QR+QR1+PP1)
      CB=CMPLX(CA7,W*PRO*CM*QP7*H*H)
      CD=QP7*(1.-.5*PRO*CM*V*H)
      CE=QP7*(1.+.5*PRO*CM*V*H)
      QQ9=R*R
      QP9=QQ9*PP1
      CA9=2.*(QQ9+QP9+PP1)
      Z=4.0686
C  SET THE INITIAL CONVERGENCE FACTOR
      AL=CMPLX(1.0,0.0)
C        £££££££££££££££££££££££££££££££££££££££££££££
C        ££                                          ££
C        ££        START ITERATIVE PROCEDURE         ££
C        ££                                          ££
C        £££££££££££££££££££££££££££££££££££££££££££££
      IIH=IH
      IF(JIJ.EQ.1) IIH=IH-1
      DO4000JIE=1,100
      ITRR=JIE
      DAMAX1=CMPLX(0.0,0.0)
      DAMAX2=CMPLX(0.0,0.0)
C    SET THE ITERATIVE SETS((EACH SET=12 ITERATION ))
      DO 1000IE=1,12
      AAA=0.0
      DAMAX=0.0
      ITR=IE
C  ££ START SCANNING THE NODES BY LAYERS                  ££
C  ££  CALCULATE THE POTENTIAL OF THE FOLLOWING NODES FOR ££
C  ££  EACH LAYER IN Z-DIRECTION                          ££
      DO5K=2,IIH
C   CONSIDER THE NODES OF THE STATOR CORE
      LL1=LL-1
      DO 16I=2,LL1
      DO 15J=2,IQ
      Q=1.018
      CC=CC1
      CA=CA1
      IF(I.LE.LL1.AND.K.LT.IV) GO TO 210
      IF(IR-1.GE.J) GO TO 210
      IF(J.GT.IR) GO TO 60
```

```
      IF(K.EQ.IV)GO TO 70
      BZ       =(2.*QP1*(S1*AZ(I,IR+1,K)+AZ(I,IR-1,K))+PP1*(1.+S1)*(AZ(
     1I+1,IR,K)+AZ(I-1,IR,K))+QQ1*(1.+S1)*(AZ(I,IR,K-1)+AZ(I,IR,K+1)))
     2/(CA*(1.+S1))
      BZ1=(AZ(I,J+1,K)+AZ(I,J-1,K))/2.
      IF(JIJ.EQ.1) BZ=BZ1
      GO TO 11
   70 BZ=(QP1*((1.+S1)*AZ(I,J+1,K)+2.*AZ(I,J-1,K))+QQ1*((1.+S1)*AZ(I,J
     1,K+1)+2.*AZ(I,J,K-1))+PP1*(1.5+.5*S1)*(AZ(I+1,J,K)+AZ(I-1,J,K)
     1))/CC
      GO TO 11
   60 IF(J.GT.IS-1) GO TO 90
      IF(K.EQ.IV) GO TO 100
      BZ       =(QP1*(AZ(I,J+1,K)+AZ(I,J-1,K))+PP1*(AZ(I+1,J,K)+AZ(I-1,
     1J,K))+QQ1*(AZ(I,J,K+1)+AZ(I,J,K-1)))/CA
      GO TO 11
  100 BZ          =(QP1* (1.+S1)*(AZ(I,J+1,K)+AZ(I,J-1,K))+PP1*(1.+S1)
     1*(AZ(I+1,J,K)+AZ(I-1,J,K))+2.*QQ1*(S1*AZ(I,J,K+1)+AZ(I,J,K-1)))
     2/(CA*(1.+S1))
      BZ1=(AZ(I,J,K+1)+AZ(I,J,K-1))/2.
      IF(JIJ.EQ.2) BZ=BZ1
      GO TO 11
   90 IF(J.GT.IS) GO TO 210
      IF(K.EQ.IV) GO TO 110
      BZ          =(2.*QP1*  (AZ(I,IS+1,K)+S1*AZ(I,IS-1,K))+PP1*(1.+S1)
     1(AZ(I+1,IS,K)+AZ(I-1,IS,K))+QQ1*(1.+S1)*(AZ(I,IS,K+1)+AZ(I,IS,K-1
     2))/(CA*(1.+S1))
      BZ1=(AZ(I,J+1,K)+AZ(I,J-1,K))/2.
      IF(JIJ.EQ.1) BZ=BZ1
      GO TO 11
  110 BZ=(QP1*((1.+S1)*AZ(I,J-1,K)+2.*AZ(I,J+1,K))+QQ1*((1.+S1)*AZ(I,J
     1,K+1)+2.*AZ(I,J,K-1))+PP1*(1.5+.5*S1)*(AZ(I+1,J,K)+AZ(I-1,J,K)
     1))/CC
      GO TO 11
  210 BZ          =(QP1 *(AZ(I,J+1,K)+AZ(I,J-1,K))+PP1*(AZ(I+1,J,K)+AZ
     1(I-1,J,K))+QQ1*(AZ(I,J,K+1)+AZ(I,J,K-1)))/CA
C   FIND OUT THE EXTRAPULATED VALUE OF THE POTENTIAL,
C       THE NORM AND THE RESIDUALS
   11 DAM=CABS(BZ       -AZ(I,J,K))
      IF(DAM.GT.DAMAX) DAMAX=DAM
      BBBB=CABS(BZ)
      IF(BBBB.GT.AAA) AAA=BBBB
      IF(ITR.EQ.11) DAMAX1=DAMAX1+(BZ-AZ(I,J,K))
      IF(ITR.EQ.12) DAMAX2=DAMAX2+(BZ-AZ(I,J,K))
      AZ(I,J,K)=AZ(I,J,K)+AL*(BZ       -AZ(I,J,K))
   15 CONTINUE
   16 CONTINUE
C    CONSIDER THE NODES OF THE PRIMARY WINDINGS AND AIRGAP
      MM1=M-1
      DO 125 I=LL,MM1
      DO 125 J=2,IQ
      XX=(J-IR)*H
C   SET THE Z-COMPONENT OF THE CURRENT DENSITY-
C       OVER THE ACTIVE ZONE
      CZ2=CS*CEXP(CMPLX(0.0,-XX*TT/WL))*(1.-CEXP(CMPLX(0.,5.*TT/12.)))
     1/(.96*.0305*2.)
      CZ4=.5*CZ2
      CZ5=.75*CZ2
      IF(J.LT.IU.OR.J.GT.IW) CZ2=CZ4
```

```
      IF(J.EQ.IU.OR.J.EQ.IW) CZ2=CZ5
C   SET THE COMPNENTS OF THE CURRENT DENSITY-
C        OVER THE OVERHANG ZONE
      TH=TT*5.*(IV-K)/(4.*6.*Z)
      CZ1=CZ2*(CEXP(CMPLX(0.,TH))-CEXP(CMPLX(0.,(5.*TT/12.-TH))))/(1.-
     1CEXP(CMPLX(0.,5.*TT/12.)))
      CZ3=CZ2*(CEXP(CMPLX(0.,TH))+CEXP(CMPLX(0.,(5.*TT/12.-TH))))/(0.86*
     1(1.-CEXP(CMPLX(0.,5.*TT/12.))))
      IF(JIJ.EQ.1) CZ2=CMPLX(0.0,0.0)
      IF(JIJ.EQ.1) CZ1=CZ3
      IF(I.GT.L) GO TO 214
      IF(I.EQ.LL)GO TO 220
      IF(I.EQ.L) GO TO 420
C   CONSIDER THE NODES OF THE PRIMARY WINDINGS
      CA=CA3
      IF(K.LT.IT) GO TO 211
      IF(IR-1.GE.J) GO TO 211
      IF(J.GT.IR) GO TO 190
      IF(K.EQ.IT) GO TO 300
      IF(K.GE.IV) GO TO 430
      BZ =(QP3*(AZ(I,J+1,K)+AZ(I,J-1,K))+PP1*(AZ(I+1,J,K)+AZ(I-1,J,K))
     1+QQ3*(AZ(I,J,K+1)+AZ(I,J,K-1))+.5*PRO*QP3*H*H*CZ1)/CA3
      BZ1=(AZ(I,J+1,K)+AZ(I,J-1,K))/2.
      IF(JIJ.EQ.1) BZ=BZ1
      GO TO 12
  430 IF(K.GT.IV) GO TO 440
      BZ=(QP3*(4.*S2*AZ(I,J-1,K)+2.*(S2+S3)*AZ(I,J+1,K))+PP1*(1.+3.*S2)
     1*(AZ(I+1,J,K)+AZ(I-1,J,K))+QQ3*(4.*S2*AZ(I,J,K-1)+2.*(S2+S3)*AZ(
     1I,J,K+1))+PRO*QP3*H*H*(PRX*CZ2+CZ1))/(CA8+3.*S2*CA3)
      GO TO 12
  440 BZ =(QP3*(S3*AZ(I,J+1,K)+S2*AZ(I,J-1,K))*2.+PP1*(1.+S2)*(AZ(I+1,J,
     1K)+AZ(I-1,J,K))+QQ3*(S3+S2)*(AZ(I,J,K+1)+AZ(I,J,K-1))+PRO*PRX*QP3
     2*H*H*CZ2)/(   S2*CA3+2.*(S3*(QP3+QQ3)+PP1))
      GO TO 12
  300 BZ =(QP3*(AZ(I,J+1,K)+AZ(I,J-1,K))+PP1*(AZ(I+1,J,K)+AZ(I-1,J,K))
     1+QQ3*(AZ(I,J,K+1)+AZ(I,J,K-1))+.25*PRO*QP3*H*H*CZ1)/CA3
      GO TO 12
  190 IF(J.GT.IS-1) GO TO 200
      IF(K.EQ.IT) GO TO 320
      IF(K.GE.IV) GO TO 450
      BZ =(QP3*(AZ(I,J+1,K)+AZ(I,J-1,K))+PP1*(AZ(I+1,J,K)+AZ(I-1,J,K))
     1+QQ3*(AZ(I,J,K+1)+AZ(I,J,K-1))+PRO*QP3*H*H*CZ1)/CA3
      GO TO 12
  450 IF(K.GT.IV) GO TO 460
      BZ=(AZ(I,J,K+1)+AZ(I,J,K-1))/2.0
      IF(JIJ.EQ.1) BZ=(QP3*(1.+S2)*(AZ(I,J+1,K)+AZ(I,J-1,K))+PP1*(1.+S2)
     1*(AZ(I+1,J,K)+AZ(I-1,J,K))+2.*QQ3*(S2*AZ(I,J,K-1)+AZ(I,J,K+1))+
     1PRO*PRY*QP3*H*H*(CZ1+CZ2))/(CA3*(1.+S2))
      GO TO 12
  460 BZ =(S3*QP3*(AZ(I,J+1,K)+AZ(I,J-1,K))+PP1*(AZ(I+1,J,K)+AZ(I-1,
     1J,K))+QQ3*S3*(AZ(I,J,K+1)+AZ(I,J,K-1))+PRO*PRX*QP3*H*H*CZ2)/(2.*
     2(S3*(QP3+QQ3)+PP1))
      GO TO 12
  320 BZ =(QP3*(AZ(I,J+1,K)+AZ(I,J-1,K))+PP1*(AZ(I+1,J,K)+AZ(I-1,J,K))
     1+QQ3*(AZ(I,J,K+1)+AZ(I,J,K-1))+.5*PRO*QP3*H*H*CZ1)/CA3
      BZ1=(AZ(I,J,K-1)+AZ(I,J,K+1))/2.
      IF(JIJ.EQ.2) BZ=BZ1
      GO TO 12
  200 IF(J.GT.IS) GO TO 211
```

```
      IF(K.EQ.IT) GO TO 340
      IF(K.GE.IV) GO TO 470
      BZ =(QP3*(AZ(I,J+1,K)+AZ(I,J-1,K))+PP1*(AZ(I+1,J,K)+AZ(I-1,J,K))
     1+QQ3*(AZ(I,J,K+1)+AZ(I,J,K-1))+.5*PRO*QP3*H*H*CZ1)/CA3
      BZ1=(AZ(I,J+1,K)+AZ(I,J-1,K))/2.
      IF(JIJ.EQ.1) BZ=BZ1
      GO TO 12
  470 IF(K.GT.IV) GO TO 480
      BZ=(QP3*(4.*S2*AZ(I,J+1,K)+2.*(S2+S3)*AZ(I,J-1,K))+PP1*(1.+3.*S2)
     1*(AZ(I+1,J,K)+AZ(I-1,J,K))+QQ3*(4.*S2*AZ(I,J,K-1)+2.*(S2+S3)*AZ(
     1I,J,K+1))+PRO*QP3*H*H*(PRX*CZ2+CZ1))/(CA8+3.*S2*CA3)
      GO TO 12
  480 BZ =(QP3*(S3*AZ(I,J-1,K)+S2*AZ(I,J+1,K))*2.+PP1*(1.+S2)*(AZ(I+1,J,
     1K)+AZ(I-1,J,K))+QQ3*(S3+S2)*(AZ(I,J,K+1)+AZ(I,J,K-1))+PRO*PRX*QP3
     2*H*H*CZ2)/(   S2*CA3+2.*(S3*(QP3+QQ3)+PP1))
      GO TO 12
  340 BZ =(QP3*(AZ(I,J+1,K)+AZ(I,J-1,K))+PP1*(AZ(I+1,J,K)+AZ(I-1,J,K))
     1+QQ3*(AZ(I,J,K+1)+AZ(I,J,K-1))+.25*PRO*QP3*H*H*CZ1)/CA3
      GO TO 12
C   CONSIDER THE NODES OF THE PRIMARY WINDINGS
C           ((THE LOWER PLANE))
  220 CA=CA2
      R=.6107
      Q=1.018
      IF(K.LT.IT) GO TO 212
      IF(IR-1.GE.J) GO TO 212
  230 IF(J.GT.IR) GO TO 240
      IF(K.EQ.IT) GO TO 250
      IF(K.GE.IV) GO TO 490
      BZ =(QP2*(AZ(I,J+1,K)+AZ(I,J-1,K))+PP2*(Q*AZ(I+1,J,K)+R*AZ(I-1,J,K
     1))+QQ2*(AZ(I,J,K+1)+AZ(I,J,K-1))+PD*PRO*QP2*H*H*CZ1)/CA2
      GO TO 12
  490 IF(K.GT.IV) GO TO 510
      BZ=(QP2*((5.+S3+S5+10.*S2)*AZ(I,J-1,K)+AZ(I,J+1,K)*(3.+2.*S1+
     13.*S5+5.
     1*S3+4.*S2))+PP2*((9.+S1+7.*S2)*AZ(I+1,J,K)*Q+R*(5.+S1+7.*S2+4.*S5
     1)*AZ(I-1,J,K))+QQ2*((5.+10.*S2+S3+S5)*AZ(I,J,K-1)+(3.+2.*S1+5.*S3+
     13.*S5+4.*S2)*AZ(I,J,K+1))+PRO*QP2*H*H*(PRX*3.*CZ2+2.25*CZ1))/CA11
      GO TO 12
  510 BZ =(QP2*(4.*S2*AZ(I,J-1,K)+2.*(S3+S5)*AZ(I,J+1,K))+PP2*(Q*2.*(S2
     1+1.)*AZ(I+1,J,K)+R*2.*(S2+S5)*AZ(I-1,J,K))+QQ2*(S3+2.*S2+S5)*(AZ(
     1I,J,K+1)+AZ(I,J,K-1))+PRO*PRX*QP2*H*H*CZ2)/CA12
      GO TO 12
  250 BZ =(QP2*(AZ(I,J+1,K)+AZ(I,J-1,K))+PP2*(Q*AZ(I+1,J,K)+R*AZ(I-1,J,K
     1))+QQ2*(AZ(I,J,K+1)+AZ(I,J,K-1))+0.25*PRO*QP2*H*H*CZ1)/CA2
      GO TO 12
  240 IF(J.GT.IS-1) GO TO 260
      IF(K.EQ.IT) GO TO 270
      IF(K.GE.IV) GO TO 540
      BZ =(QP2*(AZ(I,J+1,K)+AZ(I,J-1,K))+PP2*(Q*AZ(I+1,J,K)+R*AZ(I-1,J,K
     1))+QQ2*(AZ(I,J,K+1)+AZ(I,J,K-1))+ PE1*PRO*QP2*H*H*CZ1)/CA2
      GO TO 12
  540 IF(K.GT.IV) GO TO 550
      BZ=(QP2*(S3+2.*S2+S5)*(AZ(I,J+1,K)+AZ(I,J-1,K))+PP2*(2.*(S2+1.)*Q*
     1AZ(I+1,J,K)+2.*(S2+S5)*R*AZ(I-1,J,K))+QQ2*(4.*S2*AZ(I,J,K-1)+2.*(
     1S3+S5)*AZ(I,J,K+1))+PRO*QP2*H*H*(PRX*CZ2+CZ1))/CA12
      GO TO 12
  550 BZ =(QP2*(S6+S3)*(AZ(I,J+1,K)+AZ(I,J-1,K))+QQ2*(S6+S3)*(AZ(I,J,K
     1+1)+AZ(I,J,K-1))+2.*PP1*(AZ(I+1,J,K)+S6*AZ(I-1,J,K))+PRO*PRX*
```

```
     1QP2*H*H*CZ2)/(S6*CA2+CA5)
      GO TO 12
  270 BZ =(QP2*(AZ(I,J+1,K)+AZ(I,J-1,K))+PP2*(Q*AZ(I+1,J,K)+R*AZ(I-1,J,K
     1))+QQ2*(AZ(I,J,K+1)+AZ(I,J,K-1))+PD*PRO*QP2*H*H*CZ1)/CA2
      GO TO 12
  260 IF(J.GT.IS) GO TO 212
      IF(K.EQ.IT) GO TO 560
      IF(K.GE.IV) GO TO 570
      BZ =(QP2*(AZ(I,J+1,K)+AZ(I,J-1,K))+PP2*(Q*AZ(I+1,J,K)+R*AZ(I-1,J,K
     1))+QQ2*(AZ(I,J,K+1)+AZ(I,J,K-1))+PD*PRO*QP2*H*H*CZ1)/CA2
      GO TO 12
  570 IF(K.GT.IV) GO TO 580
      BZ=(QP2*((5.+S3+S5+10.*S2)*AZ(I,J+1,K)+AZ(I,J-1,K)*(3.+2.*S1+
     13.*S5+5.
     1*S3+4.*S2))+PP2*((9.+S1+7.*S2)*AZ(I+1,J,K)*Q+R*(5.+S1+7.*S2+4.*S5
     1)*AZ(I-1,J,K))+QQ2*((5.+10.*S2+S3+S5)*AZ(I,J,K-1)+(3.+2.*S1+5.*S3+
     13.*S5+4.*S2)*AZ(I,J,K+1))+PRO*QP2*H*H*(PRX*3.*CZ2+2.25*CZ1))/CA11
      GO TO 12
  580 BZ =(QP2*(4.*S2*AZ(I,J+1,K)+2.*(S3+S5)*AZ(I,J-1,K))+PP2*(Q*2.*(S2
     1+1.)*AZ(I+1,J,K)+R*2.*(S2+S5)*AZ(I-1,J,K))+QQ2*(S3+2.*S2+S5)*(AZ(
     1I,J,K+1)+AZ(I,J,K-1))+PRO*PRX*QP2*H*H*CZ2)/CA12
      GO TO 12
  560 BZ =(QP2*(AZ(I,J+1,K)+AZ(I,J-1,K))+PP2*(Q*AZ(I+1,J,K)+R*AZ(I-1,J,K
     1))+QQ2*(AZ(I,J,K+1)+AZ(I,J,K-1))+0.25*PRO*QP2*H*H*CZ1)/CA2
      GO TO 12
C     CONSIDER THE NODES OF THE PRIMARY WINDINGS
C           ((THE UPPER PLANE))
  420 IF(K.LT.IT) GO TO 213
      IF(IR-1.GE.J) GO TO 213
      Q=.6107
      R=.1275
      IF(J.GT.IR) GO TO 720
      IF(K.EQ.IT) GO TO 730
      IF(K.GE.IV) GO TO 740
      BZ=(QP6*(AZ(I,J+1,K)+AZ(I,J-1,K))+QQ6*(AZ(I,J,K+1)+AZ(I,J,K-1))+
     1PP6*(Q*AZ(I+1,J,K)+R*AZ(I-1,J,K))+.25*PRO*QP6*H*H*CZ1)/CA6
      GO TO 12
  740 IF(K.GT.IV) GO TO 750
      BZ  =(QP6*((S3+11.*S2+1.)*AZ(I,J-1,K)+(5.*S3+7.*S2+1.)*AZ(I,J+1,K)
     1)+PP6*
     1(Q*(11.*S2+2.)*AZ(I+1,J,K)+R*(7.*S2+6.)*AZ(I-1,J,K))+QQ6*((11.*S2+
     1S3+1.)*AZ(I,J,K-1)+(7.*S2+5.*S3+1.)*AZ(I,J,K+1))+PRO*QP6*H*H*(
     13.*PRX*CZ2+2.25*CZ1))/CA13
      GO TO 12
  750 BZ=(QP6*(2.*(S2+S3)*AZ(I,J+1,K)+4.*S2*AZ(I,J-1,K))+QQ6*(3.*S2+S3
     1)*(AZ(I,J,K+1)+AZ(I,J,K-1))+PP6*(4.*S2*Q*AZ(I+1,J,K)+2.*(S2+1.)*
     1R*AZ(I-1,J,K))+PRO*PRX*QP6*H*H*CZ2)/CA14
      GO TO 12
  730 BZ=(QP6*(AZ(I,J+1,K)+AZ(I,J-1,K))+QQ6*(AZ(I,J,K+1)+AZ(I,J,K-1))+
     1PP6*(Q*AZ(I+1,J,K)+R*AZ(I-1,J,K))+.25*PRO*QP6*H*H*CZ1)/CA6
      GO TO 12
  720 IF(J.GT.IS-1) GO TO 760
      IF(K.EQ.IT) GO TO 770
      IF(K.GE.IV) GO TO 780
      BZ=(QP6*(AZ(I,J+1,K)+AZ(I,J-1,K))+QQ6*(AZ(I,J,K+1)+AZ(I,J,K-1))+
     1PP6*(Q*AZ(I+1,J,K)+R*AZ(I-1,J,K))+PE2*PRO*QP6*H*H*CZ1)/CA6
      GO TO 12
  780 IF(K.GT.IV) GO TO 790
      BZ=(QP6*(S3+3.*S2)*(AZ(I,J+1,K)+AZ(I,J-1,K))+PP6*(4.*S2*Q*AZ(I+1
```

```
     1,J,K)+R*2.*(1.+S2)*AZ(I-1,J,K))+QQ6*(4.*S2*AZ(I,J,K-1)+2.*(S2+
     1S3)*AZ(I,J,K+1))+PRO*QP6*H*H*(PRX*CZ2+CZ1))/CA14
      GO TO 12
  790 BZ=(QP6*(S7+S3)*(AZ(I,J+1,K)+AZ(I,J-1,K))+QQ6*(S7+S3)*(AZ(I,J,K+
     11)+AZ(I,J,K-1))+2.*PP1*(AZ(I-1,J,K)+S7*AZ(I+1,J,K))+PRO*PRX*QP6*
     1H*H*CZ2)/(S7*CA6+CA4)
      GO TO 12
  770 BZ=(QP6*(AZ(I,J+1,K)+AZ(I,J-1,K))+QQ6*(AZ(I,J,K+1)+AZ(I,J,K-1))+
     1PP6*(Q*AZ(I+1,J,K)+R*AZ(I-1,J,K))+.25*PRO*QP6*H*H*CZ1)/CA6
      GO TO 12
  760 IF(J.GT.IS) GO TO 213
      IF(K.EQ.IT) GO TO 810
      IF(K.GE.IV) GO TO 830
      BZ=(QP6*(AZ(I,J+1,K)+AZ(I,J-1,K))+QQ6*(AZ(I,J,K+1)+AZ(I,J,K-1))+
     1PP6*(Q*AZ(I+1,J,K)+R*AZ(I-1,J,K))+.25*PRO*QP6*H*H*CZ1)/CA6
      GO TO 12
  830 IF(K.GT.IV) GO TO 820
      BZ  =(QP6*((S3+11.*S2+1.)*AZ(I,J+1,K)+(5.*S3+7.*S2+1.)*AZ(I,J-1,K)
     1)+PP6*
     1(Q*(11.*S2+2.)*AZ(I+1,J,K)+R*(7.*S2+6.)*AZ(I-1,J,K))+QQ6*((11.*S2+
     1S3+1.)*AZ(I,J,K-1)+(7.*S2+5.*S3+1.)*AZ(I,J,K+1))+PRO*QP6*H*H*(
     13.*PRX*CZ2+2.25*CZ1))/CA13
      GO TO 12
  820 BZ=(QP6*((S3+S2)*2.*AZ(I,J-1,K)+4.*S2*AZ(I,J+1,K))+QQ6*(3.*S2+S3
     1)*(AZ(I,J,K+1)+AZ(I,J,K-1))+PP6*(4.*S2*Q*AZ(I+1,J,K)+2.*(S2+1.)*
     1R*AZ(I-1,J,K))+PRO*PRX*QP6*H*H*CZ2)/CA14
      GO TO 12
  810 BZ=(QP6*(AZ(I,J+1,K)+AZ(I,J-1,K))+QQ6*(AZ(I,J,K+1)+AZ(I,J,K-1))+
     1PP6*(Q*AZ(I+1,J,K)+R*AZ(I-1,J,K))+.25*PRO*QP6*H*H*CZ1)/CA6
      GO TO 12
C   CONSIDER THE NODES OF THE AIRGAP
  211 Q=.6107
      BZ =(QP3*(AZ(I,J+1,K)+AZ(I,J-1,K))+PP1*(AZ(I+1,J,K)+AZ(I-1,J,K))
     1+QQ3*(AZ(I,J,K+1)+AZ(I,J,K-1)))/CA3
      GO TO 12
  213 Q=.6107
      R=.1275
      BZ=(QP6*(AZ(I,J+1,K)+AZ(I,J-1,K))+QQ6*(AZ(I,J,K+1)+AZ(I,J,K-1))+
     1PP6*(Q*AZ(I+1,J,K)+R*AZ(I-1,J,K)))/CA6
      GO TO 12
  214 Q=.1275
      BZ=(QP7*(AZ(I,J+1,K)+AZ(I,J-1,K))+QQ7*(AZ(I,J,K+1)+AZ(I,J,K-1))+
     1PP1*(AZ(I+1,J,K)+AZ(I-1,J,K)))/CA7
      GO TO 12
  212 Q=1.018
      R=.6107
      BZ =(QP2*(AZ(I,J+1,K)+AZ(I,J-1,K))+PP2*(Q*AZ(I+1,J,K)+R*AZ(I-1,J,K
     1))+QQ2*(AZ(I,J,K+1)+AZ(I,J,K-1)))/CA2
C   FIND OUT THE EXTRAPULATED VALUE OF THE POTENTIAL,
C        THE NORM AND THE RESIDUALS
   12 DAM=CABS(BZ-AZ(I,J,K))
      IF(DAM.GT.DAMAX) DAMAX=DAM
      BBBB=CABS(BZ)
      IF(BBBB.GT.AAA) AAA=BBBB
      IF(ITR.EQ.11) DAMAX1=DAMAX1+(BZ-AZ(I,J,K))
      IF(ITR.EQ.12) DAMAX2=DAMAX2+(BZ-AZ(I,J,K))
      AZ(I,J,K)=AZ(I,J,K)+AL*(BZ-AZ(I,J,K))
  125 CONTINUE
C   CONSIDER THE NODES ON THE INTERFERANCE SURFACES BETWEEN
```

```
C         THE AIRGAP AND THE SECONDARY CONDUCTOR
          DO 25J=2,IQ
          Q=.1275
          CA=CA7
          I=M
          IF(K.LE.ISW) GO TO 66
          BZ        =((Q*Q*P*P+CD)*AZ(M,J+1,K)+(Q*Q*P*P+CE)*AZ(M,J-1,K)+2.*
         1P*P*(AZ(M+1,J,K)+AZ(M-1,J,K))+Q*Q*2.*(AZ(M,J,K+1)+AZ(M,J,K-1)))/
         2(CA+CB)
          IF(JIJ.EQ.2) BZ=BZ+QP7*H*H*PRO*V*CM*BY(3,J,K)/(CA+CB)
          GO TO 68
       66 IF(K.EQ.ISW) GO TO 67
          BZ=(QP7*(AZ(I,J+1,K)+AZ(I,J-1,K))+QQ7*(AZ(I,J,K+1)+AZ(I,J,K-1))+
         1PP1*(AZ(I+1,J,K)+AZ(I-1,J,K)))/CA7
          GO TO 68
       67 BZ=((3.*QP7+CD)*AZ(I,J+1,K)+(3.*QP7+CE)*AZ(I,J-1,K)+4.*PP1*(AZ(I+1
         1,J,K)+AZ(I-1,J,K))+4.*QQ7*(AZ(I,J,K-1)+AZ(I,J,K+1)))/(3.*CA+CB)
C      FIND OUT THE EXTRAPULATED VALUE OF THE POTENTIAL,
C         THE NORM AND THE RESIDUALS
       68 DAM=CABS(BZ-AZ(M,J,K))
          IF(DAM.GT.DAMAX)DAMAX=DAM
          BBBB=CABS(BZ)
          IF(BBBB.GT.AAA) AAA=BBBB
          IF(ITR.EQ.11) DAMAX1=DAMAX1+(BZ-AZ(M,J,K))
          IF(ITR.EQ.12) DAMAX2=DAMAX2+(BZ-AZ(M,J,K))
          AZ(M,J,K)=AZ(M,J,K)+AL*(BZ        -AZ(M,J,K))
       25 CONTINUE
C      CONSIDER THE NODES OF THE SECONDARY CONDUCTOR
          Q=.1275
          MM2=M+1
          NN1=N-1
          DO 35 I=MM2,NN1
          DO 35 J=2,IQ
          IF(K.LE.ISW) GO TO 76
          BZ        =(CD*AZ(I,J+1,K)+CE*AZ(I,J-1,K)+P*P*(AZ(I+1,J,K)+AZ(I-1
         1,J,K))+Q*Q*(AZ(I,J,K+1)+AZ(I,J,K-1)))/CB
          IF(JIJ.EQ.2) BZ=BZ+QP7*H*H*PRO*V*CM*BY(I-12,J,K)/CB
          GO TO 78
       76 IF(K.EQ.ISW) GO TO 77
          BZ=(QP7*(AZ(I,J+1,K)+AZ(I,J-1,K))+QQ7*(AZ(I,J,K+1)+AZ(I,J,K-1))+
         1PP1*(AZ(I+1,J,K)+AZ(I-1,J,K)))/CA7
          GO TO 78
       77 BZ=((QP7+CD)*AZ(I,J+1,K)+(QP7+CE)*AZ(I,J-1,K)+2.*PP1*(AZ(I+1,J,K)
         1+AZ(I-1,J,K))+2.*QQ7*(AZ(I,J,K+1)+AZ(I,J,K-1)))/(CA+CB)
          BZ1=(AZ(I,J,K-1)+AZ(I,J,K+1))/2.
          IF(JIJ.EQ.2) BZ=BZ1
C      FIND OUT THE EXTRAPULATED VALUE OF THE POTENTIAL,
C         THE NORM AND THE RESIDUALS
       78 DAM=CABS(BZ-AZ(I,J,K))
          IF(DAM.GT.DAMAX) DAMAX=DAM
          BBBB=CABS(BZ)
          IF(BBBB.GT.AAA) AAA=BBBB
          IF(ITR.EQ.11) DAMAX1=DAMAX1+(BZ-AZ(I,J,K))
          IF(ITR.EQ.12) DAMAX2=DAMAX2+(BZ-AZ(I,J,K))
          AZ(I,J,K)=AZ(I,J,K)+AL*(BZ        -AZ(I,J,K))
       35 CONTINUE
C      CONSIDER THE NODES ON THE INTERFERANCE SURFACES BETWEEN
C         THE SECONDARY CONDUCTOR AND THE BACKING IRON
          DO 45J=2,IQ
```

```
      Q=.1275
      CA=CA7
      I=N
      IF(K.LE.ISW) GO TO 86
      IF(K.GE.IV) GO TO 900
      BZ =((QP7+CD)*AZ(I,J+1,K)+(QP7+CE)*AZ(I,J-1,K)+2.*PP1*(AZ(I+1,J,
     1K)+AZ(I-1,J,K))+2.*QQ7*(AZ(I,J,K-1)+AZ(I,J,K+1)))/(CA+CB)
      IF(JIJ.EQ.2) BZ=BZ+QP7*H*H*PRO*V*CM*BY(5,J,K)/(CA+CB)
      GO TO 18
   86 IF(K.EQ.ISW) GO TO 87
      BZ=(QP7*(AZ(I,J+1,K)+AZ(I,J-1,K))+QQ7*(AZ(I,J,K+1)+AZ(I,J,K-1))+
     1PP1*(AZ(I+1,J,K)+AZ(I-1,J,K)))/CA7
      GO TO 18
   87 BZ=((3.*QP7+CD)*AZ(I,J+1,K)+(3.*QP7+CE)*AZ(I,J-1,K)+4.*PP1*(AZ(I+1
     1,J,K)+AZ(I-1,J,K))+4.*QQ7*(AZ(I,J,K-1)+AZ(I,J,K+1)))/(3.*CA+CB)
      GO TO 18
  900 IF(K.EQ.IV) GO TO 910
      BZ  =((QP7*S1+CD)*AZ(I,J+1,K)+(QP7*S1+CE)*AZ(I,J-1,K)+2.*PP1*(
     1AZ(I-1,J,K)+S1*AZ(I+1,J,K))+QQ7*(1.+S1)*(AZ(I,J,K-1)+AZ(I,J,K+1))
     2)/(S1*CA+CB)
      IF(JIJ.EQ.2) BZ=BZ+QP7*H*H*PRO*V*CM*BY(5,J,K)/(S1*CA+CB)
      GO TO 18
  910 BZ  =((1.*QP7*(S1+1.)+2.*CD)*AZ(I,J+1,K)+(1.*QP7*(S1+1.)+2.*CE)*
     1AZ(I,J-1,K)+2.*PP1*(S1+1.)*AZ(I+1,J,K)+PP1*(0.+4.)*AZ(I-1,J,K)+
     2QQ7*((0.+4.)*AZ(I,J,K-1)+2.*(S1+1.)*AZ(I,J,K+1)))/(1.*CA*(S1+1.)
     3+2.*CB)
      IF(JIJ.EQ.2) BZ=BZ+QP7*H*H*PRO*V*CM*BY(5,J,K)/((1.+S1)*CA+2.*CB)
C   FIND OUT THE EXTRAPULATED VALUE OF THE POTENTIAL,
C        THE NORM AND THE RESIDUALS
   18 DAM= CABS(BZ-AZ(I,J,K))
      IF(DAM.GT.DAMAX) DAMAX=DAM
      BBBB=CABS(BZ)
      IF(BBBB.GT.AAA) AAA=BBBB
      IF(ITR.EQ.11) DAMAX1=DAMAX1+(BZ-AZ(I,J,K))
      IF(ITR.EQ.12) DAMAX2=DAMAX2+(BZ-AZ(I,J,K))
      AZ(I,J,K)=AZ(I,J,K)+AL*(BZ-AZ(I,J,K))
   45 CONTINUE
C   CONSIDER THE NODES OF THE BACKING IRON
      NN=N+1
      I=NN
      DO 105J=2,IQ
      Q=.1275
      R=1.0
      IF(K.GE.IV) GO TO 920
      BZ  =(QR*(AZ(I,J+1,K)+AZ(I,J-1,K))+2.*PR*(Q*AZ(I+1,J,K)+R*AZ(I-1,
     1J,K)) +QR1*(AZ(I,J,K-1)+AZ(I,J,K+1)))/CAA
      GO TO 19
  920 IF(K.EQ.IV) GO TO 930
      BZ  =(QR*(AZ(I,J+1,K)+AZ(I,J-1,K))+2.*PR*(Q*AZ(I+1,J,K)+R*AZ(I-1,
     1J,K)) +QR1*(AZ(I,J,K-1)+AZ(I,J,K+1)))/CAA
      GO TO 19
  930 BZ  =(QR*(S1+1.)*(AZ(I,J+1,K)+AZ(I,J-1,K))+2.*PR*(1.+S1)*(Q*AZ
     1(I+1,J,K)+R*AZ(I-1,J,K))+QR1*(AZ(I,J,K-1)+S1*AZ(I,J,K+1)))/(CAA*(
     21.+S1))
      BZ1=(AZ(I,J,K+1)+AZ(I,J,K-1))/2.
      IF(JIJ.EQ.2) BZ=BZ1
C   FIND OUT THE EXTRAPULATED VALUE OF THE POTENTIAL,
C        THE NORM AND THE RESIDUALS
```

```
   19 DAM= CABS(BZ-AZ(I,J,K))
      IF(DAM.GT.DAMAX) DAMAX=DAM
      BBBB=CABS(BZ)
      IF(BBBB.GT.AAA) AAA=BBBB
      IF(ITR.EQ.11) DAMAX1=DAMAX1+(BZ-AZ(I,J,K))
      IF(ITR.EQ.12) DAMAX2=DAMAX2+(BZ-AZ(I,J,K))
      AZ(I,J,K)=AZ(I,J,K)+AL*(BZ-AZ(I,J,K))
  105 CONTINUE
      Q=1.0
      NN2=N+2

C   CONSIDER THE NODES OF THE BACKING IRON,INTERFACE SURFACE
C   AND BETWEEN THE BACKING IRON AND THE OUTER FRAME
      DO 55I=NN2,IP
      CA=CA9
      DO 55J=2,IQ
      IF(I.EQ.IRG.AND.K.GE.IV) GO TO 971
      IF(K.EQ.IV) GO TO 950
      BZ =(QP9*(AZ(I,J+1,K)+AZ(I,J-1,K))+PP1*(AZ(I+1,J,K)+AZ(I-1,J,K))
     1+QQ9*(AZ(I,J,K+1)+AZ(I,J,K-1)))/CA
      GO TO 17
  950 BZ=(QP9*(1.+S1)*(AZ(I,J+1,K)+AZ(I,J-1,K))+PP1*(1.+S1)*(AZ(I+1,J,K
     1)+AZ(I-1,J,K))+2.*QQ9*(AZ(I,J,K-1)+S1*AZ(I,J,K+1)))/(CA*(1.+S1))
      BZ1=(AZ(I,J,K+1)+AZ(I,J,K-1))/2.0
      IF(JIJ.EQ.2) BZ=BZ1
      GO TO 17
  971 IF(K.GT.IV) GO TO 970
      BZ=(QP9*(3.+S1)*(AZ(I,J+1,K)+AZ(I,J-1,K))/2.+PP1*(2.*AZ(I+1,J,K)+(
     11.+S1)*AZ(I-1,J,K))+QQ9*(2.*AZ(I,J,K-1)+(1.+S1)*AZ(I,J,K+1)))
     1/(CA*(1.5+.5*S1))
      GO TO 17
  970 BZ =(QP9*(1.+S1)*(AZ(I,J+1,K)+AZ(I,J-1,K))+2.*PP1*(S1*AZ(I-1,J,K)
     1+AZ(I+1,J,K))+QQ9*(1.+S1)*(AZ(I,J,K+1)+AZ(I,J,K-1)))/(CA*(1.+S1))
C   FIND OUT THE EXTRAPULATED VALUE OF THE POTENTIAL,
C        THE NORM AND THE RESIDUALS
   17 DAM= CABS(BZ-AZ(I,J,K))
      IF(DAM.GT.DAMAX) DAMAX=DAM
      BBBB=CABS(BZ)
      IF(BBBB.GT.AAA) AAA=BBBB
      IF(ITR.EQ.11) DAMAX1=DAMAX1+(BZ-AZ(I,J,K))
      IF(ITR.EQ.12) DAMAX2=DAMAX2+(BZ-AZ(I,J,K))
      AZ(I,J,K)=AZ(I,J,K)+AL*(BZ-AZ(I,J,K))
   55 CONTINUE
    5 CONTINUE
C   CALCULATE THE POTENTIALS AT THE PERIHERAL NODES
  960 IF(ITRR.GT.25) GO TO 14
      DO 65I=2,IP
      AZ(I,1,1)=AZ(I,2,2)
      AZ(I,IQQ,1)=AZ(I,IQ,2)
      DO 65J=2,IQ
   65 AZ(I,J,1)=AZ(I,J,2)
      DO 75K=2,IH
      AZ(1,1,K)=AZ(2,2,K)
      AZ(IPP,1,K)=AZ(IP,2,K)
      AZ(IPP,IQQ,K)=AZ(IP,IQ,K)
      AZ(1,IQQ,K)=AZ(2,IQ,K)
      DO 75I=2,IP
      AZ(I,1,K)=AZ(I,2,K)
```

```
   75 AZ(I,IQQ,K)=AZ(I,IQ,K)
      DO 85J=2,IQ
      AZ(1,J,1)=AZ(2,J,2)
      AZ(IPP,J,1)=AZ(IP,J,2)
      DO 85K=2,IH
      AZ(1,J,K)=AZ(2,J,K)
   85 AZ(IPP,J,K)=AZ(IP,J,K)
      AZ(1,1,1)=AZ(2,2,2)
      AZ(1,IQQ,1)=AZ(2,IQ,2)
      AZ(IPP,1,1)=AZ(IP,2,2)
      AZ(IPP,IQQ,1)=AZ(IP,IQ,2)
   14 DO 185I=1,IPP
      DO 185J=1,IQQ
      AZ(I,J,IHH)=AZ(I,J,IH-1)
  185 IF(JIJ.EQ.1) AZ(I,J,IHH)=-AZ(I,J,IH-1)
C IF THE SOLUTION DIVERGE ----STOP COMPUTATION
      IF(DAMAX.GT.1000.0) GO TO 3000
      IF(ITRR.EQ.50) GO TO 23
 1000 CONTINUE
C   AT THE END OF EACH ITERATION SET CALCULATE THE NEW
C     CONVERGENCE FACTOR, ** TEST ACCURACY OF THE SOLUTION **
      DDD=DAMAX/AAA
   13 FORMAT(//10X,I5,2(4X,1PE11.4))
      WRITE(6,13) ITR,DAMAX,DDD
      IF(DDD.LT.0.00001) GO TO 23
      RR=DAMAX2/DAMAX1
      ALO=2./(1.+CSQRT(1.-(RR+AL-1.)**2/(AL*AL*RR)))
      ALMM=1.+10.*(REAL(ALO)-1.)/((5.-REAL(ALO))*(2.+REAL(ALO)))
      ALM=CMPLX(ALMM,AIMAG(ALO))
      AL=ALM
      IF(ITRR.EQ.1) AL=CMPLX(1.0,0.0)
      IF(ITRR.EQ.2) AL=CMPLX(1.35,0.1)
      WRITE(6,414) RR,ALO,ALM
  414 FORMAT(//10X,3(2X,2F12.8))
 4000 CONTINUE
      DO 95K=1,IH
      DO 95I=1,9
   95 WRITE(6,33)(AZ(I,J,K),J=1,IQQ)
   33 FORMAT(/2X,5(2X,2F10.8))
C   HAVING CALCULATE THE FIRST COMPONENT((AX)),CALCULATE AND
C      STORE THE NECESSARY VARIABLES DEPEND ON THIS COMP.
   23 IF(JIJ.EQ.2) GO TO 1500
      DO 165K=1,IH
      BXT(MI3,K)=0.0
      BYT(MI3,K)=0.0
      BZT(MI3,K)=0.0
      DO 165J=1,IQQ
      FYA(J,K)=0.0
      BXM(MI3,J)=0.0
      BYM(MI3,J)=0.0
      BZM(MI3,J)=0.0
      DO 165I=1,5
      BY(I,J,K)=CMPLX(0.0,0.0)
      IF(I.GT.3) GO TO 165
      FZ(I,J,K)=0.0
      FX(I,J,K)=0.0
      FR(I,J,K)=0.0
      PL(I,J,K)=0.0
      FYL(I,J,K)=0.0
```

```
      AZS(I,J,K)=CMPLX(0.0,0.0)
      IF(I.GT.2) GO TO 165
      PY(I,J,K)=0.0
      QY(I,J,K)=0.0
  165 CONTINUE
      BZ=CMPLX(0.0,0.0)
      DO 215J=1,IQQ
  215 X(J)=0.0
      DO 225K=1,IH
  225 ZZ(K)=0.0
      Q=.1275
      P=1./1.244444444
C      CALCULATE THE INDUCE VOLTAGE DUE TO AX-COMPONENT
      EEX=CMPLX(0.0,0.0)
      EEX2=CMPLX(0.0,0.0)
      EEX1=CMPLX(0.0,0.0)
      EEX3=CMPLX(0.0,0.0)
      DO 774K22=7,15
      DO 778J22=5,49
      SUM2(J22)=CMPLX(0.0,0.0)
      DO 778I22=LL,L
      SUM2(J22)=SUM2(J22)+AZ(I22,J22,K22)/5.00
  778 CONTINUE
      SUM1=CMPLX(0.0,0.0)
      CODD=CMPLX(0.0,0.0)
      CEVEN=CMPLX(0.0,0.0)
      DO  775 J22=6,46,2
      C22=-SQRT(2.)
      IF(J22.LT.14.OR.J22.GE.41) C22=1./SQRT(2.)
      IF(J22.GE.23.AND.J22.LT.32) C22=SQRT(2.)
      CEVEN=CEVEN+C22*SUM2(J22)
  775 CODD=CODD+C22*SUM2(J22+1)
      CEVEN=CEVEN+C22*SUM2(48)
      SUM1=H*(SUM2(5)+SUM2(49)+4.*CEVEN+2.*CODD)/3.00
      EEX=EEX+SUM1
      J3=1
      DO 704J33=1,3
      J3=J3+3
      DO 705J44=J3,48,9
      J22=J44+2
      C22=-SQRT(2.)
      IF(J22.LT.14.OR.J22.GE.41) C22=1./SQRT(2.)
      IF(J22.GE.23.AND.J22.LT.32) C22=SQRT(2.)
      IF(J33.EQ.1) EEX1=EEX1+C22*H*SUM2(J22)
      IF(J33.EQ.2) EEX2=EEX2+C22*H*SUM2(J22)
      IF(J33.EQ.3) EEX3=EEX3+C22*H*SUM2(J22)
  705 CONTINUE
  704 CONTINUE
  774 CONTINUE
      EEX=CMPLX(0.,100.*.93*W/3.0)*EEX
      EEX1=CMPLX(0.,100.*W*.93)*EEX1
      EEX2=CMPLX(0.,100.*W*.93)*EEX2
      EEX3=CMPLX(0.,100.*W*.93)*EEX3
C   CALCULATE THE FLUX DENSITY COMPONENTS DUE TO AX
      M3=M-1
      II=0
      LL1=M-4
      DO 119I=LL1,N
      IF(I.GT.11.AND.I.LE.13) GO TO 119
```

```
      II=II+1
      DO 115J=2,IQ
      DO 115K=1,IH
      BZ=-(AZ(I-2,J,K)-6.*AZ(I-1,J,K)+3.*AZ(I,J,K)+2.*AZ(I+1,J,K))/
     1(6.*Q*H)
      IF(II.EQ.1.AND.K.EQ.15) BZM(MI3,J)=CABS(BZ)
      IF(II.EQ.1.AND.J.EQ.27) BZT(MI3,K)=CABS(BZ)
      IF(K.EQ.1.OR.K.EQ.IH) GO TO 804
      BY(II,J,K)=(AZ(I,J,K+2)-6.*AZ(I,J,K+1)+3.*AZ(I,J,K)+2.*AZ(I,J,K-1)
     1)/(6.*P*H)
  304 IF(K.EQ.IH)BY(II,J,K)=(AZ(I,J,K-1)-AZ(I,J,K+1))/(2.*P*H)
      IF(K.EQ.1) BY(II,J,K)=BY(I,J,K+1)
      IF(K.LE.2) GO TO 115
      IF(I.GT.M) GO TO 365
C   CALCULATE THE AIRGAP-CROSS POWER,FORCES,CURRENT
C             DENSITIES AND LOSSES
      PY(II,J,K)=.5*REAL(W*AZ(I,J,K)*CMPLX(0.,-1.)*CONJG(BZ))
      QY(II,J,K)=.5*AIMAG(W*AZ(I,J,K)*CMPLX(0.,-1.)*CONJG(BZ))
  365 IF(I.LT.M) GO TO 115
      III=I-M3
      FYL(III,J,K)=.5*REAL(W*AZ(I,J,K)*CMPLX(0.,1.)*CM*CONJG(BZ))
      CJ=CM*W*CMPLX(0.,-1.)*AZ(I,J,K)
      PL(III,J,K)=.5*REAL(CJ*CONJG(CJ))/CM
      AZS(III,J,K)=AZ(I,J,K)
  115 CONTINUE
  119 CONTINUE
 2000 CONTINUE
 1500 II=0
C   HAVING CALCULATE BOTH COMPONENTS OF THE POTENTIAL(AX &AZ)
C   CALCULATE THE STATE VARIABLES OF THE PERFORMANCE
      M3=M-1
      Q=.1275
      P=1./1.2444444444
C   CALCULATE THE INDUCED EMF
      EEZ=CMPLX(0.0,0.0)
      DO 772J22=5,49
      DO 779K22=7,15
      SUM2(K22)=CMPLX(0.0,0.0)
      DO 779I22=LL,L
      SUM2(K22)=SUM2(K22)+AZ(I22,J22,K22)/5.00
  779 CONTINUE
      SUM1=CMPLX(0.0,0.0)
      CODD=CMPLX(0.0,0.0)
      CEVEN=CMPLX(0.0,0.0)
      DO 771K22=8,12,2
      CEVEN=CEVEN+SUM2(K22)
  771 CODD=CODD+SUM2(K22+1)
      CEVEN=CEVEN+SUM2(14)
      SUM1=P*H*(SUM2(7)+4.*CEVEN+2.*CODD+SUM2(15))/3.
      C22=-SQRT(2.)
      IF(J22.LT.14.OR.J22.GE.41) C22=1./SQRT(2.)
      IF(J22.GE.23.AND.J22.LT.32) C22=SQRT(2.)
  772 EEZ=EEZ+C22*SUM1
      EEZ=CMPLX(0.,100.*.93*W/3.0)*EEZ
      EE=EEX+EEZ
      WRITE(6,765) EE,EEX,EEZ
  765 FORMAT(//5X,3(4X,2F12.6))
      EEZ1=CMPLX(0.0,0.0)
      EEZ2=CMPLX(0.0,0.0)
```

```
      EEZ3=CMPLX(0.0,0.0)
      J3=1
      DO 706J33=1,3
      J3=J3+3
      DO 707J44=J3,48,9
      J22=J44+2
      DO 707K22=7,15
      DO 803I22=LL,L
      C22=-SQRT(2.)
      IF(J22.LT.14.OR.J22.GE.41) C22=1./SQRT(2.)
      IF(J22.GE.23.AND.J22.LT.32) C22=SQRT(2.)
      IF(J33.EQ.1) EEZ1=EEZ1+C22*H*AZ(I22,J22,K22)*P/5.
      IF(J33.EQ.2) EEZ2=EEZ2+C22*H*AZ(I22,J22,K22)*P/5.
      IF(J33.EQ.3) EEZ3=EEZ3+C22*H*AZ(I22,J22,K22)*P/5.
  803 CONTINUE
  707 CONTINUE
  706 CONTINUE
      EEZ1=CMPLX(0.,100.*W*.93)*EEZ1
      EEZ2=CMPLX(0.,100.*W*.93)*EEZ2
      EEZ3=CMPLX(0.,100.*W*.93)*EEZ3
      EE1=EEX1+EEZ1
      EE2=EEX2+EEZ2
      EE3=EEX3+EEZ3
      WRITE(6,708) EE1,EEX1,EEZ1
  708 FORMAT(//5X,3(4X,2F12.6))
      WRITE(6,709) EE2,EEX2,EEZ2
  709 FORMAT(//5X,3(4X,2F12.6))
      WRITE(6,802) EE3,EEX3,EEZ3
  802 FORMAT(//5X,3(4X,2F12.6))
      V=F*WL*(1.0-S)
      LL1=M-4
      DO 319I=LL1,N
      IF(I.GT.11.AND.I.LE.13) GO TO 319
      II=II+1
      DO 315J=2,IQ
      DO 315K=1,IH
C   CALCULATE THE FLUX DENSITY COMPONENTS
      BX=+(AZ(I-2,J,K)-6.*AZ(I-1,J,K)+3.*AZ(I,J,K)+2.*AZ(I+1,J,K))/
     1(6.*Q*H)
      IF(II.EQ.1.AND.K.EQ.15) BXM(MI3,J)=CABS(BX)
      IF(II.EQ.1.AND.J.EQ.27) BXT(MI3,K)=CABS(BX)
      IF(J.EQ.2) GO TO 805
      BY1=(AZ(I,J-2,K)-6.*AZ(I,J-1,K)+3.*AZ(I,J,K)+2.*AZ(I,J+1,K))/
     1(6.*H)
  805 IF(J.EQ.2) BY1=(AZ(I,J+1,K)-AZ(I,J-1,K))/(2.*H)
      BY2=BY(II,J,K)-BY1
      IF(II.EQ.1.AND.K.EQ.15) BYM(MI3,J)=CABS(BY2)
      IF(II.EQ.1.AND.J.EQ.27) BYT(MI3,K)=CABS(BY2)
      IF(K.LE.2) GO TO 315
      IF(I.GT.M) GO TO 375
C   CALCULATE THE AIRGAP-CROSS POWER
      PY(II,J,K)=(.5*REAL(W*CMPLX(.0,-1.)*AZ(I,J,K)*CONJG(BX          ))
     1-PY(II,J,K))/PRO
      QY(II,J,K)= (.5*AIMAG(W*CMPLX(0.,-1.)*AZ(I,J,K)*CONJG(BX))
     1-QY(II,J,K))/PRO
  375 IF(I.LT.M) GO TO 315
      III=I-M3
C   CALCULATE THE PROPULTION FORCE
      FX(III,J,K)=.5*REAL((W*AZ(I,J,K)*CMPLX(.0,1.)-V*BY2)*CM*
```

```
     1CONJG(BY2))
C    CALCULATE THE LEVITATION FORCE--REPULSION
       FYL(III,J,K)=FYL(III,J,K)+.5*
     1REAL((W*AZ(I,J,K)*CMPLX(.0,-1.)+V*BY2)*CM*CONJG(BX        ))
       IF(J.EQ.IQ) GO TO 101
C    CALCULATE THE FORCE IN LATERAL DIRECTION
  101 FZ(III,J,K)=.5*REAL(W*AZS(III,J,K)*CMPLX(0.,-1.)*CONJG(BY2)*CM)
C    CALCULATE THE CURRENT DENSITY
       CJ=CM*(W*CMPLX(0.,-1.)*AZ(I,J,K)+V*BY2)
C    CALCULATE THE COPPER LOSSES IN THE SECONDARY
       PL(III,J,K)=PL(III,J,K)+.5*REAL(CJ*CONJG(CJ))/CM
       IF(I.LT.N) GO TO 315
C    CALCULATE THE ATTRACTION FORCE
       FYA(J,K)=-REAL(BY2*CONJG(BY2))/(2.*PRO)
  315 CONTINUE
  319 CONTINUE
C     ***PRINT OUT THE RESULTS IN TABULATED FORM ***
       WRITE(6,701)
  701 FORMAT(////3X,1HX,10X,3HBXM,10X,3HBYM,10X,3HBZM,10X,3HFX ,10X,
     13HFYL,10X,3HFYA,10X,3HFZ ,10X,3HPY ,10X,3HQY ,5X,3HPL )
       DO 335J=2,IQ
       X(J)=(J-1)*H
  335 WRITE(6,183) X(J),BXM(MI3,J),BYM(MI3,J),BZM(MI3,J),FX(2,J,15)
     1,FYL(2,J,15),FYA(J,15),FZ(2,J,15),PY(1,J,15),QY(1,J,15),PL(2,J,15)
  183 FORMAT(/2X,F6.4,10(2X,1PE10.3))
       WRITE(6,702)
  702 FORMAT(////3X,1HZ,10X,3HBXM,10X,3HBYM,10X,3HBZM,10X,3HFX ,10X,
     13HFYL,10X,3HFYA,10X,3HFZ ,10X,3HPY ,10X,3HQY ,5X,3HPL )
       DO 345K=1,IH
       ZZ(K)=(K-1)*P*H
  345 WRITE(6,193) ZZ(K),BXT(MI3,K),BYT(MI3,K),BZT(MI3,K),FX(2,27,K),
     1FYL(2,27,K),FYA(27,K),FZ(2,27,K),PY(1,27,K),QY(1,27,K),PL(2,27,K)
  193 FORMAT(/2X,F6.4,10(2X,1PE10.3))
C     ***PLOT THE FLUX CONTOURS ***
       DO 444J=1,IQQ
       DO 444I=1,IPP
       IF(I.LE.5) AB1(J,I)=REAL(AZ(I,J,15))+0.005
       IF(I.GE.5.AND.I.LE.9) AB2(J,I-4)=REAL(AZ(I,J,15))+0.005
       IF(I.GE.9.AND.I.LE.18) AB3(J,I-8)=REAL(AZ(I,J,15))+0.005
       IF(I.GE.18) AB4(J,I-17)=REAL(AZ(I,J,15))+0.005
  444 CONTINUE
       CALL CONPLOT(AB1,AB2,AB3,AB4)
C       *** APPLY THE NUMERICAL INTEGRATION METHOD ***
 3100 DO 182I=1,3
       DO 182K=1,IH
  182 SUM3(I,K)=0.0
       WRITE(6,703)
  703 FORMAT(///24X,4HSLIP,12X,15HSTATE VARIABLES)
       DO 142 IJK=1,7
       DO 152 I=1,3
       DO 152J=1,IQQ
       DO 152K=3,IH
       IF(IJK.EQ.1) FR(I,J,K)=FX(I,J,K)
       IF(IJK.EQ.2) FR(I,J,K)=FYL(I,J,K)
       IF(IJK.EQ.3) FR(I,J,K)=FZ(I,J,K)
       IF(IJK.EQ.4) FR(I,J,K)=PL(I,J,K)
       IF(I.GT.2) GO TO 152
       IF(IJK.EQ.5) FR(I,J,K)=FYA(J,K)
       IF(IJK.EQ.6) FR(I,J,K)=PY(I,J,K)
```

```
      IF(IJK.EQ.7) FR(I,J,K)=QY(I,J,K)
  152 CONTINUE
      DO 32 I=1,3
      DO 32K=3,IH
      IF(IJK.GE.5.AND.I.GT.2) GO TO 32
      ODD=0.0
      EVEN=0.0
      KQQ=IQQ-3
      DO 42J=3,KQQ,2
      EVEN=EVEN+FR(I,J,K)
   42 ODD=ODD+FR(I,J+1,K)
      EVEN=EVEN+FR(I,IQ,K)
      SUM3(I,K)=H*(.5*(FR(I,1,K)+FR(I,2,K))+(4.*EVEN+2.*ODD+
     1FR(I,IQQ,K))/3.)
   32 CONTINUE
  162 DO 72 I=1,3
      IF(IJK.GE.5.AND.I.GT.2) GO TO 72
      ODD=0.0
      EVEN=0.0
      DO 102K=4,12,2
      EVEN=EVEN+SUM3(I,K)
  102 ODD=ODD+SUM3(I,K+1)
      EVEN=EVEN+SUM3(I,14)
      SUM4(I)=P*H*(SUM3(I,3)+SUM3(I,15)+4.*EVEN+2.*ODD)/3.00
      IF(IJK.EQ.5) GO TO 2300
   72 CONTINUE
      IF(IJK.GE.6) GO TO 172
      FT=.5*Q*H*(SUM4(1)+SUM4(3)+2.*SUM4(2))*2.
 2300 IF(IJK.EQ.5) FT=SUM4(1)*2.
      WRITE(6,273) S,FT
  273 FORMAT(//10X,2F20.10)
      GO TO 142
  172 DO 192I=1,2
      FT=SUM4(I)*2.00
  192 WRITE(6,283) S,FT
  283 FORMAT(//10X,2F20.10)
  142 CONTINUE
 3000 CONTINUE
 5000 CONTINUE
      CALL ENDFILM
  600 STOP
      END
C     SUBROUTINE TO PLOT FLUX CONTOURS
      SUBROUTINE CONPLOT(AB1,AB2,AB3,AB4)
      DIMENSION AB1(82,5),AB2(82,5),AB3(82,10),AB4(82,6)
      CALL CINTERP(3)
      CALL BOUNDS(0.0,117.93,0.0,22.50)
      CALL POSN(0.0,0.0)
      CALL OFFTOXY(13.54,0.3891)
      CALL ONTOXY(13.54,4.9516)
      CALL ONTOXY(68.30,4.9516)
      CALL ONTOXY(68.30,0.3891)
      CALL ONTOXY(13.54,0.3891)
      CALL ONTOXY(13.54,7.9891)
      CALL ONTOXY(68.30,7.9891)
      CALL ONTOXY(68.30,4.9516)
      CALL OFFTOXY(8.5676,8.9411)
      CALL ONTOXY(8.5676,9.2584)
      CALL ONTOXY(109.3636,9.2584)
```

```
CALL ONTOXY(109.3636,8.9411)
CALL ONTOXY(8.5676,8.9411)
CALL ONTOXY(8.5676,13.1504)
CALL ONTOXY(109.3636,13.1504)
CALL ONTOXY(109.3636,9.2584)
CALL OFFTOXY(0.0,0.0)
CALL CWHOLE
CALL WINDOW(0.0,117.93,0.0,4.5783)
CALL CONTR2(AB1,82,4,600,0.0,0.0001)
CALL ENDWIND
CALL WINDOW(0.0,117.93,3.8,8.3783)
CALL CONTR2(AB2,82,6,600,0.0,0.0001)
CALL ENDWIND
CALL WINDOW(0.0,117.93,7.8429,9.5633)
CALL CONTR2(AB3,82,10,600,0.0,0.0001)
CALL WINDOW(0.0,117.93,8.7799,16.2767)
CALL CONTR2(AB4,82,6,600,0.0,0.0001)
CALL ENDWIND
CALL NEWFRAM
RETURN
END
```

APPENDIX D

SPEED CONTROL OF THE DRIVING MOTOR

The method used for speed control is constant field - variable armature voltage[57]. See Fig. D.1.

The firing circuit comprises a voltage controlled integrated circuit. The conduction angle and motor speed are inversely proportional to the control voltage. Thus in the event of a fault condition due to a small or no control voltage, the machine any run up to a high speed. To overcome this, an inverter is used and supplied from a 7 volt P.S.U. The opto-coupled isolator which is connected to the input of the firing circuit is also supplied by the 7 volt P.S.U. In the case of a fault in the inverter circuit, the inverter output voltage (control voltage) goes high, holding the machine off. If there is a fault in the 7 volt P.S.U. the opto-isolator will be deactivated, and switching off the supply to the firing circuit.

The inverter is biased from a variable (0.1 - 7V) P.S.U. via a multi-turn pot. The active control voltage is in the range of 2-6 volt, which enable a very smooth speed control to be achieved within the acceptable range of the motor.

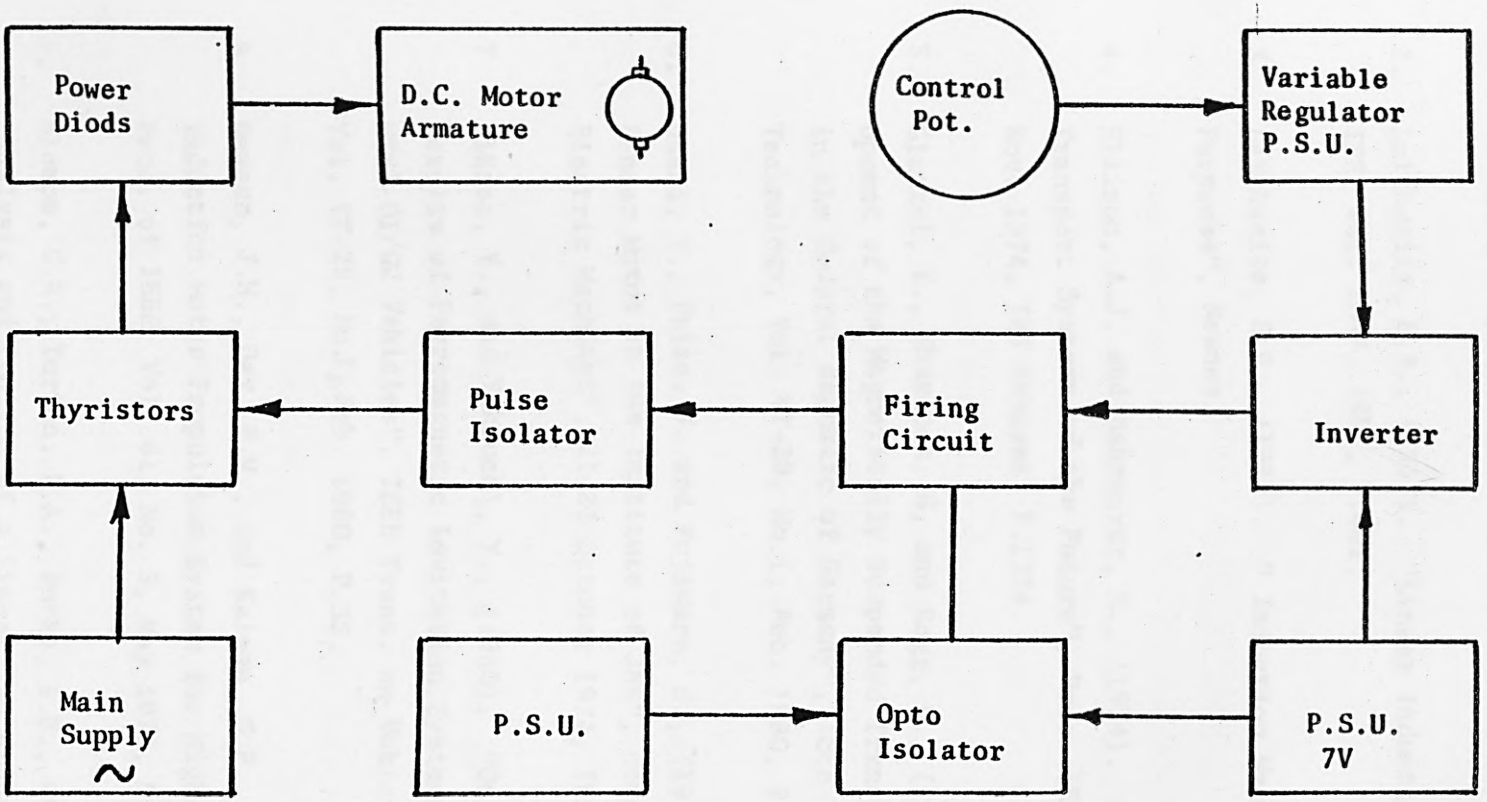

Fig. D.1. Power Electronic Speed Control

REFERENCES

1. Lowther, D.A., (1973). "A Study of the 3-axis Forces in Linear Induction Machines Using Electromagnetic Scale Models", Ph.D Thesis, Brighton Polytechnic.

2. Laithwaite, E.R., (1957). "Linear Induction Motors", Proc. IEE, Vol. 104A, 1957, P.461.

3. Laithwaite, E.R., (1966). " Induction Machines for Special Purposes", Newnes.

4. Ellison, A.J. and Bahmanyar, H., (1974). "Surface-Guided Transport Systems of the Future", Proc. IEE, Vol. 121, No. 11R, Nov. 1974, IEE Reviews, P.1224.

5. Glatzel, K., Khurdock, G, and Rogg, D., (1980). "The Development of the Magnetically Suspended Transportation System in the Federal Republic of Germany", IEEE Trans on Vehicular Technology, Vol. VT-29, No.1, Feb. 1980, P.3.

6. Usami, Y., Fujie, J. and Fujiwara, S., (1974). "Studies on Linear Motor in the Institute of JNR", conference on "Linear Electric Machines", 21-23 October 1974, IEE Publication No. 120.

7 Hikasa, Y., and Takeuchi, Y., (1980). "Detail and Experimental Results of Ferromagnetic Levitation Systems of Japan Airlines HSST-01/02 Vehicles", IEEE Trans. on Vehicular Technology, Vol. VT-29, No.1, Feb. 1980, P.35.

8. Dannan, J.H., Day, R.N., and Kalman, G.P., (1973), "A Linear-Induction Motor Propulsion System for High-Speed Ground Vehicles", Proc. of IEEE, Vol. 61, No. 5, May 1973, P.621.

9. Slemon, G.R., Turton, R.A., Burke, P.E., and Dewan, S.B., (1974). "Analysis and Control of a Linear Synchronous Motor for High-Speed Ground Transport", conference on "Linear Electric Machines", 21-23 Oct. 1974, IEE Publication No. 120.

10. Ellison, A.J. and Bahmanyar, H., (1974). "Contact-free Propulsion and Suspension Systems for Future High-Speed Surface Guided Vehicles". Presented at the International Hovering Craft, Hydrofoil and Advanced Transit Systems Conference, Birghton, Sussex.

11. Laithwaite, E.R., and Eastham, J.F., (1971). "Linear Motors with Transverse Flux". Proc. IEE, Vol. 118, No. 13 Dec. 1971, P. 1761.

12. Mahendra, S.N. (1977). "Current and Flux Distributions, Forces and Stiffnesses in Linear Induction Machines", Ph.D Thesis, The City University, London, England.

13. Borcherts, R.H., Davies, L.C., Reitz, J.R., and Wilkie, D.F., (1973). "Baseline Specifications for a Magnetically Suspended High-Speed Vehicle", Proc. IEE. Vol.61, No. 5, May 1973, P.569.

14. Thornton, R.D., (1975). "Magnetic Levitation and Propulsion, 1975", IEEE Trans. Vol. Mag-11, No. 4, July 1975, P.981.

15. Russell, R.L. and Norsworthy, K.H. (1958). "Eddy Current and Wall Lossess in Screened-Rotor Induction Motors", Proc. IEE, Vol. 105 A, April 1958, P.163.

16. Bolton, H., (1969). "Transverse Edge Effect in Sheet-Rotor Induction Motors", Proc. IEE, Vol. 116, No. 5, May 1969, P. 725.

17. Yamamura, S., (1972). "Theory of Linear Induction Motors", Wiley, J. and Sons.

18. Del Cid, J.L., (1973). "Methods of Analysis of Linear Induction Motors", Ph.D. dissertation. University of Kentucky, USA.

19. Ooi, B.T., (1973). "A Generalised Machine Theory of the Linear Induction Motor", IEE Trans. Vol. PAS-92, 1973, P.1733.

20. North, G.G., (1973). "Harmonic Analysis of a Short Stator Linear Induction Machine using a Transform Technique", IEEE Trans. paper TT2-062-5, 1973, Winter Power Meeting.

21. Preston, W. and Reece, A.B.J. (1969). "Transverse Edge Effects in Linear Induction Motors". Proc. IEE, Vol.116 No. 6, June 1969, P.973.

22. Oberetl, K. (1973). "Three-Dimensional Analysis of the Linear Motor Taking into Account Edge Effects and the Distribution of the Winding". Arch.F. Elek., Vol. 55, April 1973, (in English).

23. May, H., Mosebach, H., and Weh, H., (1978). "Three-Dimensional Numerical Treatment of Finite Width Effects In Linear Motors". International Conference on Electrical Machines, 11-13 Sept. 1978, Belgium, Paper No. L3/4.

24. Iwamoto, M. Ohno, E., Ito, T., and Shinryo, Y., (1970). "End-Effect of High Speed Linear Induction Motor", IEEE Conference, IAS Meeting 1970, p.Lt-TUE-1.

25. Dakowicz, J.K., (1977). "Analysis of Linear Induction Machines with Discrete Windings and Finite Iron Length", IEEE Trans. Vol. PAS-96, No. 1, Jan/Feb. 1977, p.66.

26. Elliot, D.G., (1972). "Numerical Analysis Method for Linear Induction Machines", 12th Symposium on the Engineering Aspects of Magnetohydrodynamics, Argonne National Laboratory, Argonne, Illinois, March 27-29 1972.

27. Al-Maayouf, M.A., (1976). "Numerical Analysis of Linear Induction Motor Performance by Finite Difference Method", M.Sc. dissertation, Queen Mary College, Nov. 1976.

28. Alwash, J.H.H. and Al-Rikabi, J.A.H. (1979). "Finite-Element Analysis of Linear Induction Machines". Proc. IEE, Vol. 126, No. 7, July 1979, p.677.

29. Dorairaj, K.R., and Krishnamurthy, M.R. (1967). "Polyphase Induction Machine with a Slitted Ferromagnetic Rotor II-Analysis". IEEE Trans., Vol. PAS-86, No. 7, July 1967, p. 844.

30. Mishkin, E. (1954). "Theory of the Squirrel-Cage Induction Motor Derived Directly from Maxwell's Field Equations", Quarterly Journal of Mechanics and Applied Mathematics 1954, Vol. 7, p. 472

31. Cullen, A.L. and Barton, T.H. (1958). "A Simplified Electromagnetic Theory of the Induction Motor, Using the Concept of Wave Impedance", Proc. of IEE, Vol.105, Part C, No. 8, Sept. 1958, p.331.

32. Laithwaite, E.R. (1975). "Linear Electric Machines- A Personal View", Proc. IEEE., Vol. 63, No. 2,Feb. 1975. p.250.

33. Matsumiya, T. and Takagi, K. (1971). "End-Effect and Equivalent Circuit of Linear Induction Machines", Electrical Engineering in Japan, Vol. 91, No. 1, 1971, p.117, Translated from Denld Gakkai Zasshi, Vol. 91, No. 2, Feb. 1971, p.299.

34. Lipo, T.A. and Mondahl, T.A. (1978). "Pole by Pole d-q Models of a Linear Induction Motor". For presentation at the 1978 IEEE PES Winter power meeting and publication in the PES Transactions.

35. Yamamura, S. and Ishikawa, H.I. (1972). "Theories of the Linear Induction Motor and Compensated Linear Induction Motor", IEEE Trans. Vol. PAS-91, No. 4, 1972, p.1700.

36. Nasar, S.A. and Boldea, I., (1976). "Linear Motion Electric Machines", Wiley, J. and Sons.

37. Deleroi, W. (1978). "Application of Balancing Waves to Describe the Magnetic Field Behaviour of a Short-Primary Linear Induction Motor", International Conference on Electrical Machines, 11-13 Sept. 1978, Belgium, paper no. L1/2.

38. Lee, C.H. and Chin, C.Y., (1979). "A Theoretical Analysis of Linear Induction Motors", IEEE Trans., Vol. PAS-98, No. 2, March/April 1979, p.679.

39. Boldea, I. and Nasar, S.A., (1975). "Quasi 1-dimensional Theory of Linear Induction Motors with Half-filled Primary Endslots". Proc. IEE, Vol. 122, No. 1, Jan. 1975.

40. Tegopoulos, J.A., (1963). "Current Sheets Equivalent to End-Winding Currents of Turbine-Generator Stator and Rotor". Trans. Am.Inst.Elec.Eng., Vol. 82, Feb. 1963, p.695.

41. Saunders, R.M. (1963). "Electromechanical Energy Conversion in Double Cylindrical Structures", Trans. Am.Inst.Elec.Eng., Vol. 82, Oct. 1963, p.631.

42. Balchin, M.J. and Eastham, J.F., (1975). "Performance of Linear Induction Motors with Airgap Windings", Proc. IEE, Vol. 122, No. 12, Dec. 1975.

43. Carpenter, C.J. (1977). "Comparison, of Alternative Formulations of 3-Dimensional Magnetic-Field and Eddy-Current Problems at Power Frequencies", Proc. IEE, Vol. 124, No. 11, Nov. 1977, p.1026.

44. Binns, K.J. and Lawerenson, P.J., (1973). "Analysis and Computation of Electric and Magnetic Field Problems", Pergamon Press, Oxford, second Edition.

45. Panizo, M., Castellanos, A. and Rivas, J., (1977). "Finite-Difference Operators in Homogeneous Anisotropic Media", Journal of Applied Physics, Vol. 48, No. 3, March 1977, p.1054.

46. Hammond, P., (1958). "Electromagnetic Energy Transfer". IEE Monograph No. 286, Feb. 1958, Part C, p.352.

47. Slepian, J., (1942). "Energy Flow in Electric Systems - the Vi Energy-Flow Postulate", Trans. Electrical Engineering, Dec. 1942, Vol. 61, p.835.

48. Say, M.G., (1970): "Performance and Design of A.C. Machines", Pitman.

49. Popovic, B.D., (1973). "Introductory Engineering Electromagnetics", Addison-Wesley publishing Company, May 1973 - second printing.

50. Young, D.M., (1954). "Iterative Methods for Solving Partial Differential Equations of Elliptic Type", Trans. Am Math.Soc., Vol. 76, 1954, p.92.

51. Carre, B.A., (1961). "The Determination of the Optimum Acceleration Factor for Successive Over-Relaxation", Computer Journal, 1961, No. 4, p.73.

52. Stoll, R.L., (1970). "Solution of Linear Steady-State Eddy Current Problems by Complex Successive Over-Relaxation", Proc. IEE. Vol. 117, No. 7, July 1970, p.317.

53. Sharples, K.O., (1978). "Personal Communication".

54. Freeman, E.M., (1974): "Equivalent Circuits from Electromagnetic Theory: Low-Frequency Induction Devices". Proc. IEE, Vol. 121, No. 10., October 1974, P.117.

55. Ooi, B.T. and White, D.C., (1970): "Traction and Normal Forces in the Linear Induction Motor", IEEE. Trans. Vol.PAS-89, No.4, April, 1970, P.638.

56. Sokdnikoff, I.S., (1941): "Higher Mathematics for Engineers and Physicists", New York, McGraw-Hill.

57. The control system has been built by Mr. P. Rajroop of Electrical Machines Laboratory, The City University